JAERI-Conf
2005-003

INDC(JPN)-195/U



JP0550241

# PROCEEDINGS OF THE 2004 SYMPOSIUM ON NUCLEAR DATA
# NOVEMBER 11-12, 2004, JAERI, TOKAI, JAPAN

March 2005

(Eds.) Yoshihisa TAHARA* and Tokio FUKAHORI

日本原子力研究所
Japan Atomic Energy Research Institute

本レポートは，日本原子力研究所が不定期に公刊している研究報告書です。
入手の問合わせは，日本原子力研究所研究情報部研究情報課（〒319-1195　茨城県那珂郡東海村）あて，お申し越しください。なお，このほかに財団法人原子力弘済会資料センター（〒319-1195　茨城県那珂郡東海村日本原子力研究所内）で複写による実費頒布をおこなっております。

This report is issued irregularly.
Inquiries about availability of the reports should be addressed to Research Information Division, Department of Intellectual Resources, Japan Atomic Energy Research Institute, Tokai-mura, Naka-gun, Ibaraki-ken, 319-1195, Japan.

© Japan Atomic Energy Research Institute, 2005

編集兼発行　　日本原子力研究所

JAERI－Conf 2005－003 INDC(JPN)-195/U

# Proceedings of the 2004 Symposium on Nuclear Data
November 11-12, 2004, JAERI, Tokai, Japan

(Eds.) Yoshihisa TAHARA* and Tokio FUKAHORI

Japanese Nuclear Data Committee
Tokai Research Establishment
Japan Atomic Energy Research Institute
Tokai-mura, Naka-gun, Ibaraki-ken

(Received February 18, 2005)

The 2004 Symposium on Nuclear Data was held at Tokai Research Establishment, Japan Atomic Energy Research Institute (JAERI), on 11th and 12th of November 2004. Japanese Nuclear Data Committee and Nuclear Data Center, JAERI organized this symposium. In the oral sessions, presented were 19 papers on topics of nuclear data for LWR and nuclear fuel cycle, nuclear data for ADS development, experiences from use of JENDL-3.3 and requests to JENDL-4, recent cross section measurements, nuclear data for life and material sciences, and nuclear data needs and activities in the World. In the poster session, presented were 21 papers concerning experiments, evaluations, benchmark tests, applications and so on. Those presented papers are compiled in the proceedings.

Keywords: Nuclear Data, Symposium, Proceedings, Nuclear Reaction, JENDL, Experiment, Evaluation, Benchmark Test, Cross Section, Nuclear Fuel Cycle.

*Engineering Development Co., Ltd.

# 2004年核データ研究会報文集
2004年11月11日～12日，東海研究所，東海村

日本原子力研究所東海研究所
シグマ研究委員会
（編）田原　義壽*・深堀　智生

（2005年2月18日受理）

2004年核データ研究会が、2004年11月11日と12日の両日、日本原子力研究所東海研究所において開催された。この研究会は、日本原子力研究所のシグマ研究委員会と核データセンターが主催して開いたものである。口頭発表では、軽水炉及び核燃料サイクルと核データ、ADS開発のための核データ、JENDL-3.3の使用経験とJENDL-4への要望、最近の断面積測定、物質生命科学と核データ、海外の核データニーズと活動についての19件の報告があった。ポスター発表では、21件の発表があり、それらは、核データの測定、評価や評価済核データのベンチマークテスト及び応用等に関するものであった。本報文集は、それらの論文をまとめたものである。

東海研究所：〒319-1195 茨城県那珂郡東海村白方白根2-4
* エンジニアリング開発株式会社

**Program Committee**

| | |
|---|---|
| Yoshihisa TAHARA (Chairman) | Engineering Development Co., Ltd. |
| Tokio FUKAHORI | Japan Atomic Energy Research Institute |
| Hideo HARADA | Japan Nuclear Cycle Development Institute |
| Osamu IWAMOTO | Japan Atomic Energy Research Institute |
| Hideki MATSUMOTO | Mitsubishi Heavy Industries, Ltd. |
| Tsuneo NAKAGAWA | Japan Atomic Energy Research Institute |
| Hiroyuki OIGAWA | Japan Atomic Energy Research Institute |
| Keisuke OKUMURA | Japan Atomic Energy Research Institute |
| Yukinobu WATANABE | Kyushu University |

**プログラム委員会**

| | |
|---|---|
| 田原　義壽（委員長） | エンジニアリング開発（株） |
| 深堀　智生 | 日本原子力研究所 |
| 原田　秀郎 | 核燃料サイクル開発機構 |
| 岩本　修 | 日本原子力研究所 |
| 松本　英樹 | 三菱重工業（株） |
| 中川　庸雄 | 日本原子力研究所 |
| 大井川　宏之 | 日本原子力研究所 |
| 奥村　啓介 | 日本原子力研究所 |
| 渡辺　幸信 | 九州大学 |

This is a blank page.

# Contents

1. Introduction ..... 1

2. Papers Presented at Oral Sessions ..... 5
2.1 PIE Analysis for Minor Actinide ..... 7
K. Suyama
2.2 Request from Nuclear Fuel Cycle and Criticality Safety Design ..... 20
M. Hamasaki, K. Sakashita and T. Natsume
2.3 Requests from Use Experience of ORIGEN Code
-Activity of the Working Group on Evaluation of Nuclide Generation and Depletion- ... 26
T. Matsumura
2.4 Nuclear Data for Innovative Reactors Having Persistent Resistance to Nuclear Proliferation ..... 32
T. Yoshida, N. Hagura, V. Toshinsky and M. Saito
2.5 Error Estimation for ADS Nuclear Properties by Using Nuclear Data Covariances ..... 38
K. Tsujimoto
2.6 Fission Cross Section Measurements at Intermediate Energies ..... 44
A. Laptev
2.7 Nuclear Data Evaluation for JENDL High Energy File and Its Benchmark ..... 50
Y. Watanabe
2.8 Criticality Benchmarks with a Continuous-energy Monte Carlo Code MVP and JENDL-3.3 ..... 56
K. Okumura, Y. Nagaya and T. Mori
2.9 Analysis of MOX Critical Experiments with JENDL-3.3 ..... 64
T. Shiraki, H. Matsumoto and M. Nakano
2.10 Analysis of Innovative Water Reactor for Flexible Fuel Cycle in FCA Using JENDL-3.3 ..... 70
M. Andoh, M. Fukushima, S. Okajima, K. Kojima, K. Kawasaki and M. Kataoka
2.11 Development of a Coupled-channels Optical Model Code "OPTMAN" and a Global CC Potential as a Base for High Energy Nuclear Data Evaluation ..... 76
E.Sh. Soukhovitski and S. Chiba
2.12 Comprehensive Study of Lattice Cell Calculations for Thorium Based Fuel Cycle in Light Water Reactors Using SRAC Code ..... 84
Le Dai Dien, Ha Van Thong and Giang Thanh Hieu
2.13 CENDL-3 and the Works Concerned ..... 90
Ge Zhigang

2.14 Monte-Carlo Simulation for the Effects of Composite Materials on Single Event Effects of Sub-100 nm Semi-conductor Devices ..... 100
E. Ibe, Y. Yahagi and H. Yamaguchi
2.15 Nuclear Data for Radiotherapy ..... 106
N. Matsufuji, Y. Kase and T. Kanai
2.16 Measurement of Fragment Production Cross-section on Nucleon-induced Reaction ..... 112
M. Hagiwara, T. Oishi, M. Baba, T. Sanami, H. Nakashima, S. Tanaka and M. Takada
2.17 The Present Status of the n_TOF Facility at CERN ..... 118
M. Igashira
2.18 Measurements of Neutron Capture Cross Sections for $^{237,238}$Np ..... 121
H. Harada, H. Sakane, S. Nakamura, K. Furutaka, J. Hori, T. Fujii and H. Yamana
2.19 Measurement of Fission Cross Sections ..... 126
M. Baba

3. Papers Presented at Poster Sessions ..... 133
3.1 $^{239}$Pu Data of JENDL-3.3 ..... 135
M. Kawai
3.2 Continuum Spectra Analysis of (*p,d*) and (*n,d*) Reactions on *Bi* in Several Tens of MeV Energy Region ..... 143
S.A. Sultana, Syafarudin, D. Maki, T. Kin, G. Wakabayashi, Y. Uozumi, N. Ikeda, Y. Watanabe, F. Aramaki, M. Matoba, T. Kawaguchi and H.M. Sen Gupta
3.3 Measurement of Deuteron-induced Activation Cross-sections for Tantalum, Iron, Nickel and Vanadium in 33-40 MeV Region ..... 148
M. Nakao, K. Ochiai, N. Kubota, N.S. Ishioka and T. Nishitani
3.4 Measurements of Double Differential Heavy Particles Production Cross Sections for 70 MeV Protons ..... 152
M. Hagiwara, T. Oishi, M. Baba, T. Sanami and M. Takada
3.5 A New Technique to Measure Double-differential Charged-particle Emission Cross Sections Using Pencil-beam DT Neutrons ..... 158
K. Kondo, S. Takagi, I. Murata, H. Miyamaru, A. Takahashi, N. Kubota, K. Ochiai and T. Nishitani
3.6 Additional Evaluation of Alpha Induced Neutron Production Nuclear Data — $^{9}$Be, $^{27}$Al, $^{28,29,30}$Si — ..... 164
T. Murata and K. Shibata
3.7 Measurements of Cross-sections of the Proton-induced Activation Reactions ..... 170
M.S. Uddin, M. Baba, M. Hagiwara, F. Tarkanyi and F. Ditroi
3.8 Neutron Production from Thin Target of Carbon and Iron by 70 MeV Protons ..... 176
T. Itoga, M. Hagiwara, T. Yamauchi, T. Oishi and M. Baba
3.9 Evaluations of Cross Sections on Zr, Nb, and W up to 200 MeV for JENDL High

Energy File ..... 182
S. Kunieda, N. Shigyo and K. Ishibashi
3.10 The Equation of State of Nuclear Matter, and Nuclei in Laboratories and in Neutron-star Crusts ..... 188
K. Oyamatsu and K. Iida
3.11 Problem on Unresolved Resonance Data in ENDF/B-VI, etc. ..... 194
C. Konno
3.12 TAGS and FP Decay Heat Calculations (II) – Impact on the LOCA Condition Decay Heat － ..... 200
A. Honma and T. Yoshida
3.13 Analysis of Plasma Material Surfaces by Means of Low Energy NRA ..... 206
K. Ochiai, N. Kubota and T. Nishitani
3.14 Elastic Recoil Detection Method Using DT Neutrons for Hydrogen Isotope Analysis in Fusion Materials ..... 210
N. Kubota, K. Ochiai, K. Kondo and T. Nishitani
3.15 Calculations of an HPGe Detector Peak Efficiency Curve up to 11 MeV with EGS4 and GEANT4 ..... 216
M. Kasaishi, A. Tojo, M. Furuta, H. Takayama, I. Miyazaki, T. Shimizu, M. Shibata, K. Kawade and A. Taniguchi
3.16 Precise Measurement of Prompt γ-ray in the $^{14}N(n, \gamma)^{15}N$ Reaction ..... 222
H. Takayama, M. Kasaishi, A. Tojo, H. Hayashi, I. Miyazaki, T. Shimizu, M. Shibata, K. Kawade, A. Taniguchi, H. Sakane and H. Harada
3.17 Integer Ratios in Resonance Energies of the Compound Nucleus Based on Time Coherency at Resonances ..... 228
M. Ohkubo
3.18 Neutron Experiment for the Re/Os Cosmochronometer ..... 233
M. Segawa, T. Masaki, Y. Temma, Y. Nagai, T. Shima, H. Makii, K. Mishima, H. Ueda, M. Igashira, T. Ohsaki, T. Shizuma and T. Hayakawa
3.19 The Measurement of Neutron Capture Cross Section of $^{62}Ni$ and Nucleosynthesis of Heavy Elements ..... 237
Y. Temma, A. Tomyo, M. Segawa, H. Makii, T. Shima, Y. Nagai, T. Ohsaki and M. Igashira
3.20 Percolation-fission Model Study of the Fragment Mass Distribution for the 1 GeV Proton Induced Reaction ..... 241
M. Katsuma, H. Kobayashi, T. Sasa and T. Sawada
3.21 Measurements of Total Cross Sections of Ta and Hf at Pohang Neutron Facility ..... 247
Guinyun Kim, A.K.M. Moniul Haque Meaze, Young Seok Lee, Moo Hyun Cho, Heung Sik Kang, In Soo Ko, Won Namkung, Tae-Ik. Ro, Won-Chung Chung, Young Ae Kim, Kun Joong Yoo and Jong Hwa Chang

Appendix : Participant List ..... 253

# 目　次

1. はじめに ..... 1

2. 口頭発表論文 ..... 5
2.1 マイナーアクチニドPIE解析からの知見 ..... 7
須山　賢也
2.2 核燃料サイクル・臨界安全設計からの要求 ..... 20
浜崎　学、坂下　毅一郎、夏目　智弘
2.3 ORIGENコード使用経験からの要求精度の調査 ..... 26
－核種生成量評価ＷＧの活動より－
松村　哲夫
2.4 核拡散抵抗性を持つ革新炉のための核データ ..... 32
吉田　正、羽倉　尚人、V. Toshinsky、斉藤　正樹
2.5 核データの共分散を用いたADSの核特性精度評価 ..... 38
辻本　和文
2.6 中高エネルギー領域の核分裂断面積の測定 ..... 44
A. Laptev
2.7 JENDL高エネルギーファイルのための核データ評価とベンチマーク ..... 50
渡辺　幸信
2.8 連続エネルギーモンテカルロコードMVPとJENDL-3.3による臨界性ベンチマーク ..... 56
奥村　啓介、長家　康展、森　貴正
2.9 JENDL-3.3によるMOX臨界実験解析 ..... 64
白木　貴子、松本　英樹、中野　誠
2.10 JENDL-3.3によるFCA革新的水冷却炉実験解析 ..... 70
安藤　真樹、福島　昌宏、岡嶋　成晃、小嶋　健介、川崎　憲二、
片岡　理治
2.11 結合チャンネル光学模型コードOPTMANと高エネルギー核データ評価のためのグローバルポテンシャル ..... 76
E.Sh. Soukhovitski、千葉　敏
2.12 SRACコードを用いた軽水炉におけるトリウムサイクルのためのセル計算の包括的研究 ..... 84
Le Dai Dien, Ha Van Thong and Giang Thanh Hieu
2.13 CENDL-3及び中国核データセンターにおける活動 ..... 90
Ge Zhigang
2.14 サブ100nm半導体デバイスシングルイベントへの複合材料効果のモンテカ

ルロシミュレーション ..... 100
伊部　英史、矢作　保夫、山口　裕功
2.15 医療照射と核データ ..... 106
松藤　成弘、加瀬　優紀、金井　達明
2.16 核子誘起核反応によるフラグメント生成断面積の測定 ..... 112
萩原　雅之、大石　卓司、馬場　護、佐波　俊哉、中島　宏、
田中　進、高田　真志
2.17 CERNのn_TOF施設の現状 ..... 118
井頭　政之
2.18 Np-237,238の中性子捕獲断面積の測定 ..... 121
原田　秀郎、坂根　仁、中村　詔司、古高　和禎、堀　順一、
藤井　俊行、山名　元
2.19 核分裂断面積の測定 ..... 126
馬場　護

3. ポスター発表論文 ..... 133
3.1 JENDL-3.3 の Pu-239 データ ..... 135
川合　將義
3.2 数十 MeV 領域における Bi の(p,d)及び(n,d)反応の連続スペクトルの解析 ..... 143
S.A. Sultana, Syafarudin、牧　大介、金　政浩、若林　源一郎、
魚住　裕介、池田　伸夫、渡辺　幸信、荒巻　富士夫、的場　優、
川口　俊郎、H.M. Sen Gupta
3.3 タンタル、鉄、ニッケル、バナジウムに対する 33～40MeV 領域での重陽子
による放射化断面積の測定 ..... 148
中尾　誠、落合　謙太郎、久保田　直義、石岡　典子、西谷　健夫
3.4 70 MeV 陽子における重荷電粒子生成二重微分断面積の測定 ..... 152
萩原　雅之、大石　卓司、馬場　護、佐波　俊哉、高田　真志
3.5 ビーム状 DT 中性子を用いた新しい荷電粒子放出二重微分断面積測定手法 ..... 158
近藤　恵太郎、高木　智史、村田　勲、宮丸　広幸、高橋　亮人、
久保田　直義、落合　謙太郎、西谷　健夫
3.6 アルファ線入射中性子生成核データの追加評価 — $^{9}$Be, $^{27}$Al, $^{28,29,30}$Si — ..... 164
村田　徹、柴田　恵一
3.7 陽子入射放射化断面積の測定 ..... 170
M.S. Uddin、馬場　護、萩原　雅之、F. Tarkanyi、F. Ditroi
3.8 70 MeV 陽子によるカーボン及び鉄の薄いターゲットからの中性子生成 ..... 176
糸賀　俊朗、萩原　雅之、山内　健、大石　卓司、馬場　護
3.9 JENDL 高エネルギーファイルのための 200 MeV までの領域における Zr、Nb、
及び W に対する断面積評価 ..... 182
国枝　賢、執行　信寛、石橋　健二
3.10 核物質の状態方程式と実験室や中性子星における中性子過剰核 ..... 188
親松　和浩、飯田　圭

3.11 ENDF/B-VI 他の非分離共鳴データの問題等 ..... 194
今野 力
3.12 全吸収ガンマ線分光法と FP 崩壊熱計算 (II)
－LOCA 条件崩壊熱への影響－ ..... 200
本間 明、吉田 正
3.13 低エネルギー核反応分析法によるプラズマ対向壁表面分析 ..... 206
落合 謙太郎、久保田 直義、西谷 健夫
3.14 核融合炉材料中の水素同位体分析のための DT 中性子を利用した弾性反跳粒子検出法 ..... 210
久保田 直義、落合 謙太郎、近藤 恵太郎、西谷 健夫
3.15 EGS4 と GEANT4 コードを用いた 11MeV までの HPGe 検出器検出効率曲線の計算 ..... 216
笠石 昌史、東條 暁典、古田 昌孝、高山 寛和、宮崎 格、
清水 俊明、柴田 理尋、河出 清、谷口 秋洋
3.16 $^{14}N(n,\gamma)^{15}N$ 反応を用いた即発ガンマ線の精密測定 ..... 222
高山 寛和、笠石 昌史、東條 暁典、林 裕晃、宮崎 格、清水 俊明、
柴田 理尋、河出 清、谷口 秋洋、坂根 仁、原田 秀郎
3.17 共鳴の時間コヒーレントに基づく複合核共鳴エネルギーにおける整数比 ..... 228
大久保 牧夫
3.18 中性子反応による Re/Os 宇宙核時計 ..... 233
瀬川 麻里子、正木 智洋、天満 康之、永井 泰樹、嶋 達志、
牧井 宏之、三島 賢二、上田 仁、井頭 政之、大崎 敏郎、
静間 俊行、早川 岳人
3.19 $^{62}Ni$ の中性子捕獲断面積測定と重元素合成 ..... 237
天満 康之、東名 敦志、瀬川 麻里子、牧井 宏之、嶋 達志、
永井 泰樹、大崎 敏郎、井頭 政之
3.20 核分裂模型を取り入れたパーコレーション模型による 1GeV 陽子入射反応の破砕片質量分布の研究 ..... 241
勝間 正彦、小林 浩、佐々 敏信、澤田 哲生
3.21 ポーハン中性子施設での Ta 及び Hf の全断面積の測定 ..... 247
Guinyun Kim, A.K.M. Moniul Haque Meaze, Young Seok Lee, Moo Hyun Cho, Heung Sik Kang, In Soo Ko, Won Namkung, Tae-Ik. Ro, Won-Chung Chung, Young Ae Kim, Kun Joong Yoo and Jong Hwa Chang

付録：参加者リスト ..... 253

# 1. Introduction

The 2004 Symposium on Nuclear Data was held at Tokai Research Establishment, Japan Atomic Energy Research Institute (JAERI), on 11th and 12th of November 2004, with about 130 participants. Japanese Nuclear Data Committee and Nuclear Data Center, JAERI organized this symposium.

The program of the symposium is listed below. In the oral sessions, presented were 19 papers on topics of nuclear data for LWR and nuclear fuel cycle, nuclear data for ADS development, experiences from use of JENDL-3.3 and requests to JENDL-4, recent cross section measurements, nuclear data for life and material sciences, and nuclear data needs and activities in the World. In the poster session, presented were 21 papers concerning experiments, evaluations, benchmark tests and so on. Those presented papers are compiled in the proceedings.

## Program of Symposium on Nuclear Data 2004

JAERI Tokai, Nov. 11-12, 2004

### Nov. 11 (Thu.)

**9:50-10:00**

1. Opening Address T. Iwamura (JAERI)

**10:00-12:00**

2. Nuclear Data for LWR and Nuclear Fuel Cycle 【Chair：Y. Tahara (EDC)】
   - 2.1 PIE Analysis for Minor Actinide [25+5] K. Suyama (JAERI)
   - 2.2 Requests from Nuclear Fuel Cycle and Critical Safety Design [25+5] M. Hamasaki (MHI)
   - 2.3 Requests from Use Experience of ORIGEN Code [25+5] T. Matsumura (CRIEPI)
   - 2.4 Nuclear Data for Innovative Reactors Having Persistent Resistance to Nuclear Proliferation [25+5] T. Yoshida (Musashi Tech.)

**12:00-13:00** Lunch

**13:00-14:30**

3. Poster Presentations

**14:30-16:00**

4. Nuclear Data for ADS Development 【Chair：T. Fukahori (JAERI)】

4.1 Error Estimation for ADS Nuclear Properties by using Nuclear Data Covariances [25+5] K. Tsujimoto (JAERI)

4.2 Fission Cross Section Measurements up to 200MeV [25+5] A.B. Laptev (JNC)

4.3 Nuclear Data Evaluation for JENDL High Energy File and its Benchmark [25+5] Y. Watanabe (Kyushu Univ.)

**16:00-16:15** Coffee Break

**16:15-17:45**

5. Experiences from Use of JENDL-3.3 and Requests to JENDL-4 【Chair：H. Matsumoto (MHI)】

5.1 Analyses of Criticality Benchmark Problems from ICSBEP Handbook with a Continuous-energy Monte Carlo Code MVP and JENDL-3.3 [25+5] K. Okumura (JAERI)

5.2 Analysis of MOX Critical Experiments with JENDL-3.3 [25+5] T. Shiraki (MHI)

5.3 Experiment and Analysis of Innovative Water Reactor for Flexible Fuel Cycle in FCA using JENDL-3.3 [25+5] M. Andoh (JAERI)

**18:00-20:30** Reception (Akogi-ga-ura Club)

## Nov. 12 (Fri.)

**10:00-11:40**

6. Nuclear Data Needs and Activities in the World 【Chair：S. Chiba (JAERI)】

6.1 Development of a Coupled-Channels Optical Model Code "OPTMAN" and a Global CC Potential as a Base for High-energy Nuclear Data Evaluation [35+5] E. Sh. Soukhovitski (JIENR)

6.2 Comprehensive Study of Lattice Cell Calculations for Thorium Based Fuel Cycle in Light Water Reactors using SRAC Code [25+5] Giang Thanh Hieu (INST)

6.3 CENDL-3 and Related Work [25+5] Ge Zhigang (CIAE)

**11:40-12:50** Lunch

**12:50-14:20**

7. Nuclear Data for Life and Material Sciences 【Chair：Y. Watanabe (Kyushu Univ.)】

7.1 Monte-Carlo Simulation for the Effects of Composite Materials on Single Event Effects of Sub-100 nm Semi-conductor Devices [25+5] E. Ibe (Hitachi)

7.2 Nuclear Data for Radiation Therapy [25+5] N. Matsufuji (NIRS)

7.3 Measurement of Fragment Production Cross-section on Nucleon-induced Reaction [25+5] M. Hagiwara (Tohoku Univ.)

**14:20-14:35** Coffee Break

**14:35-16:05**

8. Recent Cross Section Measurements 【Chair：M. Mizumoto (JAERI)】

8.1 The Present Status of the n_TOF Facility at CERN [25+5] M. Igashira (TIT)

8.2 Measurements of Neutron Capture Cross Sections for $^{237,238}$Np [25+5] H. Harada (JNC)

8.3 Measurement of Fission Cross Sections [25+5] M. Baba (Tohoku Univ.)

**16:05-16:15**

9. Closing Session Y. Tahara (EDC)

**Poster Presentations**

Nov. 11 (Thu.) 13:00-14:30

P1. $^{239}$Pu Data in JENDL-3 and its Integral Test Results M. Kawai (KEK)

P2. Continuum Spectra Analysis of (p,d) and (n,d) Reactions on Bi in Several Tens of MeV Energy Region Sadia Afroze Sultana (KyushuUniv.)

P3. Measurement of Deuteron-Induced Activation Cross-Sections for Tantalum, Iron, Nickel and Vanadium in 33-40 MeV Region M. Nakao (JAERI)

P4. Measurement of Double Differential Cross Sections of Secondary Heavy Particles Induced by 70 MeV Protons M. Hagiwara (Tohoku Univ.)

P5. A New Technique to Measure Double-differential Charged-particle Emission Cross Sections Using Pencil-beam DT Neutrons K. Kondo (JAERI/Osaka Univ.)

P6. Additional Evaluation of Alpha Induced Neutron Production Nuclear Data — $^{9}$Be, $^{27}$Al, $^{28,29,30}$Si — T. Murata (AITEL)

P7. Measurements of Cross-sections of the Proton-induced Activation Reactions on Yttrium Md. Shuza Uddin (Tohoku Univ.)

P8. Neutron Production from Thin Targets of Carbon and Iron by 70 MeV Protons
T. Itoga (Tohoku Univ.)
P9. Evaluations of Cross Sections on Zr, Nb, and W up to 200 MeV for JENDL High Energy File S. Kunieda (Kyushu Univ.)
P10. Equation of State of Nuclear Matter, and Neutron-Rich Nuclei in Laboratories and in Neutron-Star Crusts K. Oyamatsu (Aichi Shukutoku Univ.)
P11. Problem on Unresolved Resonance Data in ENDF/B-VI, etc. C. Konno (JAERI)
P12. TAGS and FP Decay Heat Calculations (II) – Impact on the LOCA Condition Decay Heat A. Honma (Musashi Tech.)
P13. Analysis of Plasma Material Surfaces by Means of Low Energy NRA
K. Ochiai (JAERI)
P14. Elastic Recoil Detection Method using DT Neutrons for Fusion Material Analysis
N. Kubota (JAERI)
P15. Calculations of an HPGe Detector Peak Efficiency Curve up to 11 MeV with EGS4 and GEANT4 M. Kasaishi (Nagoya Univ.)
P16. Precise Measurement of Prompt γ-rays in the $^{14}N(n, \gamma)^{15}N$ Reaction
H. Takayama (Nagoya Univ.)
P18. Integral Test of Xenon Cross Section for Application to Failed Fuel Detection and Location by Tagging Method in Fast Reactor C. Ito (JNC)
P19. Neutron Experiment for the Study of Re/Os Cosmochronometer
M. Segawa (Osaka Univ.)
P20. The Measurement of Neutron Capture Cross Section of $^{62}Ni$ and Nucleosynthesis of Heavy Elements Y. Temma (Osaka Univ.)
P21. Percolation-Fission Model Study of the Fragment Mass Distribution for the 1 GeV Proton Induced Reaction M. Katsuma (TIT)
P22. Measurements of Total Cross Sections of Ta and Hf at Pohang Neutron Facility
Guinyun Kim (KNU)

# 2. Papers Presented at Oral Sessions

This is a blank page.

JP0550242



## 2.1 PIE Analysis for Minor Actinide

Kenya SUYAMA
*Department of Fuel Cycle Safety Research, Japan Atomic Energy Research Institute*
*Tokai-mura, Naka-gun, 319-1195, Japan*
e-mail: kenya@cyclone.tokai.jaeri.go.jp

Minor actinide (MA) is generated in nuclear fuel during the operation of power reactor. For fuel design, reactivity decrease due to it should be considered. Out of reactors, MA plays key role to define the property of spent fuel (SF) such as α-radioactivity, neutron emission rate, and criticality of SF. In order to evaluate the calculation codes and libraries for predicting the amount of MA, comparison between calculation results and experimentally obtained data has been conducted. In this report, we will present the status of PIE data of MA taken by post irradiation examinations (PIE) and several calculation results.

### 1. Introduction

Minor Actinide (MA) has been a key issue in the nuclear data evaluation. One of the reasons is reactivity change due to MA should be considered in the fuel design, especially in high burnup MOX fuel. Another reason is MA is a main target in the strategy of partitioning and transmutation (P&T) of long-life radioactive isotopes. Of course, concerning the property of spent fuel (SF), amount of MA defines α-radioactivity, decay heat, and neutron emission rate. It also affects the criticality of SF.

Validation of calculation codes and libraries has been carried out by comparison between calculation results and experimental data. However, required data taken by Post Irradiation Examinations (PIE) are not enough, and many analyses present discrepancies between calculations and PIE data. To improve the calculation, well-organized comparison using several codes and libraries are essential. This report describes a status of measured isotopic composition data of MA taken by PIE, and several studies to obtain useful information from comparison between calculations and experimental results. It includes examples of PIE data of $UO_2$ and MOX fuel, status of PIE analysis by French institute, and comparison of MA amount between calculations using JENDL-3.2[1] and JENDL-3.3[2].

## 2. Requirement of PIE Data

**Table 1** shows the typical amount of MA in spent $UO_2$ and MOX fuel without cooling time[1]. Since fresh MOX fuel contains plutonium and $^{241}Am$, spent MOX fuel contains much $^{241}Am$ and curium isotopes. Higher burnup increases the amount of MA in SF. Current trend "higher burnup" and "using MOX" emphasize the importance of MA data.

**Table 1** Amount [g/TIHM]* of MA in PWR
(Continuous Operation of PWR under constant specific power)

| | PWR $UO_2$ | | PWR MOX | |
|---|---|---|---|---|
| | 40 GWd/t | 50GWd/t | 40GWd/t | 50GWd/t |
| $^{237}Np$ | 551.1 | 716.0 | 150.9 | 181.9 |
| $^{238}Pu$ | 184.6 | 310.2 | 2674 | 2829 |
| $^{241}Am$ | 43.64 | 56.30 | 1851 | 1726 |
| $^{243}Am$ | 106.8 | 209.4 | 1628 | 1903 |
| $^{244}Cm$ | 32.89 | 86.45 | 703.1 | 1004 |
| $^{245}Cm$ | 2.116 | 6.660 | 78.71 | 133.6 |

* Gram per Ton Initial Heavy Metal

**Table 2** shows the data concerning the MA generation. Since MA accumulates through several generation paths, to revise the calculation results, the chain analysis should be conducted to check the consistency of cross section data in each generation chain, and contribution of each path should be evaluated to determine the priority of revision of cross section data. For example, in the thermal reactor condition, most important generation path of $^{238}Pu$ is the path starting from (n,2n) reaction of $^{238}U$, instead of $^{239}Pu$ (n,2n) reaction [3].

During the cooling time, some MA increase through the decay of parent isotopes.$^{237}Np$ accumulates during long cooling time by the α-decay of $^{241}Am$, and if cooling time is longer than several thousands years, all $^{241}Am$ become $^{237}Np$. These facts imply that the improvement of one MA cross section has another effect and the importance depends on the considering time scale.

[1] MA represents actinides except for uranium and plutonium. However, considering the status of $^{238}Pu$ calculation results, we treat $^{238}Pu$ as MA in this report.

**Table 2** Basic Data Concerning the MA Generation
(PWR 17×17; $UO_2$ ; $^{235}U$ 4.1wt%; JENDL-3.3)

| | Half life [year] | Main Generation chain | $\sigma_c$ [barn]* | $\sigma_f$ [barn]* |
|---|---|---|---|---|
| $^{237}Np$ | $2.14\times10^6$ | $^{238}U(n,2n)\ ^{237}U \Rightarrow \beta^-$ (6.75day)<br>$^{236}U(n,\gamma)\ ^{237}U \Rightarrow \beta^-$ (6.75day)<br>$^{241}Am \Rightarrow \alpha$ (432year) | 32.57 | 0.5367 |
| $^{238}Pu$ | 87.7 | $^{237}Np(n,\gamma)\ ^{238}Np \Rightarrow \beta^-$(2.11day)<br>$^{242}Cm \Rightarrow \alpha$ (163day)<br>$^{239}Pu$ (n,2n) | 29.30 | 2.398 |
| $^{241}Am$ | 432 | $^{241}Pu \Rightarrow \beta^-$ (14.4year) | 118.32 | 1.211 |
| $^{243}Am$ | 7,370 | $^{241}Pu(n,\gamma)\ ^{242}Pu\ (n,\gamma)\ ^{243}Pu$<br>$\Rightarrow \beta^-$(5h) | 49.452 | 0.4439 |
| $^{244}Cm$ | 18.1 | $^{243}Am(n,\gamma)\ ^{244/244m}Am$<br>$\Rightarrow\beta^-$ (10.1h/26m)<br>$^{243}Cm\ (n,\gamma)$ | 17.57 | 0.8197 |
| $^{245}Cm$ | 8,500 | $^{244}Cm\ (n,\gamma)$ | 17.80 | 117.5 |

To collect basic data in order to contribute to develop nuclear fuel cycle facility, several post irradiation examinations were done from 1960's. **Table 3** summarizes the status of PIE data of MA. In the public-opened database on spent fuel composition SFCOMPO [4], 53 measurements of $^{237}Np$ from 7 reactors, 107 measurements of $^{241}Am$ from 10 reactors, 65 measurement of $^{243}Am$ from 7 reactors are archived. For curium isotopes, we have more than 100 data of $^{244}Cm$.

Few number of $^{245}Cm$ measurements are stored in the database. This is because $^{244}Cm$ is main contributor to neutron emission from SF and relatively short half-life (18.1 year) and amount of $^{245}Cm$ is small in normal $UO_2$ SF. However, in some case, curium isotopes would become important in spent MOX fuel reactivity estimation. In MOX fuel of 60GWd/t using initial composition of multiple recycled Pu, curium isotopes ($^{242,243,244,245}Cm$) have reactivity worth of approximately 900 pcm at 5 year cooling, even though MOX fuel of 40GWd/t using first generation Pu, it is approximately 60 pcm.[2] [5]

It seems that we have large amount of MA measurement data. However, many of them were taken in 1960's and 1970's and data that have higher burnup more than 40 GWd/t are scare. Several decades ago, European countries had large and open program of PIE[6]. However, it is difficult to find opened activity in them now. In Belgium, Belgonucleaire (BN) has been organizing several PIE activities. ARIANE [7] is the typical case conducted under international collaboration managed by BN. In the

[2] Reactivity worth is defined as pcm = $10^5\times\ln(k_{reference}/k)$ in the reference 3.

program, PIE data of 15 samples were taken from SF irradiated in two PWR and one BWR. The example of analysis of ARIANE data is shown in the reference[8]. However, the experimental data have not been freely opened and published in unclassified reports.

It is well known that France has large PIE activities to verify their codes and libraries.[9] However, data have not been opened because they are funded by French industry.

In Japan, JAERI has been conducted PIE during 1980's and 1990's. The data taken in the activities are widely used especially for benchmarking of codes and libraries [10,11,12]. Especially, the data from Takahama-3 is only published PIE data set for PWR 17×17 $UO_2$ fuel of 4.1wt% enrichment close to 50 GWd/t. However, there is no further PIE program in JAERI. Considering the situation of experimental facilities, it seems difficult to obtain new measurement data from unclassified report.

**Table 3** Number of PIE Data Stored in SFCOMPO

| | Number of Samples$ | | | Number of Assembly | Number of Fuel Pin | Burnup [GWd/t] | | | |
|---|---|---|---|---|---|---|---|---|---|
| | Total | Taken from | | | | 0 - 19.99 | 20.00 - 29.99 | 30.00 - 39.00 | 40.00 - 60.0 |
| | | PWR | BWR | | | | | | |
| $^{237}Np$ | 53 | 29(5)* | 24(2) | 12 | 15 | 14 | 12 | 19 | 8 |
| $^{238}Pu$ | 128 | 88(7) | 40(3) | 18 | 41 | 27 | 55 | 38 | 8 |
| $^{241}Am$ | 107 | 69(7) | 38(3) | 17 | 38 | 26 | 41 | 32 | 8 |
| $^{243}Am$ | 65 | 47(6) | 18(1) | 11 | 20 | 14 | 25 | 20 | 6 |
| $^{244}Cm$ | 110 | 76(6) | 34(2) | 13 | 34 | 24 | 51 | 29 | 6 |
| $^{245}Cm$ | 28 | 11(1) | 17(1) | 2 | 4 | 5 | 5 | 12 | 6 |

* Figures in ( ) are numbers of reactors.

$ Number of Sample includes Cross Check Data.

## 3. Status of Burnup Calculation

### 3.1 Numerical Benchmark

Depletion calculation is one of the most interested problems in reactor physics community. OECD/NEA/NSC has been proposing several depletion calculation benchmarks for plutonium utilization and burnup credit application [13,14,15,16]. In the benchmark calculations, MA shows larger deviation among the participants. **Figure 1** is the example of difference of calculation among benchmark participants of OECD/NEA/NSC/WPNCS burnup credit criticality safety benchmark Phase-IIIB [15]. We can understand that the difference of MA among participants is larger than uranium and plutonium.

Numerical benchmark is useful for peer review of calculation method and libraries. Unfortunately, since current international benchmark is toward to verification of complicated geometrical modeling and fuel design, such benchmark cannot give us clear information on MA generation. If we seek the

possibility to check basic data and calculation method of MA, we should propose a simple problem using single pin-cell base problem or back to previous international benchmarks.

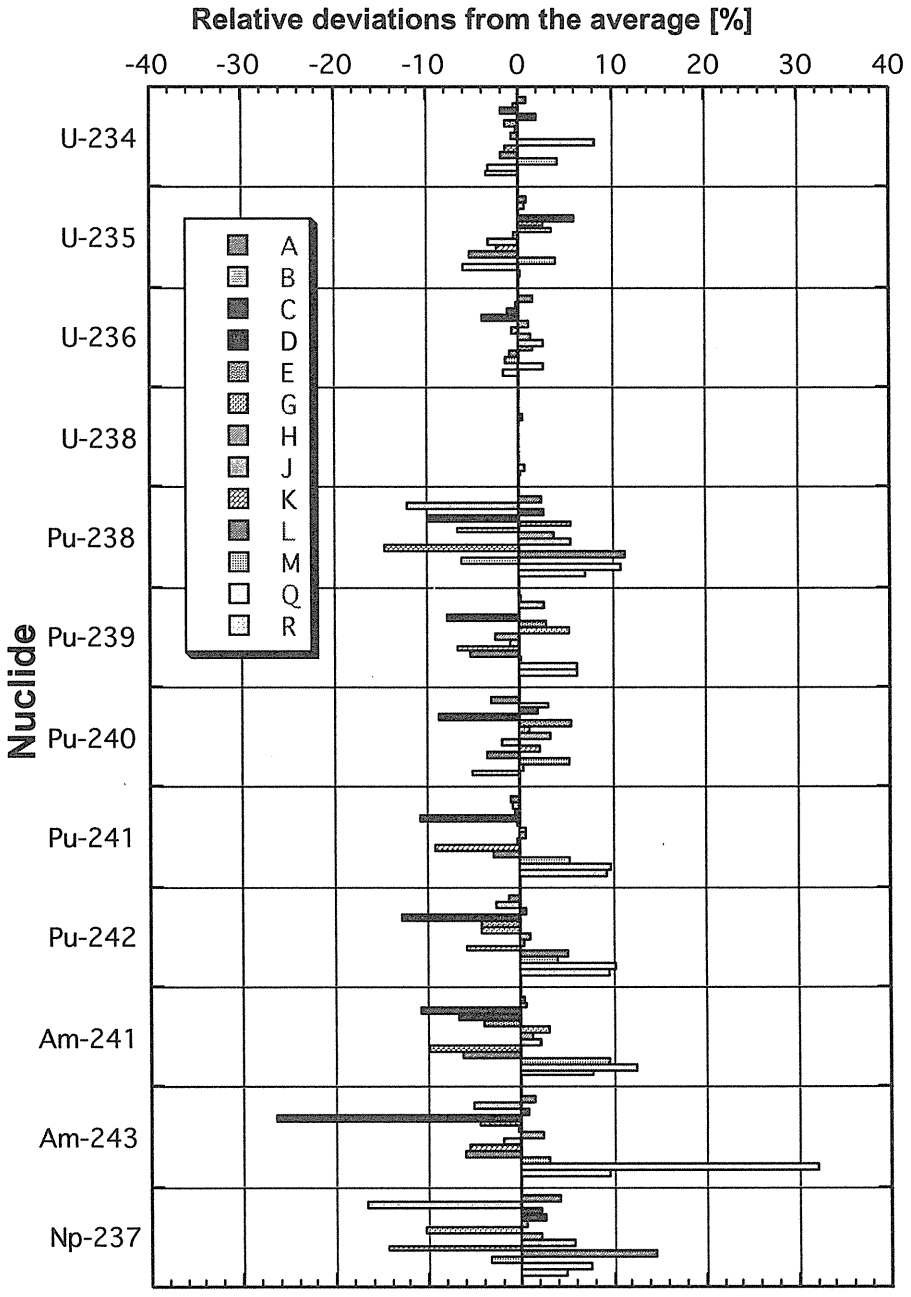



**Figure 1** Relative Difference of atomic number densities of actinides (BWR Burnup calculation: No void, 40 GWd/tHM, no cooling.) [**15**]

### 3.2 PIE analysis

#### 3.2.1 Japanese PIE Analysis

Analyses of PIE data have been conducted to verify the computer code and libraries in Japan. In the reference [**17**], systematic comparison between calculation and experimental results for PWR 15×15 $UO_2$ fuel of 3.2wt% enrichment was carried out by Okumura et. al. The data are taken by JAERI from SF irradiated in Mihama-3. [**10**] **Table 4** shows the C/E values using MVP-BURN [**17**], SWAT[**18**] and SRAC[**19**]. This analysis shows that underestimation of MA except for $^{241}$Am and $^{243}$Am irrespective of using libraries. However, it also implies that using continuous-energy monte carlo code can not improve the calculation result of MA. The authors pointed out the possibilities of small production of $^{238}$Pu and $^{244}$Cm due to small capture cross sections of $^{237}$Np or $^{236}$U and $^{243}$Am. For $^{238}$Pu, in spite of its importance, deviation from experimental results has not been solved. Previous studies in 1980's and 1990's show same underestimation of $^{238}$Pu.[**20**, **21**]

Other PIE analysis [**12**] using JENDL-3.2 is shown in the **Table 5**. The data are taken by JAERI from SF irradiated in Takahama-3. This analysis also shows the underestimation of $^{238}$Pu and $^{244}$Cm. For $^{237}$Np, underestimation seems to be relaxed for samples of BWR-$UO_2$. However, since its standard deviation of C/E value is large, we cannot conclude that the $^{237}$Np calculation results are improved definitively. The fact that $^{238}$Pu, products of capture reaction of $^{237}$Np, is underestimated should be considered.

For americium isotopes, $^{241}$Am is overestimated in the analysis. This is different from previous analysis of Mihama-3 by Okumura. Okumura also showed the overestimation in other analysis [**22**] using SRAC. Considering the analysis results by French code APOLLO2 [**23**] using JEF-2.2 [**24**] or JEFF-3.0 [**25**] shown in next sub-section presents better agreement with PIE data from Takahama-3, further discussion on this over estimation will present us important information regarding the $^{241}$Am generation.

**Table 4** Averaged C/E values of MA Calculation for Mihama-3 [**17**]

| | JENDL-3.2 | | | JEF-2.2 | ENDF/B-VI |
|---|---|---|---|---|---|
| | MVP | SWAT | SRAC | SRAC | SRAC |
| $^{237}$Np | 0.90 | 0.95 | 0.91 | 0.92 | 0.93 |
| $^{238}$Pu | 0.81 | 0.83 | 0.81 | 0.85 | 0.85 |
| $^{241}$Am | 0.97 | 0.99 | 0.97 | 0.96 | 0.98 |
| $^{243}$Am | 1.00 | 0.99 | 0.98 | 0.95 | 1.07 |
| $^{244}$Cm | 0.78 | 0.76 | 0.74 | 0.72 | 0.82 |
| $^{245}$Cm | - | - | - | - | - |

**Table 5** Averaged C/E values of MA Calculation for Takahama-PWR (SWAT with JENDL-3.2) [**12**]

| | SF95 | SF97 | SF98 |
|---|---|---|---|
| | PWR $UO_2$ | PWR $UO_2$ | BWR $UO_2$ |
| $^{237}Np$ | - | 0.96 (0.02) | 1.12 (0.12) |
| $^{238}Pu$ | 0.84 (0.04)* | 0.83 (0.02) | 0.94 (0.06) |
| $^{241}Am$ | 1.14 (0.27) | 1.21 (0.09) | 1.17 (0.14) |
| $^{243}Am$ | 0.88 (0.03) | 0.89 (0.01) | 0.98 (0.04) |
| $^{244}Cm$ | 0.75 (0.05) | 0.75 (0.02) | 0.83 (0.03) |
| $^{245}Cm$ | 0.81 (0.07) | 0.80 (0.03) | 0.94 (0.08) |

* Values in ( ) is standard deviation

### 3.2.2 French PIE Analysis

As stated in previous section, France is active in the field of research and development of fuel cycle technology. To validate their code, they have been conducting PIE in France. In the reference [**26**], instead of using French PIE data, SF97-4 sample of Takahama-3 were used for verification of APOLLO2 and new cross section data library based on JEFF-3.0. **Table 6** shows the results. It reports improvement of $^{238}Pu$, $^{237}Np$ and $^{243}Am$. For $^{238}Pu$ and $^{237}Np$, the authors explained that increase of capture resonance integral of $^{235}U$ by adopting evaluation by Leal et al [**27**] and increase of (n,2n) cross section of $^{238}U$ are the main reasons of improvement. **Figure 2** is the comparison of (n,2n) reaction cross section of $^{238}U$. Values of JEFF-3.0 is greater than those of JEF-2.2 and JENDL-3.3 between 6.5E6 to 1.2E7 eV. For $^{243}Am$, in the reference [**28**], the authors pointed out the capture cross sections of $^{241}Pu$ in JENDL-3.2 and ENDF/B-VI are better than that of JEF-2.2, however, still small considering the integral experiments data. Finally, they included new evaluation[3] from thermal to 20 eV in JEFF-3.0 producing higher $^{241}Pu$ capture cross section at the 0.26eV resonance, and $^{243}Am$ is improved.

At last, we would like to mention on $^{245}Cm$. Both **Table 5** and **Table 6** present the difference is larger than other isotopes. As shown in **Table 5**, standard deviation of calculation results is also larger than $^{244}Cm$. This is same tendency with results in **Table 6**.

[3] Reference **25** says that this evaluation is submitted to the Nuclear Science and Engineering by H. Derrien.

**Table 6** C/E-1 [%] of MA Calculation for SF97-4 from Takahama-3 PWR (APLLO2 with JEF-2.2/JEFF-3.0) [**26**]

| | JEF-2.2 | JEFF-3.0 | total 1σ |
|---|---|---|---|
| $^{237}Np/^{238}U$ | -8.1 | -3.7 | 0.7 |
| $^{238}Pu/^{238}U$ | -18.9 | -14.1 | 3.8 |
| $^{241}Am/^{238}U$ | 4.0 | 4.7 | 3.2 |
| $^{243}Am/^{238}U$ | -14.8 | -7.7 | 4.7 |
| $^{244}Cm/^{238}U$ | -26.5 | -19.3 | 6.4 |
| $^{245}Cm/^{238}U$ | -33.4 | -22.9 | 7.7 |

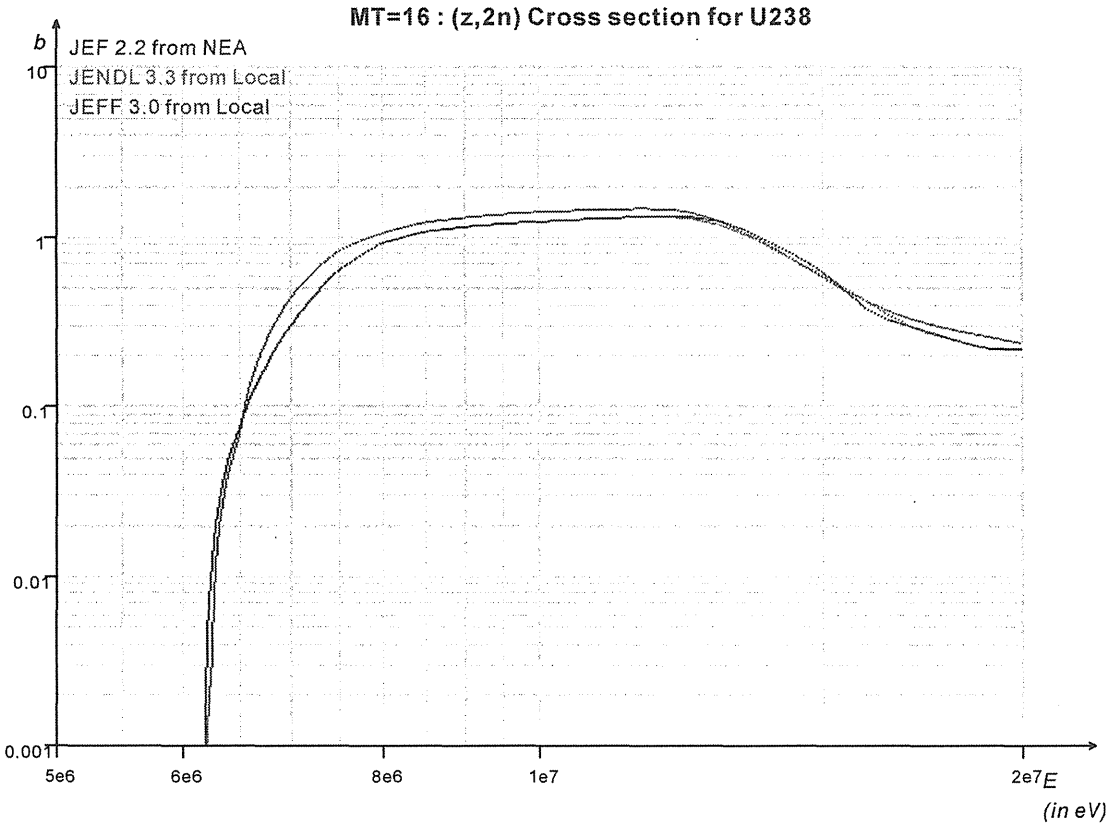



**Figure 2** (n,2n) reaction of $^{238}U$

## 4. Comparison of Calculation Results using Several Evaluated Libraries

### 4.1 Example of Chain Analysis and Comparison among Libraries

The reason of difficulty of improvement of MA calculation is MA is generated through complicated long chain. For example, as shown in section 2, $^{238}$Pu is generated through four paths.

1. $^{235}U(n,\gamma)^{236}U(n,\gamma)^{237}U(n,\gamma) \Rightarrow \beta^- \Rightarrow {}^{237}Np(n,\gamma)\,{}^{238}Np \Rightarrow \beta^- \Rightarrow {}^{238}Pu$
2. $^{238}U(n,2n)\,{}^{237}U(n,\gamma) \Rightarrow \beta^- \Rightarrow {}^{237}Np(n,\gamma)\,{}^{238}Np \Rightarrow \beta^- \Rightarrow {}^{238}Pu$
3. $^{242}Cm \Rightarrow \alpha \Rightarrow {}^{238}Pu$
4. $^{239}Pu(n,2n)^{238}Pu$

To determine the priority of evaluation and further discussion, chain analysis by burnup calculation results using several evaluated libraries was conducted. [29] **Table 7** presents the calculation results of MA using several evaluated nuclear data libraries. Authors confirmed most important reaction for $^{238}$Pu generation is (n,2n) of $^{238}$U and the difference of $^{238}$Pu depends on not only (n,2n) cross section, but also fission spectrum.

The reference also includes the discussion of $^{244}$Cm difference in **Table 7**. The authors explained that difference of capture cross section of $^{242}$Pu and $^{244}$Cm cause the difference of $^{243}$Am and $^{244}$Cm results. With the results shown in **Table 6** with APOLLO2, we could make further discussion to improve the cross section in the generation chain of $^{244}$Cm.

Results in **Table 7** show good agreement of $^{241}$Am between JENDL-3.2 and JEF-2.2 calculations, and PIE analysis using JENDL-3.2 shows large difference from experimental data shown in **Table 5**. However, $^{241}$Am results with JEF-2.2 in **Table 6** shows relatively good agreement with experimental results. Concerning this problem, we would like to point out that standard deviation of $^{241}$Am is large as shown **Table 5**. We suppose decay correction adopted to the PIE data from Takahama-3 has effect to some extent. It will be useful if we are able to compare data and calculation without decay correction. In order to determine the reason definitively, we should also back to the difference of calculation method between used codes. This fact implies that using same code system having detail chain treatment is necessary to evaluate different libraries, and collaborative work with experimental group measuring isotopic composition is helpful to do cross check the data and calculation.

**Table 7** Ratios of calculated weights using ENDF/B-VI and JEF-2.2 to those using JENDL-3.2 [29]

| | ENDF/B-VI (release 6) | JEF-2.2 |
|---|---|---|
| $^{237}$Np | 1.03 | 1.01 |
| $^{238}$Pu | 1.07 | 1.05 |
| $^{241}$Am | 1.01 | 0.99 |
| $^{243}$Am | 1.10 | 0.98 |
| $^{244}$Cm | 1.11 | 0.97 |
| $^{245}$Cm | 0.95 | 0.90 |

### 4.2 Improvement by adopting JENDL-3.3

JENDL Community may interest difference between calculations using JENDL-3.2 and JENDL-3.3. An example of comparison between PIE analysis using JENDL-3.2 and JENDL-3.3 is shown in **Table 8.** The objective data is SF97-4 selected from Takahama-3 PIE, since it was analyzed using APOLLO2.

**Table 8** C/E of MA Calculation for SF97-5 from Takahama-3 PWR
(SWAT with JENDL-3.2 /JENDL-3.3)

| | JENDL-3.2 | JENDL-3.3 | JENDL-3.3/JENDL-3.2 |
|---|---|---|---|
| $^{237}$Np | 0.97 | 1.01 | 1.04 |
| $^{238}$Pu | 0.82 | 0.86 | 1.05 |
| $^{241}$Am | 1.14 | 1.10 | 0.96 |
| $^{243}$Am | 0.89 | 0.90 | 1.01 |
| $^{244}$Cm | 0.75 | 0.75 | 1.00 |
| $^{245}$Cm | 0.80 | 0.79 | 0.99 |

$^{237}$Np and $^{238}$Pu are improved using JENDL-3.3 approximately 4%. This is because JENDL-3.3 using capture cross section of $^{235}$U evaluation by Leal et al as JEFF-3.0, and the fission spectrum of $^{235}$U became harder than JENDL-3.2. For $^{241}$Am, because of larger capture cross section of JENDL-3.3, decrease in C/E values of several percents is obtained. Smaller capture cross section of $^{243}$Am in JENDL-3.3 than JENDL-3.2 results in small increase of $^{243}$Am. Generally, MA calculation result is improved using JENDL-3.3. However, it is not sufficient. This is same conclusion with the analysis using JEFF-3.0.

## 5. Conclusion

MA calculation would be one of the most interested problem in future program of nuclear energy. However, number of PIE data of MA is not sufficient, especially for high burnup more than 40 GWd/t and we cannot access all data taken in other country. To overcome this situation, we should carry out mutual comparison among calculation results using several libraries to obtain related information.

Comparisons among codes and experimental data had been conducted. Some efforts lead to the improvement of MA calculation. However, underestimation of several MA is not solved definitively. Since MA generates by multiple paths, it is difficult to determine the main reason of the discrepancy. Using the chain analysis and sensitivity analysis, we are able to point out the main contributor to improve the analysis results.

PIE data of $UO_2$ and MOX for higher burnup $UO_2$ and MOX (40 to 60 GWd/t) should be obtained utilizing international collaborative work. But it is difficult to carry out it because of several administrative problems. And theoretical work is requied to point out the important chain and isotope. To facilitate the efficiency of nuclear data evaluation, we would like to propose following system to be used in quick check of nuclear data.

- Automated system to generate reactor constants for several neutronics codes,
- System to replace selected data (selection of isotope, reaction) in libraries to conduct sensitivity analysis of selected reaction data, and
- Development of database to compare calculation results and PIE data.

Since we are not able to access all data used in other countries, combination of international collaborative work for indirect comparison of codes and library, and efficient information/experience exchange should be pursued continuously for the improvement of MA calculation results.

## References

[1] T. Nakagawa, K. Shibata and S. Chiba et al., "Japanese Evaluated Nuclear Data Library Version 3 Revision-2: JENDL-3.2," *Journal of Nuclear Science and Technology*, **32**[12],1259 (1995).

[2] K. Shibata, T. Kawano and T. Nakagawa et al., "Japanese Evaluated Nuclear Data Library Version 3 Revision-3: JENDL-3.3," Journal of Nuclear Science and Technology, **39**[11],1125 (2002).

[3] E.D. Arthur, "Applied Nuclear Data Research and Development April 1,1982 - September 30, 1982," *LA-9647-PR*, LosAlamos National Laboratory (1983).

[4] H. Mochizuki, K. Suyama and Y. Nomura et al., "Spent Fuel Composition Database System on WWW - SFCOMPO on WWW Ver.2 -," *JAERI-Data/Code 2001-020*, Japan Atomic Energy Research Institute (2001) [in Japanese].

[5] G. O'Connor, R. Bowden and R. Thorne, "OECD/NEA Burn-up Credit Criticality Benchmark

Phase IV-A Reactivity Prediction Calculations for Infinite Arrays of PWR MOX Fuel Pincells," *NEA/NSC/DOC(2003)3,*OECD Nuclear Energy Agency, (2003).

[6] S. Guardini and G. Guzzi, "Benchmark Reference Data on Post-irradiation Analysis of Light Water Reactor Fuel Samples," *EUR7879EN*, Joint Research Centre Ispra (1983).

[7] M. Lippens, D. Boulanger and J. Basselier et al., "Source Term Assessment: ARIANE Programme," *Proceedings of CEM'01 the 8-th International Conference on Radioactive Waste Management and Environment Remediation*, September 30 - October 4, 2001 (2001).

[8] B.D. Murphy and R.T. Primm III, "Simulation of Mixed-Oxide and Low-Enriched Uranium Fuel Burnup in a Pressurized Water Reactor and Validation Against Destructive Analysis Results," *Nuclear Science and Engineering*, **142**,258 (2002).

[9] B. Roque, P. Marimbeau and P. Bioux et al., "The French Post Irradiation Examination Database for the validation of depletion calculation tools," *Proc. of 7th International Conference on Nuclear Criticality Safety (ICNC2003)*, 20-24 October 2003, Tokai-mura,Japan (2003).

[10] Dissolution Study Group in the Department of, "Dissolution Studies of Spent Nuclear Fuels," *JAERI-M 91-010* (1991) [ in Japanese].

[11] T. Adachi, Y. Nakahara and N. Kohno et al., "Comparison of Calculated Values with Measured Values on the Amount of TRU and FP Nuclides Accumulated in Gadolinium Bearing PWR Spent Fuels," *Journal of Nuclear Science and Technology*, **31**[10], 1119 (1994).

[12] Y. Nakahara, K. Suyama and T. Suzaki, "Technical Development on Burn-up Credit for Spent LWR Fuels," *JAERI-Tech 2000-071* (2000) [in Japanese].

[13] "CALCULATIONS OF DIFFERENT TRANSMUTATION CONCEPTS - An International Benchmark Exercise," NEA/NSC/DOC(2000)6, *OECD Nuclear Energy Agency*, (2000).

[14] M.D. DeHart, M.C. Brady and C.V. Parks, "OECD/NEA Burn-up Credit Calculational Criticality Benchmark Phase-IB Isotopic Prediction: Final Report," *ORNL-6901*, Oak Ridge National Laboratory, (as NEA/NSC/DOC(1996)6) (1996).

[15] H. Okuno, Y. Naito and K. Suyama, "OECD/NEA Burnup Credit Criticality Benchmarks Phase IIIB: Burnup Calculations of BWR Fuel Assemblies for Storage and Transport," *JAERI-Research 2002-001*,Japan Atomic Energy Research Institute (as of NEA/NSC/DOC(2002)2) (2002).

[16] G. O'Connor and P.H. Liem, "OECD/NEA Burn-up Credit Criticality Benchmark Phase IV-B Results of Phase IV-B Analysis," *NEA/NSC/DOC(2003)4*, OECD Nuclear Energy Agency, (2003).

[17] K. Okumura, T. Mori and M. Nakagawa et al., "Validation of a Continuous-Energy Monte Carlo Burn-up Code MVP-BURN and Its Application to Analysis of Post Irradiation Experiment," *Journal of Nuclear Science and Technology*, **37**[2], 128 (2000).

[18] K. Suyama, H. Mocizuki and T. Kiyosumi, "Revised Burnup Code System SWAT: Description and Validation Using Postirradiation Examination Data," *Nuclear Technology*, **138**[2], 97 (2002).

[19] K. Okumura, K. Kaneko and K. Tsuchihashi, "SRAC95; General Purpose Neutronics Code

System," *JAERI-Data/Code 96-015*, Japan Atomic Energy Research Institute, (1996) [in Japanese].

[20] K. Suyama, T. Iwasaki and N. Hirakawa, "Analysis of Post Irradiation Experiments in PWR Using New Nuclear Data Libraries," *Journal of Nuclear Science and Technology,* **31**[6], 596 (1994).

[21] U. Hesse, "OREST - The HAMMER-ORIGEN Burnup Program System: Method and Results," *Nuclear Technology*, **82**,173 (1988).

[22] K. Okumura, Private Communication (2003).

[23] S. Loubière, R. Sanchez and M. Coste et al., "APOLLO2 : twelve years later," *Proceedings of International Conference on Mathematics and Computation, Reactor physics and Environmental Analysis in nuclear Applications ( M&C99)*, 27-30 September 1999, Madrid, Spain (1999).

[24] C. Nordborg and M. Salvatores, "Status of the JEF Evaluated Data Library," *Proceedings of the International Conference on Nuclear Data for Science and Technology*, 9-13 May 1994, Gatlinburg, Tennessee, USA 2:680 (1994).

[25] R. Jacqmin, R. Forrest and J. Rowlands et al., "Status of the JEFF-3 Project," *Proceedings of the International Conference on Nuclear Data for Science and Technology (ND2001)*, Tsukuba, Japan, 7-12 October 2001, Journal of Nuclear Science and Technology supplement 2, 54 (2001).

[26] A. Courcelle, A. Santamarina and S. Mengelle, "Improvements of Isotopic Ratios Prediction through Takahama-3 Chemical Assays with the JEFF3.0 Nuclear Data Library," *Proc. of PHYSOR-2004 The Physics of Fuel Cycles and Advanced Nuclear Systems: Global Developments*, 25-29 April 2004, Chicago, USA (2004).

[27] L.C. Leal, H. Derrien and N.M. Larson et al., "R-Matrix analysis of U235 neutron transmission and cross section measurements in the 0 to 2.25 keV Energy Range," *Nuclear Science and Engineering*, **131**,230 (1999).

[28] H. Derrien, A. Courcelle and A. Santamarina, "Revision and validation of Pu241 resonance parameters from thermal to 20 eV," *NEA working document (http://www.nea.fr/html/dbdata/projects/jeffdoc.html) JEFDOC 916* (2002). (Restricted document. Only readable by JEFF Working Group Members)

[29] K. Suyama, J. Katakura and T. Kiyosumi et al., "Comparison of Burnup Calculation Results Using Several Evaluated Nuclear Data Libraries," *Journal of Nuclear Science and Technology* **39**[1], 82 (2002).

JP0550243



## 2.2 Request from Nuclear Fuel Cycle and Criticality Safety Design

Manabu HAMASAKI
*Core Engineering Section, Core Engineering Department*
*Nuclear Energy Systems Engineering Center, Nuclear Energy Systems Head Quarters*
*Mitsubishi Heavy Industries, Ltd.*
*3-1 Minatomirai 3chome, Nishi-ku, Yokohama, 220-8401 Japan*
e-mail: manabu_hamasaki@mhi.co.jp

Kiichiro SAKASHITA and Toshihiro NATSUME
*Core & Thermal Hydraulic Designing Section, Nuclear Fuel and Backend Designing Department,*
*Kobe Shipyard and Machinery Works, Mitsubishi Heavy Industries, Ltd.*
*1, Wadasaki-cho 1-chome, Hyogo-ku, Kobe, 652-8585 Japan*
e-mail: kiichiro_sakashita@mhi.co.jp, toshihiro_natsume@mhi.co.jp

The quality and reliability of criticality safety design of nuclear fuel cycle systems such as fuel fabrication facilities, fuel reprocessing facilities, storage systems of various forms of nuclear materials or transportation casks have been largely dependent on the quality of criticality safety analyses using qualified criticality calculation code systems and reliable nuclear data sets. In this report, we summarize the characteristics of the nuclear fuel cycle systems and the perspective of the requirements for the nuclear data, with brief comments on the recent issue about spent fuel disposal.

### 1. Introduction

Figure 1 shows the schematic flow diagram of LWR fuel cycle. We find variety of fissile materials there. Table 1 summarizes their variety. They range from gaseous form to solid and their mixture and include many indeterminate forms, resulting in demanding requirements for the modeling capability of criticality calculation codes.

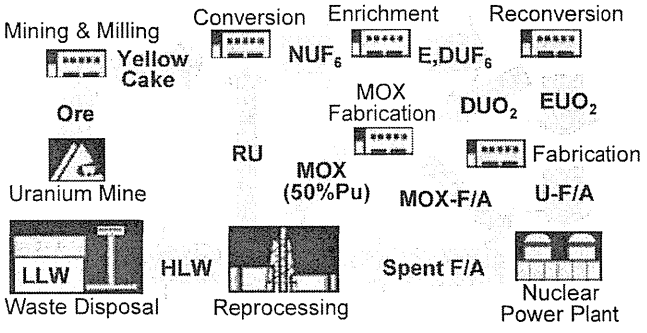



Fig.1 Schematic Flow of the LWR Nuclear Fuel Cycle

Fissile materials are sometimes dry and sometimes wet. In some processes they are in the form of aqueous solution. It means that there are variety of neutron moderation conditions according to the hydrogen content. So, variety of neutron spectra, from the fast reactor-like hardest one to the fully thermalized one must be covered. Also, they are composed of variety of resonance nuclides and their mixture, which requires appropriate treatment of resonance self-shielding and reliable resonance data.

Table 1 Variety of Fissile Materials Found in the Nuclear Fuel Cycle

| Physical / Chemical form | | Material |
|---|---|---|
| Gaseous | Hexa-Fluoride | $UF_6$ |
| Fluidal | Fluoride Solution | $UO_2F_2$aq |
| | Nitric Solution | $UO_2(NO_3)_2$aq, $Pu(NO_3)_4$aq |
| | Homo. Powder | $UO_2$/ $UO_3$-$H_2O$, MOX-$H_2O$ |
| | Slurry | ADU |
| Solid & Mixture | Pellets/Rods/Assemblies | $UO_2$-$H_2O$, MOX-$H_2O$ |
| | Dissolving Mixture | Spent $UO_2$ – Nitric Solution |

## 2. Criticality safety design practices in Japanese industries

According to the aforementioned requirements, Japanese industries have been using the standardized criticality calculation code systems with multi-group constants library and Monte Carlo codes to apply for the licensing of many nuclear fuel cycle systems.

The JACS system [1] whose main tools are KENO-IV [2] Monte Carlo code and MGCL (Multi-Group Constants Library) [3] based on ENDF/B-IV was developed by JAERI. The MGCL has 137group multi-purpose version and 26 group condensed version. JACS has been used for many licensing application.

The well-known SCALE system has been also used commonly, particularly for the design of fuel casks. The recent version of the system [4] has KENO-V.a [5] Monte Carlo code and its CSRL (Criticality Safety Reference Library) based on ENDF/B-V. The CSRL has 238 group version and condensed 44 group version. Formerly, ENDF/B-IV based 218 group and 27 group libraries were widely used.

For the design of fuel storage at power plant site, reactor core design codes (ex. PHOENIX-P/HIDRA [6]) are used. Our PHOENIX-P code is attached with ENDF-B/V based 42-group library and is used for fuel storage rack systems at PWR site for the consistency with reactor core design.

Nowadays, continuous energy Monte Carlo codes such as MCNP [7] or MVP [8] are widely used for the studies. The latest nuclear data ENDF-B/VI or JENDL-3.3 are both used.

## 3. Criticality safety design criteria

Japanese Criticality Safety Handbook [9] lays out some subcriticality criteria and associated conditions. The most commonly applied criterion for nuclear fuel systems is

$k\text{-}eff \leq 0.95$,

where *k-eff* shall be calculated with "well qualified system". The 0.95 criterion is a rather heaven-sent one that has been used since very old days. The Handbook suggests that one can rationalize it, if he/she can show the validity by quantitative data. In this validation, the quality of nuclear data is of large importance. The integral validation by some series of criticality experiments simulating the systems of interest is directly useful for this purpose. The Handbook introduced the concept of the "estimated critical lower limit *k-eff*", which includes the minimum bias to be considered for computational uncertainty and is specific to the combination of nuclear data, criticality code and fissile systems. Theoretically, we could

apply as high *k-eff* criterion as the estimated critical lower limit value, provided that sufficient backup by integral validation through criticality benchmarks is available.

## 4. Logistics in nuclear fuel cycle – fuel casks

The fuel casks are playing key roles in the logistics in the nuclear fuel cycle. They are versatile components that are used for many purposes, such as transportation, interim or long-term storage of fuels.

Since transportation or storage costs are not small among total fuel cycle cost, the economy of casks affects the total economy of fuel cycle. Furthermore, the market of fuel casks is rather open to the world. So, there has been the continuous pressure for the streamlining and sophistication of the cask design.

The economy of casks can be measured by the;

- payloads – number of fuel assemblies to be loaded,
- cost for specific materials, such as neutron absorber, gamma/neutron shielding,
- material and assembly cost to assure mechanical strength, heat resistance and radiation resistance, and
- light weight for easy handling.

The current practice of criticality safety design of spent fuel casks is often with built in neutron absorber such as boronated stainless steel, boronated aluminum etc. Usually in the criticality safety design analyses, unirradiated fuel with initial $^{235}U$ enrichment is still assumed and the 0.95 criterion is still applied.

## 5. Challenges for Burnup Credit

The front of nuclear criticality safety designs has been seeking for the application of "Burnup Credit". In Japan," A guide introducing burnup credit, preliminary version" was issued in 2001[10].In this field, it is regarded to be prudent to take the credit of the limited nuclides seen in the spent fuel. In the level-1 burnup credit, the actinides in the spent fuel are solely considered, while more ambitious level-2 burnup credit assumes the absorption by fission products (FPs)

In the criticality safety design taking credit of burnup, two categories of uncertainty are to be considered. One is the uncertainty of the assumed isotopic composition of spent fuels. Since the isotopic composition of spent fuel is obtained through depletion analysis of the power reactor, its uncertainty originates from nuclear data used in the depletion analysis, depletion code, depletion environment, as well as cooling time after reactor shutdown. And the other is the uncertainty of criticality prediction of the systems containing spent fuels. This uncertainty originates from the nuclear data used in the criticality analysis, criticality code as well as the aforementioned uncertainty of isotopic composition itself.

For the validation against the isotopic composition, the destructive analysis data of spent fuels obtained in the post-irradiation examination (PIE) are useful. As the public PIE database, the SFCOMPO[11] is available.

Although the criticality experiments using actual spent fuel are considered useful for the validation against the criticality prediction of spent fuel systems, very few numbers of such

experiments have been run because of the difficulty to handle the actual spent fuels in the experimental facility. The REBUS international project [12] is one of the few examples. This approach has intrinsic difficulty in handling the highly radioactive spent fuels and in covering the whole spectrum of depletion environment.

More strong-arm approach is the validation through the direct simulation of the power reactor with criticality codes, which is coming to be realistic these days.

## 6. Level-1: Actinide burnup credit

The level 1 burnup credit has been already applied to many examples. In Japan, Rokkasho Reprocessing Plant has the spent fuel storage pool designed for the fuel whose residual $^{235}U$ enrichment is lower than certain limit, and its head end process including the dissolver will be operated with or without gadolinium poison, according to the burnup of the fuel to be processed. The transport casks in France, Germany, Netherlands, Switzerland and USA are also the examples [13].

## 7. Level-2: FP credit

The level 2 burnup credit has been also applied to some examples. The spent fuel pit of the US nuclear power plant is an example.

The FP nuclides to be considered are preferred to be long-lived chemically stable and of course have large neutron absorption capability. Table 2 shows the examples of the selected FP nuclides. Also we have to be aware of the cooling time of interest, because the relative importance of each nuclide is not fixed with time [10].

Table 2 The examples of selected FP nuclides for the level 2 burnup credit

| Case | Nuclides |
|---|---|
| 6 FPs [14] (CEA at early stage) | Sm-149, Rh-103, Gd-155, Nd-143, Cs-133, Sm-152 |
| 12 FPs [10] (JAERI-Tech 001-055) | Sm-149, Rh-103, Gd-155, Nd-143, Cs-133, Sm-152, Tc-99, Eu-153, Nd-145, Sm-147, Mo-95, Sm-150 |
| 15 FPs [14] (OECD BUC W.G.) | Sm-149, Rh-103, Gd-155, Nd-143, Cs-133, Sm-152, Tc-99, Eu-153, Nd-145, Sm-147, Mo-95, Sm-150, Sm-151, Ag-109, Ru-101 |
| 13 FPs for Casks [15] (SAND87-0151) | Tc-99, Rh-103, Xe-131, Cs-133, Nd-143, Nd-145, Pm-147, Sm-147, Sm-149, Sm-151, Sm-152, Eu-153, Gd-155 |

## 8. Burnup credit case study – Spent fuel cask

To demonstrate the nature of the FP credit, we applied the levels of burnup credit to the spent fuel cask model designed for the intact fuel with $^{235}U$ enrichment of 4.1wt%.

Figure 2 shows the considered cask model. It has boronated aluminum spacers and flux traps. The boron in the spacer is assumed to be enriched in $^{10}B$.

The required width of flux trap and $^{10}B$ content for the 4.8wt% $^{235}U$ fuel with various burnup were surveyed. The considered levels of burnup credit are level 1, level 2A where the SAND87-0151 (13) FP nuclides are considered and the level 2B where the virtually all FP

nuclides are considered. Also the uncertainties of FP and actinide amounts were treated as the parameters.

Figure 3 shows the surveyed results of the flux trap width under various conditions. FP credit is quite attractive even with only 13 nuclides. On the other hand, in the cases with the assumed uncertainties of ±5% for actinides and/or –20% for FPs, the merits of burnup credit are significantly reduced.

Figure 4 shows the results for the $^{10}B$ content. The uncertainties reduce the merit of burnup credit here, too.

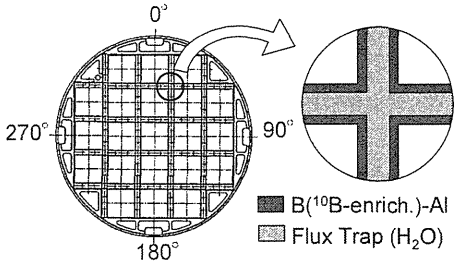



Fig.2 Spent Fuel Cask Model for the Study

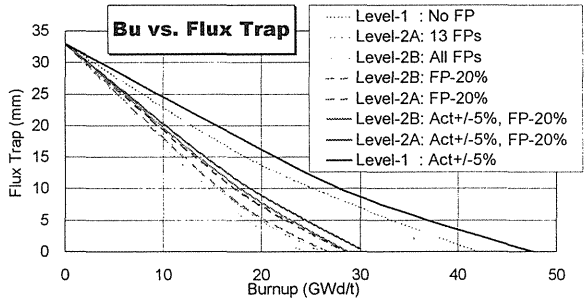



Fig.3 Required flux trap width versus burnup

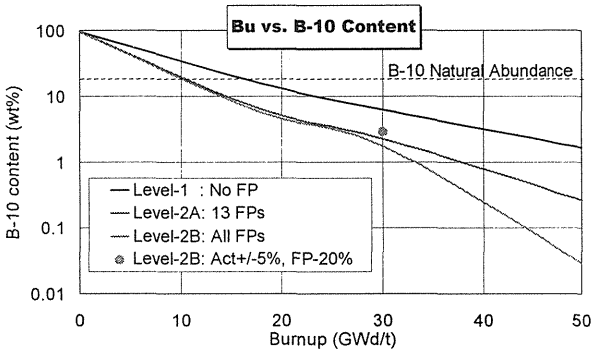



Fig.4 Required $^{10}B$ content versus burnup

## 9. Recent issue: spent fuel disposal

In the course of the periodical revision of the "Long-Term Program for Research, Development and Utilization of Nuclear Energy of Japan", the economic study on the direct disposal of spent fuels was performed [16]. In this study, major technical and non-technical challenges were studied and assessed. In the conclusion, criticality issue was identified as one of the major uncertainties of the study, since no safety evaluation criteria to prevent criticality by plutonium etc had been established yet.

Besides the safety criteria, modeling, scenario or phenomenology to be considered have not been well established. From the viewpoint of nuclear data, very long term (~$10^3$y) transient of isotopes would increase the uncertainty. Also, integral validation would be more difficult than for the postulated burnup credit design of fuel cycle systems.

## 10. Conclusions

(1) Nuclear fuel cycle consists of wide spectrum of fissile systems. Variety of resonance nuclides and neutron spectra are to be covered.
(2) Better-qualified codes and nuclear data could improve criticality safety design criteria, and give more competitive edge to nuclear fuel cycle.
(3) Burnup credit is the major front of criticality safety design of spent fuel systems.
(4) Level-2 burnup or FP credit is promising, whose efficiency depends on uncertainty of

spent fuel characteristics and their prediction.

(5) Integral tests for spent fuel systems are difficult by nature, microscopic validation would be of more importance.

(6) In the spent fuel disposal study, criticality issue was identified as one of the major uncertainties. If its reduction were necessitated, improvement of FP and actinides data would play a certain role.

**References**

[1] J.Katakura, Y.Naito and Y.Komuro,"Development of Computer Code System JACS for Criticality Safety", Trans. Am. Nucl. Soc., **41**, 329 (1982)

[2] L.M. Petrie and N.F. Cross, "KENO-IV - An Improved Monte Carlo Criticality Program", ORNL-4938 (1975).

[3] Y.Naito et al., "MGCL-Processor: A Computer Code System for Processing Multi Group Constants Library MGCL", JAERI-M9396(1981)

[4] ORNL SCALE Home Page, http://www.ornl.gov/sci/scale/

[5] L.M. Petrie and N.F. Landers, "KENO-V.a - An Improved Monte Carlo Criticality Program with Supergrouping", VOL.2, SEC. F11 ORNL/NUREG/CSD-2/V1/R2 (1984)

[6] "On the Criticality Safety Analysis for the Spent Fuel Storage at LWR Power Plant Site", MHI-NES-1003 rev.3, Mitsubishi Heavy Industries, Ltd. (1998) (in Japanese)

[7] LANL MCNP Home Page, http://laws.lanl.gov/x5/MCNP/index.html

[8] T. Mori, M. Nakagawa, JAERI-Data/Code 94-007 (1994) (in Japanese)

[9] Working group on Nuclear Criticality Safety Data, “Criticality Safety Handbook Version 2”, JAERI-1340 (1999) (in Japanese)

[10] Nuclear Fuel Cycle Safety Research Committee,“ A Guide Introducing Burnup Credit, Preliminary Version (Contract Research)”, JAERI-Tech 2001-055 (2001) (in Japanese)

[11] M. Kurosawa, Y. Naito and T. Kaneko, "Isotopic Composition of Spent Fuels for Criticality Safety Evaluation and Isotopic Composition Data Base (SFCOMPO)", Proc. Fifth International Conference on Nuclear Criticality Safety (ICNC'95), Vol.1, P.2.11, Albuquerque, NM, USA (1995)

[12] P. D'hondt et al., " The REBUS Experimental Programme for Burn-Up Credit", ICAPP'03, Cordoba, Spain, http://www3.inspi.ufl.edu/icapp03/program/abstracts/3036.pdf, (2003)

[13] International Atomic Energy Agency, "Practices and Developments in Spent Fuel Burnup Credit Applications", Proc. Technical Committee Meeting, Madrid, Spain, IAEA-TECDOC-1378 (2002)

[14] J. Raby et al., "Current Studies Related to the Use of Burnup Credit in France", Proc. ICNC2003, p.627, JAERI-Conf 2003-019(Part II)

[15] T. L. Sanders, R. M. Westfall and R. H. Jones, " Feasibility and Incentives for the Consideration of Spent Fuel Operating Histories in the Criticality Analysis of Spent Fuel Shipping Casks", SAND87-0151, UC71, TTC-0713 (1987)

[16] Atomic Energy Commission of Japan HP, http://aec.jst.go.jp/jicst/NC/tyoki/indexh2.htm, materials for 2004.10.7 technical subcommittee meeting (in Japanese)

JP0550244



# 2.3 Requests from Use Experience of ORIGEN Code -Activity of the working group on evaluation of nuclide generation and depletion-

Tetsuo Matsumura
*Central Research Institute of Electric Power Industry (CRIEPI)*
*2-11-1, Iwado Kita, Komae-shi, Tokyo 201-8511, JAPAN*
e-mail: matsu-t@criepi.denken.or.jp

A questionnaire survey was carried out through the committee members of the working group on evaluation of nuclide generation and depletion about the demand accuracy of the ORIGEN code which is used widely in various fields of design analysis and evaluation. WG committee asked each organization's ORIGEN user, and obtained the reply from various fields.

## 1. Introduction

In order to improve accuracy of nuclear data, requests of evaluation accuracy of the ORIGEN code have been discussed in the working group on evaluation of nuclide generation and depletion (WG)*. A questionnaire survey was carried out through the committee members of the WG about the demand accuracy of the ORIGEN code which is used widely in various fields of design analysis and evaluation. WG committee asked each organization's ORIGEN user, and obtained the reply. For this reason, it is thought that the opinion of each organization's business person in charge was able to be collected. The replies are obtained for following fields.

(1) Spent fuel cask (including spent fuel storage facilities)
(2) Re-processing facility
(3) Decommissioning, and waste treatment and disposal
(4) Plant decay heat analysis (accident analysis)
(5) Plant equipment design
(6) Burn-up credit

## 2. Result of the questionnaire (see Table 1)

(1) Spent fuel cask (including spent fuel storage facilities)

There are the following safety design criteria and the inspection standard concerning the demand accuracy of ORIGEN calculation about the spent fuel cask [2];

- The rate of the surface dose equivalent [< 2 mSv/h ]

*: This paper is based on chapter 6 of the WG report: JAERI-Research 2004-025 [1]

- The rate of the dose equivalent at 1m distance [< 100 μSv/h]
- In any cases, criticality [< 0.95]

The restriction temperature of a spent fuel cladding is defined with the amount of accumulation creep of 1%. These restriction temperature are about 360 $^0$C (PWR) and 380 $^0$C (BWR) as initial temperature. The questionnaire results of demand accuracy are:

- Gamma-ray source and a spectrum: 5%.
- Neutron source: 5% and 20% (there are two replies)
- Decay heat: 10% (a few $^0$C in the surface of cask)

The surface dose equivalent of a cask is calculated with radiation source of ORIGEN calculation and transportation calculation code in which a spent fuel cask is modeled with one-dimensional or two-dimensional. Neutron effective multiplication factor (criticality) is usually calculated with the Monte Carlo calculation codes of MCNP [3], KENO [4], etc. Moreover, the restriction temperature of a spent fuel cladding is evaluated with thermal conductivity calculation of general finite element programs, such as ABAQUS [5], based on the decay heat value by ORIGEN-2 calculation.

There are some evaluation errors in transportation calculation, thermal conductivity calculation, etc. However margin in safety side evaluation model and assumptions are considered to be larger than these evaluation errors such as setting higher burn-up, shorter cooling period of spent fuel than anticipated values, and safety side modeling (quality of the material, geometry, etc.) of calculations.

In case of spent fuel transport cask of FBR, the accuracy of less than 10% is required in decay heat evaluation. This request of accuracy is coming from minimum temperature margin of 18 $^0$C. The present calculation value is less than design conditions enough, and there are about 20 times margin at the surface, about 7 times at a 1m point from the cask surface.

Decay heat accuracy evaluation is necessary for 2~3 year in transportation of a LWR spent fuel, 10~50 years for spent fuel storage. Accuracy of 5% is assumed to the decay heat of an ORIGEN-2 calculation value. This is decided with the comparison result of the heat measured value and ORIGEN-2 calculation value. Mainly, Cs137 is decay heat source of spent fuel cooled for more than 10 years. From a viewpoint of neutron shielding, Cm242 (2~3 years) and Cm244 (> 4 years) are important, and 5% is required also for the prediction accuracy.

(2) Re-processing facility

ORIGEN-2 is used for radiation source evaluation of a re-processing facility. The calculation accuracy of ORIGEN-2 is not set up on radiation source, but 50% of a standard dose is used as a safety margin of a radiation shielding design. Therefore order of 10% accuracy in ORIGEN-2 can be accepted within this safety margin. Accuracy of decay heat evaluation should be within AESJ decay heat standard (1990) [6]. Moreover, for environmental radioactivity safety evaluation of FBR spent fuel Re-processing facility, inventories of $^3$H, $^{14}$C, $^{85}$Kr, $^{129}$I are important. Especially, the amount of $^{14}$C needs about 10% of accuracy, which is generation by the reaction of $^{17}$O and $^{14}$N with fast neutron.

(3) Decommissioning, and waste treatment and disposal

ORIGEN-2 is used for evaluation of activation in whole PWR and contamination source for system

equipments. In these evaluations, accuracy is estimated at about 50%, which is mainly error of neutron flux evaluation. However error of nuclear data is assumed to be less than about 5%. ORIGEN-2 is used with 1 group cross-sections from the JENDL3.2 and neutron fluxes which are evaluated in about 30 areas, such as a loop room, an operation floor and so on. Original library of ORIGEN-2 is used for a reactor core.

(4) Plant decay heat analysis (accident analysis)

The accuracy demand of decay heat is 20% for form reactor shut down to 30 days. Since U-239 (β), Np-239 (β), Pu-238 (α), Cm-242 (α), Cm-244 (α), and Am-241 (β) are main heat sources, the inventories of these nuclides should be predicts within 20% of accuracy.

(5) Plant equipment design

In evaluation of decay heat system and a SFP cooling system, decay heat of actinides accuracy is 20%. Therefore 20% of prediction accuracy of main actinides inventories is required. Decay heat of FP is evaluated with AESJ decay heat standard.

(6) Burn-up credit: To introduce burn-up credit, the accuracy of less than 3% δk (possibly within 1% δk) is expected.

3. Evaluation of the demand accuracy of ORIGEN-2

Requirements of ORIGEN2 accuracy are 5~10% in general, it became 0.5% of demand accuracy. WG discussed this number. For example, spent fuel decay heat of a highest burn-up of 55 MWd/kg and an average burn-up of 48 MWd/kg differs more than 10%. Cooling time will also decreases decay heat by 5~10% in one year. Requirements of ORIGEN2 accuracy is same order of these uncertainty of evaluation. For this reason, it is interpreted as that requirement of ORIGEN2 accuracy of 5~10% is coming from design margin of various facilities. And since concepts of design margin are different in each field/facilities, requirements of ORIGEN2 accuracy differ in each field/facilities.

It should be noticed that present replies of the questionnaire include two types of answer based on present reasonable design margin and desirable design margin request for future.

The amount prediction accuracy of generation of Cm242 and Cm244 is important, and Cs137 is important from a thermal viewpoint. As for the amount of generation of these nuclides, about 5 - 10% of accuracy is demanded. About actinides decay heat, the accuracy of a main chain nuclide is demanded in 20% of accuracy. Demand accuracy of ORIGEN-2 can be reflected to nuclear core data through the verification work of PIE data (Fig. 1).

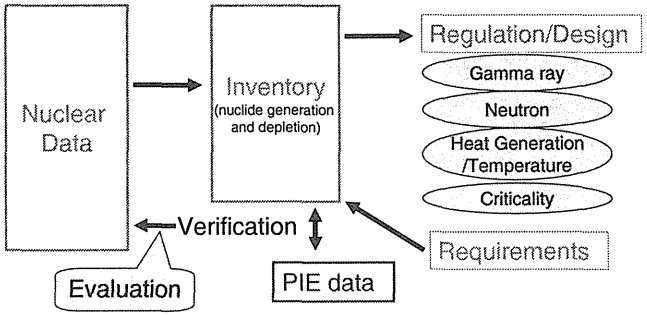



Fig. 1 Flow of Evaluation

The paper of Ando and Ohkawach [7] concludes that main U, Pu nuclides have enough (about 5%) accuracy, but TRUs are not so good. There is not enough accuracy of ORIGEN calculation in the present condition for having satisfied the demand accuracy of a questionnaire. However, the request of the industrial world which became clear as a result of the questionnaire is accepted with sincerity, and it is thought important to be reflected in future activity.

## 4. Conclusion

Questionnaire surveys were carried out about the demand accuracy of the ORIGEN code and obtained various fields of Requirements of ORIGEN2 accuracy. The questionnaire result had the reply relevant to a spent fuel cask, a storage facilities, a re-processing plant, a burn-up monitor, the criticality monitor, decommissioning ,waste processing and disposal, decay heat evaluation, the equipment design, a burn-up credit and others. These demand accuracy show request to cross-section area evaluation. For example, the following measures are required.

- Continue the verification work of the evaluation accuracy of nuclide composition in the analysis of experiment data, such as nuclide composition.
- Presume accuracy errors of ORIGEN calculation and consider relation with demand accuracy from sensitivity analysis and covariance data.
- Extract nuclide and nuclear reaction which need improvement of evaluation accuracy and covariance data, etc.

## Acknowledgements

Chapter 6 of the WG Report is contributed with Hideki MATSUMOTO (MHI), Yoshihara ANDO (Toshiba), Takufumi AOYAMA (JNC), Motoo AOYAMA (Hitach) and Yoshitaka NAITO (NAIS).

## References

[1] Keisuke OKUMURA, Shigeo OHKI, Munenari YAMAMOTO, Hideki MATSUMOTO, Yoshihara ANDO, Kazufumi TSUJIMOTO, Akihiro SASAHARA, Jun-ichi KATAKURA, Tetsuo MATSUMURA, Takufumi AOYAMA, Motoo AOYAMA, Toshiyuki KANEKO, Shinya KOSAKA, Kenya SUYAMA and Yoshitaka NAITO, "Study on Prediction Accuracy of Nuclide Generation and Depletion with JENDL (Activities of Working Group on Evaluation of Nuclide Generation and Depletion form FY 2000 to FT 2003 under Subcommittee on Nuclear Fuel Cycle of Japanese Nuclear Data Committee)", JAERI-Research 2004-025 (to be published) [in Japanese]

[2] "Standard for Safety Design and Inspection of Metal casks for Spent Fuel Interim Storage Facility: 2002", AESJ-SC-F 002:2002. (to be printed)

[3] http://drambuie.lanl.gov/~esh4/mcnp.htm

[4] http://www.ornl.gov/sci/criticality_shielding/codes.shtml

[5] http://www.hks.com/

[6] AESJ："Nuclear reactor decay heat and its recommendation value".(1992)

[7] Y. Ando, Y. Ohkawachi, "Requests on Nuclear Data in the Backend Field through PIE Analysis", JAERI-Conf 2003-006, pp. 54-60 (2003)

Table 1 (1/2) Result of the questionnaire about "the demand accuracy of ORIGEN calculation"

| Items | Demand accuracy | Notes and comments |
|---|---|---|
| Spent fuel cask (metal cask for transportation) <Reply 1> | - Gamma ray source and a spectrum: 5%<br>- Neutron source: 5% | Cask type: BWR 69 assemblies (PWR/BWR:$UO_2$ &MOX ) |
| Same as above <Reply 2> | - Decay heat : 10% (a few $^0$C in the surface of cask),<br>- Gamma ray source and a spectrum: 5% (5% of surface dose),<br>- Neutron source : 20% (20% of surface dose) | Cask type: MU<br><br>The amount of gamma ray source and a spectrum influence gamma ray shielding evaluation by 100%. |
| FBR spent fuel cask (metal cask for transportation) | - Decay heat: a design value is about 6 times of the calculation value evaluated to the safety side. (The calculation value of 91 $^0$C in fuel ciadding, design value of 650 $^0$C) however, temperature evaluation margin is about 30% at a fin tip.<br>- Gamma ray source and a spectrum: (contribution of 0.4~0.9MeV is important at about 80%)<br>- Neutron source: Cm242 is important (about 85% of the whole) | Object: Joyo Fuel<br>Type: fuel basket for reactor core fuel (8 assemblies), and blanket fuel (11 assemblies).<br><br>The present calculation value is less than design conditions enough, and there are about 20 times margin at the surface, about 10 times at a 1m point from the cask surface. |
| Spent fuel pool (including a spent fuel acceptance pool) | - Decay heat: 5% (BWR-$UO_2$ 45 GWd/t), 10% (BWR/PWR:MOX),<br>- Gamma ray source and spectrum: 10%<br>- Neutron source: no problem since it is shielded enough. | Type of spent fuel: BWR-$UO_2$ 45GWd/t,<br>BWR/PWR-MOX |
| Spent fuel storage facility | - Gamma ray source and a spectrum: 5% (since it is based on a cask surface dose, it is the same as that of a cask. spectrum is important)<br>- Neutron source: 5% | Type of storage facility: A metal cask, BWR |
| Re-processing facility | - Decay heat: decay heat evaluation curve is enough.<br>- Safety margin of 1.2 is used in a RETF design, multiplying the calculation value of ORIGEN2.<br>- Amount of generation of $^3$H and $^{14}$C, $^{85}$Kr, and $^{129}$I.in FBR: about 10% | |
| Burn-up monitor <Reply 1> | - Gamma ray source and a spectrum: 1% (for the important nuclide Cs 137: 0.5%),<br>- Neutron source: 3% (the detection method: FC, demand accuracy: 1%) | Gamma ray source influences the amount of evaluations directly. The accuracy of neutron detection influences a burn-up monitor by about 1/3 in $UO^2$ and about 1/2 in MOX. |
| Same as above <Reply 2> | - The important nuclide of neutron measurement : Cm244, (alpha, n) and spontaneous fission data.<br>- Gamma ray measurement :P r-144, Mn-54, Rh-106, Co-60, Eu-154, Cs-134, and Cs-137 (nuclear fission yield is also important in addition to cross-section data) | Considering the generation process of Cm244, the neutron capture cross section of Am243 is important. |

Table 1 (2/2) Result of the questionnaire about "the demand accuracy of ORIGEN calculation"

| Items | Demand accuracy | Notes and comments |
|---|---|---|
| Criticality monitor | - Neutron source: 5% | |
| Radioactivity concentration of decommissioning <Reply 1> | - Nuclides to be evaluated: about 57 nuclides.<br>- Co-60: about 5% for dose evaluation for the public and worker. | For all of decommissioning plant, such as a Tokai gas plant and BWR/PWR, ORIGEN2 is utilized for inventory evaluation, radiation dose evaluation of worker, de-contamination, mechanical cutting, and radioactive waste processing, etc. |
| Same as above <Reply 2> | - Nuclides to be evaluated and demand accuracy: Co-60, Cs-134, Eu-154, Eu155, about 10% of accuracy.<br>- For radiation dose evaluation: Co-60 and Cs-134 (10%),.<br>- For waste amount evaluation: Co-60, and H3 (10%).<br>- Gamma ray source and spectrum: 10% (for inner strictures of PRV) | Evaluation of Co-60 influences radiation dose evaluation accuracy by 100%. |
| Waste treatment and disposal | - For the safety evaluation of under-the-ground disposal of L1 waste generated from BWR. (although it changes with wastes for examination.). Examples: H-3, C-14, Cl-36, Ca-41, Fe- 55, Co-60, Ni-59, Ni-63, Se-79, Sr- 90, Zr-93, Nb-94, Mo-93, Tc-99, Sn-121m, I-129, Cs-137, Hf-182, Np-237, Pu-238, Pu-239, Pu- 240, Am-241, Cm-242, Cm-243, Cm-244, etc. (containing a long half-life nuclide)<br>- I-129, TRU(for public in-take): 5% of evaluation accuracy<br>- C-14: 5% for public in-take (high beta/gamma waste)<br>- Cl-36: 5% for public in-take (high beta/gamma waste) | The ORIGEN code is utilized for activation evaluation of low level radioactive waste (L1 waste etc.)<br><br>Evaluation accuracy influences scale of disposal facility (I-129 TRU influences by 90%). |
| Burn-up credit | - Since critical safe evaluation will be performed by spent fuel composition, the amount of U235, the total amount and composition of Pu, become important.<br>- Evaluation accuracy: 3% $\delta k$ in reactivity. (nuclide composition is also requested. Same for MOX fuel) | |

JP0550245



# 2.4 Nuclear Data for Innovative Reactors Having Persistent Resistance to Nuclear Proliferation

Tadashi YOSHIDA[1], Naoto HAGURA[1], Vladimir TOSHINSKY[1], Masaki SAITO[2]

[1]*Musashi Institute of Technology, Tamazutsumi 1-28-1, Setagaya-ku, Tokyo 158-8557, Japan*

e-mail: yos@ph.ns.musashi-tech.ac.jp

[2] *Tokyo Institute of Technology, 2-12-1, O-okayama, Meguro-ku, Tokyo 152-8550, Japan*

The Protected Plutonium Production ($P^3$) project has been initiated in order to realize the proliferation-resistant plutonium. The first stage of this project is based on the idea to protect plutonium by $^{238}Pu$ generated from $^{237}Np$ doped in the fresh uranium fuel. Along with the burnup going on, the doped $^{237}Np$ is transmuted via $^{238}Np$ to $^{238}Pu$, which is the intense neutron source of spontaneous fission ($2.6x10^3$ n/g/s). These neutrons will deteriorate the quality of the plutonium as the nuclear explosive material. In addition, high alpha-decay heat of $^{238}Pu$ (560W/kg) makes the processes of the explosive fabrication and its maintenance technologically difficult. In this background we surveyed the status of nuclear data relevant to the $P^3$-concept reactor design. The reliability of the capture cross section data for $^{237}Np$ and $^{238}Pu$ are far from satisfactory and more accurate experiments and evaluations are required. As fissions in these nuclides do not always play any decisive role in the $P^3$ concept LWR, we can be fairly tolerable about the uncertainty of the fission cross section data, but further study is needed.

## 1. Introduction

Converted use of reactor-fuel material to explosives is one of the most critical issues which must be resolved for the peaceful and sustainable use of the nuclear power. In this context the "Protected Plutonium Production ($P^3$)" concept has been proposed by M. Saito et. al [1,2] for the purpose of realizing the proliferation-resistant plutonium. In this $P^3$ concept, the plutonium produced in the nuclear reactors from $^{238}U$ is made highly proliferation-resistant by introducing a certain amount of the $^{238}Pu$ isotope and this is accomplished by doping some appropriate minor actinide (MA) in the fresh uranium fuel for the LWRs. The first stage of this project ($P^3$-A project [3]) focus on the transmutation of $^{237}Np$, which has a large neutron capture cross-section, into $^{238}Pu$ without deteriorating, or even with improving, of the reactor-core performances. The isotope $^{238}Pu$, which is the intense neutron source of spontaneous fission ($2.6x10^3$ n/g/s), will deteriorate the quality of the plutonium as the nuclear explosive material. In addition, high alpha-decay heat of $^{238}Pu$ (560W/kg) makes the processes of the explosive fabrication and its maintenance technologically very difficult.

Based on the preparatory studies for several years, $P^3$-A project has been initiated and carried out since 2003 by the financial support of the Ministry of Education, Culture, Sports, Science and Technology as an international cooperative work among the following organizations. They are Tokyo Institute of Technology, Idaho National Engineering and Environmental Laboratory, Musashi Institute of Technology, Japan Nuclear Cycle Development Institute, Japan Atomic Energy Research Institute, Engineering Development Co. Ltd., Mitsubishi Heavy Industries, Ltd., Nuclear Development Corporation, Advanced Reactor Technology Co., Ltd., Toshiba Corporation and Fuji Electric System Co., Ltd. The present paper describes the neutronic basis of the $P^3$-A project and then review the status and the needs of the nuclear data pertinent to this concept.

## 2. Generation and Depletion of $^{238}$Pu

In the $P^3$-A concept[3], the potential of $^{237}$Np is fully pursued as a novel fertile material which is transmutes into $^{238}$Pu through a successive neutron capture and beta-decay. If we start LWR operation with the fresh uranium fuel doped with an appropriate amount of $^{237}$Np, the plutonium generated mainly from $^{238}$U in the reactor is persistently accompanied by a sizable amount of $^{238}$Pu isotope coming from $^{237}$Np at any stage of fuel burnup, reprocessing and storage as indicated below.

$$^{237}\mathrm{Np} + \mathrm{n} \longrightarrow {}^{238}\mathrm{Pu} / {}^{239}\mathrm{Pu} \longleftarrow {}^{238}\mathrm{U} + \mathrm{n}$$

(Fuel Protection) (Fuel Production).

The isotopic presence of $^{238}$Pu makes it difficult to use the produced plutonium as the nuclear explosive material without some sophisticated isotope-separation technology, the atomic vapor laser method for example. In this sense the generated $^{238}$Pu plays the role of the fuel protector against the nuclear proliferation.

Another merit of doping $^{237}$Np in the fuel lies in the fact that it exerts a favorable effect of extending the fuel burnup. The capture cross section in $^{237}$Np is much larger than the fission cross section in the LWR environment and, therefore, it reduces the reactivity at the beginning of the burnup. Then, along with the burnup going on, it is transmuted to $^{238}$Pu, which has larger fission cross section than $^{237}$Np, and further into

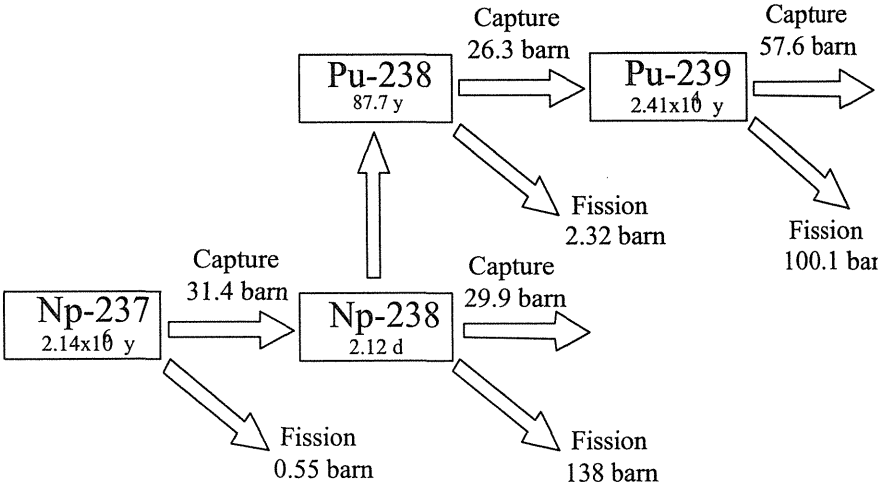



Fig. 1 Generation path of $^{238}$Pu and $^{239}$Pu from $^{237}$Np

$^{239}$Pu through neutron capture. This means the negative reactivity of $^{237}$Np is gradually replaced by the positive reactivity of plutonium. In this sense the doped $^{237}$Np plays a role of an *active* burnable poison. Figure 1 shows the generation paths of Pu isotopes from $^{237}$Np. The cross sections indicated in this figure are taken from ORIGEN-2 Library PWR47J33.LIB based on JENDL-3.3 for reference, which gives the effective one-group cross sections in PWRs with 4.7% enriched uranium fuel. As we can see here the capture reaction dominates in $^{237}$Np and the $^{238}$Np generated as the result will soon decay into $^{238}$Pu. Note that, however, the fission and capture cross sections of this short-lived isotope are very large. In reality we can not ignore the neutron reaction in $^{238}$Np under very high neutron flux though the life of this isotope is as short as 2.12 days. The quite recent measurement of the capture cross sectio of $^{238}$Np by Harada et al.[4] indicates even larger value. The produced $^{238}$Pu mainly undergoes capture reaction because the capture cross section is roughly one order larger the fission cross section.

Figure 2 indicate the fission rate in a P$^3$-A concept PWR along with the capture reaction rate in $^{238}$Pu for reference. In $^{238}$Pu the capture reaction (broken line) largely exceeds the fission reaction (triangle) at any satge of the burnup. This figure also indicates that the fission rate in $^{238}$Pu isotope, which plays the dominant role in the P$^3$ concept, is one-order maller than that of $^{239}$Pu. Even in the P$^3$ concept LWR, the reactivity is hold by $^{235}$U fission in the low burup satge and then $^{239}$Pu follows it in the later stage.

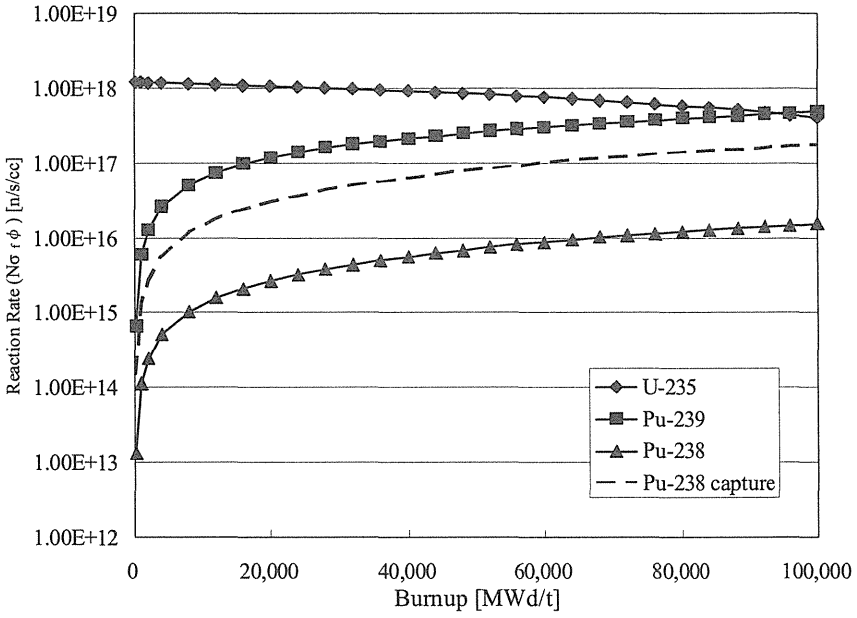



Fig. 2 Fission rate in a P$^3$-A concept PWR along with the capture reaction rate in $^{238}$Pu. The uranium enrichment and the $^{237}$Np doping fraction is 10% and 2%, respectively.

### 3. Nuclear Data

In the P$^3$ concept reactors, the isotopic fraction of $^{238}$Pu is assumed to be fairy large. The percentage becomes from ten to several tens in total plutonium[3]. It is seen also from Fig.2, where the neutron capture rate in $^{238}$Pu is comparable to $^{239}$Pu fission rate at any stage of the burnup. The capture cross sections of $^{237}$Np and $^{238}$Pu are very important because these govern the production and depletion of $^{238}$Pu, the protector of plutonium.

Figure 3 shows the capture cross section of $^{237}$Np in the thermal energy region. Two libraries, ENDF/B-VI and JEFF-3 give 181.02 barns at 0.0235 eV after the rather old experiment by Weston and Todd[5]. For this particular value, JENDL-3.3 gives 161.71 barn on the basis of the measurement by Kobayashi et al.[6]. In addition Katoh et al.[7] reported 141.7 barns in their very recent experiment. This new value is 13% lower than JENDL-3.3, which gives the 12% lower value than ENDF/B-VI and JEFF-3. Considering this situation we have to assume an uncertainty more than ±10%. Being more conservative it might be ±20%. From a preliminary sensitivity study this value of uncertainty in the capture cross section give rise to the same order of ambiguity in the $^{238}$Pu concentration generated from $^{237}$Np. As for the energy range from thermal to keV we can, however, expect a new experimental data from a new Japanese project, in which Igashira et al.[8] plan to develop a novel neutron detector and obtain the neutron data for important MAs including $^{237}$Np by applying it. Uncertainty mentioned above is expected to be remarkably reduced in a few years by their data.

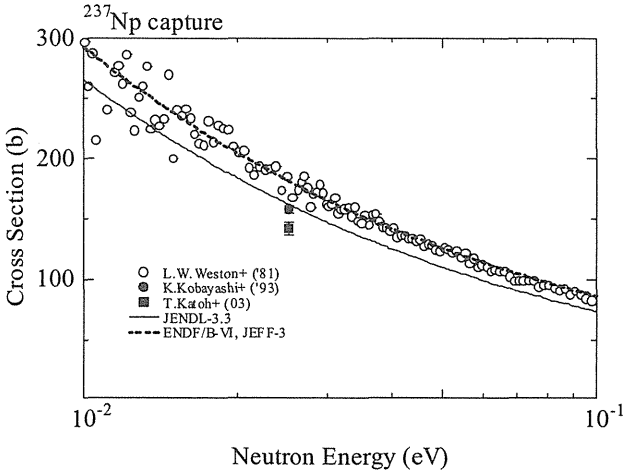



Fig.3 Capture cross section of 237Np

Another important reaction, which dominates the concentration of $^{238}$Pu, is the capture in $^{238}$Pu itself, because it is depleted mostly through this reaction. Further this reaction dominates the production of $^{239}$Pu. Remember it is also generated from $^{238}$U which is the main stream of the $^{239}$Pu production. The present status of the capture cross section data is shown in Fig. 4. Both JENDL-3.3 and JEFF-3 adopt the same value of 540.3 barns after the rather old recommendation by Mughabghab[9], which is 540±7 barns. ENDF-B/VI takes 561.08 barns, that is 4% higher than the other two libraries.

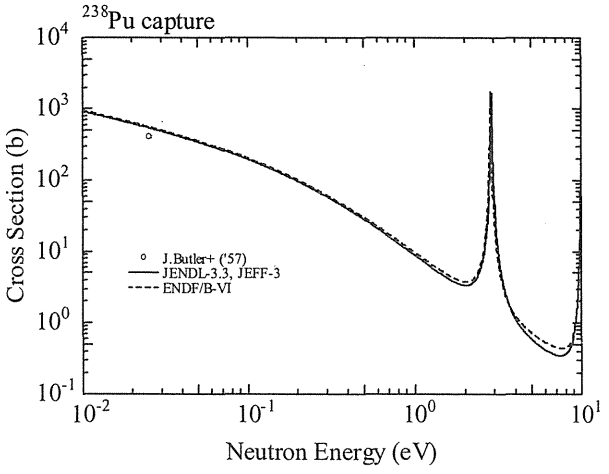



Fig. 4 Capture cross section of 238Pu

In this sense, the three libraries are rather consistent with each other because the 4% difference is not sizable. The experimental value, however, is very scarce and, then, we should expect large uncertainty in this cross section and need new reliable experimental data. Anyway, this will be one of the key cross section data in the $P^3$-concept reactor design.

As we saw in Fig. 2 the fission in $^{238}Pu$ is more than one order smaller than those in $^{235}U$ and $^{239}Pu$. This means that this reaction play only a small role in the neutronic performance of the $P^3$ concept LWR core. In this sense fairy large uncertainty is tolerable for the $^{238}Pu$ fission cross section data. This is also the case for $^{237}Np$ fission because the effective fission cross section in LWR is even four times smaller than $^{238}Pu$ as we can see in Fig. 1. The $^{237}Np$ and $^{238}Pu$ are, however, plays dominant roles in the $P^3$ concept reactor. Therefore we have to try to evaluate and validate all the nuclear data more strictly for the $P^3$ Project than ever. For validation of the nuclear data, irradiation experiments are planned at Advanced Test Reactor in INEEL and also in the Japanese fast test reactor JOYO in the framework of the $P^3$-A project[10]. Some sample reactivity measurements at critical facilities are also in the scope. We can expect that the nuclear data needed for design of $P^3$-concept reactors will be tested and improved through the analysis of these experimental data.

## 4. Concluding Remarks

Peaceful use of nuclear energy will not go forward without solving the problem of the nuclear proliferation. A new concept called $P^3$ (Protected Plutonium Production) was proposed by M Saito et al. to resolve this problem. The concept is based on the fuel protection by $^{238}Pu$ isotope generated from $^{237}Np$ doped in the fresh fuel. We surveyed the status of nuclear data relevant to $P^3$-concept reactor design. The reliability of the capture cross section data for $^{237}Np$ and $^{238}Pu$ is far from satisfactory and more accurate experiments and evaluations are required. As fissions in these nuclides do not always play any remarkable role in the $P^3$ concept LWR, we can be fairly tolerable about the uncertainty of the fission cross section data.

## Acknoledgement

This work has been supported by the Ministry of Education, Culture, Sport, Science and Technology.

## References

1) Saito, M. et al., TRANSACTIONS, American Nuclear Society, Vol. 87, 2002, pp.333-335
2) Saito, M. et al., Int. Conf. on Innovative Technology for Nuclear Fuel Cycles and Nuclear Power, Vienna, Austria, June 23-25, 2003
3) M. Saito, H. Sagara, and Y. Peryoga, TRANSACTIONS, American Nuclear Society Winter Meeting, Washington D.C, Nov. 14-18, 2004

4) H.Harada et al., *J. Nucl. Sci. Technol.*, **41 [1],** 1-6 (2004)
5) L.W. West and J.H.Todd, *Nucl. Sci. Engn.*, **79,** 184-196 (1981)
6) K. Kobayashi, A. Yamanaka, I. Kimura, *J. Nucl. Sci. Technol.*, **31 [12],** 1239-1247 (1994)
7) T.Katoh et al., *J. Nucl. Sci. Technol.*, **40 [8],** 559-603 (2003)
8) M.Igashira, "A Nuclear Data Project in Japan," Int. Conf. on Nuclear Data for Science and Technology, Fanta Fe, Sept.26-Oct.1, 2004
9) S.F.Mughabghab, "Neutron Cross sections, Vol. 1, Neutron Resonance Parameters and Thermal Cross Sections, Part B, Z=51-100", Academic Press (1984)
10) M. Itoh, et al., TRANSACTIONS, American Nuclear Society Winter Meeting, Washington D.C, Nov. 14-18, 2004

JP0550246



## 2.5 Error Estimation for ADS Nuclear Properties by using Nuclear Data Covariances

Kazufumi TSUJIMOTO
Center for Proton Accelerator Facilities, Japan Atomic Energy Research Institute
Tokai-mura, Naka-gun, Ibaraki-ken 319-1195
e-mail : ktsuji@omega.tokai.jaeri.go.jp

Error for nuclear properties of accelerator-driven subcritical system by the uncertainties of nuclear data was performed. An uncertainty analysis was done using the sensitivity coefficients based on the generalized perturbation theory and the covariance matrix data. For major actinides and structural material, the covariance data in JENDL-3.3 library were used. For MA, newly evaluated covariance data was used since there had been no reliable data in all libraries.

### *1. Introduction*

The Japanese long-term program called OMEGA has started in 1988 for research and development of new technologies for partitioning and transmutation of minor actinides (MA) and fission products. Under the OMEGA Program, for a dedicated transmutation system, the Japan Atomic Energy Research Institute (JAERI) has been proceeding with the research and development on accelerator-driven subcritical system (ADS)[1].

The uncertainties of nuclear properties of ADS are very significant both on the safety assessment and the economic evaluation. High $k_{eff}$, for example, implies small radial peaking and low proton beam current but risk of approaching criticality under accidental conditions will increase. Therefore, uncertainties on the subcriticality level must be include in the definition of the design margin. In this study, preliminary error estimation due to uncertainties of the nuclear data for ADS nuclear properties, such as the subcriticality and the coolant lead-bismuth (Pb-Bi) void reactivity, was performed.

### *2. Uncertainty Analysis*

#### *Sensitivity Analysis*

Some reactor parameter $R$, such as $k_{eff}$ or a reactivity coefficient, can be represent as a function of cross-section data. Sensitivity coefficients are defined physically such that they represent the effect on the integral parameter $R$ due to the change of the cross-section data $\sigma$. Based on the generalized perturbation theory, the sensitivity coefficients are formally given by

$$S = \frac{\partial R}{R} \times \frac{\sigma}{\partial \sigma}$$

Sensitivity analysis produce energy-dependent sensitivity coefficients that give the relative change in the integral parameter $R$ as a function of relative changes in the cross-section data by nuclide, reaction, and energy. The calculations of the sensitivity coefficients were performed using SAGEP code[2] with JENDL-3.3 library.

The calculated core was a Pb-Bi cooled ADS proposed by JAERI[3] for a dedicated transmutation system of MA. For the core fuel, mixture of mono-nitride of MA (60%) and plutonium (40%) was used with an inert matrix, ZrN. The isotopic composition of MA and Pu were assumed considering the following reprocessing scheme. The spent PWR fuel of 50 GWd/t burnup

was reprocessed after 7 years cooling, and MA and Pu were recovered. Before fabrication of the ADS fuel, additional 3-year period after recovery of MA and Pu was assumed[3]. Nitrogen with $^{15}N$ enriched (100%) was assumed to be used for both (MA,Pu)-nitride and ZrN.

The calculational results of the sensitivity coefficients for $k_{eff}$ by nuclide and reaction are shown in Fig.1. The results show that the sensitivity coefficients of fission cross section and ν-value of the actinide nuclides are significant large. The contributions of capture cross section of MA, such as $^{237}Np$ and $^{241}Am$, are also relatively large. In the structural, coolant and other material, the sensitivity coefficients of elastic scattering of $^{15}N$ and inelastic scattering of Pb and Bi are important. The energy break down of the sensitivity coefficients are presented in Fig.2 for $^{239}Pu$ and $^{241}Am$ which have relatively large sensitivity for $k_{eff}$. For $^{241}Am$, The sensitivity coefficients of fission cross section and ν-value have peak values about 1MeV because the threshold fission cross section, while that of capture cross section are large from 10keV to 1MeV.

*Covariance Matrix*

Present status of nuclear data for MA is not sufficient, and there is large discrepancy among major nuclear libraries. Although the evaluation is, recently, proceeding with variance-covariance data, such data for MA are practically non-existent in all major libraries. In this study, since the main calculations were performed using JENDL-3.3 library, variance-covariance data provided in JENDL-3.3 library for major actinide ($^{239, 240, 241}Pu$) and structural material (Fe, Cr, Mn, Ni). For MA ($^{237}Np$, $^{241}Am$ and $^{243}Am$), newly evaluated valiance-covariance data were used. The evaluations of capture, fission and number of fission neutron were done by Nuclear Data Center in JAERI based on JENDL-3.3 library. The variance data (diagonal section of covariance matrix) of capture and fission cross section processed by the ERRORJ code[4] of $^{237}Np$, $^{241}Am$ and $^{243}Am$ are shown in Fig.3 with discrepancies between other libraries (ENDF/B-VI.8 and JEFF-3.0) and JENDL-3.3. The variance data of fission cross section are relatively small above threshold energy of fission reaction. On the other hand, the variance data of capture cross section for $^{241}Am$ and $^{243}Am$ are relatively large in the energy region from 100keV to 1MeV since there is less experimental data in this energy region. The variance data value of ν-value are 0.5-1.0% for these MA nuclides. These values are much smaller than those of capture and fission cross section.

For other structural materials like Pb and Bi, and $^{242}Pu$, the covariance data in ENDF/B-VI were used for this study. For the nuclide for which there are no covariance data in all libraries, such as $^{15}N$, tentative variance (not covariance) data are estimated from the discrepancies among major nuclear data libraries. The estimations of the covariance data for not only MA but also structural material, such as Pb, Bi, and $^{15}N$ are desirable for future study.

*Error Estimations*

The error estimations of the integral reactor parameter were performed using the sensitivity coefficients S and the covariance matrix M. The uncertainties of the integral parameter can then be obtained from GMG[t] by matrix calculation. The results of the uncertainty analysis for $k_{eff}$ and Pb-Bi void reactivity are given in Fig.4 together with main contributor for the total uncertainties. Total value is the square root of the sum of the squares. The total value (±0.9%) for $k_{eff}$ is higher than corresponding values for critical fast reactor. The major contributor among the actinide nuclides is $^{237}Np$ and $^{241}Am$, and the capture cross-section of $^{241}Am$ especially play a major role. For Pb-Bi void reactivity, the capture cross-section of $^{241}Am$ is much important than Pb and Bi. The reason of little contribution of Pb and Bi for the void reactivity is that the void reactivity for only core region was estimated in this study, so that the leakage effect has relatively lsmall contribution for the void reactivity.

*3. Conclusions*

The preliminary error estimations for ADS nuclear properties were carried out using the sensitivity coefficients and the covariance matrix. As expected, the important nuclear data for the uncertainties of $k_{eff}$ and Pb-Bi void reactivity were the cross-section data of MA, especially the capture cross section of $^{241}$Am. This study is a first step to provide the guideline on priorities for new evaluations or validation experiments. From the results of this study, present status of the calculation accuracies for MA-dominant fueled ADS and required improvement on specific nuclear data were derived.

In this study, as typical nuclear properties, $k_{eff}$ and Pb-Bi void reactivity were analysis. For further work, bunrnup characteristics, such as burnup reactivity change and transmutation performance. However, for this purpose, it will be needed that the generalized perturbation theory should be extended to the system with external source. Moreover, in this study, although covariance data of capture, fission and ν-value for $^{237}$Np, $^{241}$Am and $^{243}$Am, other data, such as fission spectrum, delayed-neutron fraction, and other nuclide will be necessary.

*References*

[1] T. Mukaiyama, T. Takizuka, M. Mizumoto, Y. Ikeda, T. Ogawa, A. Hasegawa, H. Takada, and H. Takano : "Review of research and development of Accelerator-driven System in Japan for transmutation of long-lived nuclides," *Prog. Nucl. Energy*, ADS special edition, **38**, No. 1-2, p.107, (2001).

[2] A. Hara, T. Takeda, and Y. Kikuchi :"SAGEP: Two-Dimensional Sensitivity Analysis Code Based on Generalized Perturbation Theory", JAERI-M-84-27 (in Japanese).

[2] Tsujimoto K., Sasa T., Nishihara K., Takizuka T., and Takano H.,:"Accelerator-Driven System for Transmutation of High-level Waste," *Prog. Nucl. Energy*, **37**, No. 1-4, p. 339, (2000).

[3] "Accelerator-driven Systems (ADS) and Fast Reactors (FR) in Advanced Nucler Fuel Cycles : A Comparative Study," Nuclear Energy Agency, Organization for Economic Cooperation and Development (2002).

[4] G. Chiba :"ERRORJ — Covariance Processing Code Version2.2", JNC TN9520 2004-003 (2004).

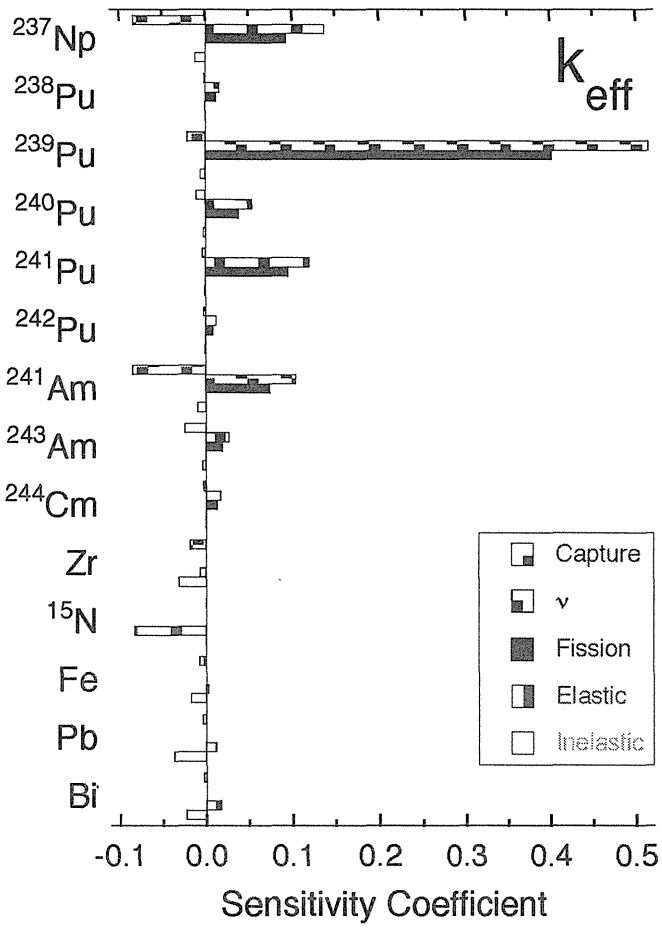



Fig.1 Sensitivity coefficients of $k_{eff}$ by nuclide and reaction.

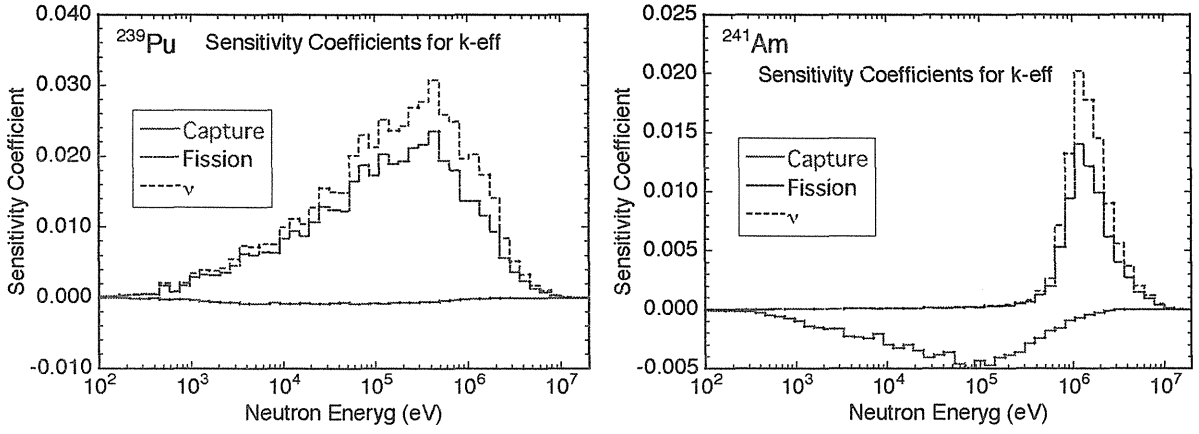
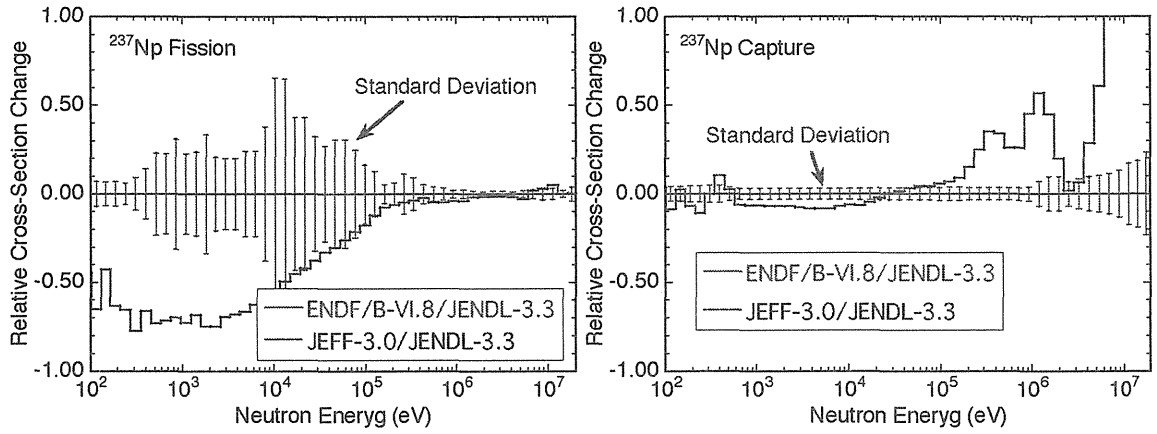
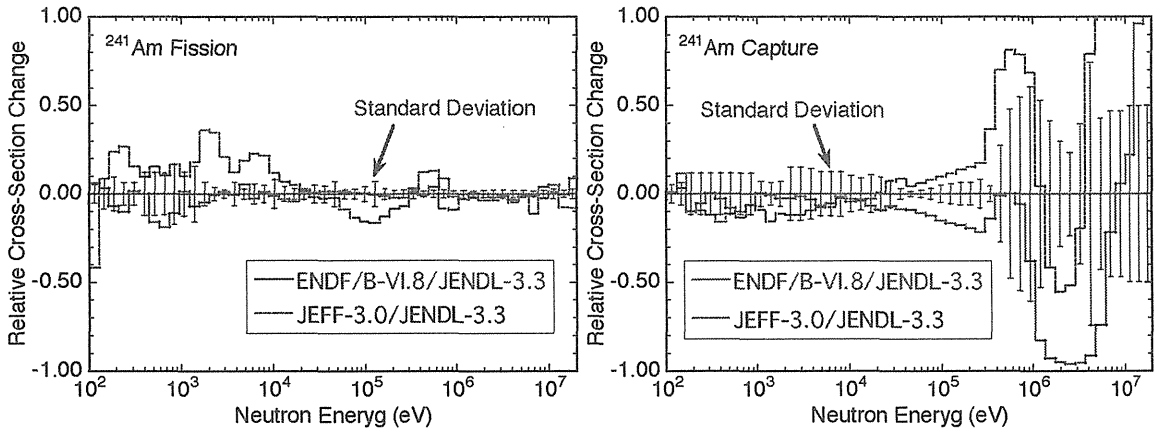


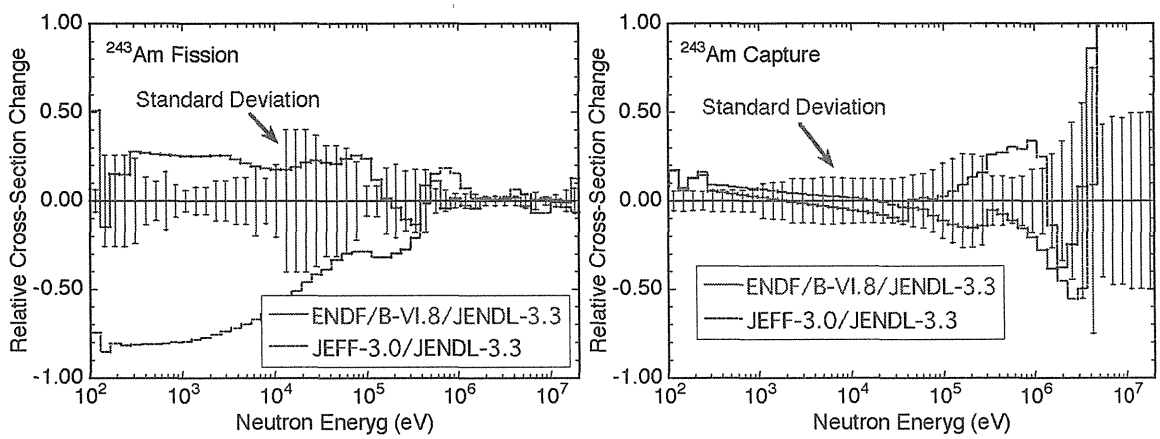

Fig.2 Energy break down of sensitivity coefficients of $^{239}$Pu and $^{241}$Am.




(a) $^{237}$Np




(b) $^{241}$Am




(c) $^{243}$Am

Fig.3 Newly evaluated variance data of capture and fission cross section for $^{237}$Np, $^{241}$Am and $^{243}$Am. Variance data is diagonal data of covariance matrix proceeded by ERRORJ code.

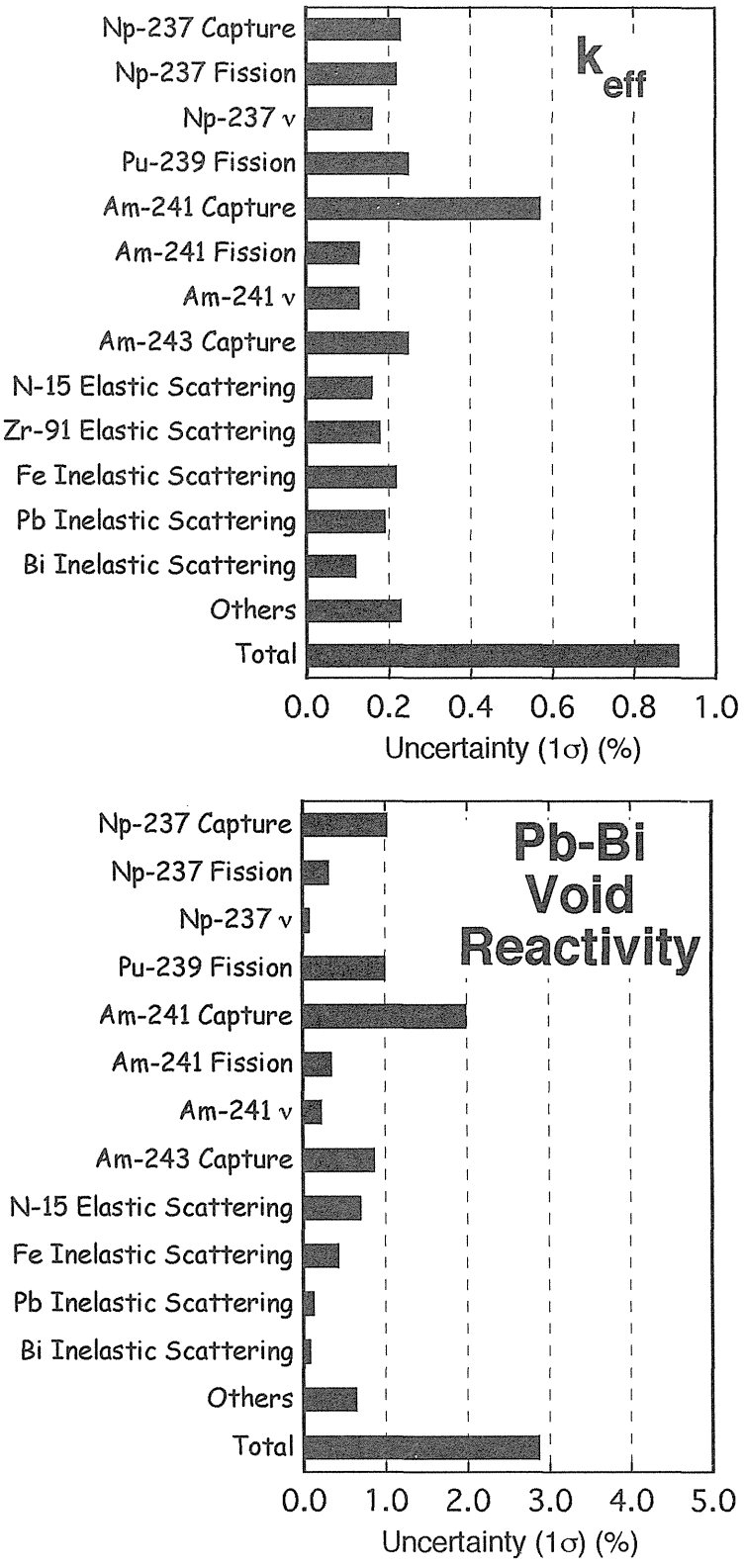



Fig.4 The results of error estimation for keff and Pb-Bi void (core only) reactivity.

JP0550247



# 2.6 Fission Cross Section Measurements at Intermediate Energies

Alexander LAPTEV*

*Japan Nuclear Cycle Development Institute*
*Tokai works, Tokai-mura, Naka-gun, Ibaraki-ken 319-1194, Japan*
*e-mail: laptev@jnc.go.jp*

The activity in intermediate energy particle induced fission cross-section measurements of Pu, U isotopes, minor actinides and sub-actinides in PNPI of Russia is reviewed. The neutron-induced fission cross-section measurements are under way in the wide energy range of incident neutrons from 0.5 MeV to 200 MeV at the GNEIS facility. In number of experiments at the GNEIS facility, the neutron-induced fission cross sections were obtained for many nuclei. In another group of experiments the proton-induced fission cross-section have been measured for proton energies ranging from 200 to 1000 MeV at 100 MeV intervals using the proton beam of PNPI synchrocyclotron.

## 1. Introduction

There is a long-standing need for information about fission reactions of heavy nuclei induced by particles at intermediate energies. Such information is required for many applications, e.g., accelerator-driven transmutation of nuclear waste, energy generation, fundamental physics, etc. To make progress in these areas requires improved accuracy and reliability of the relevant nuclear data, and many of these data needs are not yet fulfilled [1].

The Petersburg Nuclear Physics Institute (PNPI) of Russian Academy of Sciences has a big research program devoted to intermediate energies particles induced fission cross section measurements. The neutron-induced fission cross-section measurements are under way in the wide energy range of incident neutrons from 0.5 MeV to 200 MeV at the GNEIS facility [2]. During the first stage of this research the measurements of fission cross-sections of $^{233}$U, $^{238}$U, $^{232}$Th, $^{237}$Np, $^{239}$Pu, $^{nat}$Pb and $^{209}$Bi have been performed [3]. This investigation has been done jointly by PNPI and Khlopin Radium Institute (KRI) in collaboration with Nuclear Data Center of JAERI. Not long ago the new measurements of neutron-induced fission cross-section of $^{240}$Pu, $^{243}$Am and $^{nat}$W have been completed at the GNEIS facility [4,5] jointly by PNPI and KRI in collaboration with LANL. Other research team of PNPI measured the proton-induced fission cross sections of $^{233}$U, $^{235}$U, $^{238}$U, $^{232}$Th, $^{237}$Np, $^{239}$Pu, $^{nat}$Pb and $^{209}$Bi at the proton beam of PNPI synchrocyclotron energies ranging from 200 to 1000 MeV at 100 MeV intervals [6]. This article presents a brief review of these both neutron- and proton-induced fission cross-section measurements.

## 2. Neutron-induced fission

### 2.1. Experimental set-up

At works [3-5] the fission cross-section ratios for investigated nuclei relative to $^{235}$U have been measured using the neutron time-of-flight spectrometer GNEIS. This facility is based on the 1 GeV proton synchrocyclotron of PNPI and has average intensity $3\cdot10^{14}$ n/s, a burst duration 10 ns and repetition rate up to 50 Hz. The flight path was 48.5 m. The beam is shaped by a system of iron, brass and lead collimators. The measurements were carried out with the use of a sweeping magnet placed at flight path of 30 m. A schematic layout of the experimental set-up is shown in Fig. 1.

The fission reaction rate was measured using two fast parallel plate ionization chambers filled with methane (94-100 %) and $CF_4$ (6-0 %) mixture working gas at the absolute pressure of 2.5 – 3.5 atm. [3] or pure methane at about 3 atm. [4,5]. Both chambers (for actinides and sub-actinides) had

* On leave from the Petersburg Nuclear Physics Institute, Gatchina, Russia.

several sections. Each section contains one pair of cathode and anode plates spaced by 5 mm. The high quality fissionable materials have been used for actinide targets production. The target foils were 150-560 μg/cm$^2$ thick and 180 mm in diameter, deposited on one side of 0.05-mm-thick aluminum backings. Also, a weak $^{252}$Cf deposit was applied on the actinide foils to match the gains of electronics.

For each nucleus under investigation, the time-of-flight and pulse height spectra were accumulated using the data acquisition system based on a 100-MHz FLASH-ADC in each measuring channel. The start signal was provided by gamma flash-detector, a bare PMT placed in the neutron beam. This signal was also used to control a single-turn deflection of the proton beam to the neutron-producing target.

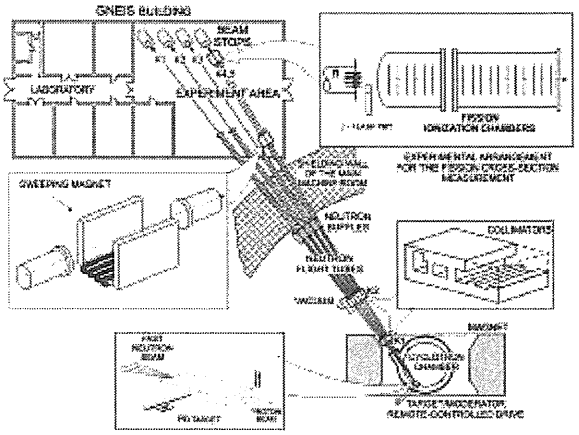



**Fig. 1** Schematic layout of the GNEIS facility and experimental arrangement for fission cross-section measurements.

## 2.2. Data processing

Identification of start (gamma flash) and stop (fission) signals on the background of electronic noise, alpha- and pile-up events in works [3-5] has been made by a method of digital filtering [7]. The raw data reduction included composing pulse height and TOF information into a 2-dimensional matrix consisting of 512 TOF channels by 128 amplitude channels. The example of this matrix in case of $^{240}$Pu is shown in Fig. 2. The average pulse height spectrum in case of $^{nat}$W and its fission and background components are presented in Fig. 3.

The "*time-of-flight vs neutron energy*" calibration was made with an accuracy 0.03 % using the positions of lead total cross section resonances and the weak gamma-flash peak observed in the TOF-spectra from which a true time-zero was derived (v. Fig. 4).

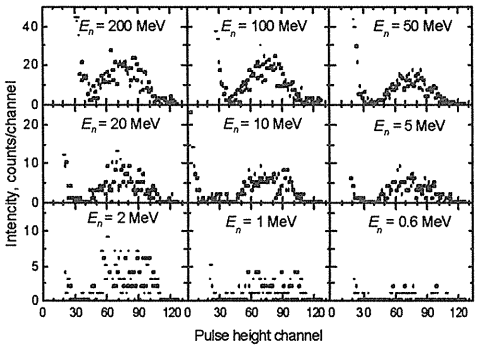



**Fig. 2** Pulse height spectra of $^{240}$Pu measured at different neutron energies.

In the data reduction process, the fission event counting rates were corrected for (1) background events, (2) the neutron flux attenuation for investigated and reference nuclei, (3) fragment losses in the targets due to finite deposit thickness, and (4) neutron momentum transfer and angular anisotropy of fission fragments. The attenuation correction was calculated using the neutron total cross-sections from ENDF/B-VI. A correction for the energy dependent linear-momentum and angular-momentum effects were calculated following a method of G. Carlson [8]. The correctness and accuracy of this approach was tested by comparison of the TOF-spectra obtained for two $^{235}$U targets placed in the chamber at 200 mm distance between them.

The fission cross-section ratios for investigated nuclei and the reference nucleus $^{235}$U obtained in the "shape" measurements have been normalized using the following methods:

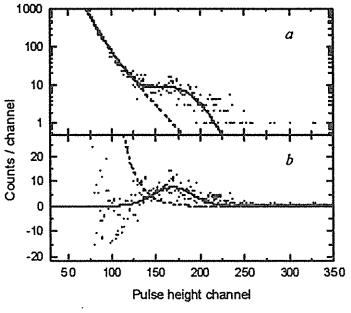



**Fig. 3** (a) Measured pulse height spectrum for one foil of $^{nat}$W; the solid curve denotes fission fragments and the dash curve shows background events; (b) pulse height spectrum for fission fragments after background subtraction; the background is shown again as the dashed curve.

1) calculation of the target thickness and detection efficiency ratios;
2) normalization to the recommended data;
3) threshold cross-section method [9].

All three methods were used, but the best accuracy was obtained using the threshold method for threshold isotopes $^{238}$U and $^{232}$Th. For this purpose, a part of the measurements [3] has been done using mixed targets. The fission cross-section ratio normalization for $^{233}$U, $^{237}$Np and $^{239}$Pu in [3] has been done in the 1.75-4.0 MeV energy interval using the data of JENDL-3.2 file. In [5] the fission cross-section ratios for investigated actinide nuclei $^{240}$Pu, $^{243}$Am and the reference nucleus $^{235}$U obtained in the "shape" measurements have been normalized using the target thicknesses. An accuracy of last normalization was 5%.

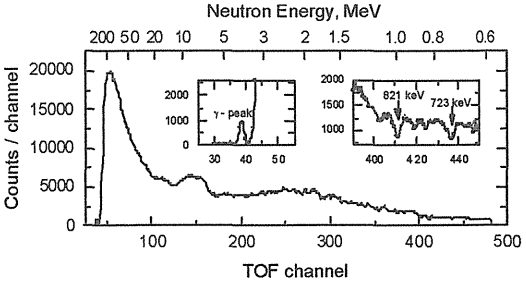



**Fig. 4** Time-of-flight spectra (10 ns channel width) obtained for $^{235}$U target after background subtraction. Inserts show TOF-spectra in regions of gamma-flash and lead resonances in more detail.

An absolute normalization of the measured cross-section ratios for sub-actinides $^{nat}$Pb, $^{209}$Bi in [3] and $^{nat}$W, $^{209}$Bi in [5] has been done using the thickness of the targets and detection efficiencies.

Finally, the normalized fission cross-section ratios have been converted to the cross-sections using the fission cross-section of $^{235}$U from JENDL-3.2 [10] below 20 MeV and the recommended data of A. Carlson *et al.* [11] above 20 MeV.

## 2.3. Results

The results of measurements [3] and [4,5] are shown in Figs. 5,6 (for actinides) and Figs. 7,8 (for sub-actinides) in comparison with other experimental data and some systematics and theoretical calculations. The error bars represent the statistical errors only (one standard deviation). These

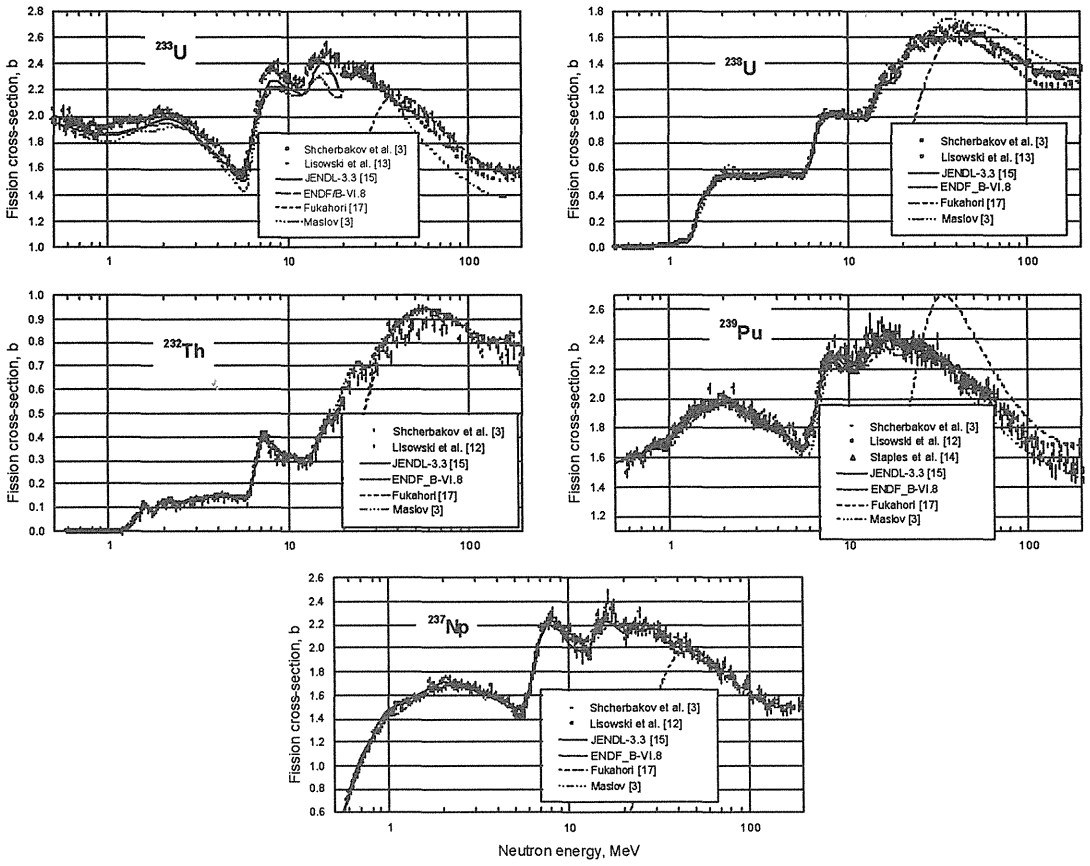



**Fig. 5** Fission cross section of $^{233}$U, $^{238}$U, $^{232}$Th, $^{239}$Pu and $^{237}$Np measured in [3] in the energy range 1-200 MeV.

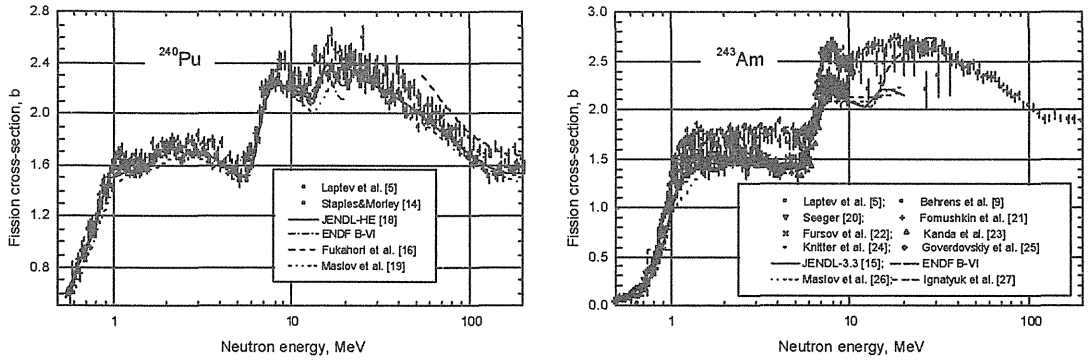



**Fig. 6** Fission cross section of $^{240}$Pu and $^{243}$Am measured in [4,5] in the energy range 1-200 MeV.

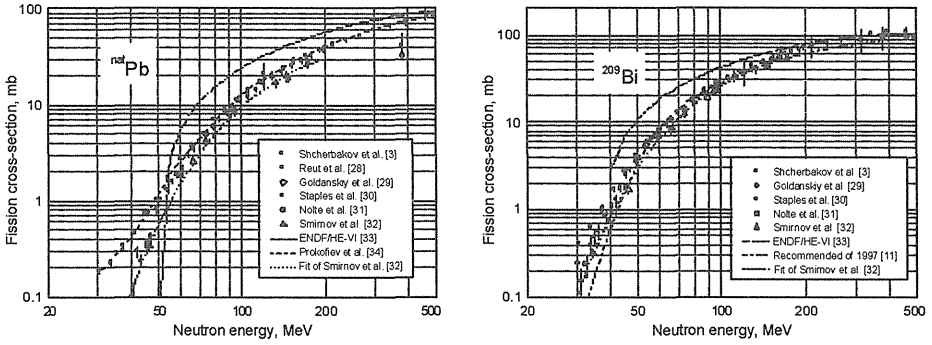



**Fig. 7** Fission cross section of $^{nat}$Pb and $^{209}$Bi measured in [3] in the energy range up to 200 MeV.

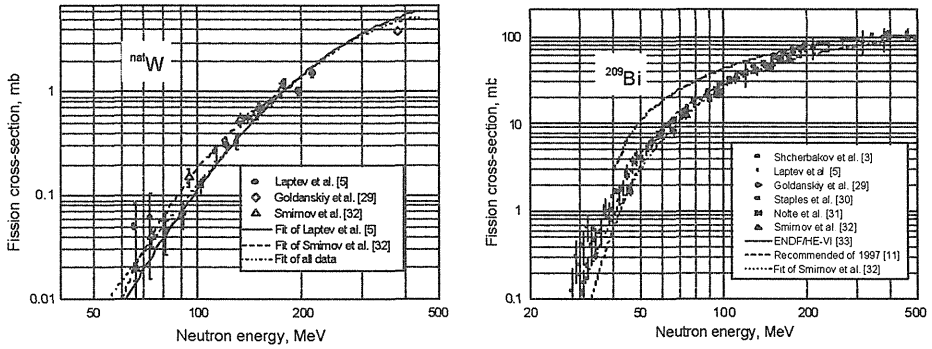



**Fig. 8** Fission cross section of $^{nat}$W and $^{209}$Bi measured in [5] in the energy range up to 200 MeV.

uncertainties are about 1-2 % at neutron energies above 1 MeV and that of sub-actinide nuclei $^{nat}$Pb and $^{209}$Bi varies from 12-20 % at 40 MeV to 1-2 % at 200 MeV but in case of $^{nat}$W it varies from 19 % at 100 MeV to 7 % at 200 MeV.

There is a some disagreement between data of [3] and that of Lisowski *et al.* [12,13] for $^{233}$U, $^{238}$U, $^{239}$Pu and $^{232}$Th above 20 MeV while both data sets are consistent for $^{237}$Np. In general, the comparison of data of [3] with results of other authors shows that in the overlapping energy regions (below 20 MeV) data of [3] are in reasonable agreement with evaluated data. The data of systematics [16,17] could be compared with experimental data only above 50 MeV and show a very strong disagreement with experiment in the case of $^{239}$Pu. The statistical model calculations of Maslov in [3] show satisfactory description of the measured fission cross-sections.

For $^{240}$Pu (Fig. 6) of [5], there is good agreement between these data and those of Staples and Morley [14] up to 70 MeV, but there are disagreements in the energy range of 70-200 MeV. Some other small differences are within stated errors. On the opinion of authors of [5], most of the differences are in normalization rather than shape. Such differences vanish, except for short ranges 1.5-3 and 7-8 MeV, after normalization of both data sets at neutron energy 14 MeV. Smooth curves

present cross section values from JENDL High Energy [18] and ENDF B-VI libraries, theoretical calculations of Maslov *et al.* [19] (Hauser-Feshbach statistical model) and systematics of Fukahori *et al.* [16]. All these evaluations show a rough agreement with data of [5] for $^{240}$Pu in the full energy range under investigation. But there are some visible disagreements in detailed data description. For example, the evaluation of JENDL-HE library [18] and the result of calculation [19] lie below data of [5] at the energy range above 40 MeV but the systematic [16] lies above these data.

For $^{243}$Am (Fig. 6) of [5], a comparison of these data with other data sets shows good agreement of the present data with that of Behrens *et al.* [9] and Goverdovskiy *et al.* [25]. There are no available previous data for the fission cross section of $^{243}$Am above ~40 MeV, these data have been obtained for the first time. In case of $^{243}$Am there are significant disagreements between previous data. The cross section values from the libraries JENDL-3.3 [15] and ENDF B-VI, theoretical calculations of Maslov *et al.* [26] and evaluation of Ignatyuk *et al.* [27] correspond to other data sets rather than [5]. Normalization of data for $^{243}$Am of [5] to libraries' 14 MeV value could not make agreement of all experimental data sets but withdraws disagreements with evaluations.

Above 50 MeV the data for $^{nat}$Pb of [3] (Fig. 7) are in a good agreement with that of Staples *et al.* [30], other data sets and the parameterization of Prokofiev *et al.* [34] based on the measurements with $^{nat}$Pb and $^{208}$Pb, including the data of Staples *et al.* [30] and other known at that moment experimental data carried out mainly in separate energy points. The ENDF/HE-VI data based on the systematics of Fukahori *et al.* [33] for $^{208}$Pb lies much higher than all experimental data.

In the case of $^{209}$Bi (Fig. 7), an agreement of the data [3] with that of other authors is good within the stated uncertainties. There is a noticeable discrepancy between data [3], as well as the data of Staples *et al.* [30], and the parameterization [11] at neutron energies below ~50 MeV and above ~120 MeV. The ENDF/HE-VI data [33] lies up to 2 times higher than all experimental data below ~150 MeV, but above this energy the tendency to agreement can be seen.

There is generally good agreement between data [5] and those of Refs. [29,32] for $^{nat}$W (Fig. 8), except for a possible discrepancy in the 90-100 MeV region. In the work [5] the neutron-induced fission cross-section of $^{nat}$W has been measured for the first time with a "white" neutron source. Smooth curves in Fig. 8 present fit of the data [5], fit of ref. [32] and fit of all data sets. Comparison (Fig. 8) of fission cross section of $^{209}$Bi measured in the experiment [5] with that obtained in previous measurement [3] shows a very good agreement.

## 3. Proton-induced fission

The proton-induced fission cross sections of the $^{233}$U, $^{235}$U, $^{238}$U, $^{232}$Th, $^{237}$Np, $^{239}$Pu, $^{nat}$Pb and $^{209}$Bi have been measured at the proton beam of PNPI synchrocyclotron energies ranging from 200 to 1000 MeV at 100 MeV intervals [6]. The measurement method is based on the registration in coincidence of both fission fragments by two parallel plate avalanche counters (PPAC's) located at very close distance from a target. To obtain the proton beams with different energies, the method of degrading of the initial 1000 MeV proton beam by copper degraders has been used.

The 100 % detection efficiency of fission fragments at a large solid angle acceptance (10 sr) has been achieved in the work [6]. The investigated targets have been produced by method of vacuum

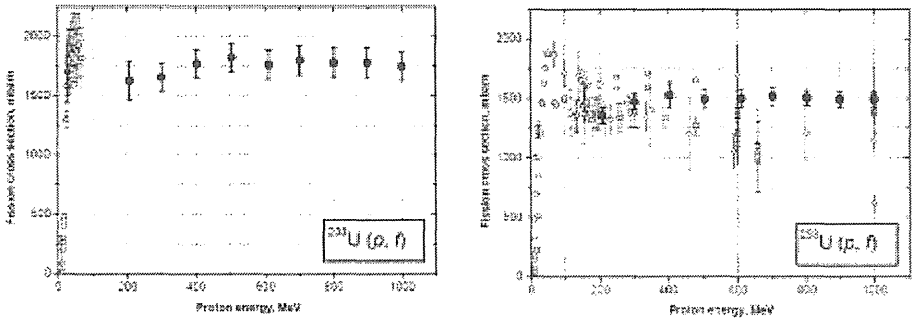



**Fig. 9** Fission cross section of $^{233}$U and $^{238}$U measured in [6] in the energy range 200-1000 MeV. Black circles are the results of [6] and open ones are previous data taken from reviews [35,36].

evaporation of fissile material. The thicknesses of targets were in the range from 100 to 450 μg/cm$^2$. The proton beam monitoring has been done at low beam intensity (~$10^5$ p/s) by direct count of scintillation telescope counters, and at high beam intensity (~$10^7$ p/s) by registration of *pp*-elastic scattering on the $CH_2$ target. The results [6] on energy dependence of total fission cross-sections of $^{233}$U and $^{238}$U targets are presented in Fig. 9. A statistical accuracy of the measured fission cross sections [6] is better than 1.5% and the total one is better than 10%. The cross sections for proton induced fission of $^{233}$U in the energy range 200-1000 MeV was obtained in [6] for the first time. According to opinion of authors [6], their results for $^{238}$U in the energy range from 300 to 900 MeV do not agree with a majority of the early-obtained data.

## References


[1] M. Salvatores, *J. Nucl. Sci. Tech.*, Suppl. 2, 4 (2002).
[2] N.K. Abrosimov, G.Z. Borukhovich, A.B. Laptev *et al.*, *Nucl. Instr. Meth.* **A242**, 121 (1985).
[3] O. Shcherbakov, A. Donets, A. Evdokimov *et al.*, *J. Nucl. Sci. Tech.*, Suppl. 2, 230 (2002).
[4] A.B. Laptev, A.Yu. Donets, A.V. Fomichev *et al.*, *Nucl. Phys.* **A 734S**, E45 (2004).
[5] A.B. Laptev, A.Yu. Donets, V.N. Dushin *et al.*, Report at the *Int. Conf. on Nucl. Data for Sci. and Tech. (ND2004)*, Santa Fe, New Mexico, USA, Sept. 26-Oct. 1, 2004.
[6] A. Kotov, Y. Gavrikov, L Vaishnene *et al.*, Report at the *XVI Int. Workshop on Physics of Nuclear Fission*, IPPE, Obninsk, Russia, October 7-10, 2003.
[7] D.D. Burgess, R.J. Tervo, *Nucl. Instr. Meth.* **214**, 431 (1983).
[8] G.W. Carlson, *Nucl. Instr. Meth.* **119**, 97 (1974).
[9] J.W. Behrens, J.C. Browne, *Nucl. Sci. Eng.* **77**, 444 (1981).
[10] T. Nakagawa, S. Shibata, S. Chiba *et al.*, *J. Nucl. Sci. Tech.* **32**, 1259 (1995).
[11] A.D. Carlson, S. Chiba, F.-J. Hambsch *et al.*, IAEA Report INDC(NDS)-368. Vienna, 1997.
[12] P.W. Lisowski, J.L. Ullmann, S.J. Balestrini *et al.*, *Proc. of Int. Conf. on Nucl. Data for Sci. and Tech.*, Mito, Japan, May 30-June 3, 1988, p.97.
[13] P.W. Lisowski, A. Gavron, W.E. Parker *et al.*, *Proc. of Int. Conf. on Nucl. Data for Sci. and Tech.*, Julich, Germany, May 13-17, 1991. Ed. S.M. Qaim, Springer-Verlag, 1992, p.732.
[14] P. Staples, K. Morley, *Nucl. Sci. Eng.* **129**, 149 (1998).
[15] K. Shibata, T. Kawano, T. Nakagawa *et al.*, *J. Nucl. Sci. Tech.* **39**, 1125 (2002).
[16] T. Fukahori, S. Pearlstein, Report BNL-45200, 1991.
[17] T. Fukahori, *private communication*, 1999.
[18] JENDL High Energy Data File 2004. Numerical data were obtained from T. Fukahori, 2004.
[19] V. Maslov, Yu. Porodzinskij, M. Baba, A. Hasegawa, *J. Nucl. Sci. Tech.*, Suppl. 2, 80 (2002).
[20] P.A. Seeger, LANL Report LA-4420. Los Alamos, 1970.
[21] E.F. Fomushkin, G.F. Novoselov, Ju.I. Vinogravdov *et al.*, *Ydernie Konstanti* **3/57**, 17 (1984).
[22] B.I. Fursov, E.Ju. Baranov, M.P. Klemyshev *et al.*, *Atomnaya Energiya* **59**, 339 (1985).
[23] K. Kanda, H. Imaruoka, H. Terayama *et al.*, *J. Nucl. Sci. Tech.* **24**, 423 (1987).
[24] H.-H. Knitter, C. Budtz-Jorgensen, *Nucl. Sci. Eng.* **99**, 1 (1988).
[25] A.A. Goverdovskiy, A.K. Gordyushin, B.D. Kuz'minov *et al.*, *Atomn. Energ.* **67**, 30 (1989).
[26] V.M. Maslov, E.Sh. Sukhovitskij *et al.*, IAEA Report INDC(BLR)-006. Vienna, 1996.
[27] A.V. Ignatyuk, A.I. Blokhin, V.P. Lunev *et al.*, *VANT, Ser. Jad. Konst.*, issue 1, 25 (1999).
[28] A.A. Reut et al., Report of the Institute of Physics Problems, 1950.
[29] V.I. Goldanskiy, E.Z. Tarumov, V.S. Penkina, *Dokl. Akad. Nauk* **101**, 1027 (1955).
[30] P. Staples *et al.*, *Bull. Am. Phys. Soc.* **40**, 962 (1995).
[31] R. Nolte, M.S. Allie, P.J. Binns *et al.*, *J. Nucl. Sci. Tech.*, Suppl. 2, 311 (2002).
[32] A.N. Smirnov, V.P. Eismont, N.P. Filatov *et al.*, Submitted to *Phys. Rev.* **C** (2004).
[33] T. Fukahori, S. Pearlstein, IAEA Report INDC(NDS)-245. Vienna, 1991.
[34] A.V. Prokofiev, S.G. Mashnik, A.J. Sierk, LANL Report LA-UR-98-0418. Los Alamos,1998.
[35] A.I. Obukhov, *Phys. Particl. Nucl.* **32**, 162 (2001).
[36] A.V. Prokofiev, *Nucl. Instr. Meth.* **A 463**, 557 (2001).

# 2.7 Nuclear Data Evaluation for JENDL High Energy File and Its Benchmark

Yukinobu Watanabe
*Department of Advanced Energy Engineering Science, Kyushu University, Kasuga, Fukuoka 816-8580, Japan*
Corresponding email: watanabe@aees.kyushu-u.ac.jp

An overview is reported of nuclear data evaluation for the JENDL High Energy (JENDL-HE) file which contains neutron and proton cross sections for energies up to 3 GeV for the whole 132 nuclides. The JENDL-HE evaluations are performed on the basis of experimental data and theoretical model calculations. For the cross section calculations, a hybrid calculation code system is constructed using some available nuclear model codes and systematics-based codes. The evaluated cross sections are compared with available experimental data and the other evaluations. Some preliminary results of benchmark tests are also presented.

## 1. Introduction

In recent years, nuclear data for energies over 20 MeV are needed from the point of view of accelerator-related applications, such as accelerator-driven transmutation system, radiotherapy with particle beams, and estimation of radiation effects induced by cosmic rays in microelectronics, *etc.* These applications require charged-particle data, particularly proton data, as well as neutron data in macroscopic transport and activation calculations. Under these backgrounds, there are several activities on high-energy nuclear data evaluations in LANL, NRG Petten, FZK, IPPE, KAERI and so on. Some of the data libraries produced in these evaluations are currently available. Among them, the LA150 library[1] is widely used in macroscopic transport calculations, which treats the nuclear interaction of neutrons and protons having energies up to 150 MeV with materials. In such calculations, the Monte Carlo codes based on microscopic simulation approach such as the intra-nuclear cascade model are built-in to deal with the nuclear processes at energies above 150 MeV, instead of the nuclear data library. Because of saving the computation time, however, the nuclear data above 150 MeV are also required in macroscopic transport and activation calculations. Thus, the Japanese Nuclear Data Committee (JNDC) has launched the JENDL High-Energy file (JENDL-HE) project[2], in which the cross sections for neutron and proton induced reactions up to 3 GeV are included for the total 132 nuclides shown in **Table 1**.

In this paper, the current status of the JENDL-HE file is reported with an outline of a nuclear model calculation code system used in the evaluation and comparisons of the JENDL-HE evaluation with available experimental data and other evaluations. Preliminary results of some benchmark tests using the transport code MCNPX are also given.

Table 1. List of nuclides to be included in JENDL High Energy file

| | |
|---|---|
| Released (66 nuclides) | $^{1}$H, $^{12,13}$C, $^{14}$N, $^{16}$O, $^{24,25,26}$Mg, $^{27}$Al, $^{28,29,30}$Si, $^{39,41}$K, $^{40,42,43,44,46,48}$Ca, $^{46,47,48,49,50}$Ti, $^{51}$V, $^{50,52,53,54}$Cr, $^{55}$Mn, $^{54,56,57,58}$Fe, $^{59}$Co, $^{58,60,61,62,64}$Ni, $^{63,65}$Cu, $^{64,66,67,68,70}$Zn, $^{90,91,92,94,96}$Zr, $^{93}$Nb, $^{180,182,183,184,186}$W, $^{196,198,199,200,201,202,204}$Hg |
| In prepartion (66 nuclides) | $^{2}$H, $^{6,7}$Li, $^{9}$Be, $^{10,11}$B, $^{15}$N, $^{18}$O, $^{19}$F, $^{23}$Na, $^{35,37}$Cl, $^{35,38,40}$Ar, $^{69,71}$Ga, $^{70,72,73,74,76}$Ge, $^{75}$As, $^{74,76,77,78,80,82}$Se, $^{89}$Y, $^{92,94,95,96,97,98,100}$Mo, $^{113,115}$In, $^{197}$Au, $^{204,206,207,208}$Pb, $^{209}$Bi, $^{232}$Th, $^{233,234,235,236,238}$U, $^{237}$Np, $^{238,239,240,241,242}$Pu, $^{241,242,242m,243}$Am, $^{243,244,245,246}$Cm |

## 2. Nuclear model calculation code system

In the present JENDL-HE evaluation, a model calculation code system combining some nuclear model codes is used to produce the high-energy cross section data. A schematic diagram of the code system is illustrated in **Fig.1**. It consists of two different parts in accordance with the incident energy. For energies below 150-250 MeV, the conventional codes used widely in the evaluations below 20 MeV are applied, and

Monte Carlo calculation codes based on the intra-nuclear cascade (INC) model or quantum molecular dynamics (QMD) are used mainly for those above 150-250 MeV.

The main code for energies below 150-250 MeV, GNASH[3], is based on statistical Hauser-Feshbach plus preequilibrium exciton models to predict nuclear reaction cross sections for particle and γ-ray emissions. A modified version of the code EXIFON[4] is used as an alternative code for N and O as well. The optical model is employed for predictions of the total, reaction, and elastic scattering cross sections. Optical model calculations are carried out using ECIS96[5] or OPTMAN[6]. The code OPTMAN is based on the coupled-channels method with the nuclear Hamiltonian parameters determined by the soft-rotator model, and is used only for C, Mg, and Si. Transmission coefficients provided by the optical model calculation are employed in the GNASH calculations of particle and γ-ray emission cross sections and isotope production cross sections. The cross sections for inelastic scattering to low-lying excited states are also calculated using ECIS96 or OPTMAN. For some cases, the code DWUCK4[7] based on DWBA is used for direct reaction calculations for discrete state transitions including deuteron pick-up and charge exchange processes as well.

In the energy range above 150-250 MeV, either JAM[8] or QMD[9] is employed for description of dynamical processes. For the statistical decay followed by the dynamical processes, the generalized evaporation model (GEM)[10] is incorporated. Both the frameworks have been demonstrated to reproduce well the measurements of double-differential nucleon and pion emission cross sections and fragment production cross sections for proton-induced reactions from 100 MeV up to 3 GeV.

In addition, the code TOTELA[11] based on systematics is used as a tool for evaluation of the total, elastic, and reaction cross sections for energies above 150-250 MeV The Niita systematics is used in TOTELA. For calculations of high-energy fission cross sections, the systematics-based code FISCAL[2] is applied. Furthermore, γ-ray energy spectra are calculated with the code ALICE-F[12].

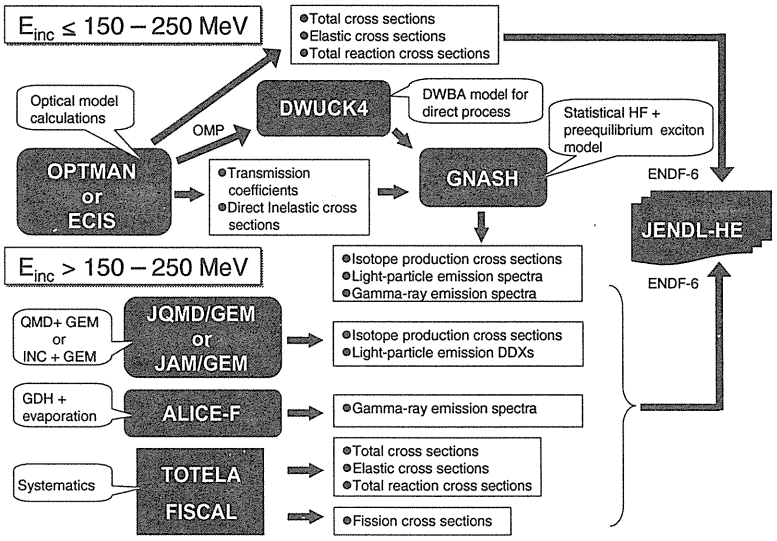



Fig.1 Nuclear model calculation code system used in the JENDL-HE evaluation

### 3. Results and comparisons with measurements and other evaluations

The cross sections were evaluated for nucleon-induced reactions on the nuclides listed in Table 1 using the above-mentioned model calculation codes. The evaluated cross sections are as follows: neutron total cross sections, nucleon elastic scattering cross sections and angular distributions, non-elastic cross sections, production cross sections and double-differential cross sections of secondary light particles (n, p, d, t, $^3$He, α, and π) and γ-rays, isotope production cross sections, and fission cross sections. Neutron total cross sections and isotope production cross sections for several nuclei are evaluated using a fitting procedure of experimental data in the case where systematic measurements are available over a broad range of incident energy.

The present status of JENDL-HE file is as follows: the evaluations for 66 nuclides among the entire 132 nuclides have been completed as shown in Table 1, and the evaluated cross section data have been

tabulated in the ENDF-6 format and released as the JENDL/HE-2004 file. For neutrons, the evaluated cross section data are merged with the data below 20 MeV taken from the JENDL-3.3[13]. For protons, the cross section data below 20 MeV are also included in the JENDL-HE. It should be noted that double-differential production cross sections of light particles are stored using the laboratory angle-energy law (LAW=7) of the ENDF-6 format.

Some representative results of the evaluated cross sections are shown below with experimental data and the other evaluations (LA150[1] and/or NRG2003[14]). Other results for the following elements are found elsewhere: C[15], Al[16], Mg and Si[17], K, Ca, Ti, V, Cr, Mn, Fe, Co, Ni and Zn[18], Cu[19], Zr, Nb and W[20].

Neutron total cross sections and proton nonelastic cross sections for Fe is shown in **Fig. 2**. Three evaluations (JENDL-HE, LA150 up to 150 MeV, and NRG2003 up to 200 MeV) are in good agreement with experimental data[21]. Among them, the JENDL-HE data provide the largest values for neutron total cross sections over the whole energy range, and the smallest values for proton nonelastic cross sections in the energy range of 30-80 MeV.

The JENDL-HE result of angular distributions of neutron elastic scattering from $^{28}$Si is compared with measurements[21] and the LA150 evaluation for nine incident energies in **Fig. 3**. Both the evaluations show excellent agreement with the experimental data to similar extent. As the incident energy increases, some differences between the JENDL-HE and the LA150 evaluations are seen at backward angles where there are no available experimental data.

Double-differential production cross sections of protons and deuterons are presented for proton-induced reactions on $^{12}$C at 68 MeV in **Fig. 4**. For protons, both JENDL-HE and LA150 evaluations show good agreement with the experimental data[22]. For deuterons, some differences are obvious in both the evaluations, and the JENDL-HE is in better agreement with the measurement than the LA150 at 30 and 60 degrees. In **Fig. 5**, evaluated double-differential neutron production cross sections are compared with experimental data[23] for the (p,xn) reaction on $^{90}$Zr at 120 MeV. The JENDL-HE evaluation is in fairly good agreement with the measurement in the continuum preequilibrium region, except for the Gamov-Teller (GT) resonance and the isobaric analog state (IAS) observed at 0 degree. The nuclear model codes used in the present evaluation are not capable of predicting such the resonance structure formed by direct charge-exchange processes.

Finally, an example of isotope production cross sections are shown in **Fig. 6**. The evaluated cross sections are compared with the experimental data[21] for $^{22}$Na produced by the proton-induced reaction on $^{nat}$Si. Both the JENDL-HE and LA150 evaluations reproduce the experimental data fairly well, although underestimation is seen for the LA150 at incident energies below 50 MeV.

## 4. Benchmark test

For validation of the evaluated cross sections, benchmark tests using the MCNPX transport code[24,25] were performed for neutron yields from stopping-length targets. Here, the preliminary result for carbon target bombarded by 113 and 256 MeV protons is shown in **Fig. 7** as an example. For 113 MeV, the MCNPX calculation using the JENDL-HE data shows excellent agreement with the measurement[26] except underestimation seen above 30 MeV at 7.5 degree, while the calculation using the LA150 data overestimates remarkably the measurement for neutrons between 3 and 20 MeV and underestimates it for neutrons above 30 MeV at 7.5 and 30 degrees. Both the MCNPX results with the JENDL-HE data and the LA150 data reproduce well the measurement[27] for 256 MeV protons to a similar extent, although overestimation is seen in the 5 to 20 MeV energy range at forward angles for the calculation with the LA150 data. It should be noted that the MCNPX calculation with the LA150 data is switched to the LAHET module automatically above 150 MeV.

## 5. Summary and conclusions

For the JENDL high-energy file (JENDL-HE), the cross sections were evaluated for neutrons and protons up to 3 GeV on the nuclides listed in Table 1, mainly on the basis of the nuclear model calculations and the systematics. The JENDL-HE evaluation were compared with the other evaluations and the experimental data, showing generally good agreement with them. Evaluations and compilations for the remaining 66 nuclides are underway. Further benchmark tests using transport codes, MCNPX and PHITS[28], are being performed for validation of the evaluated cross sections. Some preliminary results

were partly reported. Through the benchmarks, revision and updating work will continue towards completion of the JENDL-HE file.

The current version of the JENDL-HE file does not contain information for heavy recoils (A > 4). Double-differential cross sections (DDXs) of all secondary ions are required for estimation of radiation effects in structural materials, microelectronic devices, and human bodies. Therefore, it will be our future task with high priority to provide reliable DDXs of heavy recoils and complex charged particles.

**Acknowledgements**

This work has been performed by the members of High-Energy File Making Sub-Working Group in High-Energy Nuclear Data Evaluation Working Group, JNDC. The author is deeply grateful to all the members for their cooperation and valuable discussions on the JENDL-HE evaluation.

**References**

[1] M.B. Chadwick, *et al.*, *Nucl. Sci. Eng.*, **131**, 293-328 (1999).
[2] T. Fukahori, *et al.*, *J. Nucl. Sci. and Technol., Suppl.* **2**, 25-30 (2002).
[3] P.G. Young, *et al.*, LA-12343-MS, Los Alamos National Laboratory (1992).
[4] H. Kalka, *et al.*, *Z. Phys.*, **A341**, 289-299 (1992).
[5] J. Raynal, Proc. of a Specialists Meeting on Nucleon-Nucleus Optical Model Up To 200 MeV, Nov. 13-15, 1996, Buyères-le-Châtel, France, NEA Nuclear Science Committee, (1997), pp. 159-166.
[6] E.S. Sukhovitskiĭ, *et al.*, OPTMAN and SHEMMAN codes, JAERI-Data/Code 98-019 (1998).
[7] P.D. Kunz and E. Rost, DWUCK4 code, *Computational Nuclear Physics 2: Nuclear Reactions*, (Springer-Verlag, Berlin, 1993, Eds. K. Langanke, et al.), pp. 88-107.
[8] Y. Nara, *et al.*, *Phy. Rev. C* **61**, 024901 (2001).
[9] K. Niita, *et al.*, *Phy. Rev. C* **52**, 2620-2635 (1995); JAERI-Data/Code 99-042 (1999).
[10] S. Furihata, *Nucl. Inst. Method in Phys. Res. B* **171**, 251-258 (2000); S. Furihata and T. Nakamura, *J. Nucl. Sci. and Technol. Suppl.* **2**, 758-761 (2002).
[11] T. Fukahori and K. Niita, *Summary Report of the Second Research Coordination Meeting on Nuclear Model Parameter Testing for Nuclear Data Evaluation (RIPL-II)*, June 12-16, 2000, Varenna, Italy, INDC(NDS)-416, pp.97 (2000).
[12] T. Fukahori, *Proc. of the Specialists' Meeting on High Energy Nuclear Data*, JAERI-M 92-039 (1992), pp.114-122.
[13] K. Shibata, *et al.*, J. of Nucl. Sci. and Technol., **39**, 1125-1136 (2002).
[14] A.J. Koning, private communication (2004).
[15] Y. Watanabe, *et al.*, presented at Int. Conf. on Nuclear Data for Science and Technology, Sept. 26- Oct.12, 2004, Santa Fe, USA; Proc. of the 2002 Nuclear Data Symp. JAERI-Conf 2003-006 (2003), pp.183-188.
[16] Y.O. Lee, *et al.*, *J. Nucl. Sci. and Technol.*, **36**, 1125-1134 (1999).
[17] W. Sun *et al.*, presented presented at Int. Conf. on Nuclear Data for Science and Technology, Sept. 26-Oct.12, 2004, Santa Fe, USA.
[18] K. Kosako *et al.*, presented presented at Int. Conf. on Nuclear Data for Science and Technology, Sept. 26-Oct.12, 2004, Santa Fe, USA.
[19] N. Yamano, *et al.*, *Proc. of the 2002 Nuclear Data Symp.*, JAERI-Conf 2003-006 (2003), pp.195-200.
[20] S. Kunieda, *et al.*, *J. Nucl. Sci. and Technol.*, **41**, 1033-1046 (2004).
[21] EXFOR, NEA Data Bank, URL http://www.nea.fr/html/dbdata.
[22] M. Harada, *et al.*, *J. of Nucl. Sci. and Technol., Suppl.* **1**, 687-691 (2000); *J. of Nucl. Sci. and Technol., Suppl.* **2**, 393-396 (2002).
[23] W. Scobel, *et al.*, *Phys. Rev. C* **41**, 2010-2020 (1990).
[24] H.G. Hughes, *et al.*, *Proc. of the Mathematics and Computation, Reactor Physics and Environmental Analysis in Nuclear Applications*, Madrid, Spain, September 27-30, 1999, p.939; LA-UR-98-559 (1998).
[25] L.S. Waters(Ed.), MCNPX Uers's Manual, Version 2.3.0, LA-UR-02-2607 (2002).
[26] M.M. Meier, *et al.*, *Nucl. Sci. Eng.*, **102**, 310-321 (1989).
[27] M.M. Meier, *et al.*, *Nucl. Sci. Eng.*, **110**, 299-301 (1992).
[28] H. Iwasa, *et al., J. Nucl. Sci. and Technol.*, **39**, 1142-1151 (2002).

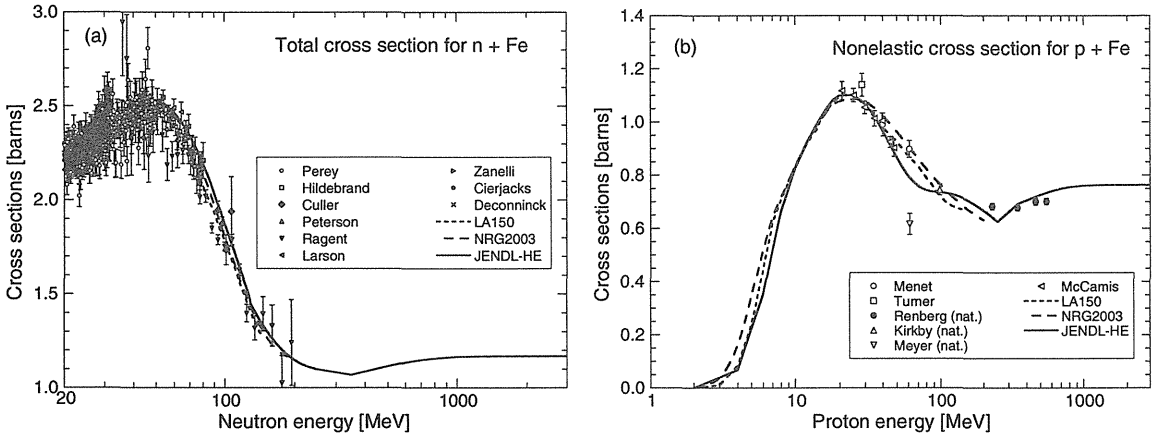



Fig.2 Neutron total cross section and proton nonelastic cross section for Fe

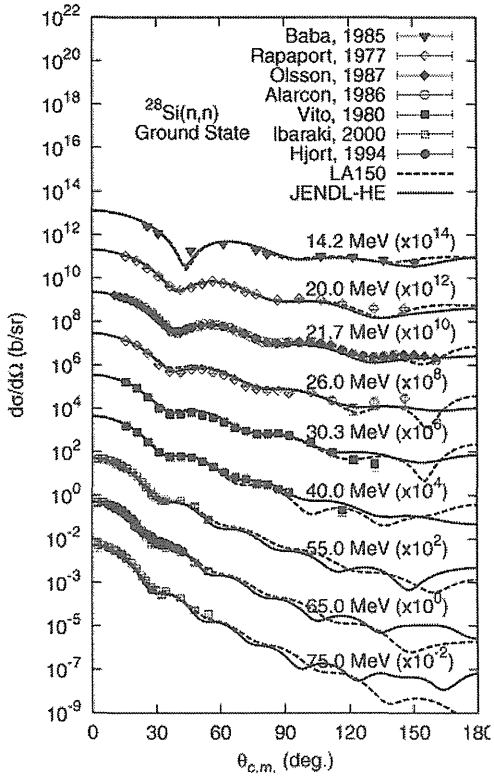



Fig.3 Angular distributions of neutron elastic scattering from $^{28}$Si

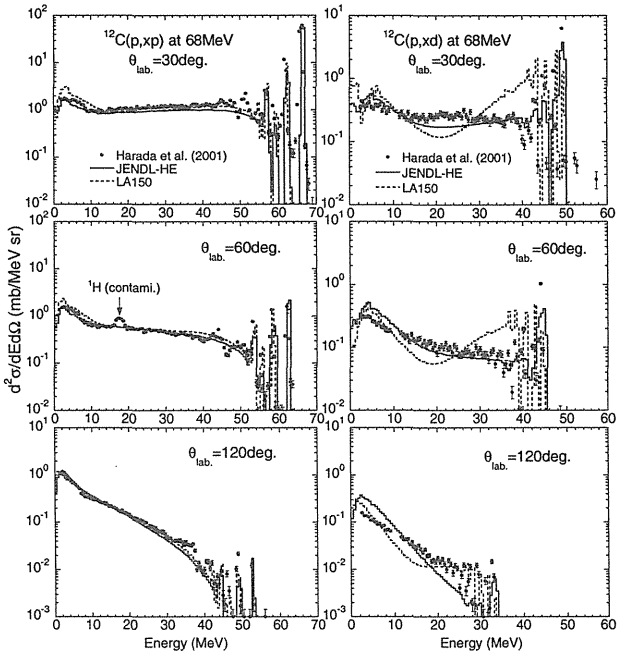



Fig.4 Double-differential proton and deuteron production cross-sections for proton-induced reactions on $^{12}$C at 68 MeV

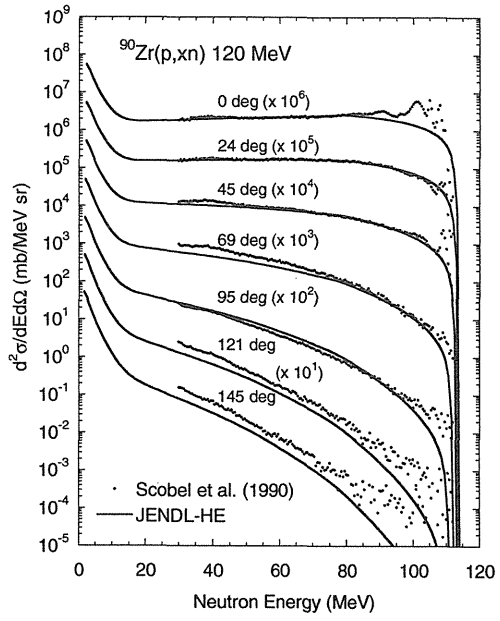



Fig.5 Double-differential neutron production cross sections for the $^{90}$Zr(p,xn) reaction at 120 MeV

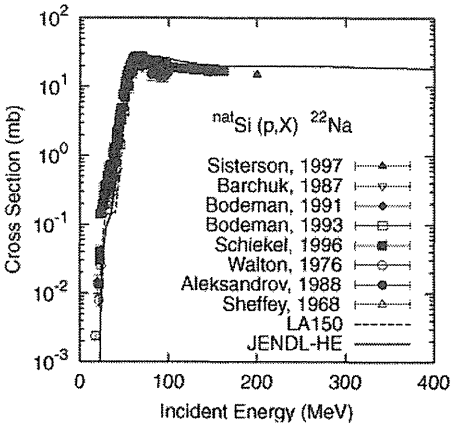



Fig.6 Production cross sections of $^{22}$Na from the proton-induced reaction on $^{nat}$Si

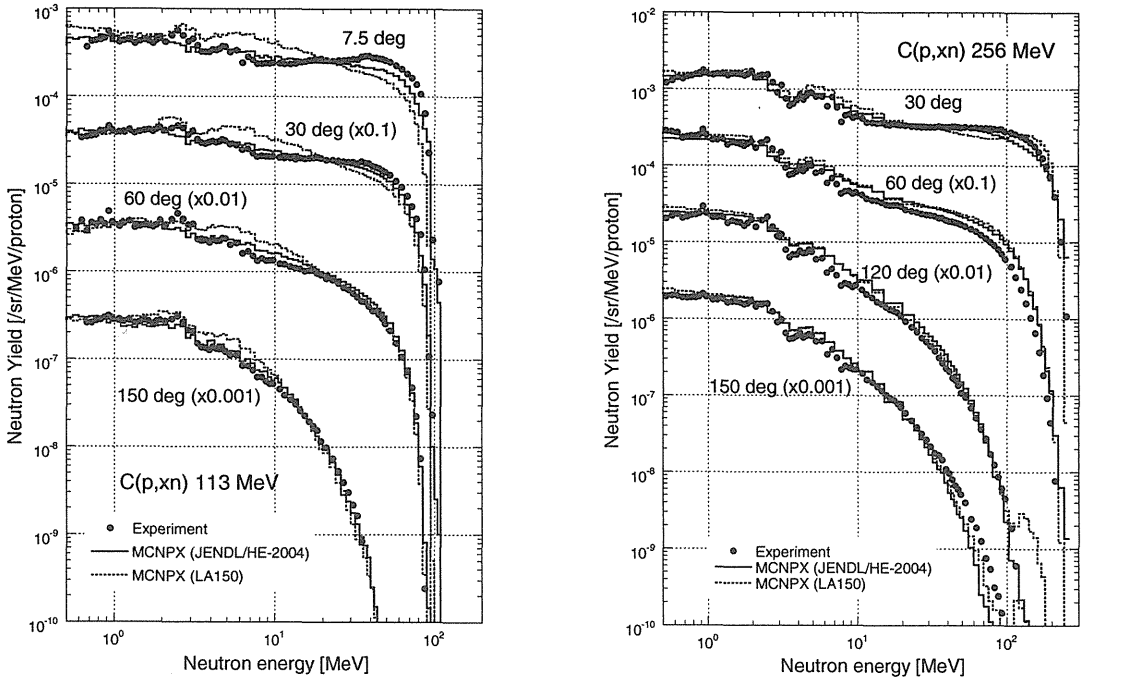



Fig.7 Comparison of MCNPX calculations and measurements for neutron yields from stopping-length carbon target for 113 MeV and 256 MeV protons.

JP0550249



# 2.8 Criticality Benchmarks with a Continuous-Energy Monte Carlo Code MVP and JENDL-3.3

Keisuke OKUMURA, Yasunobu NAGAYA and Takamasa MORI

Japan Atomic Energy Research Institute

Tokai-mura, Naka-gun, Ibaraki-ken 319-1195

e-mail: okumura@mike.tokai.jaeri.go.jp, nagaya@mike.tokai.jaeri.go.jp, mori@mike.tokai.jaeri.go.jp

**Abstract** - Criticality benchmark testing of JENDL-3.3 was performed with MVP for many critical experiments in the ICSBEP Handbook: highly enriched uranium (HEU) and low enriched uranium (LEU) fueled solutions, LEU fueled water-moderated lattices, MOX fueled water-moderated lattices and metal fueled small assemblies with hard neutron spectra. The calculations with the preliminary U235 and U238 data for ENDF/B-VII (preVII) are also made for some benchmarks to confirm their performances and to compare with the JENDL-3.3 results. The prediction accuracy of criticality with JENDL-3.3 is satisfactory, within ±0.5%Δk in most cases, except for slightly enriched uranium fueled lattices. The preVII data of U238 with lower thermal capture cross section improves the under prediction of $k_{eff}$ for the slightly enriched lattices, while slight overestimations were observed for the LEU lattices whose U235 enrichment is more than 3wt.%. On the other hand, the preVII data gives excellent results for the metal fueled assemblies compared with JENDL-3.3.

## 1. INTRODUCTION

In order to clarify problems of JENDL-3.3[1] and to prepare a database for integral testing of next JENDL, an enormous number of criticality benchmark analyses are now under way by using a continuous-energy Monte Carlo code MVP[2] and its library based on JENDL-3.3. The benchmark problems are taken from the Handbook of the International Criticality Safety Benchmark Evaluation Project, so called ICSBEP Handbook[3], which covers various fuel materials (enriched $^{233}$U, $^{235}$U, Pu, their mixtures), fuel forms (compound, metal, solution, and their mixed ones), neutron spectra (thermal, intermediate, fast). The total number of selected benchmark cases is more than 900. For these cases, MVP calculations tracing 20 million neutrons will be finished by the end of FY2004. In addition, full sets of alternative MVP libraries based on ENDF/B-VI.8 and JEFF-3.0 have been completed[4]. In the present work, a part of the benchmark results are shown from the database.

Recently, excellent benchmark results[5] are presented by R. E. MacFarlane using preliminary evaluations for ENDF/B-VII (preVII), which are opened on the web site of LANL. It is reported that the new evaluations for U235 and U238 significantly improve prediction accuracy of criticalities for small metal fueled assemblies with hard neutron spectra (Godiva, Jezebels, Flattops, etc.), and improve under prediction of low enriched uranium fueled lattices moderated by water (TCA, TRX, etc). The under prediction is common problem not only for ENDF/B-VI.8[6] but also for JENDL-3.3 and JEFF-3.0[7].

To confirm performances of the preVII data, our benchmark results with JENDL-3.3 are compared with MacFarlane's results with MCNP5. In addition, we investigated the replacement effects of the JENDL-3.3

libraries for U235 and U238 by those based on the preVII data.

## 2. HIGHLY OR LOW ENRICHED URANIUM FUELED SOLUTIONS

Table 1 shows the comparison of the C/E values of $k_{eff}$ between our JENDL-3.3 results and the preVII results[5] by MacFarlane. As far as the 27 cases of benchmark problems selected by MacFarlane are concerned, both results show very good agreement with the experimental data, and any superiority of the preVII data over JENDL-3.3 are not found, considering the uncertainties of benchmark-$k_{eff}$ in Table 1.

Table 1 Comparison of C/E* values of $k_{eff}$ between JENDL-3.3 and preVII results[5] for highly enriched uranium or low enriched solutions with thermal neutron spectra

| Benchmark ID[a] | Number of cases[b] | J33 (MVP) | | preVII (MCNP5) | | Ave. uncertainty[c] of benchmark-keff | Feature of problems |
|---|---|---|---|---|---|---|---|
| | | Ave. C/E | Std. Dev. | Ave. C/E | Std. Dev. | | |
| HST42 | 6 | 1.0011 | 0.0006 | 1.0006 | 0.0008 | ±0.0036 | Low-leakage nitrate solutions |
| HST1 | 4 | 0.9989 | 0.0025 | 1.0006 | 0.0008 | ±0.0025 | Mid-leakage nitrate solutions |
| HST9 | 2 | 1.0005 | 0.0005 | 1.0005 | 0.0000 | ±0.0057 | High-leakage Fluoride solutions |
| LST7, LST21 | 8 | 0.9993 | 0.0009 | 0.9996 | 0.0008 | ±0.0010 | Unreflected LEU solutions |
| LST4, LST20 | 7 | 1.0001 | 0.0008 | 1.0004 | 0.0009 | ±0.0009 | Reflected LEU nitrate solutions |

a) Shorthand of benchmark problem ID in ICSBEP to specify a series of experiments in a facility
(e.g. HST42 corresponds to HEU-SOL-THERM-042, LST7 corresponds to LEU-SOL-THERM-007)
b) Number of benchmark cases with different critical configurations (fuel concentrations, critical heights, etc.) selected by MacFarlane
c) Average value of evaluated uncertainties mainly caused by measurements and modeling

In the ICSBEP Handbook (Ed.2003), 432 and 90 cases of benchmark problems are stored in the HEU-SOL-THERM (HST) and LEU-SOL-THERM (LST) categories, respectively. Among them, we selected 52 and 76 cases for our database, from the viewpoints of appropriateness to benchmark testing of nuclear data, that is to say, uniformity of fuel, variety of changed physics parameters, simplicity of core configuration, easy convergence of Monte Carlo eigenvalue calculation (single unit assembly), and so on.

Figures 1 and 2 show the obtained C/E values with JENDL-3.3 plotted versus H/U235 atom ratio. The prediction accuracy of JENDL-3.3 is satisfactory (within about ±0.5%Δk) for both LEU and HEU fueled solutions. However, a slight trend of C/E values are observed in the LST cases (LST16-19: STACY 28cm-thick slab experiments), when U235 concentration, and simultaneously leakage in most cases, becomes larger. Future benchmark testing of next JENDL for solution systems should be carried out with a focus on this trend.

* In the present work, a C/E value is defined as calculated $k_{eff}$ over benchmark-$k_{eff}$ evaluated in ICSBEP which may includes small bias due to benchmark modeling. The error bar in all figures means uncertainty of benchmark-$k_{eff}$ evaluated in ICSBEP. In the error bar, statistical error of Monte Carlo calculation is not included, because it is smaller or comparable, compared with size of marker in figures.

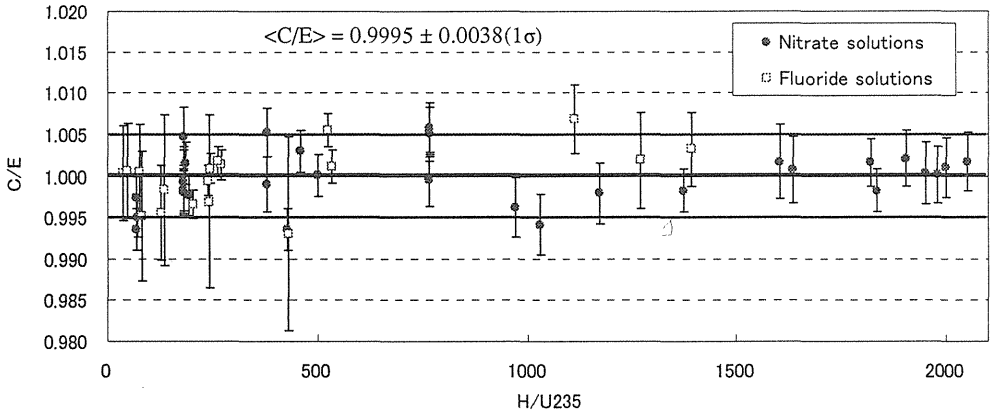



Fig.1 C/E values of $k_{eff}$ with JENDL-3.3 for highly enriched uranium fueled solutions (all configurations in HEU-SOL-THERM-1,4,9,10,11,12,13,32,35,42,43)

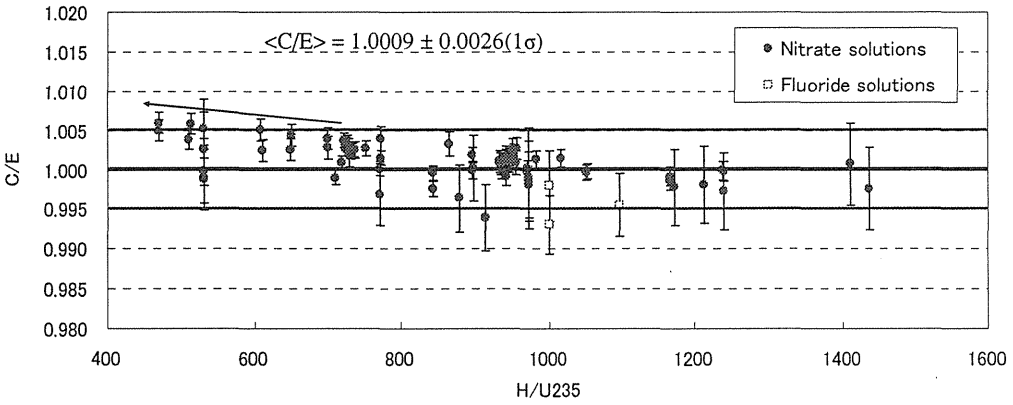



Fig.2 C/E values of $k_{eff}$ with JENDL-3.3 for low enriched uranium fueled solutions (all configurations in LEU-SOL-THERM-2, 3, 4, 5, 6, 7, 8, 9, 10, 16, 17, 18, 19, 20, 21)

## 3. LOW ENRICHED URANIUM FUELED LATTICES MODERATED BY WATER

Under prediction of $k_{eff}$ for LEU fueled assemblies moderated by water is a common problem of recent nuclear data files. As shown in Fig.3, the under prediction becomes more serious when U235 enrichment becomes lower. Therefore, it is important to select experimental data which cover wide range of U235 enrichments especially for lower ones. From this point, several benchmarks out of the ICSBEP handbook are added here, they are TRX-1&2[8], KRITZ2-1&13[9]. The MVP result for MISTRAL-1[10] by NUPEC is also added. All of the assemblies selected here are uniform lattices consist of a kind of cylindrical fuel rods, whose material forms are $UO_2$ except for TRX cores using metal-U.

Figure 4 shows the comparison among the following four sets of results: 1) all nuclide data are based on JENDL-3.3 (specified as J33), 2) U235 and U238 are based on the preVII data and others are based on JENDL-3.3 (U5U8preVII+J33), 3) only U238 is based on the preVII data (U8preVII+J33), 4) the preVII results[5] presented by MacFarlane with MCNP5.

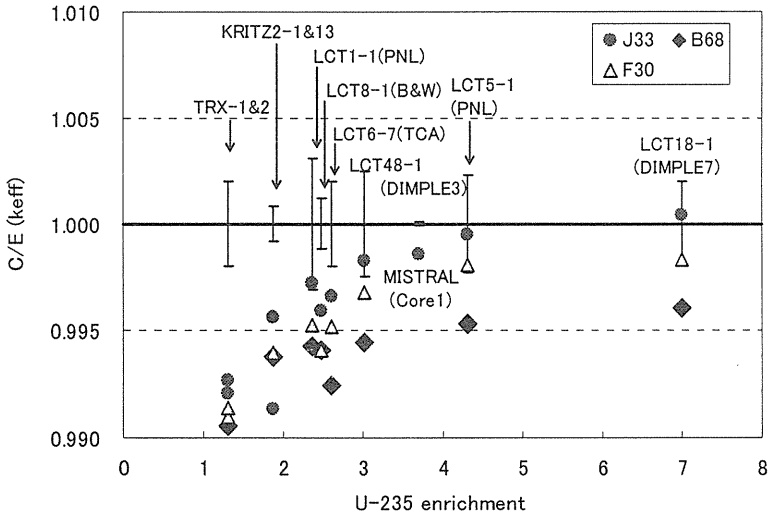



Fig.3 Dependence of C/E on U235 enrichment in LEU fueld water-moderated lattices (J33:JENDL-3.3, B68:ENDF/B-VI.8, F30:JEFF-3.0)*

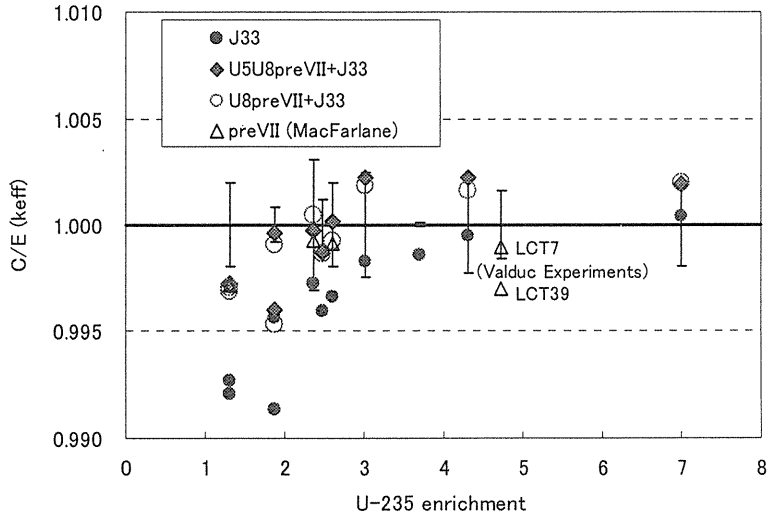



Fig.4 Comparison of C/E results by using the preVII data of U235 and U238

The dependence of the C/E on U235 enrichment is mitigated by using the preVII data of U238, while slight over predictions by about 0.25%Δk are observed for our benchmark problems (LCT48, LCT5, LCT18) where U235 enrichments are more than 3 wt.%. Benchmark data with MVP have not prepared yet for the Valduc experiments (LCT2 and LCT39), for which relatively lower C/E values are presented by MacFarlane using the preVII data.

The improvement in the preVII results is thought to be mainly due to the lower U238 thermal capture cross section (2.680 barn at 2200m/sec), compared with other evaluations (e.g. 2.717 barn in JENDL-3.3).

*For all B68 and F30 calculations in the present work, isotope-wise nuclear data library were used for the impurities or structure materials with natural compositions, where the JENDL-3.3 libraries were used only for the isotopes not evaluated in ENDF/B-VI.8 or JEFF-3.0 (isotopes of Mg, S, Cl, K, Ca, Ti, Ga).

The U238 thermal capture cross section is sensitive to dependence of $k_{eff}$ on U235 enrichment especially when the enrichment becomes lower than 3 wt.%. This can be explained by the following relation between macroscopic thermal $\eta$–value and U235 enrichment $w^{235}$.

$$\eta = \frac{N^{235}\nu\sigma_f^{235}}{N^{235}\sigma_a^{235} + N^{238}\sigma_a^{238}} \approx \left\{\frac{\nu\sigma_f^{235}}{\sigma_a^{235}}\right\} \cdot \left\{\frac{1}{1+(\frac{N^{238}}{N^{235}})(\frac{\sigma_c^{238}}{\sigma_f^{235}})}\right\} \equiv \eta^{235} \cdot F(w^{235}), \qquad \text{(Eq.1)}$$

where, $\sigma$ and $N$ denote condensed microscopic cross sections in thermal energy range and atomic number densities, respectively. The function $F(w^{235})$ has the shape like shown in Fig. 5, where 2200 m/s values of JENDL-3.3 are assumed for the condensed thermal cross sections of U235 for convenience. Thus the systematic under prediction of $k_{eff}$ observed in Fig.3 has strong correlation with thermal $\eta$–value and it is sensitive to thermal U238 capture cross section. On the other hand, other three factors ($p$, $\varepsilon$, $f$) of $k$-infinity have not strong correlations on U235 enrichments. This fact was confirmed by calculating four factors of $k$-infinities with MVP for the infinite unit cells of the benchmark problems here.

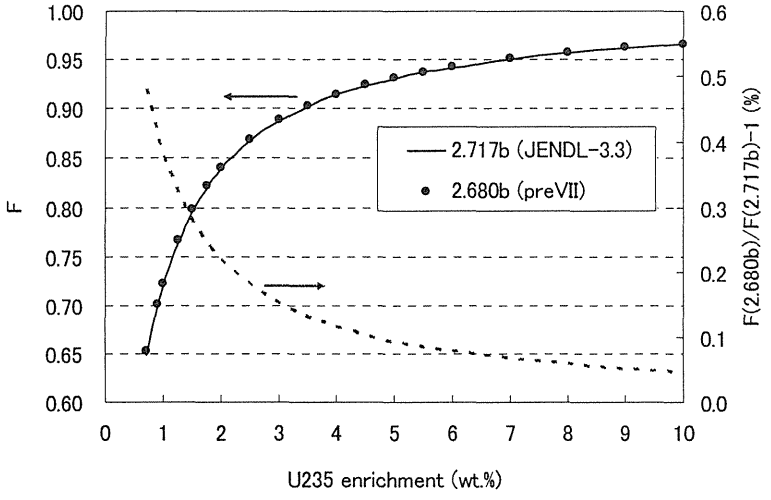



Fig.5 Dependence of function F on U235 enrichment and U238 thermal capture cross section

Further and more detailed benchmark testing including spectral indices are necessary. In addition, well-evaluated experimental data are expected for the water-moderated uranium fueled lattices whose U235 enrichment is less than 2.0 wt.%.

## 4. MOX FUELED LATTICES MODERATED BY WATER

MVP calculations with JENDL-3.3 have been carried out for 63 cases of MOX fueled water-moderated lattices selected from the ICSBEP benchmarks categorized in MIX-COMP-THERM (MCT). The selected benchmark problems and the ranges of typical physics parameters are shown in Table 2. The obtained C/E values were plotted on a graph for each of physics parameters like leakage, thermal fission rate, and so on, besides the parameters specified in Table 2. Typical graphs are shown in Fig.6(a)-(c).

Table 2 Ranges of physics parameters of thermal MOX fuel benchmarks

| Physics parameters | Range of parameter | Selected benchmark problems MIX-COM-THERM (MCT) |
|---|---|---|
| Pu/(U+Pu) | 1.5~6.6 and 22.5 [%] | MCT1 (1~4), MCT2 (1~6), MCT3 (1~6), MCT4 (1~11), MCT5 (1~7), MCT6 (1~6), MCT7 (1~5), MCT8 (1~6), MCT9 (1~6) |
| Pu239/Pu | 68~92 [%] | |
| Pu240/Pu | 8~24 [%] | |
| Am241/Pu | 590~12540 [ppm] | |
| H/H.M. | 3.5~53.4 | |

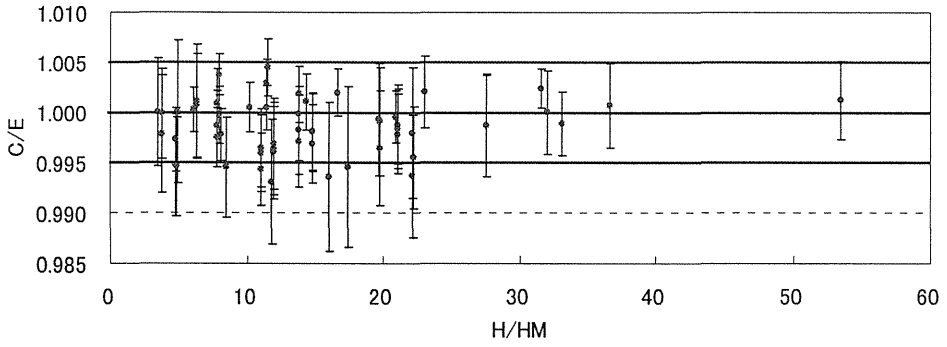



Fig. 6 (a) C/E ($k_{eff}$ with JENDL-3.3) vs H over Heavy Metal atom ratio in MCT benchmarks

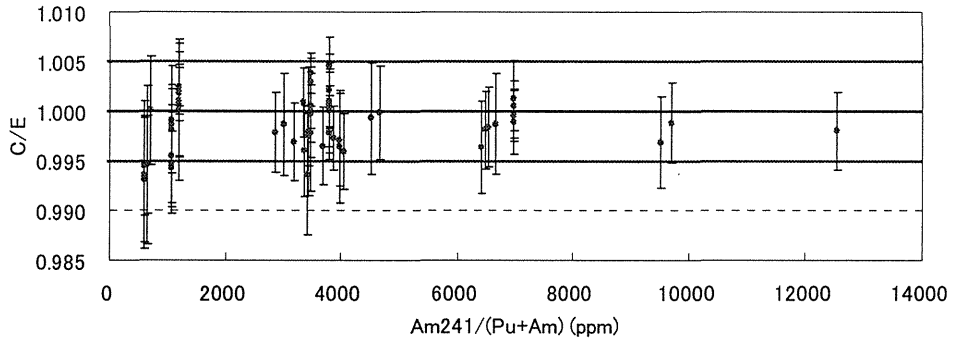



Fig. 6 (b) C/E ($k_{eff}$ with JENDL-3.3) vs Am contents in MCT benchmarks

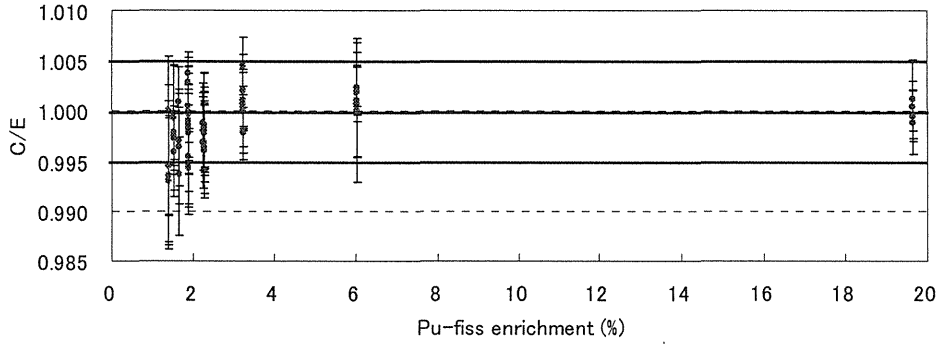



Fig. 6 (c) C/E ($k_{eff}$ with JENDL-3.3) vs fissile Pu enrichment in MCT benchmarks

The average C/E value and its standard deviation are 0.9985 and 0.0027, respectively. Although significant trends were not observed on the considered physics parameters, a slight dependence on fissile plutonium enrichment appears in lower enriched cases. If this dependence is due to the same reason concerning to the U238 thermal capture cross sections at the LEU fueled lattices, it may be eliminated by using the preVII data. The effect of the preVII data has not investigated for the MOX-thermal problems.

## 5. METAL FUELED SMALL ASSEMBLIES

At the last, benchmark results with JENDL-3.3 for metal fueled small assemblies with hard neutron spectra (See Table 3) are shown in comparison with the results obtained by using the preVII data of U235 and U238. The problems are well known fast reactor benchmarks by CSEWG[8], but benchmark-$k_{eff}$ (E-value) and calculation models are taken from the ICSBEP Handbook.

All calculated results are shown in Figure 7, where the meanings of the captions in the figure are the same as described in Chapter 1.

Table 3 Benchmark problems for metal fueled small assemblies

| Assembly names | Fuel of Core (wt.%) | Reflector | Assembly names | Fuel of Core (wt.%) | Reflector |
|---|---|---|---|---|---|
| Godiva | U235(94) | No | Flattop-Pu | Pu239(95) | Nat.U |
| Flattop-25 | U235(93) | Nat.U | PMF11(ICSBEP) | Pu239(94) | Water |
| Bigten | U235(10) | Nat.&Dep.U | Thor | Pu239(95) | Th-232 |
| HMF4(ICSBEP) | U235(96) | Water | Jezebel-233 | U233(98) | No |
| Jezebel | Pu239(95) | No | Flattop-233 | U233(98) | Nat.U |
| Jezebel-240 | Pu239(76) | No | | | |

HMF4 (HEU-METAL-FAST-004) and PMF11(PU-MET-FAST-011) are problems selected by MacFarlane[5]

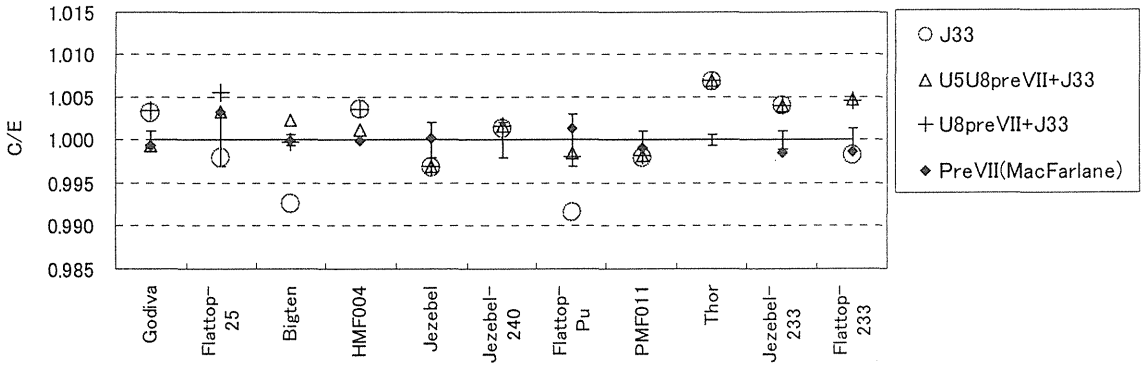



Fig.7 Benchmark results for metal fueled small assemblies

In comparison with the pure JENDL-3.3 results (J33), the U235 data of preVII has an effect to decrease $k_{eff}$ by about 0.2-0.4%Δk for the HEU fueled bare assemblies: Godiva, Flattop-25 and HFM4. On the other hand, the U238 data of preVII has an effect to increase $k_{eff}$ by about 0.7%Δk for the assemblies which have natural or depleted uranium reflectors: Flattop-25, Bigten, Flattop-Pu and Flattop-233. Consequently, the preVII data of U235 and U238 give more excellent results than JENDL-3.3 for uranium or plutonium fueled

assemblies except for Thor whose reflector is pure Th-232. Although the C/E value for Flattop-233 deviates from unity when the preVII data of U238 is used with JENDL-3.3, it seems consistent with the jezebel-233 result. It may be interesting to investigate effects of the preVII data for U233 and Th232.

## 6. CONCLUSIONS

Criticality benchmark testing of JENDL-3.3 was performed with MVP for many critical experiments in the ICSBEP Handbook: HEU and LEU fueled solutions, LEU fueled water-moderated lattices, MOX fueled water-moderated lattices and metal fueled small assemblies with hard neutron spectra. The calculations using the preliminary U235 and U238 data for ENDF/B-VII (preVII) are also made for comparisons.

The prediction accuracy of criticality with JENDL-3.3 is satisfactory, that is within ±0.5%Δk in most cases, except for slightly enriched uranium fueled lattices. The preVII data of U238 with lower thermal capture cross section improves the under prediction of $k_{eff}$ for the slightly enriched lattices, while slight overestimations were observed for the LEU lattices whose U235 enrichment is more than 3wt.%. On the other hand, the preVII data give excellent results for the metal fueled assemblies with hard neutron spectra compared with JENDL-3.3.

## REFERENCES

[1] K. Shibata, *et al.*: "Japanese Evaluated Nuclear Data Library Version 3 Revision-3: JENDL-3.3," J. Nucl. Sci. Technol. 39, 1125, (2002).

[2] Y. Nagaya, T. Mori, K. Okumura and Y. Nakagawa: "MVP/GMVP: General Purpose Monte Carlo Codes for Neutron and Photon Transport Calculations based on Continuous Energy and Multigroup Methods Version 2," to be published in JAERI report (2005).

[3] NEA Nuclear Science Committee: "International Handbook of Evaluated Criticality Safety Benchmark Experiments," NEA/NSC/DOC(95)03, Sep. 2003 Edition.

[4] T. Mori, Y. Nagaya, K. Okumura and K. Kaneko: "Production of MVP Neutron Cross Section Libraries Based on the Latest Evaluated Nuclear Data Files," JAERI-Data/Code 2004-011 (2004) [in Japanes].

[5] R. E. MacFarlane: "Testing New Actinide Cross Sections Proposed for ENDF/B-VII," Proc. of Int. Conf. on Nuclear Data for Science and Technology (ND2004), Santa Fe, Sep.26-Oct.1, (2004).

[6] (Comp. and Ed.) P.F. Rose: "ENDF-201, ENDF/B-VI Summary Documentation, " BNL-NCS-17541, 4th Edition (1991). See also WWW page of Cross Section Evaluation Working Group (CSEWG), http://www.nndc.bnl.gov/csewg/, National Nuclear Data Center, BNL.

[7] R.Jacqmin, R.Forrest, J.Rowlands, A.Nouri and M.Kellett: "Status of the JEFF-3 Project," J. Nucl. Sci. Technol., Suppl. 2, Vol.1, 54 (2002).

[8] "ENDF-202, Cross Section Evaluation Working Group Benchmark Specifications," BNL 19302 (ENDF-202), (1974).

[9] I. Remec, *et al.*: "OECD/NEA KRITZ-2 $UO_2$ and MOX Benchmark," Proc. of Int. Conf. PHYSOR2002, 11B-03, Seoul, Korea, 7-10 October, (2002).

[10] A. Zukeran: "JENDL Reactor Constant and its Application," Proc. of the 2003 symposium on Nuclear Data, pp.103-110, Nov. 27-28, 2003, Tokai, Japan, JAERI-Conf 2004-005 (2004).

JP0550250

## 2.9 Analysis of MOX Critical Experiments with JENDL-3.3

Takako SHIRAKI, Hideki MATSUMOTO and Makoto NAKANO
*Reactor Core Engineering Department, Mitsubishi Heavy Industries, Ltd.,*
*3-1, Minatomirai 3-chome, Nishi-ku Yokohama 220-8401*
e-mail:shiraki@atom.hq.mhi.co.jp

This paper reports a study to confirm the applicability of the latest version of Japanese Evaluated Nuclear Data Library (JENDL3.3[1]). For this purpose, the criticality calculations using MCNP4C[2] code are performed to evaluate middle and high plutonium content MOX (M-MOX(8.6 w/o (Pu/MOX))) and H-MOX(12.6 w/o (Pu/MOX))) experiments (VIP, VIPO and VIPEX) using the JENDL3.3. Afterward, the same calculations with ENDF/B-6[3] release 8 (ENDF/B-6.8) are performed to be compared with the results from JENDL3.3. Recently, ORNL have reevaluated U235 and U238 cross-sections in thermal and resonance energy[4]. Those new evaluations are stored in ENDF/B-pre7. The effect of the U235 and U238 cross-sections on both JENDL3.3 and ENDF/B-6.8 are evaluated. The results clarify that JENDL3.3 is superior to ENDF/B-6.8 although both libraries underestimate the criticality. In addition, the ENDF/B-pre7 data for U235 and U238 solves the underestimation.

## 1. Introduction

Mitsubishi Heavy Industries, Ltd. joined R&D international programs on MOX experiments in collaboration with the Japanese PWR utilities with the objective to validate the design codes for MOX utilization. Some programs were carried out using VENUS critical facility at the SCK/CEN in Belgium from 1990 to 1998. The criticality experiments were performed for middle- and high-plutonium content MOX (M-MOX(8.6 w/o (Pu/MOX))) and H-MOX(12.6 w/o (Pu/MOX))).

JENDL has not been used in the design of PWR core design, except for decay heat evaluations by the ORIGEN-2 code. In 2002, JENDL3.3 was released, based on the update measurement data than ENDF/B-5 or B-6. It is necessary for us to confirm the applicability of JENDL3.3 from the viewpoint of future application of the JENDL3.3 or later version of JENDL in core design.

In this study, to confirm the applicability of JENDL3.3, we performed benchmarking-calculations using Monte Carlo code against the test data from the VENUS facility.

## 2. Criticality experiment programs

The experiment data used for the benchmark calculations were obtained from the VENUS critical assembly at SCK/CEN of Belgium. The VIP was carried out as a mock up simulation of MOX and UO2 PWR assemblies. The VIPO was performed to investigate the characteristics of the core with high void fraction. The VIPEX was carried out 6 years after the VIP to measure the effect of Am or other substance using the same core configuration as the VIP.

**Table 1** shows the fuel specifications used by these programs. These are three kinds of MOX fuel and two kinds of UO2 fuel. The plutonium content of the low-plutonium content MOX (L-MOX) fuel is 4.8 w/o. The MOX fuel claddings are made of Zircaloy-4. The fuel active length is 100 cm. The contents of U235 enrichment of UO2 fuel are 3.3 w/o and 4.0 w/o, respectively. Both fuel active lengths are 50 cm. The claddings of 3.3 w/o UO2 fuel and 4.0 w/o UO2 fuel are made of Zircaloy-4 and stainless steel, respectively.

Table 1 Fuel specifications

| | | Fuel type | | | | |
|---|---|---|---|---|---|---|
| | | H-MOX | M-MOX | L-MOX | 3.3 w/o | 4.0 w/o |
| Fuel | Pu/MOX or U235/U (w/o | 12.6 | 8.6 | 4.8 | 3.3 | 4 |
| | Diamter (cm) | 0.82 | | | 0.82 | 0.89 |
| | Hight(MOX+UO2) (cm) | 100+3.6 | | | 0+50 | |
| | Density (g/cm$^3$) | 10.11 | 10.13 | 10.17 | 10.25 | 10.21 |
| Cladding | Material | Zr-4 | Zr-4 | Zr-4 | Zr-4 | Stainless steel |
| | Diamter (cm) | 0.963 | | | 0.95 | 0.978 |
| | Thickness (cm) | 0.061 | | | 0.057 | 0.038 |

The VIP core consists of one central 17 x 17 MOX fuel-bundle and four peripheral 17 x 17 3.3 w/o UO2 fuel rod bundles. These bundles are surrounded by about three rod layers with 4.0 w/o UO2 fuel. The cell pitch is 1.26cm. Aluminum microtubes and microrods are inserted between MOX fuel rods and 3.3 w/o UO2 fuel rods at the corner of each square unit cell to simulate the density of high temperature water in PWR core. The VIP configuration is shown in **Fig. 1**. The VIPEX configuration is the same as that of the VIP.

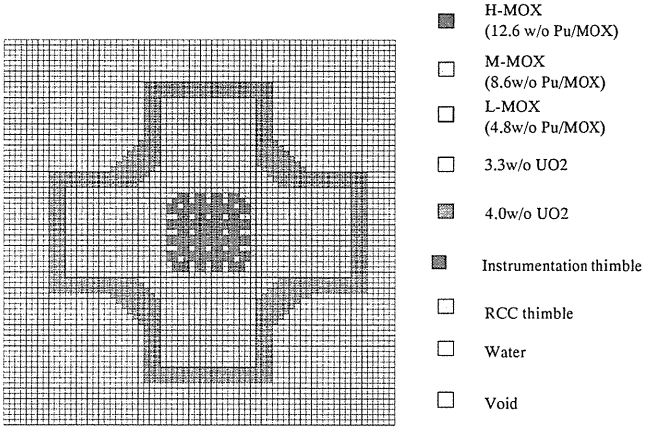



Fig.1 Cross-section view of VIP and VIPEX model

The VIPO core consists of a 14 x 14 MOX fuel assembly, surrounded by 11 rod layers of 3.3 w/o UO2 fuel and 6 rod layers of 4.0 w/o UO2 fuel as shown in **Fig.2**. The cell pitch is 1.26cm. The two rods outer layers of the MOX fuel assembly consist of H-MOX fuel, while the 10 x 10 inner part consists either of H-MOX fuel or M-MOX fuel rods. The VIPO has used a void box to simulate the void fraction between the fuel rods. This box is made of Lexan whose density is 1.2 g/cm$^3$. The height of the voided region is 15 cm and this region encloses a 10 x 10 fuel rod in the center of the core.

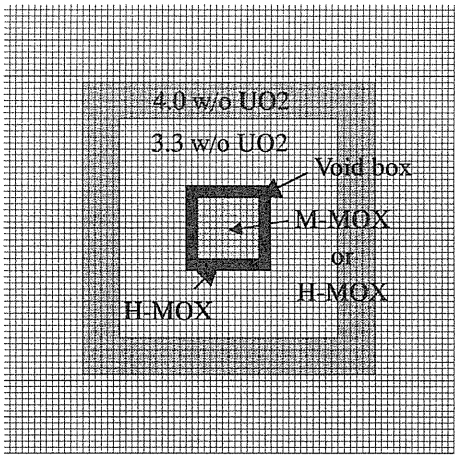



Fig.2 Cross-section view of VIPO model

In these experiments, critical water level, horizontal- and axial-power distributions, and other parameters were measured. These power distributions were obtained with γ-scanning method.

## 3. Calculation conditions

The calculation code we used is the Monte Carlo N-Particle transport code, MCNP4c3. Our calculation models cover horizontal-cross section from the core center to the water region outside of core and axial-cross section from the lower support to the upper support.

The VIP and the VIPEX calculation models are shown in **Fig. 3**. In this model, each fuel cell includes fuel, cladding, Al-microrod, Al-microtube and water. The upper and intermediate grids are modeled considering the heterogeneity. Since the core configurations are of one-eighth symmetry, correspondingly we employed one-eighth symmetry for the calculation. Pu241 decays to Am241 by β-decay with a half life of 14.4 years. Therefore VIPEX Pu241 composition decreases to 77 % and Am241 composition increases to 158 % as compared with those of the VIP.

The VIPO calculation model is shown in **Fig. 4**. The four calculations are performed on the VIPO program. These are the M-MOX fuel in the center region with a void box, the H-MOX fuel in the center region with a void box, the M-MOX fuel in the center region without a void box and the H-MOX fuel in the center region without a void box. These water levels are 146.71cm, 146.02cm, 145.47cm, 144.72cm, respectively. Since each fuel rod of VIPO is the same as that of VIP, the axial modeling such as upper, intermediate and upper grid is the same as the VIP.

In these analyses, the five kinds of cross-sections are applied as shown in **Table 2**.

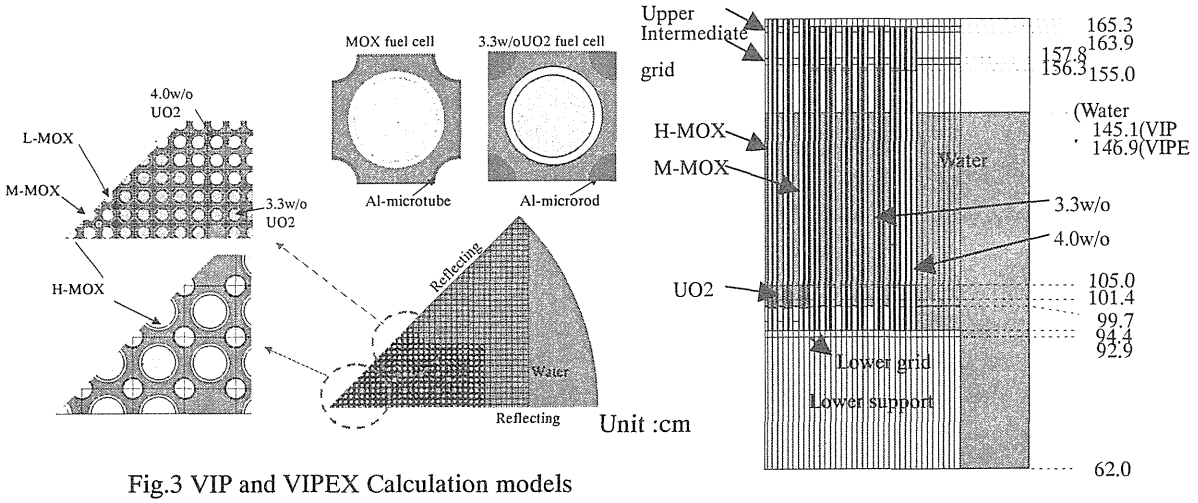



Fig.3 VIP and VIPEX Calculation models

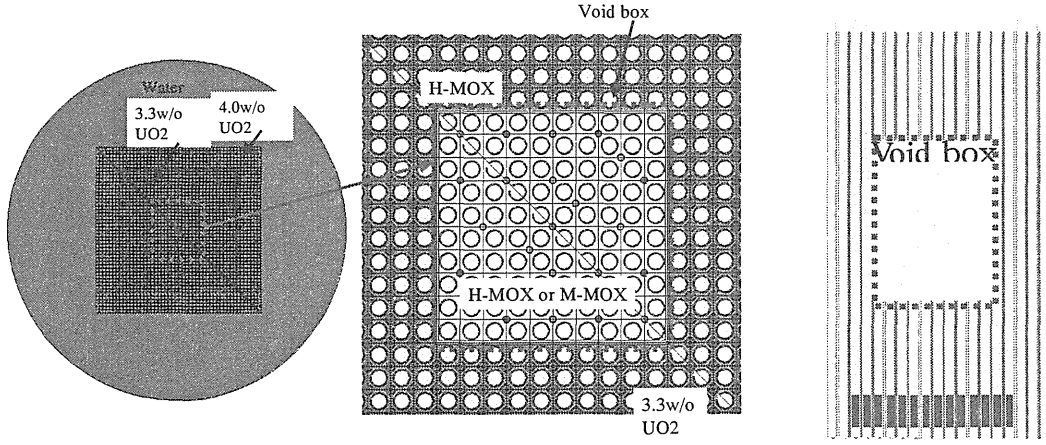



Fig.4 VIPO calculation model

The multiplication factors are calculated with the MCNP function, "KCODE". The horizontal and axial power distributions are calculated with "F4 tally" which can evaluate reaction rates, etc. in each cell.

## 4. Calculation results

### 4.1 Neutron multiplication factors

**Table 3** shows the calculated results for the neutron multiplication factors (keff). Each calculation standard deviation is less than 0.04%. The mean keff of VIP, VIPO and VIPEX obtained from JENDL3.3 is 0.9943, and the keff obtained from ENDF/B-6.8 is 0.9911. From the viewpoint of criticality evaluation for MOX, we find JENDL3.3 is superior to ENDF/B-6.8. Although both libraries slightly underestimate the keff's, the standard deviations within the 6 calculation

Table2 Cross section sets

| Nuclide | JENDL3.3 | JENDL3.3+ ENDF/B-pre7(U235,U238) | JENDL3.3+ ENDF/B-pre7(H1,O16, U235,U238) | ENDF/B-6.8 | ENDF/B-pre7 |
|---|---|---|---|---|---|
| H1 | JENDL3.3 | JENDL3.3 | ENDF/B-6.r8 | ENDF/B-6.r8 | ENDF/B-6.r8 |
| O16 | JENDL3.3 | JENDL3.3 | ENDF/B-6.r8 | ENDF/B-6.r8 | ENDF/B-6.r8 |
| U234 | JENDL3.3 | JENDL3.3 | JENDL3.3 | ENDF/B-6.2 | ENDF/B-6.2 |
| U235 | JENDL3.3 | ENDF/B-pre7 | ENDF/B-pre7 | ENDF/B-6.r5 | ENDF/B-pre7 |
| U236 | JENDL3.3 | JENDL3.3 | JENDL3.3 | ENDF/B-6.1 | ENDF/B-6.1 |
| U238 | JENDL3.3 | ENDF/B-pre7 | ENDF/B-pre7 | ENDF/B-6.r5 | ENDF/B-pre7 |
| Pu238 | JENDL3.3 | JENDL3.3 | JENDL3.3 | ENDF/B-6.2 | ENDF/B-6.2 |
| Pu239 | JENDL3.3 | JENDL3.3 | JENDL3.3 | ENDF/B-6.r2 | ENDF/B-6.r2 |
| Pu240 | JENDL3.3 | JENDL3.3 | JENDL3.3 | ENDF/B-6.r2 | ENDF/B-6.r2 |
| Pu241 | JENDL3.3 | JENDL3.3 | JENDL3.3 | ENDF/B-6.r3 | ENDF/B-6.r3 |
| Pu242 | JENDL3.3 | JENDL3.3 | JENDL3.3 | ENDF/B-6.2 | ENDF/B-6.2 |
| Am241 | JENDL3.3 | JENDL3.3 | JENDL3.3 | ENDF/B-6.r3 | ENDF/B-6.r3 |

cases are as small as 0.0008 and 0.0009 for JENDL3.3 and ENDF/B-6.8, respectively. It shows that good accuracy is maintained throughout the core configurations including those with large void and H-MOX fuel and M-MOX fuel.

By using ENDF/B-pre7 U235 and U238 data instead of original ones for these nuclides, the keff's with JENDL3.3 and ENDF/B-6.8 libraries increase by about 160pcm and 520pcm, respectively. The different effects of the new ENDF/B-pre7 cross-sections made JENDL3.3 and ENDF/B-6.8 consistent with each other, both giving the keff's of about 0.996. By using the ENDF/B-6.8 data for H1 and O16 instead of JENDL3.3 ones, the keff's decrease by about 130pcm.

**Fig. 5** shows the ratio of neutron flux with each cross-section sets to that with JENDL3.3 in the fuel of the VIP. It can be seen ENDF/B-6.8 gives the most hard spectrum. The flux with ENDF/B-6.8 is larger by 1% over 9.1keV and less by 0.6% under 9.1keV comparing with that with JENDL3.3. On the other hand, the other cases are in good agreement. The differences are less than 0.2% for all energy ranges.

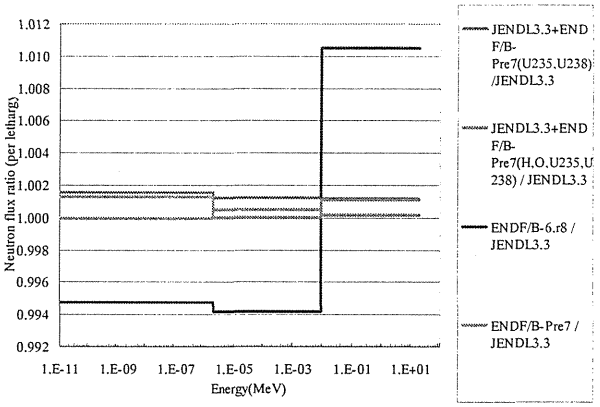



Fig.5 Ratio of neutron flux with each cross-section set to that with JENDL3.3 in the fuel (VIP)

Table 3 Multiplication factors in VIP, VIPEX and VIPO analyses with each library

| | VIP | VIPEX | VIPO | | | | |
|---|---|---|---|---|---|---|---|
| | keff | keff | 10×10 M-MOX with void box | 10×10 H-MOX with void box | 10×10 M-MOX without void box | 10×10 H-MOX without void box | Mean |
| Cross section | | | keff | keff | keff | keff | keff |
| ①JENDL3.3 | 0.99471 | 0.99535 | 0.99444 | 0.99448 | 0.99321 | 0.99368 | 0.99431 ± 0.0008 |
| ②JENDL3.3+ ENDF/B-pre7(U235,U238) | 0.99707 | 0.99808 | 0.99765 | 0.99738 | 0.99631 | 0.99665 | 0.99719 ± 0.0007 |
| ③JENDL3.3+ ENDF/B-pre7(H1,O16,U235,U238) | 0.99571 | 0.99646 | 0.99589 | 0.99699 | 0.99515 | 0.99503 | 0.99587 ± 0.0008 |
| ④ENDF/B-6.8 | 0.99114 | 0.99253 | 0.99114 | 0.99174 | 0.99003 | 0.99016 | 0.99112 ± 0.0009 |
| ⑤ENDF/B-pre7 | 0.99552 | 0.99749 | 0.99592 | 0.99689 | 0.99556 | 0.99633 | 0.99629 ± 0.0008 |
| Difference (pcm) | | | | | | | |
| ②-① | 237 | 274 | 322 | 291 | 312 | 298 | 289 |
| ③-① | 100 | 111 | 146 | 252 | 195 | 136 | 157 |
| ⑤-④ | 441 | 498 | 481 | 518 | 557 | 621 | 519 |

Table 4 Mean C/E's of horizontal power distribution with each library in VIP and VIPO

| Cross section | VIP | | | | VIPO | | | | | |
|---|---|---|---|---|---|---|---|---|---|---|
| | MOX assembly | | UO2 assembly | | MOX assembly | | | | UO2 assembly | |
| | | | | | In void box | | Out void box | | | |
| | C/E ave. | 1σ | C/E ave. | 1σ | C/E ave. | 1σ | C/E ave. | 1σ | C/E ave. | 1σ |
| ①JENDL3.3 | 1.015 | 0.009 | 0.984 | 0.011 | 0.999 | 0.025 | 1.019 | 0.026 | 0.978 | 0.011 |
| ②JENDL3.3+ ENDF/B-Pre7(U235,U238) | 1.016 | 0.016 | 0.983 | 0.017 | 1.005 | 0.031 | 1.019 | 0.069 | 0.982 | 0.031 |
| ③JENDL3.3+ ENDF/B-Pre7(H1,O16,U235,U238) | 1.015 | 0.020 | 0.983 | 0.018 | 1.003 | 0.047 | 1.014 | 0.039 | 0.981 | 0.036 |
| ④ENDF/B-6.8 | 1.014 | 0.015 | 0.986 | 0.016 | 0.986 | 0.036 | 1.018 | 0.040 | 0.980 | 0.038 |
| ⑤ENDF/B-pre7 | 1.016 | 0.016 | 0.982 | 0.015 | 0.993 | 0.035 | 1.034 | 0.048 | 0.970 | 0.027 |

4.2 Power distribution

**Table 4** shows the C/E mean values for each region with each library in the VIP and the VIPO. In the VIP, the γ intensity of 50 fuel rods in MOX region and 59 fuel rods in UO2 region were measured for horizontal power distributions. The uncertainty of measured value in MOX fuel and UO2 fuel are less than 1.8 % and 1.4 %, respectively.

In the VIPO, the γ intensity of 13 fuel rods inside the void box, 15 fuel rods outside the void box in the MOX fuel region and 28 fuel rods in UO2 region were measured for horizontal power distributions. The uncertainty of measured value is less than 1.5 %. The measured values (E) and the calculated values (C) with each library are compared in each fuel rod. **Fig.6** shows the comparison of horizontal power distribution between measurements and calculations with JENDL3.3 as example. This model is the M-MOX fuel in the center region with a void box

The calculation standard deviations are less than 0.8%. The differences with each library are small. Although the calculated values agree with the measured values within the measured and calculated errors, the C/E's in the MOX region tend to be larger than these in the UO2 region.

The axial power distributions in the VIPO H-MOX rods with the void box and 3.3 w/o UO2 fuel rods are shown in **Fig.7**. The uncertainty of measured value is less than 2%. The calculation standard deviations are less than 2%. The differences between measured and calculated values are not so large in the void box. The

calculated values are lower than the measured values by about 5 % at the maximum in the void box. These distributions agree within 3% in the UO2 fuel.

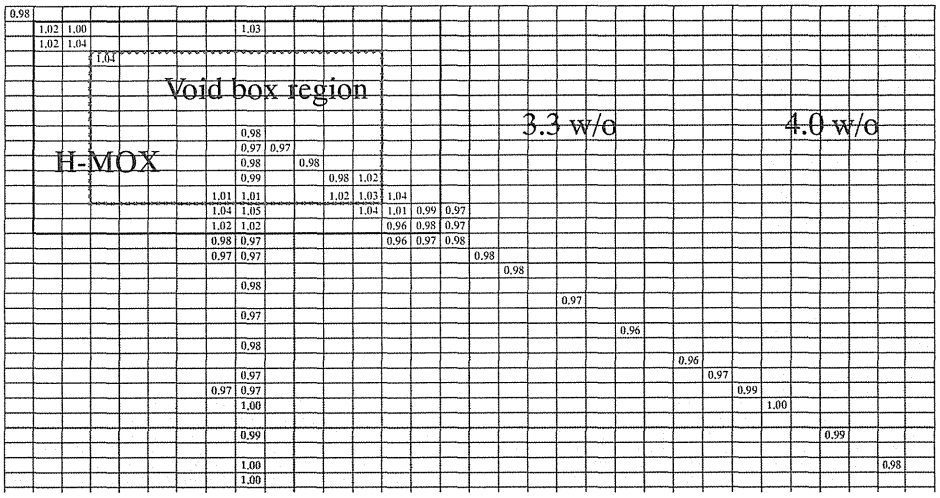
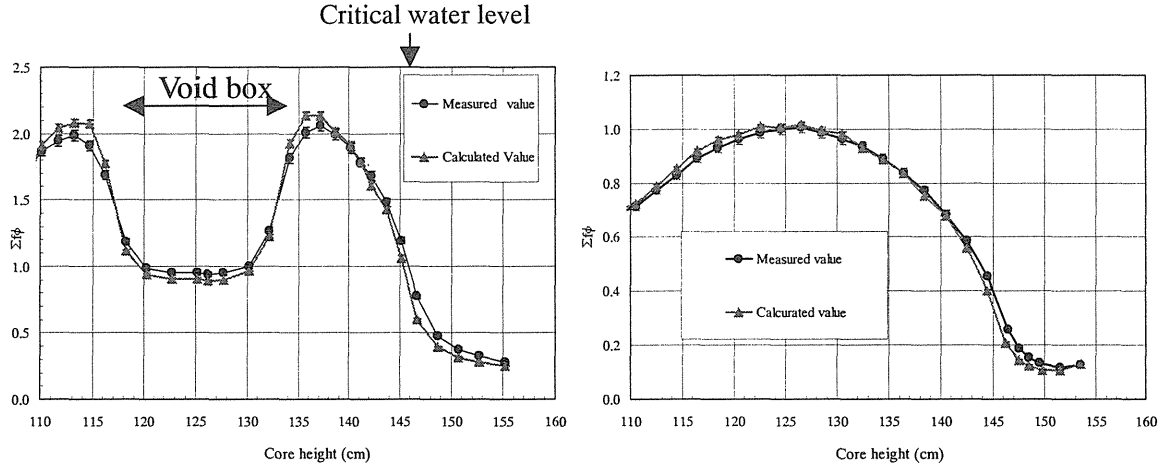



Fig.6 Comparison of horizontal power distributions with JENDL3.3 in VIPO (C/E)




H-MOX fuel inside of void box　　UO2 fuel

Fig.7 Axial power distributions in VIPO

## 5. Discussion

By using ENDF/B-pre7 U-235 and U-238 data instead of the original ones, the keff's increase by about 290pcm and 520pcm for JENDL3.3 and ENDF/B-6.8, respectively. The different effect of ENDF/B-pre7 data on keff for JENDL3.3 and ENDF/B6.8 is discussed here.

**Fig.8** shows the differences of capture and fission reaction rates of all fuel rods in the VIP with the ENDF/B-pre7 data for U235 and U238 from the original cross-section sets. The U238 capture rates are decreased when the ENDF/B-pre7 data for both libraries use. The difference in the rate for JENDL3.3 is twice larger than for ENDF/B-6.8. The U235 capture rates are increased. The difference in the rate on JENDL3.3 is twice smaller than on ENDF/B-6.8. On the other hand, the U235 fission rates are increased. The difference in the rate on JENDL3.3 is three times smaller than on ENDF/B-6.8. The capture and fission rates of other isotopes change through neutron spectrum change by using the ENDF/B-pre7 data for U235 and U238. **Fig.9** shows that those differences result in the total production, absorption and leakage rates for both libraries. The difference of total absorption including leakage by using the ENDF/B-pre7 data for U235 and U238 becomes small. It shows that the differences cancel out among isotopes. On the other hand, the difference of U235 fission reaction rate remains in total production rates. This is the cause of the difference in reactivity change due to the U235 and U238 ENDF/B-pre7 data. This increases the calculated keff of ENDF/B-6 more than JENDL3.3. As the result, keff obtained by JENDL3.3 with the ENDF/B-pre7 data for U235 and U238 agree well with ENDF/B-pre7.

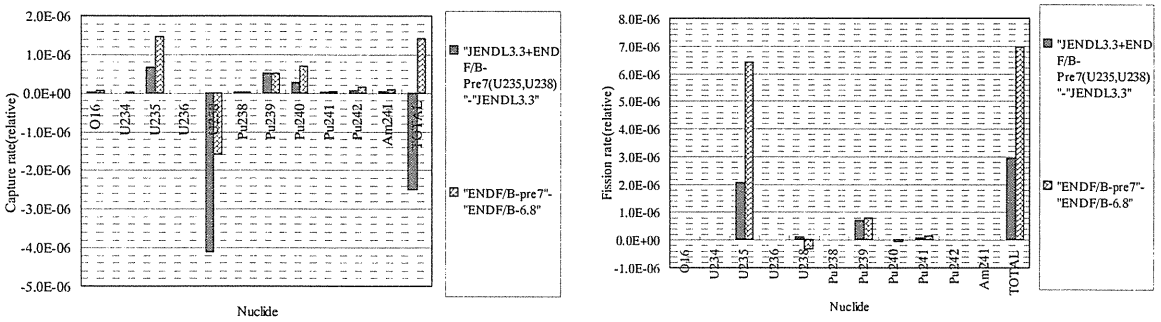



Fig.8 Reaction rate effect of ENDF/B-pre7 for U235 and U238 data

## 6. Summary

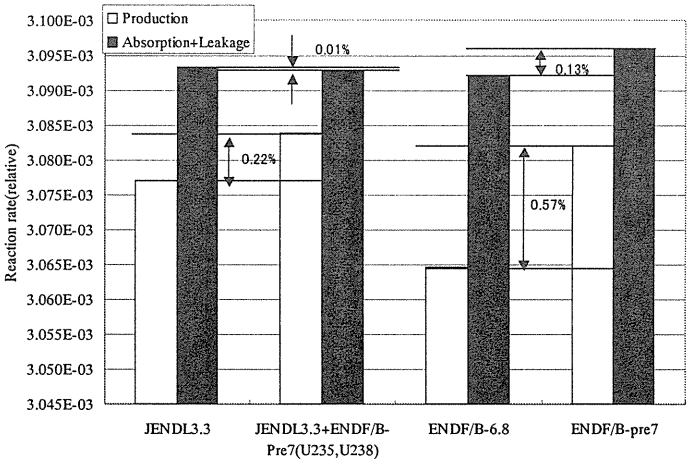



Fig.9 Detail of reaction rates

This paper reports a study to confirm the applicability of the JENDL3.3. For this purpose, the criticality calculations using MCNP4C code are performed to evaluate M-MOX and H-MOX experiments (VIP, VIPO and VIPEX) using the JENDL3.3. Afterward, the same calculations with ENDF/B-6.8 are performed. Recently, ORNL have reevaluated U235 and U238 cross-sections in thermal and resonance energy. The effect of the U235 and U238 cross-sections on both JENDL3.3 and ENDF/B-6.8 are evaluated.

As for power distribution, the calculated values agree with the measured values within the measured and calculated errors for all calculated cases. However the C/E's of power distribution in the MOX region tend to be larger than those in the UO2 region. The tendency may improve when re-evaluation of plutonium cross-section will be performed in the future.

Although the JENDL3.3 and ENDF/B-6.8 underestimate the criticality, JENDL3.3 is superior to ENDF/B-6.8. The ENDF/B-pre7 data for U235 and U238 solves the underestimation.

We expect that U235 and U238 should be re-evaluated in the future JENDL-4 as performed for ENDF/B-pre7.

## 7. References

[1] K.Shibata, et al., "Japanese Evaluated Nuclear Data Library Version 3 Revision-3: JENDL-3.3," J. Nucl. Sci. Technol., 39, 1125(2002).

[2] Los Alamos National Laboratory Los Alamos, New Mexico "MCNP4C: Monte Carlo N-Particle Transport Code System," CCC-700(April 2000).

[3] P. F. Rose, Ed., "ENDF-201, ENDF/B-VI Summary Documentation," BNL-NCS-17541,4th Edition, Brookhaven National Laboratory (October 1991).

[4] Los Alamos National Laboratory T-2 Nuclear Information Service, http://t2.lanl.gov/data/data/preVII-neutron/U/.

JP0550251



# 2.10 Analysis of Innovative Water Reactor for Flexible Fuel Cycle in FCA using JENDL-3.3

Masaki ANDOH, Masahiro FUKUSHIMA, Shigeaki OKAJIMA,
Kensuke KOJIMA, Kenji KAWASAKI and Masaharu KATAOKA
Research Group for Reactor Physics, Department of Nuclear Energy System,
Japan Atomic Energy Research Institute
Tokai-mura, Naka-gun, Ibaraki-ken 319-1195
E-mail: andoh@fca001.tokai.jaeri.go.jp

To obtain experimental data and to evaluate the prediction accuracy for the core characteristics in the design study of Innovative Water Reactor for Flexible fuel cycle (FLWR), critical experiments were carried out using a series of mock-up cores at FCA. Three mockup cores with different void fractions of the moderator were constructed to obtain experimental data in wide range of neutron spectra. Major items of the experiment are criticality, reaction rate ratios, moderator void reactivity worth and the Doppler effect. Conventional deterministic calculation systems were used to analyze the experiment with the use of the JENDL-3.2 and JENDL-3.3 libraries. The ratios of calculated and experimental (C/E) values were compared between both the JENDL libraries. The current analysis method showed good prediction accuracy in most of the experiments and no significant differences were observed in the C/E values between the libraries in this study.

## 1. Introduction

Innovative Water Reactor for Flexible fuel cycle (FLWR) [1] is a new reactor concept for the next generation proposed by JAERI. The FLWR is aimed at high breeding ratio and high burn up with the use of highly enriched MOX fuel in tight lattice. To estimate the accuracy of prediction for the core characteristics in the design study of FLWR, a program of critical experiments using the fast critical facility, FCA, was planned. This program consisted of three mock-up cores of different voidage of moderator. The principal aim of the program is focused on obtaining the nuclear characteristics of the MOX fueled core in tight lattice.

The purpose of this study is to analyze these experiments using the JENDL-3.2[2] and JENDL-3.3[3] libraries and to verify the impact of the revised nuclear data library by comparing the results.

## 2. Brief Description of Mockup cores and experiments

The FCA-FLWR mockup core, FCA-XXII-1 series core, is a coupled system of a central test zone and surrounding driver zone. The test zone is composed of a combination of uranium/plutonium fuel plates and moderator material (foamy polystyrene) plates to simulate the neutron energy spectrum of FLWR (see Fig. 1). The principal cell averaged parameters of the test zone of each core are shown in Table 1. The cell averaged enrichment of the test zone is 16 atom % of fissile plutonium and the hydrogen to heavy metal atomic number ratio (H/HM) is systematically changed from 0.09 to 0.8. The cross section view of the FCA-XXII-1(65V) core is shown in Fig. 2. The test zone is represented by a close to rectangular prism with about 38 cm in square base and 91 cm in height. It is surrounded by the enriched U driver zone and two radial blanket zones; an inner blanket zone of 30cm in thickness containing a significant amount of depleted uranium dioxide and sodium, and an outer blanket zone of 15cm in thickness containing only depleted uranium metal. The upper and lower axial blanket zones of 30cm in thickness containing natural uranium metal are also placed to cover the test zone.

The measurements were made for criticality ($k_{eff}$ value), central reaction rate ratio and central reactivity worth (e. g. moderator void reactivity worth, $^{238}U$ Doppler effect and plutonium sample reactivity worth). The central reaction rate ratio was measured with the combination of foils and fission counters[4]. The void reactivity worth was measured with changing the void fraction of the polystyrene plates from 45% (or 65%) to 80% and 95% in the central cell of the test zone. The Doppler effect was measured as the reactivity change of cylindrical natural-uranium samples (Doppler samples) with the temperature change (from room temperature to 800℃) at the core center. As for the Pu sample reactivity worth, the reactivity worth caused by the change of plutonium isotope composition from 92% to 75% (Pu-fissile) was measured at the core center.

## 3. Calculation method

The nuclear reactions in the FLWR core are dominantly occurred in the resonance energy range. Two different conventional deterministic methods, therefore, were used to analyze the experiments; the SRAC code system [5] and a standard calculation code system for a fast reactor (FR code system) [6]. The effective microscopic cross sections in the resonance energy range were calculated by the resonance shielding factors given by the table-look-up method based on the narrow resonance approximation. As for the analysis of the central reaction rate ratio, the effective microscopic cross sections were calculated with the use of the PEACO for the SRAC code system and the PEACO-X[7] for the FR code system, which provide effective microscopic cross sections more precisely by the ultra-fine energy group calculation. The effective cross sections of the cylindrical Doppler samples were also calculated with those codes. The cell averaged macroscopic effective cross sections for each cell were obtained by the collision probability calculation with a one-dimensional infinite slab model. The $k_{eff}$ values and the forward and adjoint fluxes were calculated by the diffusion calculation code CITATION[8] with considering the anisotropic effect of neutron leakage[9] and by the transport

calculation code DANTSYS[10] with $P_0$-$S_8$ approximation. Two-dimensional R-Z model was employed for the analysis of the Doppler effect, while three-dimensional X-Y-Z model was employed for the other analyses. The first order perturbation method was employed for the Doppler effect analysis and the explicit perturbation method was employed for the other reactivity worth analyses.

## 4. Comparison between Calculation and Experiment

The comparison between calculated (C) and experimental (E) results, C/E value, is shown in Table 2 to 6.

Criticality: Table 2 shows that the SRAC code system gives better agreement between the calculated and experimental results than the FR code system: the discrepancies are in the range from +0.1%Δk to +0.2%Δk with the JENDL-3.3 library by the SRAC code system, while they are from –0.5%Δk to -0.3%Δk by the FR code system. When the results are compared between JENDL-3.2 and JENDL-3.3, JENDL-3.3 gives larger C/E values than JENDL-3.2 up to 0.16% except the FCA-XXII-1(95V) core. There are no discrepancies between the results with JENDL-3.2 and JENDL-3.3 in the hard neutron spectrum considering the experimental error.

Central reaction rate ratio: There are no significant differences in the C/E values between the SRAC and FR systems. The C/E values of the fission reaction rate ratio $^{238}U/^{235}U$ (F28/F25) are larger than those of $^{239}Pu/^{235}U$ (F49/F25). From this result, the calculation code systems have a tendency to give a harder neutron spectrum. Both the calculations overestimate the ratio of the capture reaction rate of $^{238}U$ to the fission reaction rate of $^{239}Pu$ (C28/F49) by about 10% in the XXII-1 (45V) core. The contribution of the reaction rate in giant resonance peaks (in the range of 48eV~29eV, 23eV~18eV and 8.3eV~5.0eV with the 107 group energy structure) to that in the whole energy range in the capture reaction rate of $^{238}U$ is 22%, 15% and 2% for the FCA-XXII-1(45V), FCA-XXII-1(65V) and FCA-XXII-1(95V), respectively. It is considered that the calculation accuracy of the giant resonance cross section of $^{238}U$ should be investigated more precisely. When the C/E values are compared between JENDL-3.2 and JENDL-3.3, there are no large differences.

Reactivity Worth: The SRAC code system shows good agreement between the calculation and experiment for the moderator void reactivity worth in both the cores, while the FR code system shows underestimation beyond the experimental errors. The calculation accuracy in the non-leakage term of the FR code system should be improved. As for the $^{238}U$ Doppler effect, both the code system agrees with the experiment within the measurement error in most cases. In the analysis of the Pu sample reactivity worth, both the systems show C/E dependency on the voidage of the test zone and the SRAC code system shows better agreement than the FR code system. When the C/E values are compared between JENDL-3.2 and JENDL-3.3 in the analyses of the central reactivity worths, there are no large discrepances.

## 5. Conclusion

The SRAC code system showed better agreement with the measurement than the FR code system in the analysis of the criticality and the moderator void and Pu sample reactivity worths. For the central reaction rate ratio, the C/E values of F28/F25 was larger than that of F49/F25 and the calculations gave large overestimation for C28/F49. No large C/E discrepances between JENDL-3.2 and JENDL-3.3 were observes in the analyses of this study.

The further detail analyses will be carried out to solve the problems (such as the overestimation in the C28/F49) and to evaluate calculation accuracy for the design study of the FLWR.

Acknowledgements

The authors would like to thank Prof. T. Takeda of Osaka University and member of the research group for reactor physics of JAERI for the encouragement and the valuable advice. A part of the experiments in this study were carried out with the fiscal support program presented by the MEXT.

References

[1] S. Uchikawa : "Status and Future Program of Research and Development on Reduced-moderation Water Reactors", in Summary of the 6th Workshop on the Reduced-moderation Water Reactor, JAERI-Conf 2003-020 (2003). (in Japanese)

[2] T. Nakagawa, *et al.* : *J. Nucl. Sci. and Technol.*, **32**, 1259 (1995).

[3] S. Shibata, *et al.*: *ibid.*, **39**, 1125 (2002).

[4] T. Sakurai and T. Nemoto: JAERI-Research 95-054, (1995). (in Japanese)

[5] K. Tsuchihashi, et al. : JAERI 1302, (1986).

[6] M. Nakagawa and K. Tsuchihashi: JAERI 1294, (1984).

[7] S. Okajima, et al,: *J. Nucl. Sci. and Technol.*, 31, 1097-1104 (1994).

[8] T.B. Fowler, et al,: ORNL-TM-2496, (1969).

[9] P. Benoist: CEA-R-2278, (1964).

[10] R.E. Alcouffe, et al, : LA--12969M, (1995).

Table 1 Cell averaged parameters of the test zones in the FCA FLWR mockup cores

| | FCA FLWR mock-up cores | | | FLWR | |
|---|---|---|---|---|---|
| | XXII-1(45V) | XXII-1(65V) | XXII-1(95V) | Lower core | Upper core |
| Enrichment (%) | 15.8 | 15.8 | 15.8 | 10~ | 10~ |
| $V_m/V_f$ * | 0.6 | 0.6 | 0.6 | 0.18 | 0.18 |
| Void fraction (%) | 45 | 65 | 95 | 45 | 75 |
| H/Fuel ** | 0.81 | 0.52 | 0.091 | 0.93 | 0.48 |

* Volume fraction of moderator to fuel plates in a cell

** Atomic number ratio between Hydrogen and Fuel materials in a cell

Table 2 Ratio of calculated to measured criticality ($k_{eff}$ value)

| Core name | Error* | SRAC code system J-3.2 | SRAC code system J-3.3 | FR code system J-3.2 | FR code system J-3.3 |
|---|---|---|---|---|---|
| XXII-1 (45V) | ±0.02% | 1.0002 | 1.0018 | 0.9936 | 0.9949 |
| XXII-1 (65V) | ±0.02% | 1.0004 | 1.0017 | 0.9961 | 0.9970 |
| XXII-1 (95V) | ±0.02% | 1.0007 | 1.0010 | 0.9975 | 0.9971 |

* Measurement error

Table 3 Comparison of central reaction rate ratios between calculation and experiment

| Reaction | Core name | Error | SRAC J-3.2 | SRAC J-3.3 | FR J-3.2 | FR J-3.3 |
|---|---|---|---|---|---|---|
| F28/F25 | XXII-1 (45V) | ±0.9% | 1.04 | 1.04 | 1.04 | 1.03 |
| | XXII-1 (65V) | ±0.9% | 1.05 | 1.05 | 1.04 | 1.02 |
| | XXII-1 (95V) | ±1.0% | 1.04 | 1.03 | 1.02 | 1.00 |
| F49/F25 | XXII-1 (45V) | ±1.2% | 0.97 | 0.97 | 0.99 | 0.99 |
| | XXII-1 (65V) | ±1.2% | 1.01 | 1.02 | 1.02 | 1.02 |
| | XXII-1 (95V) | ±1.0% | 1.00 | 1.00 | 1.00 | 1.00 |
| C28/F49 | XXII-1 (45V) | ±1.8% | 1.09 | 1.10 | 1.09 | 1.09 |
| | XXII-1 (65V) | ±1.8% | 1.04 | 1.04 | 1.04 | 1.04 |
| | XXII-1 (95V) | ±1.7% | 1.00 | 1.01 | 1.00 | 1.00 |

Table 4 Comparison of void reactivity worth between calculation and experiment

| Core name | Void fraction | Error | SRAC J-3.2 | SRAC J-3.3 | FR J-3.2 | FR J-3.3 |
|---|---|---|---|---|---|---|
| XXII-1 (45V) | 80% | ±4.6% | 1.00 | 1.00 | 0.85 | 0.84 |
| | 95% | ±3.4% | 0.99 | 0.99 | 0.85 | 0.83 |
| XXII-1 (65V) | 80% | ±12% | 0.94 | 0.93 | 0.77 | 0.78 |
| | 95% | ±6.7% | 0.97 | 0.96 | 0.82 | 0.82 |

Table 5 Comparison of U-238 Doppler effect between calculation and experiment

| Doppler Sample | Core name | Error | SRAC J-3.2 | SRAC J-3.3 | FR J-3.2 | FR J-3.3 |
|---|---|---|---|---|---|---|
| $U_{metal}$ | XXII-1 (45V) | ±3.4% | 1.01 | 1.02 | 1.04 | 1.04 |
| | XXII-1 (65V) | ±2.6% | 0.99 | 1.01 | 1.04 | 1.05 |
| | XXII-1 (95V) | ±4.2% | 0.99 | 1.02 | 1.00 | 1.01 |
| $UO_2$ | XXII-1 (45V) | ±5.4% | 1.00 | 1.01 | 1.03 | 1.04 |
| | XXII-1 (65V) | ±4.1% | 0.99 | 1.01 | 1.05 | 1.06 |
| | XXII-1 (95V) | ±8.4% | 1.04 | 1.07 | 1.06 | 1.08 |

The Doppler samples are 2.5cmϕx15cmL in size.

Table 6 Comparison of plutonium reactivity worth between calculation and experiment

| Core name | Error | SRAC J-3.2 | SRAC J-3.3 | FR J-3.2 | FR J-3.3 |
|---|---|---|---|---|---|
| XXII-1 (45V) | ±1.0% | 0.95 | 0.94 | 0.90 | 0.89 |
| XXII-1 (65V) | ±1.4% | 0.99 | 0.95 | 0.94 | 0.92 |
| XXII-1 (95V) | ±6.5% | 1.05 | 1.02 | 1.08 | 1.07 |

Pu isotope ratio: 239/240/241/242: 91.7/8.0/0.2/0.1 -> 73.0/23.1/1.7/2.2.

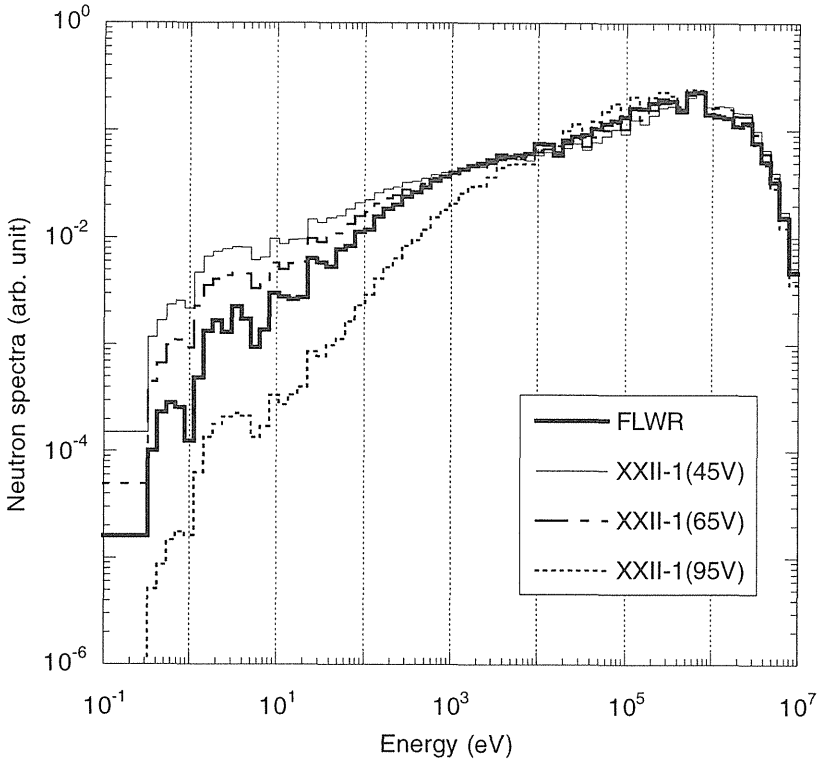



Fig. 1 Calculated neutron energy spectra in the FLWR (average of the upper and lower cores) and the FCA-XXII-1 series cores

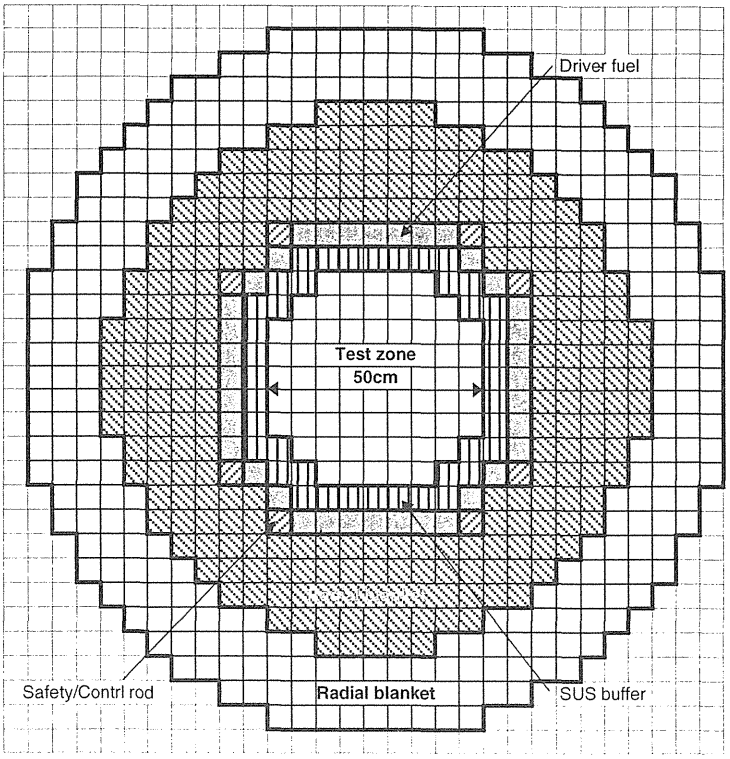



Fig. 2 Cross-section view of the FCA-XXII-1(65V) core

JP0550252



# 2.11 Development of a Coupled-Channels Optical Model Code "OPTMAN" and a Global CC Potential as a Base for High Energy Nuclear Data Evaluation

Efrem Sh. Soukhovitski[1], and Satoshi Chiba[2]
[1]*Joint Institute for Energy and Nuclear Research Sosny, Academician A.K. Krasin 99, 220109, Minsk-Sosny, Belarus*
[2]*Japan Atomic Energy Research Institute, Tokai-mura, Naka-gun,Ibaraki-ken,319-1195, Japan*
e-mail: esukhov@sosny.bas-net.by

Coupled-channels optical model code "OPTMAN" with coupling built on wave functions of the Soft-rotator nuclear Hamiltonian was completely modernized to be a base for high energy nuclear data evaluation. It was used to analyze experimental nucleon optical interaction data with A=24-122 mass nuclides. We found that all the available experimental data (total cross sections, angular distributions of elastically and inelastically scattered nucleons and reaction cross sections) for these nuclides can be described with good accuracy using smooth A-mass dependencies of optical potential values while imaginary volume potential geometry was considered to be equal real potential one, with individual properties of the nuclides accounted by individuality of the nuclear Hamiltonian parameters, Fermi energies and deformations.

## 1. Introduction

For more than twenty years an original coupled-channels optical model code OPTMAN has been developed at Joint Institute of Energy and Nuclear Research to investigate neutron-nucleus interaction mechanisms and as a basic tool for evaluation of reactor oriented nuclear data. Results of such activities for, e.g., $^{235}$U, $^{239}$Pu, $^{236}$U, $^{233}$ U, $^{238}$Pu etc., were included in evaluated Nuclear Data Library BROND[1] of former Soviet Union. Except for the standard rigid rotator and harmonic vibrator coupling scheme encoded in widely-used JUPITER[2] and ECIS[3] codes, level-coupling schemes based on a non-axial soft-rotator model are possible for the even-even nuclei in OPTMAN. This allows account of stretching of soft nuclei by rotations, which results in change of equilibrium deformations for excited collective states compared with that of the ground state. This is a critical point for reliable predictions[4, 5, 6] based on the coupled-channels method.

In 1997 in the framework of ISTC Project CIS-03-95, Financial Party of which was Japan, OPTMAN code was installed at Nuclear Data Center of Japan Atomic Energy Research Institute (JAERI) and an active collaboration started. After that time, many new options were added to the code following demands from a broad range of applications: power reactors, shielding design, radiotherapy, transmutations of nuclear wastes and nucleosynthesis.

Here we describe the activity performed under the Project Agreement B-521 of the International Science and Technology Center (Moscow). The work was requested by JAERI and is the result of a close cooperation between scientists from Joint Institute of Energy and Nuclear Research and JAERI.

## 2. Soft-Rotator Nuclear Model Coupled Channels and Optical Potential Form for Global Search

Soft-rotator nuclear model and its application to coupled-channels optical model calculations is described elsewhere[7]. We assume that the low-lying excited states observed in even-even non-spherical nuclei can be described as a combination of rotation, $\beta$-quadrupole and octupole vibrations, and $\gamma$-quadrupole vibration. Instant nuclear shapes that correspond to such excitations can be presented [8, 9] in a body fixed system:

$$R(\theta',\varphi') = R_0\left\{1+\sum_{\lambda=2,3,4\mu=even}\beta_{\lambda\mu}Y_{\lambda\mu}(\theta',\varphi')\right\}.$$

The Hamiltonian $\hat{H}$ of the soft-rotator model consists of the kinetic energy term for the rotation of the non-axial nuclei with quadrupole, hexadecapole and octupole deformations, the $\beta_2$-, $\gamma$-quadrupole and octupole vibrations, and the vibrational potentials ignoring a coupling between the three vibration modes [5]:

$$\hat{H}=\frac{\hbar^2}{2B_2}\left\{\hat{T}_{\beta_2}+\frac{1}{\beta_2^2}\hat{T}_\gamma\right\}+\frac{\hbar^2}{2}\hat{T}_r+\frac{\hbar^2}{2B_3}\hat{T}_{\beta_3}+\frac{\beta_{20}^4}{\beta_2^2}V(\gamma)+V(\beta_2)+V(\beta_3),$$

where

$$\begin{aligned}\hat{T}_{\beta_2} &= -\frac{1}{\beta_2^4}\frac{\partial}{\partial\beta_2}\left(\beta_2^4\frac{\partial}{\partial\beta_2}\right),\\ \hat{T}_\gamma &= -\frac{1}{\sin 3\gamma}\frac{\partial}{\partial\gamma}\left(\sin 3\gamma\frac{\partial}{\partial\gamma}\right),\\ \hat{T}_{\beta_3} &= -\frac{1}{\beta_3^3}\frac{\partial}{\partial\beta_3}\left(\beta_3^3\frac{\partial}{\partial\beta_3}\right).\end{aligned}$$

The symbol $\hat{T}_r$ denotes the operator of deformed nuclear rotational energy expressed in terms of the angular momentum operator and principal moments of inertia

$$\hat{T}_r=\sum_{i=1}^{3}\frac{\hat{I}_i^2}{J_i} = \sum_{i=1}^{3}\frac{\hat{I}_i^2}{J_i^{(2)}+J_i^{(3)}+J_i^{(4)}}. \qquad (1)$$

Here, $J_i^{(\lambda)}$ stands for the principal moments of inertia in the direction of the $i$-th axis in the body-fixed system due to quadrupole, octupole and hexadecapole deformations depending on $\lambda$=2, 3 and 4 respectively. The symbol $\hat{I}_i$ denotes the projection of the angular momentum operator on the $i$-th axis of the body-fixed coordinate, $\beta_{20}$ -the quadrupole equilibrium deformation parameter at the ground state (G.S.) and $B_\lambda$ -the mass parameter for multipolarity of $\lambda$. The eigenfunctions $\Omega$ of the collective energy operator are defined in the space of six dynamical variables: $0\le\beta_2<\infty$, $-\infty<\beta_3<\infty$, $\frac{n\pi}{3}\le\gamma\le\frac{(n+1)\pi}{3}$, $0\le\theta_1\le 2\pi$, $0\le\theta_2\le\pi$ and $0\le\theta_3<2\pi$ with the volume element $d\tau=\beta_2^4\beta_3^3|\sin 3\gamma|d\beta_2 d\beta_3 d\gamma d\theta_1\sin\theta_2 d\theta_2 d\theta_3$. Here $\beta_\lambda^2=\sum\beta_{\lambda\mu}\beta_{\lambda\mu}^*$ is the measure of nucleus deformation with multipolarity $\lambda$. Below we consider nuclei that are hard with respect to octupole transverse and hexadecapole vibrations. So the current version of soft-rotator model of OPTMAN takes into account the non-axial quadrupole, octupole and hexadecapole deformations, and $\beta_2$, $\beta_3$ and $\gamma$−vibrations with account of nuclear volume conservation.

By giving suitably an initial assignment of quantum numbers to low-lying levels, we can adjust the nuclear Hamiltonian parameters to describe low-lyinng experimental levels (usually first levels of 3-4 rotational bands plus levels of the first negative parity rotational band). Example of such level description for $^{28}$Si is demonstrated in Fig. 1.

Multipoles of deformed nuclear potential, with evident dependencies of deformations, necessary to built coupling appear from deformed nuclear radii, is given as follows by considering $\sum_{\lambda\mu}\beta_{\lambda\mu}Y_{\lambda\mu}(\theta',\varphi')$ small

$$V(r,R(\theta',\varphi')) = V(r,R_i) + \sum_{t=1}^{\max}\left.\frac{\partial^t V}{\partial R^t}\right|_{R=R_i}\frac{R_i^t}{t!}\{\sum_{\lambda\mu}\beta_{\lambda\mu}Y_{\lambda\mu}(\theta',\varphi')\}^t.$$

The optical nuclear potential was taken to be a standard form:

$$\begin{aligned} V(r) &= -(V_R+iW_V)f_R(r)+i4W_Da_D\frac{d}{dr}f_D(r)+V_C(r) \\ &\quad +\left(\frac{\hbar}{\mu_\pi c}\right)^2(V_{SO}+iW_{SO})\frac{1}{r}\frac{d}{dr}f_{SO}(r)\boldsymbol{\sigma}\cdot\mathbf{L} \end{aligned}$$

with the form factors given as

$$f_i=\left[1+\exp\left(r-R_i\right)/a_i\right]^{-1}, \qquad R_i = r_iA^{1/3}.$$

The symbols $i=R,V,D$ and $so$ denote the real volume, imaginary volume, imaginary surface and spin-orbit potentials respectively. One can see, that imaginary volume and imaginary surface potential form factors were considered to be equal.

In case of expansion of Coulomb potential $V_C(r)$ with evident dependences on deformations, necessary to account deformations dynamics, we follow the suggestion of Satchler *et al.* [10], using a multipole expansion of the Coulomb potential $V_C(r)$ for charged ellipsoid with a uniform charge density within the Coulomb radius $R_C$ and zero outside with some modifications (see [7, 11]).

In the mean time, energy dependence of the optical potential has been continuously improved guided by physical principles. Now, such features as the high-energy saturation behavior consistent with Dirac phenomenology, relativistic generalization of Elton and Madland, and properties stemming from the nuclear matter theory are taken into consideration[12].

$$\begin{aligned} V_R &= (V_R^0+V_R^1E^*+V_R^2E^{*2}+V_R^{DISP}e^{-\lambda_RE^*})\left[1+\frac{(-1)^{Z'+1}}{V_R^0+V_R^{DISP}}C_{viso}\frac{A-2Z}{A}\right] \\ &\quad +C_c\frac{ZZ'}{A^{1/3}}\varphi_c(E^*), \\ W_D &= \left[W_D^{DISP}+(-1)^{Z'+1}C_{wiso}\frac{A-2Z}{A}\right]e^{-\lambda_DE^*}\frac{E^{*2}}{E^{*2}+WID_D^2}, \\ W_V &= W_V^{DISP}\frac{E^{*2}}{E^{*2}+WID_V^2}, \\ V_{SO} &= V_{SO}^0e^{-\lambda_{so}E^*}, \\ W_{SO} &= W_{SO}^{DISP}\frac{E^{*2}}{E^{*2}+WID_{SO}^2}. \end{aligned}$$

Here, $E^*=(E_p-E_{fm})$, with $E_p$ - energy of the projectile and $E_{fm}$ - the Fermi energy, determined as $E_{fm}(Z,A)=-\frac{1}{2}\left[S_n(Z,A)+S_n(Z,A+1)\right]$ for neutrons and $E_{fm}(Z,A)=-\frac{1}{2}\left[S_p(Z,A)+S_p(Z+1,A+1)\right]$ for protons, where $S_i(Z,A)$ denotes the separation energy of nucleon $i$ from a nucleus labeled by $Z$ and $A$, while $Z'$, $Z$ and $A$ are charges of incident particle, nucleus and nucleus mass number, respectively. As we intend to analyze neutron and

proton scattering data simultaneously, we want to have a unique optical potential for nucleons with form suggested by [12] with a term $C_c Z Z'/A^{1/3} \cdot \varphi_c(E^*)$ describing the Coulomb correction to the real optical potential and isospin terms $(-1)^{Z'+1} C_{viso}(A-2Z)/A \cdot \varphi_{viso}(E^*)$ and $(-1)^{Z'+1} C_{wiso}(A-2Z)/A \cdot \varphi_{wiso}(E^*)$. We assumed that energy dependencies of $\varphi_{viso}(E^*)$ and $\varphi_{wiso}(E^*)$ are the same as those of real and imaginary surface potentials, while $\varphi_c(E^*)$ were considered to be the minus derivative of real potential , so that

$$\varphi_c(E^*) = (\lambda_R V_R^{DISP} e^{-\lambda_R E^*} - V_R^1 - 2V_R^2 E^*) \left[1 + \frac{(-1)^{Z'+1}}{V_R^0 + V_R^{DISP}} C_{viso} \frac{A-2Z}{A}\right].$$

All the parameters were taken to be equal for neutrons and protons. We assume that Lane model [13] works, therefore the neutron-proton optical potential difference of the suggested potential stems from the isospin terms, the Coulomb correction terms and difference of the neutron-proton Fermi energies.

Calculations with OPTMAN are now possible both for neutrons and protons as the projectile, and the upper incident nucleon energy is extended to at least 200 MeV[14]. We couple all the levels considered not only with the ground state level, but between each other as it is shown on Fig. 2 for $^{28}$Si case. With this options, OPTMAN is able to analyze the collective level structure, E2, E3, E4 $\gamma$−transition probabilities and reaction data in a self-consistent manner, which makes results of such analyses more reliable. We have found that this model was flexible enough so that OPTMAN can be applied not only to heavy rotational (actined) nuclei[15, 16], but can be applied very successfully even to a very light nucleus, namely $^{12}$C[17, 18] and light one $^{28}$Si[19], and also to vibrational nuclei such as $^{52}$Cr[20], $^{56}$Fe[21], $^{58}$Ni[22].

## 3. Global Optical Potential Global Search for A=24-122 mass region

As we can account most strongly coupled levels in our CC calculations (we call such approach as a CC with saturated coupling), our best-fit OMPs are free of errors arising from unaccount of coupling in spherical case or lack of such coupling in case of standard rotator or vibrator model is used. Thus, as we get rid of the major nuclear collective structure effects in OMP now, we can expect to get global OMP systematics with a smooth dependence of OMP on the mass number.

As the first step to carry out CC optical model calculations, we adjusted soft-rotator nuclear Hamiltonian parameters to describe experimentally observed low-lying collective levels of $^{24,26}$Mg, $^{28,30}$Si, $^{32}$S, $^{40}$Ar, $^{40}$Ca, $^{48}$Ti, $^{52}$Cr, $^{54,56}$Fe, $^{58,60,62}$Ni, $^{90,92}$Zr, $^{92,94,94,98}$Mo, $^{116,118,120,122}$Sn nuclides, by considering levels with quantum numbers $n_{\beta_2}$=0, $n_\gamma$=0, K=0$^+$( G.S. band); $n_{\beta_2}$=0, $n_\gamma$=0, K=2$^+$; $n_{\beta_2}$=1, $n_\gamma$=0, K=0$^+$ and $n_{\beta_2}$=0, $n_\gamma$=0, K=0$^-$ negative parity bands. Usually we coupled first 6-8 most strongly coupled collective levels. Nuclear wave functions with adjusted nuclear Hamiltonian parameters were used to built realistic coupling for coupled-channels calculations The best fit OMP for individual nuclides considered were found using a search option of OPTMAN code [7, 11] by minimizing the quantity $\chi^2$, incorporating neutron total $\sigma_{tot}$, proton reaction cross-sections $\sigma_{reac}$, and elastic and inelastic angular distributions. All these available experimental observables, if any, were included in $\chi^2$ search criteria. Smooth dependence of OMP for individual nuclides allowed to obtain a global OMP systematics, which is shown in Table 1. Overall $\chi^2$ for all nuclides considered was found to be about 8, the main contribution to $\chi^2$ came from excited levels other than the first $2_1^+$ one. For total, elastic scattering and angular distributions with the first excited level excitation, it was usually less than 3.

Figure 3 demonstrates the quality of neutron total and proton nonelastic cross section predictions. One can see that we face no problems in describing total cross sections, as well as proton reaction cross sections. Fig. 4 shows the angular distributions of the neutron elastic

| | |
|---|---|
| $V_R^0 = -35.93 - 0.025A$ | $V_R^{DISP} = 94.88$ |
| $\lambda_R = 0.004283$ | |
| $V_R^1 = 0.03$ | $V_R^2 = 0.00018$ |
| $W_D^{DISP} = 21.11 - 37.68A^{-1/3}$ | $\lambda_D = 0.0176$ |
| $WID_D = 11.60$ | |
| $W_V^{DISP} = 15.89$ | $WID_V = 68.54 + 0.087A$ |
| $V_{so}^0 = 5.922 + 0.003A$ | $\lambda_{so} = 0.005$ |
| $W_{SO}^{DISP} = -3.1$ | $WID_{SO} = 160.00$ |
| $r_R = 1.2450 - 0.2546A^{-1/3}$ | $a_R = 0.683 - 0.132A^{-1/3}$ |
| $r_D = 1.4217 - 0.5505A^{-1/3}$ | $a_D = 0.536 - 0.059A^{-1/3}$ |
| $r_C = 1.2607$ | $a_C = 0.360$ |
| $C_c = 0.9$ | |
| $C_{viso} = 12.0$ | $C_{wiso} = 14.00$ |
| $r_{so} = 1.18 - 0.65A^{-1/3}$ | $a_{so} = 0.59$ |

Table 1: The optical potential parameters for $24 \leq A \leq 122$ allowing the best fit of experimental data. Potential strengths in MeV; radii and diffusenesses in fm. (*Note that optical potential strengths except for the spin-orbit and Coulomb terms must be multiplied by a factor $K(E) = 2E/(E + M_p c^2)$ due to the relativistic generalization, see: Ref. [7, 11].)

scattering for $^{56}$Fe and the proton elastic scattering for $^{90}$Zr. Fig. 5 shows the angular distributions for the proton inelastic scattering leading to the first $2_1^+$ level excitation of $^{28}$Si and to the negative parity $3_1^-$ level excitation of $^{54}$Fe. Angular distributions for these levels are described by our model with high accuracy for all nuclides considered. Analogous or a little worse quality is for angular distributions with the first $4_1^+$ or the second $0_2^+$ level excitation predictions. Fig. 6 shows prediction of neutron angular distributions for the excitation of the groups of the levels for $^{32}$S and $^{92}$Zr.

Finally in Fig. 7 we demonstrate predicted inelastic scattering angular distributions for $^{24}$Mg and $^{122}$Sn nuclides, which have the lightest and the heaviest mass among the considered by our global potential search.

Calculations shown in the figures were carried out with deformations equal for neutrons and protons, while we found that for single-closed-shell nuclei: $^{52}$Cr, $^{54}$Fe, $^{58,60,62}$Ni, $^{92}$Zr, $^{92}$Mo and $^{116,118,120,122}$Sn, deformations allowing best fit are greater for the probe for which the corresponding shell of the interacting nuclei is closed. Account of difference of the deformation parameters for incident neutron and proton may improve $\chi^2$ by about 30%. This feature is consistent with the nuclear theory predictions [23].

## 4. Conclusion

We developed CC code OPTMAN within Soft-rotator nuclear model CC approach, allowing to analyze the collective level structure, E2, E3, E4 $\gamma$−transition probabilities and reaction data in a self-consistent manner. We have found that this model was flexible enough so that OPTMAN can be applied not only to heavy(actinide) nuclei, but can be applied very successfully even to a very light nucleus, and also medium weight vibrational nuclei.

Global optical potential for even-even nuclides in A=24 - 122 mass region is suggested. Expanding below A=24 and above A=122 is in progress

## Acknowledgments

The authors are grateful to the guidance of late Dr. Y. Kikuchi, who started the collaboration among the authors and would like to thank the members of nuclear data groups at JIENR and JAERI for fruitful discussions and supports to this work.

A part of this work was supported through ISTC Project B-521, with Japan as Financing Party.

## References

[1] A.I. Blokhin, A.V. Ignatjuk, V.N. Manokhin *et al.*, "BROND-2, Library of Recommended Evaluated Neutron Data, Documentation of Data Files", Yudernie Konstanty, issues 2+3 in English (1991).

[2] T. Tamura, Rev. Mod. Phys. **37**, 679 (1965).

[3] J. Raynal, "Optical Model and Coupled-Cannel Calculations in Nuclear Physics", IAEA SMR-9/8, IAEA (1970).

[4] Yu.V. Porodzinskiĭ and E.Sh. Sukhovitskiĭ, Phys. of Atom. Nucl. **59**, 247 (1996).

[5] Yu.V. Porodzinskiĭ and E.Sh. Sukhovitskiĭ, Sov. J. Nucl. Phys. **53**, 41 (1991).

[6] Yu.V. Porodzinskiĭ and E.Sh. Sukhovitskiĭ, Sov. J. Nucl. Phys. **54**, 570 (1991).

[7] E.Sh. Sukhovitskiĭ, Yu.V. Porodzinskiĭ, O. Iwamoto, S. Chiba and K. Shibata, JAERI-Data/Code 98-019 (1998); E.Sh. Soukhovitskiĭ, G.B. Morogovskiĭ, S. Chiba, O. Iwamoto, and T. Fukahori, JAERI-Data/Code 2004-002 (2004)

[8] A. Bohr and B.R. Mottelson, "Nuclear Structure, Vol. II, Nuclear Deformations", p.195, W. A. Benjamin Inc. (1975).

[9] A.S. Davydov, "Vozbuzhdennye sostoyaniya atomnykh yader (Excited States of Atomic Nuclei)", Moscow: Atomizdat (1969).

[10] R.H. Bassel, R.M. Drisko, and G.R. Satchler, Oak Ridge National Laboratory Report ORNL-3240, (1962).

[11] E.Sh. Sukhovitskiĭ, S. Chiba, J. Nucl. Sci.Technol. **Supple. 2**, 144-147 (2002).

[12] J.P. Delaroche, Y. Wang and J. Rapaport, Phys. ReV., **C39**, 391-404 (1989).

[13] A.M. Lane, Phys. Rev.Lett. **8**, 171-172 (1962); A.M. Lane, Nucl. Phys. **35**, 676-685, (1962).

[14] E.Sh. Soukhovitskiĭ and S. Chiba, J. Nucl. Sci. Technol. **Supple. 2**, 697(2002).

[15] E.Sh. Sukhovitskiĭ, O. Iwamoto, S. Chiba and T. Fukahori, J. Nucl. Sci. Technol. **37**, 120 (2000).

[16] E.Sh. Soukhovitski, S. Chiba, J. Nucl. Sci. Technol., **Supple. 2**, 144 (2002).

[17] S. Chiba, O. Iwamoto, Y. Yamanouti, M. Sugimoto, M. Mizumoto, K. Hasegawa, E.Sh. Sukhovitskiĭ, Yu. V. Porodzinskiĭ, and Y. Watanabe, Nucl. Phys. A **624**, 305 (1997).

[18] S. Chiba, O. Iwamoto, E.Sh. Sukhovitskiĭ, Yu. Watanabe and T. Fukahori, J. Nucl. Sci. Technol. **37**, 498 (2000).

[19] W. Sun, Y. Watanabe, E.Sh. Sukhovitskii, O. Iwamoto and S. Chiba, J. of Nucl. Sci. and Technol. 40, 635 (2003).

[20] E.Sh. Sukhovitskiĭ, S. Chiba, J.-Y. Lee, B.-t. Kim and S.-W. Hong, J. Nucl. Sci. Technol. 40, 69(2003).

[21] E. Sh. Sukhovitskiĭ, S. Chiba, J.-Y. Lee, Y.-O. Lee, J. Chang, T. Maruyama and O. Iwamoto, J. Nucl. Sci. Technol. **39**, 816 (2002); J.Y. Lee, E.Sh. Sukhovitskiĭ, Y.-O. Lee, J. Chang, S. Chiba and O. Iwamoto, J. Korean Phys. Soc. **38**, 88 (2001).

[22] E.Sh. Sukhovitskiĭ, Y.-O. Lee, J. Chang, S. Chiba and O. Iwamoto, Phys. Rev. **C62**, 044605 (2000).

[23] V.A. Madsen, V.R. Brown, J.D. Anderson, Phys Rev. **C12**, 1205-1211 (1975).

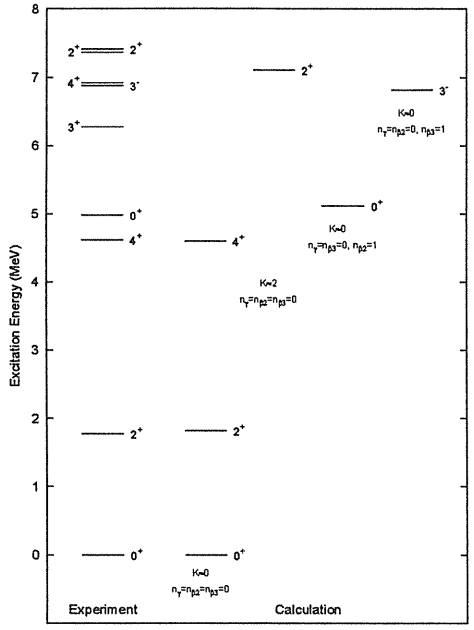



Figure 1: Comparison of the experimental and calculated $^{28}$Si level schemes. Thick lines show experimental levels described by the soft rotator model.

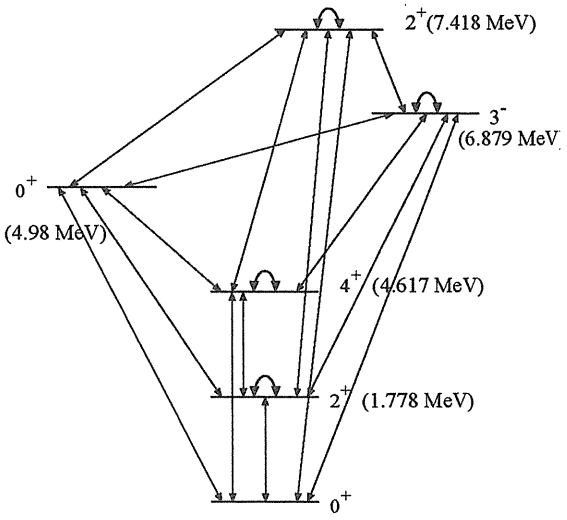



Figure 2: Coupling scheme employed in the present calculations for $^{28}$Si. Arrows show the coupling used in the parameter search procedure.

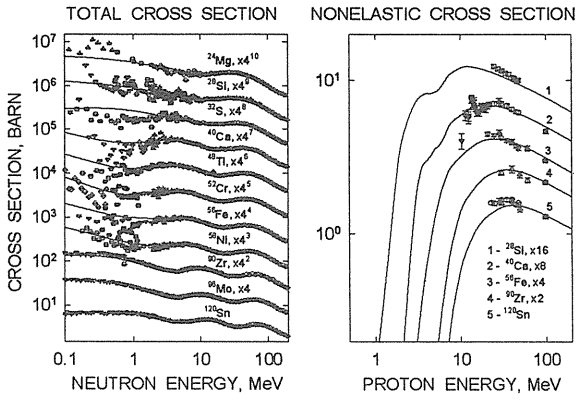



Figure 3: Comparison of neutron total and proton nonelastic cross sections: Predictions with the present global potential (solid lines), available experimental data (symbols).

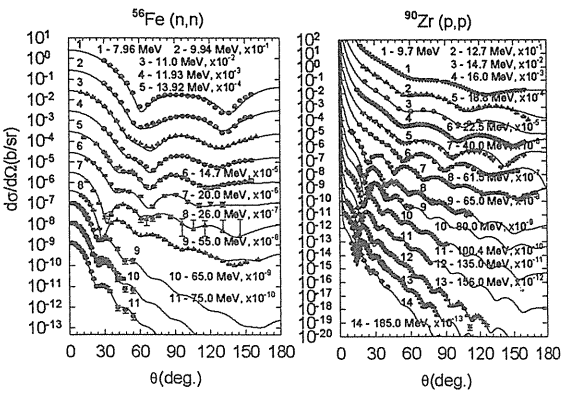



Figure 4: Comparison of experimental and predicted angular distributions of neutron elastic scattering for $^{56}$Fe (left) and proton elastic for $^{90}$Zr (right).

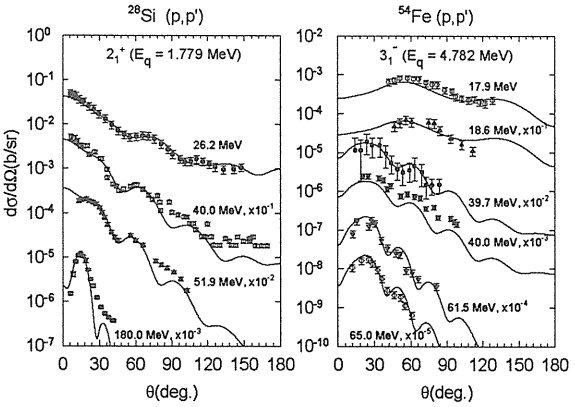



Figure 5: Comparison of experimental and predicted proton inelastic scattering angular distributions for excitation of the $2_1^+$ level of $^{28}$Si (left) and $3_1^-$ level of $^{54}$Fe (right).

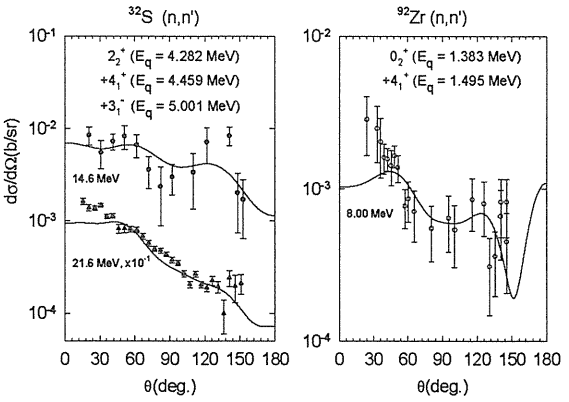



Figure 6: Comparison of experimental and predicted neutron angular distributions for excitations of groups of levels of $^{32}$S (left) and $^{92}$Zr (right).

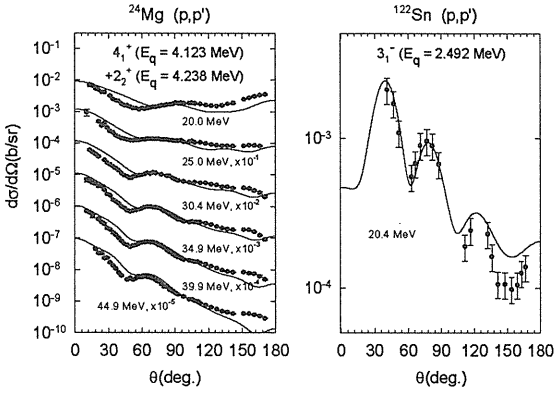



Figure 7: Comparison of experimental and predicted proton angular distributions for excitations of different levels of $^{24}$Mg (left) and $^{122}$Sn (right).

JP0550253



## 2.12 Comprehensive Study of Lattice Cell Calculations for Thorium Based Fuel Cycle in Light Water Reactors Using SRAC Code

Le Dai Dien, Ha Van Thong and Giang Thanh Hieu
*Institute for Nuclear Science and Technology, INST*
*5T-160 Hoang Quoc Viet, Nghia Do, Ha Noi-VietNam*

The designers of the innovative reactors have proposed a number of approaches to increasing resource efficiency . Adding thorium, a fertile material, to the fuel is considered in this report. Under this approach, a large portion of the reactor output is produced by fissioning of the $^{233}U$ resulting from neutron capture by thorium, which results in reduced requirements for naturally-occurring fissile uranium ($^{235}U$). The proliferation potential of the light water reactor fuel cycle may be significantly reduced by utilization of thorium as a fertile component of the nuclear fuel.

The concept of using Th-$^{233}U$ as fuel has been applied to an existing LWR design as compare with another fuel cycles (UO2 and MOX). SRAC code is extensive used to investigate the lattice cell problem.

### 1. Introduction.

Nuclear fuels used in reactors can be $^{235}U$, $^{239}Pu$ and/or $^{233}U$. The content of natural uranium contains 99.3% $^{238}U$, 0.7% $^{235}U$. The fuel irradiated in conventional light water reactors must be enriched from 2 to 4% $^{235}U$ to maintain nuclear fission chain reaction by using light water as the moderator and coolant. $^{239}Pu$ can be produced from fertile nuclide $^{238}U$, while $^{233}U$ produced from $^{232}Th$. Thorium is much more abundant in the earth's crust than uranium and the need of Pu burning from existing Pu stokpiles make the thorium based fuel cycle is widely considered for many decades.

Thorium like uranium can be used as fuel in nuclear reactors though thorium is not fissile material, but $^{232}Th$ is capable to capture slow neutrons to form $^{233}U$, a fissionable isotope. Thus, thorium based fuel cycle can be used in all proven reactor types[(1)].

$^{233}U$ produced from $^{232}Th$ in the neutronics point of view is one of the best isotope in the fissionable isotopes. In all energy range, neutron fission yield ratio ($\eta$) and the number of neutron absorbed are higher than those of $^{235}U$ and $^{239}Pu$, so that $^{233}U$ could be used as fuel for many kind of reactor.

Thorium oxide $ThO_2$ has greater stability and can be used with high temperature, longer durability due to its melting point of $3050^0C$ ($UO_2$ : 2700 - $2800^0C$) that expected to gain high burn-up.

The reactor fuelled by thorium will not reach critical but it can use a mixed core as the *seed-and-blanket* concept. $^{233}U$ would be produced which in turn fuel either the initial reactor. This feature is expected to be used to consume a large plutonium stockpiles today.

One of the advantages of $^{233}U$ as compare with $^{235}U$ and $^{239}Pu$ is that the higher neutron emitted yield when one neutron absorbed. The $^{235}U$ or $^{239}Pu$ are used to breed fissionable isotope

from thorium. $^{232}$Th absorbs neutron to become $^{233}$Th and then decay to $^{233}$Pa and finally to $^{233}$U by decay chain:

$$^{232}_{90}Th + ^{1}_{0}n \rightarrow ^{233*}_{90}Th \rightarrow ^{233}_{90}Th + \gamma_c$$
$$^{233}_{90}Th \rightarrow ^{233}_{91}Pa + ^{0}_{-1}\beta + \gamma_d + \upsilon$$
$$^{233}_{91}Pa \rightarrow ^{233}_{92}U + ^{0}_{-1}\beta + \gamma_d + \upsilon$$

The fuel is irradiated in the reactor core, in the back end of fuel cycle $^{233}$U can be extracted from thorium and reused as fuel to make a close cycle. In this study, from reactor physics calculation aspect, our work focuses on estimation of nuclear fuel conversion of $^{233}$U and those of uranium or MOX fuel cycles.

Capture cross section of $^{232}$Th and capture and fission cross sections of $^{233}$U give the fuel conversion ratio. The ratio of the number of fissionable nuclei produced from fertile material to the number of fissionable nuclei consumed in fission and non-fission reactions. It is given by:

$$N^{Fer}\sigma_c^{Fer} = N^{Fis}(\sigma_c^{Fis} + \sigma_f^{Fis})$$

Thus, ratio of fissionable content and fertile content in the fuel can be defined by:

$$\frac{N^{Fis}}{N^{Fer}} = \frac{\sigma_c^{Fer}}{\sigma_f^{Fis} + \sigma_c^{Fis}}$$

In thorium based fuel cycle, ratio of cross sections $\frac{\sigma_c^{Fer}}{\sigma_f^{Fis} + \sigma_c^{Fis}}$ identifies the capability of reproducing of $^{233}$U fuel during the fuel irradiated in the reactor core.

For a purpose of proving the advantages of the thorium fuel cycle, the preliminary reactivity calculations were performed for lattices of fuel rods containing $ThO_2$ and $(Th,U)O_2$ as well as $UO_2$ and MOX. The reactor would be water cooled and retains all design features of a LWR.

## 2. Lattice cell calculations with LWRs.

The lattice cell of LWRs has a pin cell formed a square lattice as in Figure 1. The geometry parameters are in Table 1.

**Table 1: Lattice cell parameters of LWRs.**

| Parameters | Material (temperature) | PWR | BWR |
|---|---|---|---|
| R1(mm) | Fuel (900 K) | 4.096 | 4.12 |
| R2(mm) | Clad (600 K) | 4.75 | 4.76 |
| L(mm) | Water (600 K) | 12.6 | 12.65 |

From physics calculation aspect for lattice cell problem, the difference between PWR and BWR is that the coolant in PWR is not boil while in BWR the vapor content can be up to 40% in

normal operation. The content of $UO_2$ 3% -$ThO_2$ 97% is used for Thorium fuel pin and $UO_2$ 4% used for PWR and BWR pin cell calculations.

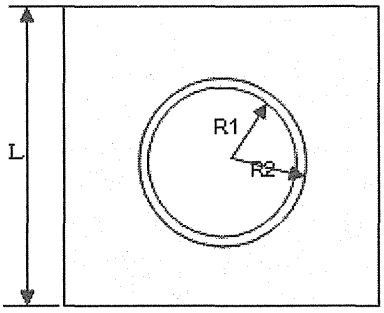



**Figure 1**: Lattice cell configuration of LWRs.

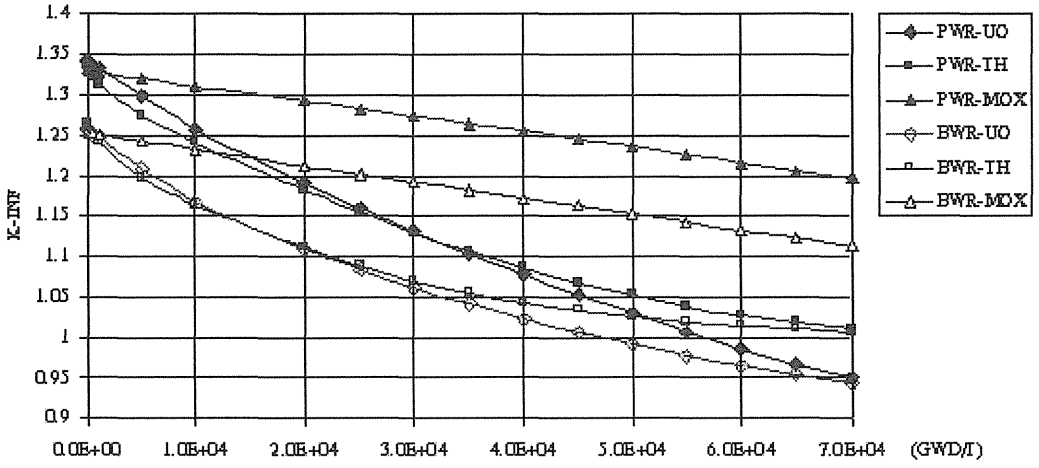



**Figure 2: K-inf vs. Fuel Burn-up.**

The variation of multiplication factor K-inf on fuel burn-up is presented in Figure 2. MOX and Th/$^{233}$U fuel can be burn up to 60GWd/T, while $UO_2$ fuel can be reach maximum at 35GWd/T – the average burn-up of present LWRs.

### 3. Estimate of fuel conversion factor.

With $UO_2$ and MOX fuels the conversion ratio is in the range of 0.5 to 0.7. Especially in MOX fuel, due to the main fission isotope is $^{239}$Pu so that the conversion factor is not so high, while the $^{232}$Th/$^{233}$U fuel it is much higher as $^{233}$U is breeded during fuel irradiation in the core, the value obviously is greater than 1. The Figure 3 illustrates the variance of conversion factor by fuel burn-up of three fuel cycles.

It should be noted that if the $UO_2$/MOX fuels are used in combination with Th/$^{233}$U in a certain configuration of the core, the fuel conversion ratio would be improved, it will make the fuel burn-up more higher and save the $^{235}$U fuel as well as the good option for consumption of plutonium.

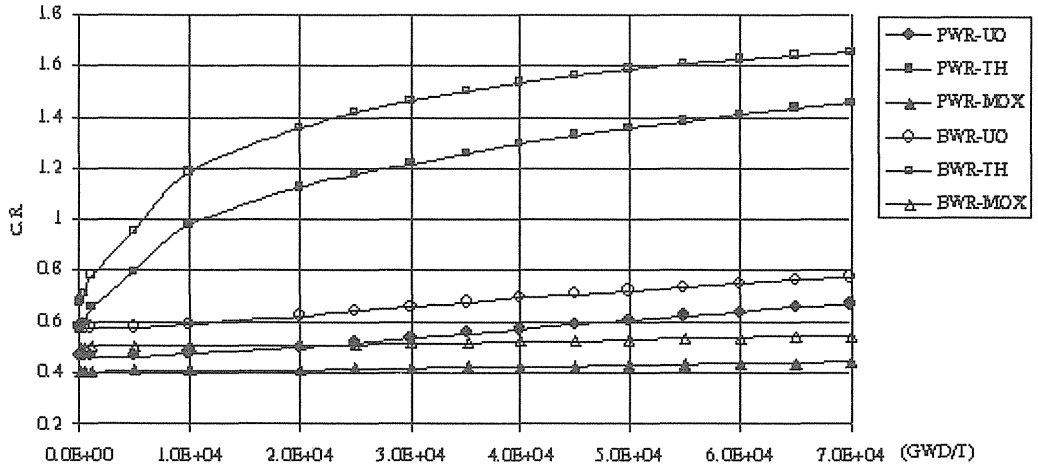



**Figure 3: Conversion ratio (C.R) vs. Burn-up.**

Further, from Table 2 we can see that the $^{239}$Pu content produced from Th/$^{233}$U cycle is much less than those formed in $UO_2$ or MOX fuel cycles. This is also an advantage of thorium based fuel cycle as plutonium can not be extracted during reprocessing.

**Table 2: $^{239}$Pu content in the fuel burn-up.**

| GWd/T | PWR | | | BWR | | |
|---|---|---|---|---|---|---|
| | $UO_2$ | Th-$^{233}$U | MOX | $UO_2$ | Th-$^{233}$U | MOX |
| 1.0E+02 | 3.725E-07 | 1.023E-09 | 6.737E-04 | 4.634E-07 | 1.101E-09 | 6.732E-04 |
| 5.0E+02 | 4.609E-06 | 1.347E-08 | 6.731E-04 | 5.697E-06 | 1.441E-08 | 6.732E-04 |
| 1.0E+03 | 1.058E-05 | 3.180E-08 | 6.720E-04 | 1.304E-05 | 3.375E-08 | 6.740E-04 |
| 5.0E+03 | 4.884E-05 | 1.542E-07 | 6.712E-04 | 5.974E-05 | 1.541E-07 | 6.803E-04 |
| 1.0E+04 | 8.198E-05 | 2.476E-07 | 6.650E-04 | 1.022E-04 | 2.293E-07 | 6.876E-04 |
| 2.0E+04 | 1.194E-04 | 3.231E-07 | 6.573E-04 | 1.553E-04 | 2.635E-07 | 7.005E-04 |
| 3.0E+04 | 1.392E-04 | 3.375E-07 | 6.341E-04 | 1.938E-04 | 2.447E-07 | 7.108E-04 |
| 4.0E+04 | 1.474E-04 | 3.648E-07 | 6.176E-04 | 2.195E-04 | 2.266E-07 | 7.187E-04 |
| 5.0E+04 | 1.495E-04 | 4.212E-07 | 6.005E-04 | 2.376E-04 | 2.187E-07 | 7.242E-04 |
| 6.0E+04 | 1.488E-04 | 5.017E-07 | 5.828E-04 | 2.512E-04 | 2.241E-07 | 7.274E-04 |
| 7.0E+04 | 1.471E-04 | 5.954E-07 | 5.646E-04 | 2.620E-04 | 2.439E-07 | 7.286E-04 |

In general, Th/$^{233}$U fuel is used in combination with $UO_2$ fuel or MOX in fuel assemblies. The practical use has been investigating in India and many modeling studies have also been applied to present exist designs as PWR, VVER, PHWR [4-9].

In this study, two kinds of fuel are combined into one fuel rod. The $UO_2$ fuel as seed is centered and surrounded by Th/$^{233}$U fuel outside.

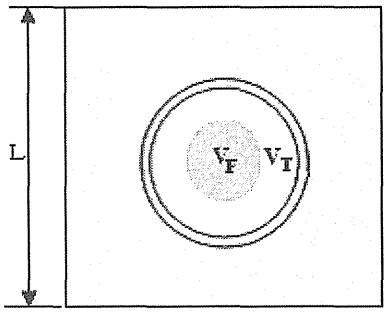



**Figure 4: Two-layer fuel pin configuration.**

The Figure 5 represents the dependence of multiplication factor K-inf and conversion ratio at the burn-up of 40 GWd/T by the volume ratio of $UO_2$ fuel alloy ($V_F$) and Th/$^{233}$U fuel ($V_T$). When the $UO_2$ volume increases, multiplication will be increased and conversion ratio decreases. However, these parameters will have minor change in the range 1.5 and 2.5 of the ratio $V_F/V_T$ values.

It should be noted that two-layered fuel rod may be one option in choosing the configurations of fuel assemblies beside well known configurations [4, 6, 7] that have been investigated. The detail investigations should be carried out to confirm the feasibility and applicability of this configuration.

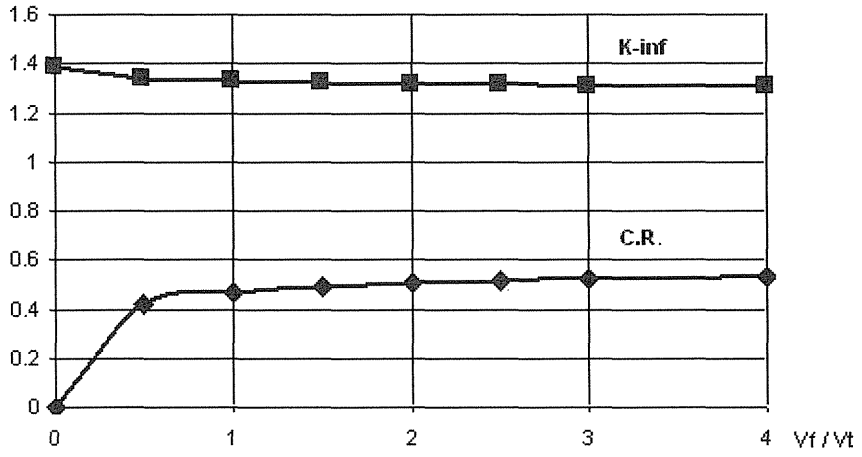



**Figure 5: The multiplication factor K-inf and conversion ratio at burn-up of 40 GWd/T vs. Volume ratio of two-layer fuel rod.**

## 4. Conclusion.

In the next several decades, the conventional LWRs based on uranium fuel cycle are still used. However, the other types of reactor are under extensive development, the typical reactors are

FBR, FBMR, HTGR etc. With the emphasize on transuranium and MA transmutation, the Th/$^{233}$U fuel cycle with the important advantages:

+ Contribute into burning of plutonium stockpiles, and $^{239}$Pu produced by this fuel cycle is much less than MOX or $UO_2$ fuel.
+ High radioactive waste with large lifetime is less than other fuel cycles.
+ High fuel burn-up.
+ Used for high temperature reactors (HTR).
+ And sustainable as compare with limited uranium resource.

It will definitely be one of the remarkable options for nuclear fuel cycle in the future.

**References.**

[1] "*Thorium based fuel options for the generation of electricity: Developments in the 1990s. (Vienna, IAEA-TECDOC-1155, May 2000).*

[2] K. Okumura, T. Kugo, K. Kaneko, K. Tsuchihashi. *SRAC: The comprehensive neutronics calculation code system. JAERI/Code 2002.*

[3] Le Dai Dien , Ha Van Thong, Giang Thanh Hieu. *Application of Pij module in SRAC code system for lattice cell problems of PWR and BWR. 2003 Report, CS/03/04-09. VAEC.*

[4] K. Okumura, H. Unesaki, T. Kitada, E. Saji - *Benchmark results of burn-up calculation for LWR next generation fuels. PHYSOR 2002, Seoul, Korea, October 7-10,2002.*

[5] D.F.Torgerson, P.G. Boczar, A.R.Dastur. *CANDU Fuel Cycle Flexibility. AECL-11129 (1994).*

[6] P.S.W.Chan, P.G.Boczar, R.J.Ellis, F.Ardeshiri. *Fuel management simulations for once-through thorium fuel cycle in CANDU reactors. IAEA Technical Commettee Meeting on "Fuel Cycle Options for LWRs and HWRs", 1998.*

[7] K. Balakrishinan. *HWR advanced fuel cycle flexibility and sustainable development, Ibid.*

[8]. D.E. Beller, W.C. Sailor, F.Venneri. *A closed ThUOX fuel cycle for LWRs with ADTT(ATW) backend for 21$^{st}$ century. LA-UR-98-4186(1998).*

[9] A.Yamamoto, T.Ikehara, T.Ito, E.Saji. *Benchmark Problem suite for reactor physics study of LWR next generation fuels. J. Nucl. Sci. Technol., 39(8), 900 (2002)*

JP0550254



# 2.13 CENDL-3 and the Works Concerned

**Ge Zhigang**

*China Nuclear Data Center (CNDC), China Institute of Atomic Energy (CIAE),*
*China Nuclear Data Coordination Network (CNDCN)*
*P. O. Box 275-41, Beijing 102413, People's Republic of China*
*Tel: +86-10-69357275, Fax: +86-10-69357787, e-mail: gezg@iris.ciae.ac.cn*

## Abstract

Chinese Evaluated Nuclear Data Library third version (CENDL-3.0) contains the nuclear data evaluated works, which were performed during the period of 1995-2000 at China Nuclear Data Center (CNDC) in cooperation with China Nuclear Data Coordination Network (CNDCN), including the neutron data for about 200 nuclides in ENDF/B-6 format in energy region of $10^{-5}$eV-20MeV. For most important nuclei the comparisons with other nuclear data libraries (ENDF, JENDL, BROND, JEF, et al.) have been performed, and the benchmark testing for the most important nuclei also have been done.

CNDC and CNDCN also have got a lot of progress in the fields of nuclear data theory study, model and code developments, and nuclear database establishment etc. The status of CENDL-3 and some progress of the nuclear data evaluation studies in the past several years will be introduced in this presentation.

## I. CENDL-3 Library

### 1.1 The view of CENDL-3

The evaluated activities of CENDL-3.0 were started in 1995 and finished in 2000. The library includes comprehensive data evaluations for all neutron reactions in the energy range from $10^{-5}$eV to 20MeV for 200 nuclides, among them, 133 nuclides are newly evaluated, and 67 nuclides are taken from CENDL-2.1.

The experimental data involved into the evaluations were taken from the EXFOR library, the literary indexed by CINDA and the experimental data measured in China domestically institutes and universities. The experimental data were evaluated carefully and corrected by using the new standard cross sections and decay data et al.

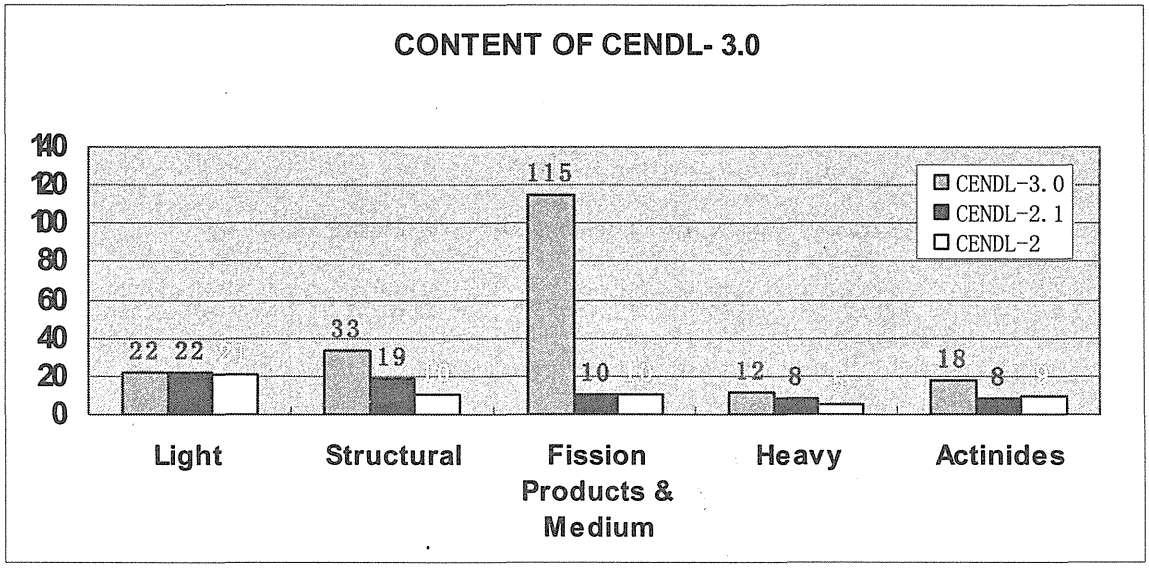
UNF series cods LUNF, UNF, SUNF, FUNF were used in the model calculations for the light elements, structural materials, fission products & medium elements, heavy elements and actinides, respectively. Most of the input model parameters are taken from the RIPL library and were adjusted based on the experimental information. APMN and APOM94 programs are used for optimal optical potential parameters automatically searching. ECIS95 is also involved for some model calculations.

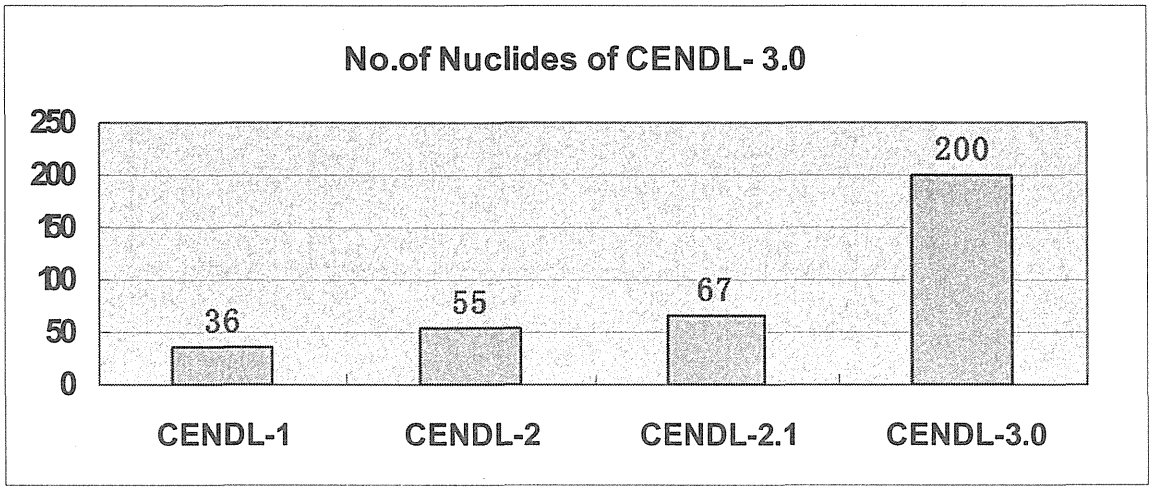
All evaluations were checked by using the ENDF facilities CHECKR, PHYCHE and FIZCON.

CENDL-3.0 was distributed inside of CNDCN and some users in China as an internal test version in 2001. After that some feedback information from benchmark testing and users has been received. These were considered in the re-evaluations for improving the data of the important nuclides, especially for the uranium and plutonium isotopes when the improvement is completed, a new version of CENDL-3.0 CENDL-3.1 will be released in the world.

Table 1. The Nuclides of CENDL-3.0

| Nucl. | Content |
|---|---|
| **Light Elements** | $^{1,2,3}H$, $^{3,4}He$, $^{6,7}Li$, $^{9}Be$, $^{10,11}B$, $^{14}N$, $^{16}O$, $^{19}F$, $^{23}Na$, $^{nat}Mg$, $^{27}Al$, $^{nat}Si$, $^{31}P$, $^{nat}S$, $^{nat}Cl$, $^{nat}K$, $^{nat}Ca$ |
| **Structural Materials** | $^{nat}Ti$, $^{nat}V$, $^{50,52,53,54,nat}Cr$, $^{55}Mn$, $^{54,56,57,58,nat}Fe$, $^{59}Co$, $^{58,60,61,62,64,nat}Ni$, $^{63,65,nat}Cu$, $^{nat}Zn$ |
| **Fission Products & Medium Elements** | $^{69,71,nat}Ga$, $^{83,84,85,86}Kr$, $^{85,87,nat}Rb$, $^{88,89,90}Sr$, $^{89,91}Y$, $^{90,91,92,93,94,95,96,nat}Zr$, $^{93,95}Nb$, $^{95,97,98,100,nat}Mo$, $^{99}Tc$, $^{99,100,101,102,103,104,105}Ru$, $^{103}Rh$, $^{105,108}Pd$, $^{107,109,nat}Ag$, $^{113,nat}Cd$, $^{115,nat}In$, $^{nat}Sn$, $^{121,123,nat}Sb$, $^{130}Te$, $^{127}I$, $^{124,129,131,132,134,135,136}Xe$, $^{133,134,135,137}Cs$, $^{130,132,134,135,136,137,138,nat}Ba$, $^{139}La$, $^{140,141,142,144}Ce$, $^{141}Pr$, $^{142,143,144,145,146,147,148,150,nat}Nd$, $^{147,148,149}Pm$, $^{144,147,148,149,150,151,152,154,nat}Sm$, $^{151,153,154,155,nat}Eu$, $^{152,154,155,156,157,158,160,nat}Gd$, $^{164}Dy$ |
| **Heavy Elements** | $^{nat}Lu$, $^{nat}Hf$, $^{181}Ta$, $^{nat}W$, $^{197}Au$, $^{nat}Hg$, $^{nat}Ti$, $^{204,206,207,207,nat}Pb$, |
| **Actinides** | $^{233,234,235,236,238,239}U$, $^{237}Np$, $^{238,239,240,241,242}Pu$, $^{241,242}Am$, $^{249}Bk$, $^{249}Cf$ |



## 1.2 The evaluation of CENDL-3

**Light elements**

Based on the updated experimental information, a series codes (LUNF) were developed for model calculations of $^{6,7}$Li and $^{9}$Be, mainly for double differential cross sections (MF-6). The full sets of neutron data, i.e. cross sections of all reactions, energy and angular distribution of secondary neutrons and differential cross sections, etc. were provided.

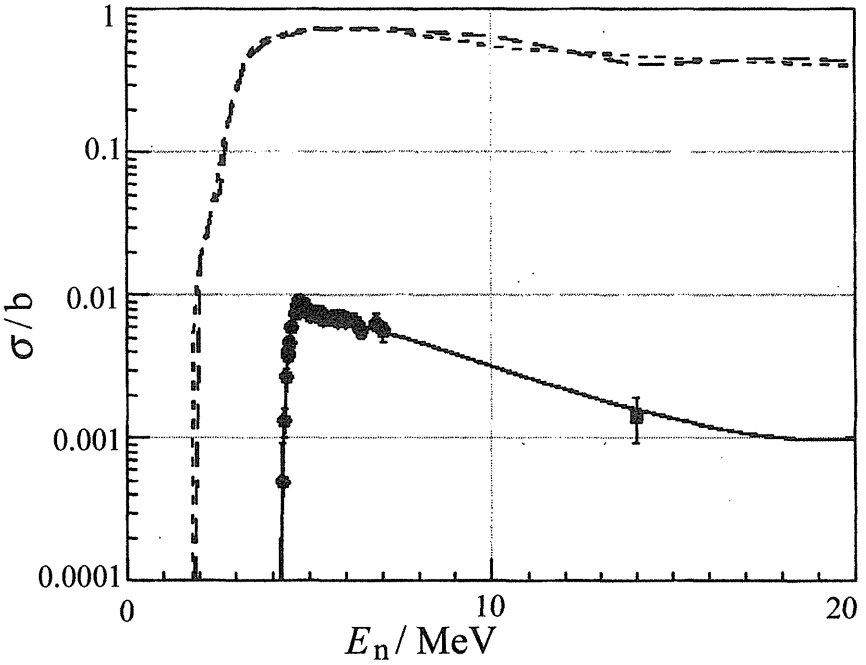



**Fig. 1 $^{6}$Li(n, n'γ) $^{6}$Li total inelastic scattering reaction**

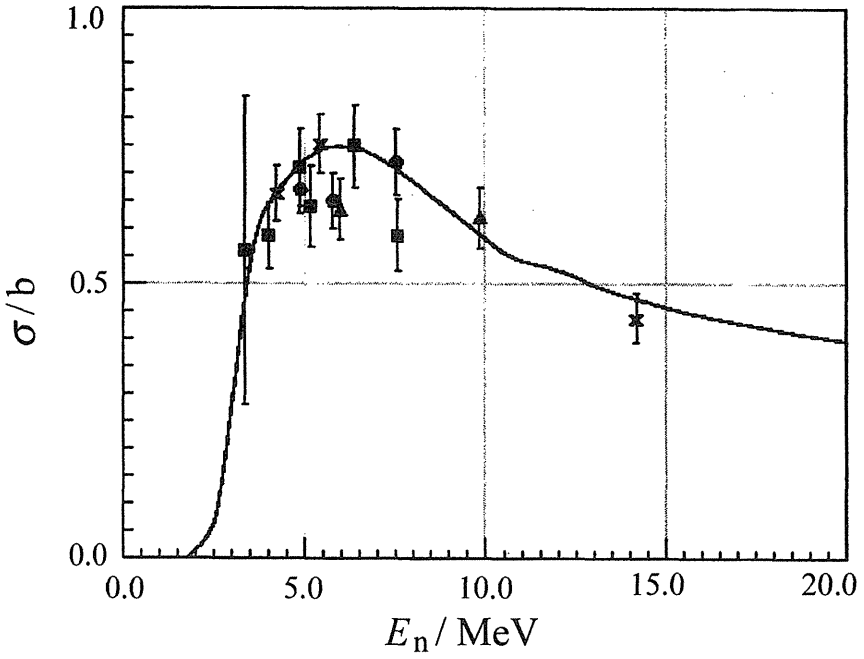



**Fig. 2 $^{6}$Li(n, nd) $^{4}$He reaction cross section**

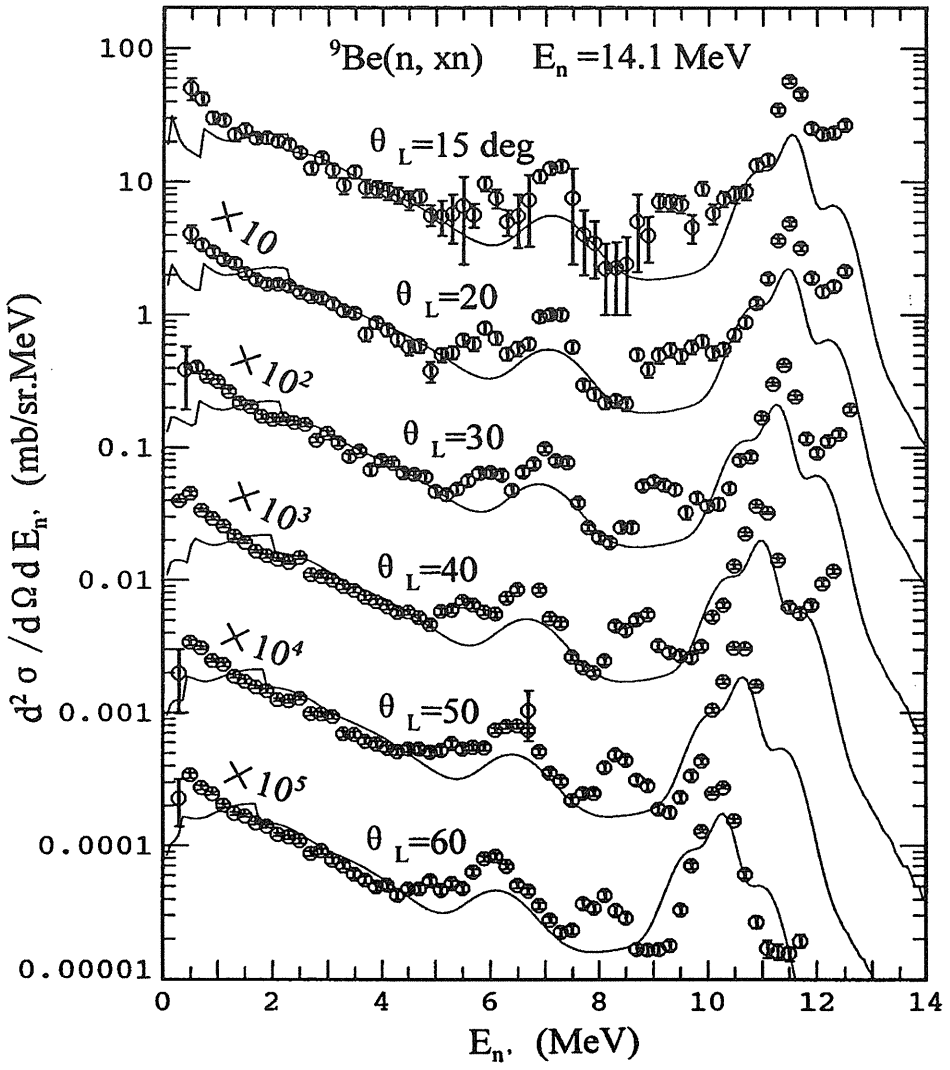



**Fig.3 n+$^{9}$Be DDX comparisons with exp. data**

**Structural materials**

According to the MUP code used in the CENDL-2 evaluations and the new results of nuclear reaction theoretical studies, a new code UNF used for structural material and medium nuclides calculation was development. With the UNF code calculations and evaluation of new experimental data, the full neutron data set (γ-production data including) are provided in ENDF/B-6 format.

Comparing to CENDL-2, the main development of CENDL-3.0 for the structured materials is that in addition to the data of natural elements, the data of their isotopes were also included, and made the data consistent between the natural elements and their isotopes.

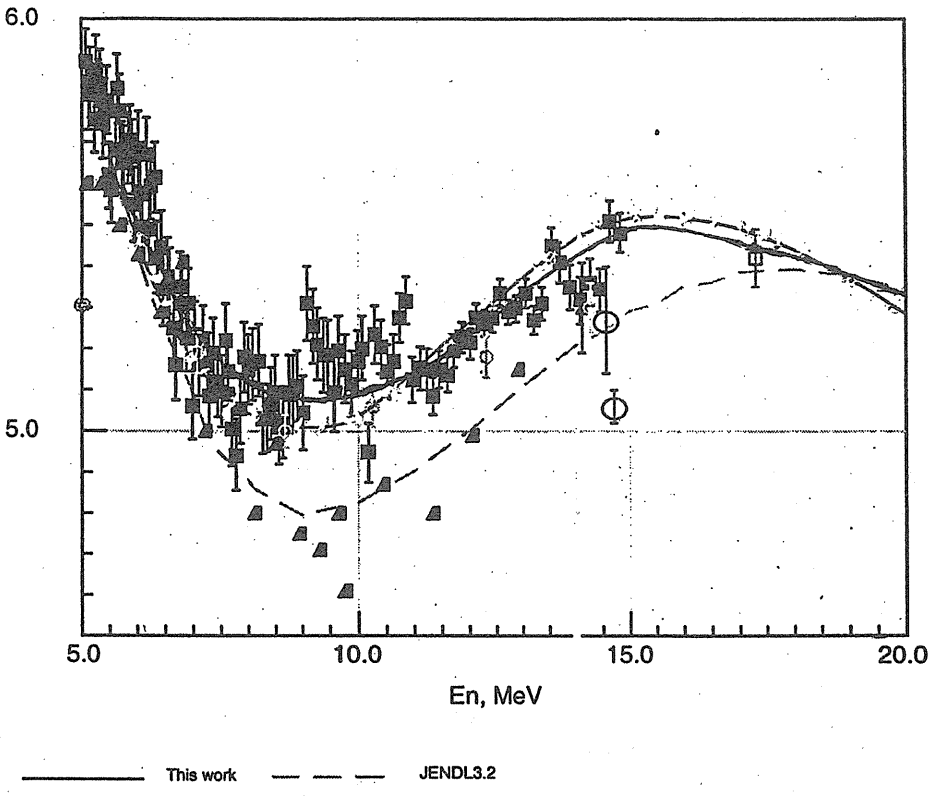



**Fig.4 Evaluated total CS of n+$^{nat}$W comparison with exp. data and JENDL3.2**

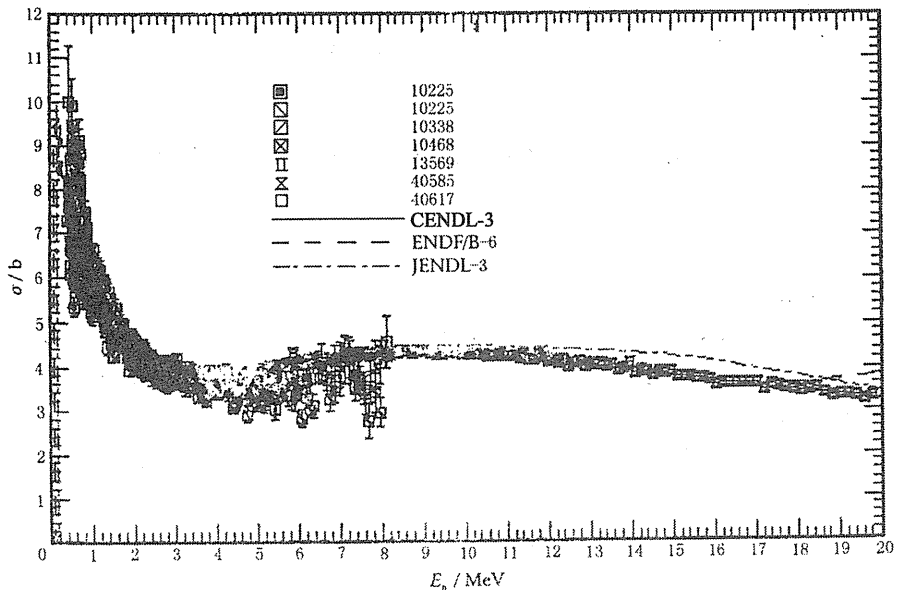



**Fig 5. The evaluated total cross section of n+$^{90}$Zr**

**Fission products**

From MF-1 to MF-5 were provided in CENDL-3.0 for most fission products nuclides, MF-1 to MF-6 are variable for others. A code SUNF, the simple version of UNF, was developed for the model calculations of fission products nuclides. The data of 101 fission products nuclides were sent to join in the international comparison of FP and coordinated by WPEC Subgroup 21, and 38 of them were selected as the data file of release 7 of ENDF/B-VI.

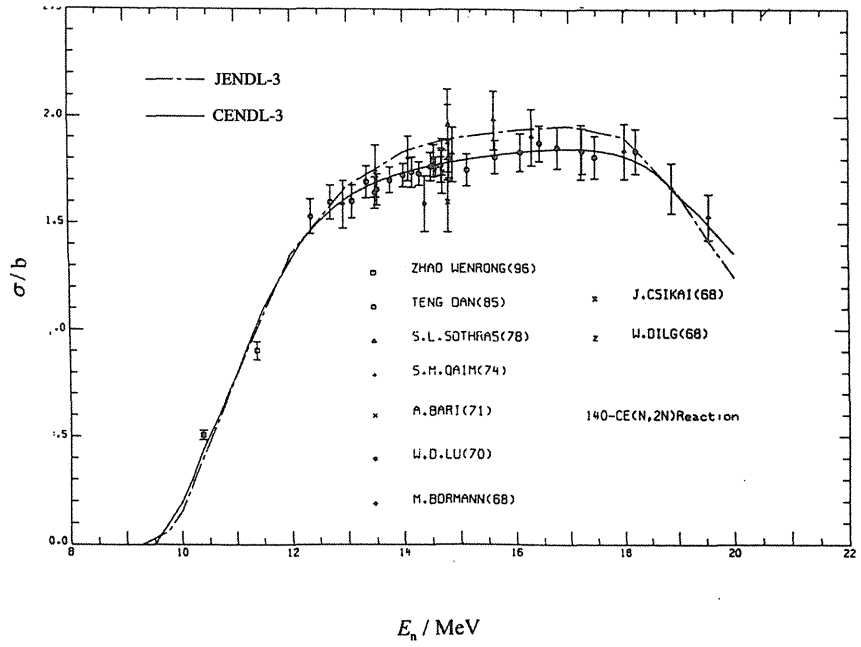



**Fig.6 The evaluated (n,2n) reaction cross section of n+$^{140}$Ce**

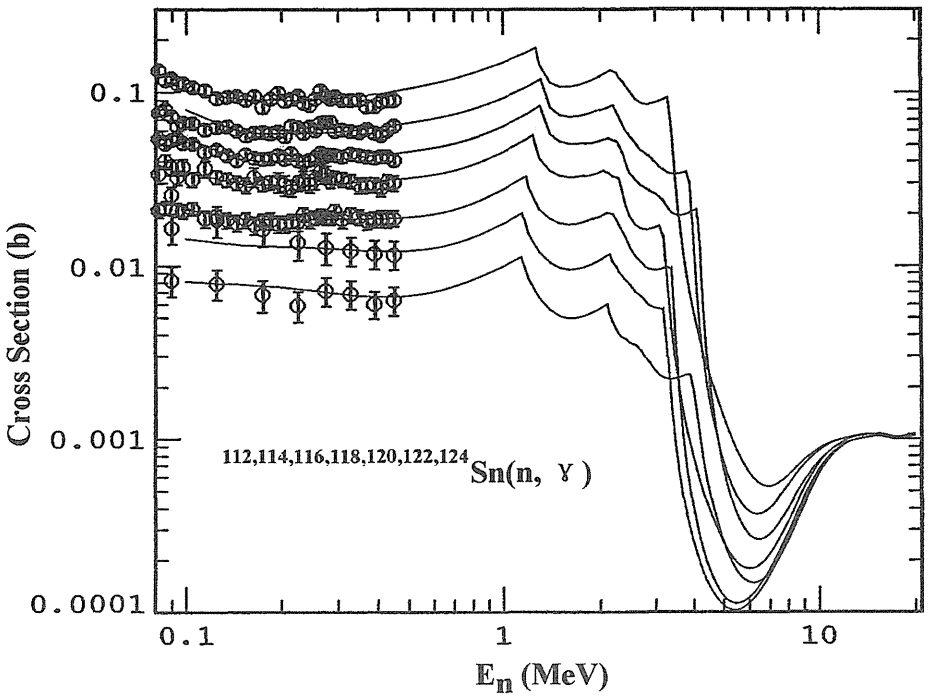



**Fig.7 Sn (n, γ) reactions evaluations comparisons with exp. data**

**Actinides**

On the basis of the model calculations with the code FUNF and adjusting the model parameters carefully, the new experimental data, 15 actinides were evaluated or re-evaluated. MF-1~6, 12~15 were included for important actinides (i.e. U, Pu isotopes), and MF-1~5 for others. The file number and nuclides were extended comparing with the pervious version of CENDL, and the results of the benchmark testing have been considered during the evaluation process.

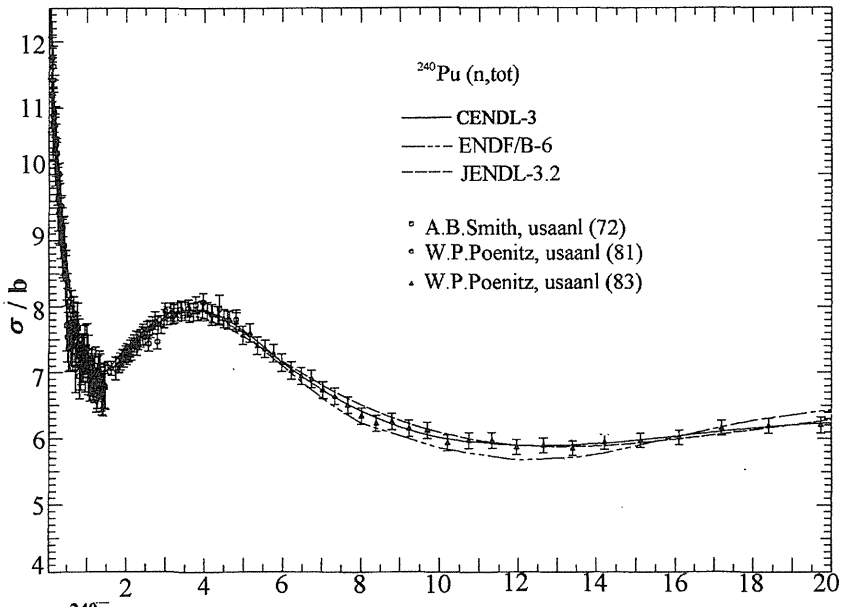



**Fig.8 $^{240}$Pu (n, tot) evaluations comparisons with exp. data and other libraries**

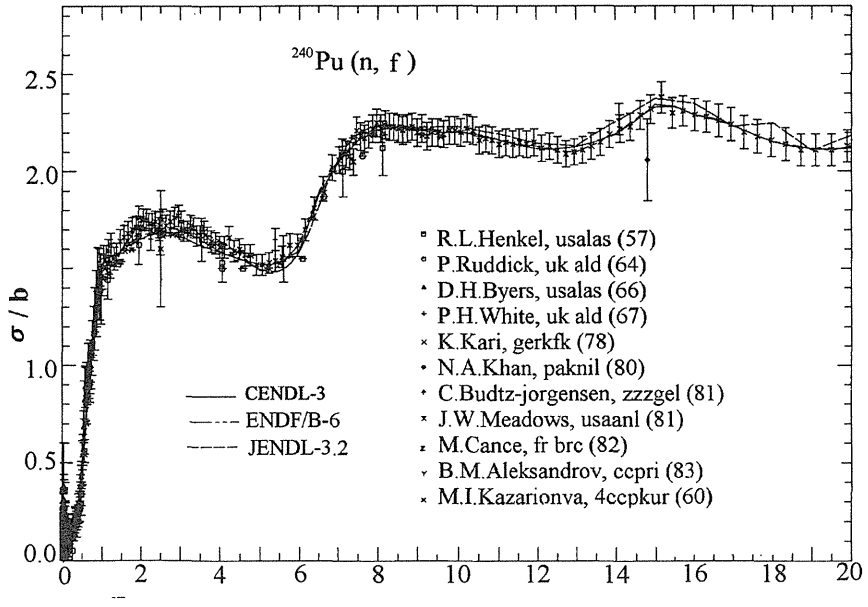



**Fig.9 $^{240}$Pu (n, f) evaluations comparisons with exp. data and other libraries**

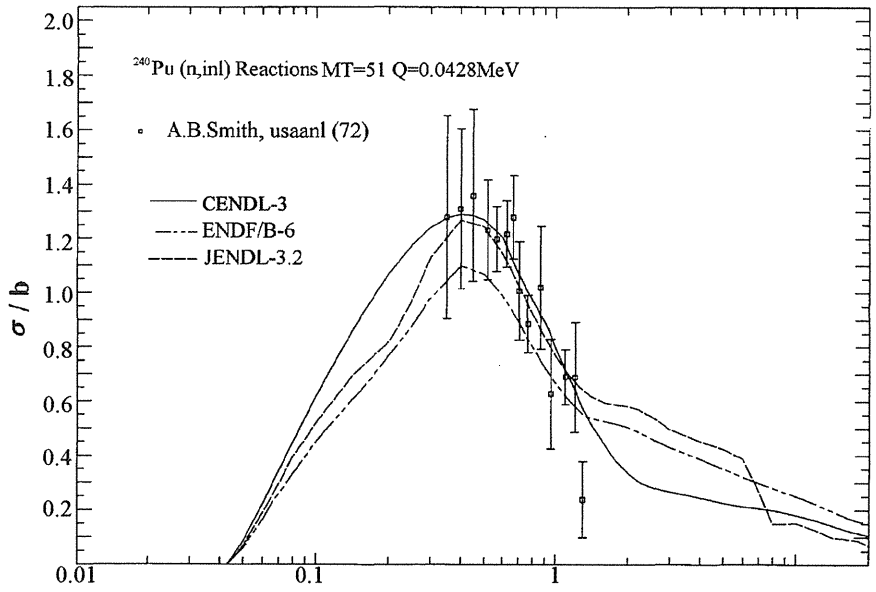



**Fig.10 $^{240}$Pu (n, inl) (MT=51)evaluations comparisons with exp. data and other libraries**

## 1.3 The benchmark testing of CENDL-3.0

In order to test the reliability of the data from CENDL-3.0, benchmark testing for some important nuclides of CENDL-3.0 has been done, the calculations and analyses of benchmarks were done with Monte Carlo code MCNP and transformation codes. The data processing was carried out by using the internationally used code system NJOY97. The results were compared with ENDF/B6, JENDL and JEF-2.2 validated CENDL-3.0 to identify the source of the discrepancies with the experimental results.

Table 1 and 2 show the results of calculation with different libraries $K_{eff}$ of $^{233}$U and $^{238}$U as the examples.

**Table 2. The Calculations of $K_{eff}$ for $^{233}$U Benchmarks**

| Assembly | Experiment | CENDL-3.0 | ENDF/B-VI | JENDL-3.2 |
|---|---|---|---|---|
| 233U Jezebel | 1.000(~0.001) | 0.99822 | 0.99235 | 1.01460 |
| 233U-F-002a | 1.000(~0.001) | 0.99518 | 0.99544 | 1.00799 |
| 233U-F-002b | 1.000(~0.001) | 0.99583 | 0.99943 | 1.00959 |
| 233U-F-003a | 1.000(~0.001) | 0.99474 | 0.99755 | 1.01168 |
| 233U-F-003b | 1.000(~0.001) | 0.99523 | 0.99989 | 1.00929 |
| 233U-F-004a | 1.000(~0.001) | 1.00715 | 1.00494 | 1.01747 |
| 233U-F-004b | 1.000(~0.001) | 1.00808 | 1.00940 | 1.01721 |
| 233U-F005a | 1.000(~0.001) | 0.99951 | 0.99409 | 1.00852 |
| 233U-F-005b | 1.000(~0.001) | 1.00204 | 0.99803 | 1.00763 |
| Flattop-23 | 1.000(~0.001) | 0.99218 | 1.00146 | 1.01140 |
| Averaging | 1.000(~0.001) | 0.99882 | 0.99926 | 1.01154 |

Table 3. The Calculations of Keff for $^{238}U$ Benchmarks of Thermal Reactor

| Assembly | CENDL-3.0 | JEF-2 | JENDL-3.2 | ENDF/B-6 |
|---|---|---|---|---|
| TRX-1 | 0.9975 | 0.9952 | 0.9901 | 0.9908 |
| TRX-2 | 0.9998 | 0.9972 | 0.9920 | 0.9924 |
| BAPL-$UO_2$-1 | 1.0010 | 1.0020 | 0.9975 | 0.9952 |
| BAPL-$UO_2$-2 | 1.0003 | 1.0014 | 0.9972 | 0.9951 |
| BAPL-$UO_2$-3 | 1.0007 | 1.0014 | 0.9976 | 0.9960 |

## 1.4 Conclusion

1. CENDL-3.0 was finished in 2000, and it has been improved since then. CENDL-3.1 is be preparing for its release.
2. Nuclides and data files of CENDL-3.1 were increased and extended compared with CENDL-2.
3. All evaluations performed based on the new experimental data and model calculations carefully. They were improved compared with CENDL-2.1.
4. The data of the most important nuclides are validated by the benchmark testing. Some of them are better than other evaluated libraries according to the results of the benchmark testing.

# II. Other progresses on nuclear data evaluations

CNDC and CNDCN also got much progress in the following related works in the past years.

## 2.1 Nuclear reaction model study

The model was improved and completed for 1p shell light nuclides, which contains the dynamics and kinematics of nuclear reactions.

A method to set up file-6 of light nuclei for evaluated neutron data in ENDF/B-6 format below 20 MeV has been established and the energy balance was strictly considered. This method has been used in the calculation of n + $^{12}C$.

The possibility of $^{5}He$ emission has been investigated in the light nuclear reactions, and the formulation for calculating of the $^{5}He$ emission was developed. Also the double differential cross sections of $^{5}He$ emission, as well as the spectra of neutron and alpha particle from the breakup of $^{5}He$, were set up and used in the series codes of LUNF.

## 2.2 Covariance study

A code EXPOV for evaluating the covariance matrix of experimental data was developed. The covariance data are output in ENDF/B-6 format. The code together with the spline fitting code SPC for multi-sets of correlative data was used to practically evaluate the covariance data for $^{58,60,61,62,64,nat}$Ni, $^{63,65,nat}$Cu and $^{27}$Al and the reasonable results have been got.

A program RAC based on the R matrix theory for calculating covariance data of light nuclide was developed. The program has been tentatively used to calculate the covariance data for $^{6,7}$Li and $^{10,11}$B, $^{16}$O the reasonable results have been got for the cross sections up to 5 MeV. The calculated data and their covariance data for $^{6}$Li, $^{10}$B have been accepted internationally as standard data of light nuclide.

Also a code has been developed for calculating the covariance data of structural material nuclides based on the statistical theory, including optical model, Hauser-Feshbach and preequilibrium emission model. The code has been used to calculate the covariance data of Ni, Cu and their isotopes in ENDF/B-6 format.

## 2.3 The systematic study of fission yield data

Based on the mass distribution data up to 200 MeV measured by Zoller, the systematic on dependence of chain yield on incident neutron energy for each mass number A was studied. And also the systematics of mass distribution on mass A and incident neutron energy was investigated by using 5 (or 3) Gaussian model. The calculated results could reproduce the experimental data used well. The investigation also shows that the correlation between the parameters of the systematic and the yields calculated with the systematics is quite complicated and, in general, is quite strong.

## 2.4 The study on the dependence of yield on energy

Taken some typical important fission products from $^{235,238}$U fission, and the dependences of fission yield on incident neutron energy were studied. The covariance data were also evaluated based on each set of experimental data and the correlation among the data due to the systematical error, such as fission rate (or normalization), detector efficiency, decay data etc., was taken into account in the fitting and the covariance matrix was obtained as a fit result. The results show that the data for most of product nuclides can be fitted with a linear function. But for some special product nuclides , the data have to be fitted with a spline function.

## 2.5 Nuclear structure and decay data

CNDC has taken permanent responsibility for evaluating and updating NSDD for A=51, and 195-198 mass chain. The data have been revised using available experimental decay and reaction data for mass chain A=197, and are being updated for mass chain A=196. Updated evaluation of A=197 has been sent to NNDC, USA and will be published in NDS in 2004. The evaluations of mass chain A=52-56 were being updated at Jilin University. The decay data of $^{233}$U were being evaluated on the basis of the new measured data.

JP0550255



# 2.14 Monte-Carlo Simulation for the Effects of Composite Materials on Single Event Effects of Sub-100 nm Semi-conductor Devices

Eishi Ibe, Yasuo Yahagi, Hironaru Yamaguchi

*Production Engineering Research Laboratory, Hitachi, Ltd.*

*292 Yoshida, Totsuka, Yokohama, Kanagawa, 244-0817 Japan*

ibe@perl.hitachi.co.jp

A Monte-Carlo simulation code SEALER was developed for neutron-induced single event upset of semiconductor devices at the ground level, in which composite material effects are fully simulated.
Any size and structures of 8 composite material such as Si, $SiO_2$, $Si_3N_4$, $Ta_2O_5$, $WSi_2$, Cu, Al, TiN can be included for analyses of nuclear spallation reactions and charge collection to storage nodes. Some preliminary implications of composite material effects are demonstrated including an apparent contribution of elastic scattering to single event upset in lower energy region as low as 2 MeV or even lower.

## 1. Introduction

Electron devices/components/systems are exposed to environmental radiation to cause single event upsets (SEU) which may further cause data corruption or even system crash at the ground level. Alpha ray from radioactive materials has been regarded as main source of such environmental radiation from late 1970s to 1990s [1,2]. Terrestrial neutrons which are produced by nuclear spallation reaction of high-energy cosmic ray with nuclei of atmospheric air in the inner space, are emerging as much more crucial radiation source as the minimum feature size of semiconductor device nose-dives toward sub-quarter microns [3,4].

A program package CORIMS (Cosmic Ray Impact Simulator) with Monte-Carlo (MC) simulation techniques for nuclear spallation reaction model (Intra-Nuclear Cascade (INC) and statistical evaporation models)[5] and charge collection models in 3D structure of major components including source, drain, isolation oxide, single/triple wells of infinite-matrix memory cells has been applied for analyses of single event effects (SEEs) of semi-conductor devices [6,7]. Experimental approaches by medium-energy (1-800 MeV) neutron irradiation experiments are also applied for commercial devices [8-10]. The simulation technique is particularly important under design phase to predict and minimize the susceptibility of semiconductor devices before mass production to the market. The simulation techniques appeared fairly satisfactory as a prediction tool for SEUs, but not so effective for SEU minimization or design tool so far.

Recently, Gasiot [11] indicated that SEU rate got higher by a factor of two when 14MeV neutron is irradiated from $SiO_2$ side than from Si substrate side. The simulation model in our precedent program package CORIMS is very limited in this viewpoint: It simulates only nuclear spallation reaction of Si nucleus and analyze secondary ion tracks and energy deposition in Si substrate.

In order to overcome such deficiency, we have made a new Monte-Carlo simulation code SEALER (Single Event Adverse and Local Effects Reliever) by which such composite material effects are fully simulated on Windows™ PCs and material/layout design of device components can be made. It is shown that extremely large database is required for this purpose. Some preliminary implications of such composite material effects are also demonstrated in this paper.

## 2. Model description

### 2.1 Nuclear spallation reaction model

In general, 8 composite materials such as Si, $SiO_2$(commonly used for isolation oxide), $Si_3N_4$(gate side wall, etc), $Ta_2O_5$(DRAM capacitor material), $WSi_2$(contact), Cu (metal line), Al (metal line), TiN (buffer, etc) are used in Si-base semi-conductor devices. Therefore, 8 nuclei (Si-natural, $^{14}N$, $^{16}O$, $^{181}Ta$, Ti-natural, $^{27}Al$, Cu-natural, $^{184}W$) are treated as target nuclei. Total and non-elastic-reaction cross section data from JENDL3.3 [12]/ JANIS2.0 [13]/ LA150 [14] are approximated as a polynomial function of neutron energy as shown in Fig. 1. Total scattering cross section of each component is calculated first for given neutron energy, and the component where neutron interaction takes place is determined by MC manner. Then type of reaction (elastic or non-elastic) and target nucleus are determined sequentially.

For elastic scattering, classic relativistic binary collision model is applied. For non-elastic nuclear reaction analyses, models similar to Tang's approach [5] is applied: Intra-nuclear cascade (INC) model in which many-body collision process is regarded as a sequential relativistic binary collisions with rexicographic processing of trees (a particle of interest is chased to the end) is applied for prompt nucleon-nucleon collision process in the target nucleus. Nucleons with energies high enough over the Fermi levels of each nucleus at the surface of the nucleus are released from the nucleus. After reaching the condition that all collided nucleons do not have such high energy, Weisskopf-Ewing type model is applied for light particle evaporation. Inverse reaction cross section is used to determine the reaction channel and is calculated based on Generalized Evaporation Model (GEM)[15]. The calculated inverse reaction cross section are fairly consistent with literature data[16] as shown in Fig.2.

### 2.2 Device and charge collection models

Bird's eye 3D view of CMOS-SRAM (static random access memory) is illustrated in Fig. 3. A pMOSFET is placed in the center between nMOSFETs. When the storage node (diffusion layer) is hit by a secondary ion, a certain amount of electrons/holes produced along the ion track is collected to the nodes typically by the funneling mechanism. Some amount of electrons and holes are also collected by diffusion process. Such charge collection models (funneling and diffusion) are incorporated into the program packages CORIMS/SEALER and SEU takes place when charge collected to the node exceeds the critical charge Qc over which the data "1(high)" in the node change to "0(low)". As device scaling proceeds, charge collected due to alpha particle decreased because charge density along alpha particle path is only about 5-10 fC/μm while charge collected due to heavier secondary ions (C,N,O,…,Ta,W) is as high as 100-200fC/μm. This is why neutron SEU is getting dominant as device size is shrunk.

The nuclear reaction models are benchmarked with 65, 180, 380 MeV proton reaction data with $^{27}Al$ and a fairly good consistency close to those in Ref.[5] .

3D device model is constructed by using common CAD algorithms based on device design parameters. Ion track analysis of secondary ions in the multi-component device structure is also carried out by specially designed algorithm. Deposited energy of any secondary ions (from proton to $^{184}W$) in any substrate material can be calculated by using polynomial approximation functions made from SRIM.

Simulated results from CORIMS are compared with test results in the field or accelerator neutron facilities (TSL, LANSCE, CYRIC, FNL, RCNP) and good agreements are obtained for all cases within 20-30 % error in average [7].

In order to evaluate the composite material effects preliminarily, a virtual (neither real nor to-scale) device model was used as shown in Fig. 4. Isolation oxides ($SiO_2$), copper metal lines, $WSi_2$ contacts over storage nodes, $Si_3N_4$ gate side walls are incorporated in the base Si substrate.

## 3. Preliminary implications from simulated results

### 3.1 Secondary ions from different materials

Figure 5 shows histograms of secondary ions from Si-base materials (Si, $SiO_2$, $Si_3N_4$) when 100 MeV neutrons are bombarded. As for Si target, heavy ions (Al, Mg) and light ions (p,α) are dominant secondary ions. Meanwhile, it is seen that medium weight ions (C,N) are produced from $SiO_2$ and $Si_3N_4$ substrates of the same order of Mg, Al from Si substrate.

Figure 6 shows energy spectra of secondary ions *produced in* the $WSi_2$ substrate. It is seen that W (though inelastic reaction) and Ta are produced from W target in $WSi_2$ with low energy but relatively high probability.

### 3.2 Results from virtual composite material device

Figure 7 shows energy spectra of secondary ions *reached at the sensitive region* (Si well). The followings are pointed out:

(1) Among heavy secondary ions, Na ion has the highest probability while Al has the highest probability of production from Si. This implies that the probability to reach at the sensitive region is determined from the rate and location (range) relative to the sensitive region.

(2) The probabilities of medium weight ions (C,N) are not so high. This is due to the assumption of the thickness of SiO2 (5μm) which is much thinner than Si substrate(50μm), so that the total amount of target nucleus in the device is another key parameter.

(3) The probabilities of Ta and W are negligibly small even though $WSi_2$ is contacted to the sensitive region. This may be due to very short range of these secondary ions, since the energy is very low as seen in Fig. 6.

Figure 8 shows calculated charge density at the inlet of the sensitive region (Well) for 2MeV neutron bombardment. Cumulative frequency over specific charge density is plotted for oxygen, silicon, elastic scattering, non-elastic scattering, and total scattering. Major findings are:

(1) Although slight charge deposition takes place by non-elastic (actually in-elastic n-n') scattering for 2MeV neutron, charge density by elastic scattering is as high as 40fC/μm. This density can cause SEU depending on the device structure/size and critical charge and thus can be major mechanism of the low SEU threshold energy

below the threshold energy of nuclear reaction of Si nucleus [17].

(2) It is also noteworthy that oxygen nucleus recoiled from $SiO_2$ by elastic scattering has major contribution to deposition density in the range of 20-40 fC/μm.

(3) For low energy neutron irradiation as in Gasiot's paper (14 MeV), contribution of elastic scattering is relatively high so that dependency of SEU on neutron beam direction may be explained in future.

4. Conclusion

(1) MONTE-CARLO simulator SEALER was developed to deal with neutron induced soft-error in all possible materials in semiconductor devices. (2) The effects of secondary ions like C,N from $SiO_2$, $Si_3N_4$ on soft-error may be underestimated by Si-only model.

(3) The amount of secondary ions passing through sensitive node depend on positions of various components with different materials; does not necessary correspond to the amount of secondary ions produced.

(4) Heavier secondary ions (from Cu, W, Ta) may have only local (spatially limited) effects.(5) Oxygen and Si nuclei recoiled by elastic scattering from $Si/SiO_2$ causes SEU when neutron energy is as low as 2MeV or even lower.

## Acknowledgements

We would like to gratefully acknowledge Prof. Emeritus T. Nakamura and Prof. M. Baba of Tohoku Univ., Prof. Y. Nagai and Dr. N. Matsuoka of Osaka Univ., Prof. Watanabe of Kyushu Univ., Dr. P.-U. Renberg, Dr. A. Prokofiev of the TSL of Uppsala Univ., Dr. S. A. Wender and Dr. B. Takala of LANSCE and other staffs at the facilities for their useful discussions and supporting the experiments.

References

[1] T.C. May, Murray H. Woods, *IEEE Transactions on Electron Device*, Vol. ED-26, No. 1, pp.2-9(1979)

[2] E. Takeda, *et al., Extended Abstracts of the 18th Conference on Solid State Devices and Materials, Tokyo*, ,pp.311-314(1986)

[3] J.F. Ziegler, , *IBM J. Res. Develop.*, Vol. 40, No. 1, pp.19-39(1996)

[4] E. Ibe, *et al., 2002 International Conference on Information Technology and Application, Bathurst*, No. 273-21(2002)

[5] H.H.K. Tang, *et al., Phys. Rev. C*, Vol. 42, No. 4, pp.1598-1622 (1990)

[6] E. Ibe, *et al., The 6th International Workshop on Radiation Effects on Semiconductor Devices for Space Application , Tsukuba, October 6 - 8, 2004*, ,pp.19-23 (2004)

[7] E. Ibe, *et al., Ionizing Radiation*, Vol. 30, No. 7, pp.263-281 (2004)

[8] Y. Yahagi, *et al., Abstract Book, RADECS 2004, CIEMAT, Madrid, Spain, Sept., 22-24*, pp.103-106 (2004)

[9] Y. Yahagi, *et al., 2002 International Integrated Reliability Workshop, Stanford Sierra Camp, S. Lake Tahoe*, pp.143-146 (2002)

[10] Y. Yahagi, *et al.,2004 IEEE International Reliability Physics Symposium, April 25-29, Phoenix, Arizona,* ,

pp.669-670 (2004)

[11] G. Gasiot, *et al., IEEE Trans. Nuc. Sci.*, Vol. 49, No. 6, pp.3032-3037 (2002)

[12] Y. Watanabe, *2004 Symposium on Nuclear Data, November 11-12, 2004, Tokai Research Esta*blishment, No. 4.3 (2004)

[13] http://www.nea.fr/janis/welcome.html

[14] http://t2.lanl.gov/publications/la150/la150.html

[15] S. Furihata, Thesis for PhD., Tohoku University, pp.18-20 (2002)

[16] C.M. Perey and F.G. Perey , *Atomic Data and Nuclear Data Tables*, Vol. 17, No. 7, pp.1-101(1976)

[17] Y. Yahagi, *et al., 2004 IRPS*, April 25-29, Phoenix, Arizona, pp.669-670 (2004)

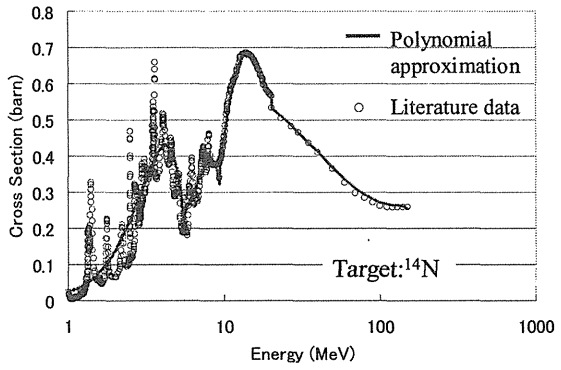



Fig.1 Literature data of non-elastic reaction cross-section and calculated results from polynomial approximation ($^{14}$N)

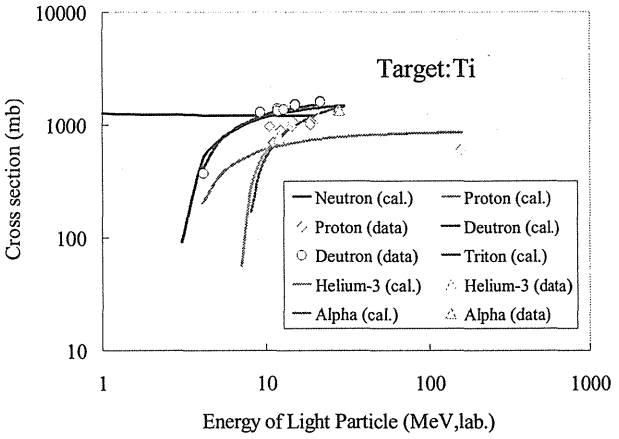



Fig.2 Literature data of inverse reaction cross-section and calculated results from GEM

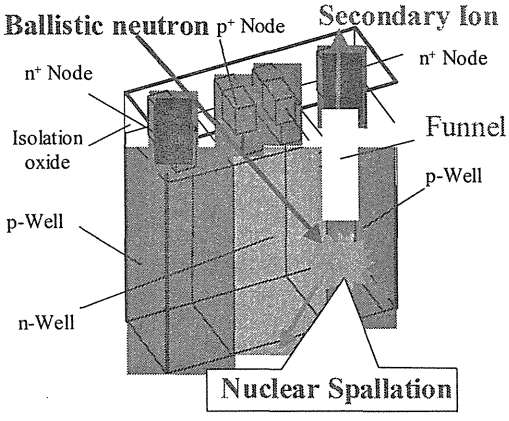



Fig.3 Bird's eye view of CMOS-SRAM device and microscopic mechanism of single event upset

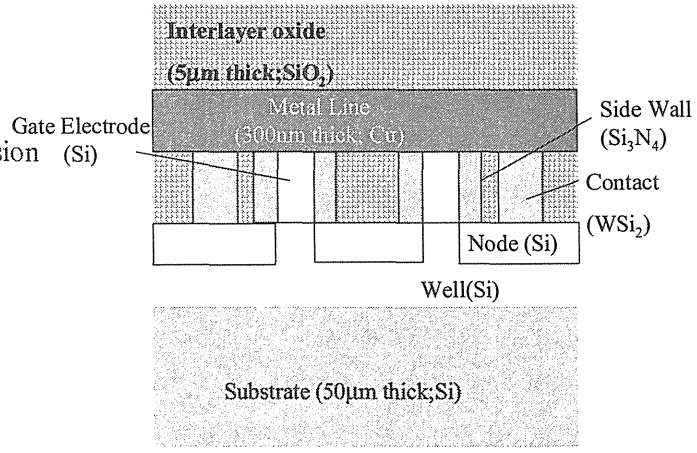



Fig.4 Cross-section of virtual composite material device model

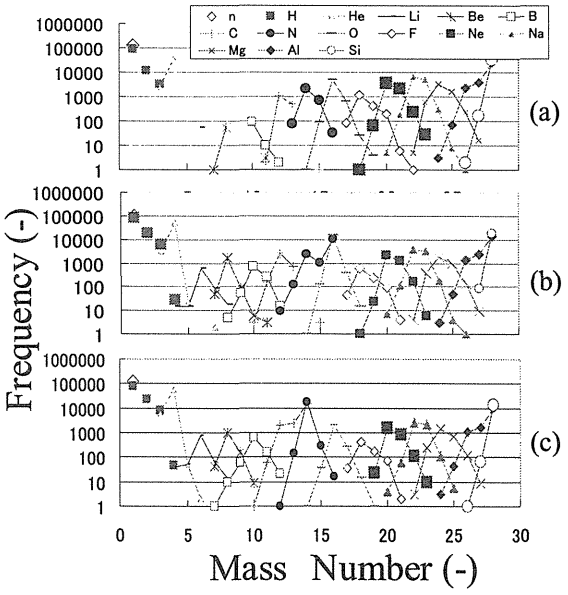



Fig.5 Histogram of secondary ion produced in Si-base material by 100 MeV neutron (a) Si, (b) $SiO_2$, (c) $Si_3N_4$

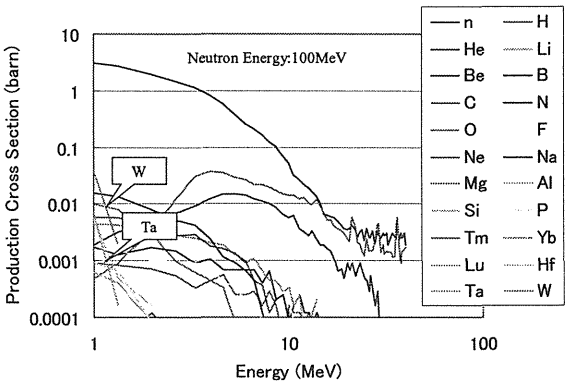



Fig. 6 Energy spectra of secondary ions produced in $WSi_2$ substrate by 100 MeV neutron

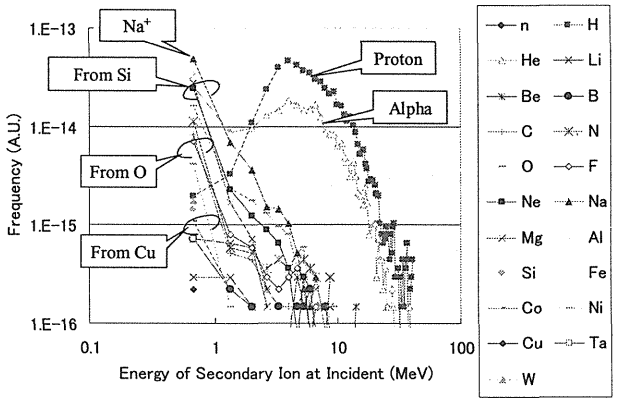



Fig. 7 Energy spectra of secondary ions at the inlet of sensitive region (Well) of the virtual SRAM device

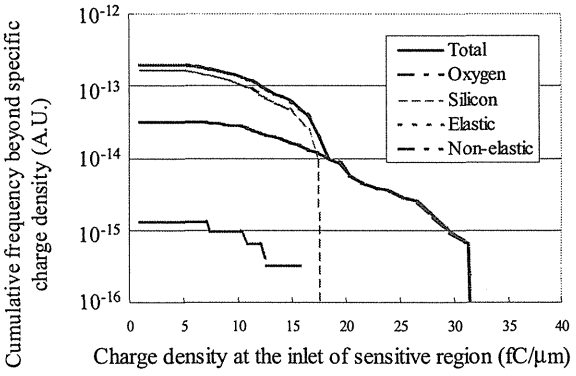



Fig.8 Charge density spectrum by secondary ions at the inlet of sensitive region

JP0550256



# 2.15 Nuclear Data for Radiotherapy

Naruhiro Matsufuji, Yuki Kase and Tatsuaki Kanai

Research Center for Charged Particle Therapy, National Institute of Radiological Sciences

9-1, Anagawa-4, Inage-ku, Chiba-shi, Chiba 263-8555 Japan

matufuji@nirs.go.jp

The production of projectile fragments is one of the most important, but not yet perfectly understood, problems to be considered when planning for the utilization of high-energy heavy charged particles for radiotherapy. The charge-changing cross section is one of the most fundamental values when describing the extent of fragmentation. Simulation codes reproduce experimental cross-section data with good precision for carbon ions. Energy and spatial distributions of fragment particle species are needed for a precise estimation of the biological effect. Microdosimetric energy-deposition information has been investigated to understand the nature of radiation effectiveness to cell nucleus. The role of neutrons has recently drawn considerable attentions to estimate the late effect of therapeutic irradiation.

## 1. Introduction

Projectile and target nuclei are broken up into fragment particles when colliding with each other. The projectile fragments reach a further region beyond the range of the primary particles, and cause unwanted exposure, known as a 'fragment tail'. It is considered that the biological effect to a cell by a charged particle is due to its ionization formed around a track of the particle. Because the track structure is characterized by the deposited energy and velocity of the particle, the resultant biological effect depends not only on LET, but also the

particle species. This fact makes it indispensable to know the *"radiation quality"*, *i.e.,* the fluence and LET on each element for a precise estimation of the biological effect of any therapeutic beam that we use.

## 2. Macroscopic effect: cross section and depth-dose distribution

The dose, quantity of radiation, is the most fundamental parameter to be controlled in radiotherapy. Fig. 1 indicates the total charge-changing cross section measured at some institutes. The solid line in the figure depicts the calculated cross section by HIBRAC[1]. HIBRAC is a simulation code of the fragment reaction, and is widely used among many particle-therapy facilities. As shown in the figure, the experimental results agree well with each other within the error bars. A slight systematic discrepancy is found between the measurements and the calculations at an energy below 150 MeV/n; however, the difference has only a small effect on the depth-dose calculation. The calculated depth-dose curve of a 290 and 400MeV/n of $^{12}C$ beam in water with HIBRAC[2] agrees well with the dose measured with an ionization chamber at NIRS, as shown in fig. 2. This clinically sufficient simulation accuracy is one of the bases for successful ongoing particle therapy.

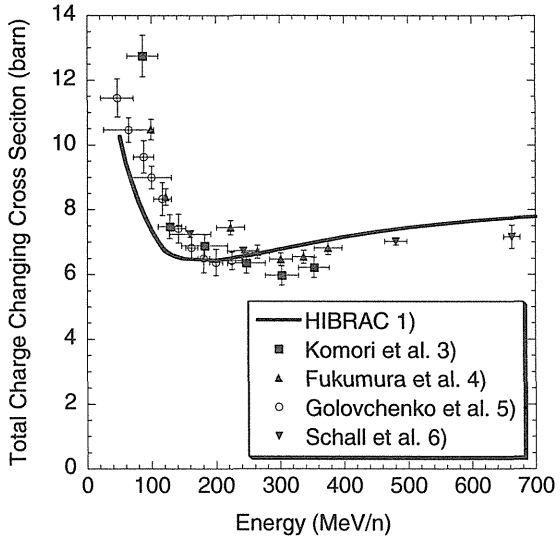



Fig.1 Total charge-changing cross section of $^{12}C$ ions in PMMA.

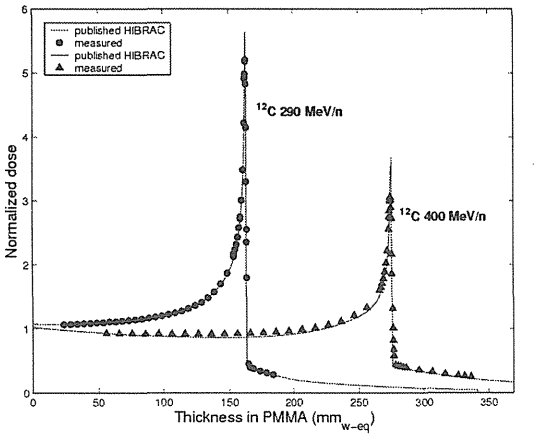



Fig.2 Depth-dose distribution of 290 and 400 MeV/n of $^{12}C$ beam in water.

### 3. Microscopic effect: fluence, LET and spatial distribution

Fig. 3 shows a normalized fluence distribution of fragments emitted from the incidence of a 290 MeV/n $^{12}C$ beam as a function of the PMMA thickness. The closed symbols and lines denote the experimental values measured at HIMAC (Heavy Ion Medical Accelerator in Chiba) of NIRS[7] and the calculational results by HIBRAC[2], respectively. For the sake of a comparison, the experimental results taken with CR-39 track detectors are plotted together as open symbols. Slight discrepancy is found on the light elements; however, HIBRAC reproduces well the experimental observations.

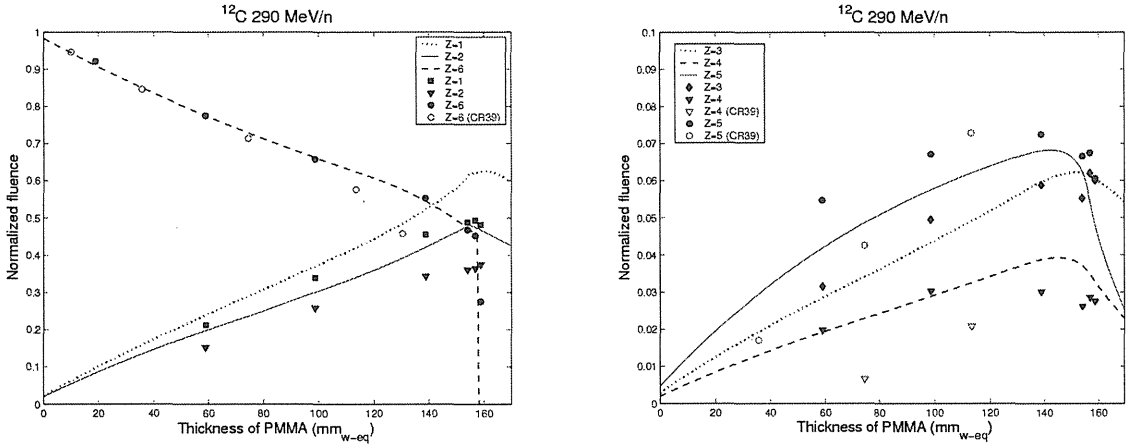



Fig. 3 Normalized fluence of fragments produced from $^{12}C$-290MeV/n in PMMA.
Symbols: experimental data lines: HIBRAC calculation

The next step for a microscopic understanding of fragmentation is to take spatial information into account. Scanning beam irradiation is materialized at some facilities according to a recent trend toward highly localized beam delivery. The usage of smaller (several mm in diameter) beam size than that of the conventionally used at broad beam (100~200 mm in diameter) enhances the importance of the information on the spatial distribution of fragments.

Multiple scattering is the most dominant factor affecting beam divergence. Because the extent of multiple scattering can be calculated by Moliéle's formula to good precision, the

divergence of primary particles in a matter can be well estimated. For fragment particles, however, one cannot overlook the effect of a momentum transfer at the reaction point.

Fig. 4 shows an example of the lateral fluence distribution of fragments for the incidence of a $^{12}$C-290 MeV/n beam to water. The development of σ of each element is reproduced well by combining multiple scattering and Fermi momentum transfer.[8)]

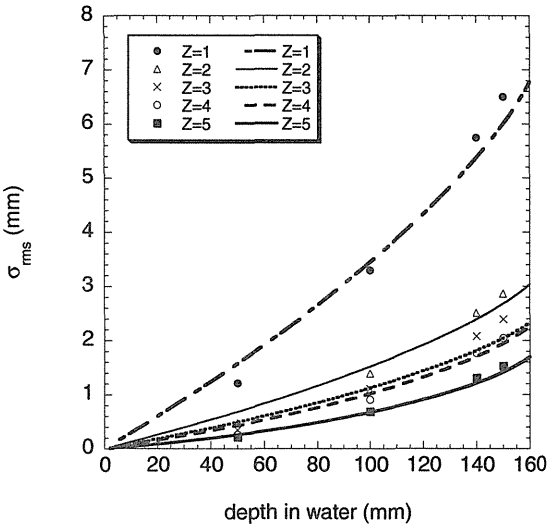



Fig. 4 Lateral spread of fragments for the incidence of $^{12}$C-290MeV/n in water.

## 4. Microdosimetry

Biological effect caused by radiations is considered to be originated from lesions caused in DNA strands. The DNA has a diameter of about 2nm and enclosed in a cell nucleus that is about 10 μm in diameter. The energy deposition in such minute size is governed by randomness. Due to large fluctuations of energy deposition, LET, a macroscopic averaged value, has little meaning to the life and death of a cell. To understand the nature of radiation effect to the biological system, such microscopic energy distribution has been investigated as microdosimetry. Microdosimetric-kinetic model[9)] is one of the attempts to explain the biological effect of radiations with microdosimetric information. Damage to a cell is characterized with specific energy (corresponds to dose in macroscopic view) in domains assumed inside a cell nucleus and parameters that reflect radiation sensitivity of the cell to X-ray. For HSG cell, its biological response to various kind and energy of ions is successfully reproduced independent of particle species with experimental specific energy spectra when assuming the domain diameter as 700 nm[10)]. The approach will make it possible to determine clinical or biological dose by physical measurement. Further investigation is required to

verify the adoptability of the model and understand the relationship between domain size and actual biological structure.

## 5. Neutrons

Unlike other charged fragment particles, produced neutrons are largely scattered out in space. As a result, neutrons show wide spatial and energetic distributions at the isocenter. Primal energy-deposition process of neutron in a matter is to collide with proton(s) and makes them recoil. The recoiled proton deposits all of its received kinetic energy around the neighbor of the collision point. The resultant high energy density deposition may locally cause significant biological damage. Their contribution to the target region is included in the measured depth-dose distribution of the therapeutic beam; however, there is little estimation at off-axis. Even the extent of energy delivered by neutrons is small compared to those by therapeutic (charged-particle) beam and affects little to the success of the tumor control, it may cause long-term side effect such as secondary cancer.[11] From the point of view, it is required to understand the spatial neutron distribution in the therapy room and estimate the risk for the induction of the secondary cancer. The information will be utilized as one of the standards when considering the optimal heavy-charged particle therapy modality.

## 6. Conclusion

10 years have passed since the beginning of clinical trials for carbon therapy at HIMAC. As the first stage, good clinical results have been derived for most cases. That is, in part, due to well understandings to the macroscopic nuclear reaction cross section. To brush up the ongoing therapy modality and establish the optimal *"heavy-ion therapy"* in the coming second stage, both theoretical and experimental efforts must be paid on the microscopic interactions of particles including neutrons with a matter. Nuclear data for the purpose has significant importance from the viewpoint.

## Acknowledgements

The authors are indebted to the skillful work of the HIMAC operation staff. We are pleased to acknowledge our colleagues in the P060 measurement group of NIRS. A part of this work was carried out as the Research Project with Heavy Ions at HIMAC.

## References

1) L. Sihver, D. Schardt, T. Kanai, "Depth-dose distributions of high-energy carbon, oxygen and neon beams in water", *Jpn. J. Med. Phys*, 18, 1 (1998).
2) L. Shiver, N. Matsufuji, T. Kanai, " Calculation of depth-dose, fluence, energy, dose and track average LET distributions of therapeutic heavy ion beams by HIBRAC", *HIMAC Report*, 99 (2004).
3) M. Komori *et al.*, "Study on the fluence and LET distribution of projectile fragments produced from heavy ion therapeutic beams", *Proc. of the 3rd Korea-Japan Joint Meeting on Med. Phys.*, 216 (2002).
4) A. Fukumura, T. Kanai, T. Murakami, N. Matsufuji, T. Kohno, T. Nakamura, "Study on nuclear fragmentation of therapeutic heavy ion beam", *2001 Annual Report of the Research Project with Heavy Ions at NIRS-HIMAC*, NIRS-M-159, 179 (2001).
5) A. N. Golovchenko *et al.*, "Fragmentation of 200 and 244 MeV/u carbon beams in thick tissue-like absorbers", *Nucl. Instr. and Meth*, B159, 233 (1999).
6) I. Schall *et al.*, "Charge-changing nuclear reactions of relativistic light-ion beams ($5 \leq Z \leq 10$) passing through thick absorbers", *Nucl. Instr. and Meth.*, B117, 221 (1996).
7) N. Matsufuji *et al.*, "Influence of fragment reaction of relativistic heavy charged particles on heavy ion radiotherapy", *Phys. Med. Biol.*, 48, 1605 (2003).
8) N. Matsufuji *et al.*, "Spatial fragment distribution from a therapeutic pencil-like carbon beam in water", *submitted to Phys. Med. Biol.* (2004).
9) R. B. Hawkins, "A microdosimetric-kinetic model of cell death from exposure to ionizing radiation of any LET, with experimental and clinical applications", *Int. J. Radiat. Biol.*, 69, 739 (1996).
10) Y. Kase, T. Kanai, M. Sakama and N. Matsufuji, "Calculation of biological effect by heavy ions with a microdosimetric-kinetic model", *Proc. of the 88th Annual Meeting of Japan Soc. of Med. Phys.* (2004).
11) H. Engels *et al.*, "Risk assessment for cancer induction after low- and high-LET therapeutic irradiation", *Strahlentherapie und Onkologie*, 175, 47 (1999).

JP0550257



## 2.16 Measurement of Fragment Production Cross-section on Nucleon-induced Reaction

M. Hagiwara, T. Oishi, M. Baba,
*Cyclotron and Radioisotope Center, Tohoku University*
E-mail: *hagi@cyric.tohoku,ac,jp*
T. Sanami
*High Energy Accelerator Research Organization (KEK)*
H.Nakashima, S.Tanaka
*Japan Atomic Energy Research Institute*
M. Takada
*National Institute of Radiological Sciences*

We introduce our activities on measurements of fragment which are secondary particles heavier than alpha-particles produced by nucleon-induced reaction and have been recognized to be a cause of serious problem to semiconductor devices and human in a space environment by using a Bragg curve spectrometer (BCS) and energy-time-of-flight method (E-TOF), together with the activities in other facilities. For these studies and estimation, it is important to know the fragment production yield including the energy and angular distribution (double-differential cross-section (DDX) data) of fragments emission.

We have resulted in success to obtain light fragments on proton- and neutron-induced reactions by using a BCS developed for neutron specially and E-TOF method. Double-differential fragment production cross-sections obtained will be applied for the analysis of SEU and dose contributions.

### 1. INTRODUCTION

The radiation effects such as a single event effect (SEE) by terrestrial cosmic ray neutrons on microelectronics as well as on board aircrafts, have recently become serious problem and attracted much attention [1]. Among SEEs, single event upsets (SEU) or soft errors are presently considered the most important effects for the electronics. The particle with strongest effects is thought to be spallation neutrons created in the atmosphere by cosmic-ray protons and heavy particles because of much higher flux than other terrestrial cosmic-rays. When a circuit is exposed to a single particle such as proton or neutron, almost all these particles pass through the device with only little effect due to its low LET (liner energy transfer), but some particles induce nuclear reaction with the component materials of the device and produce secondary charged particles. Secondary particles heavier than alpha-particle that are called ''fragment" will be important on the SEE phenomena. Production rate of fragments is lower than one of lighter particles, but fragment cause a large local ionization and can make large energy deposition in μm order region because of significantly large LET. The charge released by ionization in a sensitive device region can cause a flip of the memory content in a bit, which is called a single-event upset (SEU). Unlike radiation with large dosage, an SEU event usually does not cause a permanent damage in the circuit, but it may cause serious reliability and performance problems that must be addressed in advanced technologies.

As mentioned above, for study and estimation of SEU, it is important to know the fragment production yield with the energy and angular distribution (doubly differential cross-section (DDX) data) of fragments emission induced by neutrons and protons. The energy information of fragment is required to know the energy deposition on the sensitive area of semiconductor devices. The angular information is also important because the energy spectrum of fragment has strong angular dependence. Moreover, data are required especially in intermediate energy region (ten's of MeV – several 100 MeV) by considering the neutron flux

energy distribution and the energy dependence of SEE probability [1].

The fragment data will also be important for the dosimetry for human in space and particle beam radiotherapy (proton, carbon and so on.). Usually the estimation of dosimetry does not include the effect of the fragment production. The conventional treatment of proton beam dosimetry is based only on the ionization loss according to the Bragg curve. However, from the calculation considering the nuclear spallation reactions, the dosimetry due to the spallation products (protons, light ions and heavy recoils) is found to be larger than usually believed [2]. Therefore the contribution of secondary particles including fragments produced by spallation reaction must be checked for the precise estimation of dosimetry in space environment and radiotherapy treatment.

## 2. PRESENT STATUS OF FRAGMENT PRODUCTION DATA

For light charged particles such as p, d, t and α, several experimental data have been reported. However for the fragments heavier than alpha-particle, the spectrum data is very few, because of such difficulties in the fragments measurement as low count rate, much short range and so on. Then the most of past fragment production data were obtained by activation method which provides no information on energy and angular distributions.

For proton-induced reaction, there are several data above 1 GeV energy region by nuclear physics group, but in intermediate energy region only two experimental data has been reported for carbon (45-100 MeV protons) by C. T. Roche et al. [3] and aluminum (180 MeV protons) by K. Kwiatkowski et al. [4] using Eergy-TOF (E-TOF) method (combination of energy and time-of-flight).

### 2-1. FRAGMENT EXPERIMENTS IN PROGRESS

Experiments for fragment production are mainly performed in the field of nuclear physics by using very high energy incident beam above 1 GeV/u. These experiments are classified into two parts generally by the experimental method.

One uses the "inverse kinematics method" and a large mass separator to overcome the problems of low count rate and very short range. By using the large detection system, many fragment production data have been obtained in GSI [5], MSU [6] and so on. In the "inverse kinematics method", heavy ion is accelerated for projectile and bombard to light ion target like hydrogen. Due to the high energy of the center of mass, almost all products are transported to forward direction and the mass and charge information are obtained by using a magnetic field and ΔE, TOF measurement. The almost all data obtained by this method are limited in high energy region above 1 GeV/u. On the other hand, The Svedberg Laboratory in Uppsala has started using inverse kinematics method like GSI in the energy range of 100-470 MeV/u using a silicon projectile and a hydrogen target to study the fragment production reaction from silicon [7]. This method can perform very clear identification of isotopes over wide mass and charge range of fragments and enables to deduce production cross-section of the fragments simultaneously. This method is very effective to measure the production cross-section, but not effective to deduce the energy and angular distribution in proton-induced reaction.

Another method is recoil measurement and done at several facilities like KEK [10]. In this method, to overcome low count rate and the very short range, a Bragg curve spectrometer (BCS) [8, 9] which has flexibilities owing to be a gas counter is used for the main detector of fragments. Most experiments employing the technique are performed in very high energy region above 1 GeV/u., but below 1 GeV, PISA project [11] aims at double-differential cross-section measurement for proton induced reactions in 200 to 2,500 MeV region has been started recently.

## 2-2 CALCULATION

In the following we describe briefly the major reaction models which treat fragment production. The GNASH code developed by the Los Alamos National Laboratory [12] is constantly upgraded and has been very popular in radiation physics communities in recent years. However the code is limited to reactions of the energy below 150 MeV. For the data library, LA150 [13] which was evaluated with GNASH code is available below 150 MeV. This library is mainly used above 20 MeV regions in various fields. However, the fragment data for mass region above helium treat the angular distribution as isotropic.

As a nuclear model for application to high energy region, the JQMD code is recently developed by JAERI on the basis of quantum molecular dynamics [14]. Above 150 MeV, JQMD is recently used for SEU estimation. However these theoretical calculations treating fragment production are not validated well and uncertain due to very few experimental data. They should be examined by reliable experimental data.

## 3 PRESENT STUDIES

An important motivation of our group is to generate new data on energy and angular distribution of fragment produced from nucleon-nucleus reaction in ten's of MeV region. The fragment measurement has many difficulties such as low yields and large energy loss in sample and window and so on. In particular for neutron, which is very limited in flux compared with protons, the problem of low yield is critical for conventional counter telescope method (ΔE-E method). Therefore in the fragment measurement, large detection area, large solid angle and identification capability of fragments is required.

In this study, to overcome these problems, we adopted for the fragment measurements in ten's of MeV region 1) a Bragg curve spectrometer (BCS) [8, 9] providing various information with a single counter and 2) an energy-time of fight (E-TOF) method [3] having the capability of mass identification even in the energy region where BCS is not applicable, while the solid angle is very small. For 1), BCS was designed with special care to apply to a neutron beam as well as a charged particle beam, and resulted in success to obtain light fragments by proton- and neutron-induced reactions [15, 16]. For 2), the E-TOF method is restricted only to charged particle-induced reactions due to small detector solid angle. The dynamic range of fragment energy is higher than in BCS.

Table 1 shows the comparison to our group with other group introduced above. Our group aims to obtain energy-angular fragment production data in proton- and neutron-induced reaction with BCS and E-TOF method. The energy region is lower than in other facilities but this energy region is very important for SEU estimation and dosimetry for proton radiotherapy. For neutron, only our group has been challenging the measurements.

Table 1 Comparison with each facility in fragment measurement

| | THO | TSL | PISA | GSI etc. |
|---|---|---|---|---|
| enery range (MeV) | 30 - 90 | 100 - 470A | 200 - 2500 | >1A GeV |
| projectile | n,p | Si | p | Pb, U .... |
| method | BCS for n,p<br>E-TOF for p | inverse kinematics | BCS and E-TOF coupled | inverse kinematics |
| data | DDX | reaction XS | DDX | reaction XS |

### 3-1. BRAGG CURVE SPECTROMETER (BCS)

The details of Bragg curve spectrometer developed are described in the previous report [16]. Figure 1 shows a schematic diagram of BCS. It is a cylindrical gridded ionization chamber (GIC) [17] filled with an Ar + 10%$CH_4$ gas at a pressure of ~200 Torr. In the case of proton induced reaction, fragments produced from targets in the vacuum chamber enter the detector through a thin film window and ionize the gas in BCS. The free electrons drift to the anode by the electric field keeping a shape of Bragg curve. The time distribution of the anode signal corresponds to the reversal of the ionization distribution (Bragg curve) by the fragment. Therefore the fast part of anode signal is proportional to the Bragg peak value that is in proportion to the atomic number (Z) of the fragment. The integration of the whole anode signal represents the total charge that is proportional to the fragment energy. Therefore, BCS can provide information on the energy and the atomic number of fragments using only the anode signal.

To apply BCS to neutron-induced reactions, we put samples inside the chamber and irradiate the chamber by neutron directly to decrease the energy loss of fragments and enlarge the detection solid angle. We adopt tight neutron collimation, high-Z element (Ta) electrodes having small fragment production rate, and an additional shield electrode to reduce backgrounds due to neutron irradiation of the chamber body and counting gas.

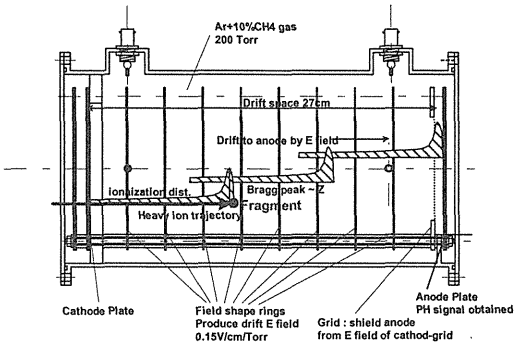



Fig. 1 Schematic diagram of the developed Bragg curve spectrometer (BCS)

Figures 2 and 3 show the measured two-dimensional spectra on the energy *vs.* Bragg peak of fragments from 4 μm thick polypropylene for 70 MeV proton and 75 MeV quasi-monoenergetic neutron [18], respectively. Excellent separation of each fragment and S/N ratio are confirmed up to Z = 6 (Carbon) for proton energy region where particles are separated by the difference of Bragg peak value. In case of neutron fragments heavier than α particle are separated distinctly, though the separation of Bragg peak is much inferior compared with proton-induced reaction due to the effects of the various emission angle. It is confirmed that we could obtain the yields of fragments with sufficient statistics using thin target (4 μm thick polypropylene) for sample and Au foil for background measurement.

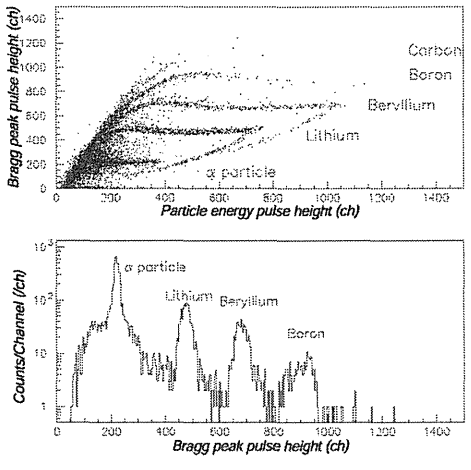



Fig.2 Energy vs. Bragg peak two-dimensional spectrum (top) and Bragg peak spectrum above separation limits (bottom) for polypropylene (4 μm) induced by 70 MeV protons.

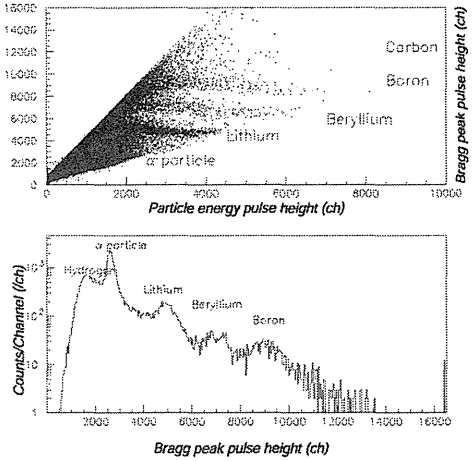



Fig.3 Energy vs. Bragg peak two-dimensional spectrum (top) and Bragg peak spectrum above separation limits (bottom) for carbon (200 μm) induced by 75 MeV quasi-monoenergetic neutron

### 3-2. ENERGY TIME-OF-FLIGHT (E-TOF METHOD)

For proton-induced reactions, we have applied an Energy-Time-Of-Flight (E-TOF) method which is used in heavy ion detection. In this method, the energy and TOF of the fragment is measured and mass number is derived by combing the energy and TOF. Therefore the dynamic range of fragment energy is higher than in BCS. These data will be useful to complement data obtained with BCS.

Up to now, we identified the fragments from polypropylene (4 μm thick) up to A=12 with the measurement system using an ultra-thin plastic scintillator and SSD with ~1 m flight path as shown in Fig.4. The energy spectra of fragments above mass of 6 were measured on the almost whole energy range. The fragments of mass number 5, 8, 9 were very few and the fragments above mass number 10 have small energy compared with lighter fragments. The time resolution of this setup was not so good because we use SSD for not only E detector but also a timing detector. We will develop the measuring system by using two timing detector for TOF measurement and E detector for energy measurement in the near future.

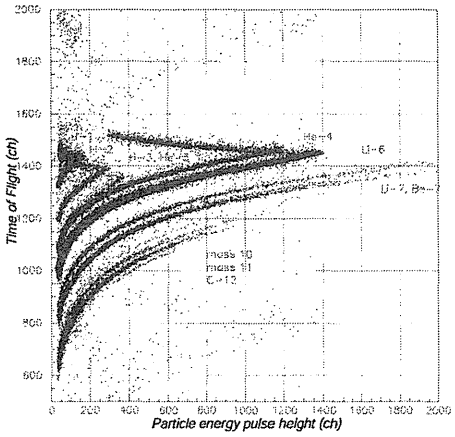



Fig.4 Energy *vs* TOF two-dimensional spectra for carbon 100 μm thick sample

## 5. SUMMARY

The present status of fragment experiment was reported for our group together with other facility. We are aiming at measurement of energy-angular spectrum of fragment induced by neutron and proton which is very important for SEU estimation and dosimetry for proton radiotherapy. For neutron, only our group has been challenging the measurements. To obtain the energy-angular spectrum of fragment by nucleon-induced reaction in ten's of MeV, we have developed a Bragg Curve Spectrometer (BCS) and E-TOF method. For BCS, excellent separation of each fragment are confirmed up to Z = 6 (carbon) for proton and neutron, respectively. Through the experiments, BCS proved to be applicable to not only proton-induced reactions but also neutron-induced reactions. We are also doing fragment production measurement for proton-induced reactions using the E-TOF technique to extend energy range and improve data quality and identified the fragments from polypropylene (4 μm thick) up to A=12 using an ultra-thin plastic scintillator for start detector and SSD for stop detector with ~1 m flight path. We intend to improve the measuring method with the refinement of data treatment and the data will be applied for the analysis of SEU and dose contributions.

## ACKNOWLEDGEMENT

The authors express their thanks to the operation crew of the NIRS and TIARA cyclotron for their cooperation.

## REFERENCES

1] IBM J. Res. Dev. 40, No.1, 1996. (Special issue on terrestrial soft errors in microelectronic systems)
[2] H.H.K. Tang and J.L. Romero, American Institute of Physics Conference Proceedings No.392 (1997) 325
[3]C.T.Roche, R.G.Clark, G.J.Mathews and V.E.Viola, Jr, Phys. Rev. C 14 (1976) 410
[4] K. Kwiatkowski et al., Phys. Rev. Lett. 50 (1983) 1648.
[5] T. Enqvist, W.Wlazlo, P. Armbruster, J. Benlliure et al. Nucl. Phys. A 686 (2001) 481
[6] J.L. Romero et al., American Institute of Physics Conference Proceedings No. 392 (1997) 655
[7] Yu.A. Murin et al., Proc. 4th ISTC Scientific Advisory Committee Seminar, Novosibirsk, April 23-27, 2001.
[8] C.R.Gruhn, et al., Nucl. Instrum. Methods, 196 (1982) 33
[9] N.J.Shenhav and H.Stelzer, Nucl.Instrm.Meth. 228 (1985) 359
[10] H. Ochiishi et al., Nucl. Instr. and Meth. A 369 (1996) 269
[11] R. Barna et al., Nucl. Instr. and Meth. A 519 (2004) 610
[12] P.G.Young, E.D.Arthur, M.B.Chadwick, LANL Report LA-12343-MS, 1992
[13] M. B. Cadwick, P. G.Young, S. Chiba et al., Nucl. Sci. Eng., 1331 (1999) 293
[14] K.Niita, S.Chiba, et al., Phys. Rev. C52 (1995) 2620
[15] T. Sanami, M. Baba, M. Hagiwara et al., J. Nucl. Sci. and Tech. Suppl. 4 (2004) 502
[16] M. Hagiwara, T. Sanami, M.Baba, T. Oishi, et al., Proc. of Nucl. data.Sym. (2003)
[17] T.Sanami, M.Baba, K.Saito, N.Hirakawa. Nucl. Instrum. Meth. A440 (2000) 403
[18] M. Baba, Y. Nauchi, T. Iwasaki, T. Kiyosumi et al., Nucl. Instrum. Meth. A428 (1999) 454

JP0550258

## 2.17 The Present Status of the n_TOF Facility at CERN

Masayuki IGASHIRA
Research Laboratory for Nuclear Reactors, Tokyo Institute of Technology
2-12-1-N1-26 O-okayama, Meguro-ku, Tokyo 152-8550, Japan
e-mail: iga@nr.titech.ac.jp

The main aim of the n_TOF facility at CERN is to provide precise neutron cross-section data relevant to the R&D of accelerator driven systems, nuclear astrophysics, etc. It is composed of a spallation neutron source, a 187.5-m flight path, a variety of detectors, a data acquisition system, etc. A 20 GeV proton synchrotron is employed together with a lead target for the spallation neutron source. The measurement of capture and fission cross sections started in 2002 and had been performed until the mid of November in 2004. The capture and fission measurements were performed for 28 and 7 isotopes, respectively. The brief history, present status, and future plan of the n_TOF facility are reported.

### 1. Introduction

C. Rubbia et al. proposed "The Energy Amplifier: A Solid-Phase, Accelerator Driven, Sub Critical, Th/233U Breeder for Nuclear Energy Production with Minimal Actinide Waste"[1]. However, more accurate neutron cross-section data in a wide energy range were necessary for the R&D of the energy amplifier. Thus, C. Rubbia et al. proposed the idea of the n_TOF facility at CERN in 1998[2].

The main aim of the n_TOF facility is to provide precise neutron cross-section data relevant to the R&D of accelerator driven systems, nuclear astrophysics, etc. It is composed of a spallation neutron source, a 187.5-m flight path, a variety of detectors, a data acquisition system, etc. A 20 GeV proton synchrotron was employed together with a lead target for the spallation neutron source.

The n_TOF facility was commissioned in 2001. Then, the background in the experimental areas was investigated and it was larger than the simulated result by about 50 times. After adding an iron shield with a thickness of 3 m and a shadow bar, the measurement of capture and fission cross sections started in 2002. The work packages from nTOF1 to nTOF10 had been performed until the mid of November in 2004. In these packages, capture and fission experiments were performed for 28 and 7 isotopes, respectively.

The brief history, present status, and future plan of the n_TOF facility are reported mainly based on the presentation at ND2004 by P. Cennini[2].

### 2. Neutron Source of the n_TOF Facility

A 20 GeV proton synchrotron was employed together with a $80\times80\times60$ $cm^3$ lead target as a

spallation neutron source. One 20 GeV/c proton can produce about 300 neutrons in the lead target. A proton pulse was delivered to the lead target every 2.4 s. The width and intensity of proton pulse depended on the operation modes of the synchrotron. In the Dedicated Mode, the width was 6 ns (rms) and the intensity was $7\times10^{12}$ protons. The performances of the n_TOF facility are shown in Table 1. The main characteristics are (1) the wide neutron-energy range, (2) the high neutron flux, and (3) the high energy resolution. The flight time of 1 eV neutron for the 187.5 m path is about 0.014 s, so only 0.006 (=0.014/2.4) of real time is the measuring time. Therefore, (4) the low duty cycle is favorable for the measurements of cross sections of radioactive samples.

Table 1 Performances of the n_TOF facility

| | |
|---|---|
| Nominal Energy Spectrum | 1 eV to 250 MeV |
| Neutron Flux | $6.2\times10^{5}$ n/cm$^2$/$7\times10^{12}$ p |
| Flight Path | 187.5 m |
| Duty Cycle | $<1\%$ |
| Energy Resolution | 0.02% at 1 keV, 0.2% at 1 MeV, 1% at 100 MeV |
| Intrinsic in-beam Contamination | Gamma Rays: 10% |
| Outside-beam Contamination | $<10^{-6}$ relative |

3. Detectors and Data Acquisition System

Parallel Plate Avalanche Counters (PPACs) and a Fast Induction Chamber (FIC) were developed for fission cross-section measurement. Four $C_6D_6$ detectors and a $4\pi$ $BaF_2$ spectrometer were developed for capture cross-section measurement.

The n_TOF data acquisition (DAQ) system is a general purpose one using flash analog-to-digital converters (FADC). The DAQ system was designed based on the proton beam repetition rates, expected event rates and detector channels, and characteristics of the detector signals. The sampling rate of FADC was usually 500 MHz and the full analogue waveform of each output of detector was stored during 16 ms for each proton pulse. Therefore, there was no dead time in measurement and the DAQ system could manage a huge data rate of 45 Mb/s. In fact, 2 Tb data were stored every day.

4. Cross Section Measurement at the n_TOF

Since the first measurement with the $C_6D_6$ detectors for the capture cross section of $^{151}$Sm, capture and fission experiments were performed for 28 and 7 isotopes, respectively, as shown in Table 2. In 2004, the capture experiments were performed with the $4\pi$ $BaF_2$ spectrometer and 25-400 mg samples. Each of radioactive samples was encapsulated in a Ti case due to the regulation of CERN.

Table 2 Capture and fission experiment performed at the n_TOF facility

| | |
|---|---|
| Capture (28 Isotopes) | |
| 2002 | $^{151}$Sm, $^{204,206,207,208}$Pb, $^{209}$Bi, $^{232}$Th |
| 2003 | $^{24,25,26}$Mg, $^{90,91,92,93,94,96}$Zr, $^{139}$La, $^{186,187,188}$Os |
| 2004 | $^{79}$Se, $^{233,234,236}$U, $^{237}$Np, $^{240,242}$Pu, $^{243}$Am |
| Fission (7 Isotopes) | |
| 2002 | $^{232}$Th, $^{234}$U |
| 2003 | $^{232}$Th, $^{233,234,235,236,238}$U, $^{237}$Np, $^{241,243}$Am, $^{245}$Cm |
| 2004 | $^{233,235,236,238}$U, $^{241,243}$Am, $^{245}$Cm |

5. Research Members at the n_TOF Facility

In 2004, the experiments at the n_TOF facility were performed by 114 researchers from 40 institutions. Most of researchers were from European institutions, but researchers from non-European institutions also participated. From Japan, M. Oshima (JAERI) and the author officially participated in the n_TOF experiments. The Maintenance and Operation (M&O) cost of the n_TOF facility was shared by all the researchers except for post-doc researchers and doctor course students.

6. Future Plan at the n_TOF Facility

The water coolant of lead target produced 2.2 MeV gamma-ray background in the time region corresponding to the keV neutron region. To reduce this background, the addition of 0.2-1% B to the coolant water or the usage of heavy water has been investigated. The usage of heavy water has another advantage: it could drastically increase the neutron flux in the keV region.

The second measuring station will be installed at about 150 m in a class A room, where one can use unsealed targets. Moreover, the second flight path will be installed to obtain higher ($\times$100) neutron flux. This flight path will be 20-25 m and orthogonal to the lead target.

All researchers hope that the next measurement will start in the summer of 2006.

References

[1] C. Rubbia, Proc. Int. Conf. on Nuclear Data for Science and Technology, 1994, Gatlinburg, USA, pp. 1065-1071 (1994).

[2] P. Cennini, Int. Conf. on Nuclear Data for Science and Technology, 2004, Santa Fe, USA.

JP0550259



# 2.18 Measurements of Neutron Capture Cross Sections for $^{237,238}$Np

*H. Harada[1)], H. Sakane[1)], S. Nakamura[1)], K. Furutaka[1)], J. Hori[2)], T. Fujii[2)], H. Yamana[2)]*

*[1)]Japan Nuclear Cycle Development Institute, Tokai-mura, Ibaraki 319-1194*
*[2)]Research Reactor Institute, Kyoto University, Kumatori-cho, Osaka 590-0494*
e-mail: harada@tokai.jnc.go.jp

Recent progress on the measurement of neutron capture cross sections performed by a JNC and Kyoto university group is reviewed focusing on $^{237}$Np and $^{238}$Np: ① on the measurement of the neutron capture cross section of $^{237}$Np for thermal neutrons, the activation method was utilized where a thin cadmium shield was introduced to minimize the errors due to a low energy resonance; ② the effective capture cross section of $^{238}$Np for thermal neutrons was measured by utilizing a double-neutron capture reaction; and ③ a total-energy detector and a flash-ADC based data-taking system have been developed and used to measure the capture cross section of $^{237}$Np by a TOF method.

## 1. The neutron capture cross section and resonance integrals of $^{237}$Np for thermal neutrons

The thermal neutron capture cross section ( $\sigma_0$) and the resonance integral ($I_0$) of $^{237}$Np have been measured by an activation method to supply basic data for the study of transmutation of nuclear waste. The neutron irradiation of $^{237}$Np samples has been done at the Research Reactor Institute, Kyoto University (KUR). Samples of $^{237}$Np were irradiated between two Cd sheets or without a Cd sheet. Since $^{237}$Np has a strong resonance at the energy of 0.49 eV, the Cd cut-off energy was adjusted as low as 0.36 eV(thickness of the Cd sheets: 0.125 mm). A high purity Ge detector was employed for the activity measurement of the irradiated sample. The reaction rate to produce $^{238}$Np from $^{237}$Np was analyzed by the Westcott's convention. The details on the experiments and analyses were described in ref. [1] Results obtained were 141.7±5.4 barns for $\sigma_0$ and 862±51 barns for $I_0$ above 0.358 eV of $^{273}$Np. **Table 1** shows the present result and previous one on the $\sigma_0$ for $^{237}$Np.

**Table 1** Comparison of $\sigma_0$ for $^{237}$Np

| Authors (year) | $\sigma_0$ (b) | Measurement method |
|---|---|---|
| Brown et al. (1956) | 172 ± 7 | $\alpha$ -ray spectroscopic method |
| Smith et al. (1957) | 170 ± 22 | Total cross section |
| Tattersall et al. (1956) | 169 ± 3 | Pile oscillation method |
| Schuman et al. (1969) | 185 ± 12 | $\alpha$ -ray spectroscopic method |
| Kobayashi et al. (1994) | 158 ± 3 | $\gamma$ -ray spectroscopic method |
| JNC-Kyoto (2003) | 141.7 ± 5.4 | $\gamma$ -ray spectroscopic method |
| JENDL-3.3 (2002) | 161.7 | Evaluation |

The measurements of the $\sigma_0$ by $\gamma$ -ray spectroscopic method give smaller values than those measured by other methods. The $\gamma$ -ray spectroscopic method requires absolute $\gamma$ -ray intensity of $^{238}$Np. Recent evaluated nuclear structure data file [2] gave about 10% smaller value for the absolute $\gamma$ -ray intensity of $^{238}$Np; if this value is used for the reduction of the $\sigma_0$, it is increased by 10 %. To

understand the discrepancy on the $\sigma_0$ of $^{237}$Np, the absolute $\gamma$ -ray intensity of $^{238}$Np should be re-investigated in detail.

## 2. The effective capture cross section of $^{238}$Np for thermal neutrons

The effective capture cross section ($\hat{\sigma}$) of $^{238}$Np for thermal neutrons has been measured as data for the burn-up analysis of irradiated fuels and for the study of nuclear transmutation of minor actinides. A sample of $^{237}$Np was irradiated for 10 hours at KUR. Neptunium-238 and –239 were produced simultaneously via the double neutron capture reaction $^{237}$Np(n, $\gamma$ )$^{238}$Np(n, $\gamma$ )$^{239}$Np as are shown in **Fig. 1**.

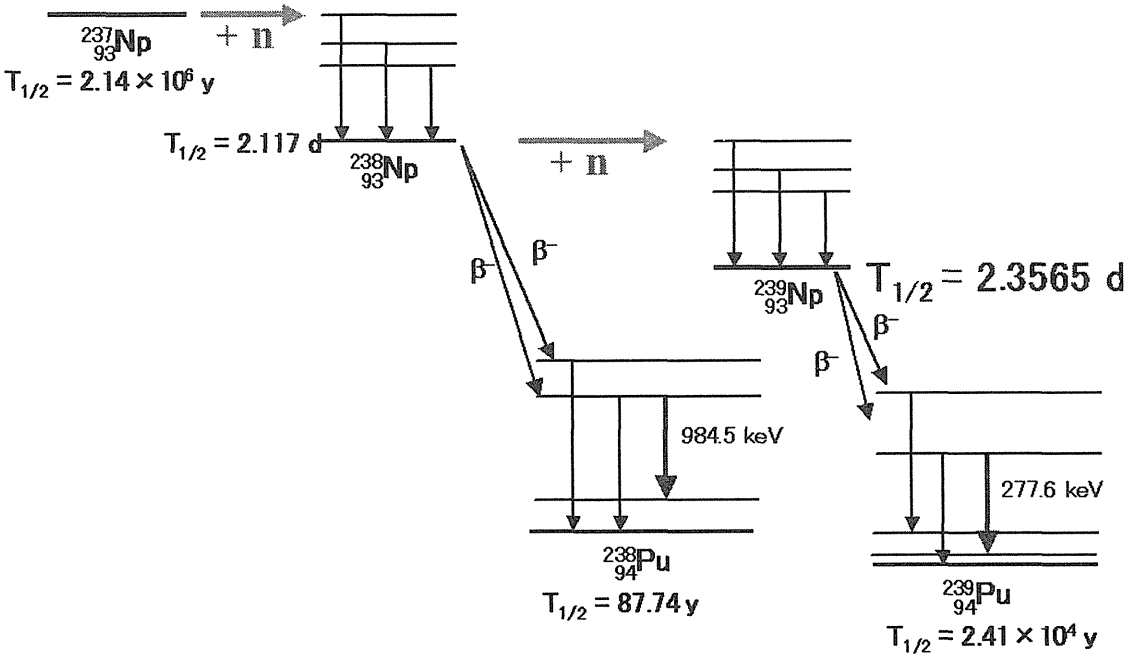



**Fig. 1** Reaction scheme of the double neutron capture reaction $^{237}$Np(n, $\gamma$ )$^{238}$Np(n, $\gamma$ )$^{239}$Np

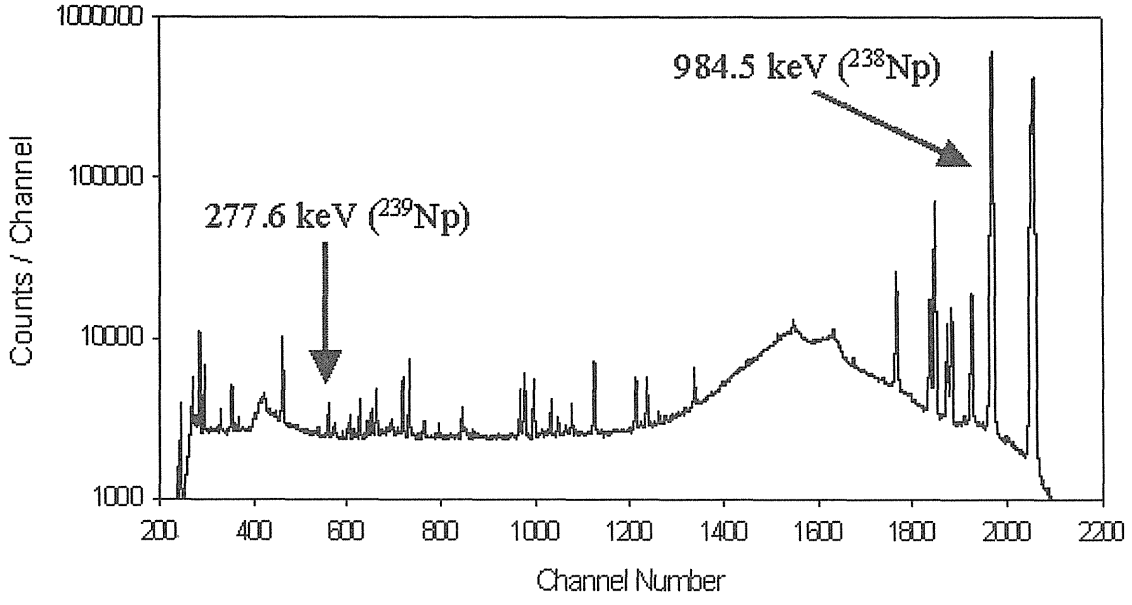



**Fig. 2** Gamma-ray spectrum from the $^{237}$Np sample irradiated during a period of 10 hours

The neutron flux at the irradiation position was monitored using Au and Co wires. The epithermal index $r\sqrt{T/T_0}$ in Westcott's convention was measured as 0.03. A high-purity Ge detector with a BGO ($Bi_4Ge_3O_{12}$) anti-coincidence shield was used to measure the activities of $^{238}$Np and $^{239}$Np. **Figure 2** shows an example of the measured $\gamma$ -ray spectrum. Both of the 277.6-keV $\gamma$ -ray from the decay of $^{239}$Np and the 984.5-keV $\gamma$ -ray from the decay of $^{238}$Np are clearly shown. The $\hat{\sigma}$ of $^{238}$Np was deduced from the ratio of these activities.

If $^{238}$U is included in the $^{237}$Np sample, $^{239}$Np is produced via the $^{238}$U(n, $\gamma$ )$^{239}$U reaction and $\beta$ decay process. It is difficult to measure $^{238}$U in the $^{237}$Np sample by measuring the radioactivities since the lifetime of $^{238}$U is much longer than that of $^{237}$Np. Therefore, the activation method using a neumatic tube of KUR has been utilyzed; the Np sample of about 1 kBq was irradiated for 3 min in the pneumatic transfer tube of KUR and the gamma-rays from the irradiated sample were measured by a HP-Ge detector. The ratio between the number of $^{238}$U and that of $^{237}$Np nuclei was determined to be less than $5.1\times10^{-5}$. The contamination of $^{238}$U contributes the neutron-capture cross section of $^{238}$Np by less than 0.4 %, and is negligible. The result obtained is 479± 24 b for the $\hat{\sigma}$ of $^{238}$Np [3]. The result is compared with data in the evaluated nuclear data libraries, ENDL-86 [4], ENDF/B-VI [5], and JENDL-3.3 [6]. To explain the present result, the evaluated capture cross sections of $^{238}$Np have to be increased about 5 times in the case of ENDL-86 and about 2.4 times in the case of ENDF/B-VI. The value in JENDL-3.3 agrees well with the present result. However, the reduced resonance integral of all libraries are equal to zero. Further fine evaluations should be required on the thermal neutron capture cross section and resonance integral of $^{238}$Np.

## 3. The measurement of neutron capture cross section of $^{237}$Np by a TOF method

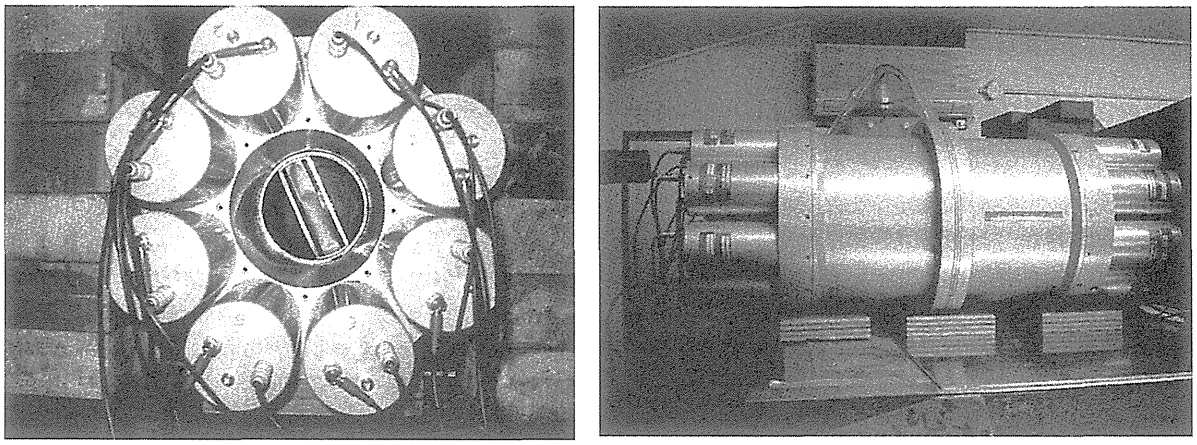


**Fig. 3** The 16-section BGO scintillation detector (back-view in left and side-view in right)

The neutron capture cross section of $^{237}$Np has been measured relative to the $^{10}$B(n,α)$^{7}$Li* cross section by the time-of-flight method in the energy range from 0.02 eV to 100 eV. The 46 MeV electron linear accelerator at the Research Reactor Institute, Kyoto University, was used as a pulsed neutron source. The 16-section BGO scintillation detector shown in **Fig. 3** having a total volume of 8.54 l and the associated 40 MHz flash-ADC–based data taking system have been developed for the measurement of the capture cross section. The BGO detector can be used as a total energy gamma-ray detector [7].

**Figure 4** shows typical waveforms for $\gamma$ -rays from a $^{137}$Cs source obtained by the flash-ADC system with 100 ns channel width (10 MHz). The input pulse was smoothed and the derived

waveform was calculated; this procedure enables to extract pulse-height information even for overlapping pulses.

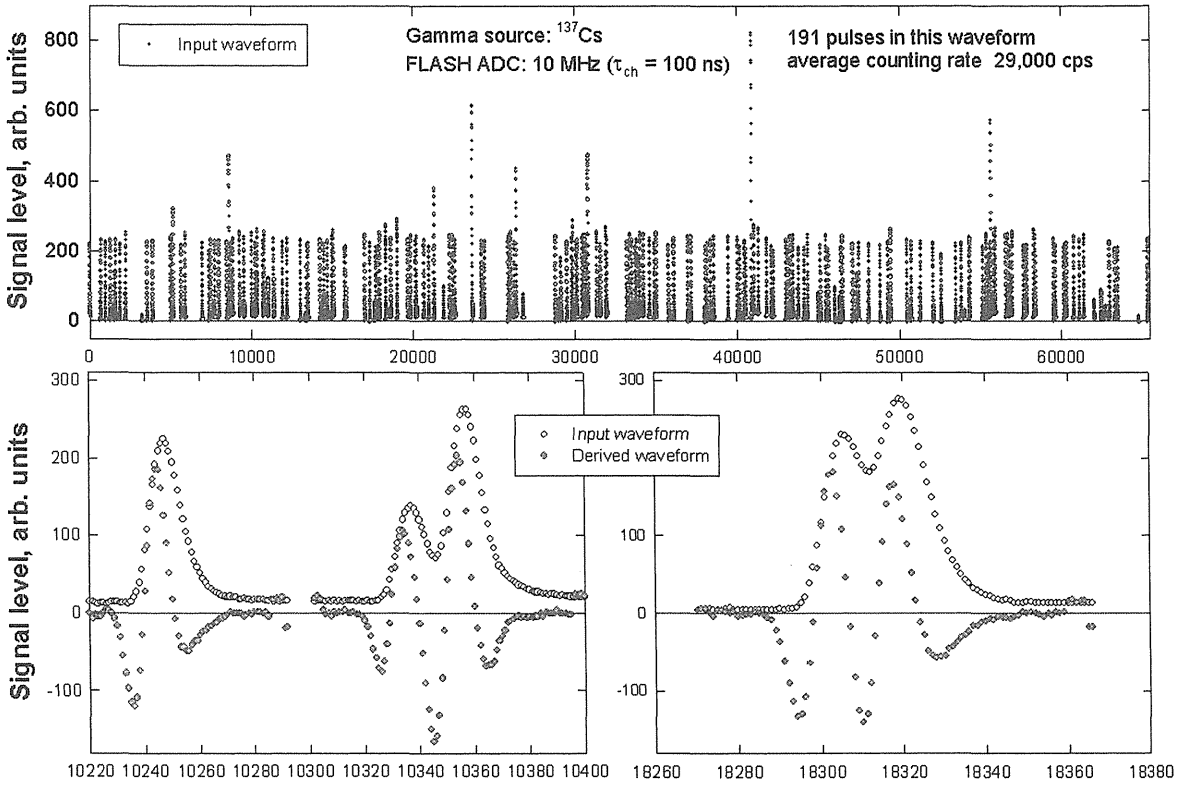



**Fig. 4** Waveforms of the BGO detector signal: (top) full-length input waveforms; (down) stretched parts of the input and derived waveforms

The capture cross section of $^{237}$Np in resonance energy range was measured using the total energy gamma-ray detector for the first time,. The result of the present measurement has been compared with the evaluated capture cross sections of ENDF/B-VI and JENDL-3.3, as well as with the data measured by other authors. **Figure 5** shows the ratio of the measured capture cross section and the other measurements or evaluated values. To make the comparison easier, the capture cross section was averaged. In the energy range from 1 to 100 eV the energy dependence of the present cross section is close to the experimental data by Weston and Todd [8]. However, there is an obvious discrepancy between the data by Kobayashi *et al.* [9] and the present data. On the otherhand, there is an agreement in the energy range 0.02 –100 eV on the energy dependence of the $^{237}$Np capture cross section between the present measurements [10] and the ENDF/B-VI. As far as the JENDL-3.3 is concerned, there is an obvious disagreement with the present data below ~ 0.3 eV, while above this energy an agreement exists, though it is worse than that of ENDF/B-VI. These comparisons show the necessity of the measurements and re-evaluations of the neutron capture cross section at especially theraml energy region.

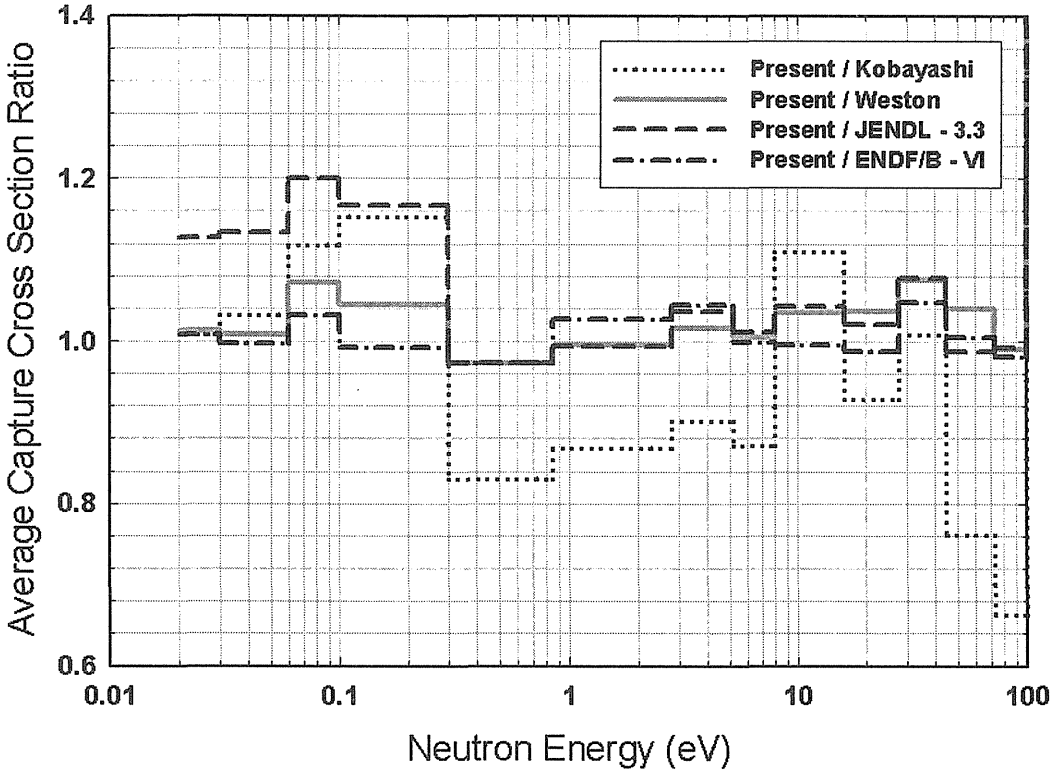



**Fig. 5** The ratio of the averaged capture cross section measured by a JNC-Kyoto group and previous measurements or evaluated values

## References

[1] T. Katoh, S. Nakamura, K. Furutaka, H. Harada, K. Fujiwara, T. Fujii, and H. Yamana, "Measurement of thermal neutron capture cross section and resonance integral of the $^{237}$Np(n, $\gamma$ )$^{238}$Np reaction", *J.Nucl. Sci. Technol.*, **40**, 559 (2003).

[2] Evaluated Nuclear Structure Data File and NUDAT, National Nuclear Data Center, Brookhaven National Laboratory, USA (2002).

[3] H. Harada, S. Nakamura, T. Fujii, and H. Yamana, "Measurement of effective capture cross section of $^{238}$Np for thermal neutrons", *J.Nucl. Sci. Technol.*, **41**, 1 (2004).

[4] Evaluated Nuclear Data Library, ENDL-86, LLNL (1986).

[5] Evaluated Nuclear Data File/B-VI, ENDF/B-VI, BNL/NNDC (1990).

[6] K. Shibata, T. Kawano, T. Nakagawa, *et al.*, "Japanese evaluated nuclear data library Version 3 Revision-3: JENDL-3.3," *J. Nucl. Sci. Technol.* **39**, 1125 (2002).

[7] O. Shcherbakov, K. Furutaka, S. Nakamura, H. Harada, K. Kobayashi, "A BGO detector system for studies of neutron capture by radioactive nuclides", *Nucl. Instru. Method*, **A517**, 269 (2004).

[8] L. W. Weston, J. H. Todd, "Neutron capture cross section of neptunium-237," *Nucl. Sci. Eng.*, **79**, 184 (1981).

[9] K. Kobayashi, S. Lee, S. Yamamoto, H. J. Cho, Y. Fujita, "Measurement of neutron capture cross section of $^{237}$Np by Linac Time-of-flight method and with Linac-driven lead slowing-down spectrometer," *J. Nucl. Sci. Technol.*, **39**, 111 (2002).

[10] O. Shcherbakov, K. Furutaka, S. Nakamura, *et al.*, "Measurement of Neutron Capture Cross Section of $^{237}$Np from 0.02 to 100 eV", to be published in *J. Nucl. Sci. Technol.*

JP0550260



# 2.19 Measurement of fission cross sections

M. Baba
*Cyclotron and Radioisotope Center, Tohoku University*
*Aoba-ku, Aramaki, 980 Sendai, Japan*
babam@cyric.tohoku.ac.jp

A review is presented on the recent progress in the experiment of fission cross section measurement, including recent activity in Japan being carried out under the project of nuclear data measurement.

## 1. Introduction

Fission plays an essential role in nuclear energy through regeneration of neutrons. For the reason, fission cross section has been a critical issue in the development of nuclear energy and still be of a key parameter for the development of new reactor system like ADS (Accelerator driven transmutation system), low moderation reactors and high burn up reactors and so on. For the reasons, cross section requirement is extending to high energy regions, proton-induced reactions and minor actinide elements (MA). However, the data accuracy is not good enough in particular for MA and high energy or proton induced reactions as shown in Fig.1 [1].

In reply to the requirement, world–wide effort is undertaken for the improvement of fission cross section data through the development of new facilities and experimental techniques. It should be noted that, in the case of fission cross sections, experimental data are of special importance for data improvement because the data accuracy required is far beyond that which can be reached by the present nuclear reaction theories.

This report summarizes recent progress in fission cross section measurement including activities in Japan conducted under the project of nuclear data measurement.

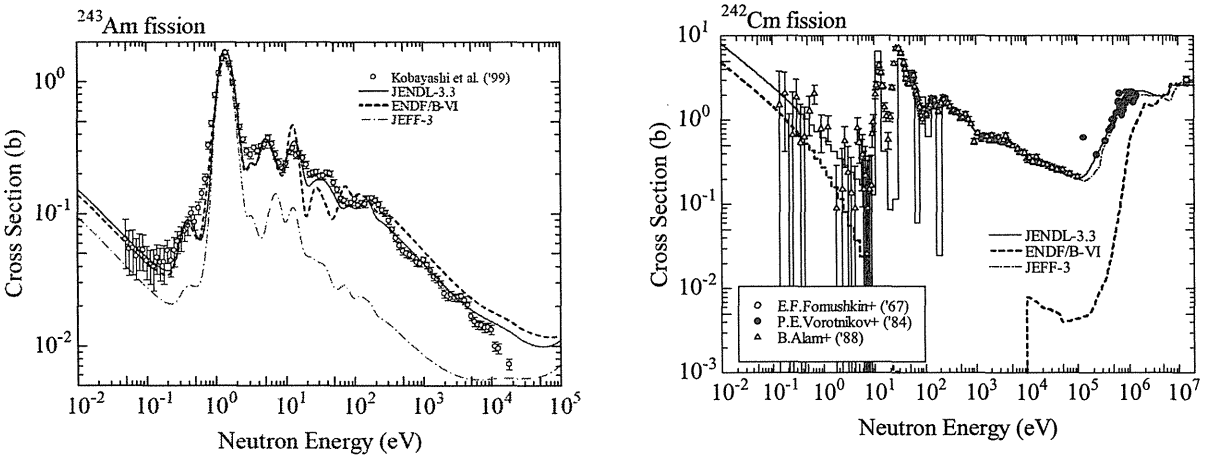



Fig.1 Present status of fission cross section data [1]

## 2. Problems in fission cross section measurement

Usually, fission cross sections are measured by detection of fission fragments with appropriate detectors because of high accuracies reached by the technique [2]. Parallel plate ionization chambers are most popular ones owing to their almost 100 % detection efficiency. In the fission cross section measurement, there are two big problems: One is very high α-activities of fissionable nuclides, in particular higher actinides elements, and the other one is the difficulty to obtain high pure samples for experiments. For some nuclides, only very little sample is available, and chemical and/or isotopic purification is indispensable.

The $\alpha$ -activities introduce serious backgrounds in fission fragment detection. For nuclides with high $\alpha$ -activity, the number of sample nuclides is also limited. Therefore, suppression of $\alpha$ -particle events have been undertaken by taking into consideration the difference of stopping power [2]. A typical one is a parallel plate ionization chamber employing sample-electrode distances shorter than $\alpha$ -particle range as shown in Fig.2. Some one adopts collimation for efficient suppression [2].

An essential solution to the problems is the employment of high neutron flux and fragment detectors with α-particle suppression for fission cross section measurement. It should be noted that recent development in digital signal processing (DSP) provides a powerful tool to obtain reliable data under high neutron flux and/or unfavorable experimental condition such as signal pile ups because it enables detailed analysis of signal wave forms.

For the second problem, a "surrogate technique" is also developed to obtain the cross sections for neutron induced reactions of unstable nuclides or nuclides for which appropriate sample is not available.

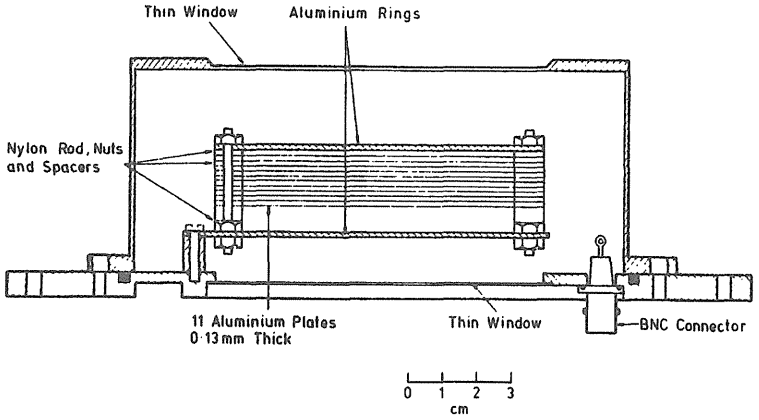



Fig.2: A multiple-plates parallel plate ionization chamber with electrode separation narrower than the $\alpha$ -particle range [2].

3. Recent progress in fission cross section studies

3-1 Utilization of intense neutron source

To obtain higher neutron flux, development has been continued for high power electron linacs like ORELA (Oak Ridge Electron Linear Accelerator) and GELINA (Geel Electron Linear Accelerator) and so on. A lead slowing down neutron spectrometer was also developed and achieved great success. It utilizes the relation between neutron slowing down time and average neutron energy inside a lead assembly around 1.5 cubic meter [3]. The neutron flux reached inside the assembly is higher than that in TOF spectrometer by more than three decades or more, although energy resolution is limited to 30-40 % as shown in Fig.2. It enabled discovery of sub-threshold fission of $^{238}$U and great progress in minor actinide cross sections via much higher neutron flux in Rensselaer polytechnique institute (RPI) and Kyoto University Research Reactor Laboratory (KUR; Fig.3) [4].

A spallation neutron source has also been used for nuclear data measurement. A spallation source at LANSCE/WNR (Los Alamos National Laboratory) driven by a 800 MeV proton beam with very short duration (< 1ns) was used effectively for fission cross section measurement in the neutron energy region from 20 MeV to 400 MeV on $^{235,238}$U, $^{239}$Pu, $^{237}$Np and so on [5]. Recently, a lead slowing down spectrometer was also assembled combined with the spallation source and enable fission cross section measurement of elements as little as ~10 ng [6]. The spallation sources in Russia have also been used for fission studies.

Recently, new high power neutron spectrometer was installed at CERN (Fig.4) [7]. Neutrons are produced by the spallation reaction of 20 GeV protons (6 ns duration) and a neutron flight path around 200 m is available. Using the facility, a "n-TOF" project is in progress through collaboration in EC and other countries. Experiments on fission cross sections are in progress on $^{209}$Bi, $^{nat}$Pb, $^{232}$Th, $^{233,234,236}$U, $^{237}$Np, $^{242,243}$Am, $^{245}$Cm for eV ~ 200 MeV energy region using a parallel-plate-avalanche-counter (PPAC) as well as fission ionization chambers to achieve higher timing resolution.

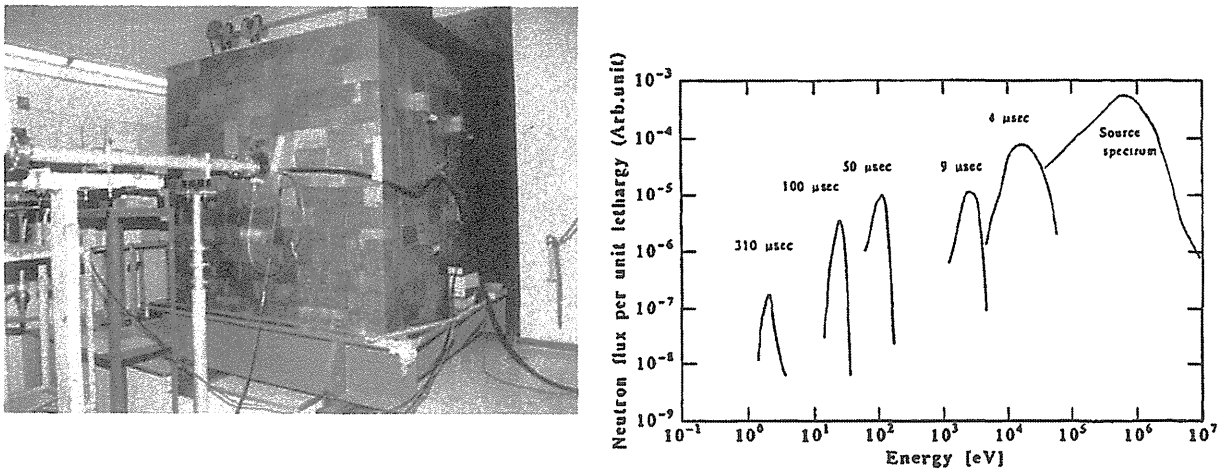



Fig.3; The lead slowing down spectrometer ate Kyoto Univ. (left) and its energy vs time (right) [4].

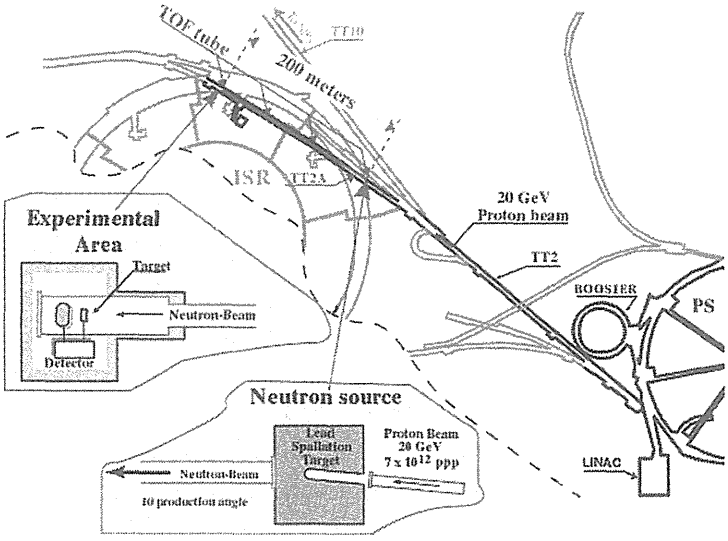



Fig.4; CERN neutron TOF spectrometer for n_TOF project.

3.2 Surrogate reaction technique [8]

Nuclear data are required also for nuclei with very short life time or with very little amount of samples for practical application like nuclear transmutation and studies on nuclear synthesis. $^{233}$Pa and $^{238}$Np are typical examples. In these cases, surrogate transfer reactions such as (d,pf), (t,pf) etc on stable nuclei are used effectively in place of direct neutron induced-reaction on unstable elements.

The neutron cross section is obtained by the following relation:

$\sigma_{nf} = \sigma_{in} \cdot P_f$, of neutron induced reaction, $\sigma_{in}$ = cross section of the surrogate reaction, $P_f$ = fission probability of the states e $P_f = \Gamma_f / (\Gamma_f + \Gamma n)$,

where $\sigma_{nf}$=fission cross section of states excited by the surrogate reaction, $\Gamma_f$ and $\Gamma n$ are, respectively, the fission width and neutron width of the state excited by the surrogate reaction. The fission probability should be obtained by the calculation using appropriate model parameters. Younes and Brit of LLNL have applied this model to many cases to obtain neutron induced fission cross sections of $^{231,232}$Th, $^{234,235,235m,236,237,239}$U, $^{240,241,243}$Pu

using the data of (t,pf), ($^3$He,df), ($^3$He,tf) reactions on the stable nuclei [8]. Figure 5 shows an example of comparison of the surrogate technique with direct reaction of $^{233}$Pa [9].

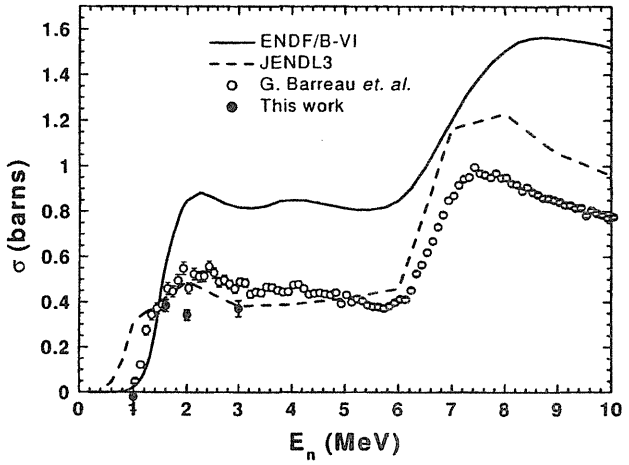



Fig.5: $^{233}$Pa(n,f) cross sections
"This work" (closed circle) shows direct results by neutron induced reaction while
"G. Barreau et al" (open circle) shows results by surrogate technique

3.3 Activities in proton induced reactions

Studies on proton induced reactions are also in progress in Uppsalla university [10] and Russian institutes. Figure 6 shows an example of the results for (p,f) cross sections of light actinides. Smirnov et al deduced the relation of fission probability in proton induced reaction and neutron induced reaction as shown in Fig.6. using the fissility parameter $Z^2/A$ [10]. The relation may be used to estimate cross section of neutron induced reaction on the basis of proton induced data.

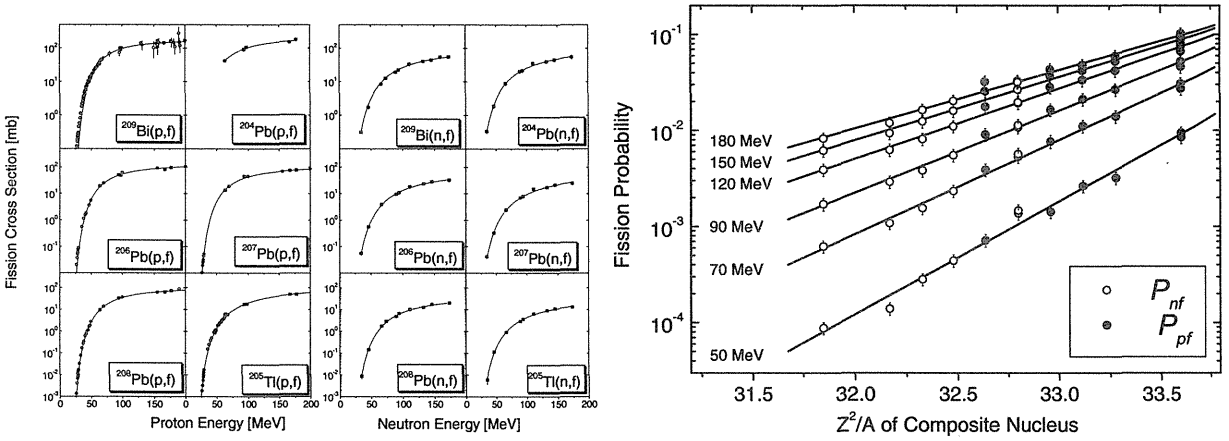



Fig.6; Proton induced fission cross sections (left) and the relation between fission probability and $Z^2/A$ (right) [10].

4. Fission cross section studies in nuclear data project

We[1] are now promoting fission cross section studies under the nuclear data project on minor actinide data which is lead by Dr. Igashira (TIT) [11]. The aim of the projects is to obtain advanced experimental data and provide data base of MA for advanced reactors through development of advanced experimental techniques.

The program covers the following subjects:

1] Neutron induced fission cross sections

1) Low energy region up to hundred of keV using Kyoto Univ. Lead Spectrometer (KULS)

2) High energy region 20-80 MeV region using a AVF cyclotron at the Cyclotron and Radioisotope Center Tohoku Univ, (CYRIC) [12] and intense $^{7}$Li(p,n) source recently installed there

3) Medium energy region (hundred of keV to 20 MeV) using Tohoku Univ., Dynamitron accelerator

2] Proton induced fission : Tohoku Univ., AVF cyclotron

1) Fission cross sections

2) Fission yields by activation, radio-chemical methods, counter technique

3] Development of experimental techniques for fission

Parallel plate avalanche counter (PPAC) for fragment detection,

Fast response/ recovery detection system, digital signal processing,

As mentioned in sect.3.1, a lead spectrometer is a powerful neutron source and useful for fission cross section measurement of MAs. For major MAs, experimental data have been reported for by Kobayashi and Yamamoto using KULS [4]. Nevertheless, the data was limited in the energy region lower than around 10 keV because of the effect of intense "$\gamma$ -flash". In the present program, therefore, the experiment is being extended to higher energies by providing electromagnetic shielding for detector-preamp lines, and employing fast recovery electronics and digital signal processing technique. In Fig.7, the extension of neutron energy range is illustrated achieved by the above mentioned means ($^{237}$Np fission cross section). Digital signal processing technique is also effective and reaches to similar results.

Recently, a new $^{7}$Li(p,n) neutron source is under development at Tohoku University CYRIC to obtain intense quasi-monoenegy neutrons by employing a geometry shown in Fig.8. In this design, the sample or fission counters can be set around 70 cm from the source, then the neutron intensity will be as high as around $10^{6}$/cm$^{2}$ · sec for 1 $\mu$A beam current that is the highest value in the world. The neutron source is now under test and adjustment for licensing. It will be opened for utilization soon.

In the Dynamitron laboratories, many fission cross section data were obtained and still can be used for the experiment from hundreds of keV to 18 MeV neutron energy region, if there is need.

For proton induced reaction studies, the beam line of Tohoku Univ. Cyclotron was upgraded to enable irradiation of fissile elements and actinide elements, and now applied to fission yield experiments using activation technique.

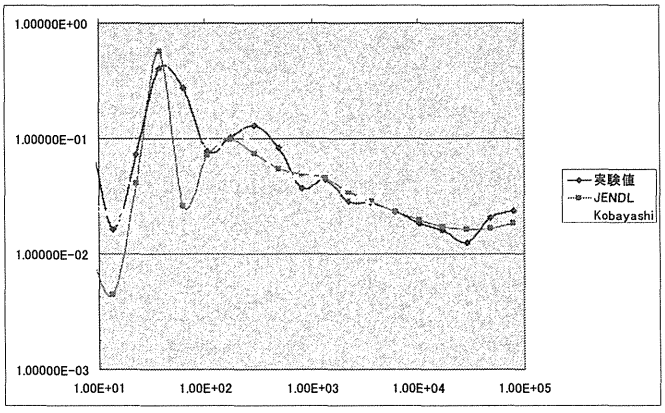



Fig.7: Extension of cross sections measurement to higher energy at KULS.

[1] The members are as follows: M. Baba, T. Yamauti, T.Oishi, M.Hagiwara (Tohoku Univ., CYRIC), T.Ohtsuki, H. Yuki (Tohoku Univ., Linear Accelerator Lab.,), J Hori, H.Yamana, K.Nakajima, M.Takamiya (Kyoto Univ,, , Research Reactor Institute)

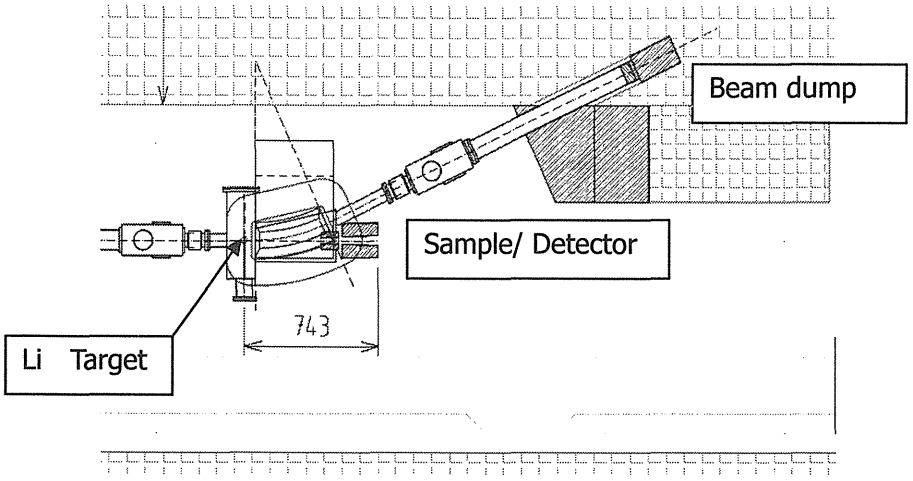



Fig.8: A new $^{7}$Li(p,n) neutron source at Tohoku Univ., CYRIC

ACKOWLEDGEMEBNT:

The author wishes to thank Drs. K. Kobayashi and S. Yamamoto for collaboration and useful information on experiments at KULS. He also expresses his thanks to Prof. H. Okamura and Mrs. S. Chiba, Y. Omiya, N. Takahashi for collaboration to installation of new Li(p,n) neutron source at CYRIC.

REFERENCES;

[1] T. Nakagawa (JAERI); "Status of Minor Actinide Nuclear Data" (2003, private communication)
[2] "Fission Cross Sections for Neutron Induced Reaction" (P. Michaudon ed.,) ,Pergamon Press.
[3] R.E.Slovacek et al.: *Nucl. Sci. Eng.*, 62, 455 (1991)
[4] K. Kobayashi et al.: *Nucl. Instrum. Methods*, A385 (1997) 145
*J. Nucl. Sci. Technol.*, 30[9], 863 (1993)
[5] n_TOF: Refer the report of M. Igashira in this proceedings.
[6] P.Lisowski; *Proc. International Conf. on Nuclear Data for Sci. Technol., 2004, Santa Fe*, to be published
[7] R.Haight et al.: *Proc. International Conf. on Nuclear Data for Sci. Technol., 2004, Santa Fe*, to be published
[8] Yoness and Britt; *Proc. International Conf. on Nuclear Data for Sci. Technol., 2004, Santa Fe*, to be published
[9] Humbsh et al.: *Proc. International Conf. on Nuclear Data for Sci. Technol., 2001, Tsukuba*
[10] Smirnov et al.: *Proc. International Conf. on Nuclear Data for Sci. Technol., 2004, Santa Fe*, to be published
[11] M.Igashira et al.: *Proc. International Conf. on Nuclear Data for Sci. Technol., 2004, Santa Fe*, to be published
[12] http://www.cyric.tohoku.ac.jp

This is a blank page.

# 3. Papers Presented at Poster Sessions

This is a blank page.

JP0550261



# 3.1 $^{239}$Pu data of JENDL-3.3

Masayoshi Kawai
KEK, 1-1 Oho, Tsukuba, Ibaraki-ken 305-0801, Japan
Masayoshi.kawai@kek.jp

**abstract**

$^{239}$Pu data of JENDL-3.3 were originally evaluated in 1987. After then, fission cross sections of important heavy isotopes, $^{233}$U, $^{235}$U, $^{238}$U, $^{239}$Pu, $^{240}$Pu and $^{241}$Pu were simultaneously evaluated and its results were adopted for JENDL-3.3. Integral test of JENDL-3.3 made by other authors showed that JENDL-3.3 well reproduced the k-eff of Pu-fuelled FBR critical cores and thermal reactors within about 0.5%. The C/E values of F25/F49 and C28/F49 in ZPPR-9 core were 1.02 and 1.04.

## 1. Introduction

$^{239}$Pu is one of the most important nuclides of nuclear fuel of fission reactors and very high accuracy of its nuclear data is required for designing the fast breeding reactors (FBR), MOX-fueled reactors and fuel re-processing facilities. Thus, the data of $^{239}$Pu were evaluated for the first version of JENDL, i.e., JENDL-1/1/. Many analyses of reactor physics experiments with JENDL-1 and ENDF/B-IV were made for MONJU and large FBR. These information was fed back to JENDL-2 evaluation/2/.

Reevaluation for JENDL-3 were made on the basis of differential data such as measured cross sections and nuclear model calculations, since there were a lot of new experimental data after completion of JENDL-2 and reactor physics calculation accuracy became higher due to applying continuous-energy Monte Carlo methods. The results of reevaluation were compiled into JENDL-3.1/3/ in 1989. Integral test was made and showed that there were not any serious problems in $^{239}$Pu data of JENDL-3.1. Then, slight modification has been made for JENDL-3.2 and 3.3. The followings are the history of the evaluation of $^{239}$data for JENDL-3:

Evaluations of $^{239}$Pu for JENDL-3.1 were made by taking into consideration of the reliability and consistency of the experimental data and by supplementing the data with the statistical model calculations in 1987. Contributions to the evaluation were as follows:

Cross sections evaluated and calculated by M. Kawai and K. Hida,

Simultaneous evaluation of fission cross section above 30 keV by Y. Kanda et al./4/

Resolved resonance parameters up to 1 keV selected by T. Yoshida,

Unresolved resonance parameters determined with ASREP code/5/ by T. Nakagawa.

For JENDL-3.2 in 1993,

Resolved resonance parameters up to 2.5 keV evaluated by Derrien./6/,

Fission spectra calculated by T. Ohsawa et al./7/

For JENDL-3.3,

Addition of direct and semi-direct capture cross sections calculated by T. Kawano,

Fission spectra above 10 MeV modified by T. Kawano et al./8/

The nuclear data evaluation and integral tests of JENDL-3.2 and 3.3 are described in the following sections.

## 2. Nuclear Data Evaluation

### 2.1 Number of prompt fission neutrons

Most of experimental data of $\nu_p$ of neutron induced fission for $^{239}$Pu were measured as a ratio to $\nu_p$ for $^{252}$Cf spontaneous fission or the thermal value of $^{239}$Pu fission. Therefore, all experimental data and previously evaluated data were renormalized to the following standard values:

$\nu_p$ for $^{252}$Cf spontaneous fission = 3.756

$\nu_p$ for $^{239}$Pu fission at thermal = 2.8781 which was derived by weighted-averaging the experimental data.

The energy dependent $\nu_p$ were evaluated based on the experimental data/9-14/ except for adopting the Frehaut's evbaluation/15/ in the energy range between 10 eV and 500 eV. Below 500 eV, $\nu_p$ has energy dependence considering an effect of the strong resonance with the spin state J=1 at 0.3 eV as shown in Fig. 1. Above 500 eV, evaluated $\nu_p$ values are given by the following polynomials which were obtained by eye-guide fitting the reliable measured data:

$\nu_p$ = 0.135 En + 2.8675 for En = 100 keV - 1.5 MeV,
0.1534 En + 2.8399 for En = 1.5 MeV - 5.3 MeV,
0.1521 En + 2.8469 for En = 5.3 MeV - 11.5 MeV
0.1305 En + 3.0953 for En = 11.5 MeV - 19.6 MeV
0.0902 En + 3.885 for En = 19.6 MeV - 30 MeV..

### 2.2 Total cross section

Below 7 MeV, JENDL-2 evaluation was adopted, which were obtained by fitting the polynomials to the experiments of refs./16 -20/ with the weighted least squares method. Above 7 MeV, experimental data by Poenitz et al./21/ were adopted.

### 2.3 Fission cross section

There were a lot of experimental data reported from the various institutes in the world. However, it should be noted that the experimental data of Gayther/22/ at Harwell and Wagemans et al./23/ at GEEL were highly accurate and quite consistent with each other. Therefore, the fission cross sections below 30 keV were evaluated based on their data. Figure 2 compares the evaluated and measured fission cross sections between 1 keV and 100 keV. Above 30 keV, it is necessary to obtain the overall consistent evaluation for absolute measurements of $^{239}$Pu fission cross sections and ratio measurements to $^{235}$U fission cross section. This requirement was needed for important nuclides such as $^{233}$U, $^{235}$U, $^{238}$U, $^{239}$Pu, $^{240}$Pu and $^{241}$Pu. Therefore, simultaneous evaluation for JENDL-3 was made/4/ to determine the fission cross sections of these nuclides with the generalized least-squares calculation by estimating the covariance matrices of the experimental data. Recently, new simultaneous evaluation performed by Kawano et al./24/ using the SOK code was adopted to JENDL-3.3.

### 2.4 Capture cross section

The cross section in the energy range below 1 MeV was derived as a product of the evaluated fission cross section and $\alpha$-value (ratio of capture to fission cross sections). After the measurement of high alpha value by Ryabov et al./25/, many experimental data of alpha values had been reported. However, evaluation of alpha

value was made on the basis of Gwin's highly accurate data/26/ below 30 keV and by least-squares fit of the experimental data above 30 MeV. Figure 3 shows comparison of the evaluated and measured α-values in the energy region between 1 keV and 1000 keV. Above 1 MeV the results of the statistical model calculation with CASTHY and ECIS were adopted. The photon strength function was normalized in the CASTHY calculation so as to reproduce the capture cross section of 280 mb at 100 keV. The results were compiled into JENDL-3.1.

For JENDL-3.3, direct and semi-direct capture cross sections were calculated by Kawano above 500 keV. Figure 4 shows the capture cross sections up to 10 MeV.

**2.5 Inelastic scattering cross sections**

The compound components were calculated with the optical and statistical model code CASTHY, taking into account level fluctuation and interference effects. The fission, (n,2n), (n,3n), and (n,4n) reactions were considered as competing processes. The neutron transmission coefficients for the incident channel were generated with ECIS, whereas those for the exit channel were calculated with CASTHY using spherical optical potential parameters adopted for JENDL-2 evaluation. The direct components were calculated with coupled channel code ECIS. Eight levels of the ground state rotational band were coupled in the calculation. Deformed optical potential parameters with a derivative Woods-Saxon absorption term were taken from Arthur et al./27/ The calculated excitation functions for the first and second levels are in general agreement with the data of Haouat et al./28/ as shown in Fig. 5.

**2.6 (n, 2n) and (n, 3n) cross sections**

The (n, 2n) and (n, 3n) cross sections shown in Figs. 6 and 7 were calculated with a modified version of GNASH to subtract the fission components from the compound cross sections and to treat transmission coefficients of the incident and exit channels separately. The neutron transmission coefficients were generated with the optical model code ELIESE-3 and the coupled channel code ECIS, respectively, using the above-mentioned spherical and deformed potentials for the evaluation of inelastic scattering cross section. The evaluated fission cross section mentioned above was fed to GNASH as a competing process. The preequilibrium process was taken into account. Though the Kalbach's constant for preequilibrium process was adjusted, the calculated (n,2n) cross section did not reproduce so well the measured data in the lower energy region. Therefore, the measured (n,2n) cross section of Frehaut et al./29/ was adopted in place of the calculated data.

Figure 6 compares the evaluated and measured (n, 2n) cross sections. JENDL-3.3 agrees with the experimental data of Frehaut et al. and shows a slight lump at 18 MeV because the competing fission cross section of JENDL-3.2 has a shape of a shallow valley. The evaluated (n, 3n) cross section of JENDL-3.3 is based on the statistical model calculation and fairly similar to ENDF/B-VI and JEF-3.0 as shown in Fig. 7.

**2.7 Resonance parameters**

For JENDL-3.3, resolved resonance parameters up to 2.5 keV were adopted from the new evaluation by Derrien/6/ using the SAMMY code fitting to the experimental data. Unresolved resonance parameters were derived by Nakagawa with the ASREP code/5/, fitting to the evaluated total, fission and capture cross sections mentioned above.

## 3. Integral test of $^{239}$Pu data of JENDL-3

### 3.1 Benchmark cores analyzed with MVP code

Integral test of JENDL-3.2 and JENDL-3.3 was made by Takano et al./30/ of JAERI, analyzing various critical experiments of FBR benchmark cores of $^{233}$U, $^{235}$U and Pu by using the continuous energy Monte Carlo code MVP. Effective neutron multiplication factor, k-eff, was calculated within the statistical errors of 0.02%. Since modification of important quantities of JENDL-3.2, such as fission cross section of $^{233}$U and $^{235}$U, total cross sections of iron etc. have been made for JENDL-3.3, improvement of k-eff of JENDL-3.3 was shown for the $^{233}$U and $^{235}$U cores compared to JENDL-3.2, but almost the same results were obtained for plutonium cores. The results of C/E-values for k-eff for Pu cores are given in Table 1. The table shows that JENDL-3.2 and -3.3 generally reproduces the k-eff values within 0.5%, while ENDF/B-VI.5 and JEF-2.2 have worse cases showing discrepancies more than 1% from the experimental values.

Similar integral test was also made for thermal reactors. Remarkably good results for k-eff of Pu-fueled cores are given in Table 2.

Table 1 Comparison of C/E-values of k-eff for Pu benchmark cores of FBR/30/

| | JENDL-3.3 | JENDL-3.2 | ENDF/B-VI.5 | JEF-2.2 |
|---|---|---|---|---|
| Small core | | | | |
| JEZBEL | 0.9971 | 0.9972 | 0.9982 | 0.9971 |
| JEZBEL-Pu | 1.0014 | 1.0015 | 0.9986 | 0.9986 |
| FLATOP-Pu | 0.9920 | 0.9928 | 1.0044 | 0.9896 |
| THOR | 1.0070 | 1.0061 | 1.0060 | 0.9806 |
| Large core | | | | |
| FCA-XVII-1 | 1.0013 | 1.0022 | 1.0114 | 1.0093 |
| ZPPR-9, | 0.9945 | 0.9939 | 1.0038 | 0.9972 |
| ZPPR-13A, | 0.9947 | 0.9938 | 1.0033 | 0.9975 |
| JOYO-MK-II | 1.0024 | 1.0003 | 1.0059 | 1.0100 |
| FCA-X-2 | 1.0012 | 1.0009 | | |

Table 2 Comparison of C/E-values of k-eff for Pu-fuel thermal cores/30/

| | JENDL-3.3 | JENDL-3.2 | ENDF/B-VI.5 | JEF-2.2 |
|---|---|---|---|---|
| TCA-242Pu | 0.9952 | 0.9959 | 0.9913 | 0.9930 |
| TCA-298Pu | 0.9960 | 0.9968 | 0.9927 | 0.9941 |
| TCA-424Pu | 0.9975 | 0.9978 | 0.9940 | 0.9950 |
| TCA-555Pu | 0.9977 | 0.9987 | 0.9945 | 0.9952 |

As for the reaction rate ratio in the ZPPR-9 core, F25/F49 was 1.02 and C28/F49 was 1.04 in case of JENDL-3.3, and they were 1.02 and 1.03 in case of JENDL-3.2. Good agreement of the JENDL-3.2 and JENDL-3.3 calculations with the experimental values were also obtained for doppler reactivities of $UO_2$ sample, sodium void reactivities and control rod worths in the FBR cores.

### 3.2 Integral test for fast reactors

Another integral test of JENDL-3.3 was reported by Chiba/31/ of JNC for several fast reactors: ZPPR (JUPITER cores), FCA, JOYO, MOZART and BFS with the JUPITER standard calculation scheme standing on the Bondarenko-type 70-group cross-section library, JFS-3-J3.3.

Figures 8 and 9 show comparison of the C/E values for k-eff of various fast reactor cores analyzed with

JENDL-3.2 and JENDL-3.3. JENDL-3.3 shows a trend of slight underestimation of k-eff but discrepancy from the experimental values are small. Moreover, it does not have any core dependence compared to JENDL-3.2. BFS cores should be classified into a uranium fueled one and difference between JENDL-3.2 and JENDL-3.3 is remarkable.

Discrepancies of calculated values from the experimental data are observed only in the $^{239}$Pu fission rate distribution in the reflector of BFS-62-2 core. However, this discrepancy can not be caused by uncertainty of $^{239}$Pu data, because BFS-62-2 is a uranium fueled core and few-group calculation likely overestimates neutron fluxes in the region outside of the core where a steep flux change occurred.

## 4. Conclusion

$^{239}$Pu data of JENDL were drastically revised from JENDL-2 to JENDL-3.1 by adopting new evaluation techniques with a simultaneous evaluation of fission cross sections with the generalized least squares method and nuclear model calculations with the combination of the CASTHY and ECIS codes. Moreover, in evaluation, reliable experimental data were selected from a lot of measured data after careful examination. For the alpha-value, JENDL-2 data were adopted to JENDL-3. This selection gave satisfactorily good results of the integral test even for early version of JENDL-3. Accordingly, for JENL-3.3, there were only modifications of the fission cross section above 30 keV due to the new simultaneous evaluation, a part of fission spectrum, a part of resolved resonance parameters evaluated by Derrien, and addition of direct and semi-direct components to the capture cross sections.

Integral tests showed that JENDL-3.3 reproduced k-eff of fast and thermal reactors within 0.5% which is a limitation of judging quality of nuclear data. The difference (which is small in case of plutonium fueled cores) in JENDL-3.2 and JENDL-3.3 results of integral tests can be attributed to other isotopes than $^{239}$Pu. It should be also noted that JENDL-3.3 gives better results than ENDF/B-VI.5.

**Acknowledgement:**

Author is highly indebted to Dr. T. Nakagawa of JAERI providing figures of comparison of the evaluated and measured cross sections for $^{239}$Pu. He also appreciates kindness of Dr. H. Takano who gave the integral test results.

**References:**

1) Igarasi, S. et al,: JAERI 1261 (1979) .
2) Nakagawa, T. (ed.): JAERI-M 84-103 (1984); Kikuchi, Y. et al.: J. Nucl. Sci. Technol. 22, 593 (1985).
3) Shibata, K., et al.: JAERI 1319 (1990).
4) Kanda, Y. et al.: Proc. Int. Conf. on Nuclear Data for Basic and Applied Science, 13 - 17 May 1985, Santa Fe, p.1567 (1985).
5) Kikuchi, Y. et al.: JEARI-data/code 99-025 (1999).
6) Derrien, H.: J. Nucl. Sci. Technol., 30, 845 (1993).
7) Ohsawa, T. et al.: Nucl. Phys. A665, 3 (2000).
8) Kawano, T. et al.: Phys. Rev., C63, 034601 (2001).
9) Gwin, R. et al.: Nucl. Sci. Eng., 94, 365 (1986).

10) Gwin, R. et al.: Nucl. Sci. Eng., 87, 381 (1984).
11) Soleilhac, M. et al.: Proc. of Second IAEA Conf. on Nuclear Data for Reactors, 15-19 Jun 1970, Helsinki, Finland, Vol. 2, p. 145 (1970).
12) Soleilhac, M. et al.: J. Nucl. Energy. 23. 257 (1969).
13) Nurpeisov, B. et al.: At. Energiya, 39, 199 (1975).
14) Vorodin, K.E. et al.: At. Energiya. 33. 901 (1972).
15) Frehaut, J.: NEANDC(E)-238/L (1986).
16) Uttely, C.A.: EANDC(UK)-40 (1964).
17) Schwartz, R.B. et al.: Nucl. Sci. Eng., 54, 322 (1974).
18) Foster, D.G.Jr. and Glagow, D.W.: Phys. Rev., C3, 576 (1971).
19) Smith, A.B. et al.: J. Nucl. Energy, 27, 317 (1973).
20) Nadolny, et al.: C00-3058-39, 33 (1973).
21) Poenitz, W.P. et al.: Nucl. Sci. Eng., 78, 333 (1981).
22) Gayther, D.B.: Conf. on Nuclear Cross Sections and Technology, 3-7 Mar 1975, Washington, D.C., , Vol. 2, p. 560 (1975).
23) Wagemans, C. et al.: Ann. Nucl. energy, 7, 495 (1980).
24) Kawano, T. et al.: JAERI-Research 2000-004 (2000).
25) Ryabov, Y.V. et al.: Atomnaya Energiya, 24, 351 (1968).
26) Gwin, R. et al.: Nucl. Sci. Eng., 59, 79 (1976).
27) Arthur, E.D. et al.: Nucl. Sci. Eng. 88, 56 (1984).
28) Haouat, W. et al. : Nucl. Sci. Eng., 81, 491 (1982).
29) Frehaut, J. et al.: CEA-N-2500 (1986); Proc. Int. Conf. on Nuclear Data for Basic and Applied Science, May 1985, Santa Fe, p.1561 (1985)
30) Takano, H. et al.: J. Nucl. Sci. Technol., Supplement 2, p. 847 (202).
31) Chiba, G.: http: JAERI-Conf 2003-006, p.22 (2004).

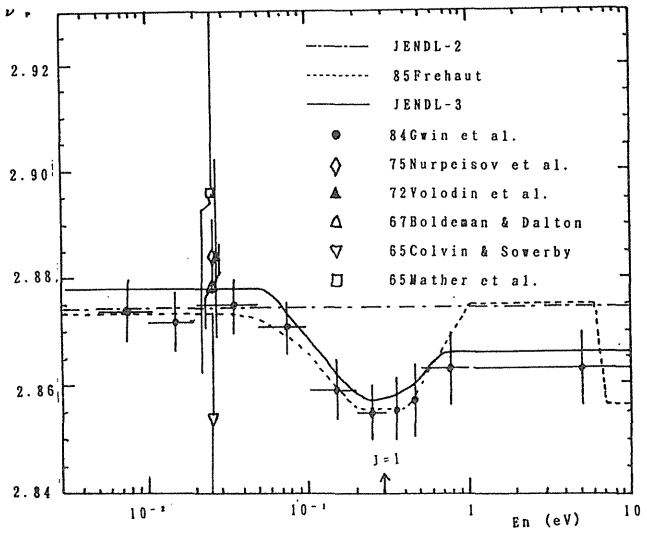



Fig. 1 Comparison of $\nu_p$ of $^{239}$Pu. Effect of the strong resonance at 0.3 eV with the spin state J=1 is observed.

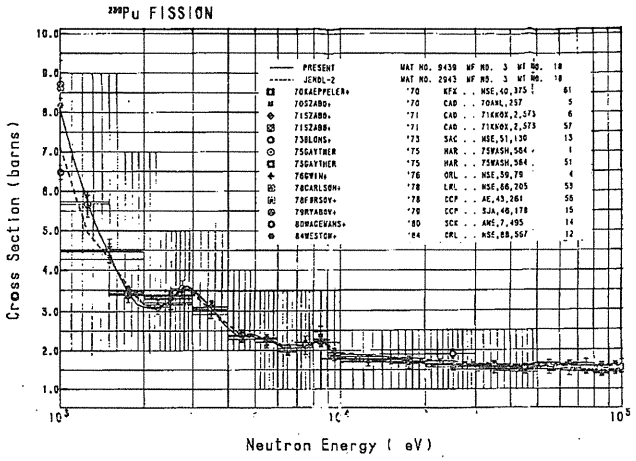



Fig. 2 Comparison of evaluated and measured fission cross sections of $^{239}$Pu

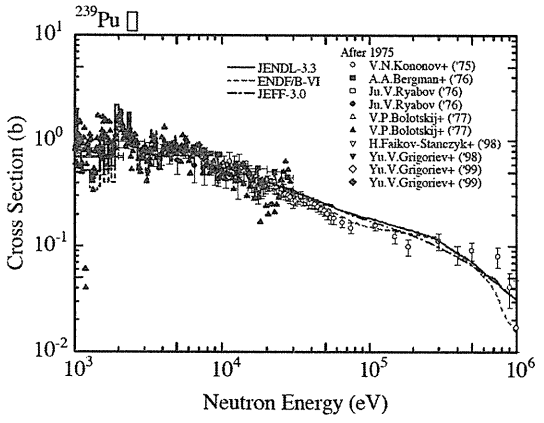



Fig. 3 Comparison of evaluated and measured α-values for $^{239}$Pu.

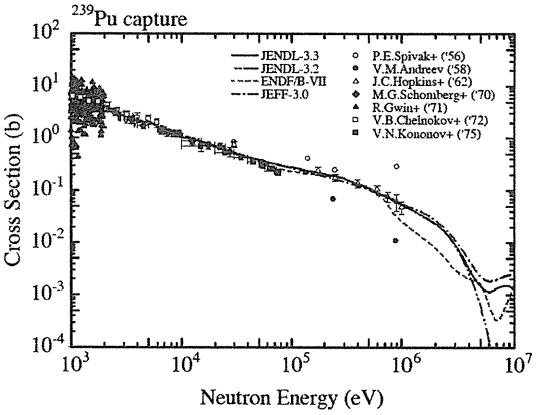
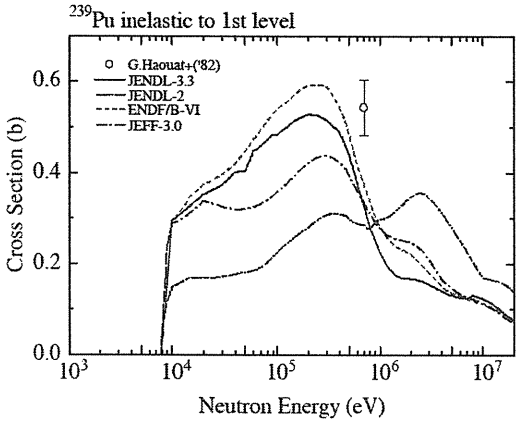
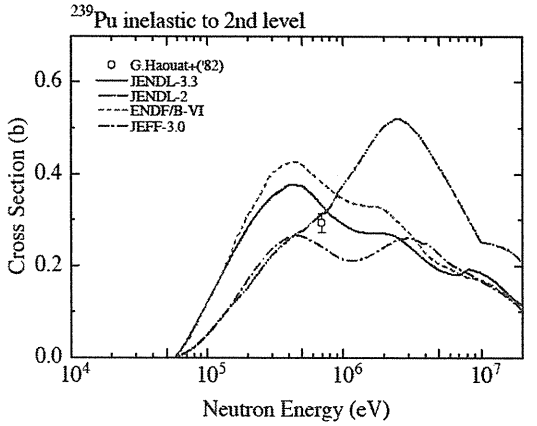



Fig. 4 Comparison of evaluated and measured capture cross sections for $^{239}$Pu.




(a) First-excited state




(b) Second excited state

Fig. 5 Comparison of inelastic excitation functions for $^{239}$Pu.

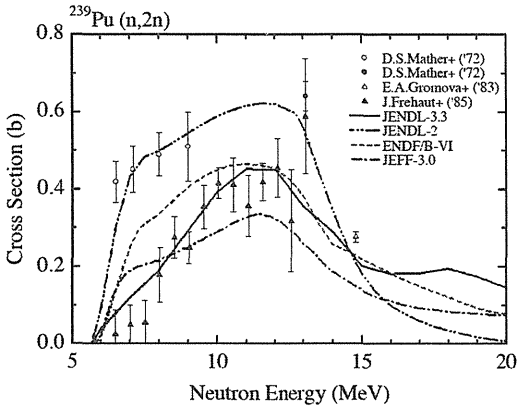



Fig. 6 Comparison of (n, 2n) cross sections

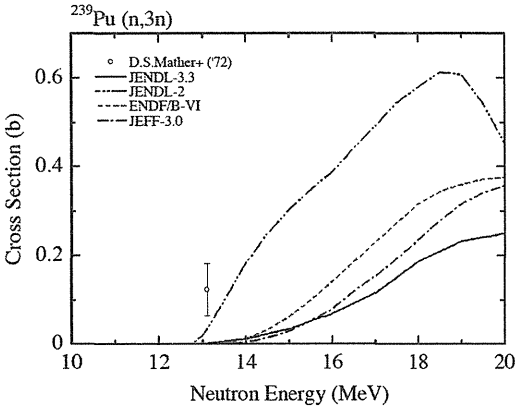



Fig. 7 Comparison of (n, 3n) cross sections

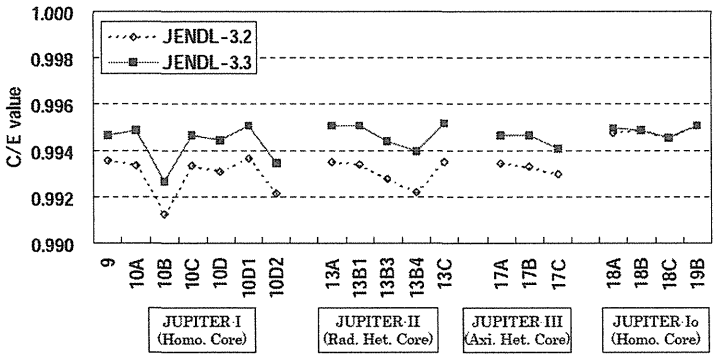



Fig. 8 C/E values of k-eff for various configuration of the JUPITER cores/31/

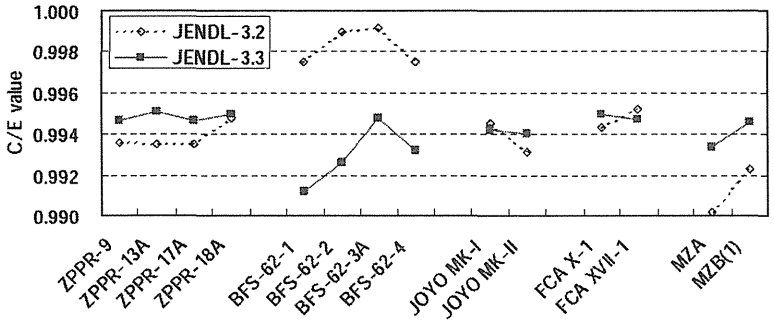



Fig. 9 C/E values of k-eff for various reactors/31/. BFS-62-1 and 62-2 are uranium-fueled.

JP0550262



# 3.2 Continuum Spectra Analysis of $(p, d)$ and $(n, d)$ Reactions on $Bi$ in Several tens of MeV Energy Region

S.A. Sultana[1], Syafarudin[2], D. Maki[1], T. Kin[1], G. Wakabayashi[1],
Y. Uozumi[1], N. Ikeda[1], Y. Watanabe[1], F. Aramaki[3], M. Matoba[4], T. Kawaguchi[4], H.M. Sen Gupta[5]
e-mail: sadia_afroze@yahoo.com

1. Kyushu University, Fukuoka, 812-8581, Japan
2. P2TKN-BATAN, Kawasan PUSPIPTEK Serpong, Indonesia
3. Kyushu Institute of Information Sciences, Dazaifu 818-0117, Japan
4. Kyushu Sangyo University, Fukuoka 813-8503, Japan
5. University of Dhaka, Dhaka, Bangladesh

**Abstract**

Theoretical analyses of the double differential cross sections for proton and neutron induced deuteron pickup reactions on $^{209}$Bi are described. Neutron induced reaction cross-section data were analyzed at incident energies from about 41 MeV to 65 MeV and at $20^0$ laboratory angle, while proton induced reaction cross-section data were analyzed at the incident energy of 42 MeV and at $25^0$ laboratory angle. Spectrum regions are treated in the direct reaction scheme, i.e., several tens of MeV energy region. The double differential cross section - energy spectra were analyzed using the DWBA-based cross sections and the asymmetric Lorentzian form strength response function having energy dependent spreading width. Both the (n,d) and (p,d) spectra are fairly well reproduced by the theoretical calculations in the tens of MeV energy region.

## I. Introduction

The nuclear data for neutron induced reactions are required in many fields of science, for accelerator driven transmutation system of nuclear waste, for nuclear heating of reactor, for clinical radiotherapy, for radiation effects in environment etc. However, this type of nuclear data at incident energies above 20 MeV or so are rather scarce because there are only a few experimental facilities having intense neutron sources suitable for the measurement.

From the above points of view, it is indispensable to devlop theoretical model for a compilation of a new nuclear data library. The code GNASH is one of the most powerful tools to estimate particle production cross sections of nucleon-induced reactions at the medium energy range that is from tens of MeV up to 100 MeV. However, since this code is based on the exciton model, it is not applicable to the particle productions via the direct reactions such as pickup and stripping reactions. The highest energy range of spectra is governed by the direct reactions. Therefore, we have developed a new theoretical model, which is based on the first-order DWBA model with a strength function of an asymmetric Lorentzian form. Hirowatari et al. [1] and Syafarudin et al. [2] firstly adopted this model to (p,d) reactions, and demonstrated its reasonable predictive ability. As a second step, it was extended to neutron-induced reactions. With a small modifications, (n,d) spectra were well reproduced.

In the present work, we investigate the applicability of the model for heavy target nuclei, since it was tested only medium mass nuclei [3]. Deuteron spectra from (n,d) and (p,d) reactions on $^{209}$Bi are analyzed with the present model and compared with experimental data. In addition, we discuss the dependence of resultant spectra on the optical model potentials [4, 5, 6] used in the DWBA calculation. Since a single-step model is valid in the excitation energy range up to about tens of MeV, we confined ourselves to the highest of 10 MeV energy domain of particle production spectra. At the lower energy range, where the multistep is the dominant, is out of the scope of this work.

## II. Analyses

### 1. Experimental Data

#### (1) $(p, d)$ reactions

The experiments were performed at the TIARA facility of JAERI. A proton beam of 68 MeV from the AVF cyclotron was led to the HB-1 beam line. Energy distributions of light ions emitted from the target were measured

using a ΔE-E counter telescope, which consisted of two thin silicon ΔE-detectors and a CsI(Tl) E-detector with photo-diode readout. Details of the experimental procedure and the results have been reported in ref [7].

**(2) $(n, d)$ reactions**

The experiments were performed at the fast neutron facility of the Louvain-la-Neuve cyclotron(CYCLONE). Details of the experimental procedure and the results have been reported in ref [8].

## 2. Theoretical Calculations

The $^{209}$Bi(n,d)$^{208}$Pb double differential cross section has been analyzed with the direct reaction model. To obtain the DDX for the (n,d) reaction we have made some slight changes in the theoretical calculations given in ref. [2].

Theoretical methods of calculating direct reactions are generally used to predict the excitation of a state having known spin-parities and existing shells of the related nucleons. To calculate spectra in the direct reaction scheme, methods are proposed by Lewis [9] and the authors' group [10, 11]. Details of our mathematical calculations for direct reaction model are given below.

Double differential cross sections for pickup reactions are assumed to be given by an incoherent sum of DWBA calculations and expressed as below

$$\frac{d^2\sigma}{d\Omega dE} = 2.30 \sum_{\ell,j} \left[ \frac{C^2 S_{\ell,j}(E)}{2j+1} \times \left( \frac{d\sigma}{d\Omega}\Big|_{\ell,j}^{DW}(E) \right) \right] \tag{1}$$

and the spectroscopic factor is as

$$C^2 S_{l,j}(E) = \left( \sum C^2 S_{l,j} \right) \times f_{l,j}(E) \tag{2}$$

where $d\sigma/d\sigma|_{l,j}^{DW}(E)$ is the cross-section calculated by the DWBA code DWUCK4 [12] and $\sum C^2 S_{l,j}$ is the sum of the spectroscopic factors of all the possible states.

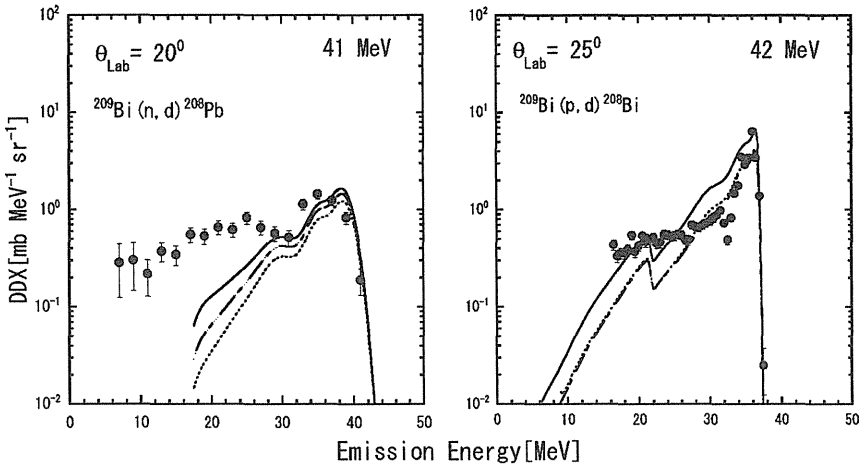



**Fig. 1** The $^{209}$Bi$(n, d)$ double differential cross section (DDX) data (left) and $^{209}$Bi$(p, d)$ double differential cross section (DDX) data (right) at 41 MeV and 42 MeV respectively. Closed circles show experimental data. Solid, dot-dashed and dotted curves refer to the prediction due to present work using Koning, Menet and Becchetti potentials respectively.

The sum rule of the spectroscopic factors of nucleon orbits for $T \pm \frac{1}{2}$ isospin states above a closed shell core is estimated with a simple shell model prescription [13]

$$\sum C^2 S_{l,j} = \begin{cases} n_n(l,j) - \dfrac{n_p(l,j)}{2T+1} & \text{for} \quad T_< = T - \frac{1}{2} \\ \dfrac{n_p(l,j)}{2T+1} & \text{for} \quad T_> = T + \frac{1}{2} \end{cases} \tag{3}$$

where $n_{n(l,j)}$ and $n_{p(l,j)}$ are the numbers of neutrons and protons respectively for each $(l,j)$ orbit and $T$ is the isospin of the target nucleus.

This sum rule of each orbit is suitable for the $(p,d)$ reaction but for the $(n,d)$ reaction, we considered the sum rule equation given by

$$\sum C^2 S_{l,j} = \frac{n_{p(l,j)}}{2T+1} \tag{4}$$

This is because here only the normal states are populated and not the analog states.

The strength function $f_{l,j}$ over the spectra is predicted by using a modified Lorentzian function [10, 11, 14] as follows

$$f_{l,j} = \frac{n_0}{2\pi} \frac{\Gamma(E)}{\left(|E - E_F| - E_{l,j}\right)^2 + \Gamma^2(E)/4} \tag{5}$$

and

$$\int_0^{\alpha} f_{l,j}(E)dE = 1 \tag{6}$$

where $E_{l,j}$ is the calculated energy of the single-particle state which varies with the spreading width Γ(E),and $n_0$ is the renormalization constant deduced from shell model calculations. The sum-rule fraction of spectroscopic factors $C^2 S_{l,j}$ and the centroid energies for $J = l \pm \frac{1}{2}$ shell-orbits are estimated by using the BCS theory, and single particle energies are calculated based on a prescription shown in ref [15]. The energy variable is taken as E-$E_F$ in consistency with the work of Hisamochi et al. in ref. [16].

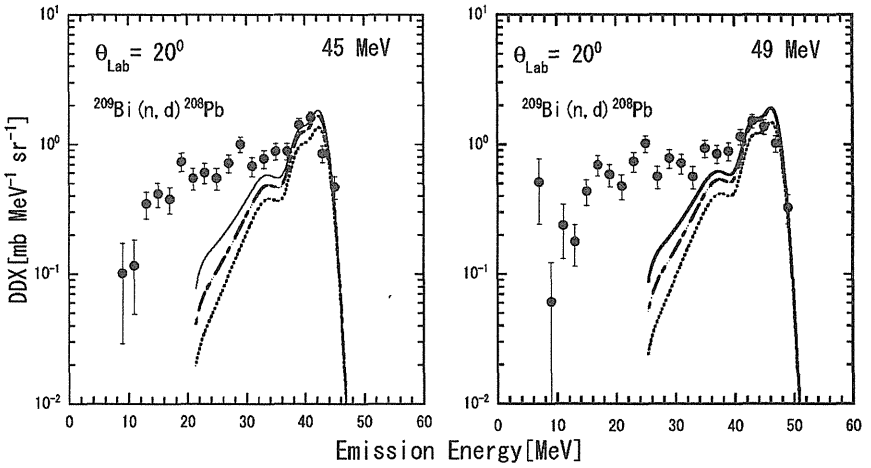



**Fig. 2** Same as fig.1 but for $^{209}$Bi$(n,d)$ reaction at 45 and 49 MeV respectively.

The spreading width is fairly well expressed with a function proposed by Brown and Rho [17] and Mahaux and Sartor [14], as

$$\Gamma(E) = \frac{\epsilon_0 \left(E - E_F\right)^2}{\left(E - E_F\right)^2 + E_0^2} + \frac{\epsilon_1 \left(E - E_F\right)^2}{\left(E - E_F\right)^2 + E_1^2} \tag{7}$$

where $\epsilon_0$, $\epsilon_1$, $E_0$ and $E_1$ are constants which express the effects of nuclear damping in the nucleus [10]. The estimated parameters [10] are

$$\begin{aligned} \epsilon_0 &= 19.4\ (\text{MeV}), \qquad E_0 = 18.4\ (\text{MeV}), \\ \epsilon_1 &= 1.40\ (\text{MeV}), \qquad E_1 = 1.60\ (\text{MeV}). \end{aligned} \tag{8}$$

## III. Results and Discussion

We applied the present method to Bi(n,d)Pb reaction data at 41-65 MeV and Bi(p,d)Bi reaction data at 42 MeV, as shown in figs. 1-3. The experimental and theoretical DDX are given by the closed circles and lines respectively.

For proton, the global optical model potentials of Becchetti and Greenlees [4], Menet et al. [5] and Koning and Delaroche [6] were used, whereas, for deuterons, the adiabatic potential constructed with the proton and neutron parameters of those three [4, 5, 6] optical model potentials were used. The results for the cross-sections are consistent with one another and presented by dotted, short-long- dashed and solid line for Becchetti and Greenlees [4], Menet et al. [5] and Koning and Delaroche [6] potentials respectively.

From fig. 1, we can see that theoretical results are in fair agreement with the experimental data for the (n,d) reaction, while for the (p,d) reaction, in the case of potential of Becchetti and Greenlees [4], it overstimates a little, may be because of using global potentials, not best fit potentials. However, in fig. 2, for the (n,d) reaction with the Koning potential, the spectrum at 45 and 49 MeV incident energies and the theoretical ones are in close agreement to each other. Again, in fig. 3, at 53.5 MeV incident energy, for potentials of Menet and Koning, the calculated energy spectra are overstimated, may be for the same reason as described for fig. 1 for the (p,d) reaction, i.e., due to not using the best fit potentials. It should be noted from figs. 1-3 that at all incident energies both for the (n,d) and (p,d) reactions the double differential cross sections, the calculated specta agree with experimental data only above tens of MeV incident energies, because our calculated energy spectrum regions are treated in direct reaction scheme.

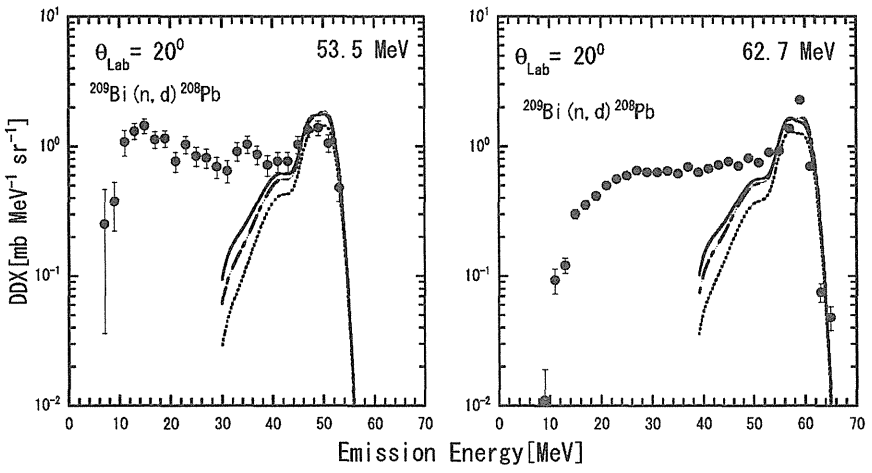



**Fig. 3** Same as fig.1 but for $^{209}$Bi$(n, d)$ reaction at 53.5 and 62.7 MeV respectively.

## IV. Conclusion

The double differential cross sections for neutron and proton induced reactions on $^{209}$Bi have been analyzed here. The bombarding energy range for neutron induced reaction is about 40 MeV$\leq E_n \leq$65 MeV and at $20^0$ Laboratory angle, while for proton it is at 42 MeV and at $25^0$ Laboratory angle. The spectra of continuum region have been analyzed consistently with direct reaction model. The overall strengths are reproduced well using asymmetrical Lorentzian form response functions having energy-dependent spreading widths. The calculated DDXs show an overall good agreement with the experimental data both in magnitude and shape.

### References

[1] S. Hirowatari et al., Nucl. Phys. A 714, (2003)3 .
[2] Syafarudin et al., J. Nucl. Sci. Technol., Suppl.2, Vol.1, (August 2002) P.377.
[3] S. A. Sultana et al., Proceedings of the 2003 Symposium on Nuclear Data, JAERI-Conf 2004-005, P.133.
[4] F.D. Becchetti, Jr. and G.W. Greenlees, Phys. Rev. 182, 1190 (1969).
[5] J.J.H. Menet, E.E. Gross, J.J. Malanify, and A. Zucker, Phys. Rev. C 4, 1114 (1971).

[6] A.J. Koning and J.P. Delaroche, Nucl. Phys. A713, 231 (2003).
[7] M. Harada, Y. Watanabe, Y. Tanaka, Y. Matsuoka, K. Shin, S. Meigo, H. Takada, T.Sasa, O. Iwamoto, T. Fukahori, S. Chiba, and S. Tanaka, J. Nucl. Sci. Technol., Suppl.2, Vol.1, P.393 (August 2002).
[8] E. Raeymackers, I. Slypen, S. Benck, J. P. Meulders, N. Nica, and V. Corcalciuc, J. Nucl. Sci. Technol., Suppl.2, Vol.1, P.354 (August 2002).
[9] M. B. Lewis, Phys. Rev., C11, 145 (1975).
[10] M. Matoba, O. Iwamoto, Y. Uozumi, T. Sakae, N. Koori, H. Ohgaki, H. Kugimiya, H.Ijiri, T. Maki, and M. Nakano, Nucl. Phys., A581, 21 (1995).
[11] M. Matoba, K. Kurohmaru, O. Iwamoto, A. Nohtomi, Y. Uozumi, T. Sakae, N. Koori, H. Ohgaki, H. Ijiri, T. Maki, M. Nakano, and H. M. Sen Gupta, Phys.Rev., C53, 1792 (1996).
[12] P. D. Kunz, Code DWUCK4, University of Colorado (Unpublished).
[13] J. B. French and M. H. Macfarlane, Nucl. Phys., 26, 168 (1961).
[14] C. Mahaux and R. Sartor, Nucl. Phys. A 493 (1989) 157; Adv. Nucl. Phys., 20, P.1 (1991).
[15] A. Bohr and B. R. Motelson, "Nuclear Structure" (W. A. Benjamin, INC., 1996, New York, Amsterdam) Vol. 1, Appendix 2D.
[16] K. Hisamochi, O. Iwamoto, A. Kisanuki, S. Budihardjo, S. Widodo, A. Nohtomi, Y. Uozumi, T. Sakae, M. Matoba, M. Nakano, T. Maki, S. Matsuki, and N. Koori, Nucl.Phys., A564, 227 (1993).
[17] G. E. Brown and M. Rho, Nucl. Phys., A372, 397 (1981).

JP0550263

JAERI－Conf 2005－003

# 3.3 Measurement of Deuteron-Induced Activation Cross-Sections for Tantalum, Iron, Nickel and Vanadium in 33-40 MeV Region

Makoto NAKAO[1], Kentaro OCHIAI[1], Naoyoshi KUBOTA[1],
Noriko S. ISHIOKA[2], and Takeo NISHITANI[1]
[1]Department of Fusion Engineering Research, Japan Atomic Energy Research Institute
Tokai-mura, Naka-gun, Ibaraki-ken 319-1195, Japan
[2]Department of Ion-beam-applied Biology, Japan Atomic Energy Research Institute
Takasaki, Gunma 370-1192, Japan
e-mail: nakao_m@fhshp.tokai.jaeri.go.jp

Activation cross-sections for deuteron-induced reactions on tantalum, iron, nickel and vanadium were measured by using a stacked-foil technique in TIARA facility, JAERI. We irradiated stacked-foil with 41 MeV deuteron beam accelerated by AVF cyclotron and the activation cross sections for the $^{181}$Ta(d,x)$^{178,180}$Ta, $^{nat}$Fe(d,x)$^{55,56}$Co, $^{nat}$Ni(d,x)$^{55}$Co, $^{60,61}$Cu and $^{51}$V(d,4n)$^{49}$Cr reactions were obtained in 33-40 MeV region. Thess data were compared with other experimental data and the calculation data in ACSELAM library.

## 1. Introduction

IFMIF (International Fusion Materials Irradiation Facility) is an accelerator-based D-Li neutron source designed to provide an intense neutron field for testing fusion reactor candidate materials. IFMIF has two 40 MeV deuteron linear accelerators with each 125 mA beam current [1]. In the design of IFMIF, the total facility availability is conceived to be at least 70 % for long-term operation. However, activation of the structural materials along the beam transport lines by deuteron beam loss limits the maintenance and makes the long-term operation difficult. Thus the accurate estimation of deuteron-induced activities and the selection of structural materials are important to determine the beam loss criteria.

We started to measure deuteron-induced activation cross-sections for IFMIF accelerator structural material in TIARA facility and had already measured the cross sections for aluminum, copper and tungsten in 22-40MeV region [2].

In this work, measurements of deuteron-induced activation cross sections for tantalum, iron, nickel and vanadium were performed by using a stacked-foil technique. Tantalum is candidate material for coating to protect the beam facing materials. Iron is used as the inner material of the drift tube. Nickel is the impurity of the steel and Vanadium is corrosion material.

## 2. Experimental Procedure and Data Processing

Activation cross sections were measured by using a stacked-foil technique. The stacked-foils consisted of natural composition tantalum, iron, nickel and vanadium foils with chemical purity more than 99.5 %. All of these foil size was 1cm x 1cm. Each thickness of foils was 10 μm for Ta, 50 μm for Fe, 20 μm for Ni and 25 μm for V. The stacked-foils were irradiated with 41MeV deuteron beam (current = 0.1 μA) accelerated by the AVF cyclotron in the TIARA facility of JAERI. After suitable cooling time, the decayed gamma-rays emitted from the irradiated foils were measured by a calibrated high purity germanium detector. The induced activities were obtained for eight nuclide ($^{181}$Ta(d,x)$^{178,180}$Ta, $^{nat}$Fe(d,x)$^{55,56}$Co, $^{nat}$Ni(d,x)$^{55}$Co, $^{60,61}$Cu and $^{51}$V(d,4n)$^{49}$Cr) from the measurement data of gamma-rays .

The energy degradation along the stack and the effective deuteron energy at the middle position of each foil were estimated by the IRACM code system [3]. The number of incident deuterons on each stacked-foil was determined from $^{65}$Zn activities produced by the $^{nat}$Cu(d,x)$^{65}$Zn reaction cross section, where we used the data reported by Takács *et al.*[4]. The elemental cross sections were derived from the induced activities and the number of incident deuterons.

The error of the present results was 13-19%. This value results from the error in the determination of continuous background for net counts of the decayed gamma-ray, the error of the standard cross sections for the $^{nat}$Cu(d,x)$^{65}$Zn reaction, the full energy efficiency of the Ge detector and the foil thickness.

## 3. Results

The production cross sections for the eight radioactive nuclei were measured and compared with previous ones by other groups and the data in ACSELAM library calculated by the ALICE-F code [5]. As the cross sections in ACSELAM library are calculated for each isotope target, the value of its cross sections were normalized by weighting with natural abundance to compare with the experimental results in figures.

### 3-1. Tantalum

The present cross sections, compared with other experimental ones and the data in ACSELAM for $^{178}$Ta ($T_{1/2}$=2.4h) and $^{180}$Ta ($T_{1/2}$=8.2h) are shown in FIGURES 1-2. For these Ta nuclide there is only one experimental data reported by Bisplinghoff *et al.*[6]. The present results were smaller than the data in ACSELAM by a factor of 2-3 for $^{178}$Ta and 2 times as high as the data in ACSELAM for $^{180}$Ta.

### 3-2. Iron

FIGURES 3-4 show the present cross sections for the $^{nat}$Fe(d,x)$^{55}$Co($T_{1/2}$=17.5h) and $^{56}$Co($T_{1/2}$=77.2d) reactions compared with other experimental ones and the data in ACSELAM. For $^{55}$Co, there are two experimental data, which are reported by Clerk *et al.* [7] and Hermanne *et al.*[8]. The present results were in agreement with the data reported by Hermanne within 20% and 4 times as low as the data in ACSELAM. For $^{56}$Co, the present results were in agreement with the data reported by Takacs *et al.* [4] within experimental error and 2 times as

low as the data in ACSELAM.

### 3-3. Nickel

Figures 5-7 show the present results for the $^{nat}Ni(d,x)^{55}Co(T_{1/2}=17.5h)$, $^{60}Cu(T_{1/2}=23.7m)$ and $^{61}Cu(T_{1/2}=3.33h)$ reactions. The present results were in agreement with the data in ACSELAM within 50% for $^{55}Co$ and 4 times as low as the data in ACSELAM for $^{60}Cu$. For $^{61}Cu$ the present results were in good agreement with the data reported by Takacs *et al.* [4] and 2 times as low as the data in ACSELAM.

### 3-4. Vanadium

Figure 8 shows the present results for the $^{51}V(d,4n)^{49}Cr(T_{1/2}=42.3m)$ reaction. The present results were 2 times as high as the data reported by Weinreich[9] and smaller than the data in ACSELAM by a factor of 4-5

## 4. Summary

The activation cross-sections for the deuteron-induced reactions had been obtained for Ta, Fe, Ni and V in 33-40 MeV region. The present results were compared with previous experimental ones and the data in ACSELAM library. For $^{nat}Fe(d,x)^{56}Co$ and $^{nat}Ni(d,x)^{61}Cu$ reaction, the present results were in good agreement with the data reported by Takacs. The data in ACSELAM were overestimation for the $^{181}Ta(d,x)^{178}Ta$, $^{nat}Fe(d,x)^{55,56}Co$, $^{nat}Ni(d,x)^{60,61}Cu$ and $^{51}V(d,4n)^{49}Cr$ reactions and underestimation for the $^{181}Ta(d,x)^{180}Ta$, $^{nat}Ni(d,x)\ ^{55}Co$ reactions. In the future we will measure these activation cross-sections below 33MeV.

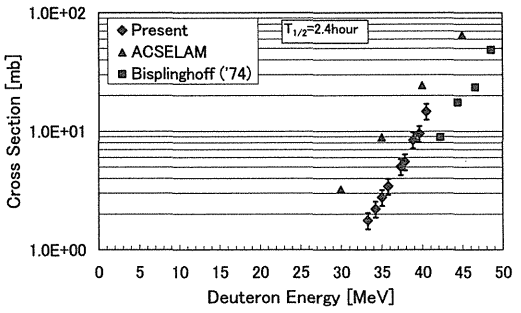



Fig. 1 Cross sections for the $^{181}Ta(d,x)\ ^{178}Ta$

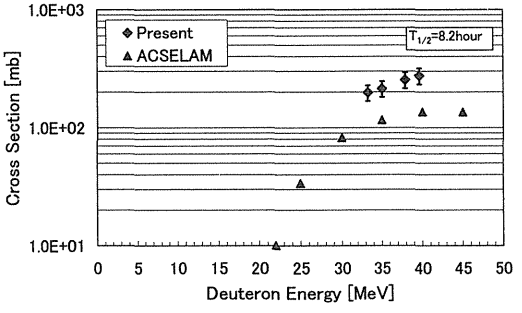



Fig. 2 Cross sections for the $^{181}Ta(d,x)\ ^{180}Ta$

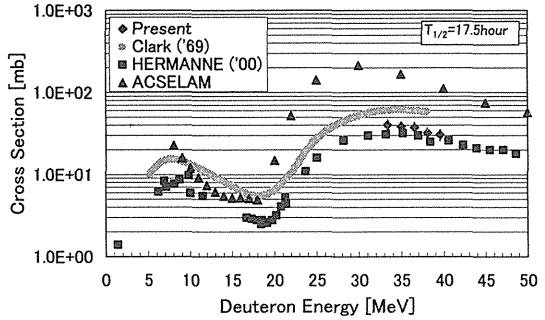



Fig. 3 Cross sections for the $^{nat}Fe(d,x)\ ^{55}Co$

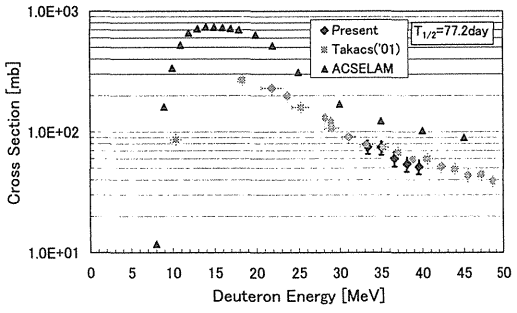



Fig. 4 Cross sections for the $^{nat}Fe(d,x)\ ^{56}Co$

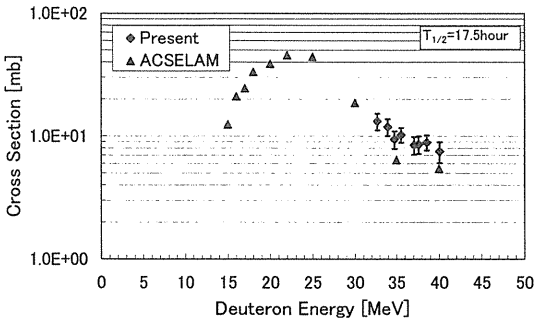



Fig. 5 Cross sections for the $^{nat}$Ni(d,x) $^{55}$Co

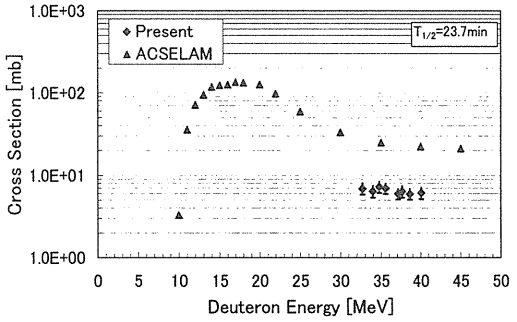



Fig. 6 Cross sections for the $^{nat}$Ni(d,x) $^{60}$Cu

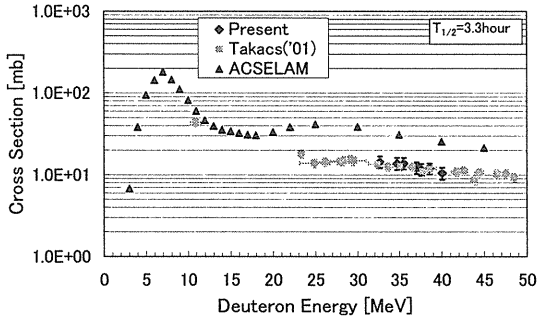



Fig. 7 Cross sections for the $^{nat}$Ni(d,x) $^{61}$Cu

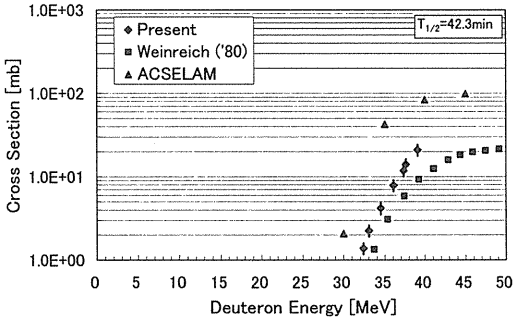



Fig. 8 Cross sections for the $^{51}$V(d,4n) $^{49}$Cr

## Acknowledgments

The authors would like to express thanks to AVF cyclotron staffs of the TIARA facility, JAERI for operating the accelerator steadily.

## References

[1] IFMIF International Team, "IFMIF-KEP; International Fusion Materials Irradiation Facility key element technology phase report," JAERI-Tech 2003-005 (2003).

[2] M.Nakao, J. Hori, *et al.*, Proc. of International Conference on Nuclear Data for Science and Technology (ND2004), Los Alamos National Laboratory (unpublished)

[3] S. Tanaka, M. Fukuda, K. Nishimura, *et al.*, "IRACM: A Code System to Calculate Induced Radioactivity Produced by Ions and Neutrons," JAERI-Data/Code 97-019 (1997).

[4] S. Takács, *et al.*, Nucl. Inst. Meth., B 174, 235-258 (2001).

[5] T. Fukahori, "ALICE-F Calculation of Nuclear Data up to 1 GeV," Proc. of the Specialists' Meeting on High Energy Nuclear Data, JAERI-M 92-039. 114-122 (1992)

[6] J.Bisplinghoff, *et. al.*, Nucl. Phys. A, Vol. 228-1, 180 (1974)

[7] J.W.Clark, *et al.*, Phys. Rev. 179, 1104 (1969)

[8] A.Hermanne *et al.*, Nucl. Inst. Meth. B. 161-163, 178 (2000)

[9] R.Weinreich, *et al.*, Appl. Rad. Isot. 31, 223 (1980)

JP0550264



# 3.4 Measurements of double differential heavy particles production cross sections for 70 MeV protons

M. Hagiwara, T. Oishi, M. Baba,
*Cyclotron and Radioisotope Center, Tohoku University*
E-mail: *hagi@cyric.tohoku,ac,jp*
T. Sanami
*High Energy Accelerator Research Organization (KEK)*
M. Takada
*National Institute of Radiological Sciences*

Measurements of differential fragment production cross sections for proton-induced reaction are described. Double-differential fragment production cross sections for carbon and aluminum induced by 70 MeV protons were obtained with a specially designed Bragg curve spectrometer (BCS) and energy-time-of-flight method (E-TOF). The present data obtained with two different methods are consistent with each other and compared with other experiment and calculations, and showed systematic trend.

## 1. INTRODUCTION

Fragments which are secondary particles heavier than alpha-particles cause a large local ionization. It is a serious problem for a semiconductor device and human in space environment. For dosimetry and the evaluation of radiation effects in devices or instruments such as single event upset (SEU) by cosmic rays, the energy and angular doubly differential fragments production cross-section data (DDX) are required. Up to now, however, experimental data of the fragment production are very scarce due to experimental difficulties in fragment detection. Thus, almost all past experimental data on fragment production were obtained by the activation method that did not provide energy and angle information. Furthermore, theoretical calculation treating fragment production is very few. Therefore, it is important to accumulate reliable experimental DDX data for fragment production.

For fragment detection, we adopted 1) a Bragg curve spectrometer (BCS) [1,2] providing various information with a single counter and 2) an energy-time of fight (E-TOF) method [3] having the capability of mass identification even in the energy region where BCS is not applicable, while the solid angle is very small. For 1), BCS was designed with special care to apply to a neutron beam, in addition to a charged particle beam and resulted in success to obtain light fragments by proton- and neutron-induced reactions [4, 5]. BCS proved very promising for fragments detection even in neutron-induced reaction, while there are still some problems that should be solved. For 2), we have succeeded in the identification of the fragment up to mass number 12 emitted from carbon bombarded with 70 MeV protons. An E-TOF method can applied only to charged particle-induced reactions due to a small detector solid-angle, but the dynamic range of fragment energy is higher than in BCS.

This paper describes energy-angular fragment production measurements in proton-induced reaction with BCS and E-TOF method. The data obtained with both methods were complementary with each other. The data were compared with other experimental data and calculations.

## 2. BRAGG CURVE SPECTROMETER (BCS)

The details of Bragg curve spectrometer (BCS) developed are described in the previous report [4]. Figure

1 shows a schematic diagram of BCS. It is a cylindrical gridded ionization chamber (GIC) [6, 7] filled with an Ar + 10%$CH_4$ gas at a pressure of ~200 Torr. In the case of proton induced reaction, fragments produced from targets in the vacuum chamber enter the detector along the axis through a thin film window and ionize the gas in BCS. The free electrons drift to the anode by the electric field keeping a shape of the Bragg curve. The time distribution of the anode signal corresponds to the reversal of the ionization distribution (Bragg curve) by the fragment. Therefore the fast part of anode signal is proportional to the Bragg peak value that is in proportion to the atomic number (Z) of the fragment. The integration of the whole anode signal represents the total charge that is proportional to the fragment energy. Therefore, BCS can provide information on the energy and the atomic number of fragments using only the anode signal.

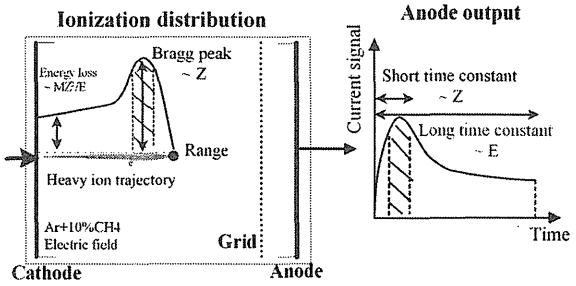



Fig. 1 Detection scheme of BCS method

To decrease the lower limit of the detection energy, BCS was improved at the part of entrance window. We use an aluminized Mylar film (2.5 μm thick) supported by tungsten wire to act as not only entrance window but also as a cathode electrode simultaneously. With the BCS developed, the new measurements of proton-induced reaction were performed using the AVF cyclotron at National Institute of Radiological Science (NIRS).

The experimental apparatus shown in Fig.2 is almost the same as one employed in the previous measurement. The fragments emitted to 30 degree direction were measured. The proton energy was 70 MeV. Proton beam current was ~10 nA. For samples, foils of aluminum 2 μm thick and polypropylene 4 μm thick were employed. In the measurement circuit, the energy signal and the Bragg peak signal were obtained from the anode signal by shaping with a long time constant (6 μsec) and a short time constant (0.25 μsec), respectively. To reduce background events and dead time of ADC, only coincidental events between anode and cathode were accumulated. The resolving time is set to 6 μsec that is equivalent to the maximum traveling time of electrons from the cathode to the grid. They are collected as a two-dimensioned data using KODAQ handler [8] with CAMAC system.

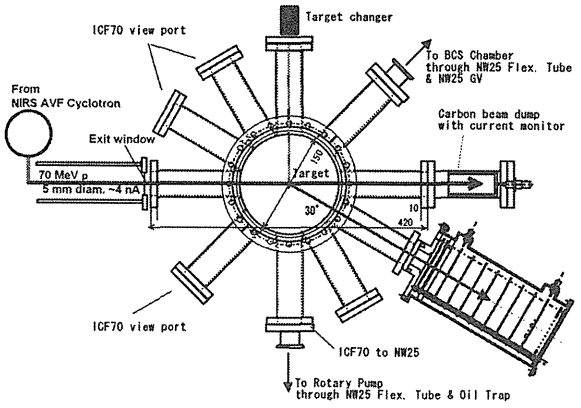



Fig2. Experimental setup of BCS in proton-induced reaction

Figures 3 and 4 show the measured two-dimensional spectra on the energy *vs.* Bragg peak of fragments from 4 μm thick polypropylene and 2 μm thick aluminum, respectively. Excellent separation of each fragment and S/N ratio are confirmed up to Z = 6 (Carbon), 9 (Fluorine) for polypropylene and aluminum sample, respectively, in the energy region where particles are separated by the difference of Bragg peak value. In case of aluminum sample, fragments heavier than fluorine could not be identified because these heavier products have too low energy to make ionization shape of Bragg peak and detected mainly below limit of identification using Bragg peak. The turning blows at maximum energy point in fig. 3 and 4 are caused by the fragments that have ranges longer than the cathode-grid distance which is the active region. It is meaningful to extend the measurable energy range by developing a correction method for this effect from the information of the energy deposit (ΔE).

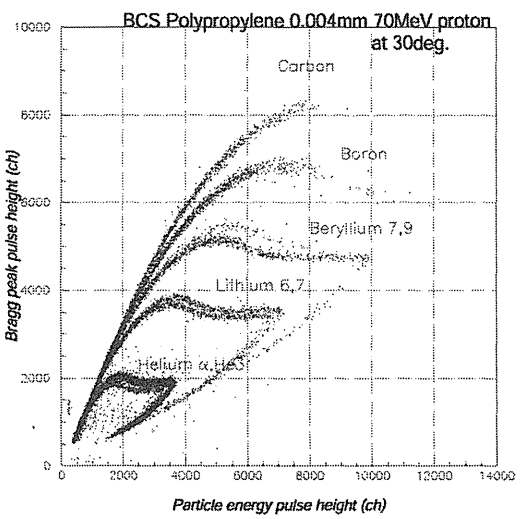



Fig.3 energy *vs* Bragg peak two-dimensional spectra for polypropylene 4 μm thick sample

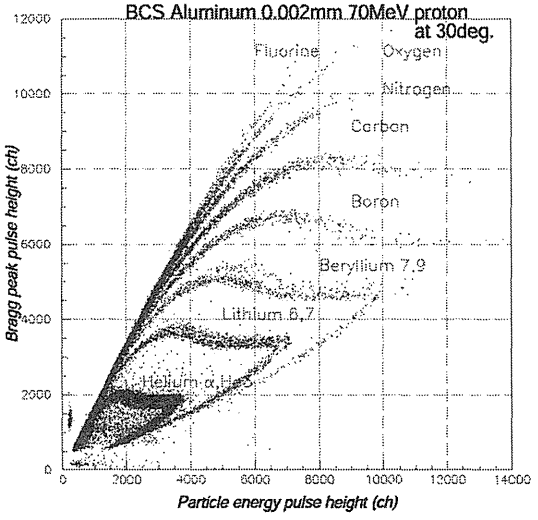



Fig.4 energy *vs* Bragg peak two-dimensional spectra for aluminum 2 μm thick sample

## 3. ENERGY TIME-OF-FLIGHT METHOD (E-TOF)

BCS method has several difficulties to cover whole energy region of fragment. We are developing to do fragment measurement for proton-induced reactions using an Energy Time-Of-Flight (E-TOF) method which is used in heavy ion detection. In this method, the energy and TOF of the fragment is measured and mass number is derived by combing the energy and TOF information. Therefore, the dynamic range of fragment energy is higher than in BCS. These data will be useful to complement data obtained with BCS.

The measurements of proton-induced reaction with E-TOF method were done also using AVF cyclotron at NIRS. The schematic view of the experimental setup is shown in Fig.5. The fragments emitted to 30 degree direction were measured. The proton energy was 70 MeV and beam current was ~10 nA, For samples, foils of aluminum 2 μm thick, and polypropylene 4 μm thick were employed similarly to the case of BCS.

It is difficult to obtain sufficient beam current (more than 10 nA) and time resolution of a beam burst (less than 1 nsec), concurrently. Therefore we use a thin detector in place of the RF signal from the cyclotron, to obtain timing signal of fragments for TOF. For a start detector of TOF, we employed an Ultra-thin plastic scintillator (Pilot-B: 5 μm thick) which had good time resolution and low energy loss for fragments. For a stop detector (E detector), a Silicon Solid State Detector (SSD) with good energy

resolution was adopted. The flight path is ~1.0 m. The scattering chamber was designed to enable simultaneous measurements of BCS and E-TOF. The combination of these methods would be powerful for the measurement of fragments induced by charged particles.

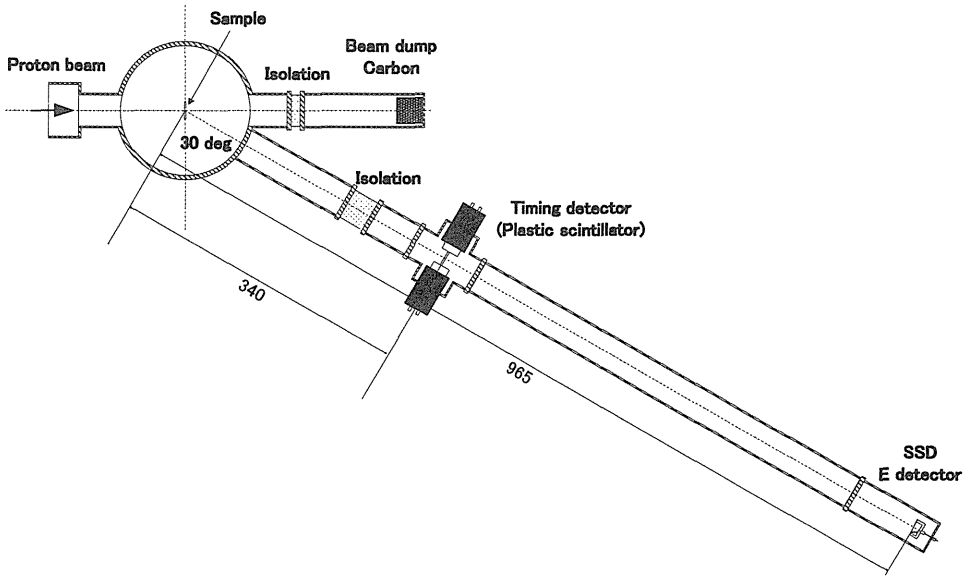



Fig.5 Schematic view of experimental setup for E-TOF measurement

Up to now, we identified the fragments from polypropylene (4 μm thick) up to A=12 with the measurement system using an ultra-thin plastic scintillator and SSD with a 0.965 m flight path as shown in fig.6. The energy spectra of fragments above mass of 6 were measured on the almost whole energy range. The fragments of mass number 5, 8, 9 were very few and the fragments above mass number 10 have very small energy. The time resolution of this setup was not good enough because we use SSD for a timing detector too. We will improve the measuring system by using two timing detectors for TOF measurement (start and stop signals) in the near future.

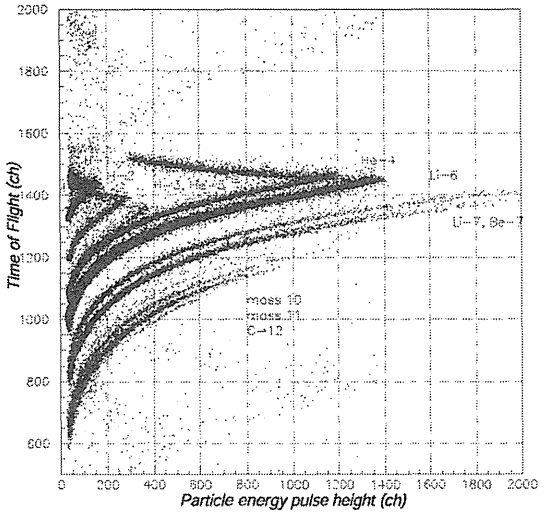



Fig.6 The energy *vs* TOF two-dimensional spectrum for carbon 100 μm thick sample

## 4. RESULTS OF FRAGMENT PRODUCTION CROSS-SECTION

The energy spectra of fragment heavier than alpha particle were obtained by both methods of BCS and E-TOF. Figure 7 shows the energy spectra of α-particle emitted to 30 degree from carbon and aluminum which were obtained with the BCS and E-TOF method. As shown in Fig.7, the data obtained with BCS and E-TOF method are consistent with each other in the overlapping region. The result of α-particle shows good agreements with LA150 [9] except for the case of aluminum above 10 MeV. Figure 8 shows the lithium spectra obtained with the BCS method. The data is compared with the previous data [4], QMD calculation with PHITS code [10] and LA150 [9]. The present data was obtained over wider energy range compared with previous one. The previous data have uncertainty due to the energy loss correction. The QMD calculation with the PHITS code show better agreement with the present one than LA150. Further, LA150 treats the angular distribution of fragment heavier than alpha particle as isotropic. Figure 9 and 10 show the energy spectra of fragments with mass number 6 and 7, respectively, obtained with E-TOF method. The present data for the mass number 6 agree with the PHITS, but not with LA150. For mass = 7, there are the experimental data by C. T. Roche et al [3]. but these data is obtained by incident energy of 45 MeV and 100 MeV. Present data agree well with the data by Roche et al. in the shape. PHITS and LA150 underestimate present data in the higher energy region.

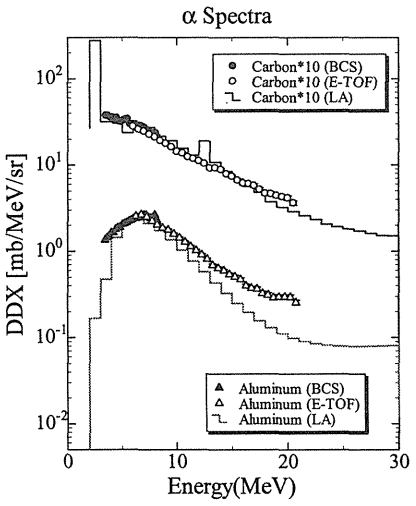



Fig.7 alpha spectra

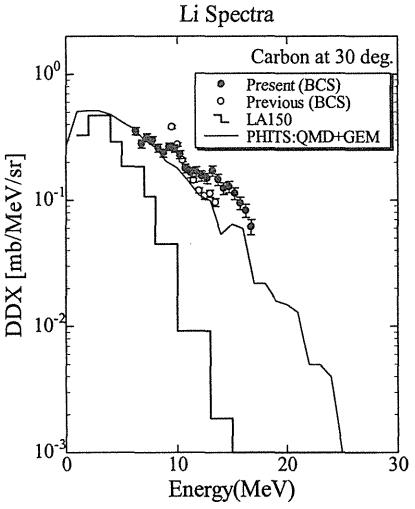



Fig.8 lithium spectra

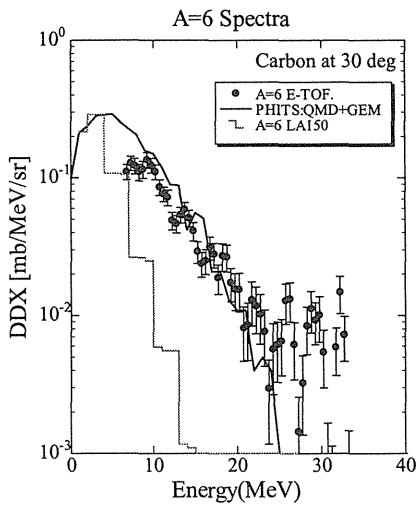



Fig.9 mass 6 spectra

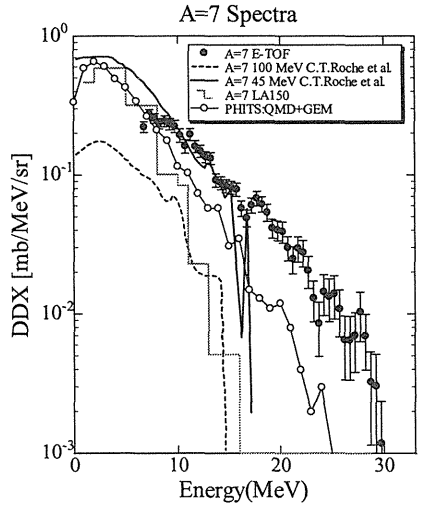



Fig.10 mass 7 spectra

## 5. SUMMARY

We developed a BCS detector and E-TOF method aiming at measurement of fragment production cross section for proton-induced reactions. For BCS, excellent separation of each fragment is confirmed up to Z = 6 (Carbon), 9 (Fluorine) for polypropylene and aluminum samples, respectively. For E-TOF, we could identify the fragments from polypropylene (4 μm thick) up to A=12 using an ultra-thin plastic scintillator for the start detector and SSD for the stop detector with ~1 m flight path. The data obtained with both methods were consistent with each other. The new results were obtained for fragment heavier than α-particle and compared with LA150 data library, QMD calculation in the PHITS code. The LA150 data agrees with the present data for α-particle but show much underestimation for fragment heavier than lithium. For fragment, QMD calculation is better than LA150 but underestimates the experimental data generally.

In the near future, we will improve the measuring method with the following refinements and the data will be applied for the analysis of SEU and dose contributions:

1) extension of the dynamic range for BCS and
2) enlarge the detection solid angle for E-TOF

For 1) we will put SSD detector backward anode electrode to detect the high energy fragments that have ranges longer than the cathode-grid distance. For 2) we will put the start detector to sample to enlarge the detection solid angle.

## ACKNOWLEDGEMENT

The authors express their thanks to the operation crew of the NIRS cyclotron for their cooperation.

## REFERENCES

[1] C.R.Gruhn, M.Binimi, R.Legrain, R.Loveman, W.Pang, M.Roach, D.K.Scott, A.Shotter, T.J.Symons, J.Wouters, M.Zisman, R.Devries, Y.C.Peng and W.Sondheim, *Nucl. Instrum. Methods*, **196** (1982) 33

[2] N.J.Shenhav and H.Stelzer, *Nucl.Instrm.Meth.* **228** (1985) 359

[3] C.T.Roche, R.G.Clark, G.J.Mathews and V.E.Viola, Jr, *Phys. Rev. C* **14** (1976) 410

[4] M. Hagiwara, T. Sanami, M.Baba, T. Oishi, M.Takada, H. Nakashima and S.Tanaka, Proc. of *Nucl. data.Sym.* (2003)

[5] T. Sanami, M. Baba, M. Hagiwara, T.Hiroishi, M.Hosokawa, N.Kawata, N.Hirabayashi, T.Oishi, H.Nakashima and S.Tanaka. *J. Nucl. Sci. and Tech.* **Suppl. 4** (2004) 502

[6] T.Sanami, M.Baba, K.Saito, N.Hirakawa. *Nucl. Instrum. Meth. A***440** (2000) 403

[7] O.Bunemann, T.E. Cranshaw, J.A. Harvey, Can. *J. Res. A***27** (1949) 373

[8] K.Omata and Y.Hujita, INS-Rep-884, Institute for Nuclear Study, University of Tokyo, 1991

[9] M. B. Cadwick, P. G.Young, S. Chiba, S.C. Frankle, G. M. Hale, H. G. Hughes, A. J. Koning, R. C. Little, R. E. MacFarlane, R. E. Praeel and L.S. Waters, *Nucl. Sci. Eng.*, **1331** (1999) 293

[10] H. Iwase, K. Niita, T. Nakamura, *J. Nucl. Sci. and Tech.* **39** No.11 (2002) 1142

JP0550265

# 3.5 A New Technique to Measure Double-differential Charged-particle Emission Cross Sections Using Pencil-beam DT Neutrons

Keitaro Kondo, Satoshi Takagi, Isao Murata, Hiroyuki Miyamaru, and Akito Takahashi
Department of Electronic, Information Systems and Energy Engineering
Osaka University, Yamada-oka 2-1, Suita, Osaka 565-0871, Japan

Naoyoshi Kubota, Kentaro Ochiai and Takeo Nishitani
Japan Atomic Energy Research Institute
Tokai-mura, Naka-gun, Ibaraki 319-1115, Japan

E-mail: kondo-kei@stu.nucl.eng.osaka-u.ac.jp

For precise measurement of Double-differential Charged-particle Emission Cross Section(DDXc), a unique technique was developed. Utilizing an anticoincidence spectrum successfully extended lower limit of measurable energy for α-particle. The validity of the present technique was confirmed from the result that the obtained total cross section agreed with the evaluated value of $^{27}$Al(n,xα) reactions. The measurements for beryllium were carried out. The results suggested more detailed analysis for $^{9}$Be(n, charged particle) reactions was required.

## 1. Introduction

For fusion reactor development, nuclear data for the interaction of 14-MeV neutrons with reactor materials are of importance. Double-differential charged-particle emission cross section (DDXc) is needed to calculate nuclear heating and fundamental value for evaluation of material damage, i.e., PKA spectra, GPA and DPA cross sections. In particular use of several light nuclei such as beryllium, carbon and lithium in large quantities is planned in the blanket region of a fusion reactor. Charged-particle emission reactions of these materials are complex due to contributions from sequential decays and multi-body breakup. From this reason, theoretical calculations of energy spectra of emitted particles are difficult. This fact makes precise measurements of DDXc quite important.

The measurement of DDXc is difficult since charged-particle emission reaction has small cross section and generally background condition is high. Until now only a few data have been accumulated. In 1960s~80s, several early studies of charge-particle emission reactions induced by DT neutrons were carried out to investigate details of direct nuclear reaction, although spectra of emitted charged-particle in the whole energy range were not obtained [1,2,3]. In the author's group, E-TOF method was developed at OKTAVIAN in Osaka University [4] and measurements of DDXc for several medium heavy materials for fusion reactor were successfully carried out [5]. However, the method was a little hard to apply for precise measurement of lighter materials. The defects of these previous methods are in the following;

1. Signal-to-noise (S/N) ratio is bad due to a large number of background signals.
2. Low net count rate decreases statistical accuracy, or needs long time measurement.

3. Energy resolution of the detector is not so good.
4. The lower limit of detecting energy is relatively high.

Therefore development of a new technique aiming at improvement of these points is strongly required in order to realize accurate measurement in the whole energy range and with acceptable high-energy resolution.

In this study, we have developed a new measurement technique of DDXc using the pencil-beam DT neutron source and E-ΔE counter telescope. In the following sections, measurements of DDXc for aluminum and beryllium are described. Aluminum was chosen as a standard sample in order to confirm the validity of the present method. Since beryllium is regarded as one of the most important materials for the fusion reactor, the detailed measurements were carried out.

## 2. Experimental procedure

We used a pencil-beam DT neutron source of Fusion Neutronics Source (FNS) in Japan Atomic Energy Research Institute (JAERI). An accelerated deuterium beam bombers a tritium target and 14-MeV neutrons are generated. A large shielding structure consisting of Fe, Pb, Cd, and polyethylene is embedded into a concrete wall with a thickness of 2m to collimate the neutrons. There is a hole of 2cm in diameter pierced through the shielding structure and a 2cm-ϕ neutron beam is extracted. Characteristics of the beam, such as intensity, profile and neutron background, are well investigated [6]. Neutron flux at the outside of the beam is about $1\times10^{4}$~$10^{6}$ times lower than at the inside of the beam. Using the neutron beam, we can arrange a detector very close to a sample material without any shield and therefore high S/N ratio and high-count rate can be achieved.

In the present study, a sample and detectors were located in an experimental vacuum chamber of 40cm-ϕ by 30cm in height. The chamber was set at the outlet of neutron beam. The distance from the neutron source to the sample was 380cm. A metal aluminum disc of 50μm thick and a metal beryllium disc of 20μm in thickness and 3cm in diameter were used as experimental samples. Figure 1 shows the experimental arrangement.

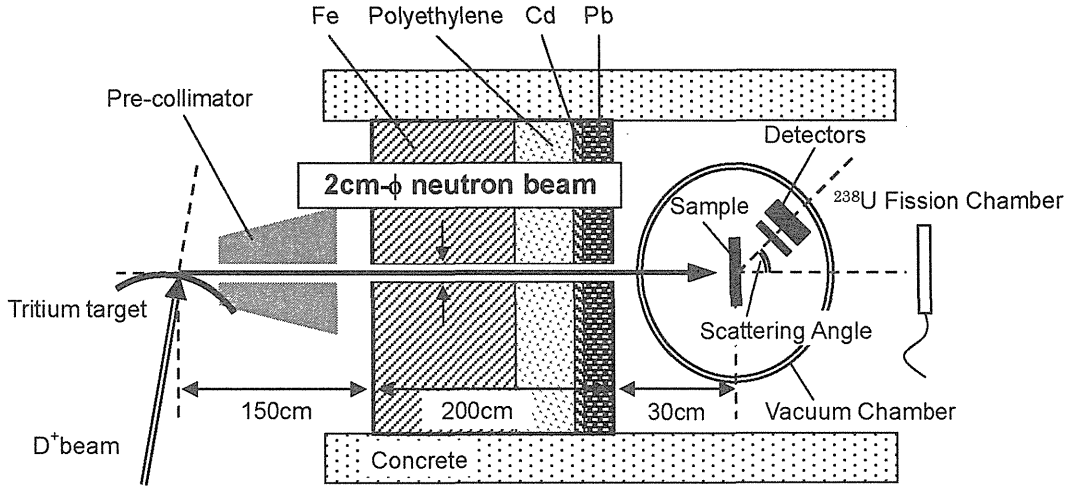



Fig. 1 Experimental arrangement

To distinguish kinds of charged particles, we used a counter-telescope system with two silicon surface barrier detectors of ΔE and E, and a two-dimensional MCA. The thicknesses of the ΔE and E detectors were 9.6μm and 700μm, respectively. The energy resolution of the telescope was about 100KeV (fwhm) for 5.486MeV α-particle from $^{241}$Am α-source. Figure 2 shows a typical two-dimensional spectrum obtained in the measurement. In the coincidence measurement for α-particles, the lower limit of detecting energy was around 2.5 MeV. In order to extend the limit of measuring energy, we utilized an anticoincidence spectrum of ΔE detector as the spectrum below the lower limit energy of coincidence measurement. The reasons why we were able to use the anticoincidence spectrum were as follows;

1. The thickness of ΔE detector was extremely thin and therefore the deposited energy of proton in the detector was up to about 600 keV.
2. The intensity of background signals in case of sample-out measurement were exceptionally low, which was only 10~15 counts per hour.

As a result, 600 keV ~ 1 MeV for the lower limit energy of α-particle measurement was achieved since only α-particle can be detected as the anticoincidence spectrum of ΔE detector over this energy. However if the sample emits heavier particles than α-particle from other nuclear reactions, it should be confirmed whether these particles are negligible. In the measurement for $^{9}$Be, since $^{9}$Be particles emitted from elastic scattering were actually measured, the effect had to be corrected.

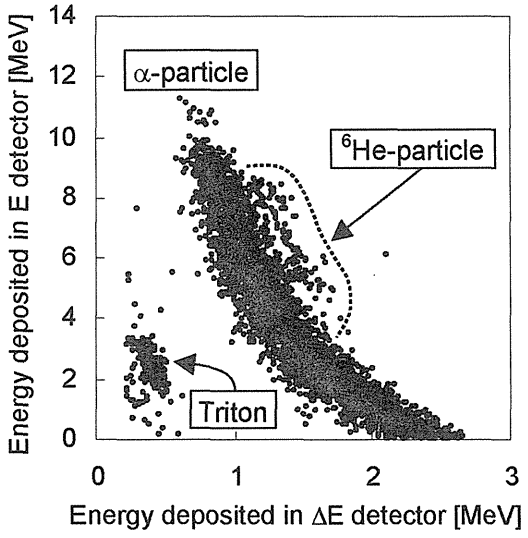



**Fig.2 2D-spectrum obtained for the measurement of $^{9}$Be(n, charged particle) reactions at 15 deg. in emitted angle**

## 3. Data analysis

In order to obtain the actual energy spectrum of emitted charged-particle, the measured spectrum must be corrected for energy loss in a sample. The relationship between real spectrum and measured spectrum is expressed in the following matrix equation;

$$M = R \cdot A \qquad (1)$$

where, A is the actual spectrum, M is the measured spectrum, R is the response function that represents effects of the energy loss in a sample and the angular resolution according to the detector geometry. The matrix R was obtained by Monte Carlo calculation with SRIM-2003 [7] and our own post-processing codes. Then spectrum unfolding was carried out with our original code based on *the spectrum type Bayes estimation method* to obtain the real energy spectrum [8,9].

DDX $\sigma(E_n \rightarrow E,\theta)$ [barn/sr/MeV] is obtained by the following equation;

$$\sigma(E_n \rightarrow E,\theta) = \frac{R(E,\theta)}{k_{\Delta E} \cdot k_E \cdot \phi_n \cdot N \cdot dE \cdot d\Omega_{\Delta E} / 4\pi} \qquad (2)$$

where, $R(E,\theta)$ is the count rate for charged particles detected in energy bin E at scattering angle $\theta$, $k_{\Delta E}$ and $k_E$ are the efficiency of the detectors (for charged-particle, $k \cong 1$), $\phi_n$ is neutron flux, $N$ is the number of target nuclei, $dE$ is the energy bin width and $d\Omega$ is the solid angle of the telescope, respectively. The angular differential cross section (ADX) was obtained by integrating DDX over energy. The total cross section (TOX) was obtained by fitting ADX with Legendre polynomials and integrating it over angle.

In the present study, neutron flux was monitored with $^{238}$U Fission Chamber relatively and absolute value was determined by the foil activation method with Al. For the standard cross section, 122.2mb for $^{27}$Al(n,α) reaction in JENDL-3.3 was used.

## 4. Results and discussion

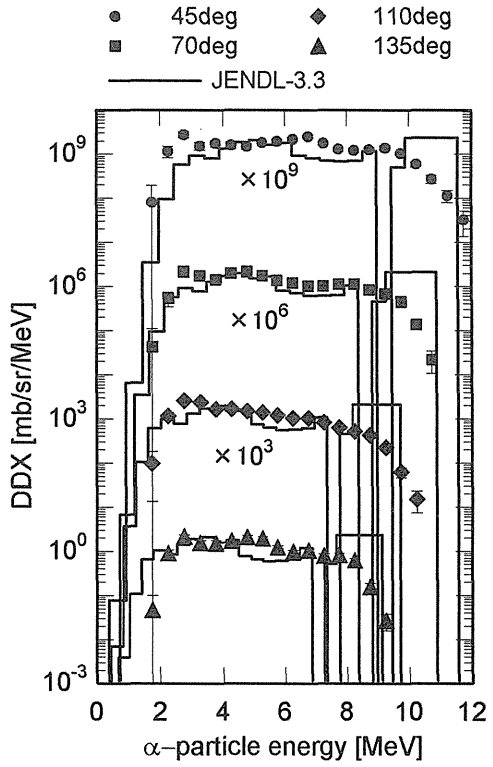



Fig.3 DDX measured for $^{27}$Al(n,xα) reactions at each scattering angles in LAB-system

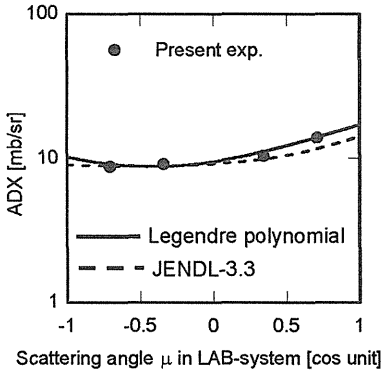



Fig.4 ADX measured for $^{27}$Al(n,xα) reactions at each scattering angles in LAB-system

Data obtained in the measurements were compared with the values evaluated for 14.2MeV neutron incidence. Error bars indicated in Figs. 3-7 include statistical error only.

Figure 3 shows DDXs obtained for $^{27}$Al(n,xα) reactions at scattering angles of 45, 70, 110 and 135 deg. There were slight differences in the details of structure between obtained DDX and the evaluation in JENDL-3.3. Figure 4 shows ADX for $^{27}$Al(n,xα) reactions. Agreement of the measured ADX with JENDL-3.3 is fairly good. Obtained TOX was 134 ± 2 mb, which was also in good agreement with JENDL-3.3 of 126.2 mb. From this result, the validity of the present experimental and analytical techniques was confirmed.

Figure 5 shows the measured DDX for $^{9}$Be(n,xα) reactions. DDX above 0.8MeV of emitted α-particle energy was obtained. The structures in the obtained DDX at backward scattering angle and in lower energy region were different from DDX reproduced from JENDL-3.3. Figure 6 shows obtained ADX. ADX evaluated in JENDL-3.3 agreed well with obtained ADX in forward scattering angles although underestimated at backward scattering angles. This disagreement would be resulting from wrongness of the branching ratio assumed

in evaluation of JENDL-3.3 for each process from which α-particle is emitted. The analysis of the obtained DDX aiming at the investigation of the branching ratio is in progress.

Figure 7 shows ADX for $^{9}Be(n,t)$ reaction. Measured ADX includes contributions from both $(n,t_0)^{7}Li_{(GS)}$ and $(n,t_1)^{7}Li^{*}_{(EX=0.48MeV)}$ reactions. Although isotropic angular distributions were assumed in JENDL-3.3 for these reactions, obtained ADX showed gentle forward peaked distribution. This result suggests that the contribution of the direct nuclear reaction process is dominant. The preliminary result of TOX obtained was 17.9 ± 0.6 mb, which was slight smaller than JENDL-3.3 of 18.9 mb. This disagreement should be caused by the uncertainty of ADX at backward scattering angle, which couldn't be obtained from the present experiment. The analysis with DWBA calculation would be desirable in order to obtain more precise information.

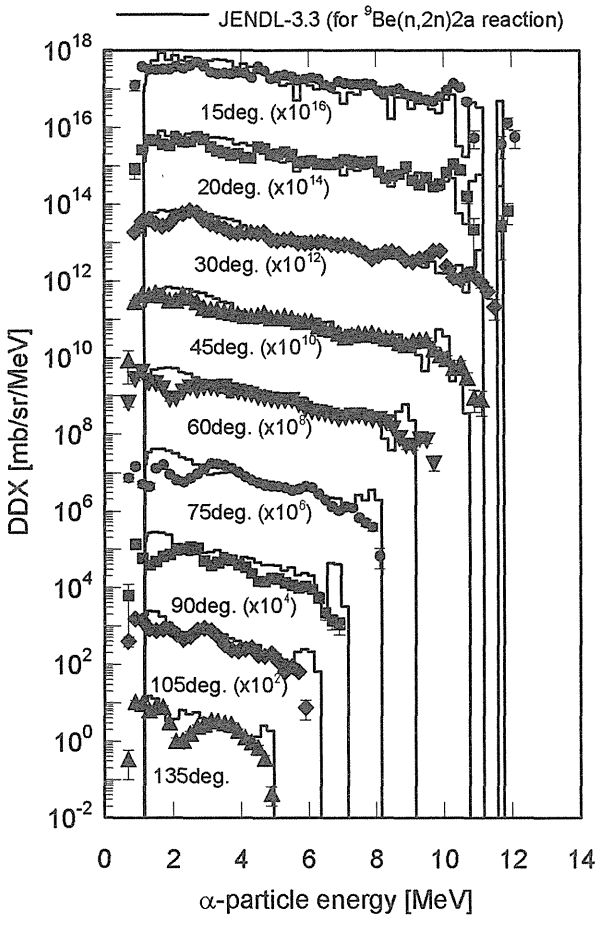



Fig.5 DDX measured for $^{9}Be(n,x\alpha)$ reactions at each scattering angles in LAB-system

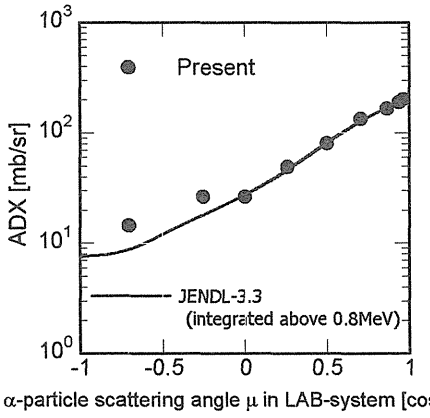



Fig.6 ADX measured for $^{9}Be(n,x\alpha)$ reactions at each scattering angles in LAB-system

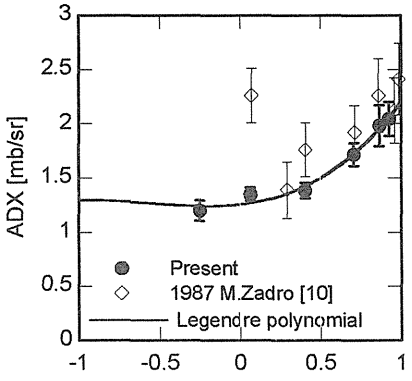



Fig.7 ADX measured for $^{9}Be(n,t)$ reactions at each scattering angles in CM-system

## 5. Conclusion

A unique technique for precise measurement of DDXc was developed. The present technique realized good S/N ratio, relatively high-count rate and good energy resolution. Since utilizing an anticoincidence spectrum extended lower limit of measurable energy for α-particle, 600KeV~1MeV for the lower limit was available. The present technique was valid from the result of measurement for the $^{27}Al(n,x\alpha)$ reactions. Detailed measurements for beryllium were carried out. Slight differences appeared between measured data and evaluation or previous experimental values. These results suggest more precise analysis for each process included in $^{9}Be(n,xa)$ reactions is required.

## Acknowledgements

The authors wish to acknowledge the FNS staff for their excellent operation of the FNS accelerator: Mr. Kutsukake, Mr. Tanaka, Mr. Abe, Mr. Seki, and Mr. Oginuma.

## References

[1] G. Paić, I. Šlaus and P.Tomaš, "Counter telescopes for the study of (n, charged particle) reactions," *Nucl. Instrum. Method.*, **34**, 40(1965)

[2] M. Brendle, M. Mörike, G. Staudt and G. Steidle, "A counter telescopes to investigate (n,α) reactions," *Nucl. Instrum. Method.*, **81**, 141(1970)

[3] S. Shirato, K. Shibata, M. Saito and S. Higuchi, "Measurements of charged particles from neutron induced reactions in the close geometry," *Nucl. Instrum. Method.*, **199**, 469(1982)

[4] A. Takahashi, I. Murata, Kokooo, *et al.*, "A time-of-flight spectrometer with pulse-shape discrimination for the measurement of double-differential charged-particle emission cross sections," *Nucl. Instrum. Method*, **A401**, 93(1997)

[5] Kokooo, I. Murata and A. Takahashi, "Measurement of double-differential cross sections of charged-particle emission reactions for several structural elements of fusion power reactors by 14.1-MeV incident neutrons," *Nucl. Sci. Eng.*, **132**, 16(1999)

[6] H. Sakane, Y. Uno, F. Maekawa, *et al.*, "A study on 14 MeV neutron beam characteristics and its applications," *Reactor Dosimetry: Radiation Metrology and Assessment, ASTM STP 1398*, John G. Williams, *et al.*, Eds., American Society for Testing and Materials, West Conshohocken, PA, p.375(2001)

[7] SRIM.EXE, (C) 1984-2000, International Business Machines Corporation, James F. Ziegler. http://www.srim.org/

[8] S. Iwasaki, "A new approach for unfolding PHA problems based only on the Bayes' Theorem," *Proc. 9th International Symposium on Rector Dosimetry*, Prague, Chezk Republic, Sep. 2-6, 1996, p.245(1998)

[9] H. Takagi, Y. Terada, I. Murata and A. Takahashi, "Measurement of double differential cross section of charged particle emission reactions by incident DT neutrons -correction for energy loss of charged particle in sample materials-," *Proc. 1999 Symposium Nucl. Data*, JAERI, Tokai, JAPAN, Nov. 18-19, 1999, JAERI-Conf 2000-005, p.178(2000)

[10] M. Zadro, S. Blagus, D. Miljanić and D. Rendić, "The (n,t) reaction on $^{9}Be$ at 14.6MeV," *Nucl. Sci. Eng.*, **95**, 79(1987)

JP0550266



# 3.6 Additional Evaluation of Alpha Induced Neutron Production Nuclear Data — $^{9}Be$, $^{27}Al$, $^{28,29,30}Si$ —

Toru Murata and Keiichi Shibata*
AITEL corp.; 8 Shinsugita-cho, Isogo-ku, Yokohama, Japan
*JAERI; Tokai-mura, Naka-gun, Ibaraki-ken, Japan
murat@green.ocn.ne.jp, * shibata@ndc.tokai.jaeri.go.jp

Alpha particle induced neutron production cross sections, emitted neutron energy spectrum and angular distributions were evaluated for the target nucleus $^{9}Be$,$^{27}Al$ and Si isotopes; $^{28}Si$,$^{29}Si$ and $^{30}Si$ in the incident energy region below 15 MeV.

## 1. Introduction

Though, JENDL (α,n) Reaction Data File 2003 has been released for 13 nuclides, additional nuclear data for the reaction are required. For $^{9}Be$, requirement of detailed angular distributions of neutrons to several excited states of $^{12}C$ was made to estimate intensity of standard radio-active neutron source. Neutron production data of $^{27}Al$ are necessary to investigate new type nuclear fuel of non-proliferate. The data for Si are necessary to estimate the neutron emission rate of high level radio-active vitrified solid which includes alpha emitting TRU.

## 2. Method of nuclear data calculation and evaluation

The neutron production nuclear data were calculated by analyzing the experimental cross sections with a resonance formula code[1] and statistical model code EGNASH2 which is developed by researchers of JAERI-NDC by combining ELIESE-3 [2] and GNASH code[3]. Evaluation of cross section was made by modifying the obtained cross section slightly to reproduce the experimental thick target neutron yields.

## 3. Results of evaluation

### 3.1 $^{9}Be+\alpha$ Reaction

The following nuclear data were already included in JENDL (α,n) reaction file.

- Total neutron production cross section
- Partial $(\alpha,n_i)$ reaction cross section; i=0,1,2,3
- The (α,α'n) reaction cross section
- Emitted neutron gross energy spectrum in Kalbach systematics[4].

In the present work,

- Experimental angular distributions [5] of neutrons emitted by the reaction $(\alpha,n_0)$, $(\alpha,n_1)$, $(\alpha,n_2)$ and $(\alpha,n_3)$ were fitted with Legendre polynomials at first. Then Legendre coefficients and partial cross section were analyzed with Blatt-

Biedenharn resonance formula. The coefficients of Legendre polynomials of angular distributions were evaluated by merging experimental and calculated coefficients.

- Continuum energy spectrum of neutrons were determined to reproduce the experimental data of Obst et al.[5] approximately.

Figure 1 shows calculated cross section of the $^{9}Be(\alpha,n_0)$ reaction and their Legendre coefficients of L=1,2,3 comparing with experimental data. Evaluation of Legendre coefficients will be made tracing experimental data with the shape of calculated values.

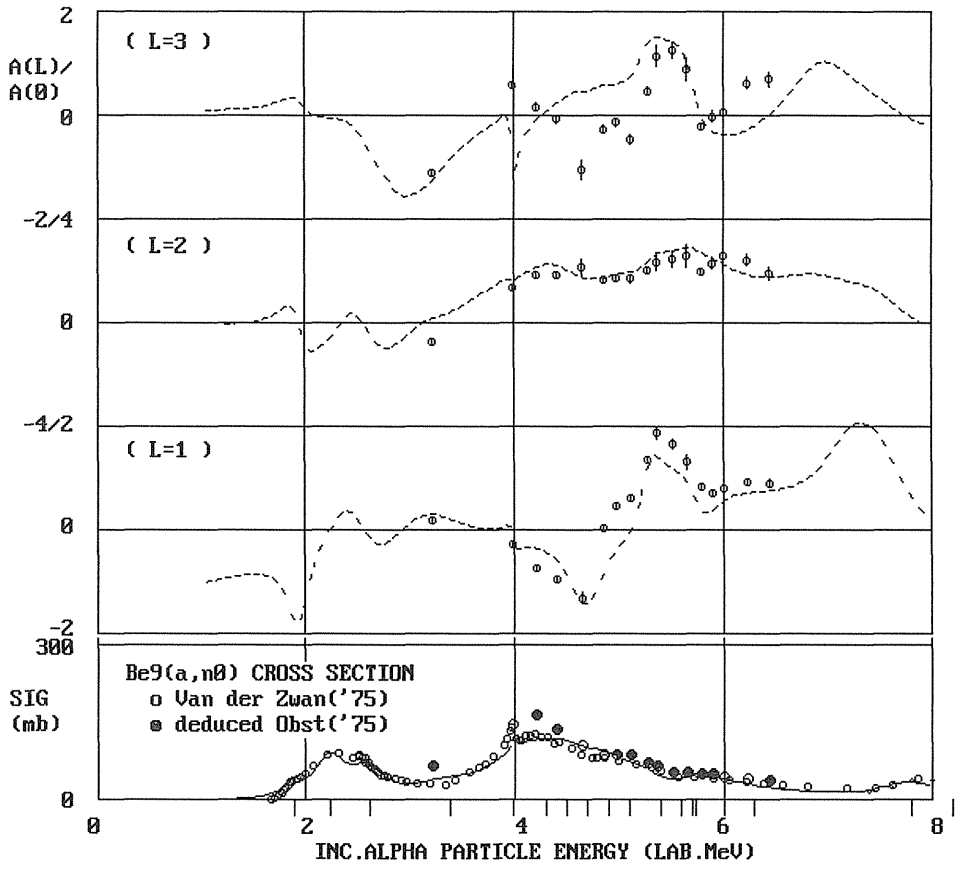



Fig.1 Present (tentative) evaluated $^{9}Be(\alpha,n_0)$ cross section is shown in the bottom figure by solid line comparing with the experimental data by Van der Zwan[6] and by Obst et al.[5] which were deduced from angular distributions. Top three figures show Legendre coefficients ratios (L=1,2 and 3) of $^{9}Be(\alpha,n_0)$ angular distributions; dashed lines show calculated results using resonance parameters to reproduce the bottom figure cross section and dots show experimental ones obtained by analyzing angular distributions by Obst et al.[5]

### 3.2 $^{27}Al+\alpha$ Reaction

Neutron production cross section was evaluated on the experimental data measured by Holmqvist and Ramstrom [7], Flynn et al.[8] and Howard et al.[9] in the resonance structure region in the incident energy below 5.5 MeV. In the higher energy region, the cross sections were measured by Stelson and Mcgowan[10] with neutron counting method

and by Sahakundu et al.[11] with activation method measuring $^{30}P$ activity. The cross sections measured by the activation method do not correspond to neutron production cross section in the high energy region where other neutron production channels are open besides the (α,n) reaction.

Evaluation was made, in the resonance structure region, to reproduce the structure with sum of Lorenz functions. In the higher energy region, calculated cross section with EGNASH-2 code was normalized to the lower energy region cross section.

Figure 2 shows the evaluated neutron production cross section comparing with the experimental cross sections. Figure 3 shows the thick target neutron yields calculated using the evaluated cross section and alpha particle stopping power、comparing with the experimental thick target neutron yields measured by Bair and Gomez del Campo[12] and by West and Sherwood[13].

Emitted neutron energy spectrum were calculated with EGNASH-2 code in the whole incident energy region, and given in the form of Kalbach systematics[4].

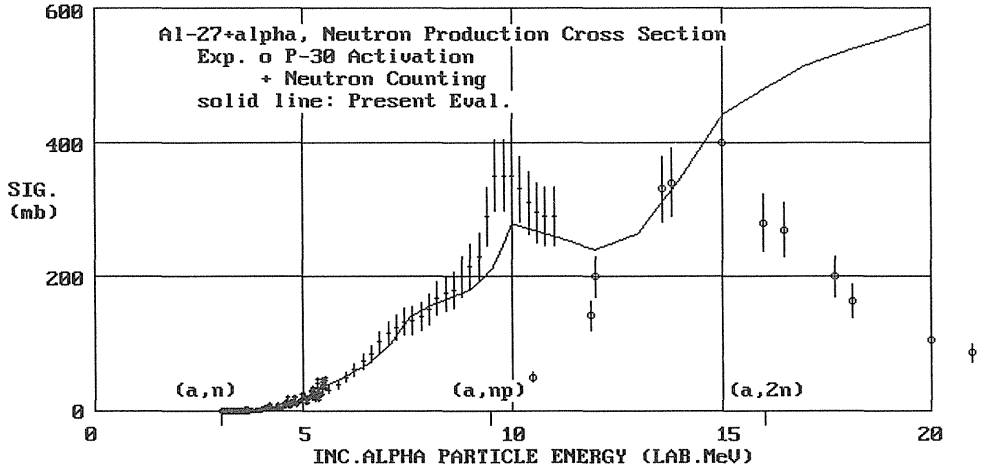



Fig.2 Neutron production cross section of $^{27}Al$+α reaction. Note that the experimental data of $^{30}P$ activity do not correspond to the neutron production cross section.

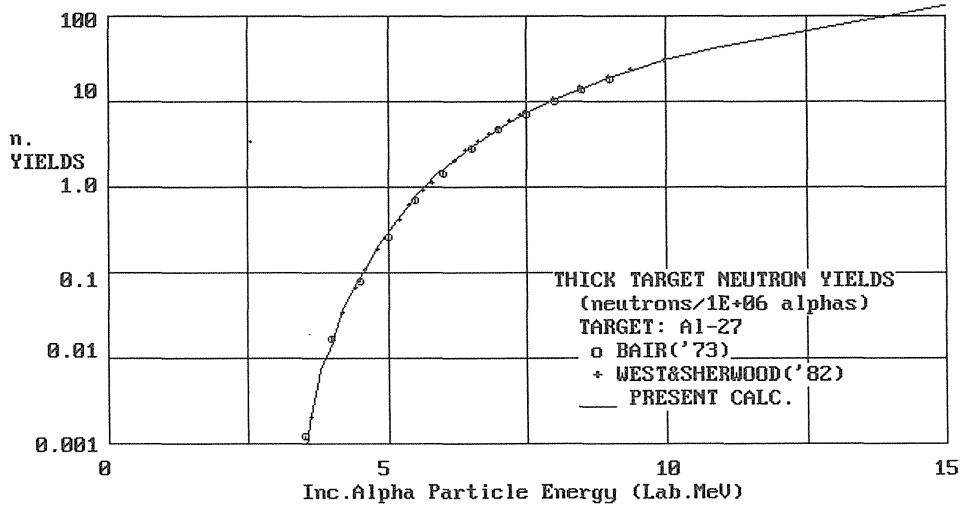



Fig.3 Thick target neutron yields (n/$10^6$α) of $^{27}Al$+α reaction.

### 3.3 Si+α Reaction

Experimental cross sections were measured by Cheng and King[14] for $^{28}$Si, by Flynn et al.[8] and by Gibbons and Macklin[15] for $^{29}$Si, by Flynn et al.[8] for $^{30}$Si. Evaluation methods are almost same as those for $^{27}$Al.

The evaluated neutron production cross sections are shown in Fig.4 for $^{28}$Si, Fig.5 for $^{29}$Si and Fig.6 for $^{30}$Si comparing with the experimental cross sections. Figure 7 shows the calculated thick target neutron yields of Si isotopes and natural Si comparing with the experimental thick target neutron yields [12), 13)].

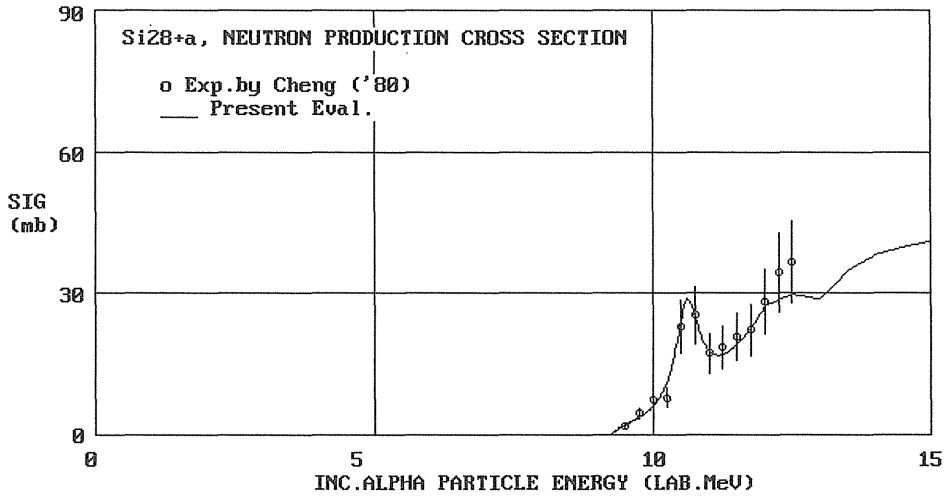



Fig.4 Neutron production cross section of $^{28}$Si+α reaction.

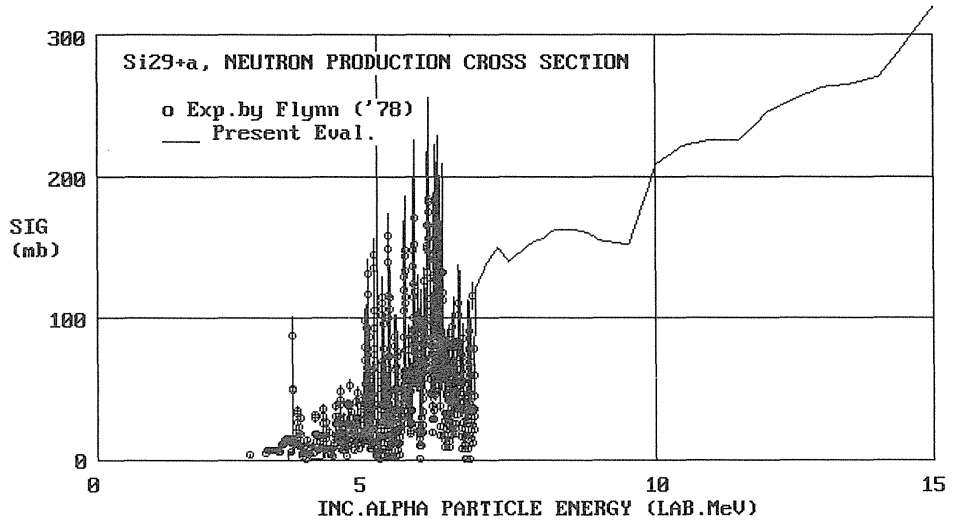



Fig.5 Neutron production cross section of $^{29}$Si+α reaction.

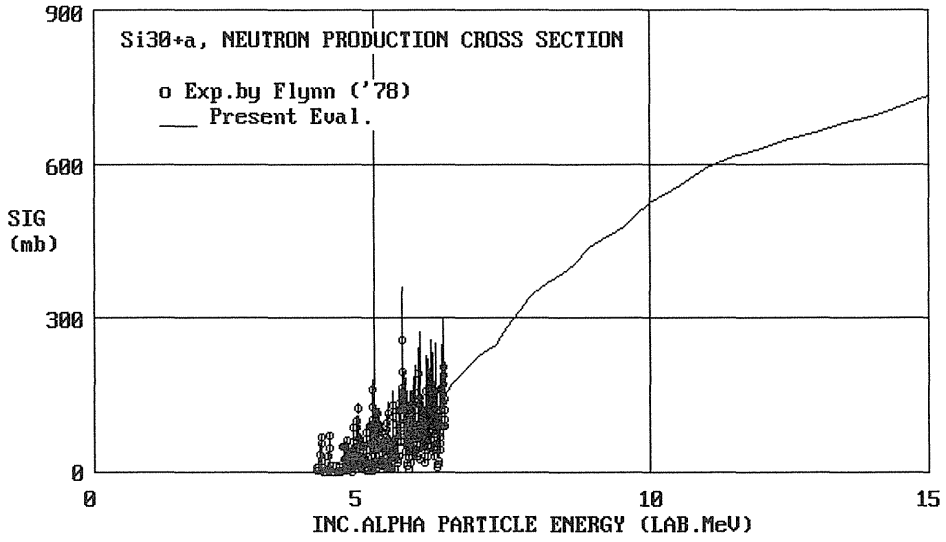



Fig.6 Neutron production cross section of $^{30}$Si+α reaction.

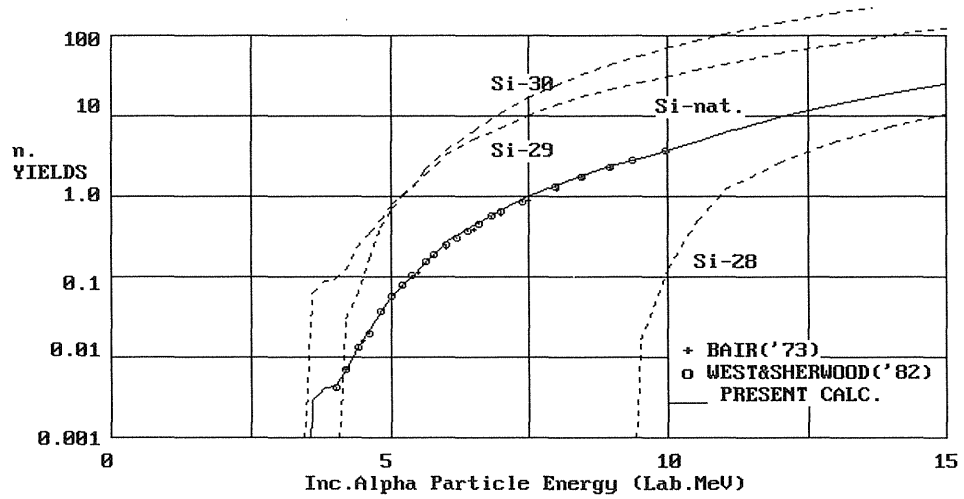



Fig.7 Thick target neutron yields (n/10$^6$α) of $^{nat}$Si+α reaction. The same quantity of each Si isotope calculated using the evaluated cross section is also shown in dashed line.

4. Conclusion

For alpha particle bombardment of $^{27}$Al,$^{28}$Si,$^{29}$Si and $^{30}$Si, neutron production cross sections and emitted neutron energy spectrum were evaluated on the experimental data and theoretical calculation. For these nuclides, though they show resonance structure in low energy region, excitation energy of the compound nuclei is so high that no spin-parity assignment was made in ENSDF (Evaluated Nuclear Structure Data Files) and definite resonance analysis cannot be applied . So, simple Lorenzian fitting was made.

Angular distributions of neutrons emitted by the $^{9}$Be(α,ni),i=0,1,2 and 3 were analyzed

with a resonance formula. But complex resonance structures make it not easy to obtain good agreement between calculated results and experimental data for the cross sections and angular distributions simultaneously with consistent resonance parameters for each final state; ground, 1st,2nd and 3rd . If it will be done successfully, alpha particle incident excited states of $^{13}C$; Ex=10-15 MeV will be determined definitely.

Acknowledgements

Thanks are due to Drs. T.Nakagawa and A.Ichihara (JAERI NDC) for helpful support in trouble shooting while utilization of EGNASH-2 code.

References

1) Murata,T. JAERI-Conf 98-003, 1998, p.215
2) Igarasi,S. JAERI 1224, 1972
3) Young,P.G.,Arthur,E.D.; LA-6947
4) Kalbach,C.: Phys.Rev.C37,2350(1988)
5) Obst,A.W.,Grandy,T.B.,Weil,J.L.: Phys.Rev.C5,738(1972)
6) Van Der Zwan,Geiger,K.W.:Nucl.Phys.A246(1975)93
7) Holmqvist,B.,Ramstrom,E.: Physica Scripta 33,107(1986)
8) Flynn,D.S.Sekharab,K.K.,Hiller,B.A.,Laumer,H.,Weil,J.L.,Gabbaed,F.: Phys.Rev.C18,1566(1978)
9) A.J.Howard et al.:Astrophysical Journal,188,131(1974)
10) Stelson,R.H.,Mcgowan,F.K.: Phys.Rev. B133,911(1964)
11) Sahakundu,S.M.,Qaim,S.M.,Stocklin,G.: Appl. Radiation and Isotopes 30,3 (1979)
12) Bair,J.K.,Gomez del Campo,J.: Nucl.Sci.Eng.71,18(1979)
13) West,D,Sherwood,A.C.: Ann.Nucl.Energy 9,551(1982)
14) Cheng,C.W.,King,J.D.: Cand.J.Phys.58,697,(1980)
15) Gibbons,J.H.,Macklin,R.L.: Phys.Rev.114,571(1959)

JP0550267



# 3.7 Measurements of cross-sections of the proton-induced activation reactions

M. S. Uddin[a], M.Baba[a] , M. Hagiwara[a], F. Tarkanyi[b] , and F. Ditroi[b]
[a]*Cyclotron and Radioisotope Center, Tohoku University, Aramaki, Aoba-ku, Sendai 980-8578, Japan.*
[b]*Institute of Nuclear Research of the Hungarian Academy of Sciences, Debrecen, H-4001, Hungary.*

Excitation functions for the $^{89}Y(p,x)^{89,88,86}Zr$, $^{89}Y(p,x)^{88,87,87m,86}Y$, $^{89}Y(p,x)^{85,83,82}Sr$ and $^{89}Y(p,x)^{84,83}Rb$ reactions were measured by a stacked foil activation technique in the energy range 15-80 MeV. The production for the long lived products like $^{88}Zr$, and $^{88}Y$ are significantly larger than that of $^{nat}Mo+p$, $^{nat}Nb+p$ and $^{nat}Zr+p$ processes. The productions of the medical isotopes, $^{85}Sr$ and $^{83}Sr$ are also effective by Y+p process using 80 MeV beam. The model calculations using ALICE-IPPE code compiled in MENDL-2P have the general trend of the measured results.

## 1. Introduction

Yttrium is widely applied to increase the strengths of alloys of important metals of nuclear technology (aluminum, magnesium and chromium). The proton-induced activation cross-section on this element is important for dose estimation in accelerator technology, for thin layer activation analysis (TLA) of yttrium alloys (especially of aluminum and magnesium) and of yttrium oxide ceramics. Yttrium is a monoisotopic element therefore ideal target material to test nuclear reaction theories.

The $^{86,87,88}Y$ radioisotopes have value for investigation of the biodistribution of $^{90}Y$ labeled therapeutic compounds. $^{88}Y$ is a recognized standard for calibration of gamma-ray detector. $^{88}Y$ is produced directly by particle-induced activation and/or via generator system from $^{88}Zr$. Yttrium can be used as target for the production of medically related radioisotopes, $^{82}Sr$, $^{83}Sr$, $^{85}Sr$ and biological tracers, $^{84}Rb$, $^{83}Rb$ (water transports in plants, etc.) and for a large- scale production of $^{88}Zr$ and $^{88}Y$ activities.

Few authors have reported data for proton-induced activation reactions on yttrium at low energies limited to maximum energies 5 MeV to 45 MeV [1-5]. A Large discrepancy is found between them.

In this work we present the new cross-sections for Y+p reactions as a part of systematic studies on particle-induced activations [6-9]

## 2. Experimental technique and data evaluation

The independent and "cumulative cross-sections" of the proton-induced reactions on yttrium were measured as a function of proton energy using a conventional stacked foil activation technique. The irradiation, the activity measurement and the data evaluation were similar as described in more details in our recent works [6-9]. Here we summarize some features specific for the investigation. Two stacks of several identical groups containing high purity thin yttrium foils (110 μm thick) were irradiated separately with 50 MeV (~165 nA for 30 min) and 80 MeV (~45 nA for 70 min) collimated protons, respectively using a K=90 MeV AVF cyclotron at Cyclotron and Radioisotope Center (CYRIC), Tohoku University, Sendai, Japan. In this way the proton beam energy range of 15-80 MeV was covered. Reactions induced on aluminum (100 and 1000 μm thick) and copper (54 μm thick) foils were used to monitor the parameters of the bombarding beam and as proton beam energy degrader.

The residual activity was measured nondestructively by the high-resolution HPGe gamma-ray spectroscopy. The efficiency *versus* energy curves of the HPGe-detector for various counting distances were established using calibrated standard gamma-ray point sources. The effective particle energy in the foils was calculated by the computer program SRIM-2003 [10] using measured thicknesses of the foils. The beam current was determined by the monitor reactions $^{nat}Cu(p,x)^{56}Co$,$^{62,65}Zn$ and $^{27}Al(p,x)^{22,24}Na$ [11]. The decay data for the investigated radionuclides were taken from NUDAT database [12].

The peak area data were corrected for the sum-coincidence effect caused by the coincidental detection of two or more gamma rays in cascade by using the SUMECC code [13]. In some cases, the contributions from overlapping peaks were separated by using the independent gammas of the contributing nuclides.

The combined uncertainty on each cross-section was estimated by taking the square root of the quadratic sum of the following errors: statistical error (0.15-6 %), error of the monitor flux (3-5 %), the error in efficiency calibration of the gamma-ray (~3 %) and foil thickness (3 %).

## 3. Results and discussion

The measured excitation functions are shown in Figs. 1-9 together with literature values. The results of this work are compared with reported experimental data and ALICE-IPPE calculation compiled in MENDL-2P [14].

*3.1 $^{89}Y(p,xn)^{89,88,86}Zr$*

The measured excitation function for the production of $^{89}$Zr is shown in Fig.1. The contribution from the decay of the 4.18 min isomeric state $^{89m}$Zr is included in the measured cross-section. Saha et al. [15] reported the $^{89}$Zr production cross-section in our investigated energy range. The results of Saha et al. moved upward in the range 18-30 MeV and out of this energy range showing consistency with this work. The results of this work are in good agreement with Birattari et al [1], Johnson et al. [2], Levkovski [3] and Mustafa et al. [4] in the lower energy region and with MENDL-2P and that fact confirm our measurements as reliable.

The independent cross-sections for the $^{88}$Zr production through $^{89}$Y(p,2n) reaction were measured that are shown in Fig.2. About 98 % consistencies of the measured values for the $^{88}$Zr production with the experimental values of Saha et al. are found above 40 MeV, but large discrepancies are present in lower energy region. The results of this work are about 62 % lower and 8 % higher than Saha et al. and ALICE-IPPE calculation in peak region, respectively. The measured data are in good agreement with Mustafa et al. who reported below 40MeV. The $^{88}$Zr production cross-sections reported by Levkovski are unexpectedly rising in peak region.

The measured cross-sections for the $^{89}$Y(p,4n)$^{86}$Zr reaction are shown in Fig.3. The present results are consistent with Saha et al. in shape, but not in magnitudes. The shape of excitation function for the production $^{86}$Zr obtained from the ALICE-IPPE calculation is not acceptable. Caretto et al. [16] reported only two points, which have common trend with this work.

*3.2 $^{89}Y(p,x)^{88,87,87m,86}Y$*

The cross-sections for the production of $^{88}$Y shown in Fig.4 were measured. The contributions in the measured values are the internal transition decay of the short-lived ($T_{1/2}$ = 13.9 ms) $^{88m}$Y isomer. The measurement was done one day after EOB. The half-life of $^{88}$Zr is 83.4 days that is so much higher than cooling time. Hence the effect of the decay of $^{88}$Zr on the $^{88}$Y production cross-section is very low that has been separated. No cumulative data are found in literature for the $^{88}$Y production in the investigated energy range.

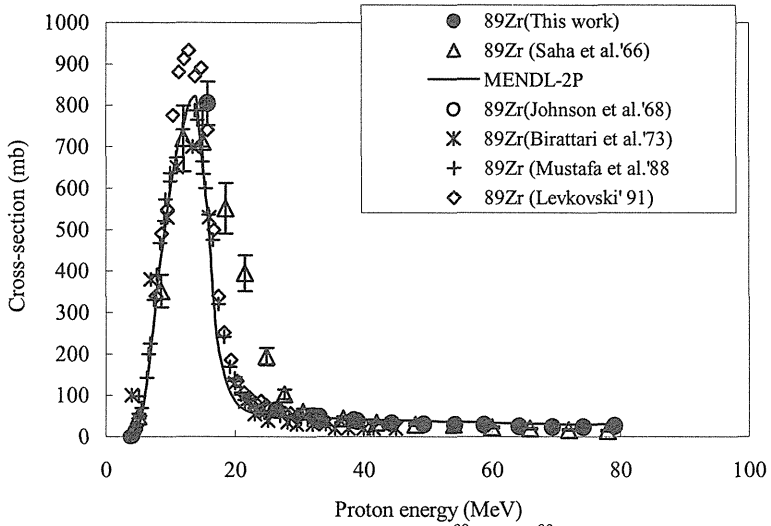



Fig. 1 Excitation functions of the $^{89}$Y(p,x)$^{89}$Zr reaction.

The measured $^{87m}$Y production cross-sections (Fig.5) are due to the direct process induced on $^{89}$Y and the decay of $^{87}$Zr. The overlapping peaks for $^{83}$Sr and $^{86}$Y on the 380.7 keV gamma energy of $^{87m}$Y were separated by using other independent gammas of the contributing nuclides. A good consistency was found between the results of this work and Michel et al. [17].

$^{87}$Y is produced by $^{89}$Y(p,p2n) reaction and by 98.43 % internal transition of the metastable state $^{87m}$Y ($T_{1/2}$=13.37 h). It was paid attention for the complete internal decay of metastable state to measure cumulative production cross- sections shown in Fig.5. Michel et al. reported cumulative cross-section. The results of this work are in good agreement with Michel et al. Saha et al. reported about two times lower values than this work. The result of ALICE-IPPE calculation shows similar overall general behavior as the experimental data.

The measured values for the production of $^{86}$Y shown in Fig.6 contain two contributions like $^{89}$Y(p,p3n) direct process and the decay of metastable state. The present results are similar to Michel et al. and MENDL-2P in shape.

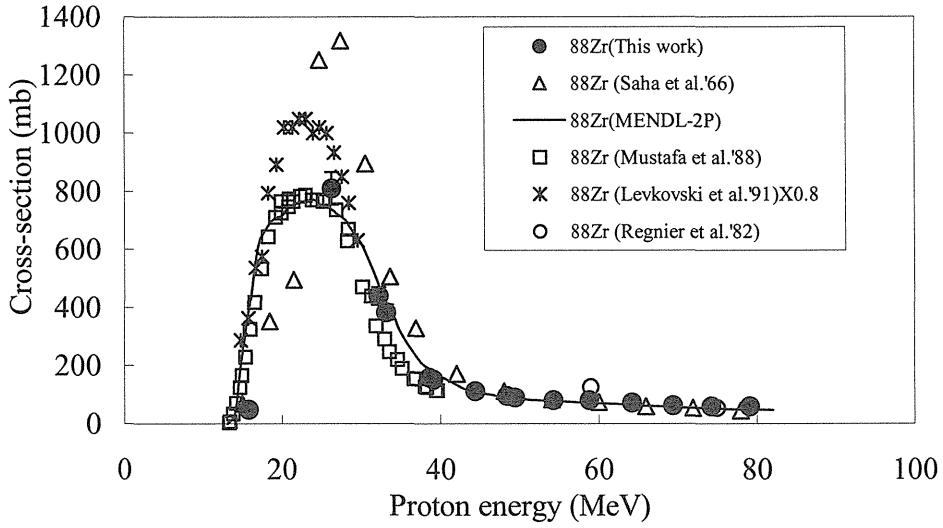



Fig. 2 Excitation functions of the $^{89}Y(p,x)^{88}Zr$ reaction.

*3.3 $^{89}Y(p,x)^{82,83,85}Sr$*

$^{85}Sr$ has a large importance in nuclear medicine as diagnostic radioisotope and for the endotherapy. The $^{85}Sr$ nuclide is also an important impurity in the application of the medical radioisotopes $^{82}Sr$ and $^{83}Sr$. The $^{85}Sr$ production cross-section was measured using 514 keV gamma. To separate the 514 keV gamma line from the strong annihilation peak (511 keV), the measurement was done about 40 days after end of irradiation and obtained separate peak through our high resolution gamma spectroscopy system. This work gives the cumulative cross-section shown in Fig.7 contained the contributions of direct process, decay of isomeric state and EC decay of $^{85}Y$. The results of this work are in good agreement with Michel et al. The calculated results compiled in MENDL-2P are also consistent with this work both in shape and magnitudes above 40 MeV

The $^{82}Sr$ ($T_{1/2}$= 25.55 d) production cross-sections shown in Fig.8 were determined by measuring 776 keV gamma line produced through the decay of its daughter radioisotope $^{82}Rb$ ($T_{1/2}$= 1.273 min). The $^{86}Y$ ($T_{1/2}$= 14.74 h), $^{83}Sr$ ($T_{1/2}$= 1.35 d) and $^{82m}Rb$ ($T_{1/2}$= 6.47 h) radionuclides emitted gamma-rays having very close energies to 776 keV which were difficult to separate by the graphical analysis of the multicomponent decay curve. After >40 days, these contributing radionuclides completely decayed out and the remaining activity was due to decay of the daughter nuclide $^{82}Rb$ in transient equilibrium with the parent $^{82}Sr$ radionuclide. The measured values are in good agreement with Michel et al. The results of ALICE-IPPE calculations have similar shape, but overestimate the experimental values.

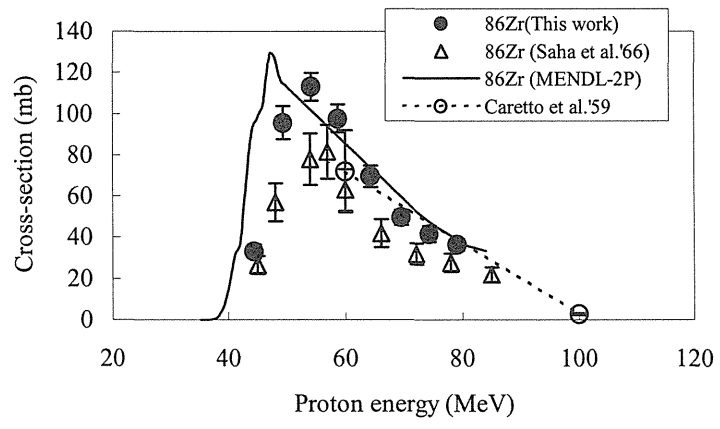



Fig. 3 Excitation functions of the $^{89}Y(p,x)^{86}Zr$ reaction.

$^{83}Sr$ is a suitable positron emitter analog of the $\beta^-$ emitting $^{89}Sr$ ($T_{1/2}$= 50.5 d) used for endotherapy. The isomeric state $^{83m}Sr$ have too short half-life ($T_{1/2}$= 4.95 s) that decayed completely to the ground state and its role as isomer in production of the ground state is negligible. $^{83}Sr$ is produced via $^{89}Y(p,2p5n)$ reaction and the decay of $^{83}Zr$ and $^{83}Y$. The results of this work are shown in Fig.8 together others. Michel et al. and ALICE-IPPE calculation well reproduce the shape of the measured excitation function.

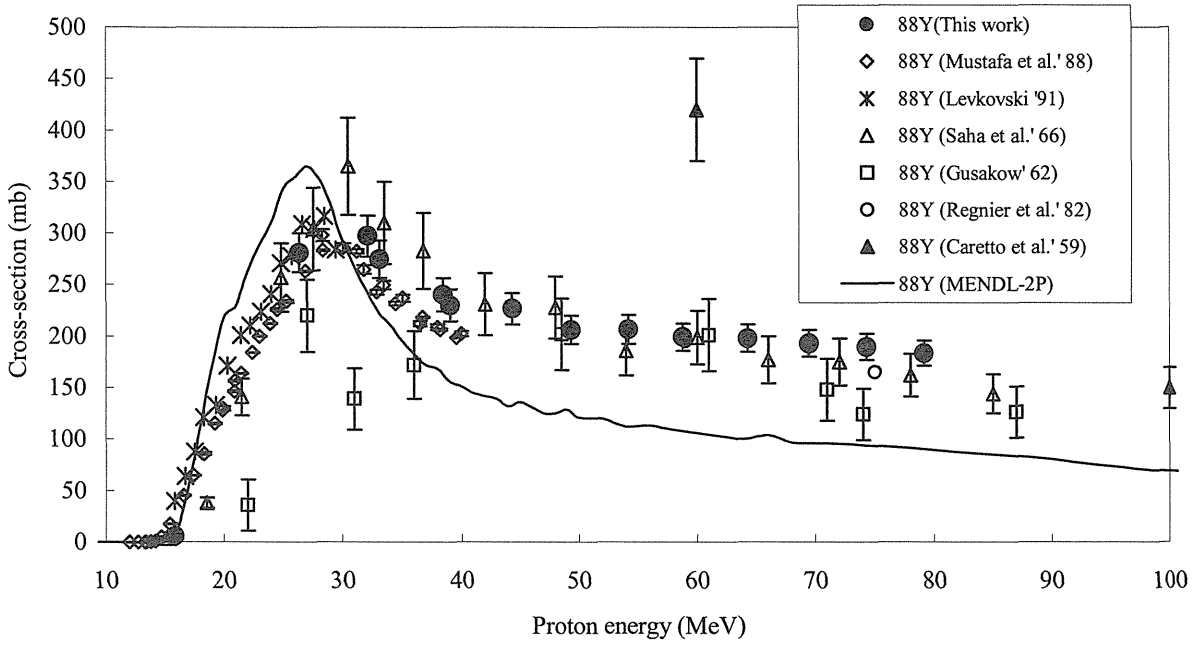



Fig.4 Excitation functions of the $^{89}Y(p,x)^{88}Y$ reaction.

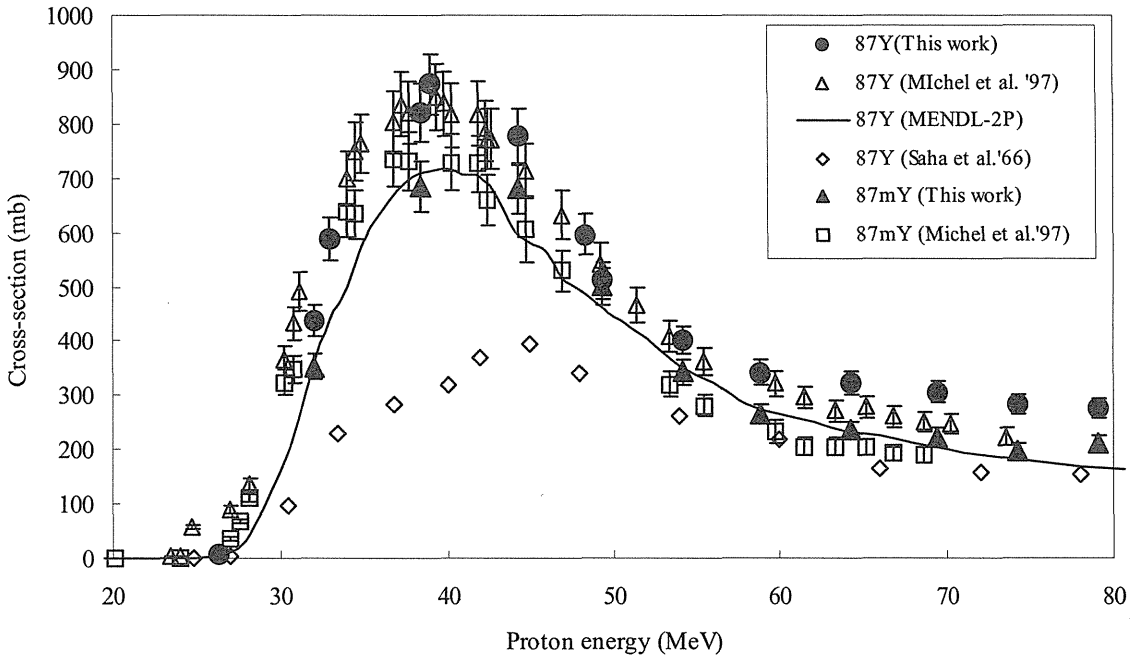



Fig.5 Excitation functions of the $^{89}Y(p,x)^{87,87m}Y$ reaction.

*3.4 $^{89}Y(p,x)^{84,83}Rb$*

The $^{84}$Rb production cross-sections shown in Fig.9 were measured after the complete decay of $^{84m}$Rb ($T_{1/2}$= 20.26 min), i.e. the obtained results are the sum of the ground and the isomeric state cross-sections. $^{84}$Rb is produced by $^{89}$Y(p,αpn) reaction. The probability of this reaction occurring is largely inhibited by the Coulomb barrier in both the entrance and exit channels. The results of this work are consistent with Michel et al. A large discrepancy is found between the measured and calculated values.

This work presents the cumulative cross-section for the production of $^{83}$Rb shown in Fig.9, which contains contribution from the decay of $^{83}$Sr. The sharply increase in excitation function above 35 MeV is probably due to more independent particle emission. Only one earlier data reported by Michel et al. are also shown in Fig.9. The results of this work are in about 97% agreement with Michel et al. The ALICE-IPPE calculation underestimates the measured values.

**4. Conclusion**

The present work gives new cross-section data for all of the investigated radionuclides. In some cases, our data are consistent with the results of Michel et al. The data in MENDL-2P calculated with the theoretical code ALICE-IPPE are consistent in shape with the measured values, but disagreement in magnitudes. Two stacks were irradiated in different conditions and observed good agreement between the obtained results in the overlapping energy range. The reliability of the data is guaranteed by using the relative method. The results of this work will play an important role to test model calculations. The cross-sections obtained in this study useful to estimate the optimal production yields and impurities in the energy range from threshold up to 80 MeV.

It seems to us the production of $^{85}$Sr will be effective by proton-induced activation on yttrium using accelerator having 80 MeV proton beam. It is also possible to give production of $^{83}$Sr through $^{89}$Y(p,x) reactions. From the point of view of the production yields the Y+p route is much more efficient to give productions of $^{88}$Zr and $^{88}$Y than $^{nat}$Mo+p, $^{nat}$Nb+p and $^{nat}$Zr+p processes.

The data base is promising to prepare recommended data sets for practical TLA applications. Among all investigated products the $^{87}$Y, $^{88}$Y, $^{88}$Zr and $^{89}$Zr radionuclides are the most suitable for thin layer activation analysis, but the $^{87}$Y and $^{89}$Zr only for investigations of short processes. It seems to us the proton-induced activation on yttrium can be effectively used for wear studies in alloys and ceramics by using TLA.

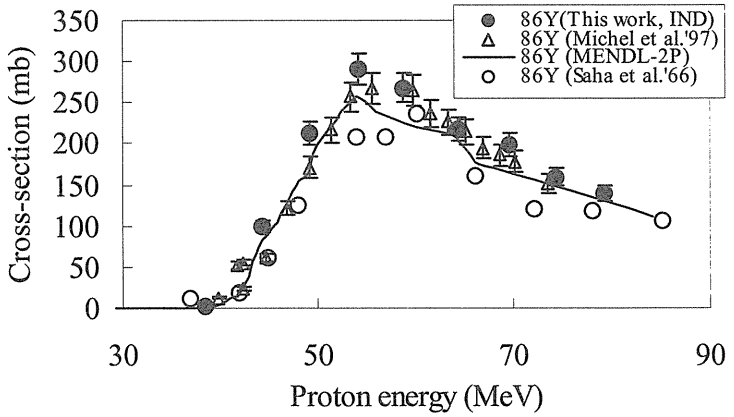



Fig.6 Excitation functions of the $^{89}$Y(p,x)$^{86}$Y reaction.

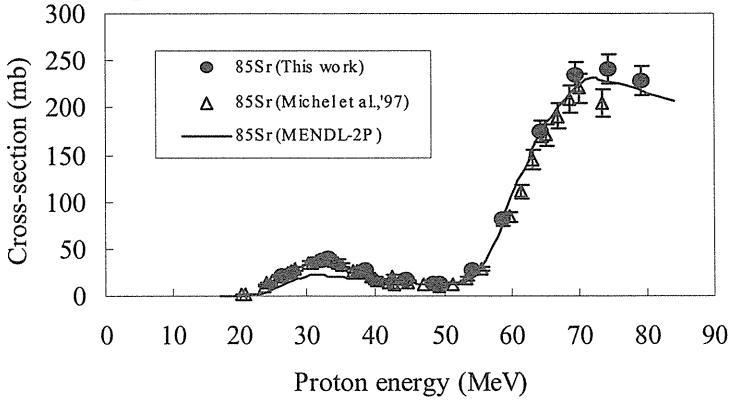



Fig.7 Excitation functions of the $^{89}$Y(p,x)$^{85}$Sr reaction.

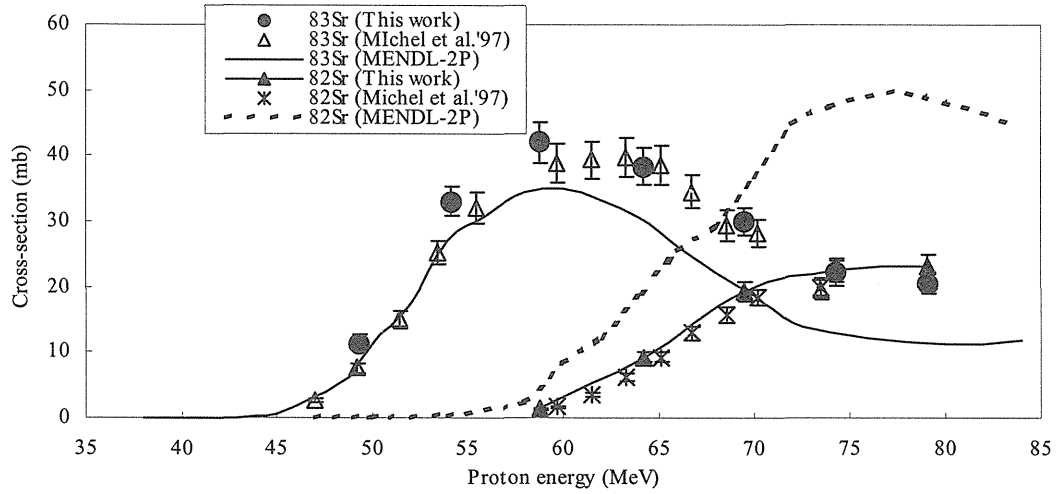



Fig.8 Excitation functions of the $^{89}Y(p,x)^{82,83}Sr$ reaction.

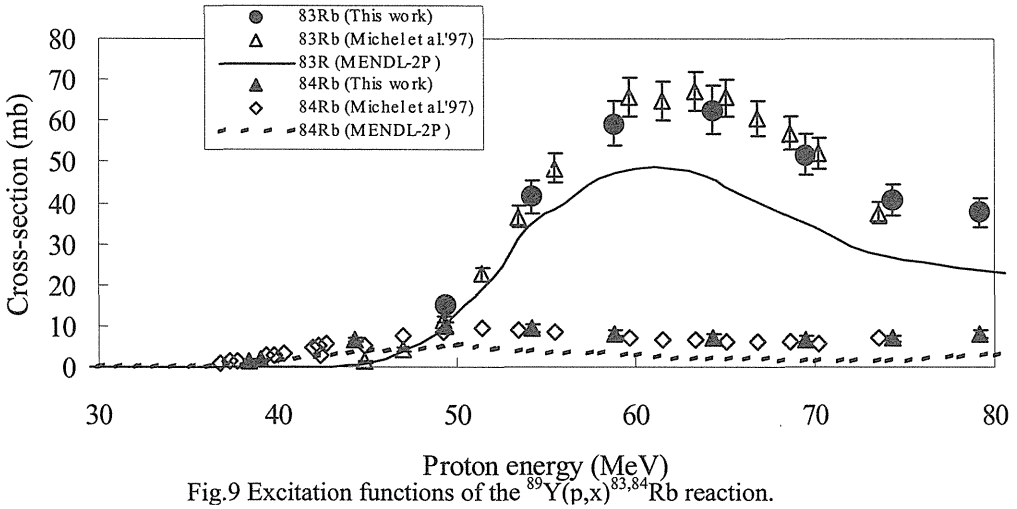



Fig.9 Excitation functions of the $^{89}Y(p,x)^{83,84}Rb$ reaction.

**References**

[1] Birattari C., et al.: Nucl. Phys., A201, 579 (1973).
[2] Johnson C.H., Kernell R.L. and Ramavataram S.: Nucl.Phys., A107, 21 (1968).
[3] Levkovski V.N.: Inter-Vesi, Moscow (1991).
[4] Mustafa M.G., West H.I. and O'Brien H., et al.: Phys. Rev., C28, 1624 (1988).
[5] Regnier S., Lavielle,B., Simonoff M. and Simonoff G.N.: Phys. Rev., C26, 931(1982).
[6] Uddin.M.S, Baba M., et al. : J. Nucl. Sci. and Tech., Supplement 4, 160 (2004).
[7] Uddin M.S., Hagiwara M., Tarkanyi F., Ditroi F. and Baba M. : Appl. Radiat. and Isot., 60, 911 (2004).
[8] Uddin M.S., Hagiwara M., Baba M.,Tarkanyi F. and Ditroi F. : Appl. Radiat. and Isot., Accepted (2004).
[9] Tarkanyi F., et al.: ND2004, Santa Fe, New Mexico.
[10] Ziegler J.F and Biersack J.P.: SRIM.com (The Stopping and Range of Ions in Matter) (2003).
[11] Tarkanyi F., et al. : IAEA-TECDOC-1211, IAEA,Vienna. <www.nds.iaea.or.at/medical>, p.49 (2001).
[12] NuDat.http:/www.nndc.bnl.gov/ nudat2/index.jsp
[13] Torii A., Uwamino Y. and Nakamura T.: INS-T-468, Institute for Nuclear Study, University of Tokyo (1987).
[14] Shubin Y.N., Lunev V.P., Konobeyev A.Y. and Dityuk A.I.: MENDL-2P, IAEA-NDS-204 (1998).
[15] Saha G.B. and Porile N.T.: Phys. Rev., 144 (3), 962 (1966).
[16] Caretto A.A. and Wiig E.O.: Phys. Rev., 115, 1238 (1959).
[17] Michel R. et al. :Nucl. Instr. and Meth. B 129, 153 (1997).

JP0550268



# 3.8 Neutron Production from Thin Target of Carbon and Iron by 70 MeV Protons

Toshiro Itoga, Masayuki Hagiwara, Takeshi Yamauchi, Takuji Oishi and Mamoru Baba

*Cyclotron and Radioisotope Center (CYRIC), Tohoku University*
*6-3, Aoba, Aramaki, Aoba-ku, Sendai-shi, Miyagi-ken 980-8578*
itogat@cyric.tohoku.ac.jp

Double differential neutron production cross section were measured at 70 MeV for the C, Fe(p, xn) reactions at four laboratory angles between 0- and 90-deg using the time-of-flight (TOF) method at the Tohoku University K = 110-MeV AVF cyclotron with a beam-swinger system and a low background TOF line. We determined neutron energy spectra from ~0.6 MeV to the highest secondary neutron energy. The experimental results were compared with the LA150 data library, and showed fairly good agreement/ or marked discrepancy.

## 1. Introduction

By the development of accelerator technology, accelerators become very reliable and high intensity and high energy accelerators are now available. Accordingly, uses of the accelerators are expanding to material studies, medical treatment, radiobiology studies and environmental science as well as nuclear physics, and some accelerators with high energy and intensity are under construction or in plan e.g., Japan Proton Accelerator Research Complex (JPARC, which is promoted by the corporation of JAERI and KEK) and Spallation Neutron Source (SNS, United States).

For the design of accelerator shielding and the accelerator-based neutron sources, differential thick target neutron yields (TTY) data are required over a wide energy and angle range with sufficiently good energy resolution. However, existing nuclear data files are not examined in quality for high energy accelerator application, and experimental data covering wide range of secondary neutron energies are very few. We have been conducting TTY measurements for proton of tens of MeV regions for the various elements shown in table 1, which are typical elements for beam-lines and beam-dumps in accelerators using a time-of-flight (TOF) method at the Cyclotron and Radioisotope Center (CYRIC), Tohoku University equipped with a K=110 AVF cyclotron and a beam-swinger system and low background TOF flight path.

These data were compared with the LA150 data library. LA150 data reproduced experimental data generally well but still shows marked disagreement in some energy and/or angular regions [1] Therefore, in the present experiment, to know the reasons of these disagreements, we measured the neutron yields for (p, xn) reactions for thin targets of carbon and iron.

Table 1: Series of TTY measurements for (p ,xn) reaction at CYRIC [1].

| Energy [MeV] | Nuclide | Angle [deg.] |
|---|---|---|
| 35 | Fe, Cu | 0, 30, 60, 90, 110 |
| 50 | C, Al, Fe, Cu, Ta, W | 0, 30, 60, 90, 110 |
| 70 | C, Al, Fe, Cu, W, Pb | 0, 30, 60, 90, 110 |

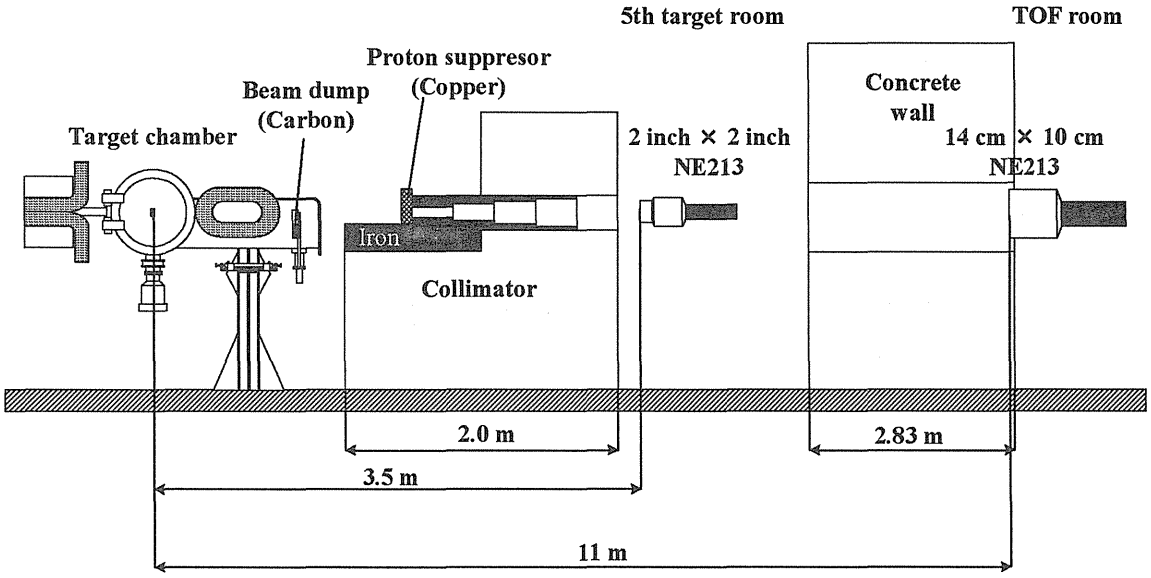



Fig. 1. Experimental setup

## 2. Experiment

The experimental setup is shown in fig. 1. A proton beam accelerated by the AVF cyclotron was transported to the target room No.5 of CYRIC equipped with a beam-swinger system and a neutron TOF channel [2]. The beam swinger system changes the incident angle of the beam onto the target from 0-deg to 120-deg and enables to measure angular distributions with a fixed detector setup. The targets of carbon and iron were plate of natural elements with sizes shown in table 2. After penetrating the target, a proton beam is bent to the beam dump made of carbon. The target chamber was shielded with a 2.5 m thick concrete wall having a beam channel for collimators to enable measurement of neutrons under a low background environment. In addition, to prevent the detection of neutral hydrogens, a copper plate is placed between the targets and detectors. Emitted neutrons were detected by an NE213 liquid scintillation detector, 14 cm-diam. × 10 cm-thick or 5 cm-diam × 5 cm-thick equipped with a pulse-shape-discriminator (PSD). The larger and smaller detectors were placed around ~11 m and ~3.5 m from the target, respectively. The measurement with a shorter flight path was adopted to obtain the low energy part (~0.6-4 MeV) of the neutron spectrum with low pulse-height bias, and that with a longer flight path was for higher energy part. The TOF, PSD and pulse-height data were collected event by event as three parameter list data for off-line analysis [3] together with the beam current at the beam dump concurrently.

Table 2: Target dimension

| Nuclide | Thickness [mm] | Density [g/cm3] | Energy loss [%] |
|---|---|---|---|
| C | 1 | 1.8712 | 2.15 |
| Fe | 0.3 | 8.058 | 2.25 |

## 3. Experimental procedures

The pulse width of proton beam was generally less than 2 ns in FWHM, and the beam interval was 492 ns by using the beam chopper to avoid frame overlap in the TOF spectra. The incident beam current on the beam dump was around 1 ~ 10 nA and was digitized and recorded by a scalar for normalization of the neutron TOF spectrum. The TOF data were obtained at four laboratory angles (0, 30, 60 and 90 deg.).

## 4. Data analysis

Neutron TOF spectra gated by the PSD signal and the lower pulse-height bias were converted into energy spectra after subtraction with flat background components. The efficiency vs. energy curves of the detectors were obtained by the calculation with a SCINFUL-R, which is revised version of the Monte Carlo code SCINFUL [4] and was verified to be accurate within ± 5 % up to 80 MeV [5]. Then the data have been corrected for the effect of neutron attenuation in the target, air, and the copper proton stopper using the ENDF/B-VI evaluated neutron data library. Finally, two neutron energy spectra obtained by two detectors were normalized with the integrated beam current and connected at 4 MeV to deduce whole energy spectrum.

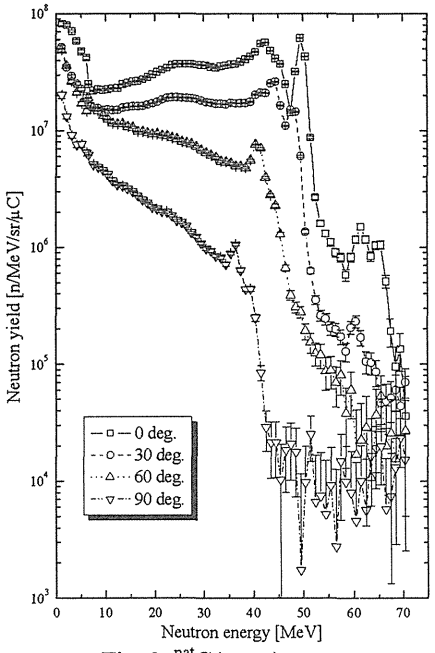



Fig. 2. $^{nat}$C(p, xn) neutron production cross section

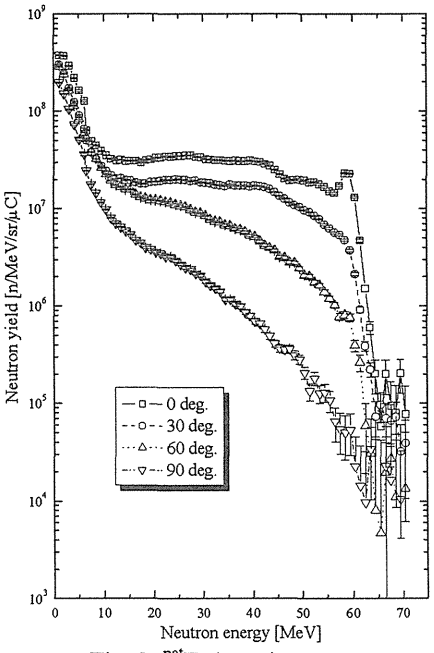



Fig. 3. $^{nat}$Fe(p, xn) neutron production cross section

## 5. Results and discussion

### 5.1 Experimental data

Figures 2 and 3 show the preliminary results of differential neutron production cross section for the $^{nat}$C and $^{nat}$Fe(p,xn) reactions at 70 MeV. The data should be confirmed for the absolute value.

In the C(p,n) spectrum shown in fig. 2, a sharp edges exist around 52 MeV due to the $^{12}$C(p,n) process which is the main components of the reaction with the Q-value of -18.1 MeV. On the other hand, there is also high energy component emitted from the $^{13}$C(p,n) process with the Q-value of -3.0 MeV from $^{13}$C whose natural content is about 1.1 %, The spectra show very strong angular dependence and energy-angle correlation because of light mass of C.

In the case of iron, as shown in fig. 3, the spectrum shows no marked structures. The neutron spectra show pronounced increase in lowest energy region because of evaporation neutrons with the yields larger than light nuclides like $^{nat}$C. The angular dependence of the spectra becomes stronger with increasing neutron energy.

### 5.2 Comparison with LA150

In this section, experimental TTY data are compared with the LA150 evaluated proton and neutron data libraries through the calculation by MCNPX [6] ver. 2.5e to take account of finite geometry and angular effects [7-8]. Figures 4 and 5 show the comparisons of our TTY experimental data and the calculations for $^{nat}$C, $^{nat}$Fe(p, xn) reactions.

In the case of $^{nat}$C(p, xn) reaction, two components ($^{12}$C, $^{13}$C(p, xn)) are visible similarly with the production cross sections, but the spectrum is generally much softer than the cross section itself. LA150 overestimates the experimental data in higher energy region and underestimates the energy region above around 50 MeV because LA150 lacks the contribution of $^{13}$C. In the case of $^{nat}$Fe(p, xn) reaction, the calculation reproduces the experimental data fairly well expect for those at backward angles.

Figure 6 and 7 show the comparisons of the present cross section data with the calculations. The calculations are normalized to the experimental data at 20 MeV. For $^{nat}$C(p, xn) reaction, LA150 underestimates experimental data in higher energy region similarly with the case of thick target. For $^{nat}$Fe(p, xn) reaction, LA150 reproduce experimental data generally well.

## 6. Conclusion and future plan

In this study, we measured the energy and angular double differential neutron emission cross sections for carbon and iron targets bombarded by 70 MeV protons using the CYRIC AVF cyclotron, Tohoku University. The data were obtained for neutron energy range down to 0.6 MeV and 0, 30, 60 and 90 deg.

The measured data were compared with calculations using MCNPX with LA150 data liberally. From these comparisons and past experimental data, LA150 reproduce generally well the experimental data while there is a room for improvement for high energy region.

We have plan to measure thin target neutron yields for Al, Cu, Ta and Pb(p, xn) reactions. In addition, we will upgrade the method of proton counting for the measurements of absolute neutron yield.

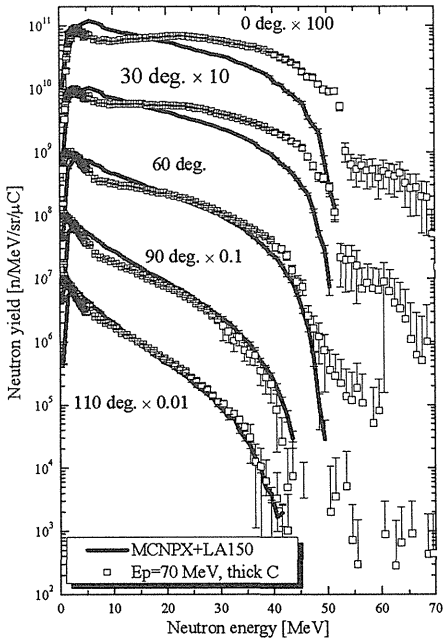



Fig. 4. Thick $^{nat}$C(p, xn)

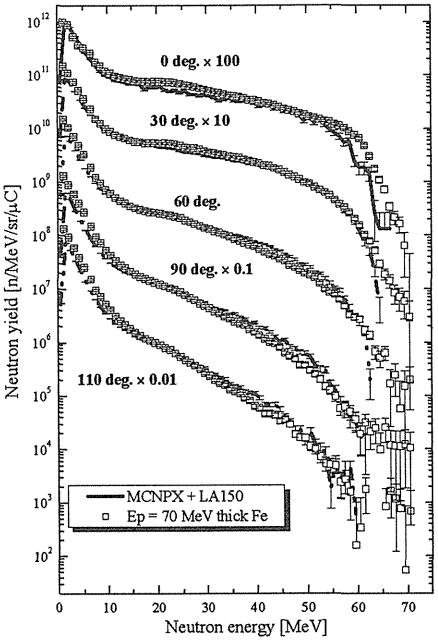



Fig. 5. Thick $^{nat}$Fe(p, xn)

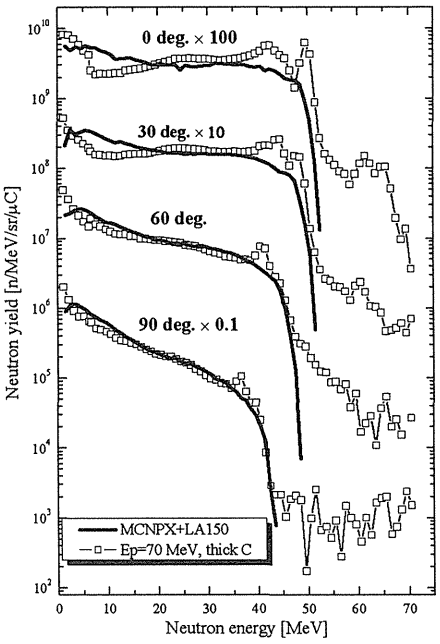



Fig. 6. $^{nat}$C(p, xn)

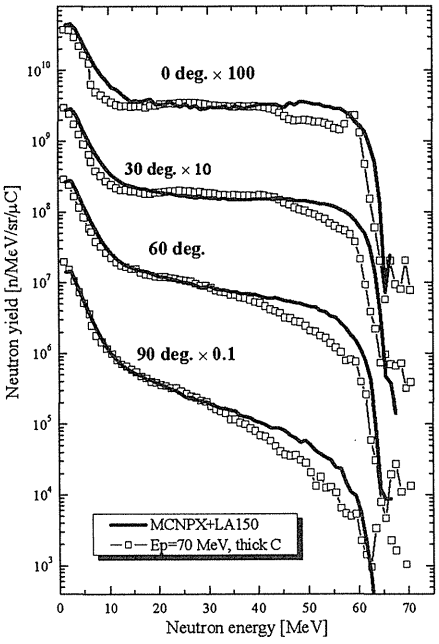



Fig. 7. $^{nat}$Fe(p, xn)

**References**

[1] T. Aoki, M. Baba, S. Yonai, *et al.*, "Measurement of Differential Thick-Target Neutron Yields of C, Al, Ta, W(p, xn) Reactions for 50-MeV Protons", *Nucl. Sci. Eng.*, **146**, 200, 2004.

[2] A. Terakawa, H. Suzuki, K. Kumagai, *et al.*, "New fast-neutron time-of-flight facilities at CYRIC", *Nucl. Instr. and Meth.*, **491**, 419, 2002.

[3] M. Ibaraki, M. Baba, S. Matsuyama, *et al.*, "Measurement of Double-differential Neutron Emission Cross Section of $^{6}$Li, $^{7}$Li and $^{9}$Be for 11.5 MeV and 18.0 MeV Neutrons", *J. Nucl. Sci. Technol.*, **35** [12], 843, 1998.

[4] J. K. Dickens. ORNL-6463. Oak Ridge National Laboratory, 1988.

[5] S. Meigo. "Measurements of the responce function and the detection efficiency of an NE213 scintillator for neutrons between 20 and 65 MeV", *Nucl. Instr. and Meth. in Phys. Res. A*, **401**, 365, 1997.

[6] L. S. Waters (Ed.), "MCNPX User's Manual version 2.5.e", LA-UR-04-0569, Los Alamos National Labolatory, 2004.

[7] M. B. Chadwick, P. G. Young, R. E. MacFarlane, *et al.*, "LA150 Documentation of Cross Sections, Heating, and Damage: Part A (Incident Neutrons)", LANL Accelerator Production of Tritium Program, 1999.

[8] M. B. Chadwick, P. G. Young, R. E. MacFarlane, et al., "LA150 Documentation of Cross Sections, Heating, and Damage: Part B (Incident Protons)", LANL Accelerator Production of Tritium Program, 1999.

JP0550269



# 3.9 Evaluations of Cross Sections on Zr, Nb, and W up to 200 MeV for JENDL High Energy File

Satoshi KUNIEDA*, Nobuhiro SHIGYO, and Kenji ISHIBASHI

*Department of Applied Quantum Physics and Nuclear Engneering, Kyushu University*

Nuclear data were evaluated on Zr isotopes, $^{93}$Nb and W isotopes for neutron- and proton-induced reactions up to 200 MeV. Optical model potential parameters were determined to give good agreements with experimental values of elastic-scattering, total, and total-reaction cross sections by the traditional phenomenological approach. The GNASH nuclear model code was used for evaluations of particle-production cross sections. Since the direct inelastic-scatterings induced by the excitations of giant resonances are not negligible for medium/heavy nuclei, the calculation was performed to take them into consideration. For composite-particle emission cross sections from pre-equilibrium states, semi-empirical models were utilized to give good agreements with experimental data. Evaluated cross sections were compared with experimental values and the LA150 evaluations.

## I. Introduction

The evaluated nuclear reaction data are required in the intermediate energy range for the designs of various accelerator-based application facilities. The program for completion of the JENDL High Energy File[1] is now ongoing under the Japanese Nuclear Data Committee to meet these needs.

In the design of accelerator-driven system, zirconium will be an useful material as a constituent of the nuclear fuel pellet or blanket tube. Niobium is one of the major elements as superconducting materials. Such compounds as NbTi or $Nb_3Sn$ are applied for the superconducting magnet of accelerators. For the sake of the design of spallation neutron source, tungsten is one of the candidate materials both for the beam window and the spallation target. Evaluating nuclear reaction data on these elements is essential for the recent and the future nuclear technologies.

Optical model potential parameters were searched to evaluate elastic-scattering, total and total-reaction cross sections, and to obtain the transmission coefficients for outgoing nucleons. The GNASH nuclear model code[2] was used for the evaluations of particle-production cross sections. Reasonable parameters were used for the Hauser-Feshbach, the exciton model, and DWBA calculations. In addition to the model calculations, the contribution of giant resonance excitation was considered by a simple way. The original GNASH code utilizes semi-empirical methods for computations of composite-particle (deuteron, triton, $^3$He and $\alpha$-particle) production cross sections from pre-equilibrium states. In spite of its frequent use for nuclear data evaluations in the intermediate energy range, a problem remained at least for $\alpha$-particle emissions from medium and heavy nuclei. The original functional forms for $\alpha$-knockout process were modified to give good agreements with experimental data in this work.

We made evaluations for such values of total, total-reaction, angular-differential elastic-scattering, energy-differential particle-production, and double-differential particle-production cross sections. Present results were compared with available experimental data and the LA150 evaluations.[3]

## II. Optical Model Analysis

The optical model is an efficient method to calculate angular-differential elastic-scattering, total and total-reaction cross sections. It also provides transmission coefficients for outgoing particles required in the statistical model. The phenomenological optical model potential (OMP) parameters were determined

* Corresponding author, Tel. +81-92-642-3765, E-mail: kuni@meteor.nucl.kyushu-u.ac.jp

in order that the model calculations could reproduce measured values for neutron and proton. The optical model calculations were performed with the ECIS-96 code.[4] To describe OMP parameters varying continuously on the incident energy, we assumed functional forms similar to that of Koning and Delaroche.[5] And local OMP parameters were obtained by an empirical way on the nuclei $A \sim 90$ and $\sim 184$, respectively. The experimental data for total-reaction cross sections were scant above $\sim$ 100 MeV. Values by the systematics derived from the TOTELA code[6] were employed as substitutional values for them. Evaluated cross sections are shown in **Figs. 1 - 4** with experimental data. [7–25]

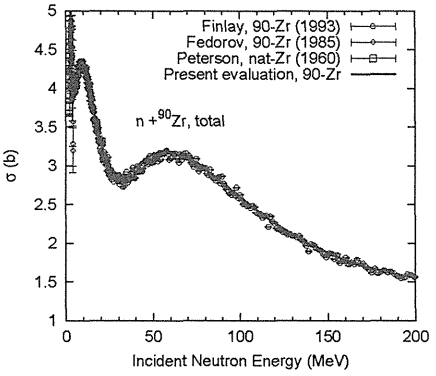



**Fig. 1** Present evaluations and experimental data[7–9] for neutron-induced total cross sections on $^{90}$Zr

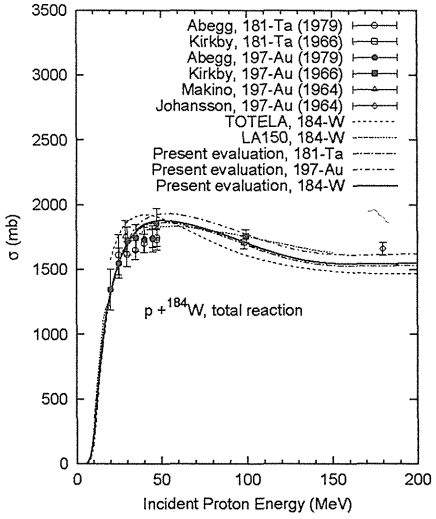



**Fig. 2** Present evaluations and experimental data[10–13] for proton-induced total-reaction cross sections on $^{181}$Ta, $^{184}$W, $^{197}$Au. The LA150[3] and TOTELA[6] prediction are also presented.

## III. Particle Production Cross Sections

The GNASH nuclear model code[2] was basically utilized for the evaluations of particle-production cross sections. In the code, the Hauser-Feshbach(H-F) statistical model is employed for the equilibrium decay, and the exciton model for the pre-equilibrium reaction. The inelastic scattering cross sections are also calculated by DWBA/CC. Productions of light particles such as neutron($n$), proton($p$), deuteron($d$), triton($t$), helium-3($^3$He), and alpha-particle($\alpha$) were considerd in this work. Because the exciton model could not calculate any emission-angle information by itself, double-differential cross sections were calculated by the Kalbach angular-distribution systematics.[26]

### 1. Nucleon production

In the H-F model, transmission coefficients of the emitted particles are derived from the optical model calculations. The local OMP parameters obtained in this study were used for neutron and proton. The global OMP of Daehnick *et al.*[27] was employed for deuteron, that of Becchetti-Greenlees[28] for triton and $^3$He, and that of Avrigeanu *et al.*[29] for alpha-particle. The level density parameter of Ignatyuk *et al.*[30] was adopted for almost all residual nuclei.

The exciton model has some adjustable parameters such as the single-particle state density parameter $g$, the average squared matrix element $|M|^2$, and the average effective potential well depth value $\overline{V}_{\rm eff}$. The standard value $A/13$ was used for $g$, and $|M|^2$ was determined on the basis of the original functional form.[2] The surface localization effect[31] of the pre-equilibrium reaction is commonly introduced in the exciton model, and also in the GNASH code. The the average effevtive well depth value $\overline{V}_{\rm eff}$ is the

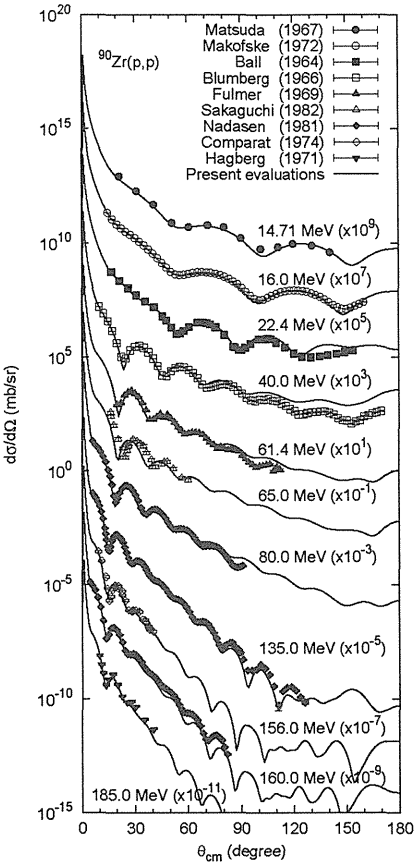



**Fig. 3** Present evaluations and experimental data[14–22] for proton-induced elastic-scattering differential cross sections on $^{90}$Zr

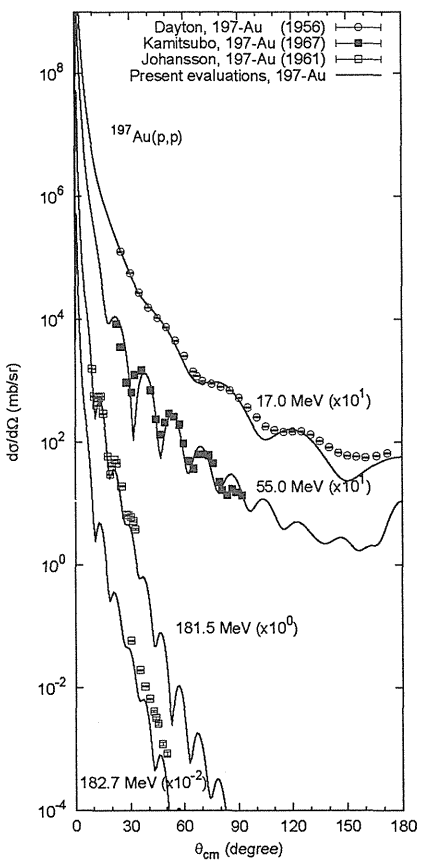



**Fig. 4** Present evaluations and experimental data[23–25] for proton-induced elastic-scattering differential cross sections on $^{197}$Au

only parameter for the effect, and the choice brings large influence on the slope of energy spectrum at around incident energy. Therefore, reasonable value was determined phenomenologically. Because neutron-induced experimental data have not been obtained above 26 MeV, the original effevtive well depth parameter[31] was used for our neutron-induced evaluations.

Inelastic scattering cross sections were calculated by DWBA. Required low-lying discrete level informations such as excitation energy, spin, parity, and deformation parameters were taken from RIPL[32] (They were the values used for JENDL-3.3). We also considered the excitations of the giant resonance, following the method of Demetriou *et al.*[33]

Evaluated double-differential cross sections are shown for $^{90}$Zr$(p, xn)$ in **Fig. 5**. Present evaluations agree with experimental data[34,35] in wide emission energies and angles. The LA150 evaluations are not shown, because they have no data for Zr isotopes. **Figure 6** stands for the results of $^{93}$Nb$(p, xp)$ double-differential cross sections. Both present and LA150 evaluations reproduce measurements[36–38] with enough accuracy. As presented in **Fig. 7** for $^{nat}$W$(p, xn)$ at 113 MeV, LA150 evaluations tend to overestimate experimental values[39] at around 100 MeV, while our evaluations give good agreements. It is ascribable to the difference of the average well depth value. The original $\overline{V}_{\rm eff}$ value[31] was employed in LA150, while $\overline{V}_{\rm eff} \sim 35$ MeV was used in this evaluation. The excitation of low-energy octupole giant resonance (LEOR) is not negligible especially on the heavy nuclei such as W isotopes. The result of $^{184}$W$(n, xn)$ energy-differential cross section is shown in **Fig. 8** at 26 MeV. The original GNASH can not reproduce experimental data,[40] since it dose not consider the giant resonance excitation. Present

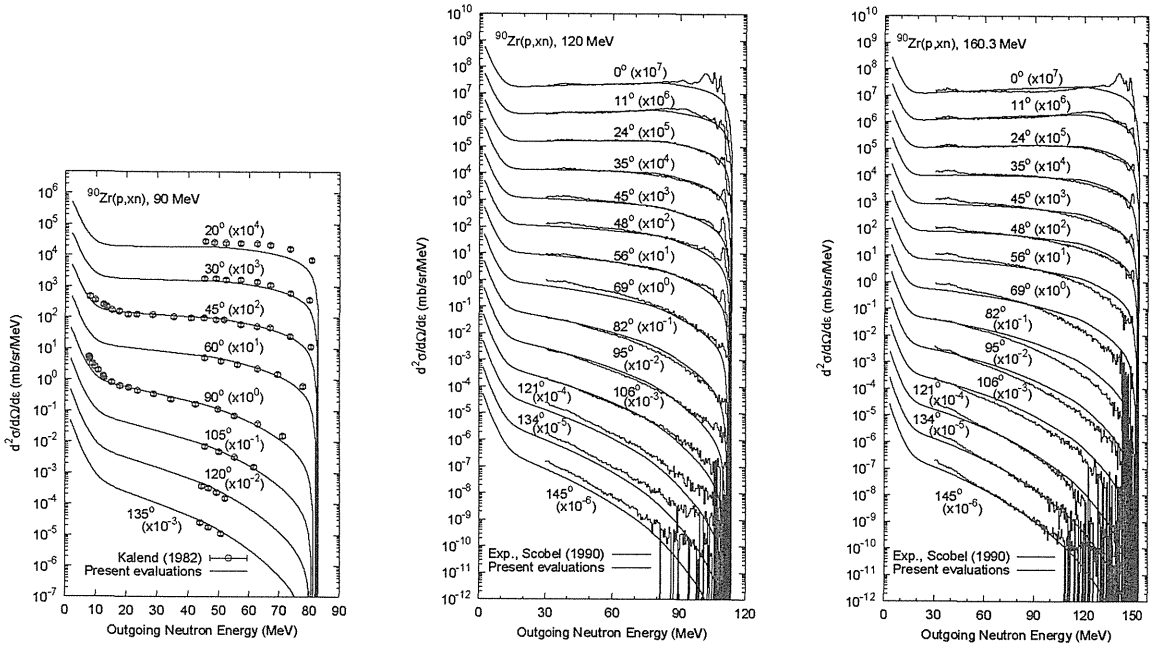



**Fig. 5** Present evaluations and experimental data[34,35] of double-differential cross sections for (*p,xn*) reactions on $^{90}$Zr at 90, 120 and 160.3 MeV.

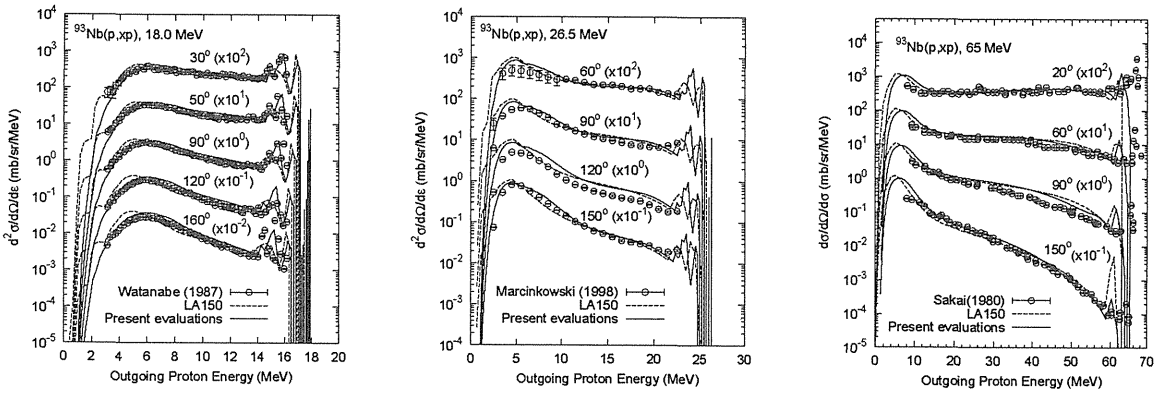



**Fig. 6** Present evaluations and experimental data[36–38] of double-differential cross sections for (*p,xp*) reactions on $^{93}$Nb at 18, 26.5 and 65 MeV. The LA150 evaluations[3] are also shown for the comparisons.

evaluation as well as LA150 agree with experimental data, because both evaluations made correction for LEOR excitaion.

## 2. Composite-particle production

We made cross section evaluations not only for the nucleon productions but also for the composite-particle ($d$, $t$, $^3$He, and $\alpha$) productions. The evaporation components were calculated by the H-F model. The GNASH employs the semi-empirical exciton model[41] for the pre-equilibrium emissions. The pickup and the $\alpha$-knockout model are considered in the semi-empirical model. **Figure 9** shows the evaluated results for $^{93}$Nb$(p, xd)$ double-differential cross sections at 65 MeV compared with experimental data[38] and the LA150 values. Our results give reasonable agreements with measurements in the overall emission energy and angle, while the LA150 results take relatively lower values at evaporation region. The difference of OMP produces such a tendency (The global OMP of Perey[42] was utilized in the LA150

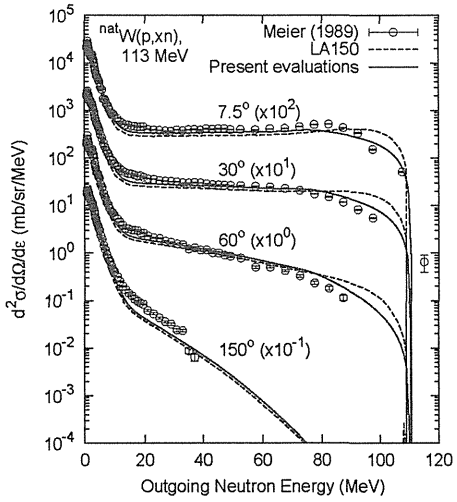



**Fig. 7** Present evaluations and experimental data[39] of double-differential cross sections for (*p,xn*) reaction on $^{nat}$W at 113 MeV. The LA150 evaluations[3] are also shown for the comparisons.

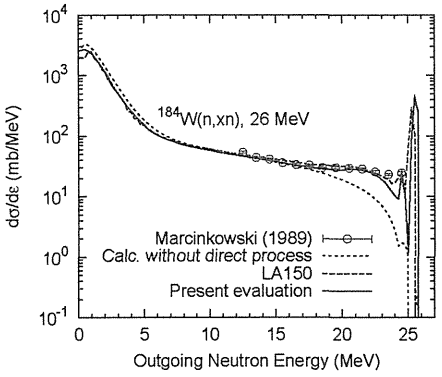



**Fig. 8** Present evaluation and experimental data[40] of energy-differential cross sections for (*n,xn*) reaction on $^{184}$W at 26 MeV. The GNASH calculation without direct reactions and the LA150 evaluation[3] are also shown for the comparison.

evaluations). We could easily confirm the validity of the pickup model. On the other hand, the original GNASH can not reproduce experimental data of $^{90}$Zr$(p, x\alpha)$ energy-differential cross sections at least on the medium and heavy nuclei as presented in **Fig. 10**. The problem arises from insufficient expression of the functional form for $\alpha$-knockout. In order to improve the calculation of $\alpha$-particle emission, the original $\alpha$-knockout functional form was modified to depend on the ratio of state densities $\omega(U)/\omega(U_{\max})$ rather than $\omega(U)/E^3$, where $E, U$, and $\omega(U)$ are the incident energy, excitation energy, and state density. And $\omega(U)$ was determined using a tentative functional form in order to get reasonable evaluated cross sections. As presented in Fig. 10, good results were obtained in this evaluation.

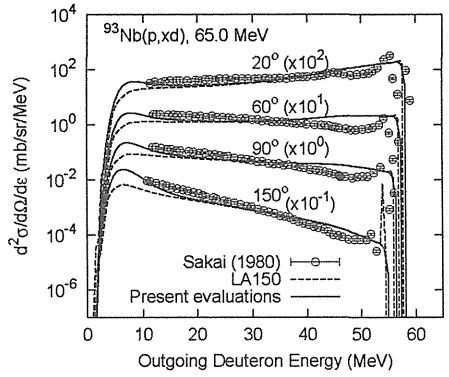



**Fig. 9** Present evaluations and experimental data[38] of double-differential cross sections for (*p,xd*) reaction on $^{93}$Nb at 65 MeV. The LA150 evaluations[3] are also presented for the comparisons.

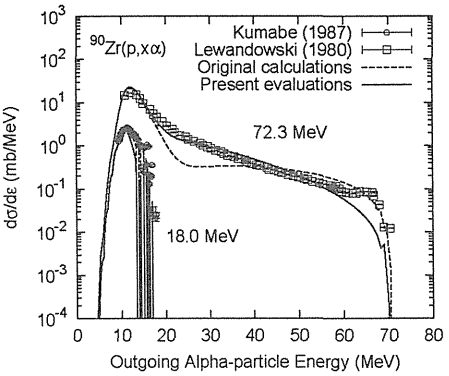



**Fig. 10** Present evaluations and experimental data[43,44] of energy-differential cross sections for (*p,xα*) reactions on $^{90}$Zr at 18 and 72.3 MeV. The original GNASH calculations are also shown.

## IV. Summary

Various cross sections were evaluated on Zr isotopes, $^{93}$Nb, and W isotopes for neutron- and proton-incidence. OMP parameters were determined by the phenomenological way. The GNASH nuclear model code was employed for the evaluations of particle-production cross sections. Reasonable parameters were utilized for the H-F, the exciton model, and DWBA calculations. Composite-particle emission cross sections were also evaluated using the H-F and the semi-empirical exciton model. The evaluated cross section data were obtained with enough accuracy.

**References**


1) T. Fukahori, Y. Watanabe, N. Yoshizawa, *et al.*, *J. Nucl. Sci. Technol. Suppl.*, **2**, 25 (2002).
2) P. G. Young, E. D. Arthur, and M. B. Chadwick, LAUR-88-382 (1988).
3) M. B. Chadwick, P. G. Young, S. Chiba, *et al.*, *Nucl. Sci. Eng.*, **131**, 293-328 (1999).
4) J. Raynal, IAEA SMR-9/8, 281 (1970).
5) A. J. Koning and J. P. Delaroche, *Nucl. Phys.*, A**713**, 231 (2003).
6) T. Fukahori and K. Niita, INDC(NDS)-416, 97 (2000).
7) R. W. Finlay, W. P. Abfalterer, G. Fink, *et al.*, *Phys. Rev.*, C**47**, 237 (1993).
8) M. B. Fedorov, V. D. Ovdienko, G. A . Smetanin, *et al.*, *Yad. Fiz.*, **69**(1) (1985).
9) J. M. Peterson, A. Bratenahl, and J. P. Stoering, *Phys. Rev.*, **120**, 521 (1960).
10) R. Abegg, J. Birchall, N. E. Davison, *et al.*, *Nucl. Phys.*, A**324**, 109 (1979).
11) P. Kirkby and W. T. Link, *Can. J. Phys.*, **44**, 1847 (1966).
12) M. Q. Makino, C. N. Waddell, and R. M. Eisberg, *Nucl. Phys.*, **50**, 145 (1964).
13) A. Johansson, U. Svandberg, and O. Sundberg, *Arkiv Fysik*, **19**, 527 (1961).
14) K. Matsuda, H. Nakamura, I. Nonoka, *et al.*, *J. Phys. Soc. Jap.*, **22**, 1311 (1967).
15) W. Makofske, G. W. Greenlees, *et al.*, *Phys. Rev.*, C**5**, 780 (1972).
16) J. B. Ball, C. B. Fulmer, and R. H. Bassel, *Pyhs. Rev.*, B**135**, 706 (1964).
17) L. N. Blumberg, E. E. Gross, A. Van Der Woude, *et al.*, *Phy. Rev.*, **147**, 812 (1966).
18) C. B. Fulmer, J. B. Ball, A. Scott, and M. L. Whiten, *Phys. Rev.*, **181**, 1565 (1969).
19) H. Sakaguchi, M. Nakamura, K. Hatanaka, A. Goto, *et al.*, *Phys. Rev.*, C**26**, 944 (1982).
20) A. Nadasen, P. Schwandt, P. P. Singh, W. W. Jacobs, *et al.*, *Phys. Rev.*, C**23**, 1023 (1981).
21) V. Comparat, R. Frascaria, N. Marty, *et al.*, *Nucl. Phys.*, A**221**, 403 (1974).
22) E. Hagberg, A. Ingemarsson, and B. Sundqvist, *Phys. Scrip.*, **3**, 245 (1971).
23) I. E. Dayton and G. Schrank, *Phys. Rev.*, **101**, 1358 (1956).
24) H. Kamitsubo, H. Ohnuma, K. Ono, A. Uchida, *et al.*, *J. Phys. Soc. Jap.*, **22**, 19 (1967).
25) A. Johansson, U. Svanberg, and P. E. Hodgson, *Arkiv Fysik*, **19**, 541 (1961).
26) C. Kalbach, *Phys. Rev.*, C**37**, 2350 (1988).
27) W. W. Daehnick, J. D. Childs, and Z. Vrcelj, *Phys. Rev.*, C**21**, 2253 (1980).
28) F. D. Becchetti Jr. and G. W. Greenlees, *Phys. Rev.*, **182**, 1190 (1969).
29) V. Avrigeanu, P. E. Hodgson, and M. Avrigeanu, *Phys. Rev.*, C**49**, 2136 (1994).
30) A. V. Ignatyuk, G. N. Smirenkin, and A. S. Tishin, *Sov. J. Nucl. Phys.*, 21, **255** (1975).
31) C. Kalbach, *Phys. Rev.*, C**32**, 1157 (1985).
32) http://www-nds.iaea.or.at/ripl .
33) P. Demetriou, A. Marcinkowski, and P. E. Hodgson, *Nucl. Phys.*, A**596**, 67 (1996).
34) A. M. Kalend, B. D. Anderson, A. R. Baldwin, *et al.*, *Phys. Rev. Lett.*, **46**, 226 (1981).
35) W. Scobel, M. Trabandt, M. Blann, B. A. Pohl, *et al.*, *Phys. Rev.*, C**41**, 2010 (1990).
36) Y. Watanabe, I. Kumabe, M. Hyakutake, *et al.*, *Phys. Rev.*, C**36**, 1325 (1987).
37) A. Marcinkowski, B. Marianski, Z. Moroz, *et al.*, *Nucl. Phys.*, A**633**, 446 (1998).
38) H. Sakai, K. Hosono, N. Matsuoka, *et al.*, *Nucl. Phys.*, A**344**, 41 (1980).
39) M. M. Meier, D. A. Clark, C. A. Goulding, *et al.*, *Nucl. Sci. Eng.*, **102**, 310 (1989). ; M. B. Chadwick and P. G. Young, *et al.*, Memo T-2-96-57, LANL (1996).
40) A. Marcinkowski, R. W. Finlay, J. Rapaport, *et al.*, *Nucl. Phys.*, A**501**, 1 (1989).
41) C. Kalbach, *Z. Phys.*, A**283**, 401 (1977).
42) C. M. Perey and F. G. Perey, *Phys. Rev.*, **132**, 755 (1963).
43) I. Kumabe, Y. Mito, M. Hyakutake, *et al.*, *Phys. Rev.*, C**35**, 467 (1987).
44) Z. Lewandowski, E. Loeffler, R. Wagner, *et al.*, *Lett. Nuo. Cim*, **28**, 15 (1980).

JP0550270



# 3.10 The Equation of State of Nuclear Matter, and Nuclei in Laboratories and in Neutron-Star Crusts

K. Oyamatsu[1] and K. Iida[2]
[1]*Department of Media Theories and Production, Aichi Shukutoku University*
*Nagakute, Nagakute-cho, Aichi-gun, Aichi 480-1197, Japan*
[2]*RIKEN BNL Reseach Center, Brookhaven National Laboratory*
*Upton, New York 11973-5000, U.S.A.*

email: oyak@asu.aasa.ac.jp

**Abstract**

We examine a relationship between the phenomenological equation of state (EOS) of nuclear matter near normal nuclear density and neutron-rich nuclei in laboratories and in neutron-star crusts. In this study, we use about 200 EOS ' s, which are systematically constructed in such a way as to provide a reasonable fit to empirical masses and radii of stable nuclei by simplified Thomas-Fermi calculations. As for neutron-rich nuclei in laboratories, matter radii and masses are shown to be functions of the symmetry energy density derivative coefficient $L$. We also find that the boundary density between the core and crust of neutron stars is a decreasing function of $L$. We expect that future systematic measurements of the matter radii and masses of neutron-rich nuclei could help deduce the $L$ value, which in turn could give useful information about nuclei in neutron-star crusts.

## 1 Introduction

The equation of state (EOS) of nuclear matter plays a key role in determining macroscopic nuclear properties of nuclei in laboratories and in neutron-star crusts. The saturation density and energy of symmetric nuclear matter, which consists of an equal number of neutrons and protons, are determined fairly well from masses and radii of stable nuclei, in which neutrons and protons are not very different in number. In the near future, a radioactive ion beam will enable us to measure nuclear masses and radii of heavy unstable nuclei with large neutron excess. This could open a door to explore extremely neutron-rich nuclei in neutron-star crusts. In order to make full use of the future experiment for the purpose of deducing asymmetric matter EOS, it is important to clarify what kind of EOS properties can be determined from stable nuclei, and what kind of EOS properties can not be determined from stable nuclei but from neutron-rich unstable nuclei. In this paper, we focus on the empirical saturation properties of the EOS that can be deduced from stable nuclei.

The energy per nucleon near the saturation point of symmetric nuclear matter is generally expressed as

$$w = w_0 + \frac{K_0}{18n_0^2}(n-n_0)^2 + \left[S_0 + \frac{L}{3n_0}(n-n_0)\right]\alpha^2. \tag{1}$$

Here $w_0$, $n_0$ and $K_0$ are the saturation energy, the saturation density and the incompressibility of symmetric nuclear matter. The neutron excess is defined as $\alpha = 1-2x$ using proton fraction $x$.

The parameters $S_0$ (the symmetry energy) and $L$ (the density symmetry coefficient) characterize the density dependent symmetry energy $S(n)$ at $n \approx n_0$ as;

$$S_0 = S(n_0), \tag{2}$$

$$L = 3n_0(dS/dn)_{n=n_0}, \tag{3}$$

From Eq. (1), the saturation density $n_s$ and energy $w_s$ of asymmetric nuclear matter with fixed proton fraction are given, up to the second order of $\alpha$, by

$$n_s = n_0 - \frac{3n_0 L}{K_0}\alpha^2, \tag{4}$$

$$w_s = w_0 + S_0\alpha^2. \tag{5}$$

## 2 Macroscopic description of nuclei

In constructing a macroscopic nuclear model, we begin with a simple expression for the bulk energy per nucleon [1, 4],

$$w = \frac{3\hbar^2(3\pi^2)^{2/3}}{10m_n n}(n_n^{5/3} + n_p^{5/3}) + (1-\alpha^2)v_s(n)/n + \alpha^2 v_n(n)/n, \tag{6}$$

where

$$v_s = a_1 n^2 + \frac{a_2 n^3}{1 + a_3 n} \tag{7}$$

and

$$v_n = b_1 n^2 + \frac{b_2 n^3}{1 + b_3 n} \tag{8}$$

are the potential energy densities for symmetric nuclear matter and pure neutron matter, and $m_n$ is the neutron mass. Here, replacement of the proton mass $m_p$ by $m_n$ in the proton kinetic energy makes only a negligible difference. Equation (6) can well reproduce the microscopic calculations of symmetric nuclear matter and pure neutron matter by Friedman and Pandharipande [2] and of asymmetric nuclear matter by Lagaris and Pandharipande [3]. Furthermore the expression can also reproduce phenomenological Skyrme Hartree-Fock and relativistic mean field EOS's.

The values of the parameters included in Eqs. (7) and (8) will be chosen below in such a way that they reproduce data on radii and masses of *stable* nuclei. In the limit of $n \to n_0$ and $\alpha \to 0$ ($x \to 1/2$), expression (6) reduces to the usual form (1) [4].

We describe a spherical nucleus of proton number $Z$ and mass number $A$ within the framework of a simplified version of the extended Thomas-Fermi theory [1]. We first write the total energy of a nucleus as a function of the density distributions $n_n(\mathbf{r})$ and $n_p(\mathbf{r})$ according to

$$E = \int d^3r n(\mathbf{r}) w\left(n_n(\mathbf{r}), n_p(\mathbf{r})\right) + F_0 \int d^3r |\nabla n(\mathbf{r})|^2 + \frac{e^2}{2}\int d^3r \int d^3r' \frac{n_p(\mathbf{r})n_p(\mathbf{r}')}{|\mathbf{r}-\mathbf{r}'|} + Nm_n + Zm_p, \tag{9}$$

where the first, second and third terms on the right hand side are the bulk energy, the gradient energy with an adjustable constant $F_0$, and the Coulomb energy, respectively. The symbol $N = A - Z$ denotes the neutron number. Here we ignore shell and pairing effects. We also neglect the contribution to the gradient energy from $|\nabla(n_n(\mathbf{r}) - n_p(\mathbf{r}))|^2$ ; this contribution makes only a little difference even in the description of extremely neutron-rich nuclei, as clarified in the context of neutron star matter [1].

For the present purpose of examining the macroscopic properties of nuclei such as masses and radii, it is sufficient to characterize the neutron and proton distributions for each nucleus by the central densities, radii and surface diffuseness different between neutrons and protons, as in Ref. [1]. We thus assume the nucleon distributions $n_i(r)$ $(i = n, p)$, where $r$ is the distance from the center of the nucleus, as

$$n_i(r) = \begin{cases} n_i^{\rm in}\left[1 - \left(\dfrac{r}{R_i}\right)^{t_i}\right]^3, & r < R_i, \\ 0\,, & r \geq R_i. \end{cases} \tag{10}$$

Here $R_i$ roughly represents the nucleon radius, $t_i$ the relative surface diffuseness, and $n_i^{\rm in}$ the central number density. The proton distribution of the form (10) can fairly well reproduce the experimental data for stable nuclei such as $^{90}$Zr and $^{208}$Pb [1].

About 200 sets of the EOS parameters $a_1$–$b_2$ and $F_0$ are determined in Refs. [4] from masses and radii of stable nuclei using the empirical values for nine nuclei on the smoothed $\beta$-stability line ranging $25 \leq A \leq 245$. All of the EOS's reproduce the input nuclear data almost equally. Although we fixed the $b_3$ value (1.58632 fm$^3$) in such a way as to reproduce pure neutron matter EOS by Friedman and Pandharipande [2], this artificial constraint on $b_3$ was found to make little difference in determining the the other EOS parameters [7].

As shown in Fig. 1, there is a strong empirical correlation between $S_0$ and $L$ [4],

$$S_0 \approx B + CL, \tag{11}$$

with $B \approx 28$ MeV and $C \approx 0.075$. It is noteworthy that a similar result, $B = 29$ MeV and $C = 0.1$, was obtained from various Hartree-Fock models with finite-range forces by Farine et al. [5]. This correlation is the only information for asymmetric nuclear matter that can be obtained from stable nuclei. This is the reason why there is significant difference in the behavior at large neutron excess among the models for asymmetric matter EOS although they reproduce the properties of stable nuclei.

As for the saturation energy and density of symmetric nuclear matter, $w_0 = -16.1 \pm 0.2$ and $n_0 \approx 0.16$ while there is a weak correlation between $n_0$ and $K_0$ [4]. This is a feature found among non-relativistic phenomenological Skyrme Hartree-Fock EOS's (see Fig. 4 of Ref. [6]).

In Fig. 2, the uncertainties in $L$ and $K_0$ are represented as a band. The upper bound reaches a large value of $L$, which increases with increase in $K_0$.

Hence it is interesting to examine how these uncertainties in $L$ and $K_0$ reflect nuclear structure calculations of neutron-rich nuclei in laboratories and in neutron stars.

## 3 Neutron-rich nuclei in laboratories

Using the nearly 200 EOS's, we calculate masses and radii of extremely neutron-rich heavy nuclei, which could be produced in laboratories in the future. For example, Figures 3 and 4 show the root-mean-square matter radius and mass excess of $^{80}$Ni ($N = 52, Z = 28, Z/A \approx 0.35$). We see clearly that the matter radius and mass of extremely neutron-rich nuclei are dependent on $L$. This reflects the fact that the saturation density and energy, which naively communicate with the radius and mass, are approximately linear functions of $L$ (see Eqs. (4), (5), (11)) [4, 8].

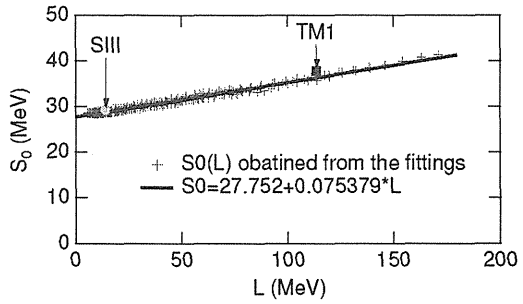



Figure 1: The correlation between $S_0$ and $L$ deduced from the mass and radius data for stable nuclei.

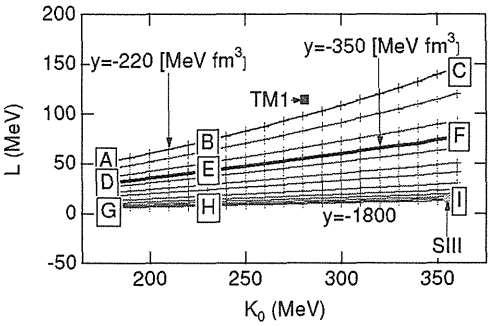



Figure 2: The $(L, K_0)$ values consistent with the mass and radius data for stable nuclei.

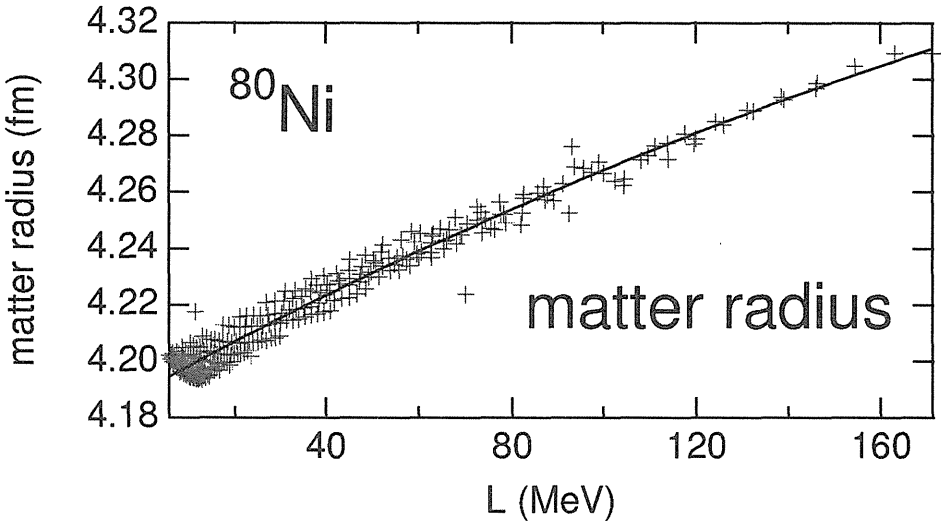



Figure 3: The calculated matter radius of $^{80}$Ni.

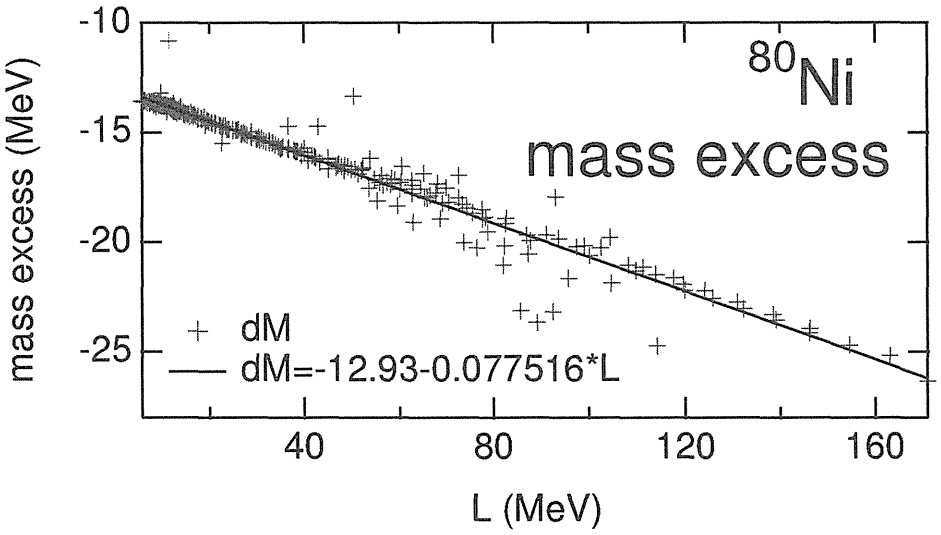



Figure 4: The calculated mass excess of $^{80}$Ni.

## 4 Inner boundary of a neutron star crust

It is also interesting to explore extremely neutron-rich nuclei in neutron-star crust, where nuclei are embedded in a gas of dripped neutrons and the nuclei may take exotic pastalike shapes. Among various interesting properties, we calculate the boundary density between the crust and the core, at which the nuclei melt into uniform matter. Here, we examine how the uncertainties of the EOS reflect the determination of the boundary density. Figure 5 shows the approximate boundary density obtained from the nearly 200 EOS's. In this calculation we follow a line of argument of Pethick et al. [9]. From Fig. 5, we see clearly that the boundary density is a decreasing function of $L$. This behvaior may be understood from the fact that $L$ acts to make shallow the single particle potential depth of bound protons in nuclei in neutron-star crusts.

## 5 Summary

We examine the macroscopic properties of neutron-rich nuclei in laboratories and in neutron-star crusts using about 200 sets of the EOS parameters that are systematically obtained from fitting to masses and radii of stable nuclei. In the series of our studies, we adopt a simplified Thomas-Fermi model allowing for large uncertainties in the $K_0$ and $L$ values.

As for the relationship between the EOS parameters, the saturation density density $n_0$ has a weak $K_0$ dependence while the saturation energy $w_0$ is essentially constant. There is a strong correlation between $S_0$ and $L$ : $S_0 = 28 + 0.075L$ (MeV). However, the $L$ value can not be constrained from stable nuclei although the upper bound of $L$ can be estimated as an increasing function of $K_0$. Since there remains uncertainties in $L$ and $K_0$, our EOS models vary significantly at large neutron excess, even though they reproduce the properties of stable nuclei almost equally.

Using the EOS's obtained for various sets of the $L$ and $K_0$ values, we systematically examine the macroscopic properties of extremely neutron-rich nuclei in laboratories and in neutron stars. As for laboratory nuclei, the predicted matter radii and masses are dependent on $L$. This $L$

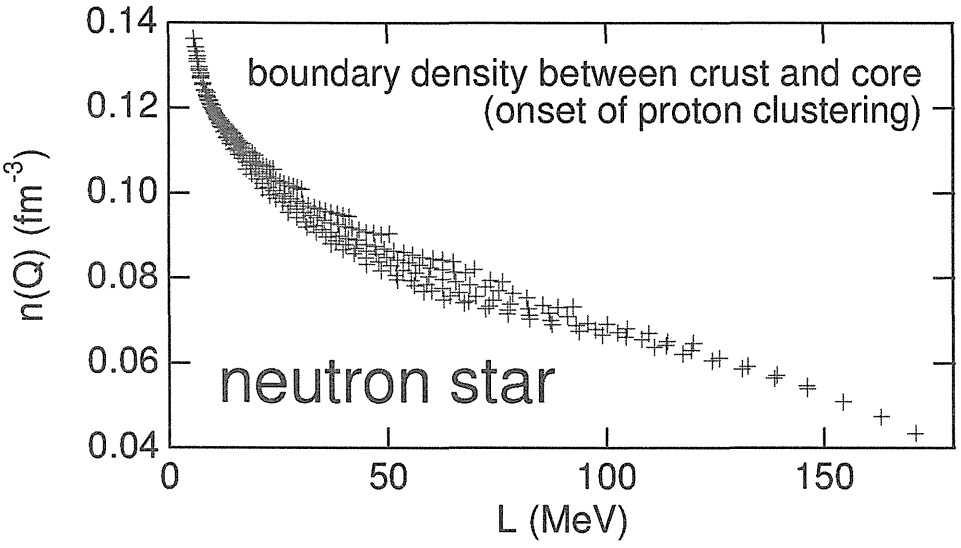



Figure 5: The crust-core boundary density in a neutron star.

dependence comes from the fact that the saturation energy and density of asymmetric matter are almost linear functions of $L$. As for nuclei in neutron-star crusts, we examine the crust-core boundary density, where nuclei melt into uniform matter. It is found that the density is a decreasing function of $L$. This is relevant to the fact that $L$ controls the proton potential depth in nuclei.

From these results, we conclude that future systematic measurements of the matter radii and masses of neutron-rich nuclei could help deduce the $L$ value, which in turn could give useful information about nuclei in neutron star crusts.

## References

[1] K. Oyamatsu, Nucl. Phys. A 561 (1993) 431.

[2] B. Friedman, V.R. Pandharipande, Nucl. Phys. A 361 (1981) 502.

[3] I.E. Lagaris, V.R. Pandharipande, Nucl. Phys. A 369 (1981) 470.

[4] K. Oyamatsu, K. Iida, Prog. Theor. Phys. 109 (2003) 631.

[5] M. Farine, J.M. Pearson, B. Rouben, Nucl. Phys. A 304 (1978) 317.

[6] J.P. Blaizot, Phys. Rep. **64**, 171 (1980).

[7] K. Oyamatsu, K. Iida, Proc. 2003 Symposium on Nuclear Data, JAERI-Conf 2004-005, (2004), 184.

[8] K. Oyamatsu, I. Tanihata, Y. Sugahara, K. Sumiyoshi, H. Toki, Nucl. Phys. A 634 (1998) 3.

[9] C.J. Pethick, D.G. Ravenhall, C.P. Lorenz, Nucl. Phys. A 584 (1995) 675.

JP0550271



## 3.11 Problem on Unresolved Resonance Data in ENDF/B-VI, etc.

Chikara KONNO
*Center for Proton Accelerator Facilities, Japan Atomic Energy Research Institute*
*Tokai-mura, Naka-gun, Ibaraki-ken 319-1195 JAPAN*
e-mail : konno@cens.tokai.jaeri.go.jp

At the 2003 symposium on nuclear data it is pointed out that the self-shielding correction for the unresolved resonances of many nuclei in JENDL-3.3 is too large around the upper energy of the unresolved resonance region. It is investigated whether ENDF/B-VI, BROND-2.2 and CENDL-2.1 have the same problem for unresolved resonance data as JENDL-3.3. More than half of nuclei with unresolved resonance data in ENDF/B-VI, BROND-2.2 and CENDL-2.1 have the same problem as JENDL-3.3.

### 1. Introduction

At the 2003 symposium on nuclear data the followings are pointed out [1];

1) Elastic scattering cross section data of many nuclei with self-shielding correction in JENDL-3.3 [2] have a large strange ramp at the upper energy of the unresolved resonance region as shown in Fig. 1.
2) Larger average reduced neutron widths are required to obtain average elastic scattering cross sections in the unresolved resonance region but they cause larger self-shielding correction in many nuclei of JENDL-3.3 with unresolved resonance data.
3) The average reduced neutron widths or the upper energy of the unresolved resonance region in JENDL-3.3 should be checked.

Other evaluated nuclear data libraries may have the same problems. ENDF/B-VI [3], BROND-2.2 [4] and CENDL-2.1 [5] are investigated in this paper.

### 2. Method

The check procedure is the same as that described in Ref. 1;

1) Matxs files of ENDF/B-VI, BROND-2.2 and CENDL-2.1 with unresolved resonance data were produced with the NJOY [6] code in the same conditions as MATXSLIB-J33 [7].
2) Multigroup libraries of elastic scattering cross section with self-shielding correction for each nuclei [100 % abundance] from the matxs files of ENDF/B-VI, BROND-2.2 and CENDL-2.1 were made with the TRANSX [8] code.
3) Multigroup elastic cross section data with self-shielding correction were checked.
4) If the elastic cross section with self-shielding correction of a nucleus has a large strange ramp at the upper energy of the unresolved resonance region, it is judged that the unresolved resonance data of the nucleus have some problems.

### 3. Nuclei with unresolved resonance data in ENDF/B-VI

All the data of nuclei (~ 80) with unresolved resonance data in ENDF/B-VI were examined. As a result, it is found out that the self-shielding correction for elastic scattering cross sections in unresolved resonance region is too large around the upper energy of the unresolved resonance region for about half of the nuclei (~ 40) as shown in Figs. 2 and 3. Table 1 summarizes all the nuclei with unresolved reso-

nance data in ENDF/B-VI. In this table unresolved resonance data of nuclei with bold character may have inadequate average reduced neutron widths or the upper energy of the unresolved resonance region.

## 4. Nuclei with unresolved resonance data in BROND-2.2

All the data of nuclei (~ 70) with unresolved resonance data in BROND-2.2 were examined. It is found out that the self-shielding correction for elastic scattering cross sections in unresolved resonance region is too large around the upper energy of the unresolved resonance region for about half of the nuclei (~ 40) as shown in Figs. 4 and 5. Table 2 summarizes all the nuclei with unresolved resonance data in BROND-2.2. In this table unresolved resonance data of nuclei with bold character have inadequate average reduced neutron widths or the upper energy of the unresolved resonance region.

## 5. Nuclei with unresolved resonance data in CENDL-2.1

All the data of nuclei with unresolved resonance data in CENDL-2.1 were examined. It seems that the self-shielding correction for elastic scattering cross sections in unresolved resonance region is too large around the upper energy of the unresolved resonance region for about half of the nuclei as shown in Figs. 6 and 7. Table 3 summarizes all the nuclei with unresolved resonance data in CENDL-2.1. In this table unresolved resonance data of nuclei with bold character have inadequate average reduced neutron widths or the upper energy of the unresolved resonance region.

## 6. Summary

It is investigated whether ENDF/B-VI, BROND-2.2 and CENDL-2.1 have the same problem for unresolved resonance data as many nuclei in JENDL-3.3 ; elastic scattering cross section data of many nuclei with self-shielding correction have a large strange ramp at the upper energy of the unresolved resonance region since the average reduced neutron widths or the upper energy of the unresolved resonance region are inadequate. The problem for unresolved resonance data appears not only in many nuclei of JENDL-3.3, but also in many nuclei of ENDF/B-VI, BROND-2.2 and CENDL-2.1. All the unresolved resonance data in ENDF/B-VI, BROND-2.2 and CENDL-2.1 should be rechecked and revised by considering self-shielding correction in the next version.

## Acknowledgments

This work was supported in part by Research Committee on Adequacy of Radiation Shielding in Atomic Energy Society of Japan and the Shielding Integral Test Working Group in Japanese Nuclear Data Committee.

## References

[1] Konno C. : JAERI-Conf 2004-005, p. 236 (2004).
[2] Shibata K., et al. : J. Nucl. Sci. Tech. 39, 1125 (2002).
[3] Cross Section Evaluation Working Group : BNL-NCS-17541 (ENDF-201) (1991).
[4] Manokhin V.N., et al. : IAEA-NDS-90 Rev. 8 (1994).
[5] Liang Qichang, et al. : IAEA-NDS-60 Rev. 3 (1996).
[6] MacFarlane R.E. and Muir D.W. : LA-12740-M (1994).
[7] Kosako K., et al. : JAERI-Data/Code 2003-011 (2003).
[8] MacFarlane R.E. : LA-12312-MS (1993).

Table 1 Nuclei with unresolved resonance data in ENDF/B-VI.

| |
|---|
| **Zr-91, Mo-nat**, Tc-99, **Ru-101, -102, Rh-103**, Ag-109, **Cd-106, -108, -110, -112, -114, -116, Xe-131, Nd-145, Pm-147**, Sm-147, **-149, -150**, -151, **-152, Eu-151**, -152, **-153**, -154, **Gd-152, -154**, -155, -157, **Dy-164, Er-167**, Hf-nat, **-174**, -176, -177, **-178**, -179, **-180, Ta-181, -182**, W-nat, **-182, -183, -184, -186,Re-185, -187, Ir-191, -193**, Th-232, Pa-231, 233, **U-232**, -233, -234, -235, -236, -237, -238, Np-238, **Pu-236, ,-238**, -239, **-240**, -241, **-242, -243, -244**, Am-241, -242, -242m, -243, **Cm-242**, -243, -244, -245,-246, -247, -248, Bk-249, Cf-249, **-250, -251, -252**, -253, **Es-253** |

**Bold** : Unresolved resonance data have some problems.

Table 2 Nuclei with unresolved resonance data in BROND-2.2.

| |
|---|
| Cr-50, -53, Fe-54, -56, -57, -58, NI-58, -60, -61, -62, -64, **Zr-nat, -90, -91, -92, -93, -94, -95, -96, Nb-93, Tc-99, Ru-101, -102, -104, Rh-103, Pd-105, -106, -107, -108, Ag-109, Sn-nat, I-129, Xe-131, Nd-143, -145**, Pm-147, Sm-nat, -147, **-148**, -149, **-150**, -151, **-152, -154**, Eu-153, **Gd-155, -157, Er-162, -164, -166, -167**, -168, -170, Ta-181, **W-182**, -183, **-184, -186, Re-nat**, Th-232, U-233, -235, -238, Pu-238, -239, **-240, -242**, Am-241, -242m, -243, Cm-242, **-244** |

**Bold** : Unresolved resonance data have some problems.

Table 3 Nuclei with unresolved resonance data in CENDL-2.1.

| |
|---|
| Zr-nat, **Mo-nat, Ag-nat, -107, -109**, In-nat, **Lu-nat, Hf-nat**, Ta-181, U-235, -238, Np-237, Pu-239, -240, **Am-241, Bk-249**, Cf-249 |

**Bold** : Unresolved resonance data have some problems.

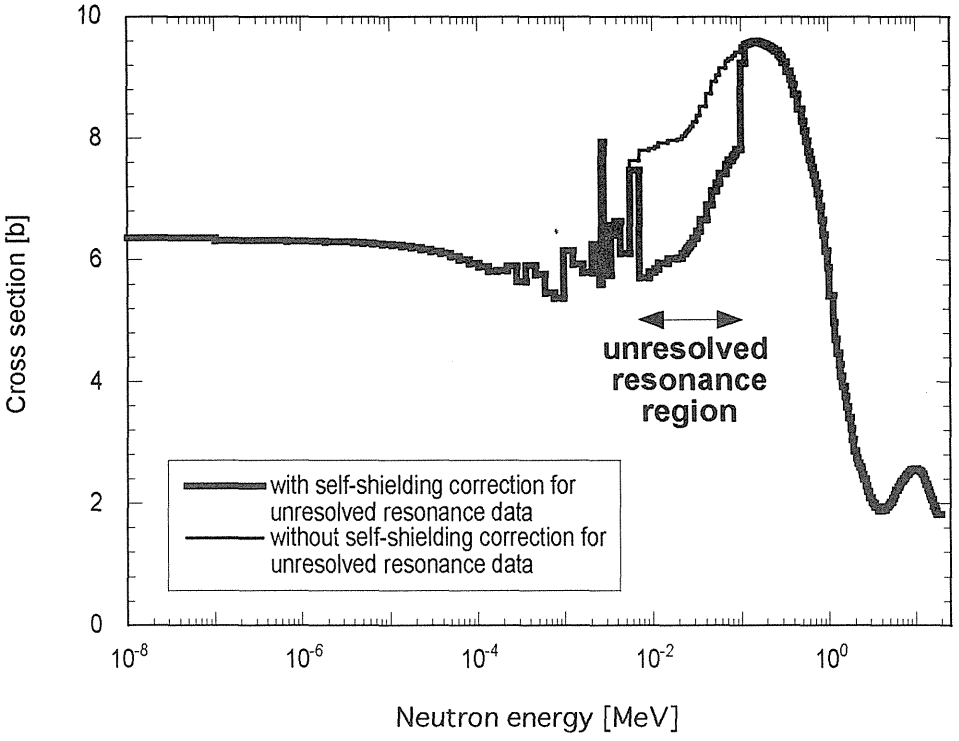



Fig. 1 Self-shielding corrected elastic scattering cross section of $^{93}$Nb in JENDL-3.3.

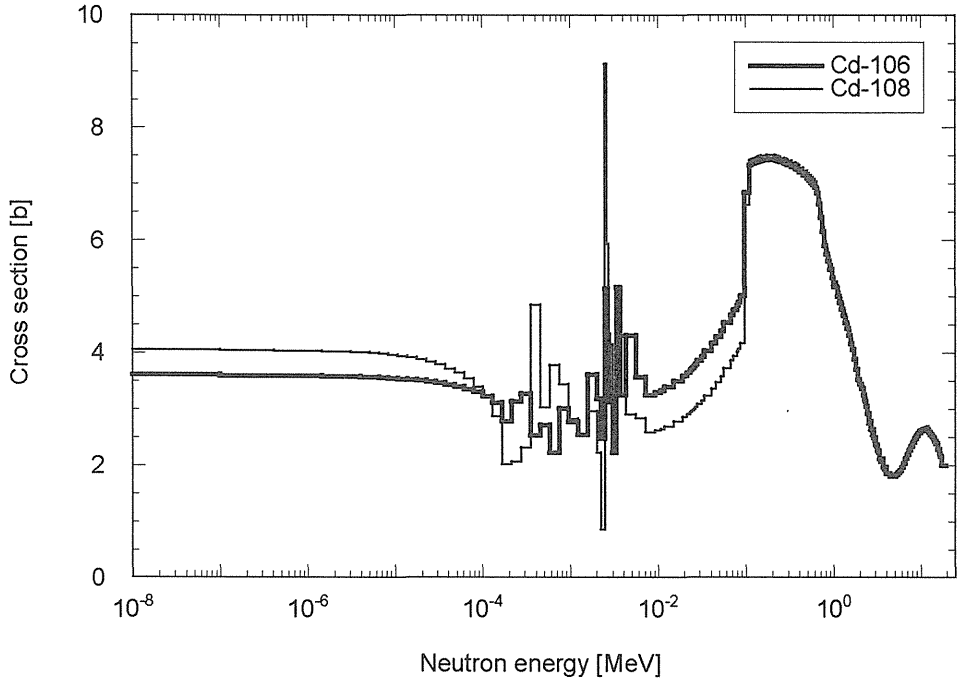



Fig. 2 Self-shielding corrected elastic scattering cross section of $^{106}$Cd and $^{108}$Cd in ENDF/B-VI.

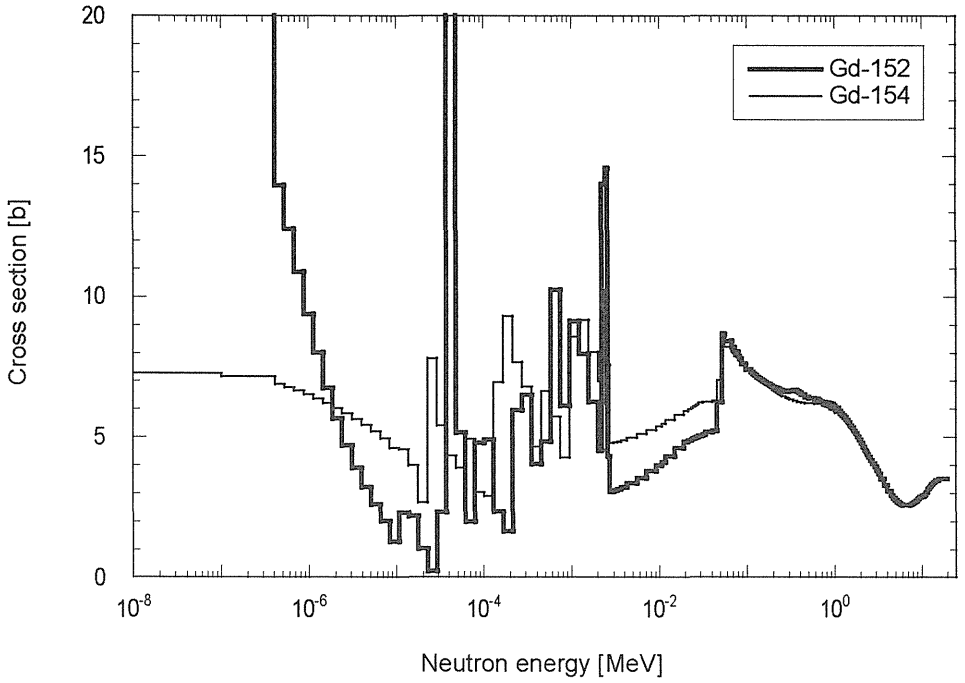



Fig. 3 Self-shielding corrected elastic scattering cross section of $^{152}$Gd and $^{154}$Gd in ENDF/B-VI.

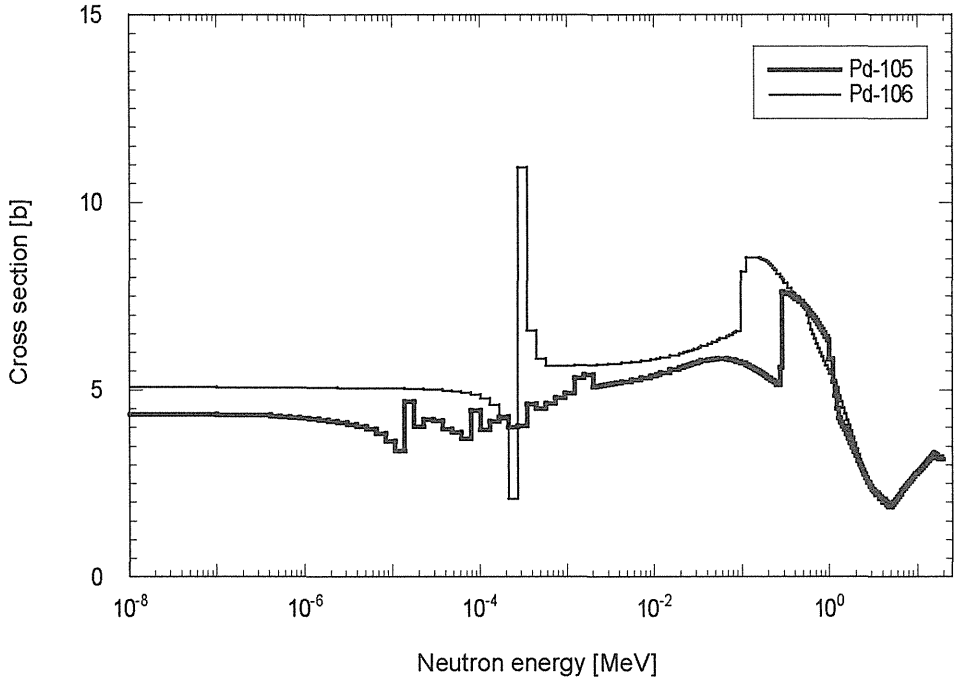



Fig. 4 Self-shielding corrected elastic scattering cross section of $^{105}$Pd and $^{106}$Pd in BROND-2.2.

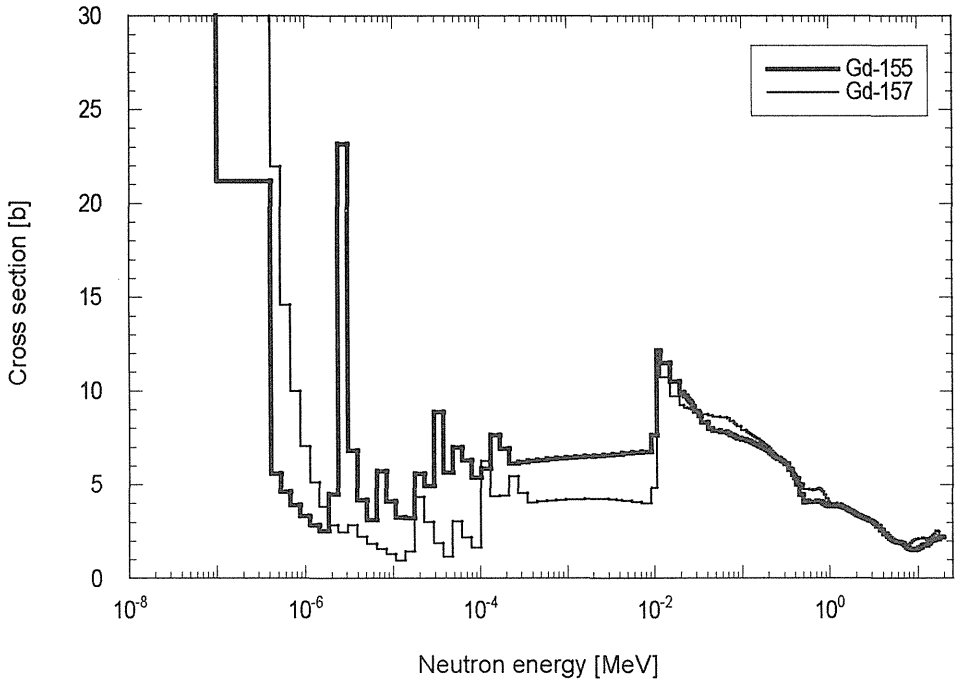



Fig. 5 Self-shielding corrected elastic scattering cross section of $^{155}$Gd and $^{157}$Gd in BROND-2.2.

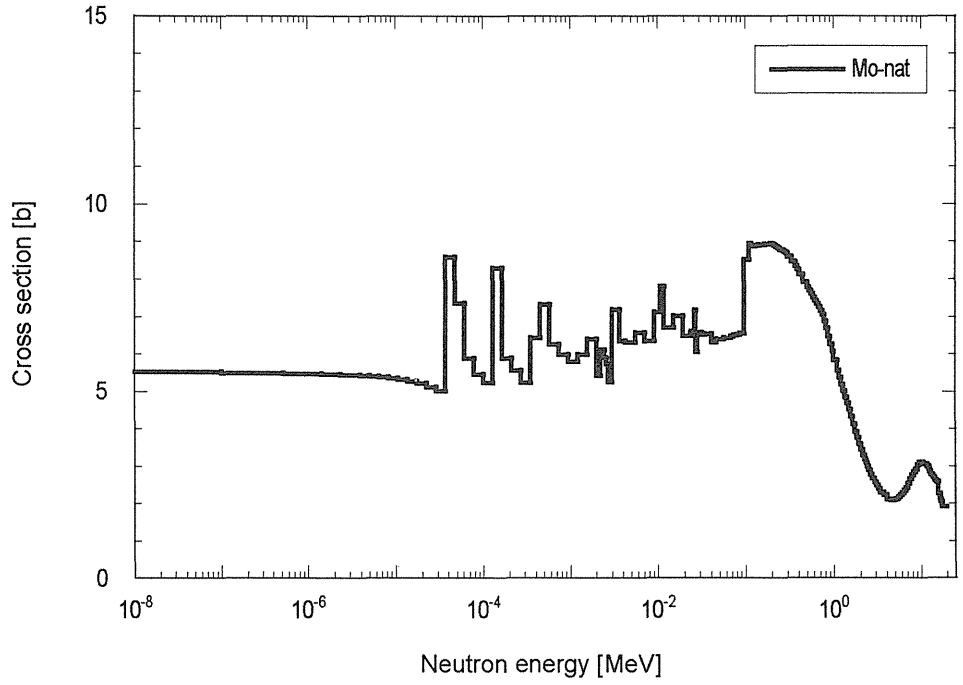



Fig. 6 Self-shielding corrected elastic scattering cross section of Mo-nat in CENDL-2.2.

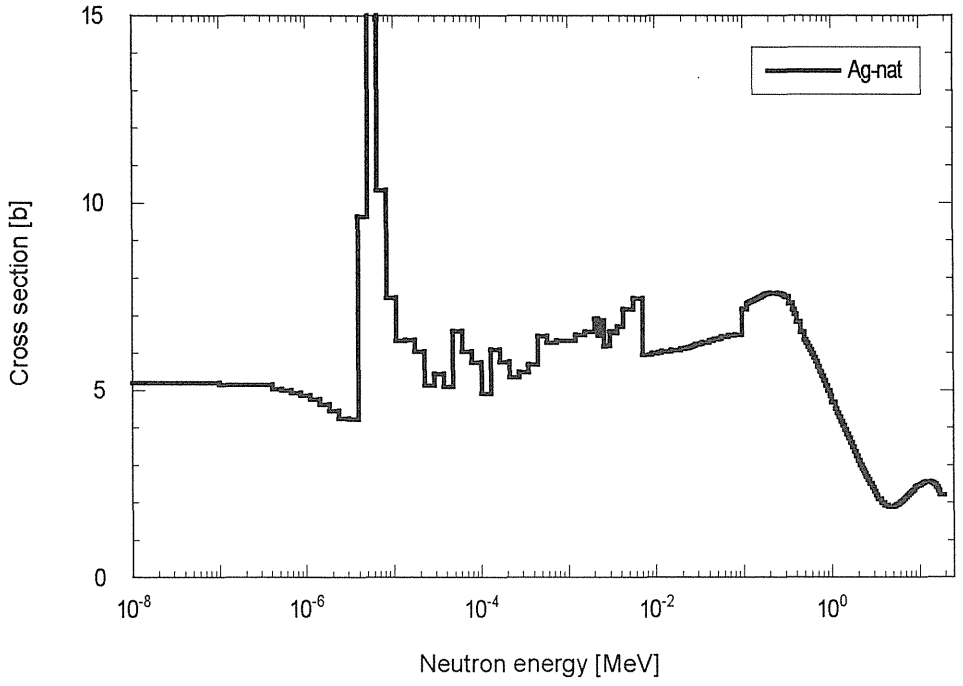



Fig. 7 Self-shielding corrected elastic scattering cross section of Ag-nat in CENDL-2.2.

JP0550272



# 3.12 TAGS and FP Decay Heat Calculations(Ⅱ) -Impact on the LOCA Condition Decay Heat-

Akira HONMA, Tadashi YOSHIDA

*Musashi Institute of Technology, Tamazutsumi 1-28-1, Setagaya-ku, Tokyo 158-8557, Japan*

e-mail: yos@ph.ns.musashi-tech.ac.jp

Introducing the TAGS (Total Absorption Gamma-ray Spectrometer) data, we calculated the FP decay heat for Pu-239, Pu-241, U-233 and U-235 after one-year irradiation. In order to see the impact of the introduction of the TAGS data on LOCA (Loss of Coolant Accident) analysis in LWRs, those results were compared with the calculations based on the original data libraries such as JENDL, JEF-2.2 and ENDF/B-VI which are widely used in the summation calculation of the FP decay heat. It was concluded that the decay heat calculation introducing TAGS data dose not exert any decisive impact on the LOCA analysis from the practical point of view. Further study is, however, required to validate the reliability of the TAGS data as the input of summation calculations.

## 1. Introduction

Summation calculations are widely used to evaluate the FP (fission product) decay heat after shutdown of power reactors. Those calculations, however, often suffer from the so-called "pandemonium problem"[1],[2]. Suppose that the $\beta$-transitions feed the very high energy levels of the daughter nuclide. These $\beta$-strengths are easily overlooked in the experimental or the evaluational procedure because of the weak and complicated nature of the $\gamma$-cascades which follow the $\beta$-transition. Then the calculation of the average $\beta$-decay energy ($E_\beta$) from this kind of data leads to overestimation and $\gamma$-decay energy ($E_\gamma$) to underestimation. In order to circumvent this problem[2], the gross theory of $\beta$-decay was applied in generating the JENDL[3] and the ENDF/B FP decay data files. As a result, the summation calculations based on JENDL and ENDF/B-VI are in very good agreement with measurements [4],[5].

In 1990's, a total absorption $\gamma$-ray spectrometer (TAGS) was developed and applied to the short-lived FP nuclides by the INEL (Idaho National Engineering Laboratory) group[6]. They measured the $\beta$-feeding as a function of the excitation energy of the daughter nuclide for 44 isotopes of 12 FP elements (Rb, Sr, Y, Cs, Ba, La, Ce, Pr, Nd, Pm, Sm and Eu) [7]. The TAGS data is, in principle, thought to be free from the pandemonium problem. In reality, however, the major libraries such as JENDL, ENDF/B and JEF have not adopted the TAGS data up to now. In this paper we try to see the impact of introducing the TAGS data on LOCA (Loss of Coolant Accident) analysis of LWRs by calculating the FP decay heat after one-year irradiation and comparing the results.

## 2. Total Absorption Gamma-ray Spectroscopy

The $\gamma$ -ray detector used by the Greenwood group was a 25.4 cm diameter × 30.5 cm long NaI(Tl) scintillator installed at the INEL on-line mass separator [7]. In principle all of the $\gamma$ -rays emitted in a cascade accompanied by a de-excitation of a certain level deposit all of their energies into the scintillator giving the level energy to which the $\beta$ -transition takes place. In this way the TAGS gives the level energy as the pulse energy and the $\beta$ -feeding rate as the pulse height at the same time. These are exactly the data required to calculate the average $\beta$ - and $\gamma$ - ray energies per one $\beta$ -decay of the parent nucleus. Therefore, if the TAGS measurements are carried out in an ideal way, the average $\beta$ - and $\gamma$ - ray energies ($E_\beta$ and $E_\gamma$) obtained from them are free from the pandemonium problem. In fact, however, there exist several difficulties which might make the TAGS data inadequate as the ideal source of information. These are the photon losses, the $\beta$ -particle contamination, the finite energy resolution of the detector, the needs for the complicated theoretical corrections and so on. Partly because of these difficulties, JENDL, ENDF/B-VI and JEF had not adopted the TAGS data as the basis of the $E_\beta$ and $E_\gamma$ calculations.

## 3. Comparison with Integral Measurement

In the previous paper[9], FP decay heat calculations based on JENDL, ENDF/B-VI and JEF-2.2[8] were carried out introducing TAGS data and the results were compared with the integral experiment. Introduction of the TAGS data was carried out by replacing the original $E_\beta$ and $E_\gamma$ values with those calculated from the TAGS data for the 44 isotopes given in the previous section. Here we briefly review the effect of TAGS introduction taking Pu-239 as an example. As shown in Fig.1 and 2, the effect of introducing the TAGS data for the 44 isotopes is not remarkable for the $\beta$ -ray component of the decay heat after a burst fission. Almost all the calculations keep fairly good consistency with the integral experiment at the Yayoi reactor[4] except JEF2.2 in the cooling-time range around several thousands seconds.

In case of the $\gamma$ -ray component, the underestimation seen in the JEF-2.2 case is conspicuous (Fig.3.), where any theoretical correction was not applied for the pandemonium effect. On the other hand the improvement by introducing the TAGS data is remarkable in the JEF-2.2 calculation as one can see in Fig.4. In the cases of JENDL and ENDF/B-VI, where the correction applied on the basis on gross theory, the good agreement with the integral measurement (Fig.3) is no more maintained and overestimation appears in the cooling-time range from 20 to 200 s (Fig.4).

As for the total decay heat, or the $\beta+\gamma$, is concerned, almost all of the calculations agree with the Yayoi measurement within the error bars both before and after the TAGS-data introduction (Figs. 5 and 6).

## 4. Impact on the LOCA Condition Decay Heat

In the preceding section, the decay heat after a burst fission have been compared with the

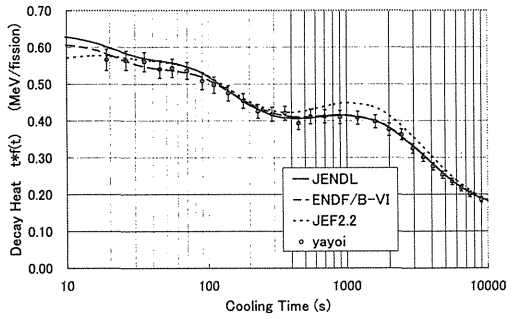



Fig.1 Decay Heat after a Burst Fission in Pu-239 before the TAGS Correction ( $\beta$ -ray Component)

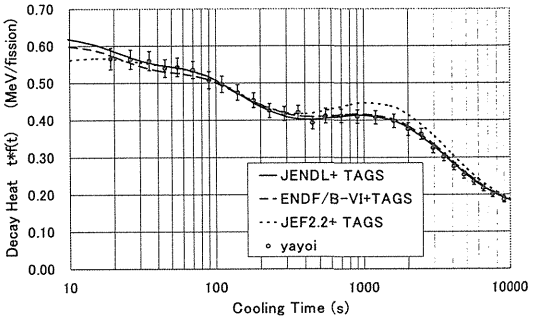



Fig.2 Decay Heat after a Burst Fission in Pu-239 after the TAGS Correction ( $\beta$ -ray Component)

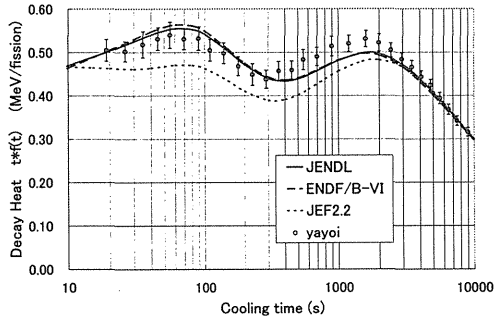



Fig.3 Decay Heat after a Burst Fission in Pu-239 before the TAGS Correction ( $\gamma$ -ray Component)

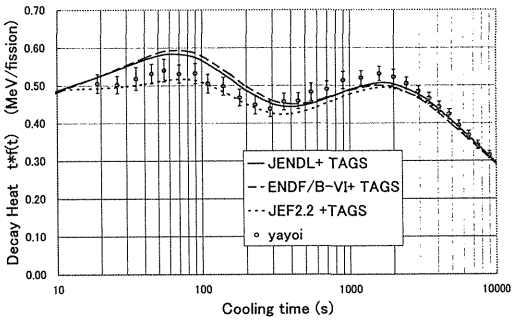



Fig.4 Decay Heat after a Burst fission in Pu-239 after the TAGS Correction ( $\gamma$ -ray Component)

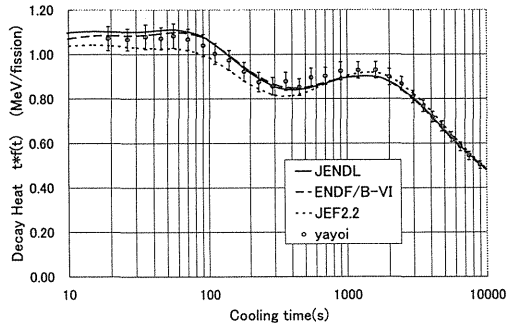



Fig.5 Decay Heat after a Burst Fission in Pu-239 before the TAGS Correction (Total)

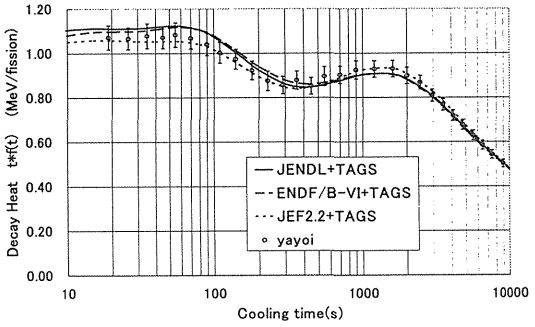



Fig.6 Decay Heat after a Burst Fission in Pu-239 after the TAGS Correction (Total)

integral measurement. In this section, the stress is put on the decay heat of cooling time range from 10 to 10000 seconds after one-year irradiation, which is very important in the LOCA analysis.

Shown in Fig. 7, 8 and 9 are the relative changes of the $\beta$- and $\gamma$-ray components and the total decay heat after one-year irradiation calculated for four major fissiles, or Pu-239, Pu-241, U-233 and U-235. As the summation calculations based on pre-JENDL have been recommended as a standard by the Atomic Energy Society of Japan (AESJ) [10], we are interested in the impact on the

JENDL calculations. Strictly speaking, the AESJ recommendation was calculated on the basis of the JNDC FP Decay Data File [11], which is the original form of the JENDL FP Decay Data File[3].

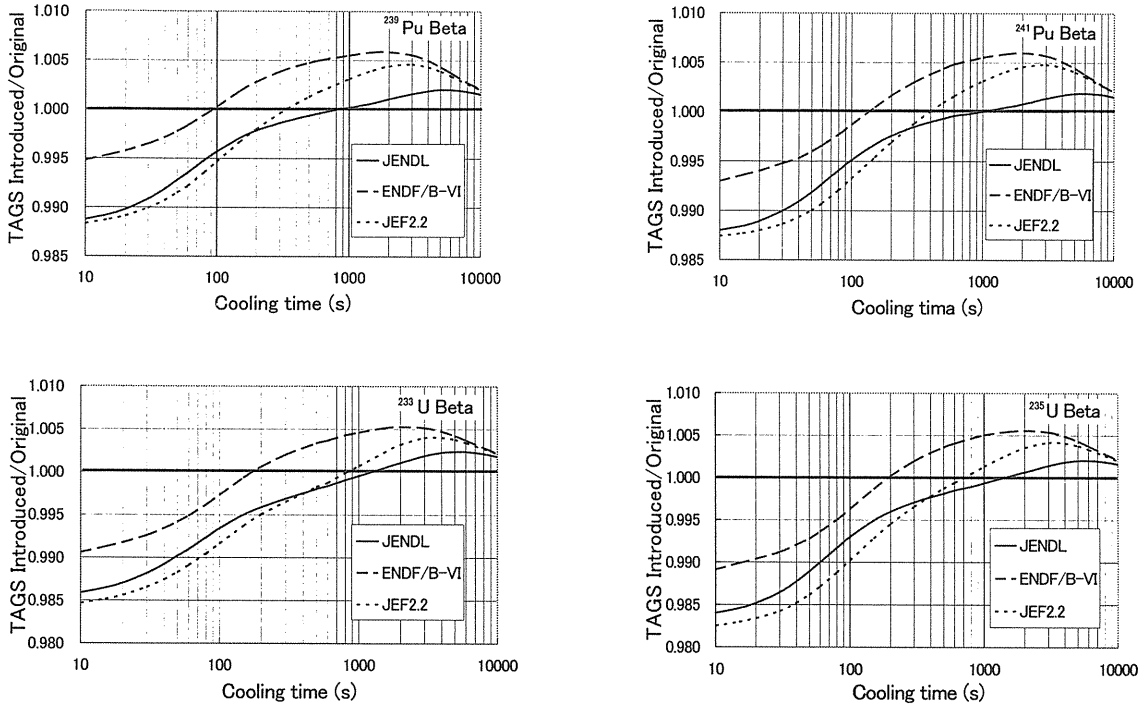



Fig. 7 Effect of Introduction of TAGS Energies into Summation Calculation ( $\beta$ -ray Component)

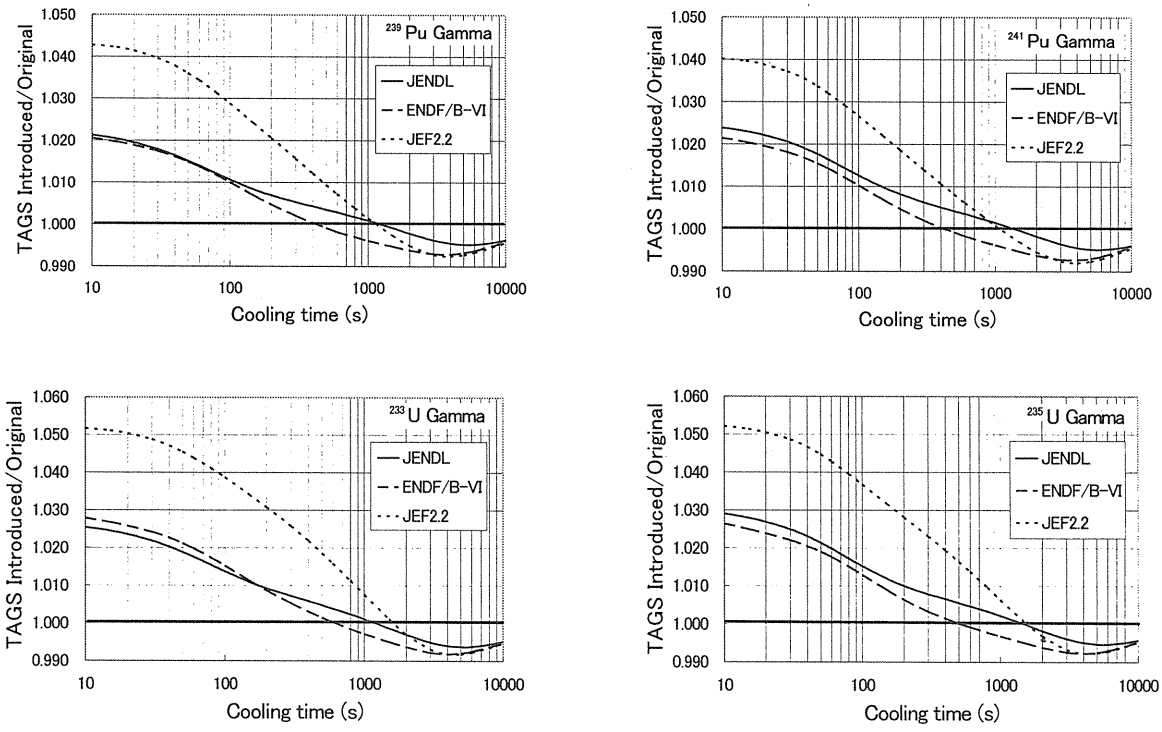



Fig.8 Effect of Introduction of TAGS Energies into Summation Calculation ( $\gamma$ -ray component)

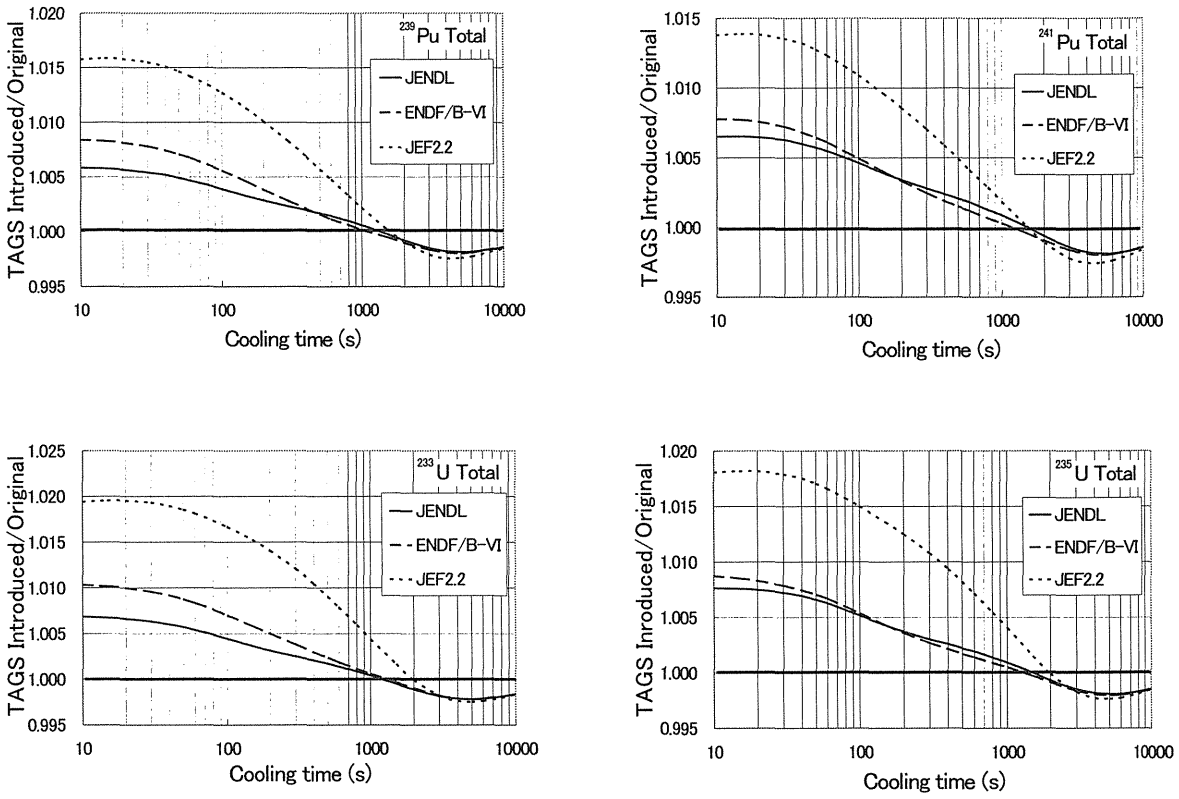



Fig.9 Effect of Introduction of TAGS Energies into Original Summation Calculation (Total or $\beta+\gamma$ decay heat)

As far as the JENDL total decay heat in Pu-239 is concerned, the effect is smaller than 0.6 % even at the maximum as is seen in Fig.9. The estimated error of the total decay heat after an infinite irradiation is given in Ref. [10]. These errors vary from 0.8% to 1.1% for Pu-239 and for U-235, and from 1.2% to 1.7% for Pu-241 in the cooling-time range from 10 to 10000s. (The error values are not provided for U-233.) The impact of introduction of the TAGS data is smaller than these error values, which AESJ recommends, as far as the total decay heat is concerned. The $\gamma$-ray component, however, is overestimated by 2 ∽3% for the cooling time range from 10 to 100 s.

## 5. Conclusion

In this paper, any decisive impact of introducing the TAGS data into JENDL in the LOCA condition was not found as far as the total, or the $\beta+\gamma$, decay heat is concerned. When we see the decay heat as component-wise, or the $\beta$-ray and the $\gamma$-ray components separately, the effects reach 2∽3% even in the JENDL case ($\gamma$-ray component, Fig.8). In this sense the effect of introduction of the TAGS data should not be ignored. In addition an European group (spokesperson: A. Algora, Valencia) started a series of the TAGS experiments at Jyvaskyla on-line mass separator for several important FP nuclides [12]. Sooner or later we will have more TAGS data for the FP region nuclides.

Therefore, the further study is required to validate the reliability of the TAGS data as the input of the summation calculation.

**References**

[1] J.C. Hardy, L.C.Carrez, B.Jonson, P.G.Hansen, *Phys. Lett.,* **71B**(1977) 307

[2] T.Yoshida, R. Nakashima, *J .Nucl. Sci. Technol.,* **18** (1981) 393

[3] J.Katakura, T.Yoshida, K.Oyamatsu, T.Tachibana, "JENDL FP Decay Data File 2000," JAERI 1343 (2001)

[4] M.Akiyama, S.An, *Proc. Int. Conf. on Nuclear Data for Science and Technology*, Antwerp, p.237 (1982) and references therein

[5] J.K.Dickens et al., *Nucl. Sci. Engn.*,**74**,(1980) 106, **78** (1981) 126

[6] R.C.Greenwood, et al., *Nucl. Instr. and Meth.*, **A314** (1992) 514

[7] R.C.Greenwood, R.G.Helmer, M.H.Putnam, K.D.Watts, *Nucl. Instr. and Meth.*, **A390** (1997) 95

[8] JEF-2.2 Radioactive Decay Data, JEF report 13, OECD NEA (1994)

[9] T. Yoshida, T.Tachibana, J.Katakura, *Proc. 2003 Symposium on Nucl Data*, Tokai, p.173 (2004)

[10] Recommended Values of Decay Heat Power and Method to Utilize the Data (Supplement to "Reactor Decay Heat and its Recommendation"), Atomic Energy Society of Japan (1990) (in Japanese); English Translation, K.Tasaka, J.Katakura, T.Yoshida, T.Kato, R.Nakasima, JAERI-M 91-034, Japan Atomic Energy Research Institute (1991)

[11] K.Tasaka et al., "JNDC Nuclear Data Library of Fission Products -Second Version-," JAERI-1320, Japan Atomic Energy Research Institute (1990)

[12] J.L.Tain, Private communication, (2004)

JP0550273



# 3.13 Analysis of Plasma Material Surfaces by Means of Low Energy NRA

K. Ochiai, N. Kubota and T. Nishitani
*Japan Atomic Energy Research Institute, Tokai-mura, 319-1195 Japan*

## Abstract

Precise investigation for the depth-profiles of the main-isotope on the plasma facing material (PFM) surface is necessary to clarify the mechanism for the fusion fuel recycling in the D-T fusion reactor. For the determination, nuclear reaction analysis (NRA) is valuable to obtain these concentrations and depth-profiles. We have carried out the depth profile analysis of the depth profile of the deuterium, tritium and lithium-isotope on the surface of the JT-60 and TFTR carbon fiber composites (CFC) tile by means of NRA with the JAERI fusion neutronics source (FNS) accelerator. In this paper, we describe the present status of the NRA activity in the JAERI/FNS and especially report the preliminary results of the deuterium and tritium depth profiles for the TFTR tiles.

## MEASUREMENT

The measurement has been carried out using the deuteron accelerator of Fusion Neutron Source in Japan Atomic Energy Research Institute (JAERI/FNS) [1]. Figure 1 shows the schematic view of the experimental set-up for NRA. The probe beam is a deuteron beam and its energy and current density are adjusted between 250 and 350 keV and 0.1~ 1$\mu$A/cm$^2$ respectively. In case of carbon samples, the detectable depth is about 1.5 $\mu$m by 350-keV deuteron. The beam spot is collimated $\phi$6.5 mm in diameter by an aperture at the upper stream of the beam. The number of incident charges is directly measured from the samples with a positive bias supply (about 150 V). A silicon solid state detector (SDD), with a deposition layer thickness of 200 $\mu$m, was used to count high energetic charged particles emitted from the samples. The solid angle for the detection was 1.1 x 10$^{-2}$ sr. The effective area of the detector was covered with a 6-$\mu$m thick aluminum foil to suppress scattered deuterons. The incident angle and the detected angle were 45 and 90 deg respectively. The energy resolution was checked with an $\alpha$-particle emitter (Am-241:$E_\alpha$ = 5.486 MeV) and the *FWHM* was below 40 keV.

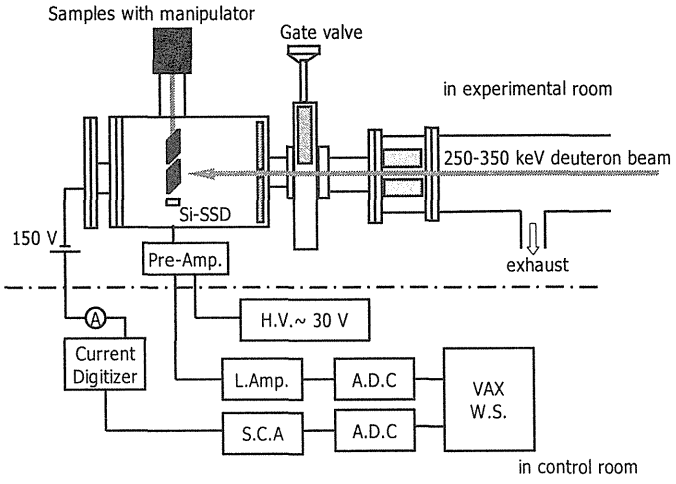



Fig.1 The NRA experimental set-up in JAERI/FNS

## SAMPLES

We have used the two plasma irradiated tiles as the sample. One is the JT-60 divertor CFC tile exposed with the D-D plasma and another is the TFTR CFC limiter tile exposed with D-T plasma [2]. Figure 2 shows the used TFTR CFC sample and the location in the TFTR. The sample was a corner peace (about 20 x 15 x 10 $mm^3$) of a CFC block named KC-16. The KC-16 block was located near the center of the TFTR inner wall in the bay-K area and the role was mainly the limiter of the plasma. The CFC tile was used in the TFTR DT plasma campaign between November 12,1999 and December 9, 1999. In the D-T plasma operation, the lithium pellet injection has been used to After the D-T plasma operation, deuterium and/or helium glow discharge cleaning and air ventilation, baking at 150 °C

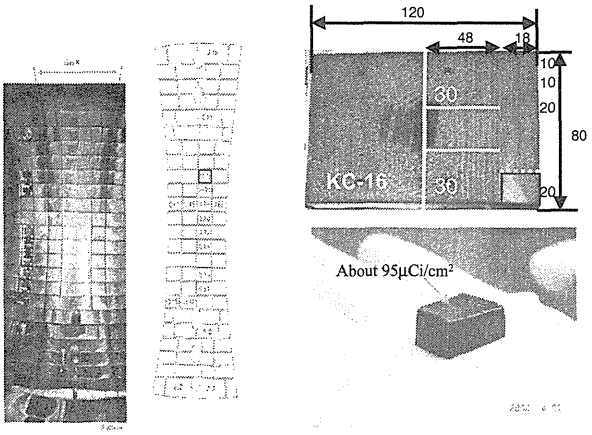



Fig.2 TFTR CFC tile sample and its location

## ANALYSIS

D($d$,$p$)T and T($d$,$\alpha$n) are used to measure the deuterium and tritium in the samples. The cross section data of D($d$,$p$)T and T($d$,$\alpha$n) were used the several references housed fusion reactions data Fusion Evaluated Nuclear Data Library (FENDL-2) [3]. From the number of the yield of each spectrum, retentions and depth-profiles can be estimated by the following equations (1)~(3).

$$E_2 = k_{(E,\theta_{out})} \times \left\{ E_0 - \left(\frac{dE}{dx}\right)_1 \frac{x_1}{\sin\theta_{in}} \right\} - \left\{ E_1 - \left(\frac{dE}{dx}\right)_2 \frac{x_1}{\sin(\theta_{out} - \theta_{in})} \right\} - \left(\frac{dE}{dx}\right)_3 \Delta x_2 \qquad (1)$$

$$N_{(x)} = \frac{\int_E^{E+\Delta E} Y dE}{\int_x^{x+\Delta x} \left(\frac{dE}{dx}\right)_1^{-1} dx \cdot \left\langle \frac{d\sigma}{d\Omega} \right\rangle \Delta\Omega \frac{\phi}{\sin\theta_{in}}} \qquad (2)$$

where $E_0$, $E_1$ and $E_2$ = incident deuteron energy, emission-particle energy by nuclear reaction at a depth point $x_1$ and detection energy, $(dE/dx)_1$, $(dE/dx)_2$ and $(dE/dx)_3$ = stopping powers for each charged-particles in the samples and in the Al (6 $\mu$m) screening foil, $k_{(E,\theta out)}$ = kinematics factor taking into account $Q$-values, $x_1$ and $\Delta x_2$ = depth point from the sample surface and unit depth in the sample taken into account the detector resolution, $\theta_{in}$ and $\theta_{out}$ = incident angle and detection angle, $N_{(x)}$ = areal density, $d\sigma/d\Omega$ = differential cross sections, $\Delta\Omega$ = solid angle (sr) and $\phi$ = the number of incident deuterons.

The cross sections of D($d$,$p$) and $^{12}$C($d$,$p$) reactions can be described by the following equation

$$\sigma(E) = \frac{S(E)}{E}\exp\left(-31.29 Z_1 Z_2 \left(\frac{\mu}{E}\right)^{-\frac{1}{2}}\right) \qquad (3)$$

where $S_{(E)}$ = astrophysical $S$-factor in MeV barn, $E$ = incident energy in MeV, $Z_1$ and $Z_2$ = atomic numbers of incident and target particles and $\mu$ = reduced mass. Since cross the section of T($d$,$n$) has a giant resonance at $E_d$ = 110 keV, we used the experimental cross section value [2].

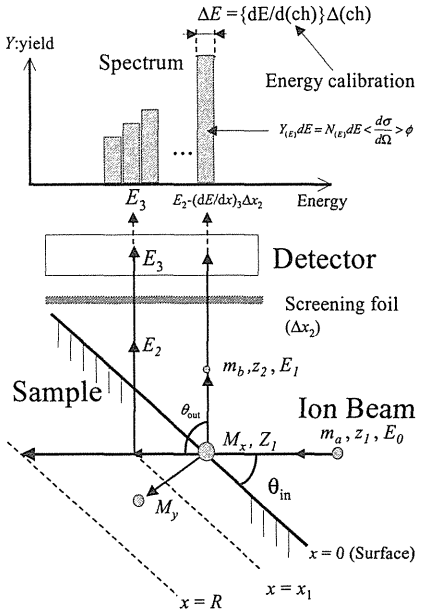



Fig.3 Schematic view for the NRA

## RESULTS AND DISCUSSION

Figure 4 shows the energy spectra of the detected charged particles from the TFTR tile sample on 300- and 150-keV deuteron implantations respectively. The Peak at the 10.2MeV is α particles with $^6$Li(d,2α) (Q = 22.37MeV) reaction and the continuous spectra below 7.5 MeV consists of α particles with $^6$Li(d, 2αn) (Q = 15.12). The 4.5-MeV and 4.1-MeV peaks are the proton $^6$Li(d,p$_0$)$^7$Li (Q = 5.03 MeV) and $^6$Li(d,p$_1$)$^7$Li* (Q = 4.55 MeV) respectively [4]. 2.9-MeV and 0.6-MeV peaks are proton and the triton spectrum from the D(d,pt) (Q = 4.03MeV) and the broad spectrum between 1.2 MeV and 2.5 is α particle with T(d,αn) (Q = 17.59 MeV).

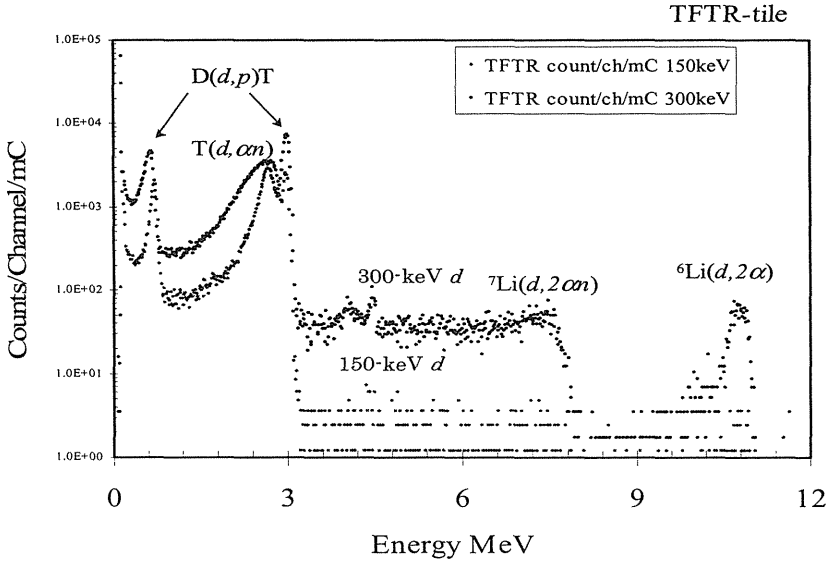



Fig.4 The energy spectra of the detected charged particles from the TFTR tile sample on 300- and 150-keV deuteron implantations

Preliminary, we have obtained the deuterium and tritium depth profile on the JT-60 and TFTR tile surfaces. Figure 5 and 6 show the deuterium and tritium depth profiles for the TFTR tile respectively. From the result of deuterium depth profile analysis, it was founds that the deuterium depth profile of the TFTR tile be uniformly distributed from the surface to 1.4-μm depth and its averaged density value was about 3.8 x $10^{21}$ deutrium/$cm^3$. The averaged value was corresponded with about 3% for the typical graphite density. Also it was found that tritium depth profile tend to have the peak of density near 0.5-μm depth and its value. We have to think more in depth about the reason of the tendency of the tritium depth profile as the future works.

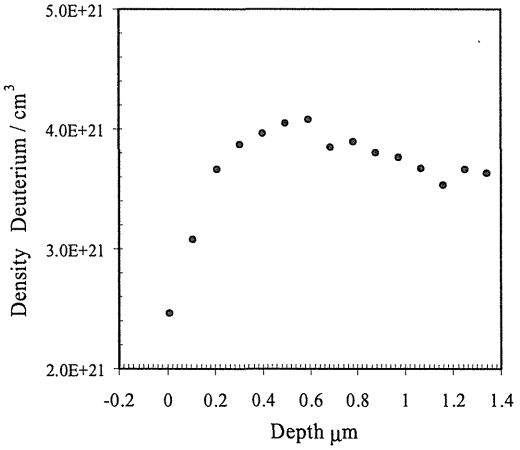



Fig.5 Deuterium depth profile on the surface, the averaged density value is 3.8 x $10^{21}$ $cm^{-2}$

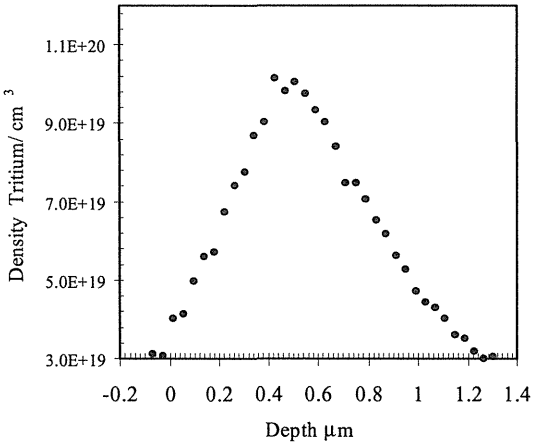



Fig.6 Tritium distribution on the surface, Activity=12.9 MBq/$cm^2$ Density peak 1 x $10^{20}cm^{-3}$ at near 0.5 μm depth

**Reference**

[1] *K. Ochiai et al. Journal of Nuclear Materials, Vol. 329-333, Part 1, 2004, p. 836-839.*

[2] *D.K. Owens et al. Journal of Nuclear Materials, Vol. 220-222, (1995) p.62-72.*

[3] For example, National Nuclear Data Center website "*http://www.nndc.bnl.gov/databases/*".

[4] *Y. Isobe et al Nucl. Instruments and Methods B Vol. 170, 2000, p.171-179.*

JP0550274



# 3.14 Elastic Recoil Detection Method using DT Neutrons for Hydrogen Isotope Analysis in Fusion Materials

Naoyoshi Kubota[1], Kentaro Ochiai[1], Keitaro Kondo[2] and Takeo Nishitani[1].

1:*Japan Atomic Energy Research Institute, Tokai-mura, Naka-gun, Ibaraki-ken 319-1195, Japan.*

2:*Department of Electronic, Information Systems and Energy Engineering, Osaka University, Japan.*

e-mail : naoyoshi@fnshp.tokai.jaeri.go.jp

## Abstract

The Fusion Neutronics Source of Japan Atomic Energy Research Institute has started the study on the hydrogen isotope analysis for fusion components since 2002 on the basis of the techniques such as nuclear activation method, ion beam method and imaging plate method. In this study, we propose the elastic recoil detection analysis (NERDA) method using 14.1 MeV neutron beam to extend the analyzable depth of hydrogen isotopes analysis up to several hundreds micrometers. An experimental setup for NERDA was constructed and a proof-of-principle experiment was then made using a standard sample of deuterated polyethylene film containing a known concentration of deuterium with thickness of 100 μm. The depth resolution of the present condition was estimated to be 158 μm for the sample.

## 1. Introduction

Hydrogen isotopes show complicated behavior on the surface of plasma facing components (PFC) in fusion devices, and the study is important for the design of the fuel recycling, the plasma control *etc.* In case that carbon based materials are used as PFC, co-deposited layers of carbon compounds are formed with the thickness of several tens of micrometers on PFC surfaces due to plasma-wall interactions [1-2]. Since these layers retain a lot of hydrogen isotopes more than the bulk in PFC, it is necessary to reveal hydrogen isotope distributions beyond co-deposited layer. However, conventional non-distractive analyses for hydrogen isotopes on the surface, *e.g.* Elastic Recoil Detection Analysis, Rutherford Backscattering Spectroscopy and Nuclear Reaction Analysis (NRA), were not appropriate in such depth region because of their shallow probing depth.

A powerful and unique method with monochromatic neutrons instead of ion beam, namely, Neutron Elastic Recoil Detection Analysis (NERDA) has been developed. This method was applied to measure hydrogen isotopes in divertor tiles of the DIII-D reactor and palladium-hydrogen system [3-4]. The advantages of neutron usages for the material analysis are to probe the deeper depth and to obtain the same sensitivity as the conventional ion beam

analysis due to large scattering cross sections for hydrogen isotopes. In addition, beam-irradiation induced degradation of hydrogen isotopes distribution could be minimized.

The Fusion Neutronics Source (FNS) of Japan Atomic Energy Research Institute (JAERI) has started the study on the hydrogen isotope analysis for fusion components since 2002 on the basis of the techniques such as the nuclear activation method, the ion beam method and the imaging plate method. So far, deuterium and tritium distributions as regards the depth from the surface of the JT-60U plasma facing components up to the range of a few micrometers were obtained by means of the deuteron induced NRA. In this study, we propose NERDA using the 14.1 MeV neutron beam produced by T(d,n)a reactions to extend the analyzing depth of hydrogen isotopes up to several hundreds micrometers. A proof-of-principle experiment was made using a standard sample of deuterated polyethylene film containing a known concentration of deuterium.

## 2. Experimental

Depth distributions are estimated with energy and yield of recoil particle from the sample by NERDA method. The detection energy $E_d$ is expressed as,

$$E_d = E_r - dE_2(x), \tag{1}$$

where $Er$ and $dE_2(x)$ are the recoil energy of the target atom and the energy loss of the recoil particle before reaching the sample surface. The energy $E_r$ is led by the energy and momentum conservation laws:

$$E_r = \left( \frac{4M_1M_2}{(M_1+M_2)^2} \cos^2\phi \right) E_1 . \tag{2}$$

where $M_1$, $M_2$, are the mass of the probe neutron and that of the target atom, $\phi$ is the recoil angle, $E_1$ is the incident energy of the probe neutron. The energy loss of $dE_2$ is expressed using stopping power $dE/dx$ for recoil particles in the sample;

$$dE_2 = \int_0^{x/\sin(\phi-\theta_0)} \left( -\frac{dE}{dx} \right) dx \tag{3}$$

where $x$ is the depth in the target, $\theta_0$ is the incident angle of the probe neutron.

On the other hand, the yield $dY$ of the recoil particles originating in the region between

a depth $x$ and $x + dx$ is expressed by;

$$dY = Q\frac{d\sigma_r(E)}{d\Omega}Ndx\Delta\Omega, \qquad (4)$$

where $Q$ is the number of incident neutrons, $d\sigma_r(E)/d\Omega$ is the angular differential recoil cross section in laboratory system, $N$ is a density of the target atom, $\Delta\Omega$ is a solid angle. Thus, the distribution of the target atoms is deduced from the detection energy and yield of the recoil particle.

Experimental setup is shown in Fig. 1. The 14.1 MeV neutrons produced by T(d,n)$^4$He reactions with 350 keV deuterons at the target of the 0° beam line of FNS were collimated with a hole of 20 mm in diameter. The collimated neutrons, *i.e.* neutron beam, were incident on the sample from the direction at an angle of 0°. Emitted particles from the sample were measured using a ΔE-E telescope system with the solid angle of $1.8 \times 10^{-2}$ sr. A pair of solid state detectors (SSDs) with the depletion layer thickness of 75 and 1500 μm was positioned at the detection angle of 25°. Output signals from each SSD were analyzed with a multi-parameter analyzer to estimate the particle mass and its energy. The energy calibration of SSDs was corrected based on an $^{241}$Am alpha source (5.486MeV). Typical fluence of incident neutrons was $4.0 \times 10^9$ neutrons/cm$^2$, which was monitored with a $^{238}$U fission chamber located behind the target chamber.

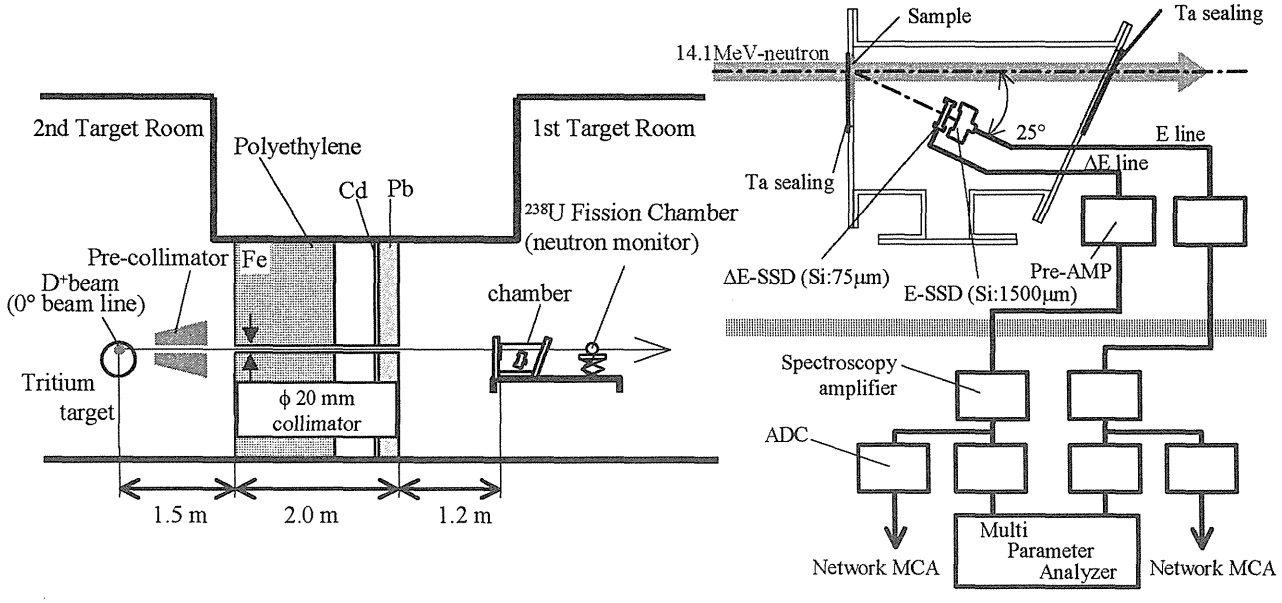



Fig. 1. The neutron beam system in FNS (left hand side) and the experimental setup of NERDA (right hand side).

A proof-of-principle experiment was performed using a standard sample of deuterated polyethylene film containing a known concentration of deuterium with the thickness of 100 μm. The deuterated polyethylene film was fabricated using a solvent-cast method. Spongelike pieces of deuterated polyethylene were solved with a toluene solution, which were controlled to become the density of 10 wt% or less. The solution was vaporized to form a film of deuterated polyethylene in air-drying at room temperature during two weeks.

## 3. Results and discussion

Typical ΔE-E contour map during the 14.1 MeV NERDA for the $(C_2D_4)_n$ sample with the thickness of 100 μm are shown in Fig. 2. The horizontal and vertical axes show the energy measured at the ΔE-SSD and the E-SSD, respectively. The D(n,d)n recoil deuterons appearing around (E, ΔE) = (180, 550) ch were recorded in the contour map. Protons originating in X(n,p) reactions with hydrogen, deuterium and other impurity on/in the target were also distinguishable. For example, D(n,p)2n reaction formed a continuum spectrum from (100, 700) ch to (400, 0) ch. Figure 3(a) and (b) show energy spectra measured with the (a) ΔE-SSD and (b) E-SSD, respectively, during the 14.1 MeV NERDA for the $(C_2D_4)_n$ sample. In each projected MPA spectrum only the recoil deuterons survived as a result of coincidence filtering.

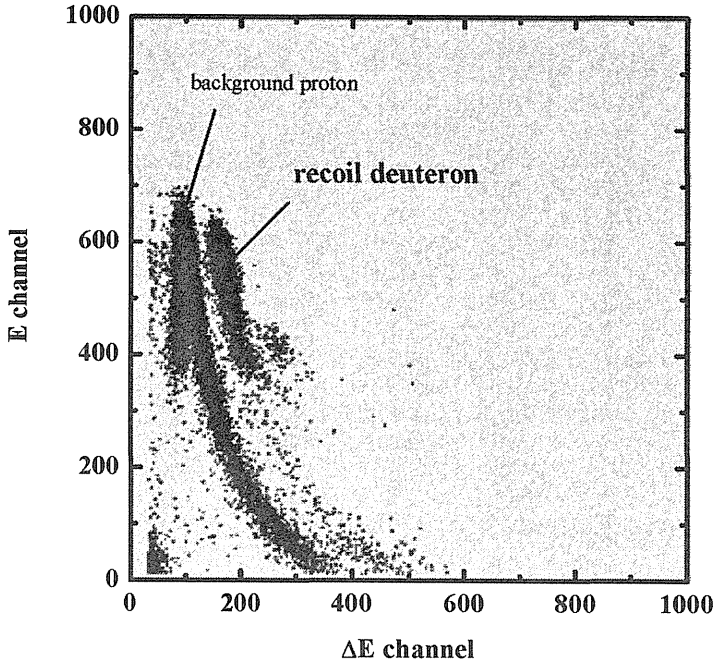



Fig. 2. The ΔE-E contour map measured with multi parameter analyzer during the 14.1 MeV NERDA for the $(C_2D_4)_n$ sample with the thickness of 100 μm.

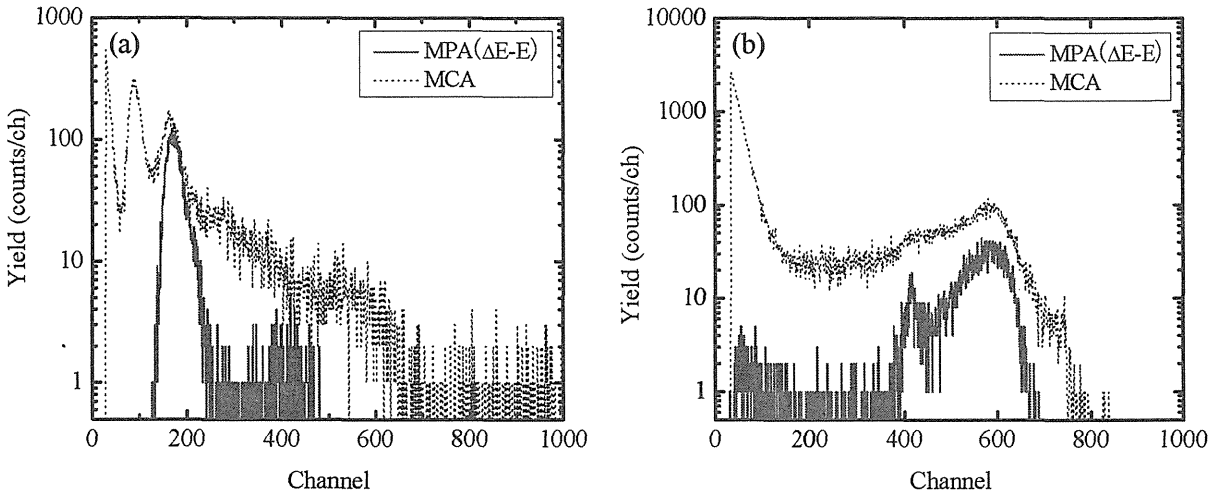



Fig. 3. Energy spectra measured with the (a) ΔE-SSD and (b) E-SSD during the 14.1 MeV NERDA for the $(C_2D_4)_n$ sample. In each MPA-spectrum only the recoil deuterons survive as a result of coincidence filtering.

A deuterium depth distribution estimated from the total energy spectrum of recoil deuterons is shown in fig. 4. In Eq. (4), the value of 53.6 mb/sr was used as the differential cross section of recoil deuterons [5]. The deuterium distribution like Gaussian was obtained for the standard sample with the homogeneous distribution of deuterium. The distribution was expressed as a Gaussian response function with a standard deviation of 67 μm. The depth resolution, which was defined as the value of a standard deviation multiplied by a factor of $2(2\ln 2)^{1/2}$ on the Gaussian response function, was then evaluated to be 158 μm corresponding to 16 % of the analyzable depth of 957 μm for the $(C_2D_4)_n$ sample.

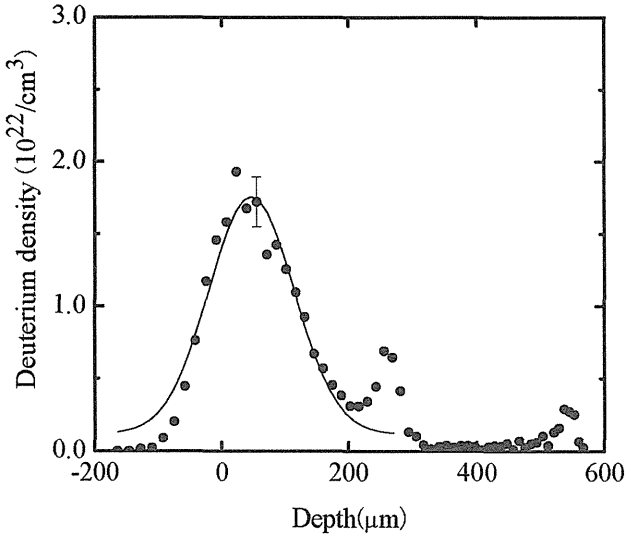



Fig. 4. Deuterium depth distribution of the $(C_2D_4)_n$ sample estimated using the total energy spectrum of deuterons. The solid line indicates the fitting curve using Gaussian.

## 4. Summary

The elastic recoil detection analysis using T(d,n) neutrons was proposed to extend the analyzing depth of hydrogen isotopes up to several hundreds micrometers. The proof-of-principle experiment was performed using the 14.1 MeV neutron beam and the standard sample of the deuterated polyethylene film containing a known concentration of deuterium. With uses of the ΔE-E system, recoil deuterons and proton spectra were obtained separately under the low background condition. The estimated depth resolution corresponded to 16 % of the analyzable depth for the standard sample, which is enough to analyze fusion materials.

## References

[1] C.H. Skinner, et al.: J. Nucl. Mater. 290-293, 486(2001)
[2] N. Bekris, et al.: J. Nucl. Mater. 313-316, 501(2003)
[3] B.G. Skorodumov, et al.: Nucl. Instr. Meth. B 85, 803 (1994)
[4] B.G. Skorodumov, et al.: J. Nucl. Mater. 233-237, 1107 (1996)
[5] S. Shirato et al.: Nucl. Phys. A120, 387(1968)

JP0550275

JAERI－Conf 2005－003

# 3.15 Calculations of an HPGe Detector Peak Efficiency Curve up to 11 MeV with EGS4 and GEANT4

M. Kasaishi[1], A. Tojo[1], M. Furuta[1], H.Takayama[1], I. Miyazaki[1], T. Shimizu[1], M. Shibata[2], K. Kawade[1], and A. Taniguchi[3]

[1]*Graduate school of Engineering, Nagoya University*

[2]*Radioisotope Research Center, Nagoya University*

[3]*Research Reactor Institute, Kyoto University*

e-mail : m-kasaishi@ees.nagoya-u.ac.jp

We determined an efficiency curve of an HPGe detector in the energy range of 0.3 - 11 MeV within 0.5 % accuracy with the measured data of the $^{14}N(n,\gamma)^{15}N$ reaction and the aid of the Monte Carlo cords EGS4 and GEANT4.

## 1. Introduction

A precise efficiency curve up to 11 MeV is needed for the precise measurements of intensities of prompt γ-rays. Methods of the determination of peak efficiency curves of HPGe detectors have been studied. The typical method is by fitting the measured data sets. Raman et al. [1] determined an efficiency curve by using fitting functions with 2 % accuracy in the energy range of 0.1 - 11 MeV (Fig.1). Recently, Helmer et al. [2] determined one by using the CYLTRAN code within 0.2 % in the energy range of 0.2 - 1.4 MeV (Fig.2). In this study, we extended to 11 MeV with the measured data of the $^{14}N(n,\gamma)^{15}N$ reaction. We attempt to determine the efficiency curve in the energy range of 0.3 - 11 MeV within 0.5 % accuracy by using of the Monte Carlo codes EGS4 [3] and GEANT4 [4].

## 2. Experiments and calculations

### *2.1 measured efficiencies*

The peak efficiencies of a 22 % coaxial HPGe detector were measured by using decay γ-rays from the $^{24}Na$, $^{56}Co$, $^{88}Y$, $^{133}Ba$ and $^{152}Eu$ sources in the energy range of 0.3 - 3 MeV. The distances from the detector face to the sources were 10 cm. The efficiencies also measured by prompt γ-rays from the $^{14}N(n,\gamma)^{15}N$ reaction up to 11 MeV with a 22 cm distance at KURRI. The intensities of prompt γ-rays from this reaction have errors of 2 % in previous papers; we used our recent data to obtain more precise measured efficiencies within 0.5 %. We ascertained that the effect of the different distances between 10 cm and 22 cm is negligible above 1.5 MeV with EGS4.

### *2.2 calculations*

Figure 3(a) shows the initial physical parameters of the detector used in

EGS4. These parameters are provided by the manufacturer (Geometry A in Fig4(a)). The EGS4 values calculated were compared with the measured efficiencies (Fig.4(b)). The values were not agreement with the measured ones. The slopes which constructed by the plots of open circles in Fig.4(b) indicate that the sensitive volume of the detector is smaller than the Geometry A. Therefore, we adjusted length and diameter of the detector for that the EGS4 values agree with the measured efficiencies (Fig.4(a),(c)). We calculated the values with the Geometry B, D and E and compared with the measured ones (Fig.4(b),(c)). As a result, the values with the Geometry E reproduced the measured ones relatively in the wide energy range. Therefore, the Geometry E was adopted for the final detector parameters used in calculations (Fig.3(b)).

We also calculated by using the GEANT4 with the same procedure. The detector parameters used in GEANT4 were a bit different than that used in EGS4.

## 3. Results

Figure 5 shows the comparison of the calculation values and the measured efficiencies. The calculated values with EGS4 agree with the measured efficiencies below 2 MeV. Above 2 MeV, the values become smaller than the measured ones. On the other hand, the calculated values with GEANT4 agree with the measured efficiencies below 6 MeV. Above 6 MeV, the values become larger than the measured ones. However, we found that the deviation between the values and the measured ones can be taken as a simple function of the energy. Therefore, we could determine the calculated values corrected by using the function.

Figure 6 shows the differences between the calculated values and the measured efficiencies. The calculated values are corrected by the deviation from EGS4. These differences were within 0.5% in the range of 0.3 - 11 MeV. Similarly, correcting the values with GEANT4 was needed. The result is also within 0.5 %

## 4. Conclusions

The calculation values with EGS4 do not agree with the measured efficiencies above 2 MeV, and the values with GEANT 4 did not agree with the measured ones above 6 MeV. However, we can correct these values with simple functions of energy. Differences between the calculated values and the measured efficiencies are within 0.5 %. Therefore, we can determine an efficiency curve of an HPGe detector within 0.5 % in the energy range of 0.3 - 11 MeV.

We can determine an precise efficiency curve up to 11 MeV with 0.5 % accuracy by the resent measured data of the $^{14}N(n,\gamma)^{15}N$ reaction and the aid of the codes EGS4 and GEANT4.

References

[1] S. Raman, C. Yonezawa, H. Matsue, H. Iimura, N. Shinohara, *Nucl. Instr. Meth.,* A 454 (2000) 389-402

[2] R. G. Helmer, J. C. Hardy, V. E. Iacob, M. Sanchez-Vega, R. G. Nelson, J. Nelson *Nucl. Instr. Meth.,* A511 (2003) 360-381

[3] W. R. Nelson, H. Hirayama, D. W. O. Rogers, SLAC Rep. 265 (1985)

[4] S. Agostinelli *et al, Nucl. Instr. Meth.,* A506 (2003) 250-303

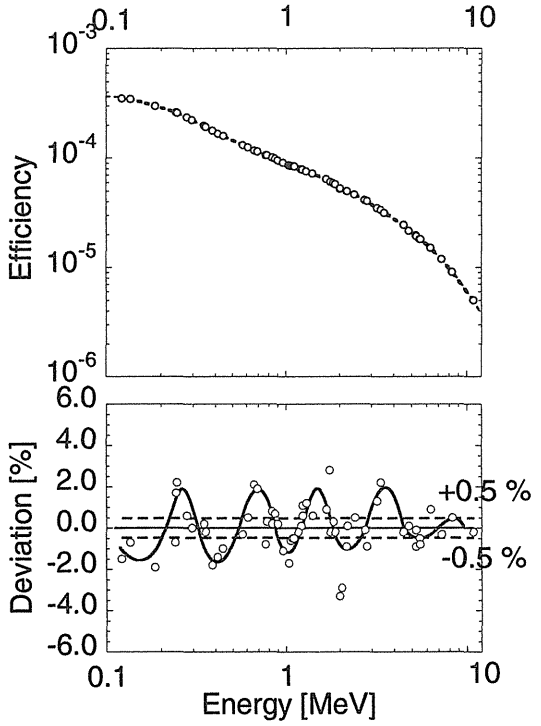



Fig.1 An efficiency curve determined by using the fitting functions up to 11 MeV [1]. In the lower panel, the oscillation caused by the non-physical fitting is shown.

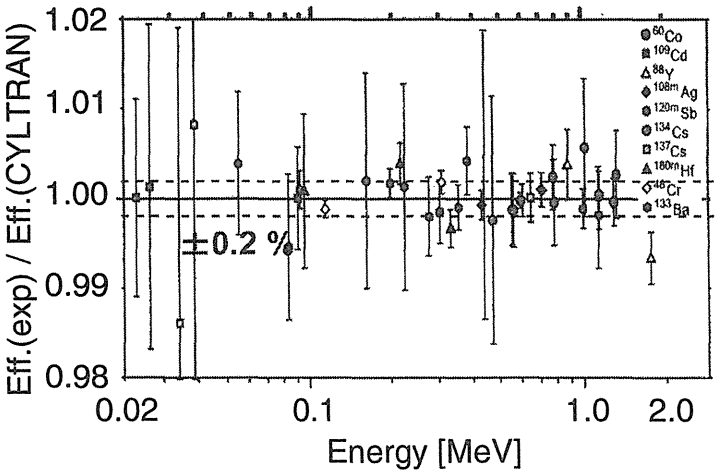



Fig.2 Comparison of the CYLTRAN values with the measured efficiencies up to 1.4 MeV [2]

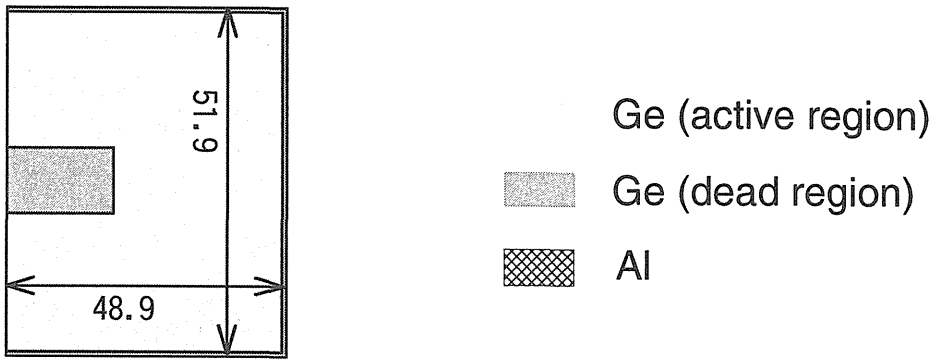



Fig.3(a) 22 % HPGe detector parameters from manufacturer (Geometry A)

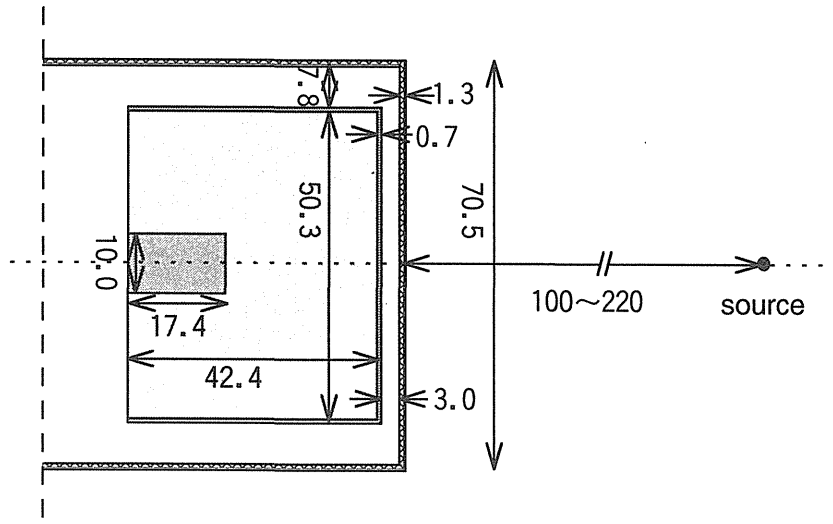



Fig.3(b) The final detector parameters used in EGS4 (Geometry E)

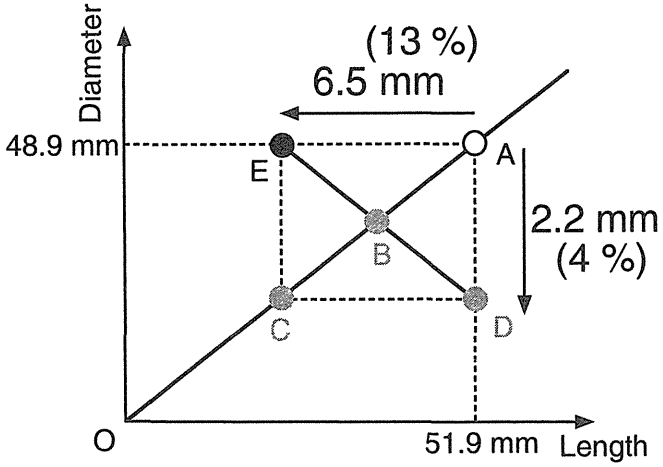



Fig.4(a) Adjustment of the detector length and diameter

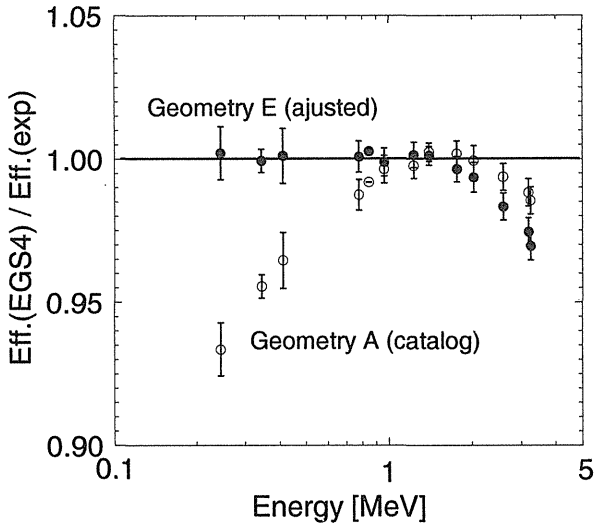



Fig.4(b) The ratio of EGS4 values to measured efficiencies

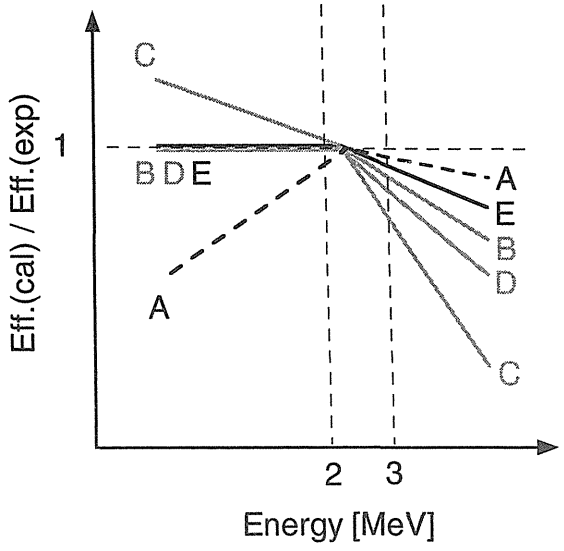



Fig.4(c) The ratio calculated with adjusted detector parameters. The Geometry E is the final parameters.

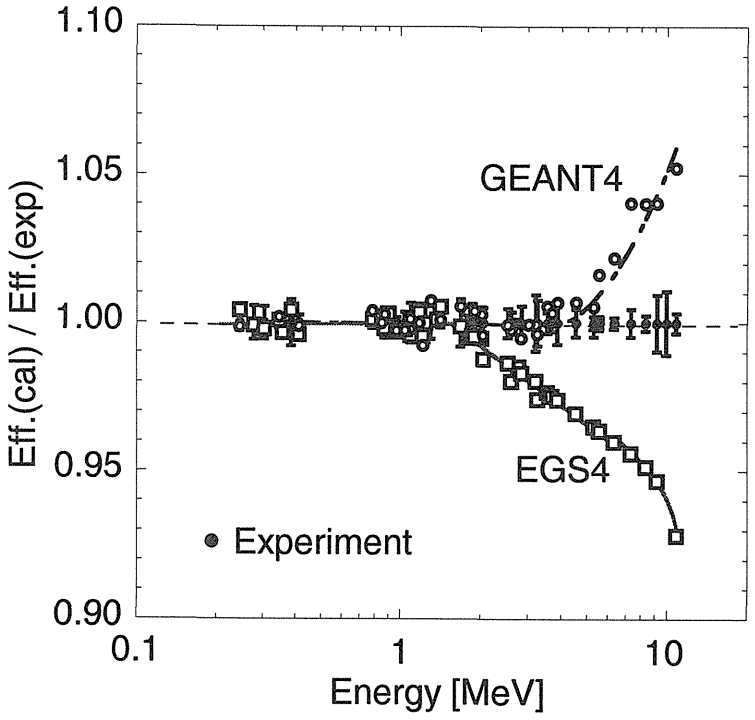



Fig.5 The ratio of the calculation values with EGS4 and GEANT4 to the measured efficiencies. The lines are eye guides.

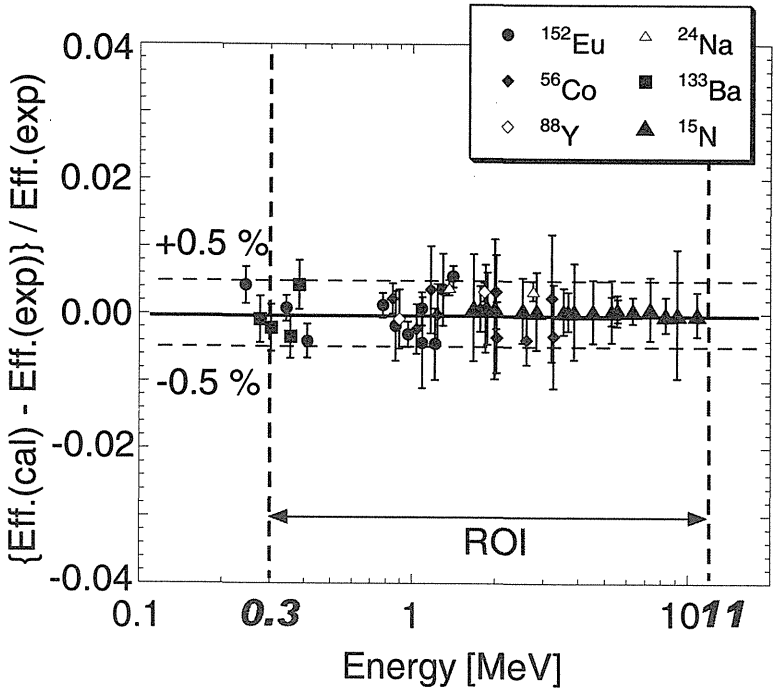



Fig.6 Differences between the calculated values and the measured efficiencies. The calculated ones are corrected by the deviation from EGS4.

JP0550276



# 3.16 Precise Measurement of Prompt γ-ray in the $^{14}N(n,\gamma)^{15}N$ Reaction

H. Takayama[1], M. Kasaishi[1], A. Tojo[1], H. Hayashi[1], I. Miyazaki[1], T. Shimizu[1], M. Shibata[2], K. Kawade[1], A. Taniguchi[3], H. Sakane[4], H. Harada[4]

[1]*Graduate school of Engineering, Nagoya University*
[2]*Radioisotope Research Center, Nagoya University*
[3]*Research Reactor Institute, Kyoto University*
[4]*Japan Nuclear Cycle Development Institute*
e-mail: h-takayama@ees.nagoya-u.ac.jp

The relative γ-ray intensities up to 11 MeV were determined within 0.2-1.0% accuracy. We used the liquid nitrogen target in the singles measurement. In order to investigate the level scheme in detail, we performed the γ-γ coincidence measurement with the deuterated melamine ($C_3D_6N_6$) target. Since these targets do not contain the $^1H$, the γ-ray from $^1H(n, \gamma)$ reaction is hardly observed. Because backgrounds were reduced, nitrogen peaks were observed clearly below 2 MeV.

## 1 Introduction

Standard radioactive nuclides such as $^{133}Ba$, $^{152}Eu$, $^{60}Co$ and $^{56}Co$ are used in the energy region below 3.2 MeV as γ-ray intensity standards, but above 3.2 MeV it is difficult to find suitable radioactive sources that have reasonably long-lives. The γ-ray intensities in the $^{14}N(n,\gamma)^{15}N$ reaction are used as the primary intensity standard up to 11 MeV.

In the previous works, the intensities were measured with 2-4% accuracy using the melamine ($C_3H_6N_6$) target [1, 2]. In this work, we performed the singles measurement with the liquid nitrogen ($N_2$) target, and the γ-γ coincidence measurement with the $C_3D_6N_6$ target in order to avoid the influence of the $^1H(n,\gamma)$ reaction.

We aimed to reduce the influence of $^1H(n,\gamma)$ reaction and determine the intensities within 1.0% accuracy.

## 2 Experiments

The γ-ray measurements were carried out at the B-4 neutron beam guide tube at KUR. The neutron flux rate at the irradiation position is about $5 \times 10^7$ n/cm$^2$·s.

In singles measurements, the liquid nitrogen target was used. Capture γ-rays were measured with 22% and 38% HPGe detectors (Fig.1). Distances between the target and the detectors were 22 and 15 cm (22% HPGe), and 24, 15 and 15 cm (38% HPGe).

The γ-γ coincidence measurements were performed with the $C_3D_6N_6$ target. A 90% HPGe, 90% GMX, and LEPS detectors were used with a 1.5 cm distance.

## 3 Results

*3.1 Background below 2 MeV*

The γ-ray from the $^{1}H(n, \gamma)$ reaction is hardly observed by utilization of the liquid nitrogen and the $C_3D_6N_6$ target. Then, backgrounds below 2 MeV are reduced as shown in Fig. 2. As a result, nitrogen peaks such as 1.678, 1.681, 1.854, 1.885 and 1.999 MeV are observed clearly. Because these γ-rays are included in the balance method, it is important that they are measured clearly.

*3.2 The singles measurement*

We determined the intensities of γ-rays from $^{15}N$ by the balance method. This method is that the intensities are determined to balance input and output intensity for each level. The scattering of the primary γ-ray intensities obtained by five measurements is shown in Fig. 3. These intensities agree within 0.5%, namely we consider that the present result is consistent and reliable.

*3.3 The γ-γ coincidence measurements*

The balance method required well-established the level scheme. If unknown γ-rays are found newly, the known γ-ray intensities are influenced. Therefore, we investigated the level scheme in detail. The latest level scheme of $^{15}N$ is shown in Fig. 4. Four γ-rays of 0.977, 3.750, 3.600 and 10.447-MeV were newly observed by the present γ-γ coincidence measurements. These γ-ray intensities were so weak. The deviation of the γ-ray intensities caused by such a weak γ-ray is less than 0.3% in the case of that we lost the γ-rays ten times as strong as the weakest γ-ray we observed.

*3.4 Comparison of the previous results with the present ones*

Comparison of the previous intensities with the present ones is shown in Fig. 5. The previous results agree with the present ones within ± 2-3%. Fig. 6 shows comparison of errors. The errors in present work were 2-8 times as improved as previous ones. The match between input and output intensity is reasonably good as shown in Fig. 7.

## 4 Conclusions

We determined the γ-ray intensities in the $^{14}N(n,\gamma)^{15}N$ reaction with 0.3-0.9 % accuracy. Since the results of the five measurements were consistent, present results were reliable.

Using this intensity, it becomes possible to determine the intensity the high energy γ-rays up to 11 MeV precisely. In the future we are planning to determine the intensities up to 7 MeV in the $^{35}Cl(n,\gamma)^{36}Cl$ reaction for the secondly standard.

## References

[1] T. J. Kennett *et al.*, Nucl. Instrum. Meth. **A 249**, 366 (1986).

[2] E. T. Journey *et al.*, Phys. Rev. **C56**, 118 (1997).

[3] S. Raman *et al.* , Nucl. Instrum. Meth.**A 454**, 389 (2000).

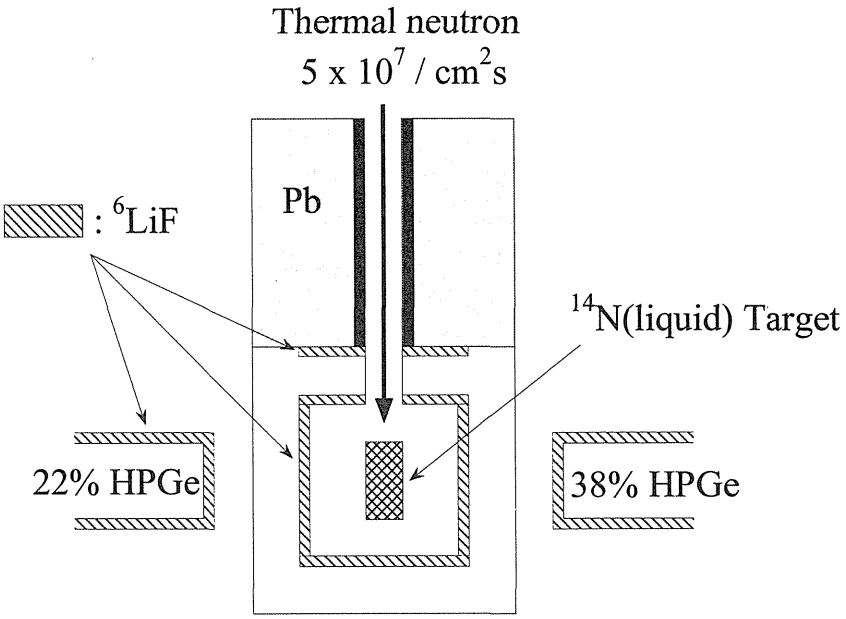



Fig. 1 Schematic view of the liquid nitrogen target system. The HPGe detectors and the target are surrounded by $^{6}$LiF. It makes for the purpose of the shield from scattered neutrons, and reduces background of prompt γ-rays from the structure materials.

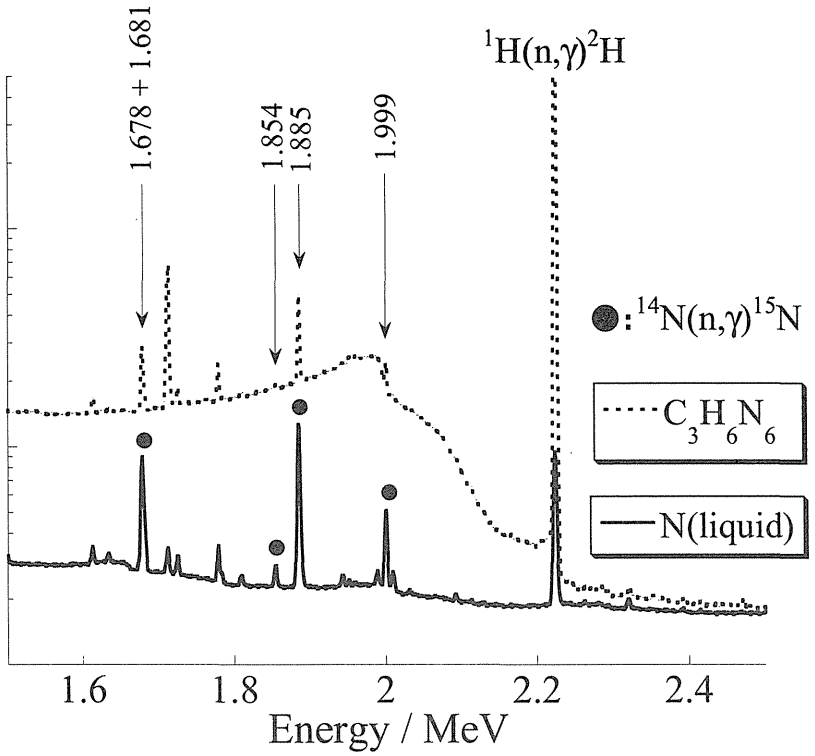



Fig. 2 The γ-ray spectra in the $^{14}$N(n,γ)$^{15}$N reaction using the melamine and the liquid nitrogen target. The melamine ($C_3H_6N_6$) target emits 2.2 MeV γ-ray strongly via $^{1}$H(n,γ) reaction. It is clearly seen that the liquid nitrogen target can reduce background.

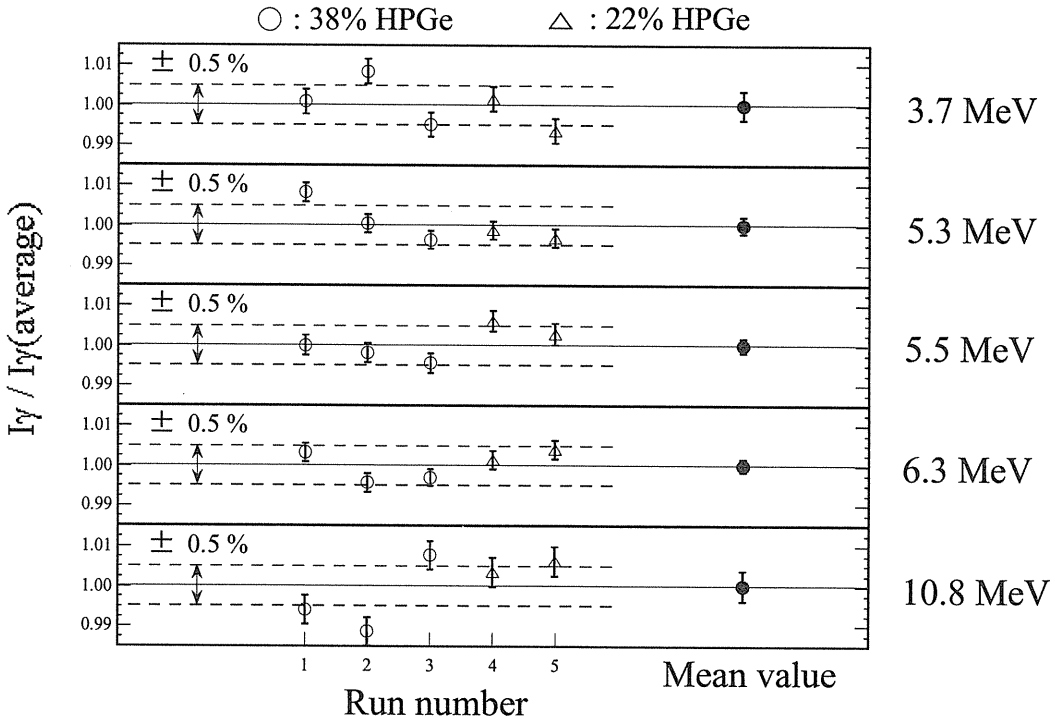



Fig.3 Scattering of intensities in the primary γ-rays. The various intensities of the five measurements differed from each other by < 0.5%.

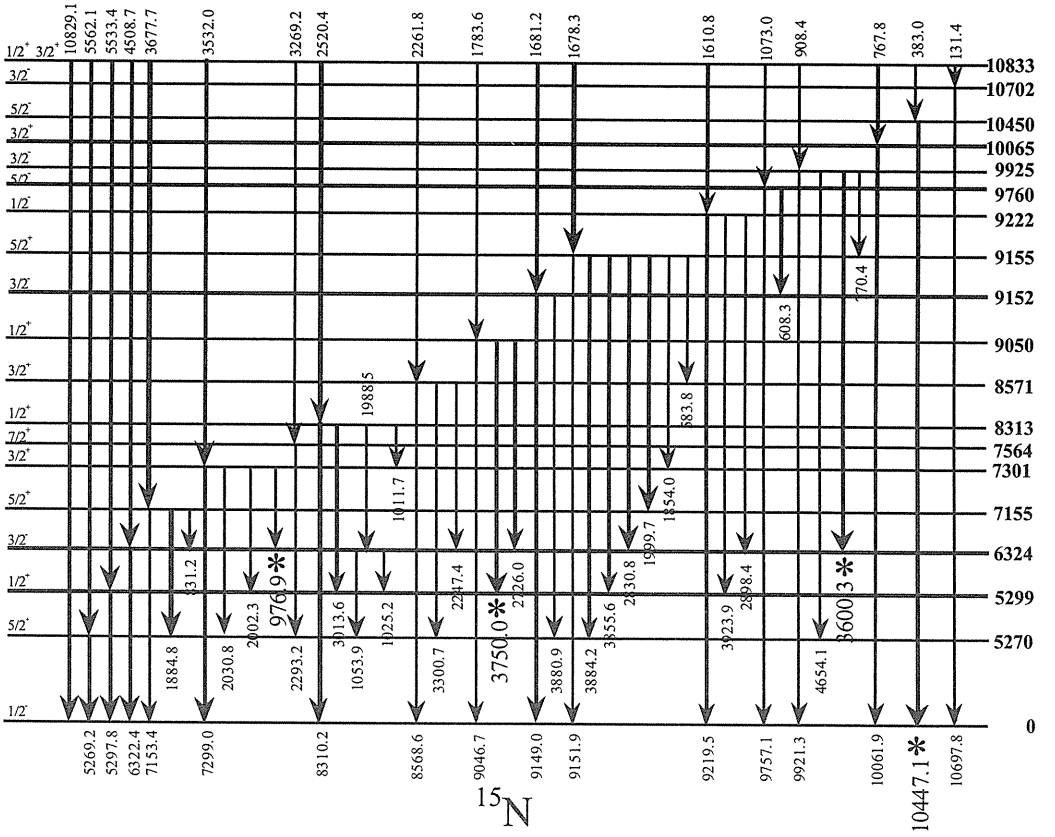



Fig.4 The latest level scheme of $^{15}$N. Asterisks indicate newly observed γ-rays.

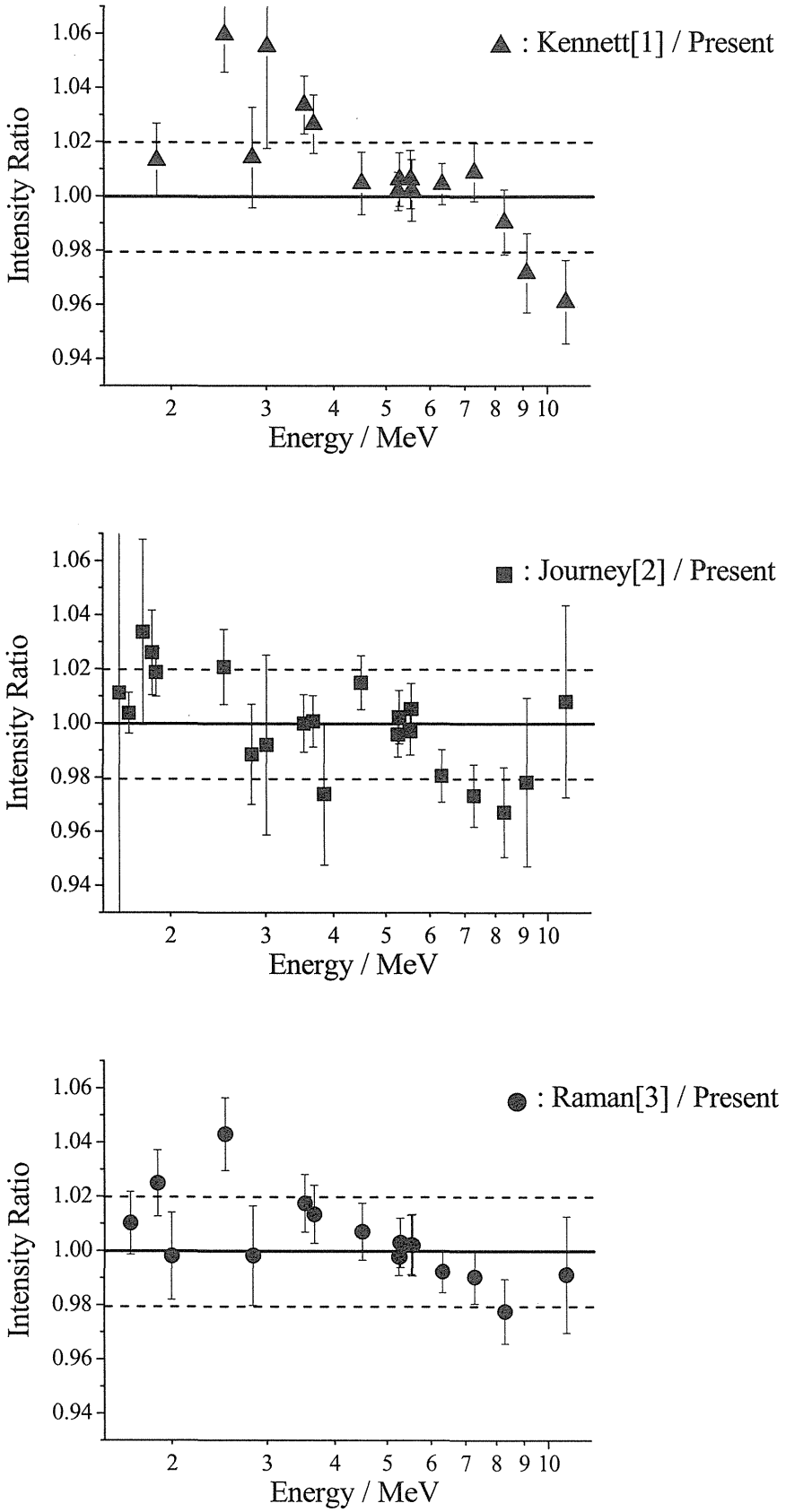



Fig. 5 Comparison of the previous intensities and the present ones.

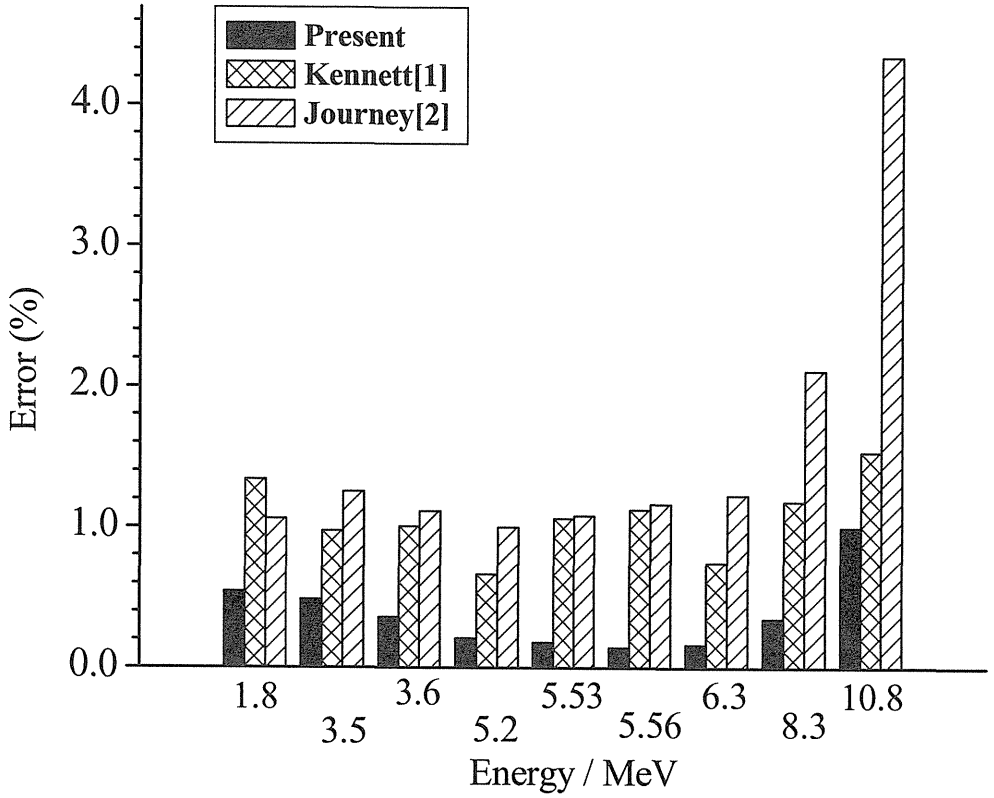



Fig. 6 Comparison of the previous errors and the present ones.

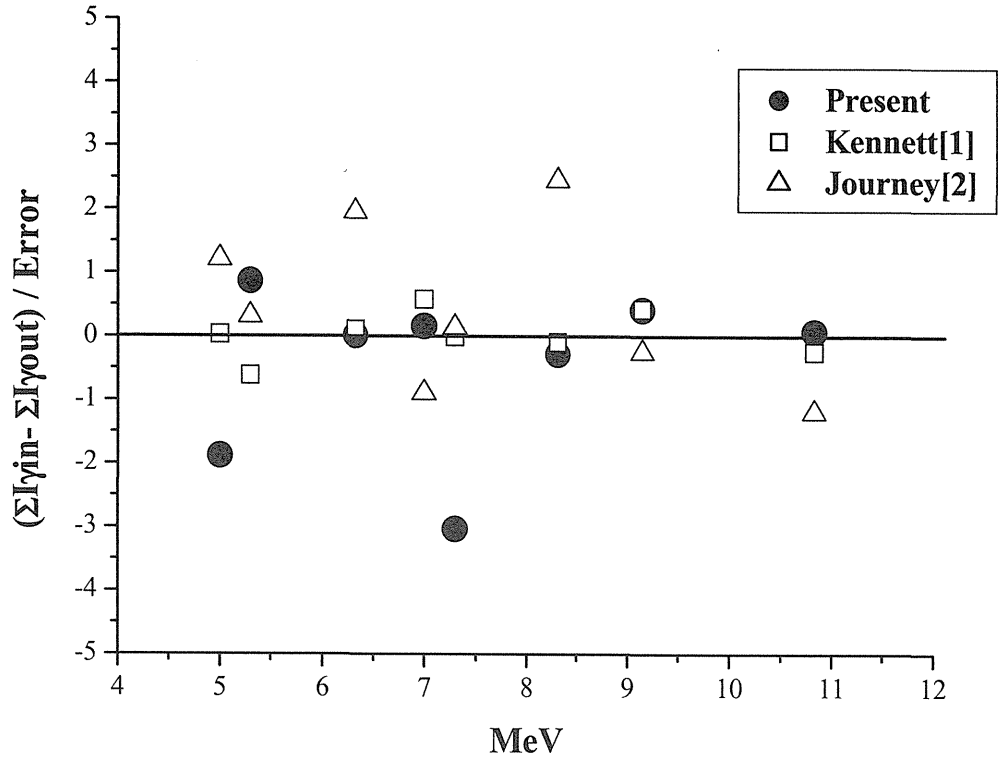



Fig. 7 Intensity balance of input and output contributors to $^{15}N$ levels.

JP0550277



# 3.17 Integer Ratios in Resonance Energies of the Compound Nucleus based on Time Coherency at Resonances

Makio OHKUBO
N.Resonance Lab, 1663-39,Senba-cyo, Mito-shi, Ibaraki-ken 310-0851 Japan

## Abstract

For an isolated neutron resonance, time coherency is required by S-matrix theory between incident wave and the response function of the compound nucleus. Dynamical behaviors of the compound nucleus, assumed to be decomposed into many normal modes, must fulfil the time boundary condition determined by the period of the de Broglie frequency of the incident neutron wave. The energies of these normal modes are restricted to be commensurable (integer ratios) with each other. Integer rations among $E_x$, $E_n^*$ and $S_n(= E_x - E_n^*)$ are deduced from these relations. Among resonance energies of the same nucleus, integer ratios are expected. $E_x/S_n$ = 4/3 or 5/3 are tabulated for resonances of light nuclei. Neutron resonance reaction mechanism is discussed.

## 1. Introduction

More than half century, neutron cross sections and resonance parameters are widely measured and compiled/evaluated for many nuclei, under the requirements of reactor engineering. We have much information about energy dependence of the cross sections in resonance region which are described by the R-matrix theory etc. However we have little information about physical meaning of each resonance; why this resonance is observed at this energy?, what happen on the compound nucleus?

We are long interested in the dispositions of the neutron resonance levels[1-9] in which equi-distant series of levels, dominant spacings etc are found, which contradict to the ordinary understanding as a quantum chaos in highly excited nuclei. For the non-statistical dispositions of resonances, we have previously investigated "Recurrence Model" of the CN [10], where time dependent properties of CN are explicitely discussed.

The model, time periodic breathing of CN coherent with the de Bloglie frequency of incident neutron wave, has been improved continuously, and a new view points for neutron resonance reaction mechanism are reported in ND2001 and SND2000-2003[11-13]. This report is a continuation. On the resonances of $^{16}O + n$ up to $E_x \leq 10MeV$, integer ratios among $E_x$, $E_n^*$ and statistical test are described in previous report. In this article, are described integer ratios among $E_x^A$ / $E_x^B$ or $E_n^A$ / $E_n^B$ for arbitrary resonances A and B of the same nuclei which come from integer ratios among $E_x$, $S_n$ and $E_n$ for each resonance. Integer ratios are tabulated in $^3He + n$, $^{6,7}Li + n$, $^{8,9}Be + n$, $^{10,11}B + n$, $^{12}C + n$, and $^{16,18}O + n$. Resonance reaction mechanism is discussed.

## 2. Time Behaviors of the Compound Nucleus

Time periodic behaviors of CN coherent with the incident wave at resonances are described previously[11]. For ease to further descriptions, basic relations are repeated briefly.

An S-matrix $S(E)$ is defined for the neutron-nucleus reaction from which cross section $\sigma_s(E) = (\pi/k^2)(2l+1) \mid 1 - S(E) \mid^2$, etc. is determined. A relation between $S(E)$ and the response function is discussed after Sitenko [14]. For an s-wave resonance, the incident wave $\psi^-(r,t)$ and outgoing wave $\psi^+(r,t)$ around the interaction region of radius $R$ are,

$$\psi^-(r,t) = \int_0^\infty dE' a(E')(1/r) exp(-ik'r - (i/\hbar)E't), \quad \text{..... (1)}$$

$$\psi^+(r,t) = \int_0^\infty dE' a(E') S(E')(1/r) exp(ik'r - (i/\hbar)E't). \quad \text{..... (2)}$$

The response function $F(\tau)$ is defined by the causality principle, as,

$$\psi^+(r,t) = \int_0^\infty d\tau F(\tau)\psi^-(r, t-\tau). \quad \text{..... (3)}$$

Mulitping Eqs.(1),(2),(3) by $exp(-iEt/\hbar)$ and integrating over t from -$\infty$ to $\infty$, $S(E)$ can be expressed

as a Fourier transform of the response function $F(\tau)$,

$$S(E)e^{2ikR} = \int_0^\infty d\tau F(\tau) e^{i\frac{E\tau}{\hbar}}, \qquad \text{..... (4)}$$

where $\tau$ is the time for the response to come back.

Eq.(4) is a basic relation on which the following discussions stand. In the continuum region, $S(E)$ has no peak, and $F(\tau)$ is expected to be a non-periodic or stochastic function of infinitely long time period. In contrast for an isolated resonance at $E_0$, $S(E)$ has a peak at $E_0$ (recoil corrected), then $F(\tau)$ must be a periodic function with a period $\tau_{rec} = 2\pi\hbar/E_0$. That is, the scattered wave $\psi^+(r,t)$ is significant if $F(\tau)$ and the incident wave $\psi^-(r,t)$ are time-coherent with each other, during life time $\sim h/\Gamma$, where $\Gamma$ is the total width of the resonance. If not, only potential scattering remains.

The response function $F(\tau)$ can be expressed by a Fourier series with higher harmonics of periods $\tau_j = \tau_{rec}/k_j$ and frequencies $\omega_j = 2\pi/\tau_j$, where $k_j$ are integers, $(j = 1, 2, ..M)$. Frequency ratios as well as time periods of these harmonics are commensurable( forming integer ratios )with each other. A unit time $\tau_0$ exist, and $\tau_j$ is written as $n_j\tau_0$, where $n_j$ is an integer. The recurrence time $\tau_{rec}$ is the least common multiple(LCM) for the ensemble $(n_j; j = 1, 2, ..., M)$ multiplied by $\tau_0$. The frequency component $\omega_j$ is propotional to the inverse integers $\omega_j = (2\pi/\tau_0)/n_j$.
The responce function $F(\tau)$ is considered to be under the influence of excitation of the compound nucleus, which is decomposed into normal modes. Total excitation energy is,

$$E_x = \hbar(\omega_1 + \omega_2 + .. + \omega_M) = \frac{2\pi\hbar}{\tau_0}\sum_{j=1}^{M}\frac{1}{n_j} = G\sum_{j=1}^{M}\frac{1}{n_j} \qquad (n_j : \text{integer}). \qquad \text{..... (5)}$$

where $G = 2\pi\hbar/\tau_0$. (For multiple excitation, the numerators 1 in (5) will be changed by small integers $a_j$.) It is considered that in Eq.(4), higher harmonics of incident wave of energy $lE_0, (l : small\ integer)$ satisfy the coherent condition without change of $F(\tau)$. It is easy to see that $E_x\ /E_0$ is in an integer ratio,

$$\frac{E_x}{E_0} = \frac{1}{l}LCM(n_1, n_2, .., n_M)\sum_{j=1}^{M}\frac{1}{n_j} \qquad (l : small\ integer) \qquad \text{..... (6)}$$

Therefore, integer ratios exist among $E_x$, $E_0$ and $S_n(= E_x - E_0)$. New parameters are defined as $X = E_x/E_0$, and $E_x/S_n = X/(X-1)$. For the resonances of many light nuclei in several hundred keV region or MeV region, the ratios will be between small integers. Inversely, for the resonances in eV region of medium and heavy nuclei, the ratios will increase to $\sim 10^{5\sim8}$ because of large $M$ and large $LCM(n_1, n_2, .., n_M)$.

For the resonances of several light target nuclei from $^3He$ to $^{18}O$, integer ratios $m/n$ are searched by equating $E_x/S_n = (m/n)(1+\Delta)$, where $|\ \Delta\ | \leq 0.01$. The $E_x$ data are from [15], where some of $E_x$ are from charge particle reactions. As shown in Fig.1, $m/n$ are marked at lattice points of $(n, m)$ plane with symbols of nuclei inserted in the figure. It is interesting that seven nuclei out of ten, there are excitations at (4,3) or (5,3) points. That is ; $^3He$, $^6Li$, $^{11}B$, $^{18}O$ commonly placed at (4,3), and $^8Be$, $^{11}B$, $^{12}C$, $^{16}O$ at (5,3). Especially $^{11}B$ placed at (4,3), (5,3), (7,3), (8,3), and (11,3). Simple integer ratios for thses nuclei are tabulated in Appendix.

There will be a question that these integer ratios are from time coherency as described above, or only by statistical chance. On this problem, we have already calculated probability of appearance of integer ratios in $^{16}O + n$ resonances in $5.0MeV \leq E_x \leq 7.5MeV$ region [13]. In this region, 11 resonances out of 13 are at integer ratios $(E_x/S_n = m/n\ ;\ n \leq 13)$ with $\Delta \leq 0.0052$. Probability of appearance was calculated by the Binary distribution to be less than 0.6% if the resonances are placed at random. Therefore, we think that the time coherency is proved at least in $^{16}O + n$ resonances, parameters of which are of high resolution and high accuracy. On the other hand, for other light nuclei, resonance parameters are not so high resolution data, and the deviations from integer ratios are rather large, and cause ambiguity on the time coherency.

## 3. Integer Ratios Among Resonance Energies

As described above, $E_x$, $E_0$ ( resonance energy in center of mass system ) and consequently separation energy $S_n$ are in integer ratios;

$$E_x\ :\ S_n\ :\ E_0 = p\ :\ p-q\ :\ q \text{ (p,q : integer)..... (7)}$$

Eq.(7) is named as holizontal relation.

By eliminating $S_n$ for other resonances, we can deduce integer relation for $E_x$ or $E_0$ between

different resonances, which we named vertical relation.
For a resonance A, holizontal relation is;

$E_{xA}/E_{0A} = S_n/E_{0A} + 1 = p_A/q_A$ ( p, q ; integer). .....(8a)

Similarly, for another resonance B, holizontal relation is;

$E_{xB}/E_{0B} = S_n/E_{0B} + 1 = p_B/q_B$ ( p, q ; integer). .....(8b)

From (8a) and (8b), an integer relations (vertical relation) are derived for $E_0$ and $E_x$ as;

$$\frac{E_{0A}}{E_{0B}} = \frac{(p_B - q_B)\, q_A}{(p_A - q_A)\, q_B} \qquad \text{..... (9)}$$

$$\frac{E_{xA}}{E_{xB}} = \frac{(p_B - q_B)\, p_A}{(p_A - q_A)\, p_B} \qquad \text{..... (10)}$$

Integer ratios in $E_0$ for first nine resonances of $^{16}O + n$ [16] are shown in Table 1. Because of accumulation of errors, deviations from the integer ratios amount to 2% for the worst case.

Table 1. Integer ratios $E_{0A}/E_{0B}$ for lowest nine resonances of $^{16}O + n$

| | $E_{0B}$ / $E_{0A}$ | 1<br>408.5 | 2<br>940.8 | 3<br>1231.7 | 4<br>1553.4 | 5<br>1588.8 | 6<br>1725.2 | 7<br>1788.5 | 8<br>2236.7 | 9<br>2717.2 |
|---|---|---|---|---|---|---|---|---|---|---|
| 1 | 408.5<br>(434.3) | * | 13/30 | 1/3 | 4/15 | 13/50 | 6/25 | 7/30 | 13/70 | 3/20 |
| 2 | 940.8<br>(1000.2) | * | * | 10/13 | 8/13 | 3/5 | 36/65 | 7/13 | 3/7 | 9/26 |
| 3 | 1231.7<br>(1309.4) | * | * | * | 4/5 | 39/50 | 18/25 | 7/10 | 39/70 | 9/20 |
| 4 | 1553.4<br>(1651.4) | * | * | * | * | 39/40 | 9/10 | 7/8 | 39/56 | 9/16 |
| 5 | 1588.8<br>(1689.1) | * | * | * | * | * | 12/13 | 35/39 | 5/7 | 15/26 |
| 6 | 1725.2<br>(1834.1) | * | * | * | * | * | * | 35/36 | 65/84 | 15/24 |
| 7 | 1788.5<br>(1901.4) | * | * | * | * | * | * | * | 39/49 | 9/14 |
| 8 | 2236.7<br>(2377.9) | * | * | * | * | * | * | * | * | 21/26 |

Observed resonance energies are in parentheses.

## 4 Discussions

a)
At a resonance, total excitation energy $E_x = S_n + E_n$ is devided into $M$ normal modes, energy ratios of which are in integer ratios. Time coherency between CN and incident wave was kept during life time of the resonance. These normal modes will be fast deformations or particles in orbit with definite frequencies. Average energies of these normal modes are $E_x/M \sim 1MeV$ for medium and heavy nuclei ($M = 6 \sim 10$ ), and more higher for light nuclei. Anyway the response function $F(\tau)$ behaves like a pulse array with a pulse separation $\tau_{rec}$, like intermittent pulses. Durind the pulse, nuclear potential deformation becomes maximum so that the neutron wave penetrates easily through the nuclear surface, and the interference takes place between pass-by component and trapped component of the incident wave. This behavior is similar to a time slit which opens periodically with $\tau_{rec}$. For incident neutron of off resonance energy, the compound nucleus does not respond and stay quietly and only potential scattering cross section is observed. By varying the incident neutron energy, sets of normal modes will be excited as resonance reactions if $\tau_{rec}$ fulfils Eq.(6). Spacial distributions of the normal modes excited on the CN and the selection rules will be next problem.

b)
As to the excitation energy $E_x$, we have considered two kinds of expressions; 1) $E_x = S_n(1 + (m/n))$ $(m, n; integer)$ where $S_n$ is neutron separation energy, and 2) $E_x = G\sum_{j=1}^{M} 1/n_j$. $G$ is defined as

$G = 2\pi\hbar/\tau_0$ where $\tau_0$ is the minimum time the response come back in nucleus, and G is near the Fermi energy the maximum energy of nucleon trapped in nuclear potential. Preliminary values of these are $\tau_0 = 1.20 \times 10^{-22}$s and $G = 34.5MeV$.
There will be integer ratio between $S_n$ and $G$. However, the situation is not clear. For $^{16}O + n$ resonances in $E_x \leq 8MeV$, $G_k = k \times S_n$ $(k = 5, 6, 7, 8)$ simplify the expression 2). For the 1st resonance $E_x = S_n(1+1/10) = G_6(1/6+1/60) = G_8(1/8+1/80)$, where $G_6 = 6S_n = 24.8MeV$ and $G_8 = 8S_n = 33.1MeV$. For 2nd resonance $E_x = S_n(1 + 3/13) = G_6(1/6 + 1/26)$. For 3rd resonance, $E_x = S_n(1 + 3/10) = G_6(1/6+1/20) = G_8(1/8+3/80)$. For 4th resonance, $E_x = S_n(1+3/8) = G_6(1/6+1/16)$. Similar expressions are possible for the resonances at higher energies.

c)
Time behaviors of CN coherent with the incident wave, is essentially important to understand resonance reactions. In order to understand precise mechanism of fine structures of nucleus including $J\pi$, strengths, and level clusters in a wide energy region, a more sophisticated approach will be needed including non-linear properties of matter wave in nuclear potential. There will be an interesting field of nuclear physics in 21-century where dynamic behaviors of the many degrees of freedom are essentially important. Neutron resonances may be a clue to this problem.

# References


[1] S.Sukhoruchkin: *Proc.Conf.Nucl.Data for Reactors, Paris,1966*,Vol 1, p159, Vienna,1967 ; S.Sukhoruchkin: *Proc. Int. Conf. on Statistical Properties of Nuclei* (Plenum, New York 1972) p.215

[2] K.Ideno, M.Ohkubo: "Nonrandom distributions of neutron resonance levels" *J.Phys.Soc.Jap.* 30,620(1971);

[3] C.Coceva, F.C.Corvi, P.Giacobbe, and M.Stefanon; *Proc. Int. Conf. on Statistical Properties of Nuclei* (Plenum, New York 1972) p.447

[4] K.Ideno: "Nonstatistical behaviours of the level spacing distributions in neutron resonances" *J.Phys.Soc.Jap* 37,581(1974)

[5] F.N.Belyaev,S.P.Borovlev: "Non-statistical effects in the distribution of distances between neutron levels", *Yad.Fiz.*27.289(1978), transl.*Sov.J.Nucl.Phys.*27(2),157(1978)

[6] G.Rohr: "The dynamics of nucleon in a nucleus studied with neutron resonances"; *Low energy nuclear dynamics*,(World Scientic,1995),p130

[7] S.Sukhoruchkin: "Tuning effect in nuclear data.II" E3-2000-192,ISINN-8,Dubna 2000, "COMNRF-Combined Nuclear Reaction File", ISINN-7,E3-98-212,Dubna 1999, Shell stabilization of excitations in odd odd nuclei"ISINN-4, E3-96-336 Dubna 1996,

[8] M.Ohkubo: "Regular level structures in s-wave neutron resonances in light or magic e-e nuclei up to several hundred keV" *INDC(JPN)* -185/U ,JAERI-Conf 2000-005, p325,

[9] M.Ohkubo: "Quantum recurrence in neutron resonances and a unit time in nuclei" *INDC(JPN)* -188/U, JAERI-Conf 2001-006, p300

[10] M.Ohkubo: "Recurrence of the compound nucleus in neutron resonance reactions" *Phys.Rev.C*, 53,1325(1996)

[11] M.Ohkubo;" Non-statistical level disposition analysis in neutron resonances" *J.Nucl.Sci.Technol. Supplement 2, Proc. Int.Conf. Nuclear Data for Science and Technology,Oct.2001,Tsukuba,Japan* p508 (2002).

[12] M.Ohkubo:"Recurrence of the excited states of nuclei and time coherency of the de Broglie wave in $^{16}$O+n resonances" *INDC(JPN)*-191/U, JAERI-Conf 2003-006, p259

[13] M.Ohkubo:"Time Periodic Behaviors of the Compound Nucleus Coherent with the Incident Wave at Resonances" *INDC(JPN)*-192/U, JAERI-Conf 2004-005, p190

[14] A.G. Sitenko: *Lecture in Scattering Theory*(Pergamon, New York 1971)

[15] *Landolt-Börnstein New Series Vol 16/B*, "Neutron Resonance Parameters", Springer(1998)
*Landolt-Börnstein New Series Vol 16/C*, "Neutron Resonance Parameters", Springer(2004)

[16] R.O.Sayer,L.C.Leal,L.M.Larson,R.R.Spencer,and R.Q.Wright: "R-Matrix Evaluation of $^{16}$O Neutron Cross Sections up to 6.3 MeV" *J.Nucl.Sci.Technol. Supplement 2, Proc. Int.Conf. ND2001* p88, (2002).

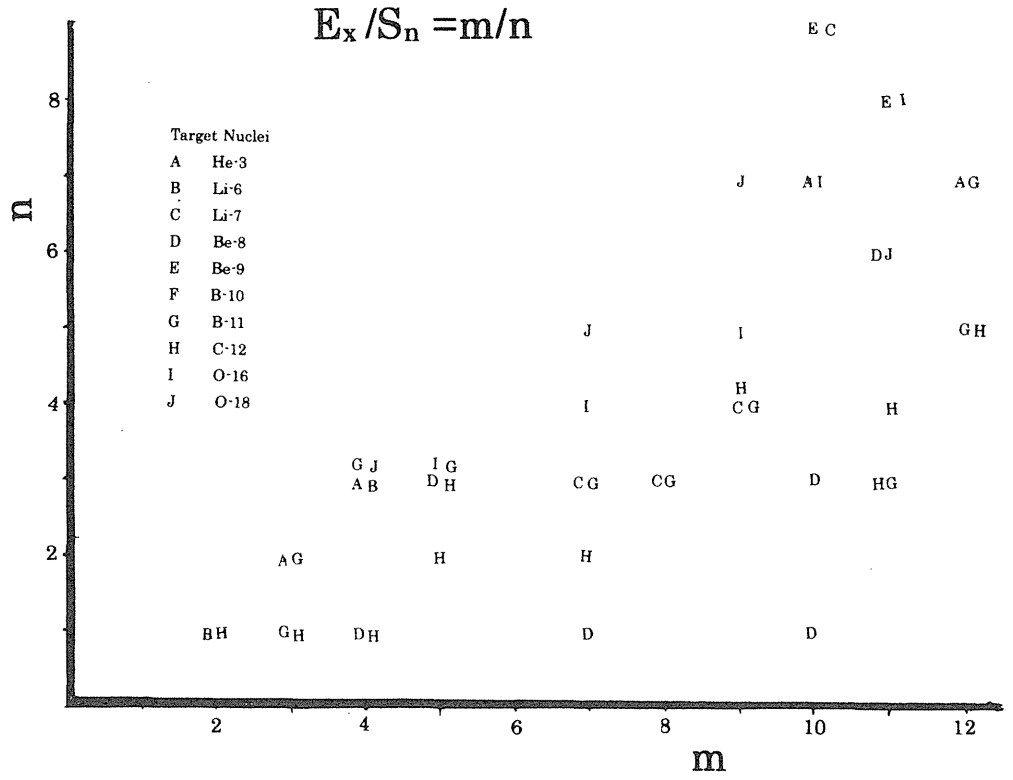



**Fig.1 Distribution of Integer ratios $E_x/S_n$ = m/n in (m,n) plane for light nuclei. Excitations at $E_x/S_n$ = 4/3 appear commonly in $^3He$, $^6Li$, $^{11}B$ and $^{18}O$, and $E_x/S_n$ =5/3 in $^8Be$, $^{11}B$, $^{12}C$ and $^{16}O$ target nuclei.**

## Appendix

**Table 1. Resonances with $E_x/S_n$ =4/3 or 5/3**

| j | Target Nuclei | $E_x$ (keV) | $S_n$ (keV) | $E_x/S_n$ | $1+\Delta$ |
|---|---|---|---|---|---|
| 1 | $^3He$ | 27500 | 20577 | 4/3 | 1.0023 |
| 2 | $^6Li$ | 9670 | 7250 | 4/3 | 1.0003 |
| 3 | $^{11}B$ | 4518 | 3370 | 4/3 | 1.0053 |
| 4 | $^{18}O$ | 5300 | 3955 | 4/3 | 1.0049 |
| 5 | $^8Be$ | 2780 | 1665 | 5/3 | 1.0015 |
| 6 | $^{12}C$ | 8200 | 4946 | 5/3 | 0.9947 |
| 5 | $^{11}B$ | 5612 | 3370 | 5/3 | 0.9992 |
| 6 | $^{16}O$ | 6860 | 4143 | 5/3 | 0.9935 |

JP0550278



# 3.18 NEUTRON EXPERIMENT FOR THE Re/Os COSMOCHRONOMETER

M.SEGAWA[1†], T.MASAKI[1], Y.TEMMA[1], Y.NAGAI[1], T.SHIMA[1],
H.MAKII[1], K.MISHIMA[1*], H.UEDA[1],
M.IGASHIRA[2], T.OHSAKI[2],
T.SHIZUMA[3] AND T.HAYAKAWA[3]

[1] *Research Center for Nuclear Physics, Osaka University,*
*10-1 Mihogaoka, Ibaraki, Osaka 567-0047, Japan*

[2] *Research Laboratory for Nuclear Reactors, Tokyo Institute of Technology,*
*O-okayama, Meguro, Tokyo 152-8550, Japan*

[3] *Japan Atomic Energy Research Institute,*
*2-4 Shirakatashirane, Toukaimura, Ibaraki 319-1195, Japan*

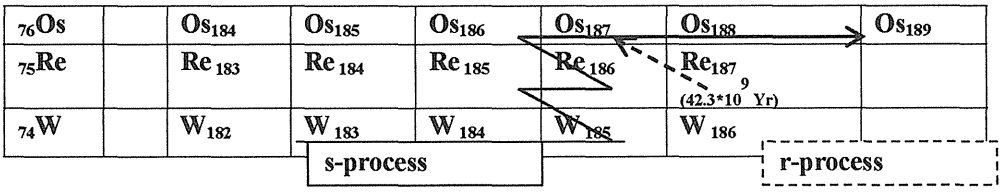
We should clarify several problems for the Re-Os pair to be used as one of the good cosmochronometers. First, since $^{187}$Os is formed and depleted by sequential neutron capture in stars, the effects should be corrected. Second, $^{187}$Os is depleted by the neutron capture process through the excited state at 10keV. It is very important to find a proper way to correct for the s-process contribution in deducing the age of the Galaxy. In order to correct for the effect mentioned above and to determine the age of the universe, we are planning to measure the neutron capture cross section of the first excited state ($E_{excited}$ = 10 keV) of $^{187}$Os, which is one of the key parameters in deducing the age of the Galaxy using the Re-Os cosmochronometer. In order to deduce the cross section we are preparing various detectors using a newly developed experimental method. In the present paper I briefly describe our experimental methods to accurately determine the neutron caprute cross section of the first excited state of $^{187}$Os.

## 1. Introduction

It has been an interesting subject to determine the age of the universe. Among three different methods to determine the age using the Hubble constant, the age of stars in globular clusters and long-lived radioactive species, the last method based on a nuclear approach is unique in a sence that the method relys on a physics observable which can trace the history of galaxies. Since one can deduce the age of the Galaxy accurately if one can construct proper models for the slow(s) and rapid(r) process nucleosynthesis in stars. Hence, the age of the universe can be obtained by adding the time interval between the Big-Bang and the start of the Galatic first generation star formation. If one could find an old star, the age of the old star can be estimated by measuring a decay rate of the abundance of a long-lived nucleus in the star during a certain period. If the old star would be one of the oldest stars in the galaxy, the life would give the lower limit of the life of our galaxy [1]. It has been considered that $^{187}$Re-$^{187}$Os pair can be one of the good cosmochronometers, since $^{187}$Re is produced by only r-process, the half life of $^{187}$Re is quite long 42.3±1.3Gyr [2] and $^{186}$Os is the s-only isotope. Therefore one should keep in mind that $^{187}$Os is produced not only by the decay of $^{187}$Re but also by slow neutron capture process by

† segawa@rcnp.osaka-u.ac.jp
* present address :Institute of Physical and Chemical Research

$^{186}$Os. Hence, principally if we know the production rate of $^{187}$Os by the s-process neutron capture of $^{186}$Os and the loss rate of $^{187}$Os, we could obtain the amount of the decay product of $^{187}$Re using the well known relation, $\sigma(^{186}\mathrm{Os})N(^{186}\mathrm{Os})=\sigma(^{187}\mathrm{Os})N(^{187}\mathrm{Os})$. Here, $\sigma(^{A}\mathrm{Os})$ and $N(^{A}\mathrm{Os})$ stand for the neutron capture cross section and the observed abundance of Os with mass number A, respectively. Consequently, we could deduce the age of the Galaxy. However, there is a problem originating from the excited state at 10 keV in $^{187}$Os (Fig. 1). The 10 keV state could be significantly populated at the stellar temperature of kT≈ 30 keV, and therefore $^{187}$Os is depleted by the neutron capture process through the excited state. Hence it is very important to find a proper way to correct for the the loss rate of $^{187}$Os through the excited state in deducing the age of the Galaxy [3,4,5,6]. In order to correct for the effect mentioned above and to determine the age of the universe we are planning to measure both the neutron capture cross sections and neutron inelastic cross sections of $^{186}$Os, $^{187}$Os and $^{189}$Os using a newly developed experimental method as described below.



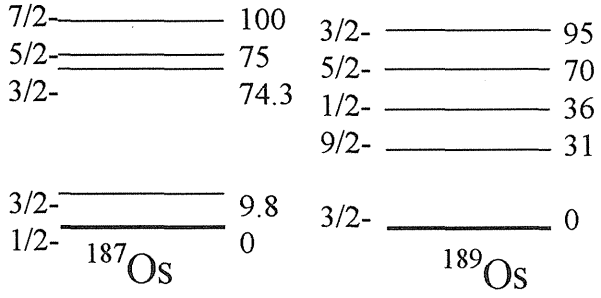




Fig.1 Partial level scheme of $^{187}$Os and $^{189}$Os

## 2. Experimental Procedure

The experiment has been carried out using keV neutrons produced by the $^{7}$Li(p,n) reaction. The proton beam was provided from the Pelletron accelerator of the Research Laboratory for Nuclear Reactors at Tokyo Institute of Technology. Pulsed neutrons from 5.5 to 90 keV were bombarded on three enriched samples of $^{186}$Os, $^{187}$Os and $^{189}$Os and $^{197}$Au and a blank position to measure the neutron capture cross section of these Os isotopes. Here gold sample was used for normalization of the absolute capture cross section, since the neutron capture cross section of gold is well known with an uncertainty of less than 3%. For the measurement of the $^{189}$Os(n,n')$^{189}$Os reaction cross section the incident neutron energy should be adjusted not to exceed the energy of the second state at 74.3keV, since $^{189}$Os has the second excited state at 74.3 keV. The neutron capture cross section of Os isotopes was measured using an anti-Compton NaI(Tl) spectrometers by detecting prompt gamma rays feeding from a neutron capture state of Os to low lying states (Fig.2). Each spectrometer consists of a central NaI(Tl) detector with a diameter of 9 inches and a length of 8 inches and an annular NaI(Tl) detector with a diameter of 13 inches and a length of 11 inches. Each spectrometer was placed at 125° with respect to the proton beam direction, and therefore a gamma ray yield detected at this angle gives an angle integrated cross section. We are now developing a detection system to measure a neutron inelastic scattering cross section of $^{189}$Os by means of four Li-glass detectors with a diameter of 50 mm and a thickness of 10 mm. Neutron energy scattered elastically and/or inelastically by $^{189}$Os is determined by employing a TOF method. The discrimination between scattered neuron by $^{189}$Os and gamma ray background can be made by their pulse heights. In order to obtain the inelastic scattering cross section of $^{189}$Os accurately, it is crucial to prevent direct neutrons from the $^{7}$Li(p,n)$^{7}$Be reaction entering into the Li-glass detector. Hence the detectors are enveloped carefully by borated paraffin blocks, Cd and Boron to attenuate neutrons. In order to find proper arrangement of these shield materials of borated polyethylene, cadmium and Boron, an extensive calculation has been made using a Monte Carlo Code, TIME-MULTI [7]. In addition, through many R&D works we have finally succeeded to construct a high sensitive measuring system of the inelastic scattering cross section of a nucleus. Using the new system we are aiming at measuring the $^{189}$Os(n,n')$^{189}$Os cross section within an uncertainty less than 15%.

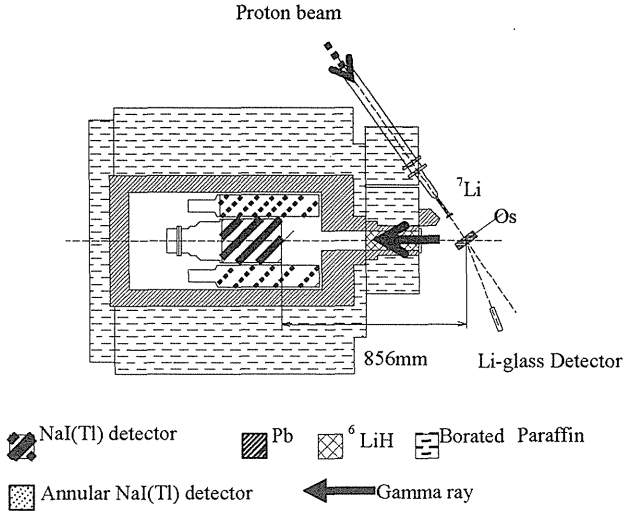



Fig.2 Schematic view of the experimental set up

## 3. Conclusion

We have for the firtst time succeeded to detect discrete gamma ray from the neutron capture reaction of $^{186}$Os, $^{187}$Os and $^{189}$Os at a stellar energy by detection a prompt discrete gamma ray from these reactions (Fig. 3). Data anaylsis to determine the neutron capture cross section of these Os isotopes is in progress. It should be added that we have also observed for the first time a bump at around 5 MeV in the gamma ray spectrum, which could be discussed in terms of a Pigny Resonance. Concerning neutron inelastic cross sections we have installed successfully a high sesitive measuring system of neutron inelastic cross sections of $^{187}$Os and $^{189}$Os. Using a newly developed method, we hope that we could determine the age of the universe within an uncertainty of one billion year.

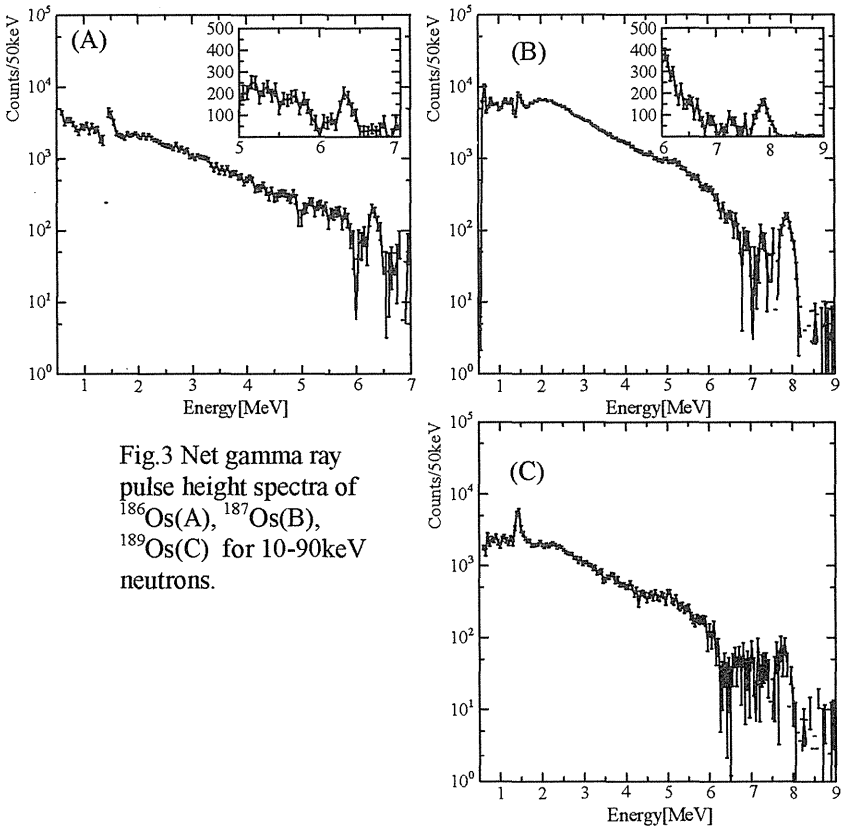



Fig.3 Net gamma ray pulse height spectra of $^{186}$Os(A), $^{187}$Os(B), $^{189}$Os(C) for 10-90keV neutrons.

## References

1. D. D. Clayton, *Astrophys. J.* **139**, 637 (1964).
2. M. Linder et al., *Geochim. Cosmochim. Acta.* **53**, 1597 (1989).
3. R. R. Winters, *Astron. Astrophys.* **171**, 9 (1987).
4. J. C. Brown, *Phys. Rev.* **C23**, 1434 (1981).
5. M. J. Harris, *Astrophy. Space. Sci.* **77**, 357 (1981).
6. S. E. Woosley, *Astrophys. J.* **233**, 411 ($^{197}$9).
7. K. Senoo, Y. Nagai, T. Shima, T. Ohsaki, and M. Igashira, *Nucl. Instr. Meth.* **A339** (1994) 556.

JP0550279

JAERI－Conf 2005－003

# 3.19 The measurement of neutron capture cross section of $^{62}$Ni and nucleosynthesis of heavy elements

Y.Temma, A.Tomyo*, M.Segawa, H.Makii, T.Shima and Y.Nagai
T.Ohsaki[1] and M.Igashira[1]
Research Center for Nuclear Physics, Osaka Univ.,
[1]Research Laboratory for Nuclear Reactors, Tokyo Institute of Technology,
e-mail: temma@rcnp.osaka-u.ac.jp

Abstract

We measured the keV neutron capture cross section of $^{62}$Ni in the energy range from 5.5 to 90 keV by using an anti-Compton NaI(Tl) spectrometer. The Maxwellian averaged cross section (MACS) is derived to be 37.2 ± 3.2 mb. This is 3.0 times larger than the value used in the calculation of s-process nucleosynthesis in massive stars.

## 1. Introduction

The overproduction of Ni isotopes has been a long standing problem in the calculations of s-process nucleosynthesis in massive stars [1], and the problem still remains in the recent nucleosynthesis calculation from the onset of central hydrogen burning through explosion as Type II supernovae [2]. Among the Ni isotopes, $^{62}$Ni has the largest overproduction factor. The origin of this problem is claimed to be due to nuclear physics inputs such as MACS of the Ni isotopes [2]. The MACS of $^{62}$Ni used in the calculation is 12.5 ± 4 mb at 30 keV [3], which is obtained by considering the interference effect of a narrow subthreshold resonance at $E_R$=-0.077 keV with the direct s-wave capture process. Theoretically, the neutron cross section of $^{62}$Ni has been calculated by taking into account not only s-wave but also p-wave neutron capture process [4]. The resultant MACS is 40.3 ± 5 mb at 30 keV. Hence, we aimed at measuring the cross section of $^{62}$Ni(n,γ) $^{63}$Ni at stellar energy, and also searching for direct γ-rays due to the possible p-wave neutron capture reaction of $^{62}$Ni.

## 2. Experimental procedure

We measured the cross section of the $^{62}$Ni(n,γ)$^{63}$Ni reaction by using pulsed keV neutrons. The neutrons were produced by the $^{7}$Li(p,n)$^{7}$Be reaction using a pulsed proton beam provided from the 3.2 MV Pelletron accelerator of the Research Laboratory for Nuclear Reactors at Tokyo Institute of Technology. We cyclically changed enriched

(96.3%) $^{62}$NiO, gold (Au) and blank samples to smear out any possible changes of the measuring system. A weight of the $^{62}$Ni sample was 2.52g. Gold was used for normalization of the absolute capture cross section of $^{62}$Ni [5]. The event rates of these three runs were connected by the neutron counts detected by the efficiency calibrated $^{6}$Li –glass detector. We used an anti-Compton NaI(Tl) spectrometer to detect a prompt γ-ray from the $^{62}$Ni(n,γ)$^{63}$Ni reaction [6]. The spectrometer was set at 125.3° with respect to the proton beam direction, where the second Legendre polynomial is zero and thus γ-ray yields detected at this angle provide an angle integrated cross section of the $^{62}$Ni(n,γ)$^{63}$Ni reaction for a dipole transition. We measured a time-of-flight (TOF) spectrum to obtain background free (net) γ-ray yields from the $^{62}$Ni(n,γ)$^{63}$Ni reaction as a function of the neutron energy by a central NaI(Tl) detector of the NaI(Tl) spectrometer.

## 3. Results

The measured TOF spectrum for $^{62}$NiO is shown in Fig.1, where the sharp peak at around 610 channel is due to the γ-rays from the $^{7}$Li(p,γ)$^{8}$Be reaction at the neutron production target position. The foreground and background γ-ray spectra from the $^{62}$Ni(n,γ)$^{63}$Ni reaction were obtained by putting the gates in the proper regions on the TOF spectrum. The net spectrum for the neutron energy range from 5.5 to 90 keV is shown in Fig.2. We observed the intense 6.8 MeV discrete γ-ray feeding from the keV neutron capture state of $^{62}$Ni to the ground state ($J^{\pi}=1/2^{-}$). However, the cascade γ-rays feeding from the predicted p-wave capture state of $^{62}$Ni to the ground state in $^{63}$Ni via the excited state ($J^{\pi}=1/2^{+}$) at $E_x$=2.955 MeV [4] were not observed.

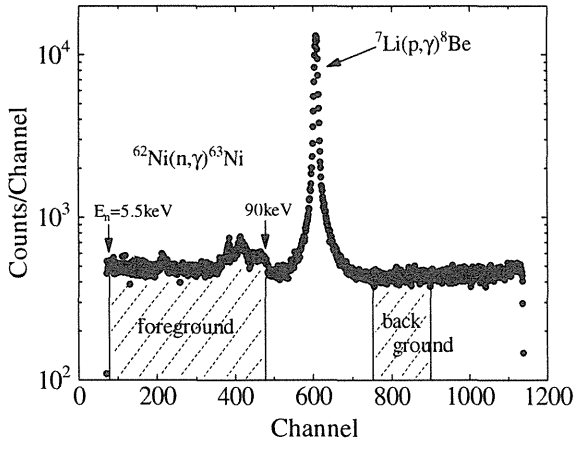



Fig.1: TOF spectrum measured by a NaI(Tl) detector for $^{62}$NiO sample.

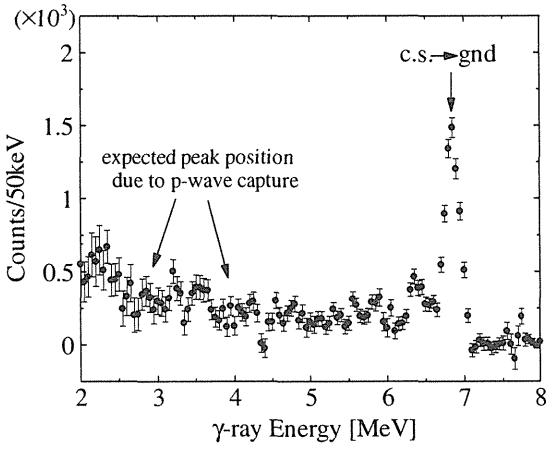



Fig.2: Background subtracted γ-ray spectrum for $^{62}$NiO sample.

We employed the pulse height weighting technique to obtain the γ-ray yield in the net spectrum [7]. Using the γ-ray yields the capture cross-section $\sigma_\gamma$(Ni) was obtained as follows.

$$\sigma_\gamma(Ni) = \frac{T_{Au}}{T_{Ni}} \frac{P_{Ni}}{P_{Au}} \frac{C_{Au}}{C_{Ni}} \cdot \frac{(r^2n)_{Au}}{(r^2n)_{Ni}} \frac{Y_\gamma(Ni)}{Y_\gamma(Au)} \cdot \sigma_\gamma(Au)$$

Here, T and P are the number of the neutron counts measured by the $^6$Li-glass detector during the measurements of the sample, and the neutron transmission of the sample, respectively, r and n are the radius and thickness (atoms/barn) of the sample, respectively, Y(Au) and σ(Au) are the γ-ray yield and the absolute capture cross section for the sample, respectively. A correction factor C was calculated using the Monte-Carlo code, TIME-MULTI [8]. The total capture cross section thus obtained is shown in Fig.3.

In order to derive the MACS we compared the present results to the evaluated cross section of the $^{62}$Ni(n,γ)$^{63}$Ni reaction, JENDL-3.3. From this comparison we multiply the cross section given by JENDL-3.3 by a factor 2 below 5.5 keV and by a factor 1.5 above 90 keV. The MACS thus obtained is shown in Fig.4. The MACS at 30 keV is derived as 37.0 ± 3.2 mb, which is larger than the value used in the s-process nucleosynthesis in massive stars by a factor of three. Since the overproduction factor of $^{62}$Ni is about three, the present MACS could significantly influence the factor and may solve the problem.

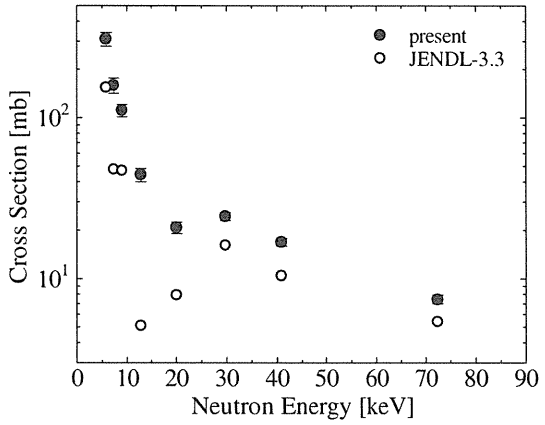



Fig.3: Neutron capture cross section of $^{62}$Ni.

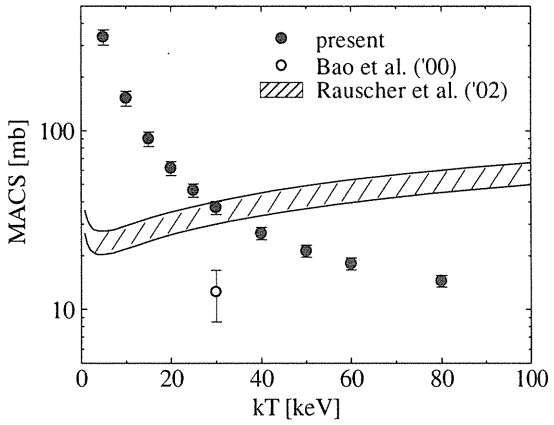



Fig.4: Maxwellian averaged cross section of $^{62}$Ni.

## 4. Summary

The neutron cross section of the $^{62}$Ni(n,γ)$^{63}$Ni reaction was measured precisely at astrophysically relevant energy. The MACS was derived as 37.0 ± 3.2 mb at 30 keV. This present value could solve the long standing problem of the overproduction of $^{62}$Ni. The predicted p-wave neutron capture process turned out to play a minor role in the present energy range. The evaluated value by JENDL played an essential role to obtain the neutron capture cross section.

*present address: Nissin Electric Co., Ltd.

References

[1] F.X.Timmes, S.E.Woosley, and T.A.Weaver, ApJS., 98, 617 (1995)

[2] T.Rauscher, A.Heger, R.D.Hoffman and S.E.Woosley, ApJ., 576, 323 (2002)

[3] Z.Y.Bao, H.Beer, F.Käppeler, F.Voss, and K.Wisshak, ADNDT, 76, 70 (2000)

[4] T.Rauscher, K.H.Guber, Phys. Rev., C66, 028802, (2002)

[5] ENDF/B-VI data file for 197Au (MAT=7925), evaluated by G. P. Young (1984)

[6] M. Igashira, K. Tanaka, and K.Masuda, in Proceedings of the 8th Int. Symp. on Capture Gamma-ray Spectroscopy and Related Topics, Fribourg, Switzerland, edited by J.Kern (World Scientific, Singapore, 1994) p.992

[7] R.L.Macklin, and J.H.Gibbons, Phys. Rev., 159, 1007, (1967)

[8] K. Senoo, Y. Nagai, T. Shima, T. Ohsaki, and M. Igashira, Nucl. Instr. Meth., A339, 556, (1994)

JP0550280



# 3.20 Percolation-fission model study of the fragment mass distribution for the 1 GeV proton induced reaction

Masahiko KATSUMA[1], Hiroshi KOBAYASHI[1], Toshinobu SASA[2] and Tetsuo SAWADA[1]

[1] *Research Laboratory for Nuclear Reactors, Tokyo Institute of Technology, Meguro-ku, Tokyo 152-8550, Japan*

[2] *Tokai Research Establishment, Japan Atomic Energy Research Institute, Tokai-mura Naka-gun, Ibaraki 319-1195, Japan*

The 1 GeV proton induced reaction on $^{208}$Pb targets is analyzed by using the percolation model combined with the Atchison fission model. The fragment mass distribution and the isotopic production cross sections obtained from our model are compared with the experimental data. The trends of the fragment mass distribution for the 1 GeV proton induced reaction can be reproduced by our calculation in some degree. The order of magnitude for the calculated isotopic production cross sections at the calculated peak positions is similar to that of the experimental peak values. The calculated peak positions of the isotopic production cross sections are shifted to the heavier region than those of the experimental data.

## 1. Introduction

Recently, in the nuclear engineering field, research activities have been launched for evaluation of yields of spallation products in target systems of accelerator driven systems (ADS) for transmutation of radioactive wastes. From the viewpoint of radiation safety, it has been necessary to estimate the amount of radiotoxicity due to rare-earth elements produced in various targets.[1)] However, we are in the lack of the experimental data for fragment mass distributions in proton induced reactions at incident energies around 1 GeV. In this situation, theoretical studies of spallation and fission in the proton induced reactions give us some helpful information about estimating of reaction products.

Conventionally, the theoretical studies of spallation and fission in the proton induced reactions have been performed by combining intranuclear cascade, evaporation and fission models.[2,3)] These studies have not perfectly accomplished yet, especially, for the reproductions of fragment mass distributions at incident energies around 1 GeV. By contrast, the percolation model works well to describe mass and energy distributions of fragments produced from multifragmentation process in pA ( $>$ 10 GeV) reactions.[4–8)] In order to study reaction products in proton induced reactions below 10 GeV, no modification to

the percolation model has been made so as to consider the possibility of spallation-fission competition in fissionable heavy nuclei.

In this paper, we apply the percolation model[4-7] to the analyses of the 1 GeV proton induced reaction on $^{208}$Pb targets,[9,10] and we make some modification to the percolation model. At the incident energy $E_{\rm inc} = 1$ GeV, we assume that fission process competes with percolation-like decay process at the stage of nuclear de-excitations. As for the fission process, we adopt the Atchison fission model[11,12] that is frequently implemented in the combined model of intranuclear cascade, evaporation and fission. The percolation model combined with the Atchison fission model will be called the percolation-fission (PF) model below. The GSI experimental data[9] of the fragment mass distribution and the isotopic production cross sections for spallation and fission products in the 1 GeV proton induced reaction will be compared with the results of the PF model.

The PF model is described in Sec. 2. The comparison between the results of the PF model calculations and the experimental data is shown in Sec. 3. The summary is in Sec. 4.

## 2. Percolation-fission model

In the PF model, target nuclei are constructed by an approximately spherical representation on a simple-cubic lattice or a hexagonal lattice.[6,7] The nucleons are taken to occupy the sites of a simple-cubic lattice or a hexagonal lattice. The site distances between two nucleons are adjusted to reproduce the root mean squared radius of target nuclei. Neighboring pairs of the sites are connected by bonds. We assume that bonds between two protons and bonds between two neutrons are initially broken in the case of a hexagonal lattice for target nuclei.

For a given impact parameter $b$, the geometry of pre-decay nuclei is schematically illustrated in Fig. 1. To construct the pre-decay nuclei, we remove nucleons on a cylindrical channel with a radius $R_{\rm E}$ from the lattice. We assume that bonds between two nucleons on a cylindrical region with a radius $R_{\rm H}$ are easily broken, because nucleons on it acquire higher energies from the incident particle shooting. The cylindrical region with the radius $R_{\rm H}$ is called the hot region.

The bond breaking probability $P_{\rm B}(b)$ of the lattice, except for the hot region, is defined as follows,

$$P_{\rm B}(b) = \frac{P_0 \int_{-\infty}^{+\infty} \rho[\boldsymbol{R}(b)] d\boldsymbol{R}}{\int_{-\infty}^{+\infty} \rho[\boldsymbol{R}(0)] d\boldsymbol{R}}. \quad (1)$$

The $P_0$ is the bond breaking probability of the central collision, $b = 0$. The $\rho(r)$ is the matter density distribution of target nuclei, which is given in a conventional Woods-Saxon form with $\rho_0 = 0.159$ fm$^{-3}$, $r_0 = 1.12$ fm, and $a_0 = 0.55$ fm for $^{208}$Pb. The bond breaking probability $P_{\rm B}(b)$ decreases as $b$ increases. The incident proton with an impact parameter

$b$ is randomly generated with Monte Carlo algorithm. The bond breaking probability $P_{\rm H}$ in the hot region of nuclei is independent of impact parameters. In our model, $R_{\rm E}$, $R_{\rm H}$, $P_0$ and $P_{\rm H}$ are the adjustable parameters in dependence on incident energies to fit the experimental data.

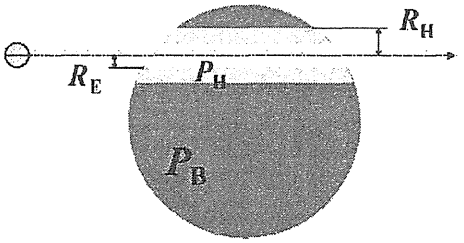



**Fig. 1** geometry of pre-decay nuclei.

In the PF model, excited nuclei after having been bombarded by an incident proton go on in the percolation-like decay process, or the fission decay process. A random number $x$ is generated, and then, the decay process is selected from the following equations,

$$\begin{array}{lll} x & > & P_{\rm fis}(E_{\rm ex}, A_{\rm i}, Z_{\rm i}) \quad \text{(Percolation-like decay)}, \\ x & \leq & P_{\rm fis}(E_{\rm ex}, A_{\rm i}, Z_{\rm i}) \quad \text{(Fission decay)}. \end{array} \tag{2}$$

Here, $P_{\rm fis}(E_{\rm ex}, A_{\rm i}, Z_{\rm i})$ is the fission probability, in dependent on an excitation energy $E_{\rm ex}$, a mass number $A_{\rm i}$, and a proton number $Z_{\rm i}$ of the pre-decay nuclei. The fission probability is given by the Atchison fission model, and it is expressed as follows,

$$P_{\rm fis}(E_{\rm ex}, A_{\rm i}, Z_{\rm i}) = \frac{C}{1 + \Gamma_{\rm n}/\Gamma_{\rm fis}}, \tag{3}$$

where $\Gamma_{\rm n}$ and $\Gamma_{\rm fis}$ are the widths for neutron emission and fission for the pre-decay nuclei. In the PF model, the $C$ is the reduction factor of the fission probability which is in inverse proportion to the number of emitted particles in percolation-like decay process, $C = (1 - E'_{\rm cm}/E_{\rm ex})/N_{\rm e}$. The $E'_{\rm cm}$ is the center-of-mass energy after decay.

When the percolation-like decay process is selected from Eq. (2), a random number $x$ is generated with Monte-Carlo algorithm. And then, whether each bond of the lattice is broken or not is decided from the following relations,

$$\begin{array}{lll} x & \leq & P_{\rm B}(b) \qquad \text{(Broken)}, \\ x & > & P_{\rm B}(b) \qquad \text{(Unbroken)}. \end{array} \tag{4}$$

It should be noted that $P_{\rm B}(b)$ is the same for each bond except for the hot region, independent of its position on the lattice. The relations in the hot region are similar to those for $P_{\rm B}(b)$,

$$\begin{array}{lll} x & \leq & P_{\rm H} \qquad \text{(Broken)}, \\ x & > & P_{\rm H} \qquad \text{(Unbroken)}. \end{array} \tag{5}$$

Note that $P_{\rm H}$ is the same for each bond in the hot region, independent of its position on the lattice and of the impact parameter. In the end of calculations for the percolation-like decay, we count the number of isolated fragments which nucleons are still connected by bonds.

When the fission decay process is selected from Eq. (2), mass and charge distributions for two fission nuclei are given from the empirical formulae in the Atchison fission model.

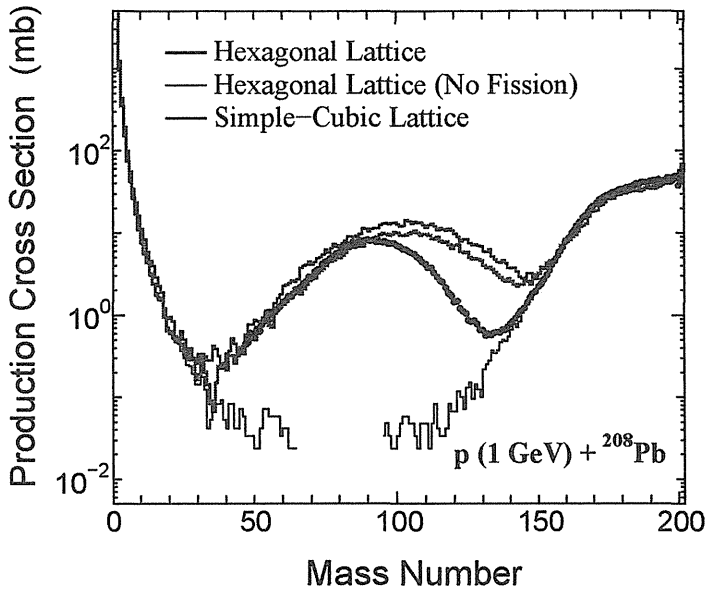



**Fig. 2** Fragment mass distribution for the 1 GeV proton induced reaction on $^{208}$Pb targets. The red and blue histograms are the results obtained from the PF model with the hexagonal lattice and the simple-cubic lattice, respectively. The black histogram is the result of the simple percolation model without the fission process. The solid circles are the experimental production cross sections, which are taken from Fig.18 of Ref. 9.

## 3. Results

Figure 2 shows the results of the fragment mass distribution for the 1 GeV proton induced reaction on $^{208}$Pb targets. The red and blue histograms are the results obtained from the PF model with the hexagonal lattice and the simple-cubic lattice, respectively. The parameter values of the PF model are listed in Table 1. In Fig. 2, one can see the small difference between the red and blue histograms. The characteristic trends in the experimental production cross section are reproduced by the red and blue histograms. However, in the mass number $90 < A < 150$ region, the production cross sections of the red and blue histograms are larger compared with that of the experimental data.

The black histogram in Fig. 2 is the result obtained from the simple percolation model with the hexagonal lattice by using the same parameters as those of the red histogram. Namely, the black histogram is the result without the Atchison fission model. In the mass number $< 30$ and $> 150$ regions, the black histogram is almost similar to the red histogram. By contrast, the production cross section in the mass number $= 40$ to 150 region is dominated by the fission process. This figure means that the fission process should be combined with the percolation model to study the 1 GeV proton induced reaction.

Figure 3 shows the isotopic production cross sections for the 1 GeV proton induced reaction on $^{208}$Pb targets as a function of neutron numbers. The calculated isotopic pro-

**Table 1** The parameters of the PF model with the simple-cubic lattice and the hexagonal lattice.

| Lattice | $P_0$ | $P_H$ | $R_E$ | $R_H$ |
|---|---|---|---|---|
| Simple-cube | 0.5 | 0.6 | 1.0 | 4.2 |
| Hexagon | 0.5 | 0.6 | 1.0 | 3.5 |

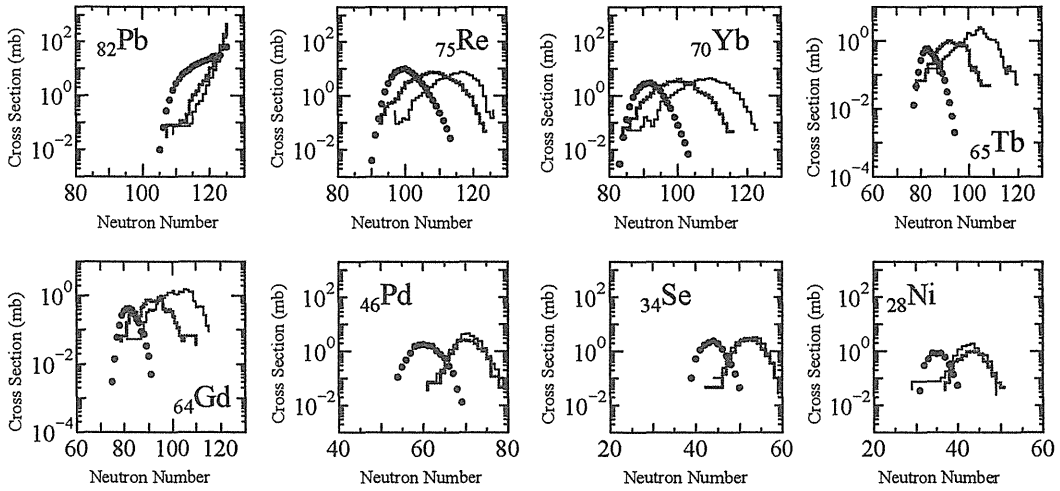



**Fig. 3** Isotopic production cross sections for the 1 GeV proton induced reaction on $^{208}$Pb targets as a function of neutron numbers. The red and blue histograms are the results obtained from the PF model with the hexagonal lattice and the simple-cubic lattice, respectively. The solid circles are the experimental isotopic production cross sections.[9)]

duction cross sections are compared with the experimental data.[9)] We select eight elements of the experimental data, $_{82}$Pb, $_{75}$Re, $_{70}$Yb, $_{65}$Tb, $_{64}$Gd, $_{46}$Pd, $_{34}$Se, and $_{28}$Ni, to see the features of the PF model. The red and blue histograms are the results obtained from the PF model with the hexagonal lattice and the simple-cubic lattice, respectively. In Fig. 3, the order of magnitude for the calculated isotopic production cross sections at the calculated peak positions is similar to that of the experimental peak values. The calculated peak positions of the isotopic production cross sections are shifted to the heavier region than those of the experimental data. For the five heavy elements in Fig. 3, the peak positions obtained from the PF model with the hexagonal lattice are better than those obtained from the simple-cubic lattice. The deviation between the hexagonal lattice and simple-cubic lattice would originate from the difference of the initial bonds. For the three light elements, the red histograms are almost similar to the blue ones.

## 4. Summary

We have applied the percolation model to the analyses of the 1 GeV proton induced reaction on $^{208}$Pb targets. In order to investigate this reaction, we have made some modification to the percolation model, which is combined with the Atchison fission model. The simple-cubic lattice and the hexagonal lattice are adopted as the nuclear lattice of $^{208}$Pb nuclei. We have compared our results obtained from the PF model with the GSI experimental data.

As shown in Fig. 2, the PF model can reproduce the trends of the fragment mass distribution for the 1 GeV proton induced reaction in some degree. In Fig. 3, the order of

magnitude for the calculated isotopic production cross sections is similar to that of the experimental data. The calculated peak positions of the isotopic production cross sections are shifted to the heavier region than those of the experimental data. As for the five heavy elements in Fig. 3, the peak positions obtained from the PF model with the hexagonal lattice are better than those obtained from the simple-cubic lattice.

The PF model should be improved further in order to make better reproductions in the near future. However, the results in this paper mean that the PF model would become a useful tool to analyze production cross sections in spallation and fission.

## Acknowledgments

We would like to express our sincere thanks to Professor A. Ohnishi and Mr. S. Yamaguchi for useful comments and giving us the numerical calculation program of the non-equilibrium percolation model. One of the authors (M.K.) thanks Professor N. Yamano for encouragement and comments. This job was funded by Ministry of Education, Culture, Sports, Science and Technology.

## References

[1] M. Saito, A. Stankovskii, V. Artisyuk, *et al.*, "Radiological hazard of spallation products in accelerator-driven system," *Nucl. Sci. Eng.*, **142**, 22 (2002).

[2] M. Lindner and A. Turkevich, "Competition between fission and neutron emission in excited heavy nuclei," *Phys. Rev.*, **119**, 1632 (1960).

[3] H.W. Bertini, "Low-energy intranuclear cascade calculation," *Phys. Rev.*, **131**, 1801 (1963).

[4] W. Bauer, "Extraction of signals of a phase transition from nuclear multifragmentation," *Phys. Rev.*, **C38**, 1297 (1988).

[5] W. Bauer, U. Post, D.R. Dean and U. Mosel, "The nuclear lattice model of proton-induced multifragmentation reactions," *Nucl. Phys.*, **A452**, 699 (1986).

[6] W. Bauer, D.R. Dean, U. Mosel and U. Post, "New approach to fragmentation reactions: The nuclear lattice model," *Phys. Lett.*, **B150**, 53 (1985).

[7] S. Yamaguchi, Master thesis, Hokkaido University (2004); S. Yamaguchi and A. Ohnishi, "Radial expansion effects on spallation IMF formation," *Prog. Theor. Phys. Suppl.*, **156**, in press (2004).

[8] Y. Hirata, A. Ohnishi, Y. Nara, *et al.*, "Sideward peak of intermediate mass fragments in high energy proton induced reactions," *Nucl. Phys.*, **A707**, 193 (2002).

[9] T. Enqvist, W. Wlazło, P. Armbruster, *et al.*, "Isotopic yields and kinetic energies of primary residues in 1 A GeV $^{208}$Pb+ p reactions," *Nucl. Phys.*, **A686**, 481 (2001).

[10] W. Wlazło, T. Enqvist, P. Armbruster, *et al.*, "Cross sections of spallation residues produced in 1A GeV $^{208}$Pb on proton reactions," *Phys. Rev. Lett.*, **84**, 5736 (2000).

[11] F. Atchison, "Spallation and fission in heavy metal nuclei under medium energy proton bombardment," *Jül-Conf-34 KFA-Jülich*, Germany, p.17 (1980); F. Atchison, "A treatment of fission for HETC," *Proceedings of a Specialists Meeting Issy-Les-Moulineaux*, France, p.199 (1994).

[12] S. Furihata, "Development of a generalized evaporation model and study of residual nuclei productions," Ph.D. thesis, Tohoku University (2003).

JP0550281



# 3.21 Measurements of Total Cross Sections of Ta and Hf at Pohang Neutron Facility

Guinyun Kim[1†], A.K.M. Moniul Haque Meaze[1], Young Seok Lee[1,2], Moo Hyun Cho[2], Heung Sik Kang[2], In Soo Ko[2], Won Namkung[2], Tae-Ik. Ro[3], Won-Chung Chung[3], Young Ae Kim[4], Kun Joong Yoo[4], and Jong Hwa Chang[4]

[1]*Department of Physics, Kyungpook National University, 1370 Sankyok-dong, Puk-ku, Daegu, 702-701, Korea*

[2]*Pohang Accelerator Laboratory, Pohang University of Science and Technology San 31 Hyoja-dong, Nam-gu, Pohang, 790 – 784, Korea*

[3]*Department of Physics, Dong-A University, Busan 604-714, Korea*

[4]*Nuclear Data Evaluation Laboratory, Korea Atomic Energy Research Institute, Daejeon 305-600, Korea*

The Pohang Neutron Facility, which consists of an electron linear accelerator, a water-cooled Ta target with a water moderator, and a time-of-flight path with an 11 m length has been operated since 2000. We report the neutron total cross-section measurements of Ta and Hf samples in the neutron energy region from 0.01 eV to 100 eV by the neutron time-of-flight method at Pohang Neutron Facility. A $^{6}$Li-ZnS(Ag) scintillator with a diameter of 12.5 cm and a thickness of 1.5 cm has been used as a neutron detector. The background level has been determined by using notch-filters of Co, Ta, and Cd sheets. In order to reduce the gamma rays from a Bremsstrahlung and that from a neutron capture, we have employed a neutron-gamma separation system based on their different pulse shape. The measured total cross-sections of Ta and Hf samples are compared with the previous ones and the evaluated data in ENDF/B-VI. The resonance parameters for Hf isotopes have been extracted from the transmission data by using the SAMMY code and compared with the previous ones.

† e-mail: gnkim@knu.ac.kr

## 1. Introduction

The Pohang Neutron Facility (PNF) was proposed in 1997 and constructed at the Pohang Accelerator Laboratory on December 1998 [1]. It consists of a 100-MeV electron linac, water-cooled Ta neutron producing target, and an 11-m-long evacuated vertical flight tube leading to the detector location. The electron linac consists of a thermionic RF-gun, an alpha magnet, four quadrupole magnets, two SLAC-type accelerating sections, a quadrupole triplet, and a beam-analyzing magnet. The overall length of the linac is about 15 m. The characteristics of PNF are described elsewhere [2].

We report the measured total cross-sections of natural Hf and Ta in the neutron energy range between 0.1 eV and 100 eV by using the neutron TOF method at the PNF. The measured results have been compared with other measurements and the evaluated data in ENDF/B-VI. The resonance parameters for Hf isotopes were determined from the fitting of transmission data by using the Multilevel R-Matrix code SAMMY [3].

## 2. Experimental Arrangement

The experimental arrangement and data acquisition system for the transmission measurements is described in elsewhere [2]. The target is located in the position where the electron beam hits its center. The target was composed of ten Ta plates with a diameter of 4.9 cm and an effective thickness of 7.4 cm. This target was set at the center of a cylindrical water moderator contained in an aluminum cylinder with a thickness of 0.5 cm, a diameter of 30 cm, and a height of 30 cm. The water level in the moderator was 3 cm above the target surface, which was decided based on a measurement of the thermal neutron flux. The neutron guide tubes were constructed by stainless steel with two different diameters, 15 cm and 20 cm, and were placed perpendicularly to the electron beam. The neutron collimation system was mainly composed of $H_3BO_3$, Pb and Fe collimators, which were symmetrically tapered from a 10-cm diameter at the beginning to a 5-cm diameter in the middle position where the sample changer was located, to an 8-cm diameter at the end of guide tube where the neutron detector was placed. There was 1.8-m-thick concrete between the target and the detector room. The sample changer consists of a disc with 4 holes; each hole is 8 cm in diameter, which matches the hole of the collimator in the neutron beam line. The sample changer is controlled remotely by the CAMAC module. The distance between centers of two opposite holes is 31 cm. The transmission samples were placed at the midpoint of the flight path and were cycled into the neutron beam by using the sample changer with four positions. The physical parameters of the samples used in the total cross-section measurements are given in Table 1. A set of notch filters of Co, In, and Cd plates with thickness of 0.5 mm, 0.2 mm, and 0.5 mm, respectively, was also used for the background measurement and the energy calibration.

**TABLE 1. Physical parameters of the samples used in the experiment.**

| Sample | Purity (%) | Size ($cm^2$) | Thickness (mm) | Weight (g) |
|---|---|---|---|---|
| Ta | 99.9 | 10×10 | 4 | 37.95 |
| Hf | 99.98 | 5×5 | 0.5 | 19.30 |

The neutron detector was located at a distance of 10.81 m from the photo-neutron target. A $^{6}$Li-ZnS(Ag) scintillator BC702 from Bicron (Newbury, Ohio) with a diameter of 127 mm and a thickness of 15.9 mm mounted on an EMI-93090 photomultiplier was used as a detector for the neutron TOF spectrum measurement.

During the measurement, the electron linac was operated with a repetition rate of 10 Hz, a pulse width of 1.5 μs and the electron energy of 60 MeV. The peak current in the beam current monitor located at the end of the second accelerator section is above 50 mA, which is the same as that in the photo-neutron target.

## 3. Data Taking and Analysis

Two different data acquisition systems were used for the neutron TOF spectra measurements: one for the NIM-based system and the other for the CAMAC-based system. The main purpose of the NIM-based system was neutron-gamma separation and the parallel accumulation of the neutron TOF spectra if necessary. The CAMAC-based system consists of a main data acquisition part and a control part of the sample changer. The 10-Hz RF trigger signal for the modulator of the electron linac was used as a start signal of the time digitizer. The details of data acquisition system are described in elsewhere[2].

The measurements were performed with two samples simultaneously. The two other positions of the sample changer were empty to collect the neutron TOF spectra without a sample (open beam). The positions of the samples were chosen in the following sequence: sample 1 – empty – sample 2 – empty. The exposition times for both sample 1 and sample 2 were 15 minutes (9000 pulses of PNF linac); for each empty position, it was 7.5 minutes. Thus, the durations for the samples were the same as those for the total open beam measurements. The interleaving sequence of free positions of the sample changer was chosen to minimize the influence of slow and/or/ small variation of the neutron beam intensity. The total data taking times for Hf and Ta were 8.5 and 21.75 hours, respectively, with the same times for the open beams.

We estimated the background level by using the resonance energies of the neutron TOF spectra of the notch-filters of Co, In and Cd. The magnitude of the background level was interpolated between

the black resonances by using the fitting function $F(I)=a+be^{-I/c}$, where $a$, $b$, and $c$ are constants and $I$ is the channel number of the time digitizer.

The neutron total cross-section is determined by measuring the transmission of neutrons through the sample. The transmission rate of neutrons at the $i$-th group energy $E_i$ is defined as the fraction of incident neutrons passing through the sample compared to that in the open beam. Thus, the neutron total cross-section is related to the neutron transmission rate $T(E_i)$ as follows:

$$\sigma(E_i)=-\frac{1}{N}\ln T(E_i), \tag{1}$$

where $N$ is the atomic density per cm$^2$ of the sample. Then, we have calculated the average total cross-sections for the same energy interval.

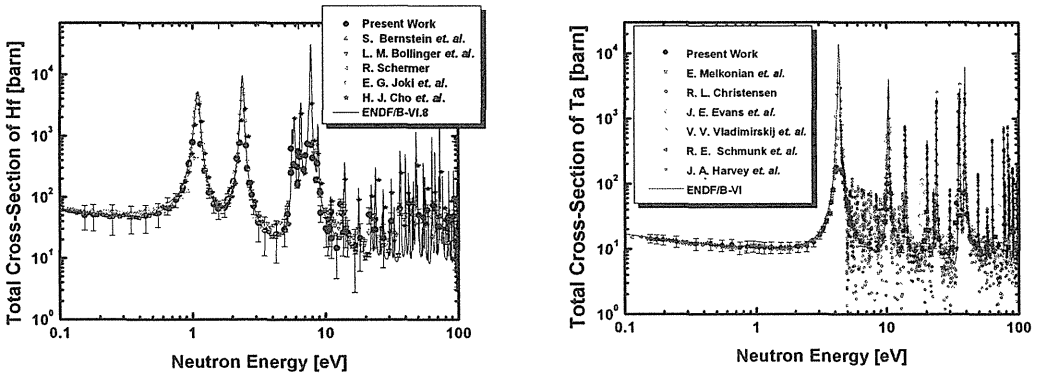



**FIGURE 1.** Comparison of the experimental total cross-sections of (a) Hf and (b) Ta with the other experiments and the evaluated one from ENDF/B-VI in the

The total cross-sections of natural Hf and Ta were obtained in the energy range from 0.1 eV to 100 eV by using the neutron TOF method as shown in **Fig. 1**. We only considered the statistical errors for the present measurements because the other sources of uncertainties, which include the detection efficiencies, the geometric factor for the sample, and the other systematic errors, are negligible.

## 4. Results and Discussion

The present measurements for the neutron total cross-sections of Hf and Ta are compared with the previous data measured by other groups [4,5] and the evaluated data in ENDF/B-VI [6]as shown in **Fig. 1**. The present measurements without any corrections are generally in good agreement with other data and the evaluated ones in the energy range between 0.1 eV and 100 eV.

There are many resonance peaks in the neutron total cross-sections for Hf and Ta. In order to get the resonance parameters of each resonance peak, we fit the transmission data with the SAMMY code [3]. Resolution function $R(E,E')$ used in this calculation is the convolution of Gaussian and exponential function. We determined the resonance parameters for Hf samples form the SAMMY fitting. In Fig. 2, the measured total cross section of natural Hf in the neutron energy range from 0.1 eV to 15 eV was compared with the SAMMY fitting results. The SAMMY prediction of total cross section and the present data are in good agreement with each other with $\chi^2$/N=0.33.

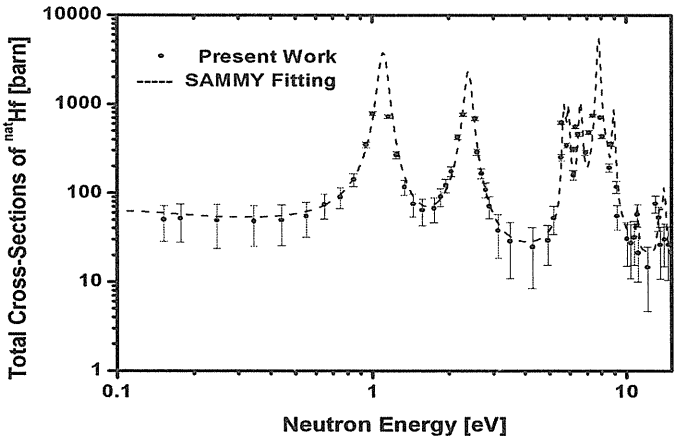



**FIGURE 2.** Comparison of the measured total cross sections of natural Hf with the predicted ones from the SAMMY fitting.

## 5. Conclusion

The Pohang Neutron Facility was constructed as a pulsed neutron facility based on an electron linac for producing nuclear data in Korea. It consists of an electron linac, a water cooled Ta target, and an 11-m long TOF path.

The neutron total cross-section of natural Hf and Ta have been measured in the neutron energy region from 0.1 eV to 100 eV by using a $^6$Li-ZnS(Ag) scintillator and the neutron TOF method at the Pohang Neutron Facility. The present results are in good agreement with the evaluated data in ENDF/B-VI and the previous measurements. The resonance parameters of Hf isotopes have been determined by fitting the transmission data with the SAMMY code.

## Acknowledgments

This work is partly supported through the Long-term Nuclear R&D program of the Korea Atomic Energy Research Institute and through the Science Research Center (SRC) program of the Institute of

High Energy Physics, Kyungpook National University. This research was also supported by Kyungpook National University Research Fund, 2004.

## References

[1] Kim G. N. *et al.*, in *Proceedings International Conference on Nuclear Data for Science and Technology*, edited by G. Reffo *et al.* (Trieste, Italy, May 19-24, 1997), p. 556.

[2] Skoy V. *et al.*, J. Korean Phys. Soc. **41**, 314 (2002); Kim G. N. *et al.*, J. Korean Phys. Soc. **43**, 479 (2003).

[3] N. M. Larson, RSICC Peripheral Shielding Routine Collection SAMMY-M2a (1999): A Code System for Multilevel R-Matrix Fits to Neutron Data Using Bayes' Equations (PSR-158, SAMMY-M2a), Oak Ridge National Laboratory.

[4] Bernstein S. *et. al.*, Phys. Rev. **87**, 487 (1952); Joki E. G. *et. al.*, J. Nucl. Sci. Eng. **11**, 298 (1961); Moore W. M., Bull. Am. Phys. Soc. **6**, 70 (1961); Schermer R., AEC reports to the NCSAG, WASH Progress Report-1031, 16 (1961); Bollinger L. M. *et. al.*, Phys. Rev. **92**, 1527 (1953); Cho H. J. *et al.*, Ann. Nucl. Energy **27**, 1259 (2000).

[5] Melkonian E. et al., Phys. Rev. **92**, 702 (1953); Christensen R. L., Phys. Rev. **92**, 1509 (1953); Harvey J. A. *et al.*, Phys. Rev. **99**, 10 (1955); Evans J. E. *et al.*, Phys. Rev. **97**, 565 (1955); Vladimirskii V. V. *et al.*, Proc. 1st Conf. on Peaceful uses Atomic Energy, Geneva, 4, pp 22 (1955); Schmunk R. E. *et al.*, Nucl. Sci. Eng., **7**, 193 (1960).

[6] Evaluated Nuclear Data, ENDF/B-VI, Brookhaven National Laboratory (2004), http://www-nds.iaea.org/point2004/.

# Appendix: Participant List

| | |
|---|---|
| ANDO Yoshihira | Toshiba Co. |
| ANDOH Masaki | JAERI |
| ARUGA Takeo | JAERI |
| ASAI Masato | JAERI |
| BABA Mamoru | Tohoku Univ. |
| CHIBA Gou | JNC |
| CHIBA Satoshi | JAERI |
| FUKAHORI Tokio | JAERI |
| Ge Zhigang | CIAE |
| Giang Thanh Hieu | INST |
| GOTO Minoru | JAERI |
| GUNJI Satoshi | JAERI |
| HAGIWARA Masayuki | Tohoku Univ. |
| HAGURA Naoto | Musashi Inst. of Tech. |
| HAMASAKI Manabu | MHI |
| HARA Kaoru-Yamasaki | JNC |
| HARADA Hideo | JNC |
| HARADA Masahide | JAERI |
| HASEGAWA Akira | JAERI |
| HONMA Akira | Musashi Inst. of Tech. |
| IBE Eishi | Hitachi Ltd. |
| ICHIHARA Akira | JAERI |
| IGASHIRA Masayuki | Tokyo Inst. of Tech. |
| ISHIKAWA Makoto | JNC |
| ITO Chikara | JNC |
| ITO Takuya | NFI |
| ITOGA Toshiro | Tohoku Univ. |
| IWAMOTO Nobuyuki | JAERI |
| IWAMOTO Osamu | JAERI |
| IWAMOTO Yosuke | JAERI |
| IWAMURA Takamichi | JAERI |
| KAI Tetsuya | JAERI |
| KASAISHI Masafumi | Nagoya Univ. |
| KATAKURA Jun-ichi | JAERI |
| KATSUMA Masahiko | Tokyo Inst. of Tech. |
| KAWADE Kiyoshi | Nagoya Univ. |
| KAWAI Masayoshi | KEK |
| KAWASAKI Hiromitsu | CRC |
| KAWASAKI Kenji | JAERI |
| Kim, Guinyun | KNU |
| KIMURA Atsushi | JAERI |
| KOJIMA Kensuke | JAERI |
| KONDO Keitaro | JAERI |
| KONNO Chikara | JAERI |
| KOSAKO Kazuaki | Shimizu co. |
| KOURA Hiroyuki | JAERI |
| KUBOTA Naoyoshi | JAERI |
| KUGO Teruhiko | JAERI |
| KUNIEDA Satoshi | Kyushu Univ. |
| Laptev, Alexander B. | JNC |
| MAKINO Takahiro | Tohoku Univ. |
| MATSUDA Norihiro | JAERI |
| MATSUFUJI Naruhiro | NIRS |
| MATSUMOTO Hideki | MHI |
| MATSUMURA Tetsuo | CRIEPI |
| MEIGO Shin-ichiro | JAERI |
| MIZUMOTO Motoharu | JAERI |
| MORI Takamasa | JAERI |
| MURATA Isao | Osaka Univ. |
| MURATA Toru | AITEL |
| NAGAI Yasuki | Osaka Univ. |
| NAGAYA Yasunobu | JAERI |
| NAITO Yoshitaka | NAIS |
| NAKAGAWA Tsuneo | JAERI |
| NAKAJIMA Hajime | JAPC |
| NAKAJIMA Ken | Kyoto Univ. |
| NAKANE Yoshihiro | JAERI |
| NAKAO Makoto | JAERI |
| Nguyen Trung Tinh | JAERI |
| NIITA Koji | RIST |
| NISHINAKA Ichiro | JAERI |
| NISHITANI Takeo | JAERI |
| NODA Hideyuki | EDC |
| NOJIRI Naoki | JAERI |
| NOMURA Yasushi | JAERI |
| OCHIAI Kentaro | JAERI |
| OHKI Shigeo | JNC |
| OHSAKI Toshiro | Tokyo Inst. of Tech. |
| OHTA Masayuki | JNC |
| OISHI Takuji | Tohoku Univ. |

| | |
|---|---|
| OKAJIMA Shigeaki | JAERI |
| OKUBO Tsutomu | JAERI |
| OKUMURA Keisuke | JAERI |
| OKUNO Hiroshi | JAERI |
| OSHIMA Masumi | JAERI |
| OTSUKA Naohiko | JAERI |
| OYAMATSU Kazuhiro | Aichi Shukutoku Univ. |
| SAKANE Hitoshi | JNC |
| SAKURAI Takeshi | JAERI |
| SANAMI Toshiya | KEK |
| SASAKI Kenji | ARTECH |
| SATO Tatsuhiko | JAERI |
| SATOH Daiki | JAERI |
| SEGAWA Mariko | Osaka Univ. |
| SEKI Yasushi | JAERI |
| SHIBATA Keiichi | JAERI |
| SHIMAKAWA Satoshi | JAERI |
| SHIRAKI Takako | MHI |
| SHONO Akira | JNC |
| Soukhovitski, Efrem Sh. | JIENR |
| SUGITA Takeshi | SSL |
| Sultana, Sadia Afroze | Kyushu Univ. |
| SUYAMA Kenya | JAERI |

| | |
|---|---|
| TAHARA Yoshihisa | EDC |
| TAKAGI Hiroyuki | Hitachi Ltd. |
| TAKAMATSU Kuniyoshi | JAERI |
| TAKAMURA Atsusi | SSL |
| TAKAYAMA Hirokazu | Nagoya Univ. |
| TAKEI Hayanori | JAERI |
| TEMMA Yasuyuki | Osaka Univ. |
| TSUBOSAKA Akira | NFI |
| TSUJIMOTO Kazufumi | JAERI |
| Uddin, Md. Shuza | Tohoku Univ. |
| Vladimir, Toshinsky | Musashi Inst. of Tech. |
| WATANABE Yukinobu | Kyushu Univ. |
| Wu Haicheng | JAERI |
| YAMAMOTO Toshihiro | JAERI |
| YAMANE Tsuyoshi | JAERI |
| YAMANE Yuichi | JAERI |
| YAMANO Naoki | Tokyo Inst. of Tech. |
| YAMASHITA Kiyonobu | JNC |
| YAMAUCHI Michinori | JAERI |
| YOKAYAMA Kenji | JNC |
| YOSHIDA Tadashi | Musashi Inst. of Tech. |
| ZUKERAN Atsushi | Hitachi Ltd. |

# 国際単位系（SI）と換算表

**表1　SI基本単位および補助単位**

| 量 | 名称 | 記号 |
|---|---|---|
| 長さ | メートル | m |
| 質量 | キログラム | kg |
| 時間 | 秒 | s |
| 電流 | アンペア | A |
| 熱力学温度 | ケルビン | K |
| 物質量 | モル | mol |
| 光度 | カンデラ | cd |
| 平面角 | ラジアン | rad |
| 立体角 | ステラジアン | sr |

**表2　SIと併用される単位**

| 名称 | 記号 |
|---|---|
| 分，時，日 | min，h，d |
| 度，分，秒 | °，′，″ |
| リットル | l，L |
| トン | t |
| 電子ボルト | eV |
| 原子質量単位 | u |

1 eV=1.60218×$10^{-19}$J

1 u=1.66054×$10^{-27}$kg

**表5　SI接頭語**

| 倍数 | 接頭語 | 記号 |
|---|---|---|
| $10^{18}$ | エクサ | E |
| $10^{15}$ | ペタ | P |
| $10^{12}$ | テラ | T |
| $10^{9}$ | ギガ | G |
| $10^{6}$ | メガ | M |
| $10^{3}$ | キロ | k |
| $10^{2}$ | ヘクト | h |
| $10^{1}$ | デカ | da |
| $10^{-1}$ | デシ | d |
| $10^{-2}$ | センチ | c |
| $10^{-3}$ | ミリ | m |
| $10^{-6}$ | マイクロ | μ |
| $10^{-9}$ | ナノ | n |
| $10^{-12}$ | ピコ | p |
| $10^{-15}$ | フェムト | f |
| $10^{-18}$ | アト | a |

**表3　固有の名称をもつSI組立単位**

| 量 | 名称 | 記号 | 他のSI単位による表現 |
|---|---|---|---|
| 周波数 | ヘルツ | Hz | $s^{-1}$ |
| 力 | ニュートン | N | m·kg/$s^2$ |
| 圧力，応力 | パスカル | Pa | N/$m^2$ |
| エネルギー,仕事,熱量 | ジュール | J | N·m |
| 工率，放射束 | ワット | W | J/s |
| 電気量，電荷 | クーロン | C | A·s |
| 電位，電圧，起電力 | ボルト | V | W/A |
| 静電容量 | ファラド | F | C/V |
| 電気抵抗 | オーム | Ω | V/A |
| コンダクタンス | ジーメンス | S | A/V |
| 磁束 | ウェーバ | Wb | V·s |
| 磁束密度 | テスラ | T | Wb/$m^2$ |
| インダクタンス | ヘンリー | H | Wb/A |
| セルシウス温度 | セルシウス度 | ℃ | |
| 光束 | ルーメン | lm | cd·sr |
| 照度 | ルクス | lx | lm/$m^2$ |
| 放射能 | ベクレル | Bq | $s^{-1}$ |
| 吸収線量 | グレイ | Gy | J/kg |
| 線量等量 | シーベルト | Sv | J/kg |

**表4　SIと共に暫定的に維持される単位**

| 名称 | 記号 |
|---|---|
| オングストローム | Å |
| バーン | b |
| バール | bar |
| ガル | Gal |
| キュリー | Ci |
| レントゲン | R |
| ラド | rad |
| レム | rem |

1 Å=0.1nm=$10^{-10}$m

1 b=100fm$^2$=$10^{-28}$m$^2$

1 bar=0.1MPa=$10^5$Pa

1 Gal=1cm/s$^2$=$10^{-2}$m/s$^2$

1 Ci=3.7×$10^{10}$Bq

1 R=2.58×$10^{-4}$C/kg

1 rad=1cGy=$10^{-2}$Gy

1 rem=1cSv=$10^{-2}$Sv

（注）

1．表1－5は「国際単位系」第5版，国際度量衡局1985年刊行による。ただし，1 eVおよび1 uの値はCODATAの1986年推奨値によった。

2．表4には海里，ノット，アール，ヘクタールも含まれているが日常の単位なのでここでは省略した。

3．barは，JISでは流体の圧力を表わす場合に限り表2のカテゴリーに分類されている。

4．EC閣僚理事会指令ではbar，barnおよび「血圧の単位」mmHgを表2のカテゴリーに入れている。

## 換算表

**力**

| N(=$10^5$dyn) | kgf | lbf |
|---|---|---|
| 1 | 0.101972 | 0.224809 |
| 9.80665 | 1 | 2.20462 |
| 4.44822 | 0.453592 | 1 |

粘度　1 Pa·s(N·s/$m^2$)=10 P(ポアズ)(g/(cm·s))

動粘度　1$m^2$/s=$10^4$St(ストークス)($cm^2$/s)

**圧力**

| MPa(=10bar) | kgf/$cm^2$ | atm | mmHg(Torr) | lbf/$in^2$(psi) |
|---|---|---|---|---|
| 1 | 10.1972 | 9.86923 | 7.50062×$10^3$ | 145.038 |
| 0.0980665 | 1 | 0.967841 | 735.559 | 14.2233 |
| 0.101325 | 1.03323 | 1 | 760 | 14.6959 |
| 1.33322×$10^{-4}$ | 1.35951×$10^{-3}$ | 1.31579×$10^{-3}$ | 1 | 1.93368×$10^{-2}$ |
| 6.89476×$10^{-3}$ | 7.03070×$10^{-2}$ | 6.80460×$10^{-2}$ | 51.7149 | 1 |

**エネルギー・仕事・熱量**

| J(=$10^7$ erg) | kgf·m | kW·h | cal(計量法) | Btu | ft·lbf | eV |
|---|---|---|---|---|---|---|
| 1 | 0.101972 | 2.77778×$10^{-7}$ | 0.238889 | 9.47813×$10^{-4}$ | 0.737562 | 6.24150×$10^{18}$ |
| 9.80665 | 1 | 2.72407×$10^{-6}$ | 2.34270 | 9.29487×$10^{-3}$ | 7.23301 | 6.12082×$10^{19}$ |
| 3.6×$10^9$ | 3.67098×$10^5$ | 1 | 8.59999×$10^5$ | 3412.13 | 2.65522×$10^6$ | 2.24694×$10^{25}$ |
| 4.18605 | 0.426858 | 1.16279×$10^{-6}$ | 1 | 3.96759×$10^{-3}$ | 3.08747 | 2.61272×$10^{19}$ |
| 1055.06 | 107.586 | 2.93072×$10^{-4}$ | 252.042 | 1 | 778.172 | 6.58515×$10^{21}$ |
| 1.35582 | 0.138255 | 3.76616×$10^{-7}$ | 0.323890 | 1.28506×$10^{-3}$ | 1 | 8.46233×$10^{18}$ |
| 1.60218×$10^{-19}$ | 1.63377×$10^{-20}$ | 4.45050×$10^{-26}$ | 3.82743×$10^{-20}$ | 1.51857×$10^{-22}$ | 1.18171×$10^{-19}$ | 1 |

1 cal= 4.18605J（計量法）

= 4.184J（熱化学）

= 4.1855J（15℃）

= 4.1868J（国際蒸気表）

仕事率　1 PS(仏馬力)

= 75 kgf·m/s

= 735.499W

**放射能**

| Bq | Ci |
|---|---|
| 1 | 2.70270×$10^{-11}$ |
| 3.7×$10^{10}$ | 1 |

**吸収線量**

| Gy | rad |
|---|---|
| 1 | 100 |
| 0.01 | 1 |

**照射線量**

| C/kg | R |
|---|---|
| 1 | 3876 |
| 2.58×$10^{-4}$ | 1 |

**線量当量**

| Sv | rem |
|---|---|
| 1 | 100 |
| 0.01 | 1 |

（86年12月26日現在）

Proceedings of the 2004 Symposium on Nuclear Data, November 11-12, 2004, JAERI, Tokai, Japan

古紙配合率100%
白色度70%再生紙を使用しています